Sag effects on protection system in distributed generation grids

Mostafa Bakkar

ADVERTIMENT La consulta d'aquesta tesi queda condicionada a l'acceptació de les següents condicions d'ús: La difusió d'aquesta tesi per mitjà del repositori institucional UPCommons (http://upcommons.upc.edu/tesis) i el repositori cooperatiu TDX (http://www.tdx.cat/) ha estat autoritzada pels titulars dels drets de propietat intel·lectual **únicament per a usos privats** emmarcats en activitats d'investigació i docència. No s'autoritza la seva reproducció amb finalitats de lucre ni la seva difusió i posada a disposició des d'un lloc aliè al servei UPCommons o TDX. No s'autoritza la presentació del seu contingut en una finestra o marc aliè a UPCommons (*framing*). Aquesta reserva de drets afecta tant al resum de presentació de la tesi com als seus continguts. En la utilització o cita de parts de la tesi és obligat indicar el nom de la persona autora.

ADVERTENCIA La consulta de esta tesis queda condicionada a la aceptación de las siguientes condiciones de uso: La difusión de esta tesis por medio del repositorio institucional UPCommons (http://upcommons.upc.edu/tesis) y el repositorio cooperativo TDR (http://www.tdx.cat/?locale-attribute=es) ha sido autorizada por los titulares de los derechos de propiedad intelectual **únicamente para usos privados enmarcados** en actividades de investigación y docencia. No se autoriza su reproducción con finalidades de lucro ni su difusión y puesta a disposición desde un sitio ajeno al servicio UPCommons No se autoriza la presentación de su contenido en una ventana o marco ajeno a UPCommons (*framing*). Esta reserva de derechos afecta tanto al resumen de presentación de la tesis como a sus contenidos. En la utilización o cita de partes de la tesis es obligado indicar el nombre de la persona autora.

WARNING On having consulted this thesis you're accepting the following use conditions: Spreading this thesis by the institutional repository UPCommons (http://upcommons.upc.edu/tesis) and the cooperative repository TDX (http://www.tdx.cat/?locale- attribute=en) has been authorized by the titular of the intellectual property rights **only for private uses** placed in investigation and teaching activities. Reproduction with lucrative aims is not authorized neither its spreading nor availability from a site foreign to the UPCommons service. Introducing its content in a window or frame foreign to the UPCommons service is not authorized (framing). These rights affect to the presentation summary of the thesis as well as to its contents. In the using or citation of parts of the thesis it's obliged to indicate the name of the author.

DEPARTAMENT D'ENGINYERIA
ELÈCTRICA

UNIVERSITAT POLITÈCNICA DE
CATALUNYA

SAG EFFECTS ON PROTECTION SYSTEM IN DISTRIBUTED GENERATION GRIDS

Doctoral Thesis

Author: Mostafa Ahmed Ahmed Mahmoud Ahmed Bakkar
Directors: Santiago Bogarra, Felipe Córcoles
Electrical Engineering Department (DEE)

Thesis presented to obtain the degree of doctorate
Polytechnic University of Catalonia (UPC)
Escuela Superior de Ingenierías Industrial, Aeroespacial y Audiovisual de Terrassa (ESEIAAT)
Terrassa, December 2021

Acknowledgment

First of all, I thank *ALLAH* for helping me throughout my research and enabling me to finish my thesis.

Then, I would like to take this opportunity to thank my supervisors of this research, Prof. Santiago Bogarra and Prof. Felipe Corcoles, for their valuable guidance and generous encouragement throughout the thesis duration, without their help this thesis could not have succeeded.

Also, I am expressing my sincerest gratitude to my parents and my sister for their support during my study, and to my love *Rania* for her unconditional love and support all the time.

A special thank goes to Dr. Alejandro Rolan Blanco and Jaume Saura, for their help during the thesis work. Their help is much indeed appreciated.

Sincerely, I would like to thank my dearest friend Mr. Reda El Mansy for his great support all the time.

Finally, I would like to express my appreciation and best wishes to my college, department, staff members, and colleagues.

Abstract

On the one hand, the penetration of Distributed Generation (DG) plants (cogeneration, small hydro, wind, and photovoltaic) increases to reduce the environmental impact. On the other hand, new types of loads (electric vehicles) lead to maintaining the connection of these generators under grid faults to balance generated and consumed power. Some of these generation plants require electronic interfaces to interconnect with the utility grid, and the control of the electronic converter significantly impacts grid dynamics. DG units are sensible to voltage sags, so the protection devices must trip fast to disconnect the faulted part of the grid. The DG disconnection will not be desirable in the near future with a large penetration, so it will be necessary to lay down new requirements for these generators and their protections. These requirements should be supported by studies based on the rule that unnecessary disconnections should be avoided. Therefore, to prevent unnecessary tripping when inverter-based DGs are connected to the Medium Voltage (MV) grid, reliable and effective protection strategies need to be developed, considering the limited short-circuit current contribution of DG. The safe operation of the grid has to be guaranteed through some requirements that must be considered to connect power converters. During grid faults -e.g., during voltage sags-, the converter's control is critical to ensure power quality and incorporate the behaviour of the DG system. One of the operational changes regards the reduced fault current contribution in electronic converters (in contrast to the large fault currents in the conventional networks based on synchronous generators), leading to conflicts in the coordination of protective devices (PDs). Other conflicts can be nuisance trips, safety degradation, and changes in the reach of PDs.

Despite most of the faults that occurred in the Transmission System (TS) are unsymmetrical (i.e., 80% of the faults could be estimated as unsymmetrical), the current grid codes for the TS do not provide any information regarding the negative-sequence currents to be injected by the DGs during the unsymmetrical faults. Only the positive-sequence components (voltages and currents) are considered in such codes. It is reasonable to consider that the future distribution grid codes could be similar to those currently used in the TS (with no mention of the negative-sequence components). To overcome all these conflicts, this research analyzes the dynamic behaviour of DGs and their controls under grid faults and the interaction between them to determine if they can stay connected during such disturbance accurately. Another essential question in this research regards the need to establish grid code requirements for connecting these DGs to Distribution System (DS), similar to those defined for the TS. As the well-established control strategies for electronic converters in the literature treat in a different way the negative-sequence components, one of the contributions of this research will be to analyze the influence of these strategies on the dynamics network behaviour, as well as the suitability of future grid codes (under the assumption that they could be similar to those of the TS).

The initial goal of this study is to employ different possible control strategies for a grid-connected inverter according to the Spanish grid code and to analyze the output voltage behaviour during symmetrical and unsymmetrical voltage sags. The analytical development of the proposed strategies shows the impacts of the sag on currents, voltages, active and reactive powers.

Another goal of this research is to propose a protection strategy based on Artificial Intelligence for a radial or ring DS with high DG penetration. The protection strategy is based on three different algorithms to develop a more secure, redundant, and reliable protection system to ensure supply continuity during disturbances in ring and radial grids without compromising system stability. In order to classify, locate and distinguish between permanent or transient faults, new protection algorithms based on artificial intelligence are proposed in this research, allowing network availability improvement disconnecting only the faulted part of the system. This research introduces the innovative use of directional relay based on a communication system and Artificial Neural Network (ANN). The first algorithm, Centralize algorithm (CE), collects the data from all the PDs in the grid in the centralized controller. This algorithm detects the power flow direction and calculates the positive-sequence current of all the PDs in the grid. Significant benefits of this system are that it consolidates the entire system's security into a single device, which can facilitate system security control. However, the CE will not pinpoint the exact location of the fault if there is any loss of information due to poor communication. Therefore, the system's redundancy can be improved by cooperating with a second algorithm, the Zone algorithm (ZO). ZO algorithm is based on zone control using peer-to-peer connectivity in the same line. The faulty line in that zone may be identified by combining the two PDs data on the same line. The most relevant advantage of this algorithm is its flexibility to adapt to any grid modification or disturbance, even if they are just temporary, unlike the CE, which is fixed to the existing grid configuration. The third protection algorithm, Local algorithm (LO), has been proposed without depending on the communication between the PDs; then, the protection system can work properly in case of a total loss of communication. Each PD should be able to detect if the fault is located in the protected line or another line by using only the local information of the PD. According to the type of fault and based on local measurements at each PD of *abc* voltages and currents, different algorithms will be applied depending on the calculation of the sequence components. The main advantage of this algorithm is the separate decision of each PD, and avoiding communication problems.

In case of radial grids, both mechanical breakers and Solid State Relays (SSRs) are used to verify the protection strategies, and in the case of ring grids, mechanical breakers are used, due to the limitations in required voltage difference of SSR.

The proposed protection algorithms are compared with conventional protections (Overcurrent and Differential) protections to validate the contribution of the proposed algorithms, especially in reconfigurable smart grids.

The author publications regarding the thesis topic are listed below:

1. M. Bakkar, S. Bogarra, F. Córcoles, J. Saura and M. Moreno: “Power Control Strategies During Voltage Sags According to Spanish Grid Code,” International Conference on Renewable Energies and Power Quality (ICREPQ’18), (16), Salamanca Spain, 2018, Proceeding. (Attend o the conference and represent the paper personally).
2. A. Rolán, P. Giménez, S. Yagüe, S. Bogarra, J. Saura, M. Bakkar: “Voltage recovery influence on three-phase grid-connected inverters under voltage sags”, IET Generation, Transmission & Distribution, 2019, 13, (3), pp. 435–443.
3. M. Bakkar, S. Bogarra, A. Rolán, F. Córcoles, J. Saura: “Voltage sag influence on controlled three-phase grid-connected inverters according to the Spanish grid code,” IET generation transmission & distribution, accepted, unpublished, 2020.
4. M. Bakkar, S. Bogarra, F. Córcoles, and J. Iglesias: “Overcurrent protection based on ANNs for smart distribution networks with grid-connected VSIs”, IET Generation Transmission & Distribution, Dec. 2020, Online.
5. M. Bakkar, Ahmed Aboelhassan, M. Abdel-Geliel, and Michael Galea: “PV Systems Control Using Fuzzy Logic Controller Employing Dynamic Safety Margin under Normal and Partial Shading Conditions”, Energies, 2021, 14, x.
6. A. Rolan, S. Bogarra, M. Bakkar: “Integration of Distributed Energy Resources to Unbalanced Grids under Voltage Sags with Grid Code Compliance”, IEEE Transactions on Smart Grid, 2021.

Keywords: Artificial Neural Network-based relay, distributed generators, distribution system, protection algorithms, smart grids, three-phase controlled Voltage Source Inverter.

Table of Contents Page

Acknowledgment... i

Abstract iii

Table of contents... vi

List of figures xi

List of tables xxii

List of symbols xxv

List of abbreviations xxix

CHAPTER 1 Introduction 1

1.1. Overview.. 1

1.2. DG techniques 5

1.3. Protective devices 5

1.4. Motivation 7

1.5. Thesis Objectives 7

1.6. Thesis Outline 8

CHAPTER 2 State of the art of DG penetration impact on MV DS protection systems.. 10

2.1. DGs impact on MV distribution grid.................................. 10

2.1.1. Impact of fault ride-through requirements..................... 10

2.1.2. Impact of DG on MV distribution grid protection............ 10

2.2. State of the art... 12

2.2.1. State of the art on the reference current control strategies of VSI during grid faults.. 12

2.2.2. State of the art of the protection schemes of MV DS with DGs penetration.. 14

CHAPTER 3 Medium voltage distribution system construction, modeling, and analysis during faults with DG penetration 21

3.1. Modeling of DS components 21

3.2. Analysis of PV penetration impact on the DS behaviour 28

CHAPTER 4 Analysis of a three-phase grid-connected converter under voltage sags according to the Spanish grid code 35

4.1. Spanish grid code P.0. 12.2 application with symmetrical and unsymmetrical sags 35

4.2. Three-phase grid-connected inverter 37

4.2.1. Reference current control strategies using *Park*

transformation…… 37

4.2.2. Reference current control strategies in *Ku* transformation.. 43

4.3. Analysis and discussion…… 45

CHAPTER 5 Proposed fault protection scheme…… 58

5.1. Introduction …… 58

5.2. Conventional protections (OCR/DR)…… 59

5.3. Proposed fault protection algorithms…… 61

5.3.1. Centralize control algorithm (CE)…… 67

5.3.2. Zone control algorithm (ZO)…… 69

5.3.3. Local control algorithm (LO)…… 71

5.3.3.1. Fault classification algorithm…… 72

5.3.3.2. LO algorithm in case symmetrical and unsymmetrical faults and the MV side of the (HV/MV) transformer is not isolated…… 75

5.3.3.3. LO algorithm in case of symmetrical and unsymmetrical faults and the MV side of the (HV/MV) transformer grounded through a zigzag…… 86

5.3.4. PD priority strategy…… 93

CHAPTER 6 Analysis and test results of the proposed protection algorithms…. 97

6.1. Analytical and test results for CE, ZO, and LO protection algorithms…… 97

6.1.1. CE-ZO protection algorithms…… 98

6.1.2. LO protection algorithm…… 102

6.2. Comparative study…… 117

CHAPTER 7 Experimental implementation and results…… 124

7.1. Experimental implementation of the three-phase grid-connected converter…… 124

7.1.1. Experimental implementation of the current control strategies…… 124

7.2. Experimental implementation of the proposed protection algorithms…… 128

7.2.1. Protection algorithms practical verification using dSPACETM and DSP…… 131

7.2.2. Experimental implementation and verification of the proposed protection algorithms using the physical scaled grid….. 133

7.2.2.1. Calculation of system parameters…… 134

7.2.2.2. Experimental results discussion of the proposed

protection algorithms (CE, ZO, and LO) …………………………. 136
7.2.2.3. Simplified radial grid without DG……………………………… 141
7.2.2.4. Simplified radial grid with DG……………………………. 144
7.2.2.5. Complete radial grid without DG……………….……….... 147
7.2.2.6. Complete radial grid with DG…………………………….... 152
7.2.2.7. Complete ring grid without DG…………………………… 158
7.2.2.8. Complete ring grid with DG……………………………….. 166
CHAPTER 8 Conclusions and recommendation future work…………………. 176
8.1. Conclusions…………………………………………………………... 176
8.2. Recommendation for future work………………………………….. 177
List of references ……………………………………………………………….... 180
Appendix A Analysis of the ring grid behaviour during faults…………….…. 193
A.1. System behaviour with isolated transformer and different types of faults……………………………………………………………….. 193
A.2. Test the algorithm with different types of HV/MV Transformer configurations………………………………………………………... 195
A.3. Examples for analysed ring grid with faults in different locations. 197
A.4. The behaviour of the ring grid during fault and disconnection….. 202
Appendix B Tested cases and simulation results……………………………… 210
B.1. Tested cases……………………………………………………….. 210
B.2. Results……………………………………………………………... 214
B.3. Demonstration of DPF in various grid scenarios………………….. 235
B.4. ANN fault classification……………………………………………... 244
Appendix C Solid State Relay and Mechanical breaker demonstration………. 247
C.1. Solid-state relay features…………………………………………. 247
C.2. Available topologies………………………………………………. 248
C.3. Evaluation of SSR response……………………………………… 248
C.4. Troubleshooting…………………………………………………….... 249
Appendix D Experimental verification of the protection algorithms…………... 253
D.1. Total number of analysed cases…………………………………….. 253
D.2. Implementation on dSPACE……………………………………….... 257
D.3. Experimental results (Continue)…………………………………… 268
Appendix E Converter control…………………………………………………. 286
E.1. Mathematical model of grid-connected inverter system in *Park* transformation……………………………………………………… 286
E.2. Mathematical model of grid-connected inverter system in *Ku* transformation……………………………………………………… 291

E.3. Relation between *Ku* and Park components………………………. 293

E.4. Phase Lock Loop (PLL)…………………………………………….. 298

E.5. Modification of the current control strategy………………………. 299

Appendix F Experimental setup………………………………………………….. 304

F.1. System connection…………………………….……………………... 304

Appendix G Calculation of the system parameters and pu values……………... 313

G.1. Calculation of line parameters……………………………………… 313

G.2. Calculation of zigzag impedance…………………………………… 314

G.3. Calculation of fault resistance……………………………………… 314

G.4. Calculation of pu values…………………………………………….. 315

Appendix H Proposed MPPT technique during partial shading……………….. 318

H.1. State of the art of the MPPT techniques during partial shading… 318

H.2. Chopper control employing MPPT control………………………... 319

H.3. MPPT employing adaptive FLC and DSM (practical Case Study) 324

H.4. Mathematical inference of the MPPT under partial shading mode………………………………………………………………….. 327

List of publications…………………………………………………………………….. 331

List of figures

Fig. 1.1 Long-range world population projections, source: Global Energy Perspectives ITASA/WEC 1
Fig. 1.2 Renewable energy projects in Spain, source: greenpeace.org 1
Fig. 1.3 World electricity generation, source: IRENA, 2019.. 2
Fig. 1.4 Renewable Energy Electricity Generation Costs as Percentage [16]... 2
Fig. 1.5 Smart grid DS, source: printerest (electrical-engineering-pics.blogspot.co.at) 3
Fig. 1.6 ANN (a) principle of operation (b) structure 4
Fig. 1.7 Renewable energy-based DG system. 5
Fig. 2.1 Radial grid (a) no DG penetration, (b) with one DG, and (c) with two DGs.............................. 11
Fig. 2.2 Ring grid (a) no DG penetration, and (b) with DG penetration 11
Fig. 2.3 Short circuit current in case of ring grid (a) without DG (b) with DG penetration during a fault at DL2 12
Fig. 3.1 Main grid structure 21
Fig. 3.2 Equivalent single-phase circuit of the linear HV/MV transformer 22
Fig. 3.3 Zigzag connection at the secondary of the (HV/MV) transformer [141], [142] 22
Fig. 3.4 Zigzag transformer connection 23
Fig. 3.5 Distribution line model 24
Fig. 3.6 three-phase fault modeling 24
Fig. 3.7 Star connected three-phase CT set 25
Fig. 3.8 Equivalent circuit of a practical PV device including the series and parallel resistances, (a) with a single-diode model, (b) of Double exponential model [146] 25
Fig. 3.9 PV characteristic influence of the ambient irradiation (a) I-V curve (b) P-V curve 26
Fig. 3.10 General scheme of a three-phase grid-connected inverter supplied by PV................................ 27
Fig. 3.11 Single line diagram of the analysed DS with DG penetration (a) ring grid, (b) radial grid 28
Fig. 3.12 Transient period of the *abc* current during symmetrical fault 29
Fig. 3.13 DPF in the analysed ring grid (a) no DG (b) with DG... 29
Fig. 3.14 Single line diagram of the analysed grid during a fault in DL4 (a) power flow without DG (b) power flow with DG 30
Fig. 3.15 Short-circuit currents during three-phase fault at DL4, with fault resistance $r = 1\ \Omega$ (a) without DG (b) with DG penetration 30
Fig. 3.16 Short-circuit currents during three-phase fault at DL4, with $r = 0.1\ \Omega$ (a) without DG (b) with DG penetration.. 31
Fig. 3.17 Short-circuit currents during three-phase fault at DL3, with $r = 0.1\ \Omega$ (a) without DG (b) with DG penetration.. 31
Fig. 3.18 Short-circuit currents during single-phase to ground (AG) fault at DL3, with r = 0.1 Ω (a) without DG (b) with DG penetration 32
Fig. 3.19 Short-circuit currents during two-phase to ground fault (ABG) at DL5, with $r = 0.1\ \Omega$ (a) without DG (b) with DG penetration 32
Fig. 3.20 Short-circuit currents during a two-phase fault (AB) at DL4, with $r = 0.1\ \Omega$ (a) without DG (b) with DG penetration... 33
Fig. 3.21 Short circuit current paths in case of (a) single-phase fault (b) three-phase fault...................... 33
Fig. 4.1 Block diagram of the grid-connected photovoltaic (PV) system 35
Fig. 4.2 Active (I_a) and reactive (I_r) currents to be injected during grid faults, according to Spanish grid code P.O. 12.2... 36
Fig. 4.3 Current control considering unbalanced conditions for positive- and negative-sequence components 38
Fig. 4.4 Three-phase inverter control for unbalanced conditions... 38
Fig. 4.5 Calculation of the reference currents considering grid code requirements 43
Fig. 4.6 Three-phase inverter grid connected equivalent circuit: inverter (right controlled soured), *RL* filter, and faulted grid connection (left controlled source), for the proposed CPC and BCC control strategies 44
Fig. 4.7 General scheme of a three-phase grid-connected inverter, and its control, supplied by a PV installation 45
Fig. 4.8 Different control strategies for type G sag depth 0.6 47

Fig. 4.9 Spanish grid code P.O. 12.2: active and reactive currents and powers in pu with different control strategies for type G sag of depth 0.6 48
Fig. 4.10 Comparison of types G and D sags, both of depth 0.6, under BCC strategy 49
Fig. 4.11 CPC and BCC strategies during a 2-phase fault (type C sag) for sag depth (a) $h = 0.7$, (b) $h = 0.5$ and (c) $h = 0.3$ 51
Fig. 4.12 Flowchart to adapt Spanish grid code to a grid-connected inverter 52
Fig. 4.13 Comparison between (a) limiting strategy proposed in [71], and (b) the proposed limiting strategy 53
Fig. 4.14 THD of the injected current during steady state of three-phase fault 54
Fig. 4.15 abc and the complex plane of grid voltage, injected current and inverter reference voltage for unsymmetrical sag (type C) with h=0.5 sag depth 54
Fig. 4.16 Differences between type A, type C, and type G sags using transformed variables with h=0.7 sag depth, and 200ms duration. (a) abc variables, (b) transformed variables and (c) complex plane 55
Fig. 4.17 Sag depth and sag duration influences (a) abc variables (b) transformed variables (c) complex plane 56
Fig. 5.1 Single line diagram of the analysed radial DS with DG penetration 59
Fig. 5.2 Single line diagram of the analysed ring DS with DG penetration 59
Fig. 5.3 Short-circuit current of OCR, and DR behaviour during a three-phase fault in DL3 with fault resistance r = 0.1 Ω (a) with two DGs, (b) with one DG, (c) without DG 60
Fig. 5.4 Short-circuit current of DR behaviour during single-phase fault in DL3 with fault resistance r = 0.1 Ω (a) without DGs, (b) with two DG 61
Fig. 5.5 Distribution levels of the proposed protection algorithm for grounded/ isolated power transformer 61
Fig. 5.6 Single line diagram of the analysed radial DS with DG penetration and CE/ZO algorithms 62
Fig. 5.7 Single line diagram of the analysed ring system with DG penetration and CE/ZO algorithms 62
Fig. 5.8 Concept diagram of the proposed algorithm 63
Fig. 5.9 Structure of the ANN for fault location scheme 63
Fig. 5.10 ANN training environment 64
Fig. 5.11 short-circuit currents in PSCAD and MATLAB^{TM} SIMULINK simulation platforms 64
Fig. 5.12 Flowchart of ANN training procedure 65
Fig. 5.13 ANN aspects for different trained ANN 65
Fig. 5.14 Decision of different ANN models and the estimated output 66
Fig. 5.15 Concept diagram for implementing directional element (a) abc current and voltage signals (b) square wave of current and voltage (c) current and voltage multiplication (d) integrator output (e) decision 66
Fig. 5.16 Simulation diagram for DPF during fault 67
Fig. 5.17 Single phase to ground fault 67
Fig. 5.18 Positive-sequence values for two-phase to ground fault at DL3, with fault resistance r = 0.1 Ω 68
Fig. 5.19 Concept diagram of CE algorithm 68
Fig. 5.20 ANN connection in case of CE 69
Fig. 5.21 Delay components of the total fault clearing time 69
Fig. 5.22 Concept diagram of ZO algorithm 70
Fig. 5.23 Zone identification for ZO algorithm, and ANN connection in case of CE 71
Fig. 5.24 Single line diagram of the analysed radial DS with DG penetration and LO 72
Fig. 5.25 Single line diagram of the analysed ring DS with DG penetration and LO 72
Fig. 5.26 preprocessing module block diagram and ANN to classify the fault 73
Fig. 5.27 Flowchart of fault classification algorithm 73
Fig. 5.28 Positive-sequence current magnitude in case of healthy and faulty conditions in case of an isolated grounded transformer during a single-phase to ground fault at DL3 75
Fig. 5.29 Sequence current components during a single-phase to ground fault at DL4 (a) the first disconnection, (b) the second disconnection 76
Fig. 5.30 Fault isolation steps in case of a single-phase to ground fault 76
Fig. 5.31 Flowchart of LO for unsymmetrical fault and recloser algorithm 77
Fig. 5.32 Sequence current single-phase fault at DL3 (a) before disconnection (b) after the first disconnection during 78

Fig. 5.33 Zero-sequence current profile with one DG connected at bus 3 (a) the first disconnection, (b) second disconnection when a single-phase fault at DL3, (c) second disconnection when a single-phase fault at DL5 79
Fig. 5.34 Fault isolation steps in case of two-phase or two-phase to ground faults 79
Fig. 5.35 Zero-sequence current profile during two-phase fault at DL4 and two-phase to ground fault at DL2, with one DG connected at bus 3 (a) the first disconnection, (b) second disconnection 80
Fig. 5.36 Inverse time-current characteristic curve for unsymmetrical faults 80
Fig. 5.37 Three-phase fault at DL3 81
Fig. 5.38 Flowchart of LO for symmetrical fault and recloser algorithm 81
Fig. 5.39 Positive-sequence voltage profile during three-phase fault with one DG connected at bus 3 (a) the first disconnection, (b) second disconnection 82
Fig. 5.40 Recloser algorithm explanation when the fault in different lines 83
Fig. 5.41 Recloser algorithm behaviour when a three-phase fault at the middle of the DL 83
Fig. 5.42 Flowchart of the proposed CE, and ZO protection algorithms 84
Fig. 5.43 Flowchart of the LO proposed protection algorithm 84
Fig. 5.44 measurement signals (a) behind the breaker, (b) in front of the breaker 85
Fig. 5.45 Difference in trip signals with and without recloser algorithms 86
Fig. 5.46 Flowchart of proposed LO algorithm without recloser 86
Fig. 5.47 Single-phase to ground fault at DL3 with fault resistance r =0.1 Ω 87
Fig. 5.48 Single-phase to ground fault at DL3 with fault resistance r =0.1 Ω, after 1st disconnection of PD5 87
Fig. 5.49 Fault isolation steps in case of single-phase to ground fault 88
Fig. 5.50 Flowchart of the proposed LO algorithm with YNd11 transformer connection grounded through a zigzag transformer 88
Fig. 5.51 Negative-sequence voltage profile during single-phase fault with one DG connected at bus 3 (a) the first disconnection, (b) the second disconnection 89
Fig. 5.52 Negative-sequence voltage profile during two-phase fault with one DG connected at bus 3 (a) the first disconnection, (b) the second disconnection 89
Fig. 5.53 Three-phase to ground fault at DL3, with fault resistance r = 0.1 90
Fig. 5.54 Three-phase to ground fault at DL3 with fault resistance r =0.1 Ω, after 1st disconnection of PD5 90
Fig. 5.55 Three-phase fault at DL3 91
Fig. 5.56 Voltage profile during three-phase fault with one DG connected at bus 3 91
Fig. 5.57 Definite time curve (a) Positive-sequence voltage, (b) Negative-sequence voltage 92
Fig. 5.58 Concept diagram of (a) CE algorithm, (b) each PD fault location controller including ZO and LO algorithms, (c) post-processing algorithm 92
Fig. 5.59 Concept diagram of (a) analysed ring grid with a three-phase fault at DL3, (b) ZO algorithm, (c) CE algorithm, and (d) PD priority algorithm 94
Fig. 5.60 Analysed ring grid when a three-phase fault at DL3 and LO algorithm with YNd11 transformer connection grounded through a zigzag transformer 95
Fig. 6.1 Single line diagram of the analysed ring system with DG penetration 97
Fig. 6.2 Flowchart of the studied cases 98
Fig. 6.3 CE and ZO behaviour during a three-phase fault in DL3 with fault resistance *r* = 0.1 Ω, (a) with two DGs, (b) without DG 99
Fig. 6.4 Ring grid with two DGs during (a) three-phase fault in DL3, (b) single-phase fault in DL4 99
Fig. 6.5 CE and ZO behaviour during different fault resistance, with two DGs during a three-phase fault in DL3 (a) r = 2 Ω, (b) r = 0.05 Ω 101
Fig. 6.6 CE and ZO behaviour during two-phase to ground fault in DL3, and r = 0.1 Ω, with two DGs, in case of (a) stiff grid, (b) weak grid 101
Fig. 6.7 The analysed ring grid with 2 DG connected at buses 3 and 7 for CE-ZO algorithm, in case of (a) single-phase to ground fault at DL3, and (b) three-phase fault at DL4 101
Fig. 6.8 Flowchart of the studied cases 102
Fig. 6.9 System behaviour during symmetrical fault at DL4 with CE-ZO with r = 0.1 Ω 103
Fig. 6.10 LO scheme 104
Fig. 6.11 Flowchart of the LO proposed protection algorithm 104

Fig. 6.12 Definite time curve (a) Positive-sequence voltage, (b) Negative-sequence voltage 105
Fig. 6.13 abc voltages, abc currents, and trip signals for LO, with the analysed ring grid (a) with 2 DGs during 1 ph to ground (AG) at DL5, (b) without DG during 2 ph (BC) at DL1 106
Fig. 6.14 abc voltages, abc currents, and trip signals for LO, with the analysed ring grid (a) with 2 DGs during three-phase fault at DL3, (b) with 2 DGs during single-phase to ground fault (BG) at DL4 107
Fig. 6.15 abc voltages, abc currents, and trip signals for LO, with the analysed ring grid (a) without DG during 2 ph (BC) at DL1, (b) without DG during two-phase to ground fault (ABG) at DL2 108
Fig. 6.16 Ring grid with 2 DGs during 3 ph (abc) at DL3, (a) fault, (b) trip. 109
Fig. 6.17 Ring grid with 2 DGs during 1 ph (BG) at DL4, (a) fault, (b) trip. 110
Fig. 6.18 ring grid with 2 DGs during (a) 3 ph (abc) at DL3, (b) 1 ph (BG) at DL4 111
Fig. 6.19 Single line diagram of a radial DS with DG penetration 111
Fig. 6.20 abc voltages, abc currents, and trip signals for LO, with the analysed radial grid (a) with2 DGs during 1 ph to ground (AG) at DL5, (b) without DG during 2 ph (BC) at DL1 112
Fig. 6.21 abc voltages, abc currents, and trip signals for LO, with the analysed radial grid (a) with 2 DGs during three-phase fault at DL3, (b) with 2 DGs during single-phase to ground fault (BG) at DL4 113
Fig. 6.22 abc voltages, abc currents, and trip signals for LO, with the analysed radial grid (a) without DG during 2 ph (BC) at DL1, (b) without DG during two-phase to ground fault (ABG) at DL2 114
Fig. 6.23 Radial grid with 2 DGs during (a) 3 ph (abc) at DL3, (b) 1 ph (BG) at DL4 115
Fig. 6.24 Radial grid with 2 DGs during 3 ph (abc) at DL3, (a) fault, (b) trip... 116
Fig. 6.25 Radial grid with 2 DGs during 1 ph (BG) at DL4, (a) fault, (b) trip... 117
Fig. 6.26 Single line diagram of a radial DS with DG penetration 118
Fig. 6.27 Flowchart of the studied cases 118
Fig. 6.28 Short-circuit current of OCR, DR, CE-ZO behaviour during a three-phase fault in DL3 with fault resistance r = 0.1 Ω (a) with two DGs, (b) with one DG, (c) without DG 119
Fig. 6.29 Trip signal of OCR, DR, CE-ZO behaviour during symmetrical and unsymmetrical faults with different fault resistance (a) with two DGs, (b) with one DG, (c) without DG...................................... 120
Fig. 6.30 Short-circuit current of DR behaviour during single-phase fault in DL3 with fault resistance r = 0.1 Ω (a) without DGs, (b) with two DG.. 120
Fig. 7.1 Experimental setup. (a) Real setup, (b) Electrical scheme. 124
Fig. 7.2 Measured abc grid voltages and injected currents during the unfaulty steady-state condition ... 125
Fig. 7.3 Simulated and measured abc grid voltages and injected currents for a type A sag with BCC strategy.. 125
Fig. 7.4 Simulated and measured abc grid voltages and injected currents for a type D sag with BCC strategy.. 126
Fig. 7.5 Simulated and measured abc grid voltages and injected currents for a type G sag with BCC strategy.. 126
Fig. 7.6 Experimental results of grid voltage and injected current with the sag of h = 0.5 depth and 200 ms duration for (a) CPC strategy and (b) BCC strategy. I and II are the reactive and active current references, respectively, imposed by the Spanish grid code 127
Fig. 7.7 (a) Theoretical, (b) simulation, and (c) experimental results of CPC and BCC control strategies during unsymmetrical sag (type C). T = period. 128
Fig. 7.8 Equivalent circuit of Crydom SSR with an interface circuit 129
Fig. 7.9 Concept diagram of SSR 130
Fig. 7.10 Connection between the relay and mechanical contactor 131
Fig. 7.11 Logic representation of laboratory scheme.. 131
Fig. 7.12 Conceptual diagram of the algorithm schemes tested in the laboratory 131
Fig. 7.13 Procedure of the experimental verification (a) Analysed grid, (b) Concept diagram of the proposed algorithms practically, (c) Laboratory setup 132
Fig. 7.14 *abc* voltages and currents of PD9 and PD10 during a single-phase fault at DL5 (a) generated from SIMULINK, (b) Output of dSPACE^{TM} DAC. 133
Fig. 7.15 Digital output of the fault location algorithm decision and fault occurrence in case of three-phase fault, and single-phase fault for (a) CE and (b) ZO 133
Fig. 7.16 Implemented ring grid in the laboratory 134
Fig. 7.17 Simplified radial grid.. 137
Fig. 7.18 Complete Radial grid.. 137

Fig. 7.19 Ring grid 137
Fig. 7.20 Flowchart of the studied cases 137
Fig. 7.21 Flowchart of the proposed CE-ZO protection algorithms 138
Fig. 7.22 Flowchart of the LO proposed protection algorithm 138
Fig. 7.23 Procedure of the experimental verification (a) Concept diagram of the proposed algorithms (b) Analysed grid, (c) Laboratory setup 139
Fig. 7.24 Complete laboratory setup 139
Fig. 7.25 delay between experimental and simulated *abc* voltage at PD1 141
Fig. 7.26 Scheme of the simplified radial grid without DG 141
Fig. 7.27 Flowchart of the priority algorithm 142
Fig. 7.28 Behaviour of CE-ZO control for single-phase to ground fault 142
Fig. 7.29 Behaviour of CE-ZO control for three-phase fault 142
Fig. 7.30 Behaviour of LO control for three-phase fault 143
Fig. 7.31 Definite time curve (a) Positive sequence voltage, (b) Negative sequence voltage 143
Fig. 7.32 Trip time difference between CE-ZO and LO 144
Fig. 7.33 Scheme of the Simplified radial grid with DG 144
Fig. 7.34 Behaviour of CE-ZO control for single-phase to ground fault with BCC 145
Fig. 7.35 Behaviour of CE-ZO control for three-phase fault with BCC 145
Fig. 7.36 Behaviour of LO control for three-phase fault with BCC 146
Fig. 7.37 Behaviour of CE-ZO control for single-phase to ground fault with CPC 146
Fig. 7.38 Behaviour of CE-ZO control for three-phase fault with CRC 147
Fig. 7.39 Scheme of the complete radial grid without DG 147
Fig. 7.40 Behaviour of OCR for single-phase to ground fault when the fault at F1 148
Fig. 7.41 Behaviour of OCR for the three-phase fault when the fault at F1 148
Fig. 7.42 Behaviour of DR for single-phase to ground fault when the fault at F1 149
Fig. 7.43 Behaviour of DR for the three-phase fault when the fault at F1 149
Fig. 7.44 Behaviour of CE-ZO for single-phase to ground fault when the fault at F1 150
Fig. 7.45 Behaviour of CE-ZO for the three-phase fault when the fault at F1 150
Fig. 7.46 Behaviour of OCR for the three-phase fault when the fault at F2 151
Fig. 7.47 Behaviour of DR for the three-phase fault when the fault at F2 151
Fig. 7.48 Behaviour of CE-ZO for the three-phase fault when the fault at F2 152
Fig. 7.49 Scheme of the complete radial grid with DG 152
Fig. 7.50 Behaviour of OCR for single-phase to ground fault when the fault at F1 153
Fig. 7.51 Behaviour of OCR for the three-phase fault when the fault at F1 153
Fig. 7.52 Behaviour of DR for single-phase to ground fault when the fault at F1 154
Fig. 7.53 Behaviour of DR for the three-phase fault when the fault at F1 154
Fig. 7.54 Behaviour of CE-ZO for single-phase to ground fault when the fault at F1 155
Fig. 7.55 Behaviour of CE-ZO for the three-phase fault when the fault at F1 155
Fig. 7.56 Behaviour of OCR for the three-phase fault when the fault at F2 156
Fig. 7.57 Behaviour of DR for the three-phase fault when the fault at F2 156
Fig. 7.58 Behaviour of CE-ZO for the three-phase fault when the fault at F2 157
Fig. 7.59 Digital output of OCR, DR, and CE-ZO with DG during (a) Single-phase fault, (b) Three-phase fault 157
Fig. 7.60 Digital output of OCR, DR, LO, and CE-ZO with DG during Three-phase fault 158
Fig. 7.61 Simulation and Experimental *abc* voltages and currents of PD5, PD6, and Trip signals of the CE-ZO algorithm decision in case of three-phase fault, and single-phase 158
Fig. 7.62 Scheme of ring grid without DG 159
Fig. 7.63 Behaviour of CE-ZO for single-phase to ground fault when the fault at DL1 160
Fig. 7.64 Behaviour of CE-ZO for the three-phase fault when the fault at DL1 160
Fig. 7.65 Behaviour of LO without recloser for single-phase to ground fault when the fault at DL1 161
Fig. 7.66 Behaviour of LO without recloser for the three-phase fault when the fault at DL1 161
Fig. 7.67 Behaviour of LO with recloser for single-phase to ground fault when the fault at DL1 162
Fig. 7.68 Behaviour of LO with recloser for the three-phase fault when the fault at DL1 162
Fig. 7.69 Behaviour of PD1, PD2, and PD3 for single-phase to ground fault when the fault at DL1 163
Fig. 7.70 Behaviour of PD1, PD2, and PD3 for the three-phase fault when the fault at DL1 163

Fig. 7.71 Behaviour of PD1, PD2, and PD6 for single-phase to ground fault when the fault at DL1 164
Fig. 7.72 Behaviour of PD1, PD2, and PD6 for the three-phase fault when the fault at DL1 164
Fig. 7.73 Scheme of ring grid when the fault at DL3 165
Fig. 7.74 Behaviour of CE-ZO for the three-phase fault when the fault at DL3..................................... 165
Fig. 7.75 Scheme of ring grid when the fault at DL2 165
Fig. 7.76 Behaviour of CE-ZO for single-phase to ground fault when the fault at DL2.......................... 166
Fig. 7.77 Scheme of ring grid with DG.. 166
Fig. 7.78 Behaviour of CE-ZO for single-phase to ground fault when the fault at DL1.......................... 167
Fig. 7.79 Behaviour of CE-ZO for the three-phase fault when the fault at DL1..................................... 167
Fig. 7.80 Behaviour of LO without recloser for single-phase to ground fault when the fault at DL1 167
Fig. 7.81 Behaviour of LO without recloser for the three-phase fault when the fault at DL1 168
Fig. 7.82 Behaviour of LO with recloser for single-phase to ground fault when the fault at DL1 168
Fig. 7.83 Behaviour of LO with recloser for the three-phase fault when the fault at DL1 169
Fig. 7.84 Scheme of ring grid with DG.. 170
Fig. 7.85 Behaviour of PD1, PD2, and PD3 for single-phase to ground fault when the fault at DL1 170
Fig. 7.86 Behaviour of PD1, PD2, and PD3 for the three-phase fault when the fault at DL1 170
Fig. 7.87 Behaviour of PD1, PD2, and PD6 for single-phase to ground fault when the fault at DL1 171
Fig. 7.88 Behaviour of PD1, PD2, and PD6 for the three-phase fault when the fault at DL1 171
Fig. 7.89 Behaviour of CE-ZO control for single-phase to ground fault with CPC................................ 172
Fig. 7.90 Behaviour of CE-ZO control for single-phase to ground fault with CRC 172
Fig. 7.91 Scheme of ring grid with DG when the fault at DL3... 173
Fig. 7.92 Behaviour of CE-ZO for the three-phase fault when the fault at DL3..................................... 173
Fig. 7.93 Scheme of ring grid when the fault at DL2 173
Fig. 7.94 Behaviour of CE-ZO for single-phase to ground fault when the fault at DL2.......................... 174
Fig. A.1 Single-phase to ground fault at DL3, when the secondary part of the MV transformer is isolated, and low load consumption 193
Fig. A.2 Single-phase to ground fault at DL6, when the secondary part of the MV transformer is isolated, and low load consumption 194
Fig. A.3 Three-phase to ground fault at DL6, when the secondary part of the MV transformer is isolated, and low load consumption 194
Fig. A.4 Three-phase fault at DL3, when the secondary part of the MV transformer is isolated, and high voltage consumption 195
Fig. A.5 Two-phase to ground fault at DL3, $r = 0.1\ \Omega$ (Transformer connection YNd11 “grounded”).. 196
Fig. A.6 Two-phase to ground fault at DL3, $r = 0.1\ \Omega$ (Transformer connection YNyn) 196
Fig. A.7 Single-phase to ground fault at DL3, $r = 0.1\ \Omega$ (transformer connection YNyg grounded through a resistor) 197
Fig. A.8 Short-circuit current during three-phase fault at DL3, with r =0.1 Ω fault resistance 198
Fig. A.9 Short-circuit current during single-phase to ground fault at DL3, with r =0.1 Ω fault resistance 198
Fig. A.10 Short-circuit current during two-phase to ground fault at DL6, with r =0.1 Ω fault resistance 199
Fig. A.11 Short-circuit current during single-phase to ground fault at DL3, with r = 4 Ω fault resistance 199
Fig. A.12 Short-circuit current during three-phase fault to ground at DL4, with r =0.1 Ω fault resistance 200
Fig. A.13 Short-circuit current during single-phase to ground fault at DL4, with r =0.1 Ω fault resistance 200
Fig. A.14 Short-circuit current during single-phase to ground fault at DL6, with r =0.1 Ω fault resistance 201
Fig. A.15 Short-circuit current during two-phase to ground fault at DL2, with r =0.1 Ω fault resistance 201
Fig. A.16 RMS short-circuit currents during three-phase fault at DL3, with r = 0.1 Ω (a) without DG (b) with DG penetration.. 202
Fig. A.17 Single-phase to ground fault at DL3, r =0.1 Ω (Transformer connection YNd11 zigzag) (a) before disconnection, (b) after 1st disconnection 202
Fig. A.18 Two-phase to ground fault at DL3, r =0.1 Ω (Transformer connection YNd11 zigzag) 203

Fig. A.19 Two-phase fault at DL3, r =0.1 Ω (Transformer connection YNd11 zigzag) 203
Fig. A.20 Three-phase to ground fault at DL3, r =0.1 Ω (Transformer connection YNd11 zigzag) 204
Fig. A.21 Single-phase to ground fault at DL3, r =2 Ω (Transformer connection YNd11 zigzag) 204
Fig. A.22 Single-phase to ground fault at DL3, r =0.1 Ω with one DG (Transformer connection YNd11 zigzag) 205
Fig. A.23 Two-phase to ground fault at DL3, r =0.1 Ω with one DG (Transformer connection YNd11 zigzag) 205
Fig. A.24 Three-phase to ground fault at DL3, r =0.1 Ω with one DG (Transformer connection YNd11 zigzag) 206
Fig. A.25 Single-phase to ground fault at DL5, r =0.1 Ω (Transformer connection YNd11 zigzag) 206
Fig. A.26 Two-phase to ground fault at DL6, r =0.1 Ω with one DG (Transformer connection YNd11 zigzag) 207
Fig. A.27 Single-phase to ground fault at DL5, r =0.1 Ω with two DG (Transformer connection YNd11 zigzag) 207
Fig. A.28 Two-phase to ground fault at DL4, r =2 Ω with two DG (Transformer connection YNd11 zigzag) 208
Fig. B.1 Analysed ring grid with CE (a) 2 DGs during single-phase to ground fault (AG) at DL5, (b) No DG during two-phase fault (BC) at DL1 222
Fig. B.2 Analysed radial grid with CE (a) 2 DGs during single-phase to ground fault (BG) at DL4, (b) No DG during two-phase to ground fault (ABG) at DL2 223
Fig. B.3 Analysed ring grid behaviour during symmetrical fault at DL4 with CE-ZO with r = 0.1 Ω.... 224
Fig. B.4 Analysed ring grid behaviour during symmetrical fault at DL5 with CE-ZO with r = 0.1 Ω.... 225
Fig. B.5 Analysed ring grid behaviour during symmetrical fault at DL2 with CE-ZO with r = 0.1 Ω.... 226
Fig. B.6 Analysed ring grid behaviour during single-phase to griund fault at DL3 with CE-ZO with fault resistance r = 0.1 Ω.. 227
Fig. B.7 Analysed ring grid behaviour during two-phase to ground fault at DL1 with CE-ZO with fault resistance r = 0.1 Ω.. 228
Fig. B.8 Analysed ring grid behaviour during two-phase fault at DL6 with CE-ZO with fault resistance r = 0.1 Ω 229
Fig. B.9 Analysed radial grid behaviour during symmetrical fault at DL3 with CE-ZO with fault resistance r = 0.1 Ω.. 230
Fig. B.10 Analysed radial grid behaviour during two-phase to ground fault at DL1 with CE-ZO with fault resistance r = 0.1 Ω.. 231
Fig. B.11 Analysed radial grid behaviour during symmetrical fault at DL6 with CE-ZO with fault resistance r = 0.1 Ω.. 232
Fig. B.12 Analysed ring grid with ZO (a) 2 DGs during single-phase to ground fault (AG) at DL5, (b) No DG during two-phase fault (BC) at DL1 233
Fig. B.13 Analysed radial grid with ZO (a) 2 DGs during single-phase to ground fault (BG) at DL4, (b) No DG during two-phase to ground fault (ABG) at DL2 234
Fig. B.14 Ring grid 235
Fig. B.15 Ring grid 236
Fig. B.16 Ring grid 237
Fig. B.17 Radial grid... 238
Fig. B.18 Radial grid with one DG 239
Fig. B.19 Radial grid with two DG.. 240
Fig. B.20 Analysed ring grid with one DG = 4 MW connected at bus 2 241
Fig. B.21 Analysed ring grid with one DG = 4 MW connected at bus 4 242
Fig. B.22 Ring grid 243
Fig. B.23 Ring grid 244
Fig. B.24 ANN training steps 245
Fig. C.1 SSR block diagram 247
Fig. C.2 SSR response vs. input pulse signal (a) during on/off state, (b) On-state zooming 248
Fig. C.3 disconnection SSR disconnect at zero-crossing 248
Fig. C.4 One line radial grid 248
Fig. C.5 ring grid 249

Fig. C.6 Current at PD1 249
Fig. C.7 Behaviour of CE-ZO for single-phase to ground fault when the fault at DL1 250
Fig. C.8 Scheme of ring grid without DG 250
Fig. C.9 *abc* voltage, current and impedance of PD1 251
Fig. D.1 Scheme of the Simplified radial grid with DG 253
Fig. D.2 Scheme of the complete radial grid with DG 253
Fig. D.3 Scheme of ring grid with DG 253
Fig. D.4 Simulink file of the currents at each PD located at the faulted line 257
Fig. D.5 Connection of dSPACE 1104, OP-AMP, and DSP 258
Fig. D.6 SIMULINK program for fault type identification 259
Fig. D.7 SIMULINK program for fault location (CE) 259
Fig. D.8 SIMULINK program for fault location (ZO) 260
Fig. D.9 SIMULINK program for fault location (LO) 260
Fig. D.10 *abc* voltages from dSPACE in case of a three-phase fault (Control desk) (PD1 and PD2) 261
Fig. D.11 abc voltages from dSPACE in case of single-phase to ground fault (Control desk) (PD1 and PD2) 261
Fig. D.12 *abc* voltages to ADC of DSP in case of a three-phase fault (Scope) (PD1) 262
Fig. D.13 *abc* voltages to ADC of DSP in case of single-phase fault to the ground (Scope) (PD1) 262
Fig. D.14 *abc* voltages to ADC of DSP in case of a three-phase fault (Scope) (PD2) 262
Fig. D.15 *abc* voltages to ADC of DSP in case of single-phase fault to the ground (Scope) (PD2) 263
Fig. D.16 abc voltages to DSP in case of a three-phase fault (inside Code Composer) (a) for PD1, (b) for PD2 263
Fig. D.17 *abc* voltages to DSP in case of single-phase fault to the ground (inside Code Composer) (a) for PD1, (b) for PD2 264
Fig. D.18 *abc* voltages vs. fault occurrence for three-phase voltage 264
Fig. D.19 Digital output of the algorithm decision vs. fault occurrence (Three-phase fault) 264
Fig. D.20 Digital output of the algorithm decision vs. fault occurrence (Single-phase fault) 265
Fig. D.21 *abc* current from dSPACE in case of a three-phase fault (Control desk) 265
Fig. D.22 *abc* current from dSPACE in case of single-phase fault to the ground (Control desk) 265
Fig. D.23 *abc* current to ADC of DSP in case of a three-phase fault (Scope) (PD1) 266
Fig. D.24 *abc* current to ADC of DSP in case of single-phase fault to the ground (Scope) (PD1) 266
Fig. D.25 *abc* current to ADC of DSP in case of a three-phase fault (Scope) (PD2) 266
Fig. D.26 *abc* current to ADC of DSP in case of single-phase fault to the ground (Scope) (PD2) 267
Fig. D.27 *abc* current to DSP in case of a three-phase fault (inside Code Composer) (a) for PD1, (b) for PD2 267
Fig. D.28 *abc* current to DSP in case of single-phase fault to the ground (inside Code Composer) (a) for PD1, (b) for PD2 267
Fig. D.29 Digital output of the algorithm decision vs. fault occurrence (Three-phase fault) 268
Fig. D.30 Digital output of the algorithm decision vs. fault occurrence (Single-phase fault) 268
Fig. D.31 Scheme of Simplified radial grid (one line) without DG 268
Fig. D.32 LO control in case of single-phase to ground without DG 269
Fig. D.33 LO control in case of single-phase to ground with DG and BCC control 269
Fig. D.34 CE-ZO control in case of three-phase with DG and CPC control 270
Fig. D.35 CE-ZO control in case of three-phase with DG and CRC control 270
Fig. D.36 Scheme of the radial grid (three-line) without DG 271
Fig. D.37 OCR control in case of single-phase to ground without DG 271
Fig. D.38 OCR control in case of three-phase without DG 272
Fig. D.39 DR control in case of single-phase to ground without DG 272
Fig. D.40 DR control in case of three-phase to the ground without DG 273
Fig. D.41 OCR control in case of single-phase to ground without DG 273
Fig. D.42 DR control in case of single-phase to ground without DG 274
Fig. D.43 CE-ZO control in case of single-phase to ground without DG 274
Fig. D.44 Scheme of the radial grid (three-line) with DG 275
Fig. D.45 OCR control in case of single-phase to ground with DG 275
Fig. D.46 DR control in case of single-phase to ground with DG 276

Fig. D.47 CE-ZO control in case of single-phase to ground with DG and BCC 276
Fig. D.48 Scheme of ring grid without DG.. 277
Fig. D.49 CE-ZO control in case of two-phase to ground 277
Fig. D.50 Scheme of ring grid without DG when fault DL3 278
Fig. D.51 CE-ZO control in case of single-phase to ground.. 278
Fig. D.52 LO control in case of single-phase to ground 279
Fig. D.53 LO control in case of three-phase to ground... 279
Fig. D.54 Scheme of ring grid without DG when fault DL2 280
Fig. D.55 CE-ZO control in case of three-phase to ground 280
Fig. D.56 Scheme of ring grid with DG.. 281
Fig. D.57 CE-ZO control in case of two-phase to ground with DG and BCC 281
Fig. D.58 CE-ZO control in case of three-phase with DG and CPC... 282
Fig. D.59 CE-ZO control in case of three-phase with DG and CRC 282
Fig. D.60 Scheme of ring grid with DG.. 283
Fig. D.61 CE-ZO control in case of single-phase to ground with DG and BCC 283
Fig. D.62 Scheme of ring grid with DG.. 283
Fig. D.63 CE-ZO control in case of single-phase to ground with DG and BCC 284
Fig. E.1 Three-Phase grid-connected VSC with RL filter 286
Fig. E.2 Equivalent electric circuits of three-phase inverter with RL filter in Park transformed variables 289
Fig. E.3 Obtaining the symmetric components of an unbalanced system... 292
Fig. E.4 Three-phase inverter control for balanced conditions 294
Fig. E.5 Park transformation of the symmetric components to obtain constant variables 295
Fig. E.6 PLL Components 298
Fig. E.7 PLL using transformed quadrature voltage 298
Fig. E.8 PLL Model according to [201].. 299
Fig. E.9 abc injected current (initial condition) 300
Fig. E.10 Short-circuit currents at the start and the recovery of the sag 300
Fig. E.11 Grid code modifications.. 301
Fig. E.12 comparison between the initial and the enhanced *abc* injected inverter current 302
Fig. F.1 Experimental setup 304
Fig. F.2 Hardware connection.. 305
Fig. F.3 Controller connection 305
Fig. F.4 Experimental components (from left to right): AC Source, inverter, and dSPACE, contactor and relay 306
Fig. F.5 Experimental components smart source, resistive load, current and voltage sensors................ 306
Fig. F.6 Complete laboratory setup... 307
Fig. F.7 Box construction 308
Fig. F.8 DSP, Op-Amp and power supply 309
Fig. F.9 Scheme of the complete laboratory connection of the complete ring grid 310
Fig. F.10 Scheme of the inverter connection 311
Fig. G.1 analysed grid with fault 314
Fig. G.2 Analysed grids (a) Real grid, (b) Laboratory grid 315
Fig. H.1 PV curve under different weather conditions for the KYOCERA KC200GT PV 319
Fig. H.2 General configuration of MPPT using DSM based FLC 322
Fig. H.3 Flowchart of the proposed DSM based FLC MPPT 322
Fig. H.4 PV power curves for (a) three modules (b) four modules at normal and partial shading conditions 323
Fig. H.5 PV power curve for different PV modules for DSM based FLC at partially shaded mode....... 323
Fig. H.6 PV voltage for (a) one PV module (b) two PV modules (c) four PV modules at partial shading conditions.. 324
Fig. H.7 Flowchart of the proposed DSM based FLC MPPT 325
Fig. H.8 Practical system setup... 325
Fig. H.9 Practical and theoretical curves of the PV module at 80 W.. 326
Fig. H.10 The measured PV voltage of DSM based FLC at normal condition....................................... 326

Fig. H.11 PV voltage simulation of DSM based FLC at normal condition 326
Fig. H.12 PV curve at normal and partial shading conditions 327
Fig. H.13 PV power for (a) DSM based FLC, (b) FLC at partial shading condition 327
Fig. H.14 DSM definition 329

List of tables

Table 1.1 Occurrence percentage of power system component faults [25] 6
Table 2.1 Comparison between different current control techniques 14
Table 2.2 Comparison between different protection strategies. 15
Table 2.3 Comparison of AI techniques. [25] 17
Table 3.1 YNd11 connection schemes and vector representation 22
Table 3.2 Dyg11 connection schemes and vector representation 23
Table 3.3 Load values at the end of each line 27
Table 3.4 Grid parameters 27
Table 3.5 short circuit current during three-phase fault at DL4 with and without DG penetration. 30
Table 4.1 Advantages and disadvantages of each control strategy during the sag 41
Table 4.2 behaviour of each control strategy 41
Table 4.3 Equation of reference active and reactive power and negative sequence current of control strategies according to grid codes. 42
Table 4.4 Reference active and reactive power, and negative-sequence current equations for the proposed control strategies. 45
Table 5.1 OCR settings with 2 DG 60
Table 5.2 DR settings with 2 DG 60
Table 5.3 CE ANN fault location parameters 68
Table 5.4 ZO ANN fault location parameters 70
Table 5.5 Some of the cases used to verify the protection algorithm 71
Table 5.6 ANN fault classification parameters 73
Table 5.7 Some of the cases used to test the classification algorithm 74
Table 5.8 Results of ANN decision in different fault scenarios 74
Table 5.9 Grounding connection of the HV/MV power transformer 74
Table 5.10 Parameters for IEEE extremely inverse curve 80
Table 5.11 Fault clearing time 85
Table 6.1 Some of the scenarios used to test the protection algorithms 98
Table 6.2 Single-phase to ground, and two-phase to ground short-circuit currents, when loads consumption are: (L1 = 5, L2 =2, L3 = 1, L4 = 1, L5 = 4) MVA, and with fault resistance r = 0.1 Ω.... 100
Table 6.3 Disconnections in case of single-phase fault at DL2 105
Table 6.4 OCR settings with 2 DG 119
Table 6.5 DR settings with 2 DG 119
Table 6.6 Comparison between different protection strategies. 121
Table 6.7 Comparison of the proposed method with other methods for a similar problem. 121
Table 7.1 System parameters 124
Table 7.2 Specifications of SSR 129
Table 7.3 List of grid components and their parameters: 134
Table 7.4 System parameters 136
Table 7.5 Comparison between the real grid and the laboratory grid parameters 136
Table 7.6 Some of the experimentally tested cases for radial grids 140
Table 7.7 Some of the experimentally tested cases for ring grid 140
Table B.1 number of cases considering fault resistance 210
Table B.2 Total number of cases 213
Table B.3 Fault identifier results for some operation conditions 215
Table B.4 Fault location results for some operation conditions 217
Table B.5 CE decision for the analysed ring grid without DG 235
Table B.6 ZO decision for the analysed ring grid without DG 235
Table B.7 CE decision for the analysed ring grid with DG 236
Table B.8 ZO decision for the analysed ring grid with DG 236
Table B.9 CE decision for the analysed ring grid with DG and high load consumption 237
Table B.10 CE decision for the analysed ring grid with DG and low load consumption 237
Table B.11 ZO decision for the analysed ring grid with DG and high load consumption 237
Table B.12 ZO decision for the analyzed ring grid with DG and low load consumption 237

Table B.13 CE decision for the analysed radial grid without DG 238
Table B.14 ZO decision for the analysed radial grid without DG 238
Table B.15 CE decision for the analysed radial grid with one DG 239
Table B.16 ZO decision for the analysed radial grid with one DG 239
Table B.17 CE decision for the analysed radial grid with two DG 240
Table B.18 ZO decision for the analysed radial grid with two DG 240
Table B.19 ZO decision 241
Table B.20 CE decision 242
Table B.21 ZO decision 242
Table B.22 CE decision 243
Table B.23 ZO decision 243
Table B.24 CE decision 244
Table B.25 ZO decision 244
Table D.1 shows the total number of the implemented cases in the laboratory 254
Table E.1 Unsymmetrical voltage sag types (obtained from [202]): faults of origin, phasors, and symmetrical components 296
Table F.1 Inverter system parameters 307
Table F.2 System parameters 308
Table G.1 System parameters 315
Table G.2 Comparison between the real grid and the laboratory grid parameters 316
Table H.1 Comparison between different MPPT Techniques 318
Table H.2 Summary of simulation results. 324
Table H.3 List of experimental components 325

List of symbols

Symbols	**Definition**
C	Capacitor
E_m	Peak value of the phase voltage
f_s	The switching frequency
G_n	Nominal irradiation
h	Sag depth
$i^+_{d\,REF}, i^+_{q\,REF}$	The reference positive currents
i^+_d, i^+_q	*dq* positive current components
$i^+_{f\,REF}, i^-_{f\,REF}$	Forward Positive- and negative-reference currents
i^0, i^1, i^2	Zero, positive, and negative sequence currents
I_a	Injected active current
$I_{a\,max}$	Maximum active current
i_a, i_b, i_c	Injected *abc* currents
I_a, I_r	Active and reactive currents
$I_{base,Park}$	Park transformation current
i_d	Direct current
$i^-_{d\,REF}, i^-_{q\,REF}$	The reference negative currents
i^-_d, i^-_q	*dq* negative current components
i_f	Transformed injected current
i_f	The transformed injected current
$I_{nominal}$	Nominal current
I_{ph}	Photo current source
I_{Ph}	PV photo-current " light-generated current"
$I_{pv,n}$	Light-generated current at the nominal condition (usually 25 ◦C and 1000W/m2)
i_q	Quadrature current
I_r	Injected reactive current
i_s	Grid current
$K(\Psi)$	*Ku* transformation
$K_f(s)$	Gain of the PI
K_I	Integration constant of PI controller
K_P	Proportional constant of PI controller
L, R	Filter resistance and inductance
L_f	Inverter interfacing inductance
N_p	Number of parallel cells
N_{pm}	Number of parallel module
N_s	Number of series cells
N_{sm}	Number of series modules
$P(\Psi)$	Transformation matrix
p, q, s	Instantaneous active, reactive and apparent powers
P_{a0}	Supplied active power before sag
P_{REF}	The reference active power
Q_{REF}	The reference reactive power
$Re(i_f), Im(i_f)$	Real and imaginary parts of the transformed injected current
R_s	Series resistor
R_{sh}	Shunt resistor
T	Actual temperatures [K]
$t(I)$	Trip time
T_D	Time dial
T_n	Nominal temperatures [K]
$V(t)$	Instantaneous value of the RMS remaining voltage
v^+_d, v^+_q	Positive sequence voltage
v^+_{gf}, v^-_{gf}	Grid voltage positive- and negative-sequence components

v^0, v^1, v^2	Zero, positive and negative sequence voltages
$v_a(t)$, $v_b(t)$, $v_c(t)$	Instantaneous RMS voltages
v_a, v_b, v_c	The *abc* grid voltages
$v_{abc\ pu}(t)$	Per-unit *abc* voltages
$v_{abc\ Ref}$	Reference inverter *abc* voltages
V_{base}	Voltage base value
v_d	Direct voltage
v^{-}_{d}, v^{-}_{q}	Negative sequence voltage
V_{dc}	DC link voltage
$v_{f\ pu}(t)$	Per-unit transformed voltage
$v_{f\ Ref}$	Transformed inverter reference voltage
v_{fd}	Transformed inverter direct voltage
v_{fq}	Transformed inverter quadrature voltage
$v_{g\ abc}(t)$	Grid *abc* voltages
v_{gb}	Backward grid voltage by Ku
v_{gd}	Transformed grid direct voltage by Park
v_{gf}	Forward grid voltage by Ku
v_{gq}	Quadrature grid voltage Transformed by Park
v_L	Transformed load voltage
v_{s0}	Zero transformed voltage by Park
v_{sa}, v_{sb}, v_{sc}	*abc* grid voltages
v_{sd}	Direct voltage by transformed Park
v_{sq}	Quadrature voltage transformed by Park
X	Number of inputs
x	Input to neuron
Y	Number of outputs

Greek symbols

Symbols	**Definition**
ξ	Damping factor
ω_n	Natural frequency of the voltage
Ψ	Transformation angle
Ψ_0	Transformation's initial angle
θ^+	The positive angles
θ^-	The negative angles
ω	Pulsation
ΔV	Symmetrical voltage range
Ψ	Transformation angle
ω	Grid pulsation
$\Delta \mathbf{T}$	Temperature difference
$\boldsymbol{\theta}_{\mathbf{estimate}}$	Estimated angle
$\boldsymbol{\theta}_{\mathbf{m}}$	Phase angle
$\boldsymbol{\sigma}$	A constant between (1~10)
$\boldsymbol{\omega}$	Frequency in (Rad./second)
$\boldsymbol{\omega}_{\mathbf{g}}$	Grid pulsation

Other symbols

Superscript	**Definition**
*	Conjugate
$^{-1}$	Inverse of a matrix
^{t}	Transpose of a matrix or vector

Subscript	**Definition**
$_{012}$	Conjugate
$_{0dq}$	Inverse of a matrix
$_{0fb}$	Transpose of a matrix or vector
$_{abc}$	Phases of a three-phase system
$_{pu}$	Per unit
$_{REF}$	Reference

List of abbreviations

Abbreviations	**Nomenclatures**
A, C, G	Voltage Sag Types
AARC	Average Active Reactive Control
AC	Alternating Current
AI	Artificial Intelligent
ANN	Artificial Neural Networks
ANSI	American National Standard Institute
As	Arsenic
a-Si	Amorphous Silicon
a-Si:H	Amorphous Hydrogenated Silicon
AVC	Automatic Voltage Control Relay
b	Bias
BCC	Balanced Current Control
BIPV	Building Integrated Photovoltaic
BPSC	Balanced Positive-Sequence Control
CAGR	Compound Annual Growth Rate
CB	Circuit Breaker
CdTe	Cadmium Telluride
CE	Centralize Algorithm
CIGSS	Cadmium Indium Gallium Serenide Solar Cell
CPC	Constant Active Power Control
CSC	Current Source Inverter
CTs	Current Transformers
CuInSe2	Copper Indium Dieseline
DC	Direct Current
DE	Differential Evolution Algorithm
DG	Distributed Generation
DL	Distributionl Line
DN	Distribution Network
DOCR	Directional Overcurrent Relay
DPF	Direction Of The Power Flow
dq	Direct-Quadrature
DR	Differential Relay
DS	Distribution System
DSO	Distribution System Operator
DSP	Digital Signal Processor
DT	Definite Time
DWT	Discrete Wavelet Transform
EHV	Extra High Voltage
EPIA	European Photovoltaic Industry Association
FFT	Fast Fourier Transform
FLC	Fuzzy Logic Controller
FRT	Fault Ride Through
Ga	Gallium
GA	Genetic Algorithm

GaAs	Gallium Arsenide
GCs	Grid Codes
GCV	Grid Code Current Verification
GOOSE	Generic Object Oriented Substation Event
GPV	Grid Code Power Verification
GSC	Grid-side converter
HV	High Voltage
IARC	Instantaneous Active Reactive Control
ICT	Information And Communication Technologies
IEA	International Energy Agency
IEC	International Electro Technical Commission
IED	Intelligent Electronic Device
IEEE	Institute Of Electrical And Electronics Engineers
IGBT	Insulated Gate Bipolar Transistor
ILP	Integer Linear Programming
INC	Incremental Conductance Algorithm
ISL	Instantaneous Saturation Limit
IT	Information Technologies
IT	Inverse Time
I-V	Photovoltaic Current Versus Voltage
kVA 's	Kilo Volt Amperes
LL	Latched Limit
LO	Local Algorithm
LP	Linear Programming
LV	Low Voltage
LVRT	Low Voltage Ride-Through
MAS	Multi-Agent System
MGs	Microgrids
MLP	Multilayer Perceptron
MMS	Manufacturing Message Specification
MPP	Maximum Power Point
MPPT	Maximum Power Point Track
MOV	Metal-Oxide Varistor
MSE	Mean Square Error
MV	Medium Voltage
MVA's	Mega Volt Amperes
OCR	Overcurrent Relay
P and O	Perturb And Observe
PCC	Point Of Common Coupling
PCS	Power Conditioning System
PDs	Protective Devices
PF	Power Factor
PI	Proportional-Integral Controller
PLL	Phase-Lock Loop
PNSC	Positive-Negative-Sequence Control
PSO	Particle Swarm Optimization
PSOs	Power System Operators
PV	Photovoltaic

P-V curve	Power Voltage Curve
PWM	Pulse Width Modulation
RBFNN	Radial Basis Function Neural Network
RE	Renewable Energy
REE	Red Eléctrica Española
RL filter	Resistance Inductance Filter
RMS	Root Mean Square
SGs	Smart Grids
SICW	Sinusoidal Current Waves
SRF-PLL	Synchronous Reference Frame PLL
SSFID	Solid-State Fault Interruption Device
SSRs	Solid-State Relays
STATCOM	Static Compensator
Std	Standard
SVM	Support Vector Machine
SVP	Sampled Values Protocol
SYCW	Symmetrical Current Waves
$t(I)$	Trip Time
TCP/IP	Transmission Control Protocol/Internet Protocol
T_D	Time Dial
THD	Total Harmonic Distortion
VSC	Voltage Source Converter
VSI	Voltage Source Inverter
VT	Voltage Transducer
W	Weight
Wi-Fi	Wireless Fidelity
ZO	Zone Algorithm

1 Introduction

This chapter presents the overview and motivations to classify, locate the fault, and protect the Medium Voltage (MV) electrical Distribution System (DS), followed by the objectives and tasks needed to achieve this goal. Finally, the structure of the thesis and the contents of each chapter are briefly indicated.

1.1. Overview

The main aim of electric utilities is to improve the quality of service continuously. Nowadays, the electricity demand is increasing day after day, especially with the increasing trend regarding smart homes and electric vehicles, elevating the electricity demand. The International Energy Agency (IEA) estimates that by 2040, the energy demand will increase by 40 %, as shown in Fig. 1.1 [1]. Therefore, the quality of the electrical grid must be enhanced and the fault detection and the restoration must be efficient [2], [3].

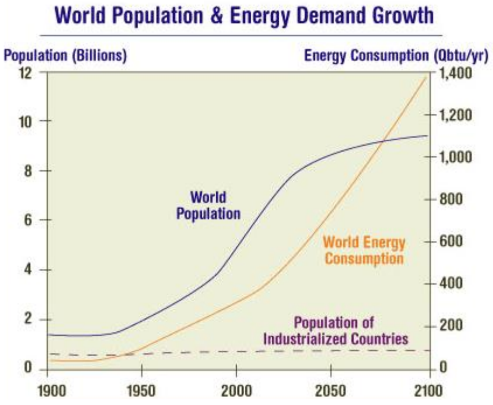

Fig. 1.1 Long-range world population projections, source: Global Energy Perspectives ITASA/WEC

Spain is among the highest number of sunshine hours in Europe, accounting for nearly a third of the country's installed solar power capacity, making this type of energy preferable in this part of the world. Also, Spain was one of the first countries to deploy large-scale solar Photovoltaics (PVs) and, as of 2018, the first country for concentrated solar power (CSP) in the world [4]. Fig. 1.2 shows the locations of renewable energy projects in Spain.

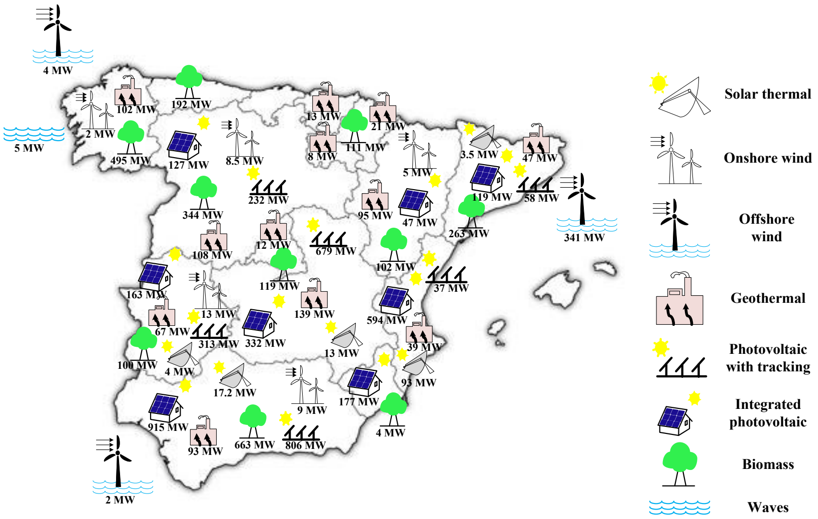
4 MW
102 MW
192 MW
2 MW
5 MW
495 MW
127 MW
8.5 MW
13 MW
21 MW
8 MW
111 MW
3.5 MW
47 MW
5 MW
119 MW
58 MW
232 MW
344 MW
95 MW
47 MW
263 MW
341 MW
108 MW
12 MW
679 MW
102 MW
37 MW
163 MW
119 MW
139 MW
13 MW
594 MW
67 MW
313 MW
332 MW
13 MW
39 MW
100 MW
4 MW
17.2 MW
9 MW
177 MW
93 MW
915 MW
93 MW
663 MW
806 MW
4 MW
2 MW
Solar thermal
Onshore wind
Offshore wind
Geothermal
Photovoltaic with tracking
Integrated photovoltaic
Biomass
Waves

Fig. 1.2 Renewable energy projects in Spain, source: greenpeace.org

In particular, the penetration of Distributed Generation (DG) in DSs has increased dramatically over the last decade [2]. As shown in Fig. 1.3, world electricity generation is expected to be more dependent on renewable energy, especially solar and wind energies [5].

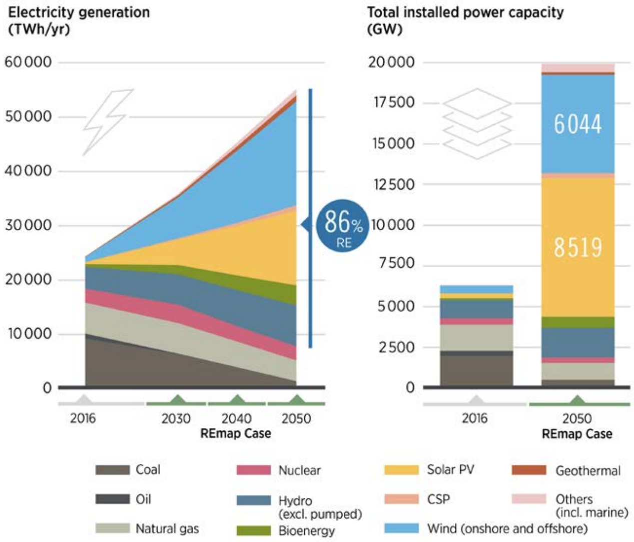

Fig. 1.3 World electricity generation, source: IRENA, 2019.

DG is described as power generation ranging from a few kWs to MWs, connected to a substation, distribution feeder, or customer level. DG systems include PV, wind turbines, fuel cells, micro turbines, gas turbines, and internal combustion engines [6]. Renewable energy resources will take significant importance in the electricity market in the next decades due to their ability to be directly connected to the DS located close to the consumers. DG also has some technological advantages as: improving the reliability, improving the voltage profile, power quality and voltage support of weak DSs, rapid installation in the grid, and taking shorter payback time, some DG technologies have low emissions and good overall efficiencies and contribute to greenhouse gas reduction. However, the drawbacks of DGs can be summarized as follow: DG's connection may cause overvoltage, fluctuation, and system voltage unbalance if synchronization with the utility supply is not appropriately achieved when a DG connects to the network, short-circuit currents are modified, which modify the relay settings [7]. Inverter interfaced DGs, such as PV, are commonly connected to DS. As seen from Fig. 1.4, PV has recently experienced rapid growth worldwide due to mass production, which makes the cost relatively low. During the last decade, Smart Grids (SGs) concept has been considered an effective approach to improve the challenges in the energy domain. However, many obstacles emerge on the route to realizing those accomplishments [2].

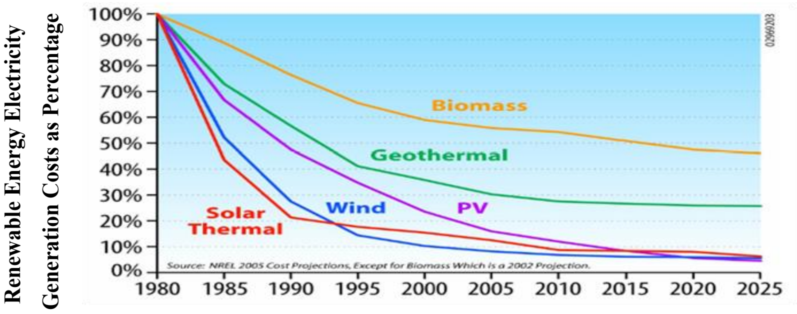

Fig. 1.4 Renewable Energy Electricity Generation Costs as Percentage [16]

The advantages of PV systems can be summarized as follow: quit, have no polluting environmental effects, are highly durable, and requires minimal maintenance [8]. Some of the disadvantages of PV systems are: need large areas to install PV arrays to generate sufficient power; have low efficiency, however, the efficiency of the PV panels have increased significantly in the previous decade, and it is predicted to continue enhancing in the following decade [9].

The DG unit owners are usually private individuals or enterprises not related to the DS operator (DSO), which usually cannot have authority over the operation of the DG units. The two sections have some level of competing interests. Usually, the DG-owners are based on generating power, optimizing income, and holding low network interconnection costs. On the other hand, the DSO's focus is on maintaining stability, high reliability, and sufficient power quality in the network. After connecting a DG unit, the DSO must make interconnection specifications that ensure the proper operation of the DS. The goal of DSO is to utilize the ability to control voltage levels and reduce losses in the DS through control of the reactive power generation of the DG units. However, DG-owners see little gain from reactive power generation or consumption. Therefore, the systems are often run at a constant power factor near one. Currently, DSO asked all DG units to disconnect when a fault is detected. This situation is not adequate when the level of DG penetration rises. In this case, instead of disconnecting the DG, it should help support and restore the network during fault [10].

The penetration of DG will also affect the behaviour of MV DS for both radial and ring configurations, in the next section, both configurations are discussed.

➢ Radial and ring grids

For radial grids that did not contain DGs, the unidirectional power flow topology simplifies the implementation of reactive power compensation for voltage regulation; it also simplifies the systems bus characteristics calculations, and the short-circuit current computations. However, the radial system suffers a major disadvantage, as the system's reliability is low due to the single power flow to the loads. In the case of a failure, the affected circuit will remain isolated from the source as long as the fault is repaired. For present radial systems that contain DG, the power flow can change based on generation and consumption. The radial DS will greatly benefit from the incorporation of DG by the ability to function in isolated mode as well as the enhanced system voltage profile. Another aspect regarding the DG integration in radial topology is still constrained by the maximum amount of power that can be exported, which cannot exceed the feeder rating that has been originally sized during the design stage for the busload.

The meshed (ring) topology provides a significant increase in efficiency over the radial topology by providing alternative power paths to the load, which improves the system reliability, as the power outage duration is reduced significantly. On the other side, bidirectional power flow complicates the power system protection, which introduces the need to use directional relay elements to compensate for the safety of the bus according to the direction of the power flow. Fig. 1.5 shows the DS, including the operation control center and communication signals.

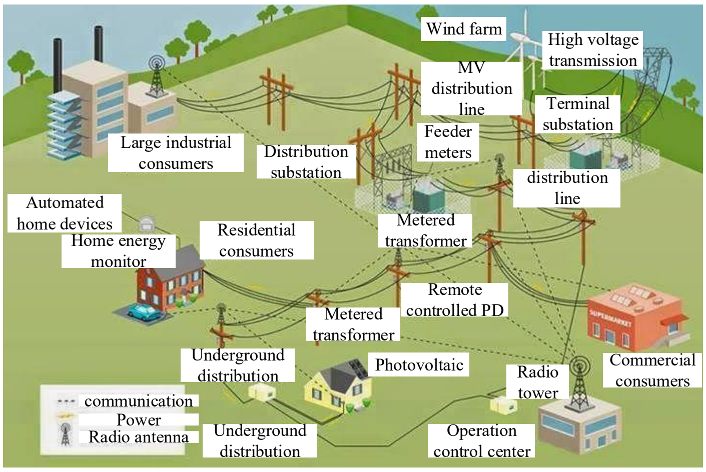
Wind farm
High voltage transmission
MV distribution line
Terminal substation
Feeder meters
Large industrial consumers
Distribution substation
distribution line
Automated home devices
Home energy monitor
Residential consumers
Metered transformer
Remote controlled PD
Metered transformer
Underground distribution
Photovoltaic
Radio tower
Commercial consumers
communication
Power
Radio antenna
Underground distribution
Operation control center

Fig. 1.5 Smart grid DS, source: printerest (electrical-engineering-pics.blogspot.co.at)

SGs bring together the demands and abilities of all generators, grid operators, end-users, and stakeholders to function as efficiently as possible, reducing costs and environmental consequences while increasing system dependability, resilience, and stability. Recently, due to the evolution of Information and Communication Technologies (ICT), Artificial Intelligence (AI), and fast Internet availability especially with the contribution of the 5G technology, the trend toward Smart Grid (SG) is increasing every year [11]. Therefore, the DSO has increased the number of sensors in the network, especially in SGs, to have more information and enhance the grid's commercial quality [12]. Accordingly, the moment has come to introduce new protection algorithms and procedures to enhance the availability of the grid [2]. The rapid development of communication system standards such as IEC 61850 and emerging communications technologies will give more creativity to adapt to new challenges. IEC 61850 began to be in DS when the idea of SG is started to develop [8]. Wherefore, new solutions are needed to propose fault location algorithms in modern DS [2].

One of the most used AI techniques in the protection of MV DS is the Artificial Neural Networks (ANNs) that will be used in this thesis. In the following subsection, the general explanation and the principle of operation will be presented.

- Artificial Neural Network

Because of their nonparametric, adaptive, and noise-tolerant properties, ANN's built credibility in modeling and analyzing complex systems. As biologically inspired analytical techniques, they have the capability of learning and modeling very complex nonlinear relationships. Neural networks are simultaneous implementation of static or dynamic nonlinear systems, and their numerous independent operations can be performed at the same time. The function of an ANN is dictated by the arrangement of neurons, the characteristics of the connection, and the type of processing performed at the elements or nodes. The output to be expected in classification tasks is a categorical variable, while output is a quantitative variable in regression problems. ANN's unique feature is to the extent it is devoted to parallel computation. In addition, it is programmed to generalize the observable inputs and will provide a valid input-output mapping even though in the learning phase the data has not been introduced to the network [13]. Fig. 1.6 shows the general principle and structure of ANN. ANNs are utilized in a wide range of applications, such as pattern recognition, approximation of functions, data compression, associative memory, optimization, prediction, modeling, and control of nonlinear systems [14].

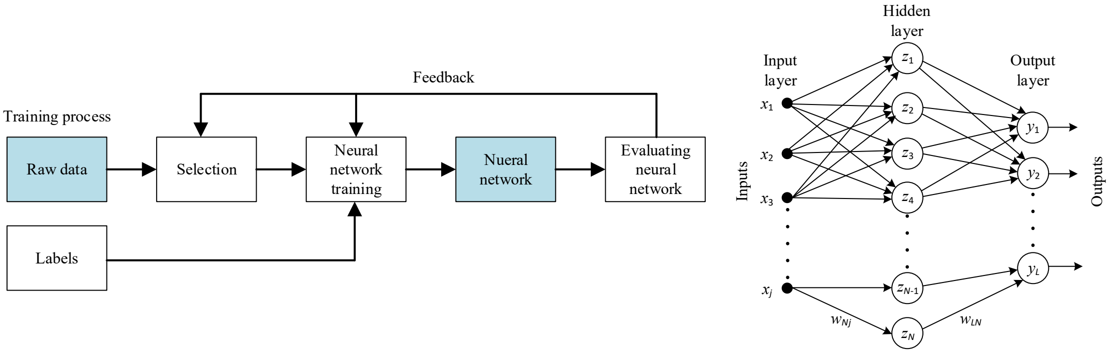

(a) (b)

Fig. 1.6 ANN (a) principle of operation (b) structure

Since ANNs can provide excellent pattern recognition, several researchers suggest performing multiple tasks in power-system relaying for signal processing and decision-making [14].

There are generally three categories of artificial neural networks: feedforward, feedback, and competitive learning. Neural network learning strategies to identify patterns can be divided into two broad categories: unsupervised and supervised learning. The desired set of outputs is determined along with the set of inputs during supervised learning, and the associated output is linked with each input. The neural network in this scenario learns to align inputs with desired targets by adjusting the network's weights. However, desired outputs are not considered during unsupervised learning, and the network learns to recognize the similarity of input patterns by changing the weights of the network before similar inputs begin to generate related outputs [15]. However, the main disadvantage with ANNs is that there is no precise guide for selecting the number of hidden layers and neurons per hidden layer. On the other hand, one of the key benefits of employing ANNs is the ability to generalize flexibility.

In this research, Multilayer Perceptron (MLP) is used, as it has an excellent ability to approximate any nonlinear mapping to some degree of precision [16]. In addition, they do not require a priori assumptions to be made about the properties of the data [17]. MLP is the most frequently used form of feedforward neural network [41]. It is composed of numerous layers of parallel neurons, with one or more hidden layers and an inner product of inputs, weights, and biases, and nonlinear transfer functions, followed by an output layer with an internal product of the inputs, weights, and biases, and linear/nonlinear transfer functions. Also, the back-error propagation method is used in this research, as the neuron weights are adjusted in consecutive steps to achieve minimal global error between the network's real and predicted reaction [14].

1.2. DG techniques

DG can consist of generators directly connected to the MV grid through a transformer, such as the synchronous generators of the combined heat and power plants, or electronic converters, such as the PV generators, wind turbines, and fuel cells [7].

Green and renewable energy sources with virtually no polluting environmental effects are highly durable and require minimal maintenance, modular and versatile in ratings and applications, and PV systems are quiet and visually unobtrusive. The efficiency of PV modules is approximately around 25 %. However, higher efficiencies are anticipated soon as technology and manufacturing processes continue to develop. The following subsection will focus on PV technology as it is the main core of the DGs studied in this thesis.

Two stages grid-connected is a traditional photovoltaic system. It consists of a photovoltaic panel, DC/DC converter, and DC/AC inverter. This topology has the merits of amplifying the solar array voltage, providing galvanic isolation and power decoupling. In applications such as grid-connected systems, the output current needs to be controlled, even though a Voltage Source Inverter (VSI) is often used [18]. The main advantage of the current control technique is the output current limiting. As shown in Fig. 1.7, inverters, solid-state devices that convert DC power to AC, must be used to convert Direct Current (DC) from PV cells to Alternating Current (AC). [19]. Thus, developing a PV grid-connected inverter system is important for the mitigation of energy and environmental issues.

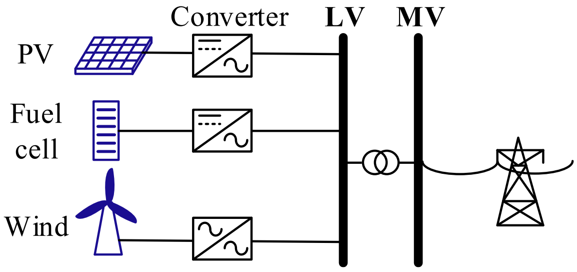

Fig. 1.7 Renewable energy-based DG system.

PV systems are categorized as stand-alone PV systems and PV systems connected to the grid. The PV stand-alone system matches the load, and the PV grid-connected system matches the load and grid [20]. The inverter uses a tracking feature with a maximum power point to identify the ideal operating voltage for the array. Based on the available sunlight and temperature conditions, the inverter operates in phase with the grid (unity power factor) and typically delivers as much power as it can [21].

1.3. Protective devices

The electric lines in a DS are subject to various events such as severe weather conditions, interaction with wildlife, falling trees, human errors, malfunctions of equipment, and so on. For example, MV overhead lines may fail due to ice sleeves on conductors during snowfall or tree fall during windstorms, while overheating may cause the catastrophic failure of underground cables [22]. Such disasters could lead to fault events that could cause to trip the network Protective Devices (PDs), such as power switches, reclosers, circuit breakers, and fuses [23]. Rapid service restoration and excellent pinpoint accuracy during a fault clearance play an important role in the regular operation of the power system to reduce overall costs and increase the safety of the entire system [24]. When disconnection occurs, it can cause temporary or sustained power interruptions [2]. Due to multiple power generation, which will affect PDs settings, the issue of fault location in DSs is critical and complicated, particularly with DG penetration. The performance of those networks can be significantly improved if the exact location of the fault is detected utilizing smart protection technologies. The DS usually operates at two levels of voltage, MV and Low Voltage (LV). The MV voltage DS is the focal point of this research. As shown in Table 1.1, most of the power system component faults are located in the cables or lines, so more effort is required to improve performance and reduce errors in this topic.

Table 1.1 Occurrence percentage of power system component faults [25]

Power system elements	%
Generators and Transformers	17
Overhead lines and underground cables	59
Switchgear	12
Relays, etc.	12

PDs aim to hold currents under normal operating conditions and interrupt currents rapidly under abnormal operating conditions. The PDs are installed at the ends of each Distribution Line (DL) to isolate the faulted line from the grid [26]. PDs are intended to reduce the impact of power system outages by maintaining service quality and minimizing damage to equipment. One of the essential features of any PD is isolating faults quickly because the damage caused by a fault is mainly proportional to its duration. PD must precisely determine the type and location of faults in a short time, and provide a circuit breaker opening order to interrupt failed phases accordingly [26].

Protection of power system is achieved primarily using overcurrent (due to overload or short-circuit) protection devices [27]. This class of protection relays is widely used in DS protection. In most protective systems, overcurrent relays (OCRs) have to be coordinated with other protection devices. This has to be done in such a way that sensitivity and selectivity are guaranteed for a wide range of faulted system conditions. To meet this requirement various relay characteristics are applied.

It is important to say the overcurrent protection needs to be adjusted for radial grid with DGs penetration, and also for the ring grid. Another class of overcurrent protection devices, especially applied in DSs consisting mostly in overhead lines is the recloser [28]. In these grids, the highest percentage of faults is temporary and a permanent disconnection feeder is unnecessary [3].

In radial or ring grids with DGs, disturbances can lead to fault currents, which can flow in both directions through a power system component and causes unnecessary disconnection of circuits. A directional relay is added to the OCR to provide proper protection of these grid structures and cope with bi-directional fault currents.

In ring DSs, differential protection is used more widely than in radial grids. A drawback of the protection is the necessity for a communication channel to compare the current quantities. Moreover, it needs additional backup protection [29]. Typical applications of differential protection are transformers and busbars where there is a short distance between current transformers.

Modern breakers particularly used in medium- and higher-voltage applications have separate relays that sense and activate the tripping. Digital and numerical relays have customized functions and offer improved network and equipment protection [3], [26]. These types of relays are used in this research as a PD, to ensure the fast disconnection of the faulted part of the system. The numerical PD is designed to combine functions such as monitoring, metering, controlling, and recording events, as well as being economical and adaptable to communicate with peers [13]. A specialized Digital Signal Processor (DSP) is used to incorporate numerical PD as computational hardware, using DSP as a relay processor, enabling it to meet basic protective requirements such as reliability, sensitivity, selectivity, and speed, which can dramatically boost the efficiency of the protection operation [30]. Therefore, the use of numerical PDs would soon replace previous PD technology such as digital PDs, static PDs, or electromechanical PDs [31].

1.4. Motivation

As the number of DG increases, the complexity of the network increases, which requires a more sophisticated protection system. Faults on such DS can have severe consequences on the stability of the power system. Since the severity of the consequences is based on the location of the fault, and equipment response, a deep analysis is needed to investigate all of the fault conditions and create a robust network protective system. DS can start exporting electrical power to neighboring grids that transform the power system into a bidirectional power system [32]. There are currently some DGs connected to DS, however, in the future, the level of penetration is expected to increase rapidly [3]. Power systems studies must then be carried out to optimize the proposed DG integration by location and penetration level, and it is also necessary to model, evaluate and understand its impact on the reliability of existing power systems to incorporate these resources without degrading the reliability and power quality of the existing systems [3]. One of these solutions is to use Artificial Intelligent methods like ANN, Fuzzy Logic Controller (FLC), Particle Swarm Optimization (PSO) … and so on. ANNs typically gain the ability to capture complex and nonlinear interactions through a learning mechanism between inputs and outputs. ANNs are particularly useful for solving the complex problems of signal processing and pattern recognition, ANNs will increase the possibility to accurately determine the type and location under a variety of operating conditions [26].

Conventional techniques find limitations due to fault resistance, the influence of pre-fault load conditions, and signal contamination due to noise [33]. The major reason for searching for a new solution is that an accurate fault location can reduce the time required to restore power supply to customers. Complicated calculations are used in conventional techniques, which might lead to errors in the anticipated fault location. These can be overcome with the use of ANN [34].

In addition, due to DG’s wide penetration into the ring DS, regulation of the DG converters during an abnormal condition plays an essential role in the stability behaviour of the whole network. Power converters are designed and controlled to inject power into the grid under normal conditions and support the grid during transient operation by reducing the active power injection and increasing the injection of reactive power according to grid codes [7]. As DGs contribution to fault is limited around the rated current of the applied inverters, it may appear that the short-circuit current of DG-based inverters has no effect on MV protections [35]. However, a change in the power flow will occur. Moreover, in the case of high DG penetration, the relay short-circuits current value will be affected, impacting the coordination of the protection system [36].

The behaviour of the protective system in the case of a ring grid with high penetration of DG-based inverter has been the subject of very little research. No previous research has created a protection algorithm based on an ANN communication system with a directional relay system. Therefore, a perfect, efficient, and secure technique is still required. This protection algorithm allows the detection of symmetrical and asymmetrical faults in an MV ring DS, resulting in a more secure, reliable, and robust protection environment. This thesis aims to propose several algorithms based on numerical PD to identify and locate the fault in the MV DS grid by using different technologies as communication between PDs that can be employed in SGs. Moreover, in order to have a secure, redundant, and efficient protection system another autonomous algorithm is proposed depending only on the local information of every PDs [2].

1.5. Thesis objectives

The proposed Ph.D. thesis aims to study the problems resulting from the implementation of DG systems in DSs on both ring and radial grid configurations, more precisely the effect of DG penetration on DS short-circuit currents, and DG converter control during faults. The main objectives can be summarized in the following steps:

- Analysis of sag effects in a DS with DG penetration

Analyze the behaviour of a DS with DGs based on power electronic converters due to voltage sags. Different control strategies have been studied. The safe operation of the grid during the disturbance has been considered, by using different control strategies, and different sag depths and types.

- Analysis of DG penetration on the protection of MV ring DS

The impact of DG penetration on MV DS protection has been studied and new protection algorithms based on AI have been analysed, in order to ensure supply continuity and availability during abnormal grid conditions, and without compromising system performance. A decision-making algorithm is developed and proposed for detecting, locating, and isolating the faulted part of the grid, the new technique is based on the direction of the power flow recognition and ANN.

- Propose new protection algorithm using ANN

The proposed strategy proposes three algorithms that work in parallel to increase the reliability and redundancy of the protection system. The first algorithm named Centralize algorithm (CE) is based on gathering all the data of the PDs in the grid and then giving the appropriate decision. The second algorithm named Zone algorithm (ZO) is based on data exchange between the peer PDs. Finally, the third algorithm named Local algorithm (LO) is based only on the local data of each PD and does not depend on the communication, which gives more security to the system in case of communication problems. The proposed strategy was intended to ease the system's decision-making by presenting a fast and accurate method for classifying and identifying fault locations in MV DS [37].

- Simulate and practically validate the new protection algorithms, and advocate them through a comparison with conventional protection

A comprehensive evaluation of algorithms for multiple tests has been studied. Several fault detection and diagnosis methods have been investigated, and proposed algorithms have been tested for multiple scenarios. Finally, extensive studies and detailed experiments have been carried out to validate the proposed protection strategies. In addition, a comparative study has been presented to show the merits of the proposed protection algorithms over the conventional protections.

1.6. Thesis outline

This section presents an outline of the thesis.

Chapter 2 – State of the art of DG penetration impact on MV DS protection systems

Introduces the impact of DG on the MV radial and ring DS protection using classical and AI techniques.

Chapter 3 – Medium voltage distribution system construction, modeling, and analysis during faults with DG penetration

An overview of the analysed MV ring DS is given. Also, the general structure and parameters of the grid are presented.

Chapter 4 – Analysis of a three-phase grid-connected converter under voltage sags according to the Spanish grid code

Treats the control of DG during voltage sags and proposes several control strategies to guarantee fault ride-through capability of DG unit. The test of the proposed control strategies will be presented.

Chapter 5 – Proposed Fault protection scheme

Explains in detail the proposed fault classification and location algorithms.

Chapter 6 – Analysis and test results of the proposed protection algorithms

The proposed protection strategy will be analysed and investigated and the discussion of the test results will be presented.

Chapter 7 – Experimental implementation and results

The experimental verification of the proposed fault protection algorithms will be analysed.

Chapter 8 – Conclusions, and recommendations for future work

General conclusions and recommendations for further research are presented.

2 State of the art of DG penetration impact on MV DS protection systems

In this chapter, the impact of DGs on the behaviour of the MV distribution grid and the protection system will be studied. Following the state of the art of the VSI control during abnormal grid conditions will be addressed. In addition, the evolution and the modifications of the protection systems (conventional / AI) with DGs penetration will be introduced.

2.1. DGs impact on MV distribution grid

The DG's connection to the DS results in several sources of fault current, which might affect fault detection. The DG's contribution to the fault current is highly dependent on the DG's type and connection to the DS. As stated earlier, the converter interfaced DG hardly contributes to the fault current. In the following points, the most critical impacts of DG on system behaviour will be summarized.

2.1.1. Impact of fault ride-through requirements

As the number of DG units connected to DS increases, some grid operators have defined Low Voltage Ride Through (LVRT) capabilities and grid code standards to maintain DGs connected to the grid during fault. Nevertheless, the disconnection of DG during a grid disruption can no longer be ignored, therefore, converter control during grid abnormal conditions becomes essential.

Power converters are designed and controlled to inject power into the grid during normal conditions and support the grid during transient operation by reducing the active power injection and increasing the reactive power injection according to the grid codes [38]. By applying fault ride-through criteria, the DG units must be able to survive the voltage sags without losing stability, so the conventional protective system needs to be modified to guarantee this task [32].

2.1.2. Impact of DG on MV distribution grid protection

Specific requirements have to be defined by the utility if DGs are connected to the grid to ensure the grid's stability. The utility does not generally own DGS, and hence, their protection is the owner or operator's responsibility. In the following, some requirements of the DG protection system are introduced: DG must be protected from utility disturbances, DG units have not to disturb circuits owned by the utility, and DG should support the grid during faults. In addition, the protection system of any DG source has to involve the following devices: under-voltage and overvoltage protection, short-circuit current protection, and frequency protection [39].

DG can have significant impacts on the protection system as follows [40], [41]: DGs may feed faults after protection opens (protection blinding) [42], disturb PDs coordination resulting in coordination loss [43], cause PD speed loss, and unintentional islanding [44], and have a significant impact on the voltage profile, power quality, and power loss [45]. Another significant impact of DG penetration is the change in the power flow direction [46]. This situation was not considered when designing the present DS's protection systems based on radial power flow. Also, the change of fault currents in the DS will affect the proper functioning of the existing protection system [47]. The DG impact will be studied if conventional relays (OCR / DR) are used in the protection system of the grid shown in Fig. 2.1.

- DGs impact on a radial grid

In Fig. 2.1(a), if no DG is connected, and a fault occurs at DL2, then in the case of OCR, PD3 will trip to disconnect DL2, and in the case of DR, both PDs (PD3 and PD4) will trip.

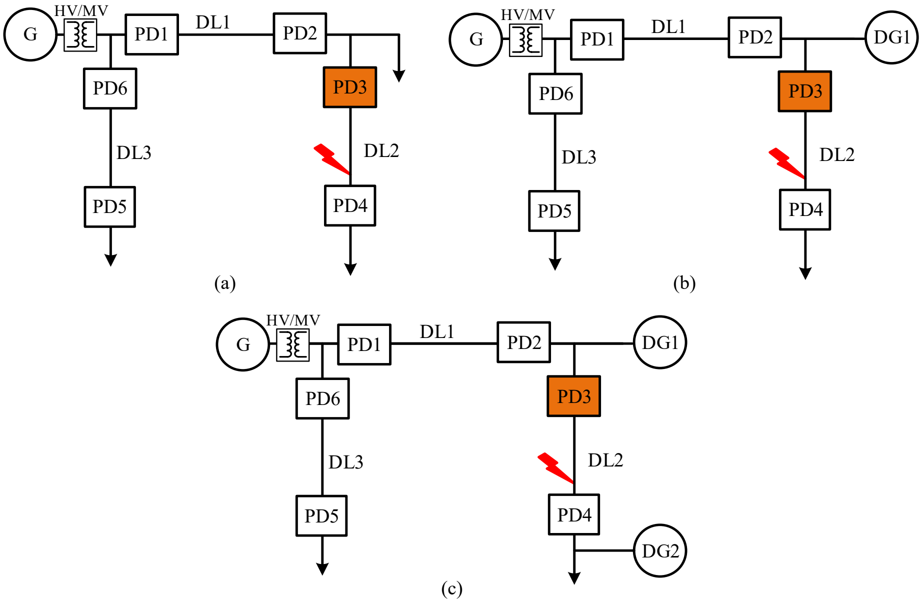

(a) (b) (c)

Fig. 2.1 Radial grid (a) no DG penetration, (b) with one DG, and (c) with two DGs

For the same network, if a DG is added and considered a fault in DL2, as shown in Fig. 2.1(b), the fault current will increase due to the upstream DG unit. In this case, PDs coordination will not be affected, because the short circuit current in DL2 is higher than other lines.

In the network discussed above, DG2 is connected as shown in Fig. 2.1(c). If an OCR is used, PD3 will be disconnected; however, the fault will be supplied from DG2, as PD4 will not trip because the short circuit current is not high to trip the PD4. However, if a DR is used, both PD3 and PD4 will trip without problems.

In the case of single-phase to ground fault, and if the (HV/MV) transformer is connected through a zigzag transformer with grounding impedance, the fault current during single-phase fault will be limited. Therefore, the DR will not trip in this case. However, during a three-phase fault, the fault current will be high in both cases (with and without DGs), this case will be studied in detail in chapter 6 to show the limitation of DR in this case.

- DGs impact on a ring grid

The network discussed above is changed to a ring grid with two DGs connected as shown in Fig. 2.2(a). In this case, for an OCR, PD8 will be disconnected first, then PD7 will trip, as the short-circuit current passing through PD8 is higher than PD7. However, for a DR, both PD7 and PD8 will trip at the same time.

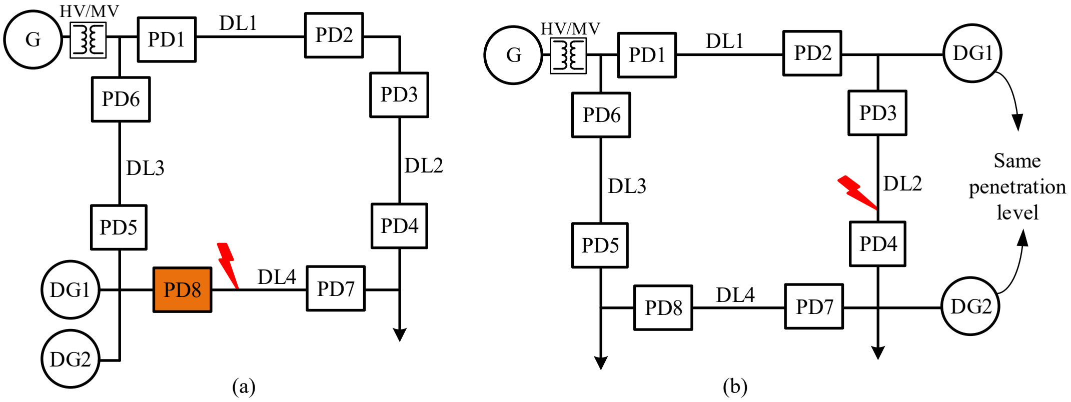

(a) (b)

Fig. 2.2 Ring grid (a) no DG penetration, and (b) with DG penetration

DG penetration can also affect the coordination of the protection. In some cases, if the DG penetration of DG1 and DG2 are approximately equal, as shown in Fig. 2.2(b) when the fault comes from both ends of the lines are approximately the same, conventional relays (OCR / DR) will face problems to disconnect the faulted part of the system, especially in case of weak grids and high DG penetration [32], [48].

When a short-circuit occurs at DL2, and a DG is connected to the ring grid shown in Fig. 2.3, both the grid and the DG unit contribute to the fault current. The current contribution is divided based on network configuration, grid impedance, and the power generated by the DG unit. Due to the DG unit's contribution, the total fault current will increase. However, the grid contribution decreases ($I_{SC1} > I'_{SC1}$), as shown in Fig. 2.3. The DG presence can lead to fault current detection problems. As the penetration of DG changes the value and Direction of the system's Power Flow (DPF) and the fault current, which can lead to poor relay coordination [49].

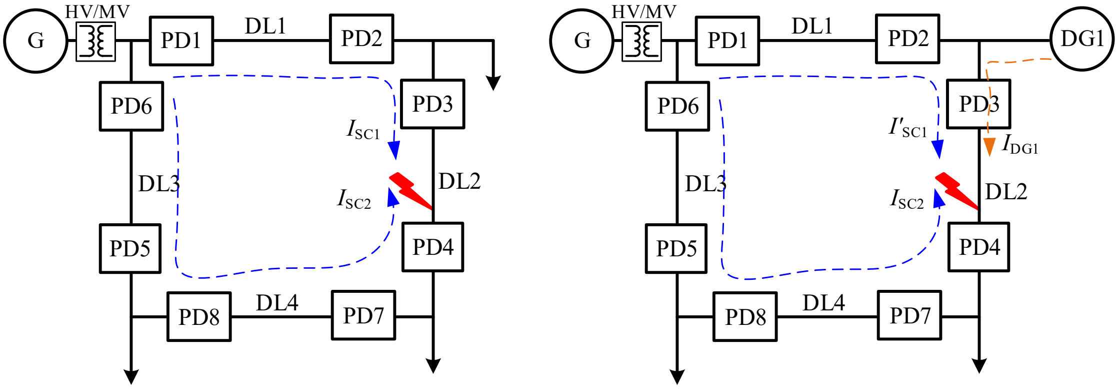

(a) (b)

Fig. 2.3 Short circuit current in case of ring grid (a) without DG (b) with DG penetration during a fault at DL2

2.2. State of the art

In this section, the review is classified into two parts. The first part gives a literature review about the reference current control strategies of VSI during abnormal grid conditions especially voltage sags, and the second part gives a literature review about the protection scheme of MV DS with DG penetration.

2.2.1. State of the art on the reference current control strategies of VSI during grid faults

A literature review is presented to identify the injected current control topologies of DGs during sags due to grid short circuit faults.

The majority of grid faults are unbalanced faults, which degrade the performance of grid-connected converters, significantly impacting grid power quality [50]. Unsymmetrical voltage sags cause grid current peaks and DC-bus voltage fluctuations, since a pulsation of twice the fundamental frequency emerges in both voltages and currents due to the negative-sequence components, causing a ripple in the DC-bus voltage and the injected power to the grid [51], [52]. As a result, negative-sequence currents must be controlled in order to inject more reactive power into the grid during faults and improve grid power quality standards. So, several studies have been published to control the reference current during unbalanced conditions to increase the injected reactive current [38], [53]–[59]. In most of the references, the converter current control is done using *Park* transformation, while in [60] published by the authors of this thesis, *Ku* transformation is used to analyze the converter behaviour during sags in a simple way. The *Ku* transformation offers a clear visual representation of the electrical variables, making it easier to assess the most relevant information about sag depth and type than the *dq* representation, as will be explained in Section 4. Next, the aforementioned references will be discussed.

In [53], [61], a positive- and negative-sequence current control method is proposed to meet the LVRT requirement under unsymmetrical sags employing an instantaneous grid voltage feedforward control; in addition, a rapid voltage sag detecting method is proposed. A similar idea has been discussed in [54] based on unbalanced voltage control of positive and negative sequence components of a large-scale grid-connected PV system. This research was carried out to provide constant active power during sags. A symmetrical component-based generalized power control technique is proposed in [55]; the goal is to control the instantaneous power delivered under unbalanced voltage sags. In [56], [57] during unbalanced grid faults, several methods for injecting reactive current have been investigated. During such transient unbalanced grid conditions, mathematical expressions have been established to set the reactive power limit given by a static compensator. In [38], four reactive power injection control strategies have been analysed to determine how much active and reactive power is delivered to the grid during unbalanced conditions: average active reactive control, balanced positive-sequence control, instantaneous active reactive control, and positive-negative-sequence control, named average active reactive control, balanced positive-sequence control, instantaneous active reactive control, and positive-negative-sequence control. In [58], the same control strategies represented in [38] have been used in order to reduce the DC voltage oscillations and accomplish current limiting control. A couple of reactive power reference values have been calculated for each control strategy to meet the peak current limitation and maximum DC voltage oscillations criteria. The supplied reactive power reference was determined by comparing reference values that accounted for both DC voltage oscillation and peak current limitation.

In [62], PV inverters' performance during unbalanced voltage sags has been investigated using three alternative control algorithms. The use of continuous values for control parameters in a control strategy is presented for variable power quality characteristics. Reference [63] focuses on the impact of grid-connected PV systems on system transient stability. The PV system is usually controlled to keep both active and reactive power at the reference set points. This can be achieved by controlling the inverter using the current reference signals. The PV system may have to be disconnected when its terminal voltage drops below the specified threshold voltage. This reference points out that, the faults ride-through capability of the PV system is significant to the power system transient stability. The PV system operational characteristics have impacted the transient state during the fault and the subsequent steady-state.

Current limiting strategies are used to avoid exceeding the converter's limits; however, careful attention should be paid to avoid obtaining distorted injected current or increasing the transient periods. In [64], a current limiting factor is applied to the reference current, a current limiting technique for inverter-based islanded microgrids (MGs). The drawback of that strategy is that it should be equipped with an instantaneous saturation limit (set to double the inverter rated peak current), which distorts the injected current in some cases due to crest clipping. In [65] instantaneous limiting and latched limiting with a variety of reset mechanisms are investigated for inverter-interfaced generators during and after faults. To limit the fault current, the proposed limiting strategy requires a long transient time, which will result in distorted currents for many periods.

Reference [66] proposes a generalized active power control strategy for DG inverters operating under unbalanced grid faults. Based on derived formulas and graphic representations, the contributions of symmetric-sequence components to the instantaneous power and the interactions between symmetric sequences have been explained in detail. In [67], an adjustable parameter between the reference currents and the grid voltages is introduced, a strategy can control the DC-link ripples, the symmetry of currents, or the power factors in terms of controllable oscillating active and reactive powers. Reference [68] presents a reference generator for three-phase grid-connected inverters operating under unbalanced voltage sags. Two control objectives are simultaneously accomplished: to control the amplitude of the injected currents and to exploit the power capacity of the inverter. Therefore, DG power plants can avoid overcurrent tripping while flexibly helping to mitigate the adverse effects of grid faults. The main contribution is the development of a reference generator either for active or reactive power for any given unbalanced voltage sag. In [69], the transient stability behaviour of the droop-controlled VSC is theoretically explained. In [70], two control strategies for three-phase power electronics interfaced DG systems are proposed to compensate the grid steady-state unbalanced voltage. In the first method, to reduce the adverse effects of compensation on the DGs operation, DGs active power oscillation is minimized in the compensation strategy. In the second method, to effectively reduce the negative-sequence voltage of the grid, DGs negative-sequence current is set to be in phase with the grid negative-sequence current. In [71], a current limiting strategy is proposed to instantaneously limit the injected *abc* current at a pre-defined threshold. However, the current limiting technique needs many calculation steps, besides only limit the *abc* current at the beginning of the sag, not at the start and the end of the sag.

It should be noted that the previous studies do not consider either the limit of the reference currents according to the grid code requirements or the implementation of a control strategy according to such requirements. This is becoming very important nowadays due to the increase in DG systems connected to the grid.

Several researchers discuss the application of grid codes to control converters based on *Park* transformation to derive reference currents using various methods [59], [68], [72]–[77]. For example, in [59], only symmetrical voltage sags were taken into account to meet the Spanish grid code criteria for grid-connected PV power plants. References [68], [72]–[76] take symmetrical and asymmetrical voltage sags into account. In [68], [72], [73] unbalanced currents and fluctuating active power are produced. Reference [78] provides a detailed overview of electrical protection requirements for PV-based DG, from the LV to the HV-EHV level. In addition, the study of national and regional codes that have been suggested and approved in several countries where high PV penetration levels have been achieved. The protection relays and their settings are the subjects of the study. In [74], power injection scenarios have been proposed in two different ways. The first is intended to inject balanced currents; however, both active and reactive powers fluctuate, as mentioned in [76]. The second way seeks to inject consistent active power during sags. However, the injected current is unbalanced and the reactive power oscillates, as mentioned in [75]. In [79], the performance requirements for single- and two-stage grid-connected inverters in grid-connected PV power plants under fault conditions have been addressed. According to the grid codes, modifications have been proposed to control and incorporate the PV power plant ride-through compatible with any type of fault. These modifications include applying current limiters and controlling the DC-link voltage by different methods. In [59], a control system for a PV installation connected to the grid is developed to accomplish the requirements raised in the 2010 draft version of the Spanish grid code P.O. 12.2. The flexibility of the developed control permits its adaptation to future versions and modifications in the grid code. Moreover, the control loops proposed can be implemented in another grid-connected DG. Table 2.1 gives a comparison between various references to differentiate easily between them.

Table 2.1 Comparison between different current control techniques

Grid code fulfill	Current limiting	Experimental verification	Transformation technique	References
Yes	No	No	*Park*	[38]
No	Yes	Yes	*Clarke*	[65]
No	Yes	Yes	*Park*	[64]
Yes	Yes	Yes	*Clarke*	[68]
No	Yes	Yes	*Clarke*	[70]
No	Yes	Yes	*Clarke*	[76]
No	Yes	Yes	*Clarke*	[75]
No	Yes	Yes	*Park*	[69]
Yes	Yes	Yes	*Park*	[74]
Yes	Yes	Yes	*Clarke*	[73]
No	Yes	Yes	*Park*	[71]
Yes	Yes	Yes	*Ku*	[60]

2.2.2. State of the art of the protection schemes of MV DS with DGs penetration

A literature review of the research is presented to identify the protection schemes of MV DS with DGs penetration during grid faults.

Various approaches for locating and detecting faults in DSs with DG have been proposed. As shown in Table 4 of [80], these methods can be divided into two categories: conventional and Artificial Intelligence (AI) techniques. Conventional techniques include the traveling wave method [81], synchronize voltage and current measurement, fundamental frequency method, knowledge-based methods, and impedance-based method. Some of the AI techniques employed for fault location in DSs are [25], [82], [83]: Artificial Neural Network (ANN), Support Vector Machine (SVM), Fuzzy Logic Controller (FLC), Genetic Algorithm (GA), matching approach, Discrete Wavelet Transform (DWT) technique including

Wavelet-Neural networks, Wavelet-Fuzzy and Neuro-Fuzzy. Table 2.2 illustrates different protection techniques from different aspects as the DG connection, the grid configuration the speed of tripping decision.

Table 2.2 Comparison between different protection strategies.

Inverter based	**Grid reconfiguration**	**Experimental verification**	**Trip signal**	**Strategy**	**References**
Yes	Yes	Yes	Very fast	Directional based ANN	Proposed method [37]
Yes	Yes	No	Fast	Linear programming	[110]
Yes	No	Yes	Very fast	Deep learning ANN (DNN)	[111]
Yes	No	No	Moderate	Directional relay	[112]
Yes	No	No	Fast	Discrete wavelet transform (DWT)	[114]
No	No	Yes	Not specified	Support Vector Machine (SVM) and ANN	[113]
No	No	No	Very fast	ANN	[115]
No	No	No	Moderate	communication-based	[116]
No	No	No	Moderate	OCR with DR	[109]

The conventional protection strategies for the DS and the limitations of those techniques are addressed in [84]. These limitations include a change in the power flow, resulting in unpredictable operating times leading to possible coordination loss. In addition, connecting variable DGs to the system will produce variable fault levels, resulting in protection blinding and false tripping. In [85], various DS protection strategies have been proposed to utilize the advantages of DG entirely. The common protection challenges associated with integrating DG into MV DSs were discussed in [86]. A comparison between different fault classification methods has been presented in Table IV of [85]; also, a comparison between artificial intelligence is presented in Table III of [87], and the protection schemes for microgrids are presented in Table IV of [87]. The main focus of conventional relays used in this research will be on OCR and DR protection as they are the most commonly used schemes in distribution protection systems.

- Conventional Protection Strategies

Current research trends indicate that the addition of DG is threatening conventional protection, so the settings and the parameters need to be updated. One of the most common protection systems in DS is overcurrent protection. The relay setting for OCR depends on the fault level that relies on the DG penetration, load consumption, and grid configuration [88]. The inverse time characteristic allows the relay to discriminate between permissible and non-permissible conditions.

Several types of research have been developed to calculate the OCR parameters with DG penetration [89]. Some of them use a microprocessor-based relay without communication as presented in [90]. Another way is to use linear programming with communication as in [91]. Previous studies focus on the non-based inverter DS. In [92], a new communication-assisted OC protection scheme has been proposed for inverter-based microgrids; the algorithm is developed for DC microgrids. The real drawback is that the fault is delayed, resulting in more damage to the faulty equipment and an increased risk of damage to healthy equipment. Reference [93] investigates the impact of PV systems on the coordination between OCRs in a PV-dominated distribution feeder. In [94], [95] the impact of DG on the directional OCR is studied, using the adaptive protection method. However, this process's complexity is high, and a suitable communication medium is needed, especially with grid reconfigurations and DG penetration into DS.

Differential protection is one of the preferred methods of protecting DS, especially with DG penetrations [86], because it solves the issue of bidirectional power flow. The DR merits can be summarized as follows: its operation concept of the internal zone of protection does not require information on the fault currents from the DS analysis [85]. However, providing a backup protection scheme is necessary, as the communication system may fail [96]. A line differential protection uses the differential current between both end lines and compares it to a threshold. However, if the CTs are saturated or their ratios are not matched correctly, the differential signal may assume considerably large values. A second signal called “restraining signal” is created to prevent false trips, which is much higher during external faults than during internal faults. Moreover, with increasing DG penetration, the threshold current also increases, and the sensitivity of the relays is thus decreased. Also, if the contribution of DG comes from one end of the faulted line is approximately equal to the current from the other end, the DR could face tripping problems, especially with weak grids and high DG penetration [48], [97].

Some methods based on signals matching using voltages or currents will be presented. In [98], a novel algorithm based on both sinus matching and differential protection in DS with DG non-based inverter penetration is proposed. The algorithm guarantees the consistency and alacrity required for recovery. However, due to the matching process, the processing of the data needs more time and calculation; in addition, the DR uncertainty in some cases especially with DG penetration as mentioned in the previous paragraph.

Standards’ advent, such as IEC 61850, and Ethernet-based communication capabilities, has evolved traditional protection schemes into new features. Also, using Multi-Agent System (MAS) [99] or wireless networks [100]. A two-terminal pilot channel could be employed to reduce communication costs, and a multi-terminal current differential protection technique is used. Previous studies targeted the DS non-based inverter.

The evolution of a centralized controller with DR is one of the main concepts in smart grids. As in [100] and [101], the concept of a hybrid protection system is presented, which implements traditional differential protection along with adaptive protection via a central controller, for a PV-based inverter system. However, the system was not tested with high PV penetration nor with high fault resistance.

Many researchers propose different techniques to update the settings of conventional relays with DG penetration to solve this issue. In [102], inverse time-current characteristics are provided by dual setting relays. However, these studies did not focus on the PV-based inverter. In [103], the same idea was used with different network reconfigurations, but the reliability evaluation and stability improvement need to be carefully studied.

Adaptive protection enables relays to react to any changes in the DS. However, this process’s complexity is high, and a suitable communication medium is needed, especially with grid reconfigurations and DG penetration into DS. In [104], [105]**,** a two-stage optimization approach has been presented by including automated online readjustment of the relay settings to better suit various DS operating conditions.

One way to rapidly update the relay setting is to use communication, as presented in [106], [107], which employs the current differential principle with an adjusted restrain characteristic to locate the fault. Another idea is based on preprocessing of the faulted current and voltage signals using Fourier transform. In [108], a data-mining-based differential protection scheme is proposed, using discrete Fourier transform to estimate the most affected features during faults.

Differential evolution algorithm (DE) is an effective way to solve the Directional OCR (DOCR) coordination problem, as in [109], [110] an enhanced DE is proposed, and comparisons among different versions of DE are presented. Previous research focuses on non-based inverter DG. However, the protection system’s behaviour during grid reconfigurations has not been studied.

- AI Protection Strategies

Unlike conventional protections, smart protection techniques can locate the fault for any fault resistance or load condition impact, even when the grid could be reconfigured. The implementation of ANN will solve these. Not much research has been done about the behaviour of the protection system with high penetration of DG-based inverter [111]–[116]. The difficulties in determining the fault current and voltage profiles on high penetration of DG-based inverter systems have been discussed in [117]. One trend is to use directional relays to isolate the grid’s faulted part [110]. Another trend is the application of AI techniques. One of these trends is the use of ANNs to locate faults in inverter-based DG networks without PD communications requirements [111]. However, the problems concerning system dynamics have received little attention. MAS has recently been used to coordinate PDs [118]. MAS is also used in conjunction with ANN to locate asymmetrical faults by integrating the fault direction discriminating approach with the communication system [36]. Instead of ANN, a similar concept has been employed with directional relay [110], [119]. A comparison of the aforementioned methods can be found in [33], [34], [87].

Recently, AI techniques have gained more importance in the protection of DS. Mainly because of their ability to operate fast and deal with a large number of inputs. Table 2.3 shows the advantages and disadvantages of the most common techniques. The FLCs used to enhance the current differential protection scheme are presented in [120]. Another way is to use Particle Swarm Optimization (PSO), as in [121], an adaptive protection approach is proposed. Integer Linear Programming (ILP) and PSO are used in this research. One of the most efficient approaches for resolving protection problems consists of ANNs [122]. In [123], a smart differential protection scheme using a nonlinear signal transformation based on ANN is proposed.

Table 2.3 Comparison of AI techniques. [25]

AI techniques	Advantages	Disadvantages
ANN	- Dealing with nonlinearity.	- Results depend on the training quality of the NN. - The parameters such as hidden layers, neurons, and learning rate are identified using trial and error.
SVM	- Faster even for large-size problems. -minimize error bound.	- Performance depends on the choice of kernel function and hyper parameters.
FLC	- Handles uncertainties. - Interpret input/output relationship.	- Determining the global minimum. - Feature definition and extraction have to be enhanced.
GA	- Slow Simulation speed. - Large dimension of possible solutions.	- Not consistent results over time, because almost all processes are random.
Matching approach	- More economical method.	- Dependent on the simulated data for matching with actual data. - Time-consuming process of creating a database.

Considering the studies mentioned above do not focus on DGs-based inverters. Different approaches have recently been developed that take into account the existence of DGs-based inverters. In [124], a centralized algorithm with mixed-integer linear programming is proposed to obtain the relay setting. However, no backup protection is introduced, and the algorithm was not tested experimentally. In [125], a fault detection system using DWT and ANN has been presented. Despite this, the error percentage (6.43%) has to be improved due to the large amount of transient data used to train the ANN. Reference [126] presents a new method for solving the problem of DOCRs coordination in DSs with high penetration of DG, using a hybrid PSO with linear programming (LP) algorithm. Reference [127] uses a combination of Adaptive Network-Based Fuzzy Inference System (ANFIS) and DWT, and this research proposes an accurate technique for finding defects in an MV underground power cable. The suggested method employs five ANFIS networks and is divided into two stages: fault categorization and precise fault location. In [128], [129] a new automated fault location method by using Radial Basis Function Neural Network (RBFNN) for a DS with DGs has been presented to determine the fault location, and two-staged RBFNNs have been developed for locating various fault types. The first RBFNN is used to calculate the fault distance from each power source, while the second RBFNN is utilized to determine the specific location of the faulty line. The third stage RBFNN is also created for fault isolation and determining circuit breakers' open and close states. In [130], a new objective function within the GA approach is presented to solve the coordination of OCRs and distance relays. The existing objective function of OCRs coordination is improved and extended to include the coordination of OCR and distance relays [131]. Various OCRs parameters are considered within the approach to select the best of them by GA for optimal coordination. Two separate power system networks are used to test the proposed strategy. Reference [132] presents an attempt to design an automatic voltage control (AVC) relay based on FLC. The structure of the proposed FLC based-AVC relay is presented, and the results with and without integrated DG into DS are discussed. It has been found that the proposed FLC-based AVC relay has the ability to control the voltage magnitude of DS as load changes. It has also shown that the relay's performance is not affected by the connection of DG, and its setting does not require re-adjustment as DGs are connected to the network.

Another concept is to use MAS with ANN to interact between PDs [36]. The concept focused on integrating the distinguishing method of fault direction with its communication mechanism to identify asymmetric faults. A similar concept was used with the use of a directional relay rather than using ANN. Previous studies give more flexibility to connect DG-based inverters to DS; however, these studies are limited to radial grids.

In [99], micro-grid protection for radial and ring grids is presented using a MAS protection strategy based on a variable differential protection scheme. However, for inverter-based DG with high fault resistance, the protection scheme has not been tested. In [98], a unique approach based on both sine matching and differential protection is proposed, in DS with DG penetration. The algorithm ensures the speed and accuracy required for restoration. However, the protection scheme will take longer to decide when there is a high DG penetration or a high fault resistance.

Many recent studies have concentrated on investigating ring grid protection challenges; for example, in [115], an ANN with PD communication has been proposed, or in [133], directional relays have been studied. In [134], MAS has been used to indicate the faulted part of the grid. Considering the studies mentioned above do not focus on DGs-based inverters.

Different approaches have recently been developed that take into account the presence of DGs-based inverters. In [135], a protection system based on communication is developed according to the IEC61850 communication standard. However, more information has to be provided to analyze the dynamic behaviour and the communication characteristics of the system. In [112], [136], a communication-based DC directional overcurrent protection scheme is employed to isolate the faulted part of the grid for an islanded MVDC. In [137], the investigation of a communicated protection coordination scheme using Wireless Fidelity (Wi-Fi) 's feasibility is presented. However, the Wi-Fi protocol's security and interference proneness need to be considered, followed by the experimental validation.

Previous research has mainly focused on communication, with no solutions provided in the case of poor communication. In [138], high PV penetration protection requirements have been studied. The suggested protection strategy to eliminate the fault relies on communication between overcurrent protections. Only symmetrical faults were shown in the demonstration. As seen in the review, most of the research focuses on the behaviour of the protection schemes, and they aim to improve the system's reliability by adding an artificial intelligence system to the controller instead of the classical control to indicate the type and location of faults.

It can be seen from the aforementioned, the behaviour of the protection system in the case of a ring grid with high DG-based inverter penetration has been analysed in very few studies. In addition, none of the previous studies designed a protective algorithm using an ANN-based communication relay system to locate different types of faults in an MV ring DS, which will ensure a more secure, reliable, and redundant environment for protection. Therefore, the need for a perfect, reliable, and secure method is still in demand.

The proposed ANN can identify and locate the fault using a simple training algorithm, with a minimum number of layers to minimize the training time. The new approach can improve the system's effectiveness, reliability, and accuracy, moreover, for the sudden changes in the grid (addition of new parts, temporary modifications, network reconfiguration due to failures or maintenance) it can simultaneously speed up the response of protection system. The proposed strategy can also be used for the most common neutral connection of the HV/MV transformers. Therefore, the proposed PDs must adapt to the changes introduced by connected DGs to the grid, which implies the possible use of PDs with directional capabilities with several characteristics as rapid reactions, sensitivity, selectivity, and reliability improving DG fault ride through [86]. The proposed protection schemes in this thesis present the characteristics mentioned above for the inverter-based DG using: CE and an ANN-based backup ZO, and LO algorithms.

The use of CE and ZO algorithms, which are modeled and adapted by ANN to automatically coordinate the PD setting and locate the interference on the faulty line, will be explained in this research, depending on changing load consumption conditions, DG penetration, different fault locations, fault types, fault resistance and (HV/MV) transformer configuration. To implement this idea, the communication- and data-processing-based protection system should have a secure, high-speed communication system, wide area measuring devices, and remote control devices. The response of the inverter controller was assessed under grid faults integrating the capabilities of LVRT and the requirements of Spanish grid code. The proposed strategy is based on evaluating CE and ZO algorithm decisions to have a more efficient and consistent process. The CE unit will use network-wide comparison measures to locate the fault location and trip the relevant breakers to isolate the fault. The security and redundancy of the protection system are increased using a second controller working in parallel, and both controllers' decisions will be evaluated. The algorithm is based on peer PDs communicating in the same line and transmitting data to the ZO at each PD [37]. In addition, LO will be used as a backup for CE-ZO algorithms using only the local measurements of each PDs and without communication. The *abc* voltages are used to calculate the positive and negative sequence components required to decide the trip actuation in each PD. The benefits of these approaches are that it has a more secure protection scheme and can be adapted for temporary adjustments in the grid.

In the next chapter, the analysis and modeling of the DS used in this research are presented. Also, the analysis of the short-circuit DS with high PV penetration will be investigated.

3 Medium voltage distribution system construction, modeling, and analysis during faults with DG penetration

In this chapter, the DS components' models and their parameters are presented. Also, the modeling of the PV generator is introduced. Finally, the short-circuit faults with high PV penetration on the analysed MV DS are studied.

3.1. Modeling of DS components

Power systems are usually mathematically constructed in the form of nonlinear, bulk structures, which contain subsystems often not readily identifiable as models. There is no adequate analytical technology to overcome this degree of difficulty, and the number of computational possibilities is too high resulting in unsatisfactory solutions [139]. It is important to mention that the MATLAB™ 2015b SIMULINK platform is used to model the analysed DS. So, the SIMULINK models are adapted to the level of MV DS. The main components used to model the MV DS will be explained in the following points, and the calculation of its parameters will be presented.

- Main grid

Two main grid situations have been studied. First, the main grid is supposed to be a stiff grid, which means that the grid is strong enough to get over any load variation. Second, the system is studied under a weak grid situation. The point is that if the grid is very weak, the DGs do not have enough inertia to overcome any load variation (which will create, in turn, a frequency variation from its steady-state value), but this case is not analysed in this thesis. The model of the three-phase main grid is shown in Fig. 3.1.

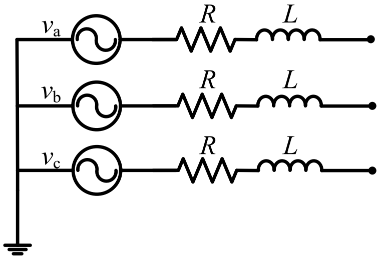

Fig. 3.1 Main grid structure

Internal *R*-*L* impedance in a balanced three-phase voltage source is implemented and linked to a grounded neutral connection (Yg). The source internal resistance and inductance are calculated by specifying the source inductive short-circuit level and *X*/*R* ratio. The grid base phase-to-phase voltage is 66 kV with a 50 Hz frequency. The grid voltage is reduced to the voltage of the MV grid (20 kV) through an HV/MV YNd11 connected transformer [140]. The internal inductance *L* is computed from the three-phase short-circuit power S_{sc}, which equals 3600 MVA as follows:

$$L = \frac{V_{\text{base}}^2}{S_{\text{SC}}} . \frac{1}{2\pi f} = \frac{\left(66 * 10^3\right)^2}{3600 * 10^6} . \frac{1}{2\pi(50)} = 3.9 \text{ mH}. \tag{1}$$

The internal resistance R is computed from the source reactance *X*, and *X*/*R* ratio as follows:

$$R = \frac{X}{\left(\frac{X}{R}\right)} = \frac{2\pi * 50 * 0.0039}{(7)} = 0.175\ \Omega. \tag{2}$$

The base values for the MV side were obtained as the following:

$$V_{\text{Base}} = 20\text{ kV},\ S_{\text{Base}} = 25\text{ MVA},\ I_{\text{Base}} = \frac{S_{\text{Base}}}{\sqrt{3}\cdot V_{\text{Base}}} = 721.69\text{ A},\ Z_{\text{Base}} = \frac{V_{\text{Base}}}{\sqrt{3}\cdot I_{\text{Base}}} = 16\ \Omega. \tag{3}$$

- Power transformers

The main grid is connected to the DS through an HV/MV three-phase transformer to reduce the 66 kV (primary side) until the level of the DS voltage's which is 20 kV (secondary side), the rated power of the transformer is 25 MVA. The MV transformer connection is YNd11. Table 3.1 shows the connection scheme and vector representation of YNd11 transformer configuration.

Table 3.1 YNd11 connection schemes and vector representation

Connection index	**Connection group**	**Vector diagram**		**Connection schemes**		**Transformer ratio**
		High voltage	Low voltage	High voltage	Low voltage	
11	Yd11	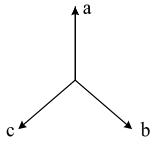	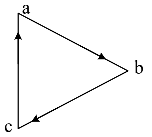	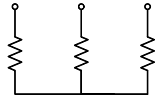	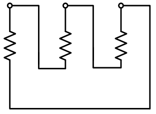	$\sqrt{3}\frac{n_1}{n_2}$

The three-phase transformer consists of three linear transformers, its model is shown in Fig. 3.2 and consists of three windings that are connected and wound on the same core, where R_1 and L_1 are the resistance and the inductance of the primary winding respectively, R_2, and L_2 are the parameters of the secondary winding, and R_m and L_m are the magnetization resistance and the inductance respectively.

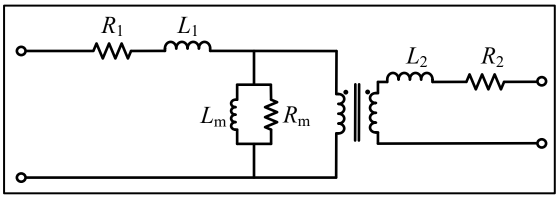

Fig. 3.2 Equivalent single-phase circuit of the linear HV/MV transformer

Another aspect that must be considered is the ground connection of the (HV/MV) transformer because this connection will affect the short circuit current, which will lead to a change in the protection system behaviour. According to several connections obtained from several companies, different connections have been studied in this research [141]. In this research, two connections are considered. The most common connection used is to connect a zigzag transformer to the neutral of the delta side of the MV transformer (YNd11 grounded thorough zigzag) as shown at Bus 1 in Fig. 3.3 [141], [142], which will be explained further in the next point. The other connection is (YNyn), and its neutral is connected directly to the ground; some cases have been studied using this connection; however, the main concern is to study the (YNd11) transformer connection grounded through a zigzag transformer.

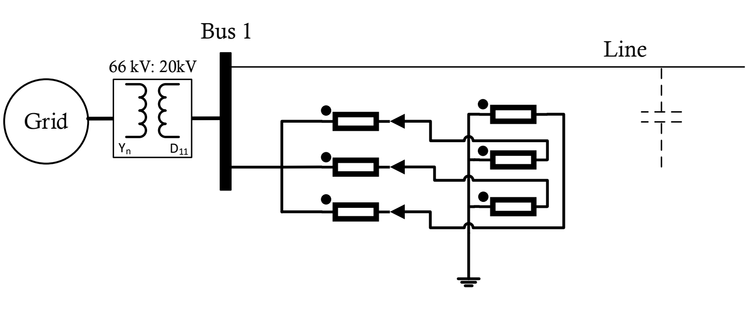

Fig. 3.3 Zigzag connection at the secondary of the (HV/MV) transformer [141], [142]

For the low voltage side transformer (MV/LV), the connection for all the loads and DGs connected to the grid must be delta star grounded on the low voltage side (Dyg11), as shown in Table 3.2 [143]. The three-phase transformer, 20/0.4 kV, 2 MVA, is used to connect loads and PV generation units.

Table 3.2 Dyg11 connection schemes and vector representation

Connection index	**Connection group**	**Vector diagram**		**Connection schemes**		**Transformer ratio**
		High voltage	Low voltage	High voltage	Low voltage	
11	Dy11	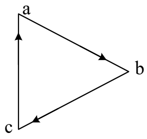	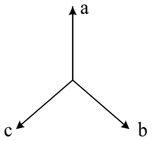	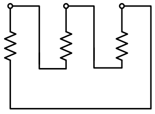	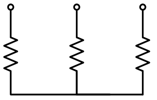	$\frac{1}{\sqrt{3}}\frac{n_1}{n_2}$

- Zigzag transformer

The grounding transformer offers a low impedance in zero-sequence while maintaining a very high impedance to positive and negative-sequence due to the zig-zag connection and the opposite winding polarities of upper and lower windings. Therefore, only a zero-sequence current can flow through the three windings, as seen in Fig. 3.4 [144].

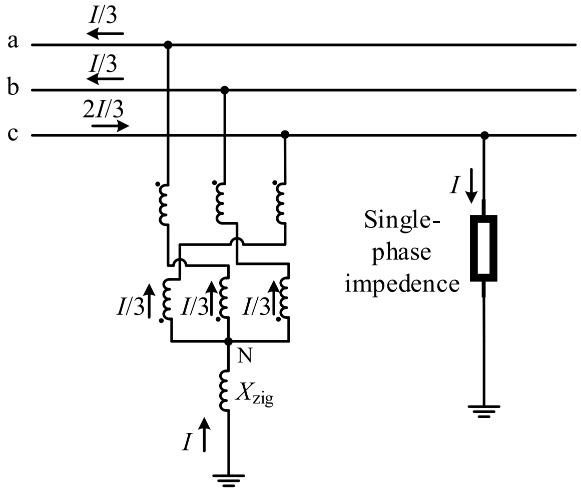

Fig. 3.4 Zigzag transformer connection

The zigzag impedance (X_{zig}) calculation for a fault current (I_f) = 500 A, is obtained using the following equations:

$$X_{\text{zigzag\_real}} = \frac{V_{\text{base}_{\text{ph}}}}{I_f/3} = \frac{20000/\sqrt{3}}{500/3} = 69.282\ \Omega. \tag{4}$$

- Distribution lines

The DL of the MV DS is assumed to be modeled as a PI section of underground cables and without three-phase conductor couplings, as shown in Fig. 3.5. The values of the DL are obtained from [145] to be equal to MV grid lines, as shown in Table 3.2.

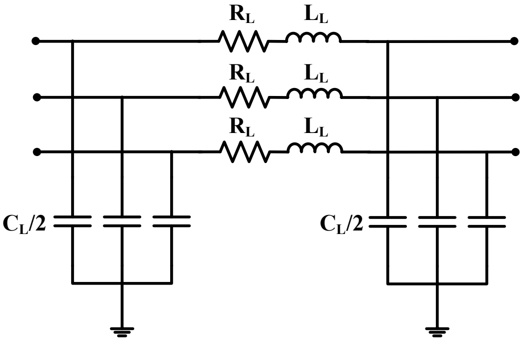

Fig. 3.5 Distribution line model

Positive- and zero-sequence parameters are used to specify the parameters of the line R_L, L_L, and C_L. The positive- and zero-sequence of the RLC parameters are used to obtain the self-resistance and inductance of the three coupled inductors (R_L, L_L), respectively, besides the phase capacitance (C_L), as follows:

$$R_1 = r_1 * l_{sec},\ L_1 = l_1 * l_{sec},\ C_1 = c_1 * l_{sec},\ R_0 = r_0 * l_{sec},\ L_0 = l_0 * l_{sec},\ C_0 = c_0 * l_{sec}, \tag{5}$$

where r_1, l_1, and c_1 are positive resistance, inductance, and capacitance per unit length, respectively. Also, r_0, l_0, and c_0 are the zero-sequence resistance, inductance, and capacitance per unit length, besides, l_{sec} is the line section length (km).

The RLC line section parameters are then computed as follows:

$$\begin{gathered} R_L = \frac{(2R_1 + R_0)}{3},\ L_L = \frac{(2L_1 + L_0)}{3},\ C_L = C_1 \\ R_L = 0.16\ \Omega/\text{km},\ L_L = 0.34696\ \text{mH}/\text{km},\ C_L = 0.309\ \mu\text{F}/\text{km}. \end{gathered} \tag{6}$$

In order to calculate the pu values of the resistance, inductance, and capacitance of the DL, the SI values are divided by the impedance base value of the grid, as follow:

- The line resistance is 0.32 Ω, for 2 km, and the base value is 16 Ω. Therefore, the pu value is $R_{pu} = \frac{0.32}{Z_{Base} = 16} = 0.02$
- The line inductance is 0.34696 mH. So, $X_L = 0.218\ \Omega$ for 2 km, and the base value of the real grid is 16 Ω. So, the pu value is $X_{Lpu} = \frac{0.218}{16} = 0.0136$
- The line capacitance is 0.309 µF, So, $X_C = 10.301\ \text{k}\Omega$ for 2 km, and the base value of the real grid is 16 Ω. Therefore, the pu value is $X_{Cpu} = \frac{10301}{16} = 643.8307$

➢ Fault modeling

Three breakers that can be separately switched to program all forms of faults. They can be used to represent a single-phase fault (phase-to-ground), two-phase fault, two-phase-to-ground fault, or three-phase fault, ground connected or isolated, as shown in Fig. 3.6.

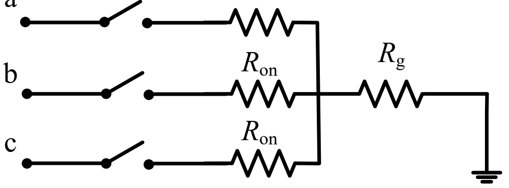

Fig. 3.6 three-phase fault modeling

The fault resistance (R_{on}) can be set from a very small (few milliohms) to a very large value (multiple of ohms), but not equal to zero. Also, the ground resistance (R_g) could be a small value if the fault is connected to the ground, or a very high value if the fault is isolated from the ground.

- Instrument transformers (current and voltage transformers)

Instrument transformers obtain voltage and current measurements and optimize the distribution level signals to suitable lower-level signals convenient for relay use. In order to measure the instantaneous voltages and currents of each phase, voltage transducer (VT) and current transducer (CT) are used. Fig. 3.7 gives an example of the connection of a star-connected three-phase CT set to the PD. In the proposed (CE-ZO) protection algorithms, the values are used directly without CT ratio, as these methods are not sensitive for the *abc* values and can function in both high or reduced levels. However, with the LO algorithm and with conventional protections (OCR and DR) CTs are used, because these methods depend on the level of the *abc* values. On the other hand, by changing the desired *abc* values, any protection algorithm can be quickly, easily, correctly adapted, and implemented.

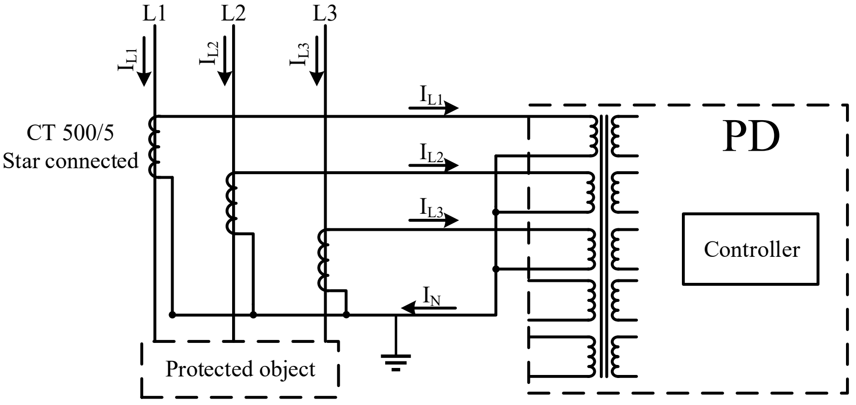

Fig. 3.7 Star connected three-phase CT set

- Grid-connected PV System Modeling

The most common equivalent circuit for a solar cell is a current source parallel with one or two diodes. A single-diode form of PV cell model is shown in Fig. 3.8(a), including four components: an "I_{ph}" photocurrent source, a parallel source diode, an "R_s" series resistor, an "R_{sh}" shunt resistor [146].

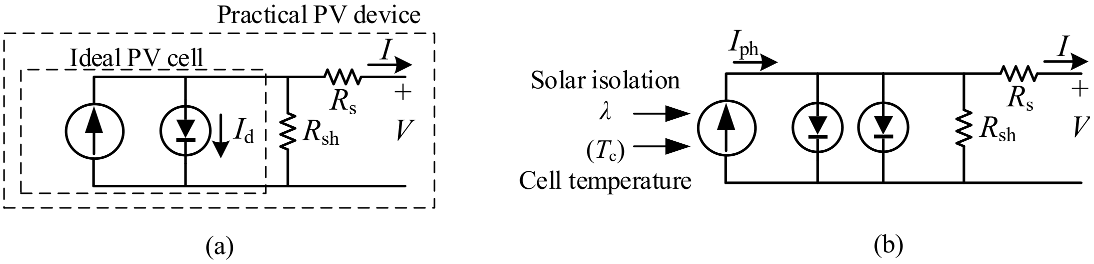

(a) (b)

Fig. 3.8 Equivalent circuit of a practical PV device including the series and parallel resistances, (a) with a single-diode model, (b) of Double exponential model [146]

A solar cell exposed to light generates "I_{ph}" DC that linearly depends on solar irradiance. In general, the PV efficiency is insensitive to variation in R_{Sh} and it can be assumed that the shunt-leakage resistance approaches infinity without leakage current to ground, and some authors [147] propose to neglect this resistance to simplify the model. On the other hand, due to the current flow, a slight variation in R_S would significantly affect the PV output capacity [146]. The value of R_S is very low, and sometimes, this parameter is neglected too. According to (7), the light generated current, apart from directly depending on solar irradiation, it is also influenced by temperature [148]:

$$I_{\text{PV}} = \left(I_{\text{PV,n}} + \text{K}_1 \Delta T\right)\frac{G}{G_{\text{n}}}, \tag{7}$$

where: $I_{\text{pv,n}}$ [A] is the light-generated current at the nominal condition (25ºC and 1000W/m^2), K$_1$ is the short-circuit current coefficient, $\Delta T = T - T_{\text{n}}$ (being T and T_{n} the actual and nominal temperatures [K]), G [W/m^2] is the irradiation on the panel surface, and G_{n} is the nominal irradiation.

As illustrated in Fig. 3.8(b), a second diode may also be included in the PV equivalent circuit, as it provides an even better curve fitting of the I-V curve, which represents a difference in current flow at low current values due to recombination charges in the depletion region of the semiconductor.

I-V curve is changing according to the solar irradiation and temperature, solar irradiance (W/m^2) is directly proportional to the PV module photocurrent (A) with a small variation of the PV cell voltage (V). Fig. 3.9 depicts sun irradiance and temperature influences on the I-V Curve.

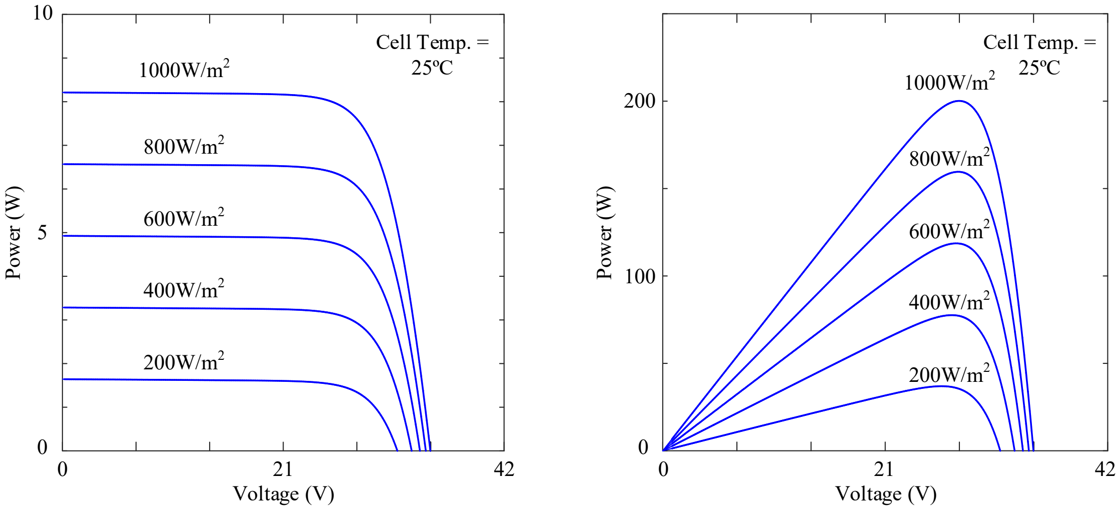

(a) (b)

Fig. 3.9 PV characteristic influence of the ambient irradiation (a) I-V curve (b) P-V curve

The characteristic of the solar cell I-V is nonlinear and varies with irradiation and temperature. The Maximum Power Point (MPP) is a unique point on the I-V or P-V curve when the entire PV system (array, converter, and so on) operates at maximum efficiency and provides maximum output. Calculation models and search algorithms can both be used to find the MPP's location. As a result, measures such as Maximum Power Point Tracking (MPPT) are required to keep the PV array's operating point at its MPP (Appendix H). Various algorithms can be used to achieve automatic tracking [149], [150].

In this research, the PV model has been simplified to a constant current source in the analysis of the protection system, in order to simplify the system and reduce the total calculation time of the simulated cases. Besides, during the fault (voltage sag), the weather condition is supposed to be constant.

The structure of the DG grid-connected converter may be single or multiple stages. A multiple-stage topology has been considered that consists of PV arrays, DC/DC converter to adapt the PV voltage to the input of the inverter, three-phase inverter, RL filter, and (MV/LV) transformer, as shown in Fig. 3.10. On the other hand, single-stage topology does not contain DC/DC converter, as the DC voltage of the PV array is converted directly to AC using inverters [151].

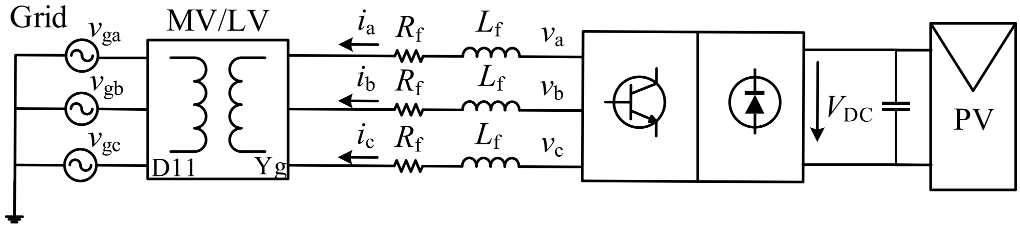

Fig. 3.10 General scheme of a three-phase grid-connected inverter supplied by PV

- Analysed DS complete grid

In this research, the IEEE 9-bus standard is modified and adapted to an electrical ring and can be changed to operate as a radial DS, where the system includes a single main grid and several DGs connected to different buses. Table 3.3 shows the load values at each bus; the presented values are examples of the most used load values, as in order to verify the system, different load consumptions have been used. Table 3.4 shows the system parameters for (main grid, HV/MV Transformer, zig-zag transformer, DL, MV/LV transformer, loads, and DG). The analysed ring and radial grids with the maximum number of buses are shown in Fig. 3.11(a), and Fig. 3.11(b), respectively. Nevertheless, these two grids are used with different configurations (fewer buses, different HV/MV connections, fewer DLs, different DG connection points, and variable DG penetration).

Table 3.3 Load values at the end of each line

Loads	**Line 1**	**Line 2**	**Line 3**	**Line 4**	**Line 5**
Active Power	4.5 MW	1.8 MW	7.2 MW	0.9 MW	3.6 MW
Reactive Power	2.18 MW	0.87 MW	3.49 MW	0.4359 MW	1.74 MW
Resistance	72 Ω	180 Ω	45 Ω	360 Ω	90.1 Ω
Inductance	0.11 H	0.28 H	0.69	0.56 H	0.139 H

Table 3.4 Grid parameters

Main grid	Rated voltage: 66 kV, Short circuit power: 3600 MVA
HV/MV Transformer (YNd11)	Rated power: 25 MVA. Rated voltage: 66/20 kV. Ucc (%): 11. Windings (1, 2) parameters (resistance/leakage inductance): 0.0018 pu/ 0.055 pu.
Zig-zag	Grounding reactance: 69.282 Ω, Single-phase fault current: 500 A
Distribution line (DL)	Resistance: 0.16 Ω/km. Reactance: 0.109 Ω/km. Capacitance: 0.309 µF/km. Line length: 2km.
MV/LV Transformer (Dyn11)	Rated power: 2 MVA. Rated voltages: 20/0.4 kV. Ucc (%): 4.5. Windings (1, 2) parameters (resistance/leakage inductance): 0.00075 pu/ 0.0225 pu.
DG	Rated power: 2 MVA. Rated voltage: 400 V.

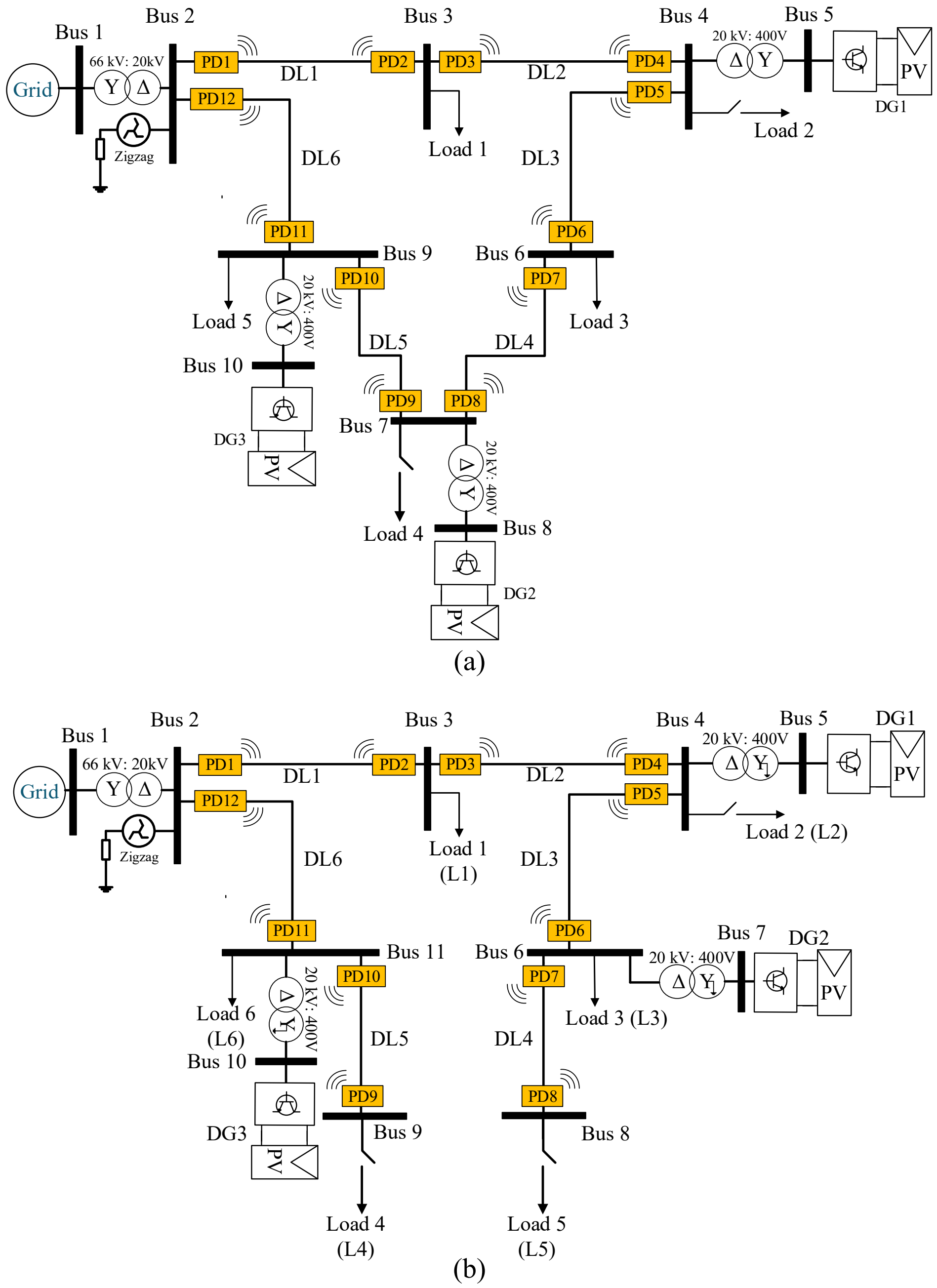
Bus 1
Bus 2
Bus 3
Bus 4
Bus 5
Grid
66 kV: 20kV
Y
Δ
Zigzag
PD1
PD2
PD3
PD4
PD5
PD6
PD7
PD8
PD9
PD10
PD11
PD12
DL1
DL2
DL3
DL4
DL5
DL6
20 kV: 400V
PV
DG1
Load 1
Load 2
Load 3
Load 4
Load 5
Bus 6
Bus 7
Bus 8
Bus 9
Bus 10
DG2
DG3
(a)
Bus 11
Load 1 (L1)
Load 2 (L2)
Load 3 (L3)
Load 4 (L4)
Load 5 (L5)
Load 6 (L6)
(b)

Fig. 3.11 Single line diagram of the analysed DS with DG penetration (a) ring grid, (b) radial grid

3.2. Analysis of PV penetration impact on the DS behaviour

In this section, the analysed ring grid will be studied with different PV penetration to demonstrate the impact of the DG on the analysed grid, and the possibility to use this grid as an MV DS to show the issues of high DG penetration in these types of networks. Moreover, to use the analysed ring grid as a platform to prove the functionality of the proposed protection algorithms.

The literature review shows that most authors use transient values to identify the fault type and location. In this research, the steady-state values of the voltages and currents will be used as inputs to the fault identifier and localizer schemes. Which provide a benefit to simplify the control algorithm to be used in different grids without the need to adjust the algorithm for each grid, in advance, enhance the reliability, as other methods that depend on harmonics, for example, will face problems in the dynamic behaviour study of the system, especially in sophisticated grids with high DG-based inverter penetration. Moreover, the difference of the RMS value between transient and steady-state is slight, as illustrated in Fig. 3.12**,** using a normal case with one DG connected as bus 4 as shown in Fig. 3.11.

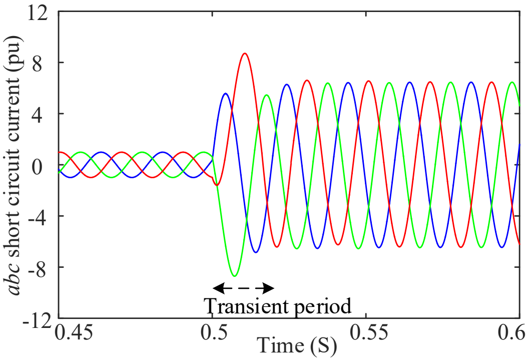

Fig. 3.12 Transient period of the *abc* current during symmetrical fault

It is important to note that, in a DG-based inverter, the transient period is shorter and the short circuit currents are not high so that this study will concentrate on the system's steady-state behaviour during the fault period [152].

DG location and penetration in DS affect the Direction of the Power Flow (DPF). This change in the DPF will have a significant impact on the behaviour of the protection systems. The demonstration of DG impact on DPF in ring and radial grid can be seen in Appendix B. Fig. 3.13 shows the DPF in the case of ring grid with and without DG penetration for a specific value of the loads and DGs.

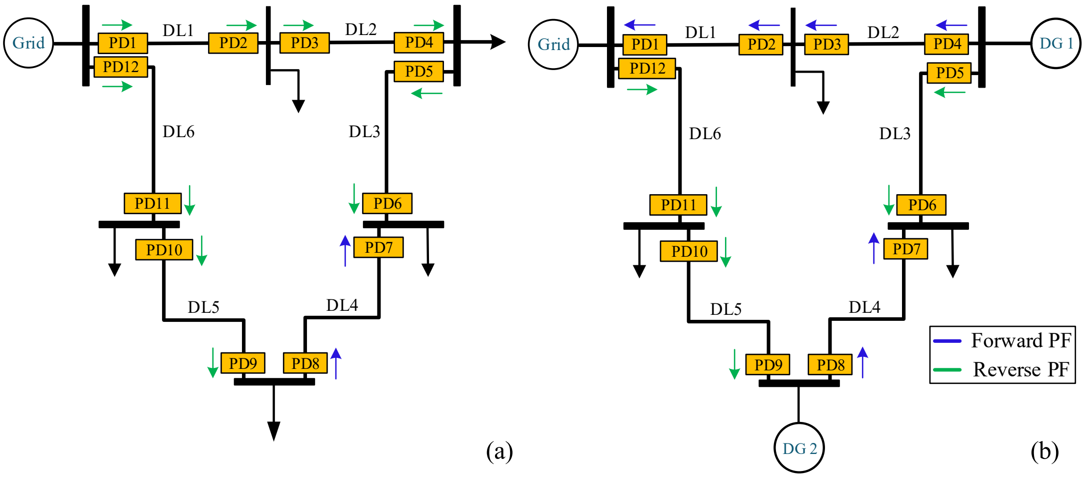

Fig. 3.13 DPF in the analysed ring grid (a) no DG (b) with DG

The values of short-circuit currents without DG penetration and with high DG penetration will change significantly, which will affect the settings of the protection system. When a short-circuit occurs at the indicated location in Fig. 3.15, both the grid and the DG unit contribute to the fault current. Fault current increases due to the DG unit's contribution, and its value depends on network configuration, grid impedances, and DG-generated power. However, the grid contribution decreases, as shown in Fig. 3.15, with fault resistance $r = 1\ \Omega$. For example, when a symmetrical fault occurs at DL4 as shown in Fig. 3.16 with fault resistance $r = 0.1\ \Omega$, the short-circuit current through PD7 increases from 3923 A without DG to 4071 A with DG. This can lead to poor relay coordination [49]. As discussed in the literature, the penetration of DG changes the value and direction of the system's power flow (DPF) and the fault current as shown in Fig. 3.14, which leads to the miss-coordination of the relays [110], [133]. Also, Table 3.5 gives an example when two DGs connected at buses 3, and 6 as shown in Fig. 3.14; in this case, the penetration of DG will affect the short-circuit current.

Table 3.5 short circuit current during three-phase fault at DL4 with and without DG penetration.

DG penetration (MVA)			Grid current (pu)	DL1 current (pu)	DL2 current (pu)	DL3 current (pu)	DL4 current (pu)	DL5 current (pu)	DL6 current (pu)
DG 1	DG 2	DG 3							
0	0	0	I_{Grid}=5.1	I_{PD1}= I_{PD2}=1.7	I_{PD3}= I_{PD4}=1.7	I_{PD5}= I_{PD6}=1.7	I_{PD7}=1.7 I_{PD8}=3.3	I_{PD9}= I_{PD10}=3.4	I_{PD11}= I_{PD12}=3.4
6	0	6	I_{Grid}=4.8	I_{PD1}= I_{PD2}=1.6	I_{PD3}= I_{PD4}=1.6	I_{PD5}= I_{PD6}=2.1	I_{PD7}=2 I_{PD8}=3.8	I_{PD9}= I_{PD10}=3.9	I_{PD11}= I_{PD12}=3.2

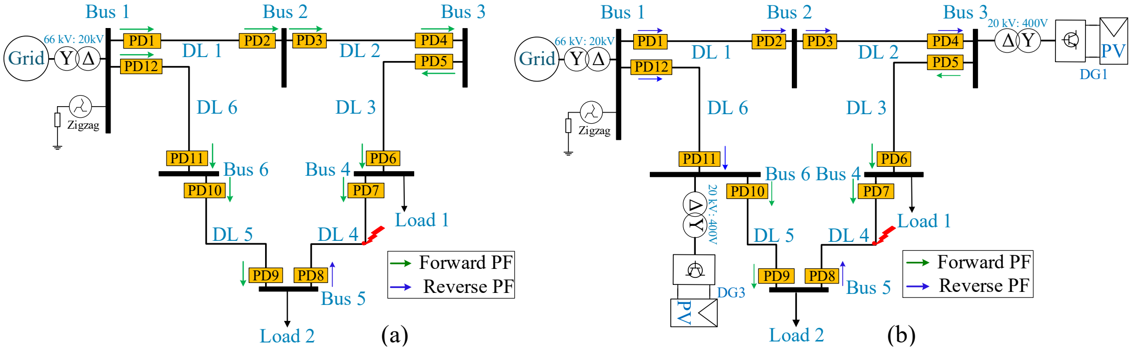
Bus 1
Bus 2
Bus 3
Grid
66 kV: 20kV
Zigzag
PD1
PD2
PD3
PD4
PD5
PD6
PD7
PD8
PD9
PD10
PD11
PD12
DL 1
DL 2
DL 3
DL 4
DL 5
DL 6
Bus 4
Bus 5
Bus 6
Load 1
Load 2
Forward PF
Reverse PF
20 kV: 400V
PV
DG1
DG3
20 kV: 400V
(a)
(b)

Fig. 3.14 Single line diagram of the analysed grid during a fault in DL4 (a) power flow without DG (b) power flow with DG

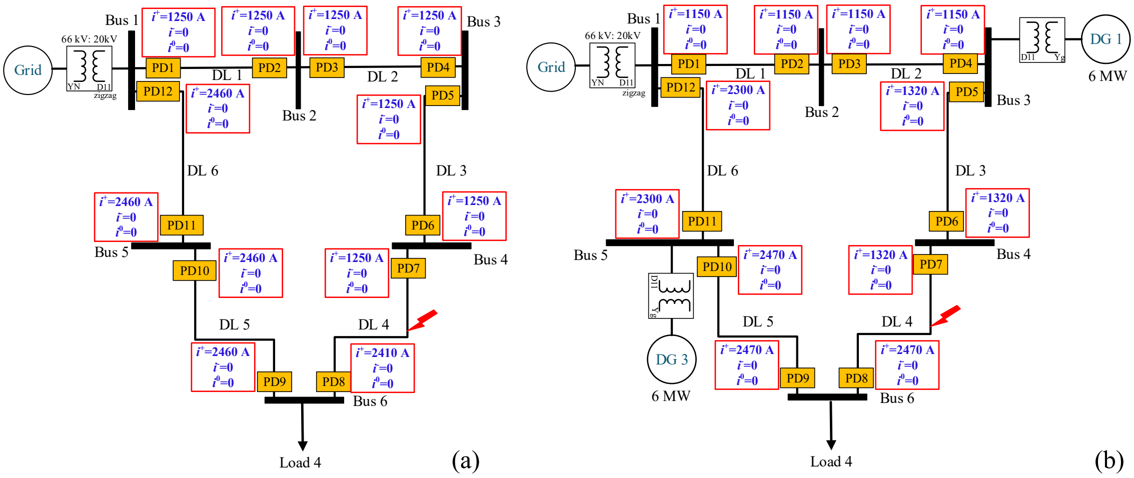
Grid
66 kV: 20kV
YN
D11
zigzag
Bus 1
Bus 2
Bus 3
Bus 4
Bus 5
Bus 6
PD1
PD2
PD3
PD4
PD5
PD6
PD7
PD8
PD9
PD10
PD11
PD12
DL 1
DL 2
DL 3
DL 4
DL 5
DL 6
i⁺=1250 A
i⁻=0
i⁰=0
i⁺=2460 A
i⁺=2410 A
Load 4
(a)
i⁺=1150 A
i⁺=2300 A
i⁺=1320 A
i⁺=2470 A
DG 1
6 MW
D11
Yg
DG 3
6 MW
(b)

Fig. 3.15 Short-circuit currents during three-phase fault at DL4, with fault resistance r = 1 Ω (a) without DG (b) with DG penetration

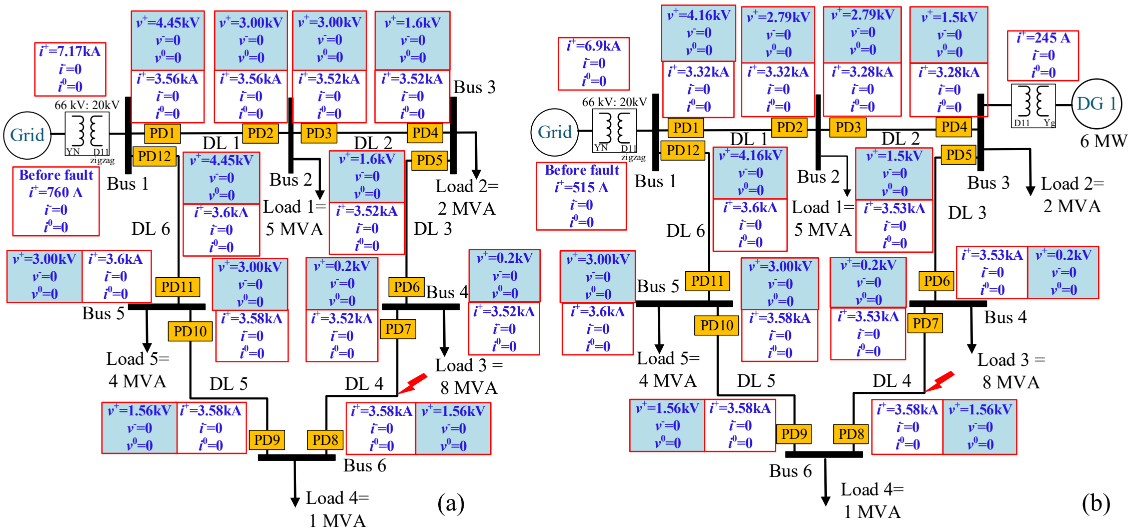
Grid
66 kV: 20kV
YN D11 zigzag
Before fault i⁺=760 A i⁻=0 i⁰=0
i⁺=7.17kA i⁻=0 i⁰=0
v⁺=4.45kV v⁻=0 v⁰=0
v⁺=3.00kV v⁻=0 v⁰=0
v⁺=1.6kV v⁻=0 v⁰=0
i⁺=3.56kA i⁻=0 i⁰=0
i⁺=3.52kA i⁻=0 i⁰=0
i⁺=3.6kA i⁻=0 i⁰=0
i⁺=3.58kA i⁻=0 i⁰=0
v⁺=0.2kV v⁻=0 v⁰=0
v⁺=1.56kV v⁻=0 v⁰=0
PD1 PD2 PD3 PD4 PD5 PD6 PD7 PD8 PD9 PD10 PD11 PD12
DL 1 DL 2 DL 3 DL 4 DL 5 DL 6
Bus 1 Bus 2 Bus 3 Bus 4 Bus 5 Bus 6
Load 1= 5 MVA
Load 2= 2 MVA
Load 3 = 8 MVA
Load 4= 1 MVA
Load 5= 4 MVA
(a)
Before fault i⁺=515 A i⁻=0 i⁰=0
i⁺=6.9kA i⁻=0 i⁰=0
v⁺=4.16kV v⁻=0 v⁰=0
v⁺=2.79kV v⁻=0 v⁰=0
v⁺=1.5kV v⁻=0 v⁰=0
i⁺=3.32kA i⁻=0 i⁰=0
i⁺=3.28kA i⁻=0 i⁰=0
i⁺=3.53kA i⁻=0 i⁰=0
i⁺=245 A i⁻=0 i⁰=0
D11 Yg
DG 1
6 MW
(b)

Fig. 3.16 Short-circuit currents during three-phase fault at DL4, with $r = 0.1\ \Omega$ (a) without DG (b) with DG penetration

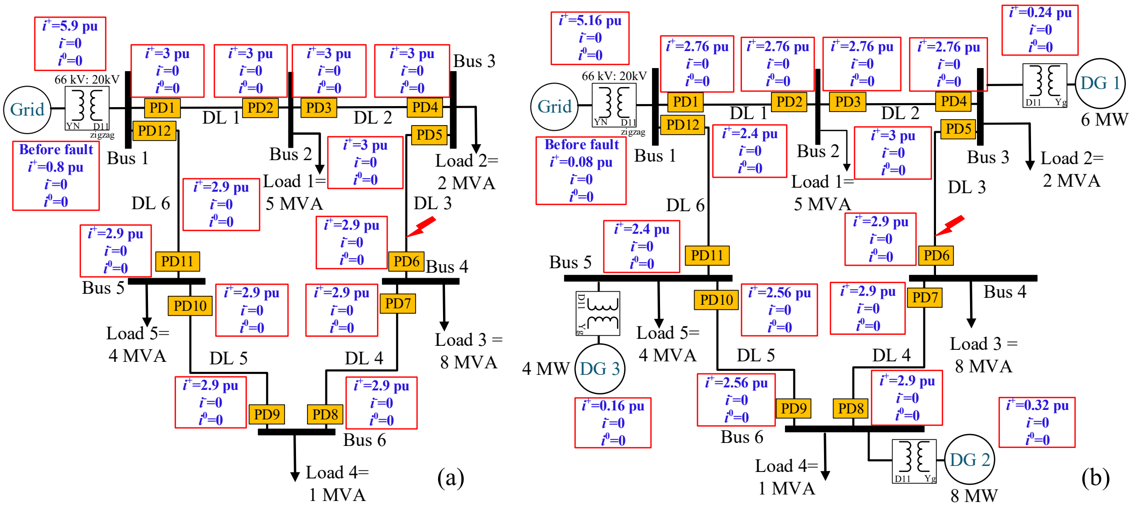
Grid
66 kV: 20kV
YN D11 zigzag
Before fault i⁺=0.8 pu i⁻=0 i⁰=0
i⁺=5.9 pu i⁻=0 i⁰=0
i⁺=3 pu i⁻=0 i⁰=0
i⁺=2.9 pu i⁻=0 i⁰=0
PD1 PD2 PD3 PD4 PD5 PD6 PD7 PD8 PD9 PD10 PD11 PD12
DL 1 DL 2 DL 3 DL 4 DL 5 DL 6
Bus 1 Bus 2 Bus 3 Bus 4 Bus 5 Bus 6
Load 1= 5 MVA
Load 2= 2 MVA
Load 3 = 8 MVA
Load 4= 1 MVA
Load 5= 4 MVA
(a)
Before fault i⁺=0.08 pu i⁻=0 i⁰=0
i⁺=5.16 pu i⁻=0 i⁰=0
i⁺=2.76 pu i⁻=0 i⁰=0
i⁺=2.4 pu i⁻=0 i⁰=0
i⁺=2.56 pu i⁻=0 i⁰=0
i⁺=0.24 pu i⁻=0 i⁰=0
i⁺=0.16 pu i⁻=0 i⁰=0
i⁺=0.32 pu i⁻=0 i⁰=0
DG 1 6 MW
DG 2 8 MW
DG 3 4 MW
D11 Yg
(b)

Fig. 3.17 Short-circuit currents during three-phase fault at DL3, with $r = 0.1\ \Omega$ (a) without DG (b) with DG penetration

Fig. 3.17 shows the pu values of the positive sequence current in all the DLs in the grid with and without DGs. The total number of loads consumption in the grid is 20 MVAR, and the maximum DG penetration is 18 MW. In case of steady-state and no DG penetration, the main grid delivers 0.8 pu to supply the loads (Fig. 3.17(a)); however, in case of DG penetration, the grid delivers 0.08 pu as the rest of the power consumption is supplied by the DGs (Fig. 3.17(b)). In the case of a three-phase fault at DL3, the grid penetration is reduced from 5.9 pu without DG to 5.16 pu with DG penetration.

In order to illustrate the effect of DG penetration on the analysed distribution grid, the values of positive, negative, and zero sequence voltages and currents are presented with and without DG penetration. The behaviour has shown during single-phase to ground fault (Fig. 3.18), two-phase to ground fault (Fig. 3.19), two-phase fault (Fig. 3.20). In the case of single-phase faults, the short-circuit current values do not increase significantly as the zigzag grounding transformer limits the fault current in this case. However, as shown in the rest of the figures, considering other types of faults, the short-circuit current varies depending on the amount of PV penetration into the DS. More results can be seen in Appendix A.

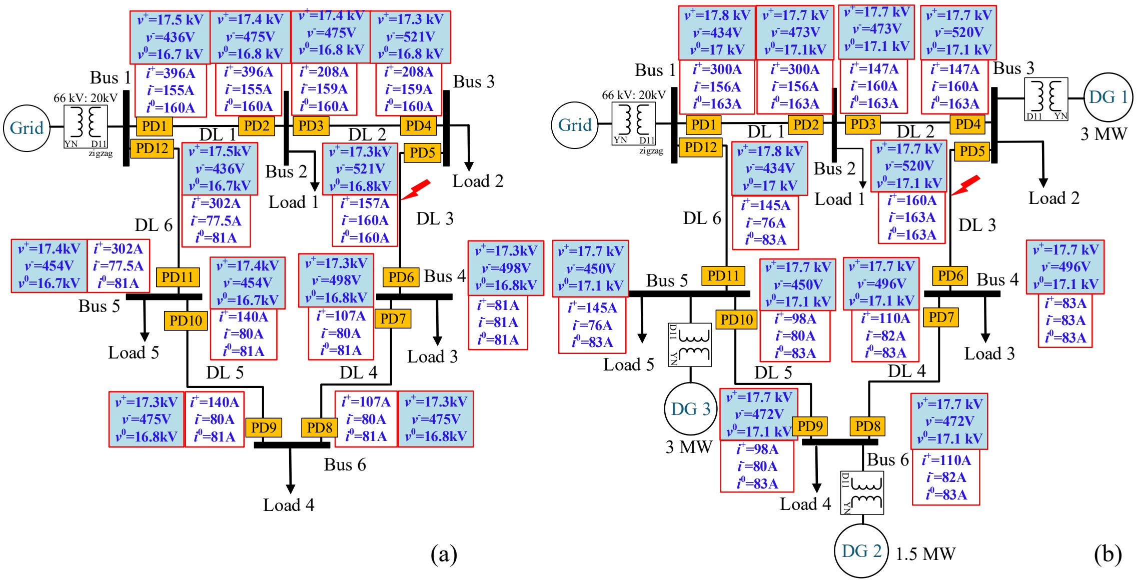
v^{+}=17.5 kV v^{-}=436V v^{0}=16.7 kV
v^{+}=17.4 kV v^{-}=475V v^{0}=16.8 kV
v^{+}=17.4 kV v^{-}=475V v^{0}=16.8 kV
v^{+}=17.3 kV v^{-}=521V v^{0}=16.8 kV
i^{+}=396A i^{-}=155A i^{0}=160A
i^{+}=396A i^{-}=155A i^{0}=160A
i^{+}=208A i^{-}=159A i^{0}=160A
i^{+}=208A i^{-}=159A i^{0}=160A
Bus 1
66 kV: 20kV
Grid
YN D11 zigzag
PD1
DL 1
PD2
PD3
DL 2
PD4
Bus 3
PD12
v^{+}=17.5kV v^{-}=436V v^{0}=16.7kV
Bus 2
v^{+}=17.3kV v^{-}=521V v^{0}=16.8kV
PD5
Load 2
Load 1
i^{+}=302A i^{-}=77.5A i^{0}=81A
i^{+}=157A i^{-}=160A i^{0}=160A
DL 3
DL 6
v^{+}=17.4kV v^{-}=454V v^{0}=16.7kV
i^{+}=302A i^{-}=77.5A i^{0}=81A
PD11
v^{+}=17.4kV v^{-}=454V v^{0}=16.7kV
v^{+}=17.3kV v^{-}=498V v^{0}=16.8kV
PD6
Bus 4
v^{+}=17.3kV v^{-}=498V v^{0}=16.8kV
Bus 5
PD10
i^{+}=140A i^{-}=80A i^{0}=81A
i^{+}=107A i^{-}=80A i^{0}=81A
PD7
i^{+}=81A i^{-}=81A i^{0}=81A
Load 5
Load 3
DL 5
DL 4
v^{+}=17.3kV v^{-}=475V v^{0}=16.8kV
i^{+}=140A i^{-}=80A i^{0}=81A
PD9
PD8
i^{+}=107A i^{-}=80A i^{0}=81A
v^{+}=17.3kV v^{-}=475V v^{0}=16.8kV
Bus 6
Load 4
(a)
v^{+}=17.8 kV v^{-}=434V v^{0}=17 kV
v^{+}=17.7 kV v^{-}=473V v^{0}=17.1kV
v^{+}=17.7 kV v^{-}=473V v^{0}=17.1 kV
v^{+}=17.7 kV v^{-}=520V v^{0}=17.1 kV
i^{+}=300A i^{-}=156A i^{0}=163A
i^{+}=300A i^{-}=156A i^{0}=163A
i^{+}=147A i^{-}=160A i^{0}=163A
i^{+}=147A i^{-}=160A i^{0}=163A
Bus 3
DG 1
3 MW
D11 YN
Bus 1
66 kV: 20kV
Grid
YN D11 zigzag
PD1
DL 1
PD2
PD3
DL 2
PD4
PD12
v^{+}=17.8 kV v^{-}=434V v^{0}=17 kV
Bus 2
v^{+}=17.7 kV v^{-}=520V v^{0}=17.1 kV
PD5
Load 1
i^{+}=145A i^{-}=76A i^{0}=83A
i^{+}=160A i^{-}=163A i^{0}=163A
Load 2
DL 6
DL 3
v^{+}=17.7 kV v^{-}=450V v^{0}=17.1 kV
Bus 5
PD11
v^{+}=17.7 kV v^{-}=450V v^{0}=17.1 kV
v^{+}=17.7 kV v^{-}=496V v^{0}=17.1 kV
PD6
Bus 4
v^{+}=17.7 kV v^{-}=496V v^{0}=17.1 kV
i^{+}=145A i^{-}=76A i^{0}=83A
PD10
i^{+}=98A i^{-}=80A i^{0}=83A
i^{+}=110A i^{-}=82A i^{0}=83A
PD7
i^{+}=83A i^{-}=83A i^{0}=83A
Load 5
Load 3
D11 YN
DL 5
DL 4
DG 3
3 MW
v^{+}=17.7 kV v^{-}=472V v^{0}=17.1 kV
PD9
PD8
v^{+}=17.7 kV v^{-}=472V v^{0}=17.1 kV
i^{+}=98A i^{-}=80A i^{0}=83A
Bus 6
i^{+}=110A i^{-}=82A i^{0}=83A
Load 4
D11 YN
DG 2
1.5 MW
(b)

Fig. 3.18 Short-circuit currents during single-phase to ground (AG) fault at DL3, with $r = 0.1\ \Omega$ (a) without DG (b) with DG penetration

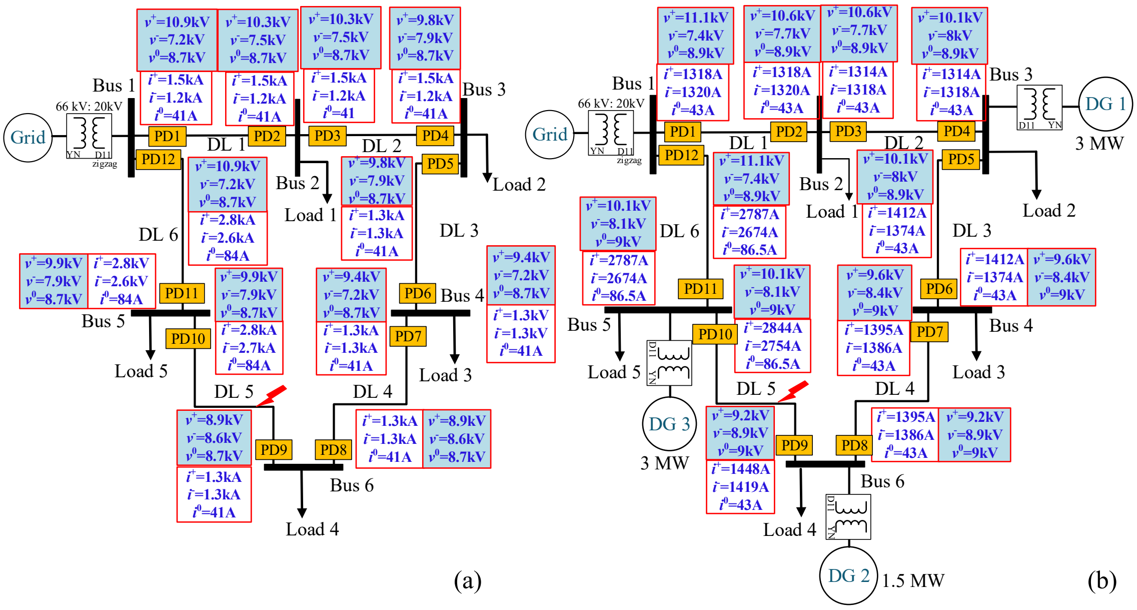
v^{+}=10.9kV v^{-}=7.2kV v^{0}=8.7kV
v^{+}=10.3kV v^{-}=7.5kV v^{0}=8.7kV
v^{+}=10.3kV v^{-}=7.5kV v^{0}=8.7kV
v^{+}=9.8kV v^{-}=7.9kV v^{0}=8.7kV
i^{+}=1.5kA i^{-}=1.2kA i^{0}=41A
i^{+}=1.5kA i^{-}=1.2kA i^{0}=41A
i^{+}=1.5kA i^{-}=1.2kA i^{0}=41
i^{+}=1.5kA i^{-}=1.2kA i^{0}=41A
Bus 1
66 kV: 20kV
Grid
YN D11 zigzag
PD1
DL 1
PD2
PD3
DL 2
PD4
Bus 3
PD12
v^{+}=10.9kV v^{-}=7.2kV v^{0}=8.7kV
Bus 2
v^{+}=9.8kV v^{-}=7.9kV v^{0}=8.7kV
PD5
Load 2
Load 1
i^{+}=2.8kA i^{-}=2.6kA i^{0}=84A
i^{+}=1.3kA i^{-}=1.3kA i^{0}=41A
DL 6
DL 3
v^{+}=9.9kV v^{-}=7.9kV v^{0}=8.7kV
i^{+}=2.8kV i^{-}=2.6kV i^{0}=84A
PD11
v^{+}=9.9kV v^{-}=7.9kV v^{0}=8.7kV
v^{+}=9.4kV v^{-}=7.2kV v^{0}=8.7kV
PD6
Bus 4
v^{+}=9.4kV v^{-}=7.2kV v^{0}=8.7kV
i^{+}=1.3kV i^{-}=1.3kV i^{0}=41A
Bus 5
PD10
i^{+}=2.8kA i^{-}=2.7kA i^{0}=84A
i^{+}=1.3kA i^{-}=1.3kA i^{0}=41A
PD7
Load 5
Load 3
DL 5
DL 4
v^{+}=8.9kV v^{-}=8.6kV v^{0}=8.7kV
PD9
PD8
i^{+}=1.3kA i^{-}=1.3kA i^{0}=41A
v^{+}=8.9kV v^{-}=8.6kV v^{0}=8.7kV
i^{+}=1.3kA i^{-}=1.3kA i^{0}=41A
Bus 6
Load 4
(a)
v^{+}=11.1kV v^{-}=7.4kV v^{0}=8.9kV
v^{+}=10.6kV v^{-}=7.7kV v^{0}=8.9kV
v^{+}=10.6kV v^{-}=7.7kV v^{0}=8.9kV
v^{+}=10.1kV v^{-}=8kV v^{0}=8.9kV
i^{+}=1318A i^{-}=1320A i^{0}=43A
i^{+}=1318A i^{-}=1320A i^{0}=43A
i^{+}=1314A i^{-}=1318A i^{0}=43A
i^{+}=1314A i^{-}=1318A i^{0}=43A
Bus 3
DG 1
3 MW
D11 YN
Bus 1
66 kV: 20kV
Grid
YN D11 zigzag
PD1
DL 1
PD2
PD3
DL 2
PD4
PD12
v^{+}=11.1kV v^{-}=7.4kV v^{0}=8.9kV
Bus 2
v^{+}=10.1kV v^{-}=8kV v^{0}=8.9kV
PD5
v^{+}=10.1kV v^{-}=8.1kV v^{0}=9kV
DL 6
Load 1
i^{+}=2787A i^{-}=2674A i^{0}=86.5A
i^{+}=1412A i^{-}=1374A i^{0}=43A
Load 2
DL 3
i^{+}=2787A i^{-}=2674A i^{0}=86.5A
i^{+}=1412A i^{-}=1374A i^{0}=43A
v^{+}=9.6kV v^{-}=8.4kV v^{0}=9kV
PD11
v^{+}=10.1kV v^{-}=8.1kV v^{0}=9kV
v^{+}=9.6kV v^{-}=8.4kV v^{0}=9kV
PD6
Bus 5
PD10
i^{+}=2844A i^{-}=2754A i^{0}=86.5A
i^{+}=1395A i^{-}=1386A i^{0}=43A
PD7
Bus 4
Load 5
Load 3
D11 YN
DL 5
DL 4
DG 3
3 MW
v^{+}=9.2kV v^{-}=8.9kV v^{0}=9kV
PD9
PD8
i^{+}=1395A i^{-}=1386A i^{0}=43A
v^{+}=9.2kV v^{-}=8.9kV v^{0}=9kV
i^{+}=1448A i^{-}=1419A i^{0}=43A
Bus 6
Load 4
D11 YN
DG 2
1.5 MW
(b)

Fig. 3.19 Short-circuit currents during two-phase to ground fault (ABG) at DL5, with $r = 0.1\ \Omega$ (a) without DG (b) with DG penetration

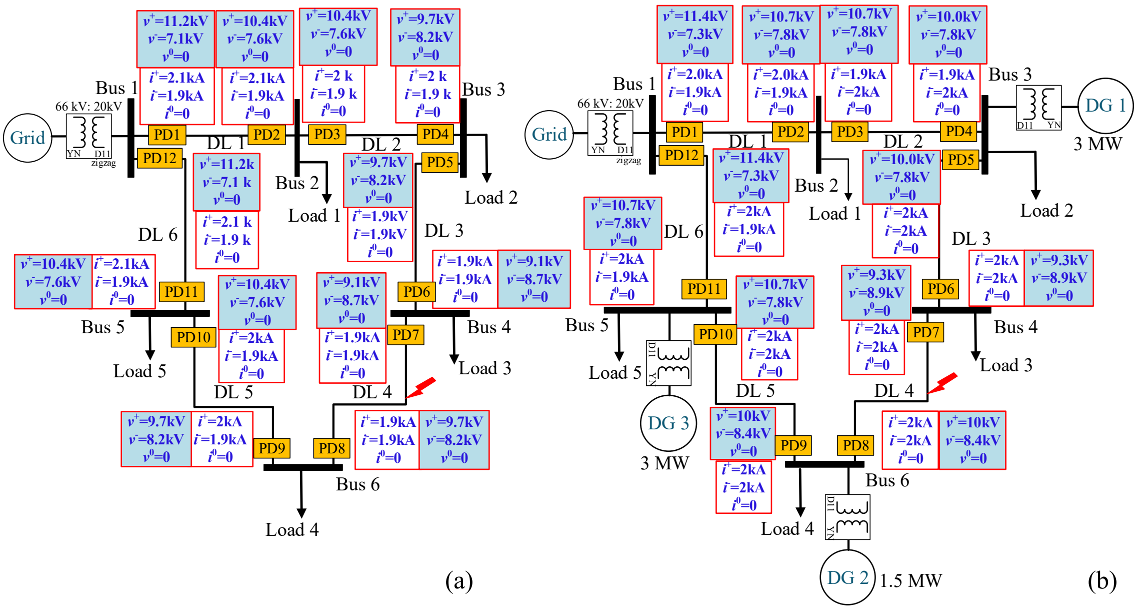
Grid
66 kV: 20kV
YN
D11
zigzag
Bus 1
Bus 2
Bus 3
Bus 4
Bus 5
Bus 6
DL 1
DL 2
DL 3
DL 4
DL 5
DL 6
PD1
PD2
PD3
PD4
PD5
PD6
PD7
PD8
PD9
PD10
PD11
PD12
Load 1
Load 2
Load 3
Load 4
Load 5
v^+=11.2kV v^-=7.1kV v^0=0
i^+=2.1kA i^-=1.9kA i^0=0
v^+=10.4kV v^-=7.6kV v^0=0
i^+=2.1kA i^-=1.9kA i^0=0
v^+=10.4kV v^-=7.6kV v^0=0
i^+=2 k i^-=1.9 k i^0=0
v^+=9.7kV v^-=8.2kV v^0=0
i^+=2 k i^-=1.9 k i^0=0
v^+=11.2k v^-=7.1 k v^0=0
i^+=2.1 k i^-=1.9 k i^0=0
v^+=9.7kV v^-=8.2kV v^0=0
i^+=1.9kV i^-=1.9kV i^0=0
v^+=10.4kV v^-=7.6kV v^0=0
i^+=2.1kA i^-=1.9kA i^0=0
i^+=1.9kA i^-=1.9kA i^0=0
v^+=9.1kV v^-=8.7kV v^0=0
v^+=10.4kV v^-=7.6kV v^0=0
i^+=2kA i^-=1.9kA i^0=0
v^+=9.1kV v^-=8.7kV v^0=0
i^+=1.9kA i^-=1.9kA i^0=0
v^+=9.7kV v^-=8.2kV v^0=0
i^+=2kA i^-=1.9kA i^0=0
i^+=1.9kA i^-=1.9kA i^0=0
v^+=9.7kV v^-=8.2kV v^0=0
(a)
DG 1
3 MW
DG 3
3 MW
DG 2
1.5 MW
v^+=11.4kV v^-=7.3kV v^0=0
i^+=2.0kA i^-=1.9kA i^0=0
v^+=10.7kV v^-=7.8kV v^0=0
i^+=2.0kA i^-=1.9kA i^0=0
v^+=10.7kV v^-=7.8kV v^0=0
i^+=1.9kA i^-=2kA i^0=0
v^+=10.0kV v^-=7.8kV v^0=0
i^+=1.9kA i^-=2kA i^0=0
v^+=11.4kV v^-=7.3kV v^0=0
i^+=2kA i^-=1.9kA i^0=0
v^+=10.0kV v^-=7.8kV v^0=0
i^+=2kA i^-=2kA i^0=0
v^+=10.7kV v^-=7.8kV v^0=0
i^+=2kA i^-=1.9kA i^0=0
i^+=2kA i^-=2kA i^0=0
v^+=9.3kV v^-=8.9kV v^0=0
v^+=10.7kV v^-=7.8kV v^0=0
i^+=2kA i^-=2kA i^0=0
v^+=9.3kV v^-=8.9kV v^0=0
i^+=2kA i^-=2kA i^0=0
v^+=10kV v^-=8.4kV v^0=0
i^+=2kA i^-=2kA i^0=0
i^+=2kA i^-=2kA i^0=0
v^+=10kV v^-=8.4kV v^0=0
(b)

Fig. 3.20 Short-circuit currents during a two-phase fault (AB) at DL4, with $r = 0.1\ \Omega$ (a) without DG (b) with DG penetration

As shown in Fig. 3.18(a) and Fig. 3.18(b) in the case of single-phase faults, the differences in the short-circuit currents are not significant due to the zigzag connection, which maintains the short circuit current to a limited value. However, for two-phase, two-phase to the ground, and three-phase fault, the values are significantly different due to the ground fault or the different path of the fault current, which means the current can path through the ground fault and not through the zigzag, as shown in Fig. 3.21.

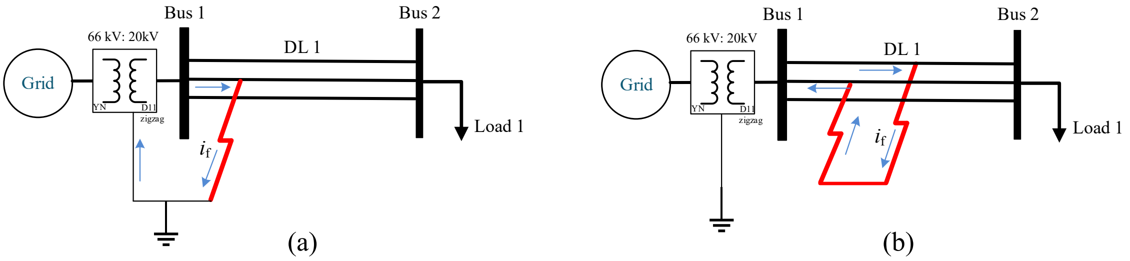
Grid
66 kV: 20kV
YN
D11
zigzag
Bus 1
Bus 2
DL 1
Load 1
i_f
(a)
Grid
66 kV: 20kV
YN
D11
zigzag
Bus 1
Bus 2
DL 1
Load 1
i_f
(b)

Fig. 3.21 Short circuit current paths in case of (a) single-phase fault (b) three-phase fault

In the case of large penetration of DG in the DS, DG converters control during abnormal conditions plays a significant role in the entire system's behaviour. Power converters are designed and controlled to inject power into the grid during normal conditions and support the grid in transient operation by reducing the active power injection and increasing the reactive power injection according to the grid codes [38], [153]. The inverter controller response was evaluated under grid faults incorporating LVRT capabilities, and as specified by Spanish grid code. The behaviour of grid-connected converter under grid faults according to Spanish grid code is discussed in the next chapter.

4 Analysis of a three-phase grid-connected converter under voltage sags according to the Spanish grid code

As mentioned in the preceding chapter, the structure of the DG grid-connected converter could be single or multiple stages. A multiple-stage converter (chopper/inverter) is used in this research as shown in Fig. 4.1. The inverter control during grid sags is studied utilizing different control strategies following grid code requirements.

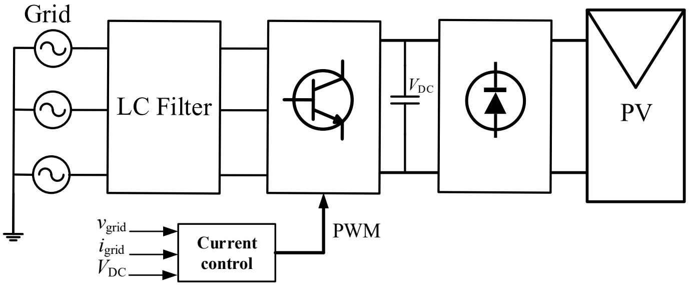

Fig. 4.1 Block diagram of the grid-connected photovoltaic (PV) system

It is important to state that in this research, the PV model has been simplified to a constant current source in the analysis of the protection system, in order to simplify the system and reduce the total calculation time of the simulated cases, because a massive number of cases have been studied to analyze the protection system in different grid behaviour. Besides, during the faults (sags), the weather condition is supposed to be constant, as the sag lasts for a short period of time. The proposed method can be incorporated in the analysis of the protection system in future work by considering different generation scenarios (Appendix H).

In the next section, the inverter control during sags accomplished with grid codes is demonstrated in detail.

4.1. Spanish grid code P.0. 12.2 application with symmetrical and unsymmetrical sags

In MV-grids, including DG units, voltage sags can cause desirable or undesirable disconnection of some lines in the DS or even disconnect DG units. Voltage sags are characterized by the depth, duration, and frequency of occurrence. A detailed definition of sag and its characteristics can be found in [32]. In this thesis only sags caused by grid faults are considered.

The majority of grid faults are unbalanced faults, affecting grid-connected converters' performance, severely impacting grid power quality. Unsymmetrical voltage sags cause grid current peaks and DC-bus voltage fluctuations, as a pulsation of twice the fundamental frequency occurs in both voltages and currents due to the negative-sequence components, creating a ripple in the injected power to the grid and in the DC-bus voltage [51]. Therefore, negative-sequence currents must thus be controlled in order to inject more reactive power into the grid during faults and satisfy the grid's power quality standards.

Recently, the number of DG units is increased significantly. Therefore, the balance between power consumption and power generation must be achieved during grid faults by maintaining DG systems connected to the DS [154], [155]. These requirements raise the need for the new standard and grid codes, to satisfy these requirements. Therefore, the combination of introducing efficient control strategies and improving the PV power planet structure with LVRT capabilities is necessary. Distribution grid codes are required in a similar way to the grid codes used in the transmission system [156]. Grid codes require DG converters to maintain the connection to the grid during faults to support the grid, minimizing active power injection and boosting reactive power injection [157].

Measured RMS voltage does not present significant oscillations during symmetrical voltage sags, but it oscillates during unsymmetrical voltage sag. As a result, the reference reactive current oscillates, and the value of the active current increases during the voltage sag to sustain active power generation. However, the inverter's apparent power must not exceed its limitations. However, the active power must be restricted according to the grid code to keep the grid in service during the fault period.

In 2005, Spanish governments promoted a legal framework for technical requirements for grid access and connection, especially renewable energy sources [158]. In 2008, the required active and reactive current injection (Fig. 4.2) was defined in the draft version of response requirements to voltage sags from production facilities under the special regime (P.O.12.2). [157].

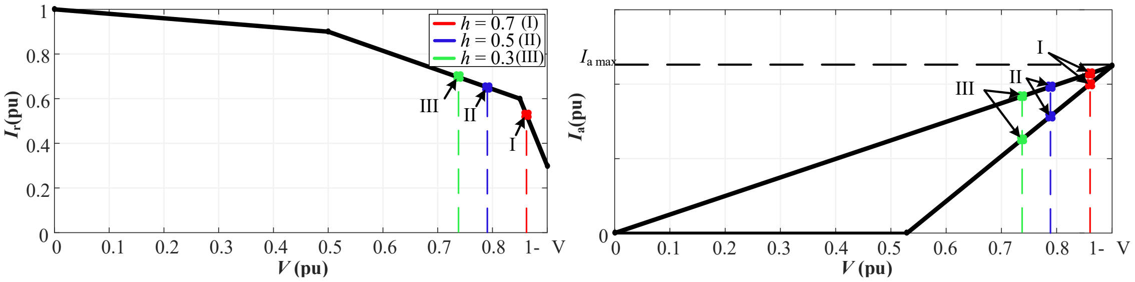

Fig. 4.2 Active (I_a) and reactive (I_r) currents to be injected during grid faults, according to Spanish grid code P.O. 12.2.

The inverter must be controlled during sags according to the injected active current I_a and reactive current I_r. The RMS remaining voltage's instantaneous value $V(t)$ is calculated according to (8), [159].

$$V(t) = \sqrt{\frac{v_a(t)^2 + v_b(t)^2 + v_c(t)^2}{3}}, \tag{8}$$

where: $v_a(t)$, $v_b(t)$, and $v_c(t)$ are the instantaneous RMS values of the *abc* voltages.

When unsymmetrical faults occur, the grid code does not provide a clear explanation of how to proceed. As a result, a proposal for using the grid code for both symmetrical and unsymmetrical faults is developed in this thesis. An explanation is provided assuming a two-phase fault, which produces type C sags, in order to explain how to proceed in the event of unsymmetrical sags, according to [153]. The sag depth parameter, h, is assumed to be 0.3 for point III in Fig. 4.2. This parameter is described in Table 1 from reference [160]. The per-unit RMS values during the steady-state of the fault, assuming a sag depth h = 0.3 for type C sag, are calculated using (9).

$$v_a(t) = 1,\ v_b(t) = \sqrt{\left(-\frac{1}{2}\right)^2 + \left(-\frac{\sqrt{3}}{2}h\right)^2} = 0.5635,\ v_c(t) = \sqrt{\left(-\frac{1}{2}\right)^2 + \left(\frac{\sqrt{3}}{2}h\right)^2} = 0.5635. \tag{9}$$

By substituting the values of (9) in (8) it is obtained $V(t) = 0.739$ pu. According to this voltage, the active I_a and reactive I_r currents can be obtained from Fig. 4.2. It is assumed that these values correspond to the positive sequence. The maximum active current $I_{a\ max}$ is determined by the maximum value of the converter power before the sag.

The magnitude of $I_{a\ max}$ depends on the weather conditions in the case of renewable energy resources, and its value can be obtained employing the following equation [157]:

$$I_{a\ max} = \frac{P_{a0}}{1 - \Delta V}, \tag{10}$$

where: ΔV is the allowable voltage drop (which equals 7.5% in distribution grids [157]), and P_{a0} is the active power supplied by the installation before the sag.

The converter limits are verified to not exceed the maximum contributory fault current (I_{fault_max} specified for the converter) from the active and reactive current values obtained using the grid code:

$$\sqrt{I_r^2 + I_a^2} \le I_{fault\_max}\ \text{pu}. \tag{11}$$

In this study, the converter limit is set to 1 pu in steady-state during the fault, for safety reasons, as seen in (12).

$$\sqrt{I_{\mathrm{r}}^{2}+I_{\mathrm{a}}^{2}} \leq 1 \text{ pu.} \tag{12}$$

If the current obtained from (11) exceeds the maximum contributory fault current, then more priority is given to the reactive current to support the grid, as shown in (13). In this study $I_{\mathrm{fault\_max}} = 1$ pu.

$$I_{\mathrm{a}} = \sqrt{I_{\mathrm{fault\_max}} - I_{\mathrm{r}}^{2}}. \tag{13}$$

4.2. Three-phase grid-connected inverter

The control of power converters in DG systems may have a significant impact on grid behaviour. In addition, the inverter system must acquire the capability to operate with high speed and frequency in generating the pulse-width modulation (PWM) signals. In general, the converters can be classified as (a) Voltage Source Converters (VSC) & (b) Current Source Converters (CSC), depending upon the input and output. In VSC, the input voltage is kept constant, and the output voltage amplitude is unaffected by the load. However, the waveform of load current, and its magnitude, are determined by the load impedance. In CSC, the input current is constant but adjustable. The amplitude of CSI's output current is unaffected by the load. The amplitude and waveform of the output voltage, on the other hand, are determined by the load impedance. In this research, VSC is used, as the objective is to control the injected *abc* current to the grid during voltage sags.

For these reasons, it is crucial to establish analytical models that can help explain how grid-connected equipment behaves to voltage sags. In order to develop the proposed control strategy, a mathematical study of the currents during voltage sag is carried out in Appendix E. *Park* and *Ku* transformations are used to analyze the converter behaviour during sags and are utilized to control the converter current. The *Ku* transformation provides a clear visual representation of the electrical variables, making it easier to evaluate the essential information regarding sag depth and type than the *dq* representation.

4.2.1. Reference current control strategies using *Park* transformation

Few studies investigated the performance of control strategies under grid codes during unsymmetrical sags, as indicated in the literature review [68], [72]–[76]. So, additional study is needed in this field, particularly for unsymmetrical voltage sags. Unlike earlier studies, the author studied the behaviour of a three-phase grid-connected inverter under symmetrical and unsymmetrical voltage sags as presented in [161], [162]. In addition, four different control strategies are developed to accomplish with the Spanish grid code. These control strategies offer reference voltages determined based on grid code reference currents to avoid active and reactive power oscillation since their values vary from the pre-faulted steady-state values. Another variation is that the current study considers converter limitations and presents a methodology for limiting injected current during faults. According to *Park* and *Ku* transformations, positive- and negative-sequence reference values of converted currents are computed using the instantaneous power theory described in [163]. Different control algorithms for three-phase inverters have been implemented based on this concept under unsymmetrical sags [38].

The current control strategies analysed are Balanced Current Control (BCC) that seeks to inject symmetrical current by imposing zero values for *dq* negative current, Constant Active Power Control (CPC) that aims to deliver constant instantaneous active power, Constant Reactive Power Control (CRC) that aims to deliver constant instantaneous reactive power and Constant Active Reactive Control (CPRC) that aims to impose null values for both terms of power oscillations. These strategies aim to calculate *dq* current references during voltage sags based on grid codes requirements, and study grid codes based on both positive- and negative-sequence reference currents; then, the active reference current is obtained to maximize its value without exceeding the converter limits. Also, compare the different control strategies that allow the converter to remain connected under different types of abnormal grid behaviour based on the grid codes.

As said previously, the unsymmetrical sags are characterized by the appearance of a negative-sequence component. Therefore, independent control must be performed to the positive- and the negative-sequence components of the currents. Two current control loops are needed for positive- and negative-sequence controls. Each loop contains two PI controllers and decoupling terms (ωL) and feed-forward terms from the *dq*, transformed grid voltages. The summations of these components produce *dq* positive- and negative-sequence voltage references; finally these references are transformed to *abc* voltages to the inverter, as shown in Fig. 4.3; also, the overall control scheme is shown in Fig. 4.4.

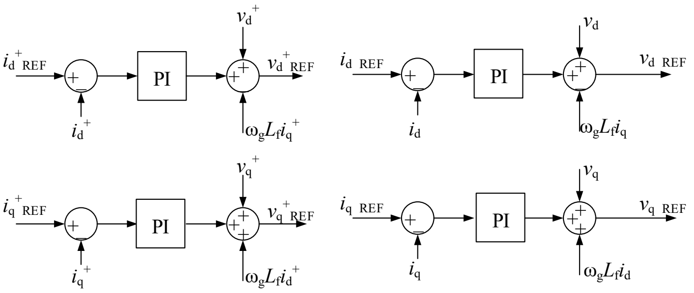
v_d^+
$i_{d\,REF}^+$
PI
$v_{d\,REF}^+$
i_d^+
$\omega_g L_f i_q^+$
v_d^-
$i_{d\,REF}^-$
PI
$v_{d\,REF}^-$
i_d^-
$\omega_g L_f i_q^-$
v_q^+
$i_{q\,REF}^+$
PI
$v_{q\,REF}^+$
i_q^+
$\omega_g L_f i_d^+$
v_q^-
$i_{q\,REF}^-$
PI
$v_{q\,REF}^-$
i_q^-
$\omega_g L_f i_d^-$

Fig. 4.3 Current control considering unbalanced conditions for positive- and negative-sequence components

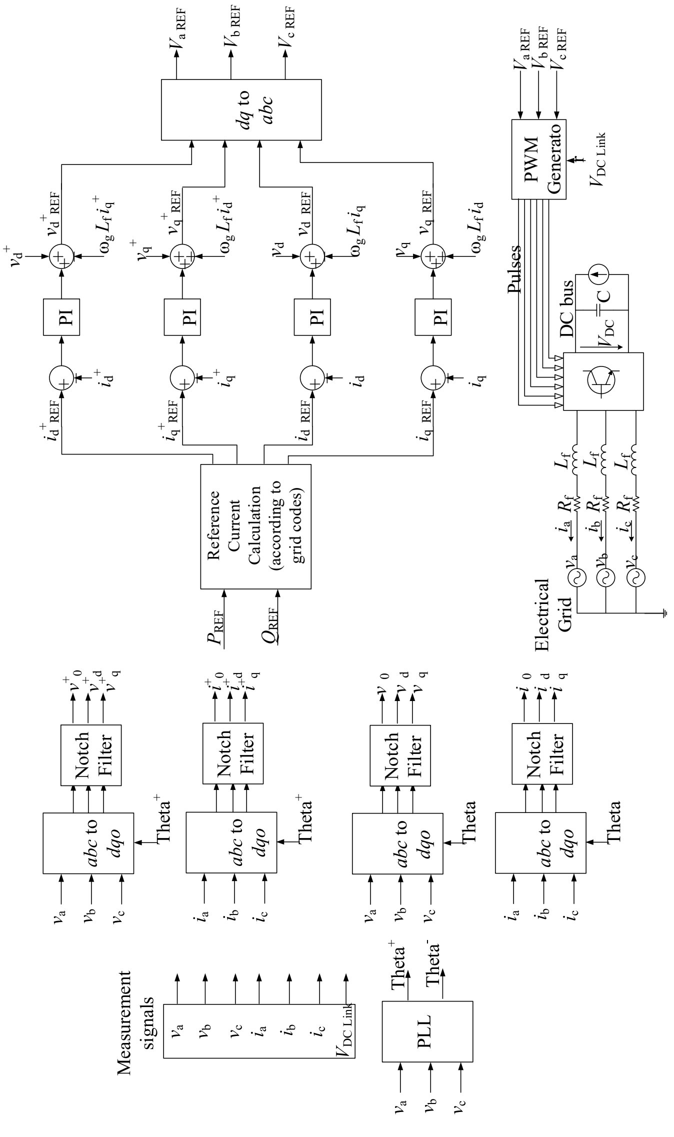
$V_{a\,REF}$
$V_{b\,REF}$
$V_{c\,REF}$
dq to abc
PI
$\omega_g L_f i_q$
$\omega_g L_f i_d$
Reference Current Calculation (according to grid codes)
P_{REF}
Q_{REF}
PWM Generato
$V_{DC\,Link}$
Pulses
DC bus
C
V_{DC}
L_f
R_f
Electrical Grid
Notch Filter
abc to dqo
Theta
Measurement signals
v_a
v_b
v_c
i_a
i_b
i_c
$V_{DC\,Link}$
PLL
Theta^+
Theta^-

Fig. 4.4 Three-phase inverter control for unbalanced conditions

where: v_{d}^{+}, v_{q}^{+}, v_{d}^{-} and v_{q}^{-}, are the positive and negative sequence grid voltage, $i_{\mathrm{d\,REF}}^{+}$, $i_{\mathrm{q\,REF}}^{+}$, $i_{\mathrm{d\,REF}}^{-}$ and $i_{\mathrm{q\,REF}}^{-}$ are the reference positive and negative sequence currents, i_{d}^{+}, i_{q}^{+}, i_{d}^{-} and i_{q}^{-} are the positive and negative injected sequence currents, $v_{\mathrm{d\,REF}}^{+}$, $v_{\mathrm{q\,REF}}^{+}$, $v_{\mathrm{d\,REF}}^{-}$ and $v_{\mathrm{q\,REF}}^{-}$ are the reference positive and negative sequence voltage, ω_g is the grid pulsation, and L_{f} is the filter inductance.

The following section will give a brief discussion about the four reference current control strategies during voltage sags.

- Constant Active Reactive Control (CPRC)

This method indicates that it is possible to control the instantaneous active and reactive power because the equations of this method are in a balanced regime, this means that the negative-sequence components are canceled.

$$i_{\mathrm{d\,REF}}^{+} = \frac{1}{v_{\mathrm{mod}}} v_{\mathrm{d}}^{+} P_{\mathrm{REF}} + \frac{1}{v_{\mathrm{mod}}} v_{\mathrm{q}}^{+} Q_{\mathrm{REF}} \quad , \quad i_{\mathrm{q\,REF}}^{+} = \frac{1}{v_{\mathrm{mod}}} v_{\mathrm{q}}^{+} P_{\mathrm{REF}} - \frac{1}{v_{\mathrm{mod}}} v_{\mathrm{d}}^{+} Q_{\mathrm{REF}} \tag{14}$$

$$i_{\mathrm{d\,REF}}^{-} = \frac{1}{v_{\mathrm{mod}}} v_{\mathrm{d}}^{-} P_{\mathrm{REF}} + \frac{1}{v_{\mathrm{mod}}} v_{\mathrm{q}}^{-} Q_{\mathrm{REF}} \quad , \quad i_{\mathrm{q\,REF}}^{-} = \frac{1}{v_{\mathrm{mod}}} v_{\mathrm{q}}^{-} P_{\mathrm{REF}} - \frac{1}{v_{\mathrm{mod}}} v_{\mathrm{d}}^{-} Q_{\mathrm{REF}}, \tag{15}$$

where v_{mod}

$$v_{\mathrm{mod}} = v_{\mathrm{d}}^{+^2} + v_{\mathrm{q}}^{+^2} + v_{\mathrm{d}}^{-^2} + v_{\mathrm{q}}^{-^2} + 2\sqrt{v_{\mathrm{d}}^{+^2} + v_{\mathrm{q}}^{+^2}}\sqrt{v_{\mathrm{d}}^{-^2} + v_{\mathrm{q}}^{-^2}}\cos\left(2\omega t + \theta^{+} + \theta^{-}\right), \tag{16}$$

where: v_{d}^{+}, v_{q}^{+}, v_{d}^{-} and v_{q}^{-}, are the positive and negative sequence voltage, $i_{\mathrm{d\,REF}}^{+}$, $i_{\mathrm{q\,REF}}^{+}$, $i_{\mathrm{d\,REF}}^{-}$ and $i_{\mathrm{q\,REF}}^{-}$ are the reference positive and negative sequence currents, θ^{+} and θ^{-} are the positive and negative angles, P_{REF} is the reference active power, Q_{REF} is the reference reactive power, and ω is the pulsation. The calculation of the instantaneous powers is done by:

$$\begin{gathered} p = v_{\mathrm{a}} i_{\mathrm{a}} + v_{\mathrm{b}} i_{\mathrm{b}} + v_{\mathrm{c}} i_{\mathrm{c}} \\ q = \left(\left[v_{\mathrm{a}} - v_{\mathrm{b}}\right] i_{\mathrm{c}} + \left[v_{\mathrm{b}} - v_{\mathrm{c}}\right] i_{\mathrm{a}} + \left[v_{\mathrm{c}} - v_{\mathrm{a}}\right] i_{\mathrm{b}}\right)\left(\frac{1}{\sqrt{3}}\right) \end{gathered} \tag{17}$$

$$\begin{gathered} p = v_{\mathrm{d}}^{+} i_{\mathrm{d}}^{+} + v_{\mathrm{q}}^{+} i_{\mathrm{q}}^{+} + v_{\mathrm{d}}^{-} i_{\mathrm{d}}^{-} + v_{\mathrm{q}}^{-} i_{\mathrm{q}}^{-} \\ q = v_{\mathrm{q}}^{+} i_{\mathrm{d}}^{+} - v_{\mathrm{d}}^{+} i_{\mathrm{q}}^{+} + v_{\mathrm{q}}^{-} i_{\mathrm{d}}^{-} - v_{\mathrm{d}}^{-} i_{\mathrm{q}}^{-}, \end{gathered} \tag{18}$$

where: v_{a}, v_{b}, v_{c}, i_{a}, i_{b} and i_{c} are the *abc* grid voltages and currents, and p, q are the instantaneous active and reactive powers.

The current references are perfectly sinusoidal under balanced sinusoidal conditions. However, voltage and current transformed variables oscillate at the double fundamental grid frequency under unbalanced operating conditions. This oscillation produces distorted reference currents consisting of high-order harmonics. Due to this issue, this method required the implementation of a more complex control method. There are some strict restrictions for injecting harmonic current into the grid for the high power grid-connected converter. Moreover, additional problems can arise such as extra deterioration of the grid voltage at the Point of Common Coupling (PCC). Therefore, this method has an obvious advantage: the highest degree of control on the instantaneous powers exchanged with the grid. However, on the other hand, it is not suitable for generating sinusoidal reference currents of grid-connected converters because it produces distorted current shapes with harmonics. Then the reference currents are not adequately controlled.

- Constant Reactive Power Control (CRC)

The reference currents are calculated using both positive and negative sequence components in this strategy. The instantaneous reactive power injected into the grid is controlled accurately without oscillation. However, the active power has oscillation during voltage sag. The injected reference current used both positive- and negative-sequence components of the voltage and currents during the sag, as seen in (19).

$$
\begin{aligned}
i_{\mathrm{d\,REF}}^{-} &= \frac{1}{\left(v_{\mathrm{d}}^{+^2}+v_{\mathrm{q}}^{+^2}\right)-\left(v_{\mathrm{d}}^{-^2}+v_{\mathrm{q}}^{-^2}\right)} v_{\mathrm{d}}^{-} P_{\mathrm{REF}} - \frac{1}{\left(v_{\mathrm{d}}^{+^2}+v_{\mathrm{q}}^{-^2}\right)-\left(v_{\mathrm{d}}^{+^2}+v_{\mathrm{q}}^{-^2}\right)} v_{\mathrm{q}}^{-} Q_{\mathrm{REF}} \\
i_{\mathrm{q\,REF}}^{-} &= \frac{1}{\left(v_{\mathrm{d}}^{+^2}+v_{\mathrm{q}}^{+^2}\right)-\left(v_{\mathrm{d}}^{-^2}+v_{\mathrm{q}}^{-^2}\right)} v_{\mathrm{q}}^{-} P_{\mathrm{REF}} + \frac{1}{\left(v_{\mathrm{d}}^{+^2}+v_{\mathrm{q}}^{-^2}\right)-\left(v_{\mathrm{d}}^{+^2}+v_{\mathrm{q}}^{-^2}\right)} v_{\mathrm{d}}^{-} Q_{\mathrm{REF}}.
\end{aligned}
\tag{19}
$$

This method gives the advantages of control reactive power; this means cancel oscillations of reactive power, but noticeably fluctuation of active power, since the terms are not controlled and inject unsymmetrical sinusoidal current into the grid.

- Constant Active Power Control (CPC)

This method aims to cancel the effect of the second-order component from the calculation of reference current. So, the harmonics in the reference currents will be canceled as well. In order to achieve this goal, throughout one period, the average value of the instantaneous conductance and susceptance is calculated, and then determines the reference for the active and reactive current, as seen in the following equations.

$$
\begin{aligned}
i_{\mathrm{d\,REF}}^{+} &= \frac{1}{v_{\mathrm{d}}^{+^2}+v_{\mathrm{q}}^{+^2}+v_{\mathrm{d}}^{-^2}+v_{\mathrm{q}}^{-^2}}\left(v_{\mathrm{d}}^{+} P_{\mathrm{REF}}+v_{\mathrm{q}}^{+} Q_{\mathrm{REF}}\right) \\
i_{\mathrm{q\,REF}}^{+} &= \frac{1}{v_{\mathrm{d}}^{+^2}+v_{\mathrm{q}}^{+^2}+v_{\mathrm{d}}^{-^2}+v_{\mathrm{q}}^{-^2}}\left(v_{\mathrm{q}}^{+} P_{\mathrm{REF}}-v_{\mathrm{d}}^{+} Q_{\mathrm{REF}}\right)
\end{aligned}
\tag{20}
$$

$$
\begin{aligned}
i_{\mathrm{d\,REF}}^{-} &= \frac{1}{v_{\mathrm{d}}^{+^2}+v_{\mathrm{q}}^{+^2}+v_{\mathrm{d}}^{-^2}+v_{\mathrm{q}}^{-^2}}\left(v_{\mathrm{d}}^{-} P_{\mathrm{REF}}+v_{\mathrm{q}}^{-} Q_{\mathrm{REF}}\right) \\
i_{\mathrm{q\,REF}}^{-} &= \frac{1}{v_{\mathrm{d}}^{+^2}+v_{\mathrm{q}}^{+^2}+v_{\mathrm{d}}^{-^2}+v_{\mathrm{q}}^{-^2}}\left(v_{\mathrm{q}}^{-} P_{\mathrm{REF}}-v_{\mathrm{d}}^{-} Q_{\mathrm{REF}}\right).
\end{aligned}
\tag{21}
$$

This method injects unsymmetrical sinusoidal current waveform into the grid, with the advantages of controlled active power; this means cancel oscillations of active power, but noticeably fluctuation of reactive power, since the terms are not controlled.

- Balanced Current Control (BCC)

Considering the same principle used in the CPC strategy, other methods for adjusting the conductance and susceptance values in the expressions used to compute the reference currents can be found to achieve different goals. The main aim is to use only positive-sequence components, while the negative-sequence components are forced to be null in order to have symmetrical sinusoidal reference current signals. As negative-sequence currents are not injected, balanced sinusoidal currents are obtained. The main advantage of this method is the ability to inject a perfectly controlled current into the grid during the sag. However, the main disadvantage is the oscillation of both active and reactive power under unbalanced grid conditions. This method is advantageous in the application when the injection of a perfectly symmetrical sinusoidal current waveform is essential.

$$
\begin{aligned}
i_{\mathrm{d\,REF}}^{+} &= \frac{1}{v_{\mathrm{d}}^{+2} + v_{\mathrm{q}}^{+2}} \left(v_{\mathrm{d}}^{+} P_{\mathrm{REF}} + v_{\mathrm{q}}^{+} Q_{\mathrm{REF}} \right) \\
i_{\mathrm{q\,REF}}^{+} &= \frac{1}{v_{\mathrm{d}}^{+2} + v_{\mathrm{q}}^{+2}} \left(v_{\mathrm{q}}^{+} P_{\mathrm{REF}} - v_{\mathrm{d}}^{+} Q_{\mathrm{REF}} \right)
\end{aligned}
\tag{22}
$$

$$
\begin{aligned}
i_{\mathrm{d\,REF}}^{-} &= 0 \\
i_{\mathrm{q\,REF}}^{-} &= 0.
\end{aligned}
\tag{23}
$$

In the previous methods, null P or Q reference values means less oscillation in P or Q. On the other hand, in BCC, the null value of either the P or Q reference does not give less power oscillation. In conclusion, this method is the only one that injects perfectly symmetrical sinusoidal controlled reference current, not only sinusoidal but also balanced currents to be obtained, but the control of the active and reactive power is not achieved, because there is a noticeable oscillation in the injected power during voltage sag.

Table 4.3 shows the active and reactive power reference values, as well as the reference positive and negative sequence currents, for the four control strategies. Each control strategy has some advantages and disadvantages, Table 4.1 gives a brief comparison between every control strategy showing the merits and demerits of every control strategy. Table 4.2 shows the behaviour difference between every control strategy.

Table 4.1 Advantages and disadvantages of each control strategy during the sag

Control strategy	Advantages	Disadvantages
CRC	• Constant instantaneous reactive power	• Unsymmetrical sinusoidal injected currents • Oscillating instantaneous active power
CPC	• Constant instantaneous active power	• Unsymmetrical sinusoidal injected currents • Oscillating instantaneous reactive power
BCC	• Sinusoidal and symmetrical injected currents	• Fluctuating instantaneous active and reactive powers
CPRC	• Constant instantaneous active and reactive powers	• Distorted injected currents

Table 4.2 behaviour of each control strategy

Control strategy	GCV	GPV	SICW	SYCW	*p*(*t*)	*q*(*t*)
CRC	×	×	✓	×	×	✓
CPC	×	×	✓	×	✓	×
BCC	✓	×	✓	✓	×	×
CPRC	×	✓	×	×	✓	✓

GCV - Grid code current verification, GPV - Grid code power verification, SICW - Sinusoidal current waves, SYCW - Symmetrical current waves, $p(t)$ instantaneous active power, and $q(t)$ instantaneous reactive power.

Table 4.3 Equation of reference active and reactive power and negative sequence current of control strategies according to grid codes.

Control Method	Positive Component	Reference Active and Reactive Power	Negative Component
CRC	$i_{\mathrm{d\,REF}}^{+} = I_{\mathrm{a}}$ $i_{\mathrm{q\,REF}}^{+} = I_{\mathrm{r}}$	$P_{\mathrm{REF}} = \frac{\left(v_{\mathrm{d}}^{+2} + v_{\mathrm{q}}^{+2} + v_{\mathrm{d}}^{-2} + v_{\mathrm{q}}^{-2}\right) v_{\mathrm{d}}^{+} I_{\mathrm{a}}}{v_{\mathrm{d}}^{+2} + v_{\mathrm{q}}^{+2}} + \frac{\left(v_{\mathrm{d}}^{+2} + v_{\mathrm{q}}^{+2} + v_{\mathrm{d}}^{-2} + v_{\mathrm{q}}^{-2}\right) v_{\mathrm{q}}^{+} I_{\mathrm{r}}}{v_{\mathrm{d}}^{+2} + v_{\mathrm{q}}^{+2}}$ $Q_{\mathrm{REF}} = \frac{\left(v_{\mathrm{d}}^{+2} + v_{\mathrm{q}}^{+2} - v_{\mathrm{d}}^{-2} - v_{\mathrm{q}}^{-2}\right) v_{\mathrm{q}}^{+} I_{\mathrm{a}}}{v_{\mathrm{d}}^{+2} + v_{\mathrm{q}}^{+2}} - \frac{\left(v_{\mathrm{d}}^{+2} + v_{\mathrm{q}}^{+2} - v_{\mathrm{d}}^{-2} - v_{\mathrm{q}}^{-2}\right) v_{\mathrm{d}}^{+} I_{\mathrm{r}}}{v_{\mathrm{d}}^{+2} + v_{\mathrm{q}}^{+2}}$	$i_{\mathrm{d\,REF}}^{-} = \frac{\left(v_{\mathrm{d}}^{+} v_{\mathrm{d}}^{-} - v_{\mathrm{q}}^{+} v_{\mathrm{q}}^{-}\right) i_{\mathrm{d}}^{+}}{v_{\mathrm{d}}^{+2} + v_{\mathrm{q}}^{+2}} + \frac{\left(v_{\mathrm{d}}^{+} v_{\mathrm{q}}^{-} + v_{\mathrm{q}}^{+} v_{\mathrm{d}}^{-}\right) i_{\mathrm{q}}^{+}}{v_{\mathrm{d}}^{+2} + v_{\mathrm{q}}^{+2}}$ $i_{\mathrm{q\,REF}}^{-} = \frac{\left(v_{\mathrm{d}}^{+} v_{\mathrm{q}}^{-} + v_{\mathrm{q}}^{+} v_{\mathrm{d}}^{-}\right) i_{\mathrm{d}}^{+}}{v_{\mathrm{d}}^{+2} + v_{\mathrm{q}}^{+2}} + \frac{\left(-v_{\mathrm{d}}^{+} v_{\mathrm{d}}^{-} + v_{\mathrm{q}}^{+} v_{\mathrm{q}}^{-}\right) i_{\mathrm{q}}^{+}}{v_{\mathrm{d}}^{+2} + v_{\mathrm{q}}^{+2}}$
CPC	$i_{\mathrm{d\,REF}}^{+} = I_{\mathrm{a}}$ $i_{\mathrm{q\,REF}}^{+} = I_{\mathrm{r}}$	$P_{\mathrm{REF}} = \frac{\left(v_{\mathrm{d}}^{+2} + v_{\mathrm{q}}^{+2} - v_{\mathrm{d}}^{-2} - v_{\mathrm{q}}^{-2}\right) v_{\mathrm{d}}^{+} I_{\mathrm{a}}}{v_{\mathrm{d}}^{+2} + v_{\mathrm{q}}^{+2}} + \frac{\left(v_{\mathrm{d}}^{+2} + v_{\mathrm{q}}^{+2} - v_{\mathrm{d}}^{-2} - v_{\mathrm{q}}^{-2}\right) v_{\mathrm{q}}^{+} I_{\mathrm{r}}}{v_{\mathrm{d}}^{+2} + v_{\mathrm{q}}^{+2}}$ $Q_{\mathrm{REF}} = \frac{\left(v_{\mathrm{d}}^{+2} + v_{\mathrm{q}}^{+2} + v_{\mathrm{d}}^{-2} + v_{\mathrm{q}}^{-2}\right) v_{\mathrm{q}}^{+} I_{\mathrm{a}}}{v_{\mathrm{d}}^{+2} + v_{\mathrm{q}}^{+2}} - \frac{\left(v_{\mathrm{d}}^{+2} + v_{\mathrm{q}}^{+2} + v_{\mathrm{d}}^{-2} + v_{\mathrm{q}}^{-2}\right) v_{\mathrm{d}}^{+} I_{\mathrm{r}}}{v_{\mathrm{d}}^{+2} + v_{\mathrm{q}}^{+2}}$	$i_{\mathrm{d\,REF}}^{-} = \frac{\left(-v_{\mathrm{d}}^{+} v_{\mathrm{d}}^{-} + v_{\mathrm{q}}^{+} v_{\mathrm{q}}^{-}\right) i_{\mathrm{d}}^{+}}{v_{\mathrm{d}}^{+2} + v_{\mathrm{q}}^{+2}} + \frac{\left(-v_{\mathrm{d}}^{+} v_{\mathrm{q}}^{-} - v_{\mathrm{q}}^{+} v_{\mathrm{d}}^{-}\right) i_{\mathrm{q}}^{+}}{v_{\mathrm{d}}^{+2} + v_{\mathrm{q}}^{+2}}$ $i_{\mathrm{q\,REF}}^{-} = \frac{\left(-v_{\mathrm{d}}^{+} v_{\mathrm{q}}^{-} - v_{\mathrm{q}}^{+} v_{\mathrm{d}}^{-}\right) i_{\mathrm{d}}^{+}}{v_{\mathrm{d}}^{+2} + v_{\mathrm{q}}^{+2}} + \frac{\left(v_{\mathrm{d}}^{+} v_{\mathrm{d}}^{-} - v_{\mathrm{q}}^{+} v_{\mathrm{q}}^{-}\right) i_{\mathrm{q}}^{+}}{v_{\mathrm{d}}^{+2} + v_{\mathrm{q}}^{+2}}$
BCC	$i_{\mathrm{d\,REF}}^{+} = I_{\mathrm{a}}$ $i_{\mathrm{q\,REF}}^{+} = I_{\mathrm{r}}$	$P_{\mathrm{REF}} = v_{\mathrm{d}}^{+} I_{\mathrm{a}} + v_{\mathrm{q}}^{+} I_{\mathrm{r}}$ $Q_{\mathrm{REF}} = v_{\mathrm{q}}^{+} I_{\mathrm{a}} - v_{\mathrm{d}}^{+} I_{\mathrm{r}}$	$i_{\mathrm{d\,REF}}^{-} = 0$ $i_{\mathrm{q\,REF}}^{-} = 0$
CPRC	$i_{\mathrm{d\,REF}}^{+} = I_{\mathrm{a}}$ $i_{\mathrm{q\,REF}}^{+} = I_{\mathrm{r}}$	$P_{\mathrm{REF}} = \frac{v_{\mathrm{mod}}^{2}}{v_{\mathrm{d}}^{2} + v_{\mathrm{q}}^{2}} \left(v_{\mathrm{d}}^{+} I_{\mathrm{a}} + v_{\mathrm{q}}^{+} I_{\mathrm{r}}\right)$ $Q_{\mathrm{REF}} = \frac{v_{\mathrm{mod}}^{2}}{v_{\mathrm{d}}^{2} + v_{\mathrm{q}}^{2}} \left(v_{\mathrm{q}}^{+} I_{\mathrm{a}} - v_{\mathrm{d}}^{+} I_{\mathrm{r}}\right)$	$i_{\mathrm{d\,REF}}^{-} = \frac{1}{v_{\mathrm{mod}}^{+\,2}} \left(v_{\mathrm{d}}^{-} P_{\mathrm{REF}} + v_{\mathrm{q}}^{-} Q_{\mathrm{REF}}\right)$ $i_{\mathrm{q\,REF}}^{-} = \frac{1}{v_{\mathrm{mod}}^{+\,2}} \left(v_{\mathrm{q}}^{-} P_{\mathrm{REF}} - v_{\mathrm{d}}^{-} Q_{\mathrm{REF}}\right)$

The reference currents are evaluated according to the Spanish grid code, discussed in Section (4.2.), using the four commented strategies. Fig. 4.5 shows the method graphically to calculate the reference currents. The positive sequence reference currents are directly calculated from the grid code for the four control strategies, applying equations (24) and (25).

$$i_{\mathrm{d\,REF}}^{+} = I_{\mathrm{a}} \tag{24}$$

$$i_{\mathrm{q\,REF}}^{+} = I_{\mathrm{r}}. \tag{25}$$

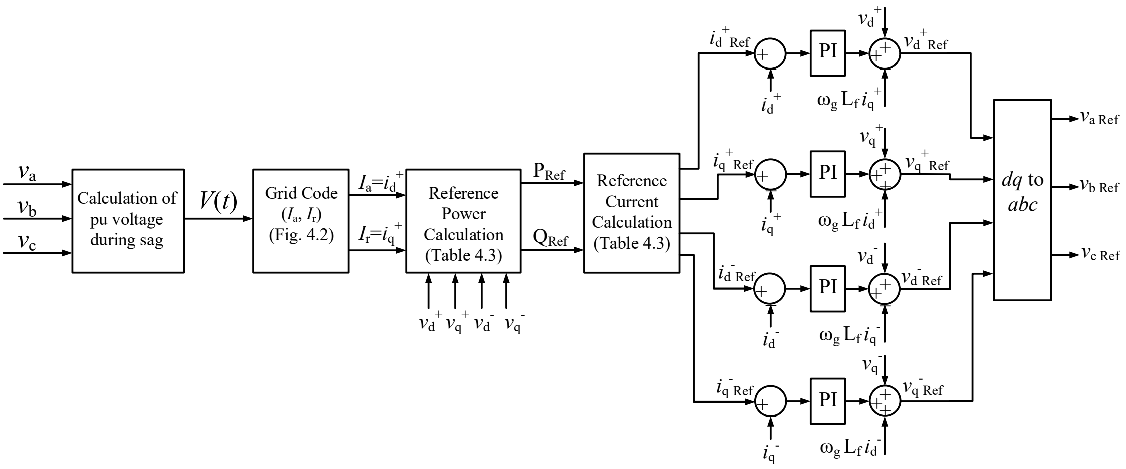
v_a
v_b
v_c
Calculation of pu voltage during sag
$V(t)$
Grid Code (I_a, I_r) (Fig. 4.2)
$I_a = i_d^+$
$I_r = i_q^+$
Reference Power Calculation (Table 4.3)
v_d^+ v_q^+ v_d^- v_q^-
P_{Ref}
Q_{Ref}
Reference Current Calculation (Table 4.3)
$i_{d\,Ref}^+$
i_d^+
PI
v_d^+
$\omega_g L_f i_q^+$
$v_{d\,Ref}^+$
$i_{q\,Ref}^+$
i_q^+
v_q^+
$\omega_g L_f i_d^+$
$v_{q\,Ref}^+$
$i_{d\,Ref}^-$
i_d^-
v_d^-
$\omega_g L_f i_q^-$
$v_{d\,Ref}^-$
$i_{q\,Ref}^-$
i_q^-
v_q^-
$\omega_g L_f i_d^-$
$v_{q\,Ref}^-$
dq to abc
$v_{a\,Ref}$
$v_{b\,Ref}$
$v_{c\,Ref}$

Fig. 4.5 Calculation of the reference currents considering grid code requirements

The reference active and reactive powers for each control method are calculated using positive reference currents (column 3 of Table 4.3. The negative reference currents can be determined using the equations of column 4 of Table 4.3 to calculate negative reference currents.

The *dq* sequence currents are calculated by using equations (26) and (27).

$$i_d = i_d^+ + i_d^- \cos(2\omega t) + i_q^- \sin(2\omega t) \tag{26}$$

$$i_q = i_q^+ + i_q^- \cos(2\omega t) - i_d^- \sin(2\omega t), \tag{27}$$

where: i_d^+, i_q^+, i_d^-, i_q^- are *dq* positive and negative current components.

To obtain the sequence currents in SI units, they must be multiplied by the base current, which for the transformed variables of *Park* is obtained as:

$$I_{\text{base,Park}} = \sqrt{3} I_{\text{nominal}}, \tag{28}$$

where: $I_{\text{base,Park}}$ is the park transformation current, I_{nominal} is the nominal current

In case of imposing zero negative currents, i_d and i_q will not oscillate; otherwise, i_d and i_q will oscillate. The verification of grid code is done by considering that the reactive current (I_r) relates to i_q, and the active current (I_a) relates to i_d. The currents I_a and I_r are adjusted during the faults to meet with the grid code, thus the active and reactive powers will change [18]. A renewable energy system must provide the required active and reactive currents during the fault to support the grid. In transient conditions, the inverter must be controlled considering the injected active current (I_a) and reactive current (I_r), according to the Spanish grid code P.O. 12.2, as shown in Fig. 4.2.

Negative sequence control during faults could be one of the future requirements for grid codes [164]. When working with sequence components (during the unsymmetrical sags), the I_a and I_r currents are related to the positive-sequence components of the direct and quadrature currents (24) and (25). The proposed control strategies might well be applied to grid codes from other countries; the main changes will be in Fig. 4.2, since various grid codes might result in different amounts of active and reactive currents being injected during the sag [165]. Therefore, the values of I_a and I_r have given in Fig. 4.2 maybe change.

4.2.2. Reference current control strategies in *Ku* transformation

In the authors' previous work [60], [162], the three-phase inverter injected currents are calculated using a mathematical model based on *Ku* transformation, for symmetrical and unsymmetrical voltage sags. In [162], the transformed inverter voltage is expected to remain constant in the synchronous reference frame at its pre-fault steady-state value. In addition, another paper has been published by the authors [166], to demonstrate the necessity of complying with grid code standards for DGs operating in a faulty grid, as well as ensuring power converter voltage and current limitations. Furthermore, the controllability of grid-connected DGs was investigated utilizing three different types of control for a PV system's grid side converter: constant forward voltage control, balanced current control, and the proposed balanced current control with grid code requirements. The *Ku* transformation was employed in [60] to calculate the reference currents and provide an optimal visual representation of the electrical parameters. The analytical demonstration of *Ku* transformation is presented in Appendix E.

Two control strategies have been studied using *Ku* transformation; these two strategies are CPC, and BCC. Because using CPC strategy offers a constant active power and more reactive power injections than other strategies, which will help to support the grid during faults. Also, BCC strategy is the only strategy that injects symmetrical and balanced *abc* currents during unsymmetrical sags.

Fig. 4.6 shows the equivalent circuit, where the *abc* components of the inverter are given by their reference value. In addition, with the two control strategies considered, a visual example of how the behaviour of the electrical variables is impacted during a two-phase fault is also presented in Fig. 4.6. The grid-connected three-phase inverter scheme using *Ku* transformation is shown in Fig. 4.7. The reference current evaluation is performed according to the Spanish grid code discussed in Section 4.2. The inverter control system is shown at the bottom of Fig. 4.7. Active and reactive currents (I_a and I_r) are achieved, according to (8) and Fig. 4.2, depending on the grid voltages measures at the point of common connection ($v_{g\ abc}$). The grid code is used to impose the reference positive-transformed currents (29):

$$i^{+}_{f\ REF} = \frac{1}{\sqrt{2}}(I_a + jI_r), \tag{29}$$

where the subscript f indicates the forward component of the transformed *Ku* variable. The active and reactive currents (I_a and I_r) corresponds to the real and imaginary parts of the positive-transformed forward reference current. Reference active and reactive powers (P_{REF} and Q_{REF}) are calculated, for each control technique, using the positive reference currents, as it is shown in Table 4.4.

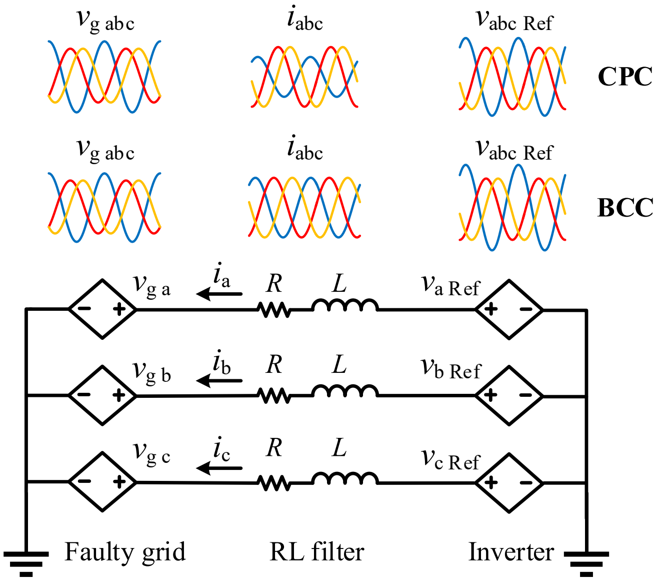

Fig. 4.6 Three-phase inverter grid connected equivalent circuit: inverter (right controlled soured), *RL* filter, and faulted grid connection (left controlled source), for the proposed CPC and BCC control strategies

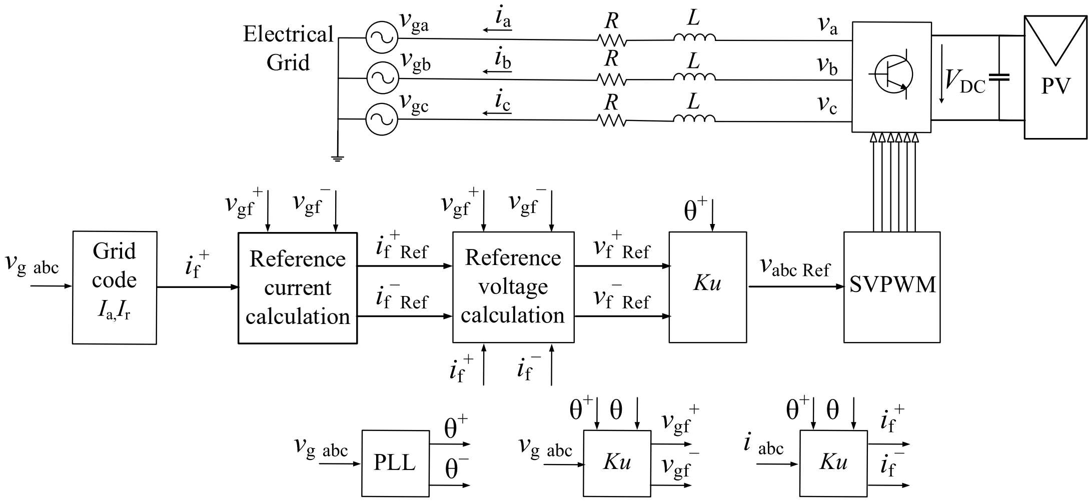

Fig. 4.7 General scheme of a three-phase grid-connected inverter, and its control, supplied by a PV installation

Table 4.4 Reference active and reactive power, and negative-sequence current equations for the proposed control strategies.

Control method	**Positive-sequence component**	**Negative-sequence component**	**Reference active and reactive powers**
CPC	$i^{+}_{\mathrm{f\,REF}} = \frac{1}{\sqrt{2}}\left(I_{\mathrm{a}} + \mathrm{j}I_{\mathrm{r}}\right)$	$i^{-}_{\mathrm{f\,REF}} = \frac{1}{2}\left(\begin{array}{l} \mathrm{Re}\{i^{+}_{\mathrm{f\,REF}}\}\left(\frac{-\mathrm{Re}\{v^{+}_{\mathrm{gf}}\}\mathrm{Re}\{v^{-}_{\mathrm{gf}}\}+\mathrm{Im}\{v^{+}_{\mathrm{gf}}\}\mathrm{Im}\{v^{-}_{\mathrm{gf}}\}}{\lvert v^{+}_{\mathrm{gf}}\rvert^{2}}\right) \\ +\mathrm{Im}\{i^{+}_{\mathrm{f\,REF}}\}\left(\frac{-\mathrm{Re}\{v^{+}_{\mathrm{gf}}\}\mathrm{Im}\{v^{-}_{\mathrm{gf}}\}-\mathrm{Im}\{v^{+}_{\mathrm{gf}}\}\mathrm{Re}\{v^{-}_{\mathrm{gf}}\}}{\lvert v^{+}_{\mathrm{gf}}\rvert^{2}}\right) \end{array}\right) + \mathrm{j}\left(\begin{array}{l} \mathrm{Re}\{i^{+}_{\mathrm{f\,REF}}\}\left(\frac{-\mathrm{Re}\{v^{+}_{\mathrm{gf}}\}\mathrm{Im}\{v^{-}_{\mathrm{gf}}\}-\mathrm{Im}\{v^{+}_{\mathrm{gf}}\}\mathrm{Re}\{v^{-}_{\mathrm{gf}}\}}{\lvert v^{+}_{\mathrm{gf}}\rvert^{2}}\right) \\ +\mathrm{Im}\{i^{+}_{\mathrm{f\,REF}}\}\left(\frac{-\mathrm{Re}\{v^{+}_{\mathrm{gf}}\}\mathrm{Re}\{v^{-}_{\mathrm{gf}}\}-\mathrm{Im}\{v^{+}_{\mathrm{gf}}\}\mathrm{Im}\{v^{-}_{\mathrm{gf}}\}}{\lvert v^{+}_{\mathrm{gf}}\rvert^{2}}\right) \end{array}\right)$	$P_{\mathrm{REF}} = \frac{\lvert v^{+}_{\mathrm{gf}}\rvert^{2}-\lvert v^{-}_{\mathrm{gf}}\rvert^{2}}{2\cdot\lvert v^{+}_{\mathrm{gf}}\rvert^{2}}\left(\begin{array}{l} \mathrm{Re}\{v^{+}_{\mathrm{gf}}\}\mathrm{Re}\{i^{+}_{\mathrm{f\,REF}}\} \\ +\mathrm{Im}\{v^{+}_{\mathrm{gf}}\}\mathrm{Im}\{i^{+}_{\mathrm{f\,REF}}\} \end{array}\right)$ $Q_{\mathrm{REF}} = \frac{\lvert v^{+}_{\mathrm{gf}}\rvert^{2}+\lvert v^{-}_{\mathrm{gf}}\rvert^{2}}{2\cdot\lvert v^{+}_{\mathrm{gf}}\rvert^{2}}\left(\begin{array}{l} \mathrm{Im}\{v^{+}_{\mathrm{gf}}\}\mathrm{Re}\{i^{+}_{\mathrm{f\,REF}}\} \\ -\mathrm{Re}\{v^{+}_{\mathrm{gf}}\}\mathrm{Im}\{i^{+}_{\mathrm{f\,REF}}\} \end{array}\right)$
BCC	$i^{+}_{\mathrm{f\,REF}} = \frac{1}{\sqrt{2}}\left(I_{\mathrm{a}} + \mathrm{j}I_{\mathrm{r}}\right)$	$i^{-}_{\mathrm{f\,REF}} = 0$	$P_{\mathrm{REF}} = \frac{1}{2}\left(\begin{array}{l} \mathrm{Re}\{v^{+}_{\mathrm{gf}}\}\mathrm{Re}\{i^{+}_{\mathrm{f\,REF}}\} \\ +\mathrm{Im}\{v^{+}_{\mathrm{gf}}\}\mathrm{Im}\{i^{+}_{\mathrm{f\,REF}}\} \end{array}\right)$ $Q_{\mathrm{REF}} = \frac{1}{2}\left(\begin{array}{l} \mathrm{Im}\{v^{+}_{\mathrm{gf}}\}\mathrm{Re}\{i^{+}_{\mathrm{f\,REF}}\} \\ -\mathrm{Re}\{v^{+}_{\mathrm{gf}}\}\mathrm{Im}\{i^{+}_{\mathrm{f\,REF}}\} \end{array}\right)$

4.3. Analysis and discussion

Each of the control strategies is applied to all sag types and considers the sag depth to highlight the differences between each control strategy and comprehend their consequences. The results obtained from this analysis for several sag types (sag type G will be used as an example) and all strategies, are presented in the following figures. Fig. 4.8 illustrates the instantaneous voltage, current, active and reactive powers, in pu for CRC, CPC, BCC, and CPRC strategies for sag type G of 0.6 depth. All the strategies have oscillation in active power, reactive power, or both, and the only strategy that can inject constant active and reactive power is CPRC, as shown in the figure. However, BCC has the advantage of injecting symmetrical sinusoidal current waves.

If negative-sequence currents are considered, BCC is the only strategy that can accomplish the grid code without any oscillations, because the other strategies have oscillation in *dq* currents, due to the negative-sequence components. Fig. 4.9 shows the active current, reactive current, active power, and reactive power versus sag magnitude in pu, and Fig. 4.10 shows the voltage, current, active power, reactive power, and *dq* current of type G and type D sags, with sag depth 0.6 and BCC control strategy.

On the other hand, if the active and reactive grid curves are assumed to be related to power rather than current, then the only strategy that can give constant active and reactive power is CPRC, as shown in Fig. 4.9; however, the disadvantage is the poor current control. Fig. 4.9 corresponds to the most unfavorable situation of the grid. When more priority is given to the reactive power than the active power, that means that CRC strategy can be a good option, because by using this strategy, reactive power can be controlled without any oscillation as shown in Fig. 4.9, but for active power, there are noticeable oscillations.

In order to use CRC strategy, active power can be reduced to a lower limit than the upper limit of Fig. 4.9, so, the oscillation of active power did not exceed the limit of grid code. However, this strategy gives sinusoidal unsymmetrical currents. In order to inject sinusoidal symmetrical current during voltage sag, the only strategy to obtain this is the BCC. On the other hand, by using BCC, the active and reactive power must be reduced to different limits below the active power limit and above the reactive power limit. Controlling the positive- and negative-sequence reference currents are required to manage active and reactive power during abnormal grid behaviour. Different control strategies for controlling power during voltage sags are investigated in this thesis. Furthermore, two scenarios are considered to validate the Spanish grid code using these strategies: the first scenario suppose only positive-sequence current is imposed, and the second scenario assumes that positive- and negative-sequence current are imposed [167].

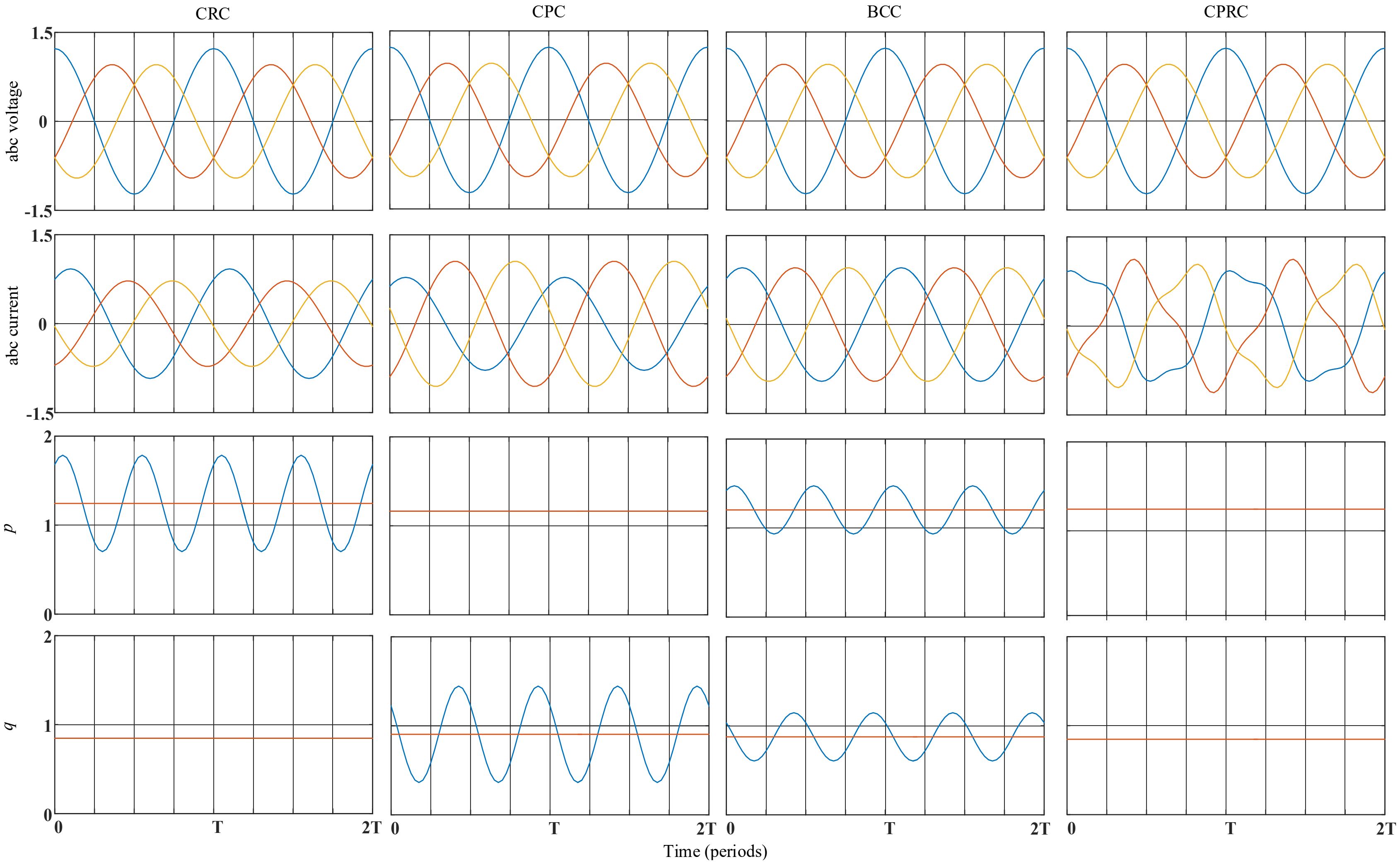

Fig. 4.8 Different control strategies for type G sag depth 0.6

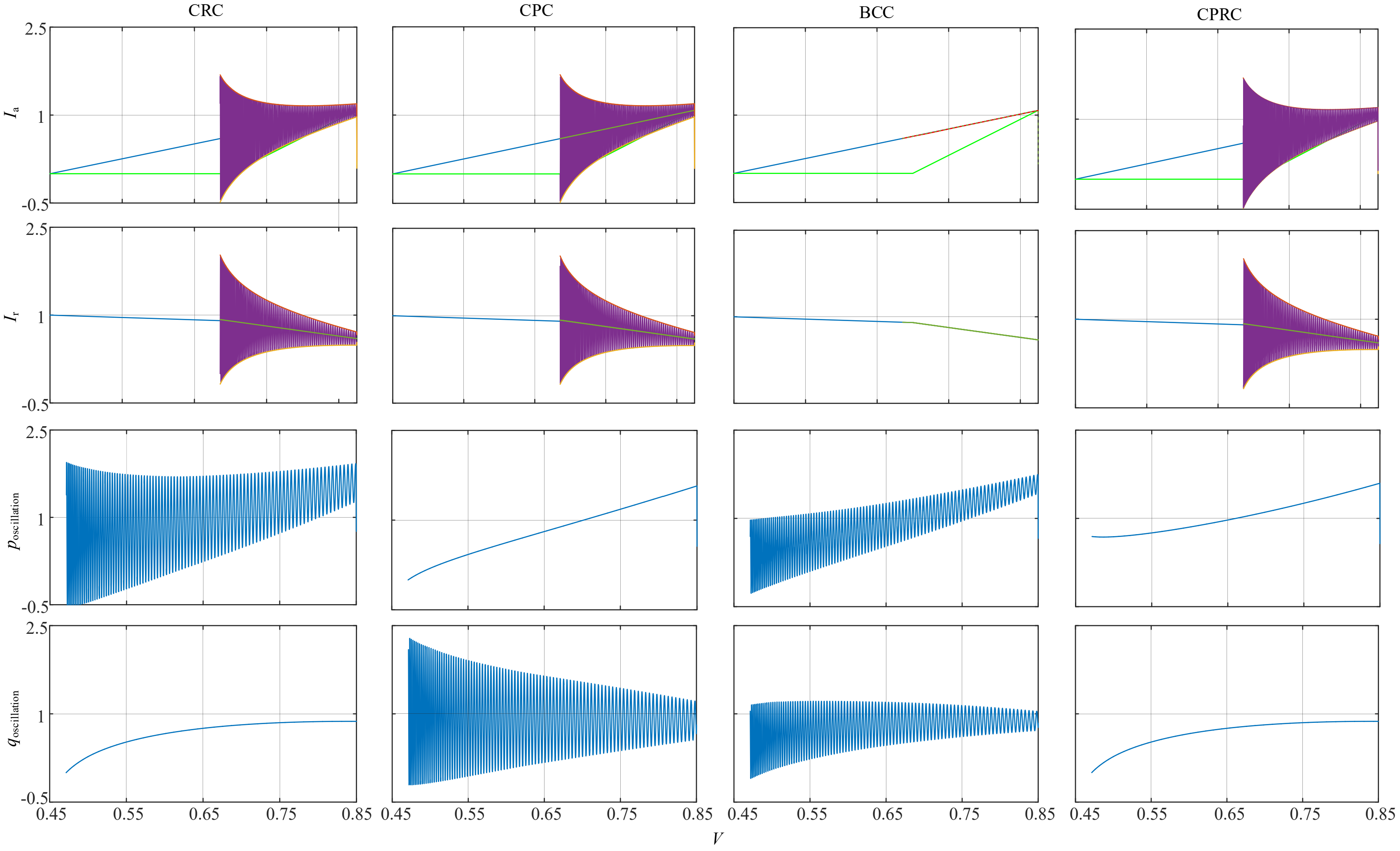

Fig. 4.9 Spanish grid code P.O. 12.2: active and reactive currents and powers in pu with different control strategies for type G sag of depth 0.6

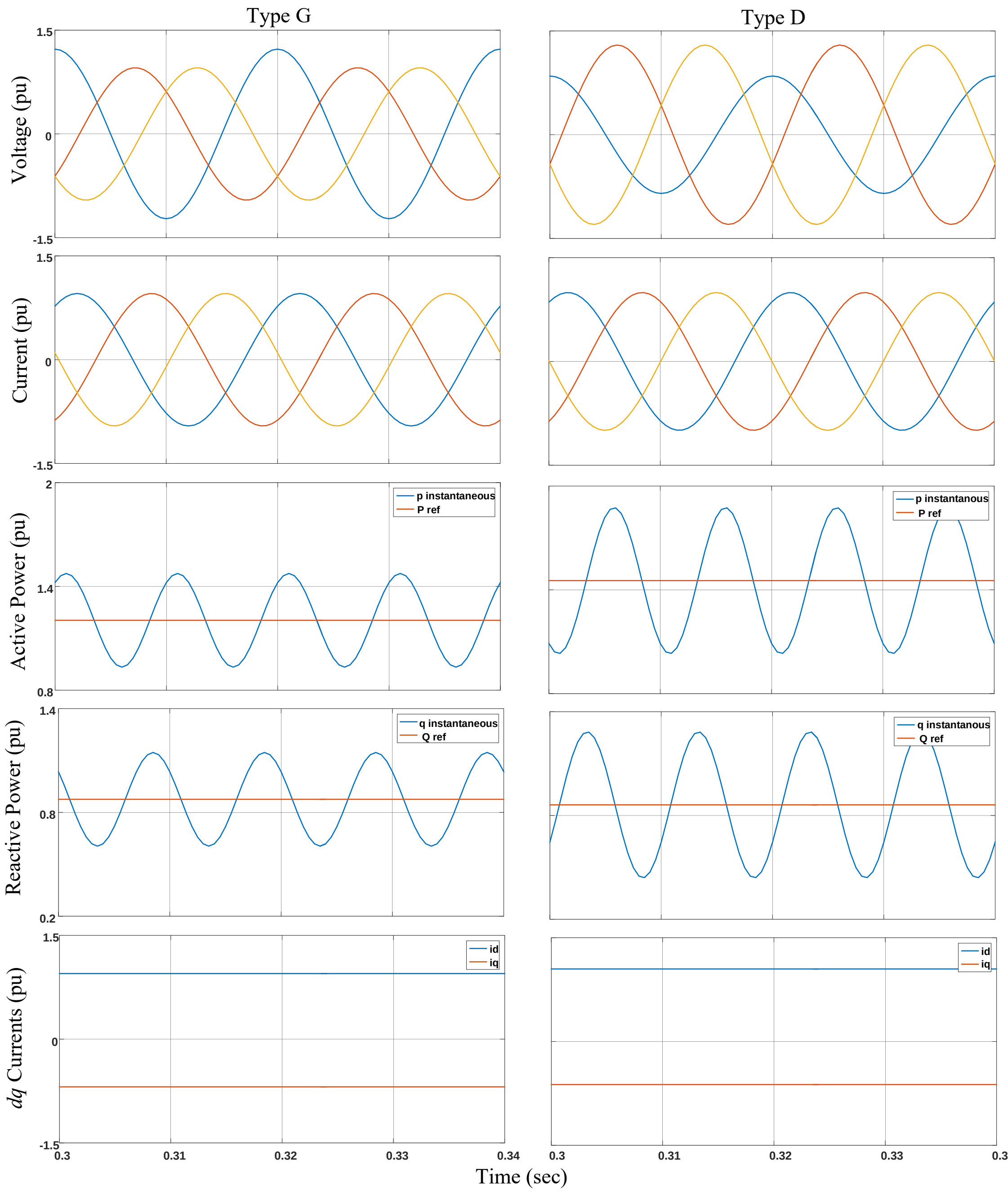

Fig. 4.10 Comparison of types G and D sags, both of depth 0.6, under BCC strategy

As seen in Fig. 4.10, BCC strategy has been tested for type D, and type G sags to demonstrate the functionality and the grid code validation of the proposed strategy in different scenarios. As seen in the third and fourth row of Fig. 4.10, the average active and reactive powers are constant; however, both instantaneous powers are oscillating.

It can conclude from previous results that, BCC is the only strategy that can provide the exact specified limits of active and reactive currents, and average active and reactive powers to inject the grid's most adverse scenario. It does, however, have the drawback of instantaneous power oscillation. On the other hand, if the grid code curves are considered to be linked to active and reactive power rather than currents, CPRC can validate the grid code. In addition, various controls with appropriate limitations can be employed to avoid violating grid codes.

In addition, in order to test the behaviour of the control strategies using *Ku* transformation, another test has been made with type C sag and with different sag depth for CPC and BCC to ensure that these strategies are carried out in accordance with grid code standards.

Negative reference currents are obtained for two control strategies. The first is to use BCC strategy to impose zero negative reference currents, and the second is to use CPC strategy to calculate the negative reference currents using the formulas of the third column of Table 4.4. If zero negative currents are imposed, i_f will not oscillate, but the active and reactive powers will change when I_a and I_r currents are adjusted to fit the grid code during the faults.

The behaviour of each control strategy during a two-phase fault (type C sag) with different sag depths of $h = 0.7$, 0.5, and 0.3 is shown in Fig. 4.11, whose *abc* voltage components are indicated in the first row. It is assumed that $P_{a0} = 0.7$ in (10), then the converter injects 70 % of its rated power before the fault. The second row of Fig. 4.11 illustrates that the *abc* currents are unbalanced when using CPC strategy. However, when using BCC strategy during unsymmetrical sags, the injected *abc* currents are balanced.

The injected current limits for both cases are the converter's rated current. The real and imaginary parts of the transformed forward component of the reference current are shown in the third and fourth rows of Fig. 4.11. It is noticed that *abc* currents for CPC strategy oscillate. This indicates that this strategy may not validate the grid code for unsymmetrical sags in some cases. Furthermore, for severe sags, these limits can be increased in a small amount (for example 1.1 ~ 1.2 pu). Whereas for the BCC strategy, the *abc* current remains constant, indicating that the grid code has been validated.

The I, II, and III limits in the third and fourth rows of Fig. 4.11, correspond to the grid code limits for active and reactive currents given in Fig. 4.2. The control sets the upper limit for the active current if the imposed *abc* current does not exceed 1 pu, i.e. real part of the positive component of the injected current, according to (29). Nevertheless, if that current exceeds 1 pu, the control must limit the injected active current until it drops below the limit shown in Fig. 4.2. According to Fig. 4.2, there is only one feasible value for the reactive current, i.e. the imaginary part of the positive component of the injected current, as illustrated in (29). For example, the control imposes the upper limit of the active current for the sag with depth $h = 0.7$, in the second row of Fig. 4.11(a), ensuring that the *abc* current does not exceed 1 pu. However, if the upper limit of the active current is injected as seen in Fig. 4.11(b) for $h = 0.5$, , the *abc* current exceeds 1 pu, thus a limit must be imposed in this case to inject always *abc* current within 1 pu (solid black line in the third row of Fig. 4.11. In some cases, even though the control injects the lower limit of the active current, the injected *abc* current can surpass 1 pu, as illustrated in the second row of Fig. 4.11(c). The CPC strategy cannot always accomplish the grid code, as seen in the third and fourth row of Fig. 4.11 since the injected currents exceed the aforementioned limitations, while for the BCC strategy the limits are not exceeded [60].

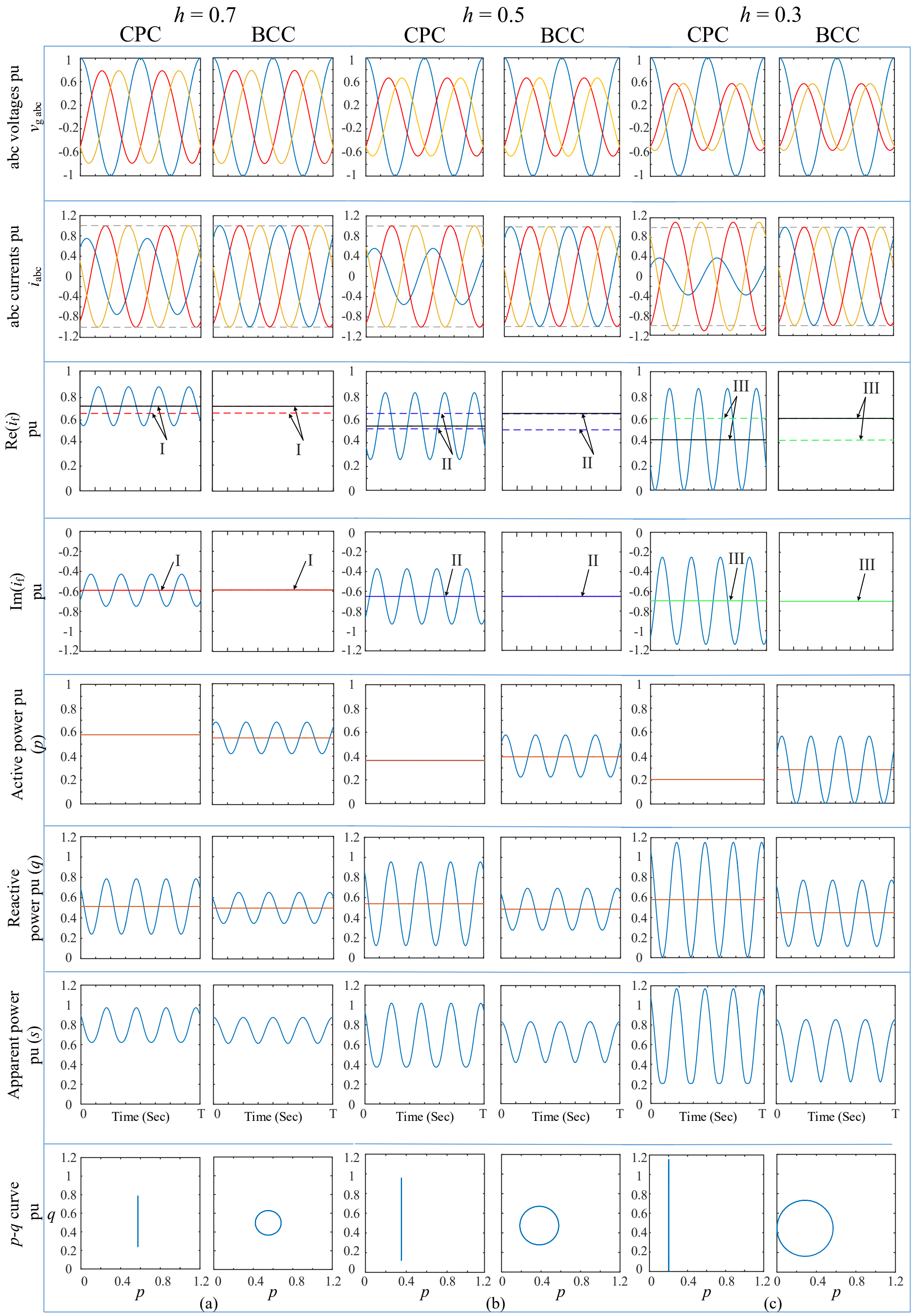

Fig. 4.11 CPC and BCC strategies during a 2-phase fault (type C sag) for sag depth (a) $h = 0.7$, (b) $h = 0.5$ and (c) $h = 0.3$

It is observed that the negative sequence of the injected current has a value other than zero for CPC strategy, while this value is zero for the BCC strategy. In this regard, the authors' previous work [167] has demonstrated that BCC strategy is the only strategy that can validate the grid code without restrictions for unsymmetrical sags. Both strategies will verify the grid code for symmetrical sags since the negative sequence component will be zero. However, as seen in the fifth row of Fig. 4.11, this strategy has the drawback of oscillation in the instantaneous active power (p), whereas the CPC strategy has no oscillation in that power. The instantaneous reactive power (q) oscillates, as seen in the sixth row of Fig. 4.11, but the power oscillation is larger with CPC strategy. In both control strategies, there is an oscillation in the instantaneous apparent power (obtained from (30)) as seen in the seventh row of Fig. 4.11, and since both active and reactive powers oscillate, this oscillation cannot be removed.

$$s = \sqrt{p^2 + q^2}. \tag{30}$$

The active-reactive (p-q) curve is shown in the last row of Fig. 4.11. It is observed that because there is no oscillation in the active power, this curve is represented as a straight line for the CPC strategy. However, for the BCC strategy, both powers oscillate, transforming the straight line into a circle.

The results indicate that neither the CPC nor the BCC strategies for symmetrical sags violate the grid code. Only the BCC strategy achieves grid code requirements for unsymmetrical sags at the price of oscillations in instantaneous active and reactive powers. On the other hand, the CPC strategy provides constant active power under unsymmetrical sags, but it does not fulfill grid code requirements, because transformed current oscillations are always outside the grid code limits. Fortunately, only under the most severe unsymmetrical sags cause the average transformed current to exceeds the code limitations [60].

To summarize the theoretical study, the process for implementing the Spanish grid code in the control system is described below. The flowchart for that purpose is shown in Fig. 4.12.

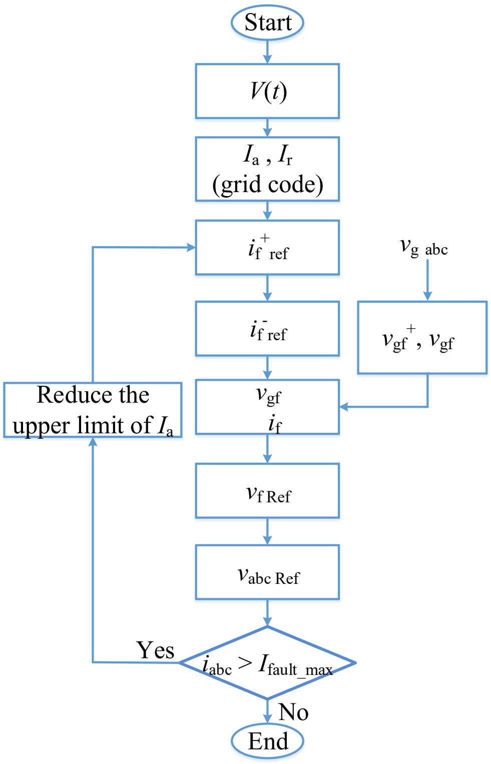

Fig. 4.12 Flowchart to adapt Spanish grid code to a grid-connected inverter

The process starts calculating, using (8), the per-unit instantaneous value of the RMS remaining voltage during the sag. Second, the active and reactive currents are calculated using the preceding value according to the Spanish grid code, depicted in Fig. 4.2. The active current's upper limit is then chosen. Third, according to Table 4.4, these currents are utilized to obtain the *Ku* transformed positive reference current. Table 4.4 is used to calculate the *Ku* transformed negative reference current, which depends on the chosen control strategy. Fourth, the *Ku* transformed grid voltage and injected current components are determined (note that to obtain the transformed grid voltage *Ku* transformation equation has to be used, as explained in Appendix E). Then, the entire system's mathematical model is obtained. Finally, the *abc* components of the inverter's reference voltage are calculated as follows:

$$\left[v_{\mathrm{abc\,Ref}}\right]=\left[\mathbf{K}\left(\Psi\right)\right]\left[v_{\mathrm{f\,Ref}}\right]. \tag{31}$$

The *abc* currents are calculated in this study to ensure that the value does not exceed 1 pu. If the value exceeded that limit, the active current would need to be reduced within the limits of the grid code as shown in Fig. 4.2, until the *abc* current equals the desired limit.

It should be emphasized that the proposed analytical model represents the behaviour of a three-phase grid-connected inverter with *RL* filter under unsymmetrical voltage sags. Note that this model is also valid for symmetrical sags. In this situation, the negative-sequence component of the grid voltage is zero, i.e. $v_{\mathrm{gf}}^{-}=0$.

The functionality of the proposed limiting strategy is guaranteed by comparing it with the strategy presented in [71] that is used to limit the injected current is presented in Fig. 4.13. As seen, the proposed limiting strategy gives the same performance with less calculation effort to limit the injected *abc* current.

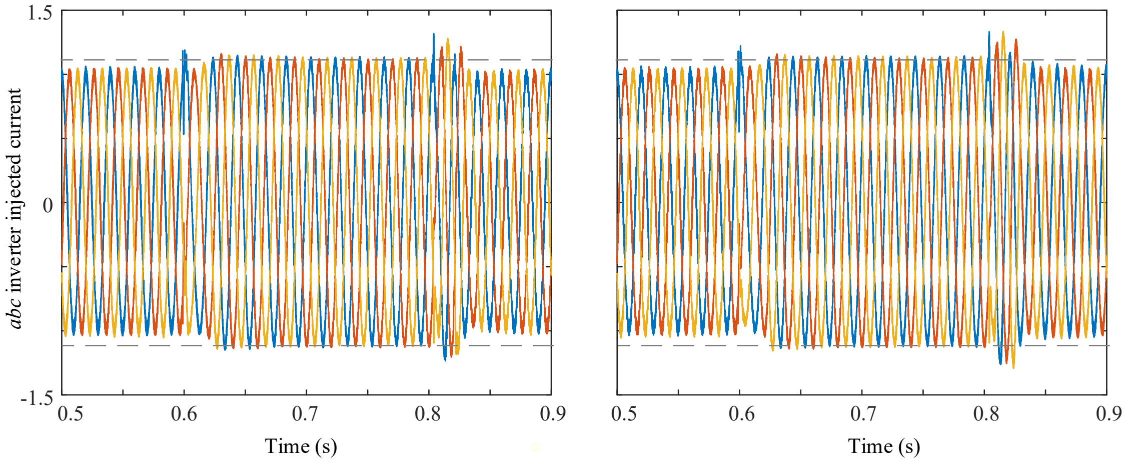

(a) (b)

Fig. 4.13 Comparison between (a) limiting strategy proposed in [71], and (b) the proposed limiting strategy

The utility industry's guideline for harmonic levels in the system is generally less than 5%, as shown in Table 2 of [168]. Furthermore, as shown in Table 3 of [169], the harmonics of the injected current from DG depend on the inverter's control technique. In this thesis, the THD of the injected current during fault is less than 4 %, as shown in Fig. 4.14.

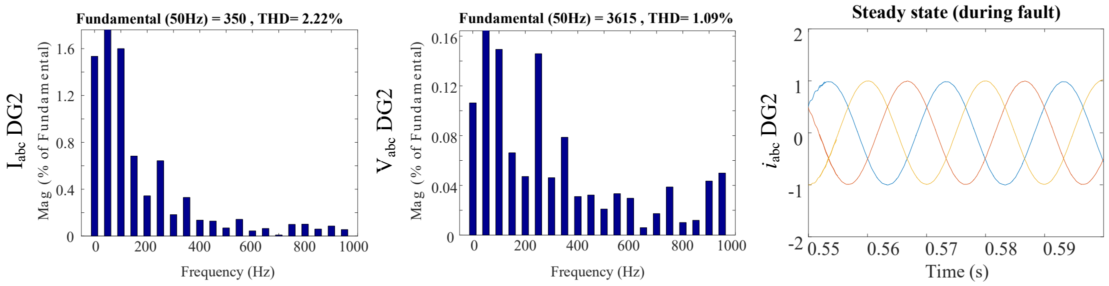

Fig. 4.14 THD of the injected current during steady state of three-phase fault

- Analysis of sag parameters impact using *Ku* transformation

If voltages are represented in the complex plane, i.e. *Ku* plane, different types of faults may be clearly distinguished, making it easier to know and recognize the sag type and depth. The *abc* and transformed voltages are represented in per-unit values in this section, as follows:

$$v_{\text{f pu}}(t) = v_{\text{f}}(t) \Big/ \left(\sqrt{3/2}V_{\text{base}}\right)$$
$$v_{\text{abc pu}}(t) = v_{\text{abc}}(t) \Big/ \left(\sqrt{2}V_{\text{base}}\right), \tag{32}$$

where V_{base} is the voltage base value, which corresponds to the phase voltage.

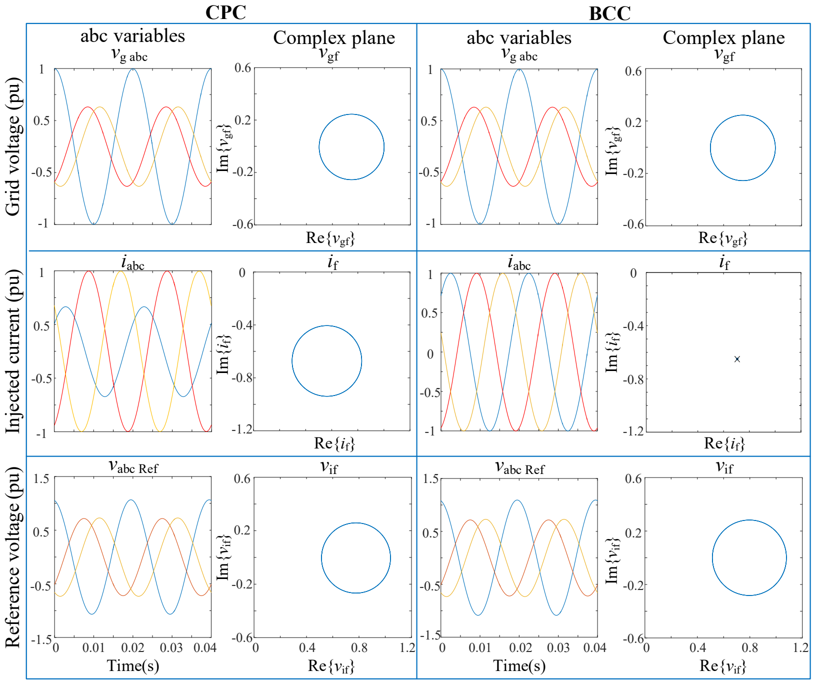

Fig. 4.15 *abc* and the complex plane of grid voltage, injected current and inverter reference voltage for unsymmetrical sag (type C) with h=0.5 sag depth

During unsymmetrical sags (type C sag), Fig. 4.15 shows the time evolution of the waveform in *abc* and transformed variables of the grid voltage, injected current, and reference inverter voltage. The transformed variables of the grid voltage and reference inverter voltage oscillate due to the phase unbalance, as seen by the circle waveform in the complex plane. However, the BCC strategy always imposes a symmetrical current, thus the transformed current does not oscillate (In the complex plane of the current, the is a single point, not a circle). Furthermore, because the current in the CPC strategy is unbalanced during the sag, an oscillation will appear, as indicated by the circle.

The exponential term $e^{-j2\omega t}$, dependent on twice the fundamental pulsation, explains this phenomenon. CPC and BCC strategies provide the same time evolution in the *abc* and complex planes for symmetrical sags (type A sag) (imaginary part vs. real part), because the grid voltage is balanced during the sag, there is no oscillation in the transformed variables of voltage or current, which will be represented as a single point in the complex plane [60].

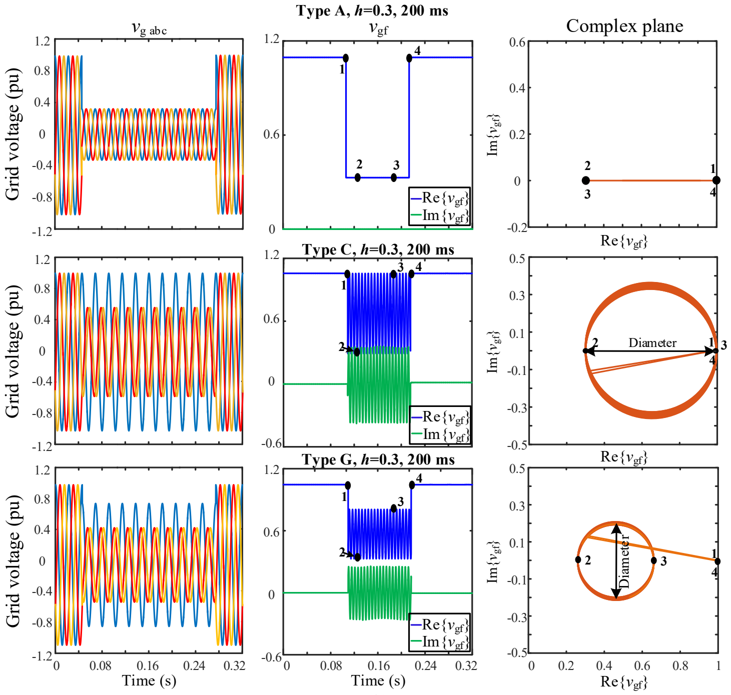

(a) (b) (c)

Fig. 4.16 Differences between type A, type C, and type G sags using transformed variables with h=0.7 sag depth, and 200ms duration. (a) *abc* variables, (b) transformed variables and (c) complex plane

Fig. 4.16 illustrates the time evolution of both *abc* components and transformed components of the grid voltage before, during, and after a fault, taking into account: symmetrical sags (type A sags, caused by three-phase faults) and unsymmetrical sags (type C, caused by phase-to-phase faults, and type G, caused by phase-to-phase-to-ground faults after two Dy transformers). In this figure, point 1 indicates the sag's beginning, while points 2 and 3 represent the sag's minimum and maximum oscillations, respectively, and point 4 illustrates the sag's end. Note that because there is no oscillation in the representation of the real and imaginary parts, points 2 and 3 in Fig. 4.16(b) for type A sag are in the same position in Fig. 4.16(c). As a result, the complex plane of the voltages forms a straight line, indicating that the fault is symmetrical. However, because only two phases have a voltage reduction, for type C sag points 1, 3, and 4 are all at the same level, as shown in Fig. 4.16(b). Due to this fact, the representation in the complex plane is a circle rather than a straight line (as in the case of symmetrical sags). However, it should be emphasized that this representation changes depending on the type of unsymmetrical sag. Points 1, 3, and 4 are not at the same level for type G sag as they are for type C sag, as shown in Fig. 4.16(b). This is because as shown in Fig. 4.16(a) for type G sag, the voltage is reduced in all phases. As a result, that the circle shifts to the left in this case, as shown in Fig. 4.16(c), since the voltage is reduced in all the phases. The sag depth affects the length of the diameter, as shown in Fig. 4.16, for the same sag type and using the complex plane. For unsymmetrical sag, the diameter of the circle in the complex plane may be utilized to determine the phase unbalance. For example, the phase unbalance for type C sag is higher than that for type G sag. As a result, the diameter of the circle for type C is larger than for type G [60].

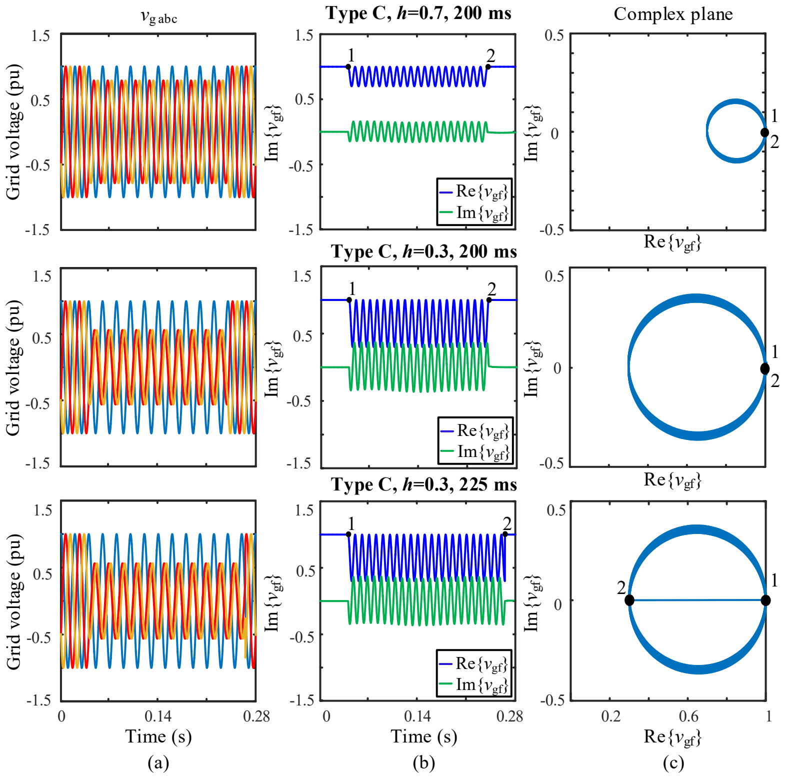

Fig. 4.17 Sag depth and sag duration influences (a) *abc* variables (b) transformed variables (c) complex plane

Another benefit of representing grid voltages on the complex plane, i.e. Ku plane, is that it provides information about the location of the sag's endpoint (point-on-wave). For example, when looking at Fig. 4.17 the following conclusions can be drawn: when the sag duration is a multiple of a period, the sag's starting point (point 1) and ending point (point 2) are in the same place in the complex plane (Fig. 4.17(c)), whereas when the sag duration is not a multiple of a period, points 1 and 2 are in different places for unsymmetrical sags. Indeed, both points 1 and 2 are located at the rightmost part of the circle (Fig. 4.17(c)), for unsymmetrical sag type C when the sag duration is 200 ms (multiple of a period). However, points 1 and 2 are in different locations if the sag duration is 225 ms (not a multiple of a period), since the point-on-wave where the sag ends is different for various durations. Points 1 and 2 are always in the same location for symmetrical sags (type A sags) because the point-on-wave when the sag ends is always the same. To summarize, the location of the sag's endpoint in the complex plane will always be the same for symmetrical sags, but it is a valuable tool to visualize the exact endpoint of the sag for unsymmetrical sags. The previous results demonstrated that visualizing grid voltages in the complex plane provides a much better visual representation of the effects of sag parameters [60].

In this chapter, different control strategies to control DG-based inverters during voltage sags have been proposed to fulfill the Spanish grid code requirements. In addition, a proposed limiting strategy is demonstrated. In the next chapter, different protection algorithms to protect MV DS underground cables will be presented and explained in detail.

5 Proposed fault protection scheme

In this chapter, the proposed protection algorithms will be explained in detail for radial and ring DS with inverter-based DG. First, the conventional protections (OCR/DR) will be presented and discussed to show the limitation of these protection strategies in the case study. Then, the proposed protection algorithms that consist of three levels of protection will be explained, starting with CE, then ZO, and at the end LO and fault classification method.

5.1. Introduction

Nowadays, several researchers proposed to apply communication standards for resolving protection issues. This chapter presents a novel use of a communication-based DR system with ANN. A protection strategy has been proposed using three algorithms. The first algorithm depends on analyzing data from all of the PDs in the grid and sending it to a CE, whereas the second algorithm is based on a ZO employing peer-to-peer communication. The proposed strategy is based on comparing both algorithms' decisions to create a more reliable and redundant system. If there is a miscommunication, the decision priority is handed to the other algorithm. One of the most significant benefits of the ZO is that it avoids the need to change the PD setting in temporary grid reconfigurations. Furthermore, in the case of poor communication, a new algorithm named LO will be employed to provide a more secure protection system. The algorithm will analyze the local data (voltage and current) of each PD in order to isolate the grid fault. All algorithms for the ring and radial grids have been evaluated in a variety of scenarios involving fault types, fault locations, fault resistance, the number of DGs and their location and contribution, load consumption, and different neutral connections for the MV side of the HV/MV transformer.

Thus, the objectives of this chapter can be summarized as follows:

1. The proposed ANN protection controller can locate the fault using a simplistic training algorithm, a minimal number of layers, and hidden layers to reduce training time. The new approach can improve the system's availability, reliability, and accuracy while also accelerating the protection system's response to unexpected grid changes (new parts being integrated, transitory adjustments, and network reconfiguration due to faults or maintenance).
2. A novel protection scheme is proposed, unlike [138], the algorithm is evaluated for both symmetrical and unsymmetrical faults. Furthermore, unlike [112], [125], [137], the proposed strategy may be used for multiple HV/MV transformer neutral connections. Besides, unlike [98], [99], the protection algorithms are evaluated for low and high fault resistance. In addition, the protection algorithms have been tested for stiff where the voltage and frequency of the grid are expected to be fixed by the stiff grid, and weak grids where a frequency or voltage variation from its steady-state value can occur during faults. Moreover, variations in load profile, DG penetration, fault locations, fault types have all been considered.
3. The application of CE, and ZO algorithms will be analysed, modeled, and optimized by ANN to coordinate the PD setting and pinpoint the faulty line automatically.
4. Evaluating both algorithm decisions (CE-ZO) results in a more accurate and consistent procedure, as well as backup protection, as one algorithm acts as a backup for the other.
5. No coordination system with a DR approach based on ANN was employed in any of the prior studies. This protection method enables the detection of multiple fault types (symmetrical and unsymmetrical) in the MV DS, resulting in more reliable and redundant protection.
6. Novel use of the local measurements (voltages/currents) of each PD is used to propose a protection algorithm named LO, which is genuine and communication-free. The use of LO gives another degree of reliability for both radial and ring grids.

The analysed grids shown in Fig. 5.1 and Fig. 5.2 are used as a DS (radial/ring), and DGs are connected in different parts of the grids to validate the proposed protection algorithms. The grid was introduced in chapter 3.

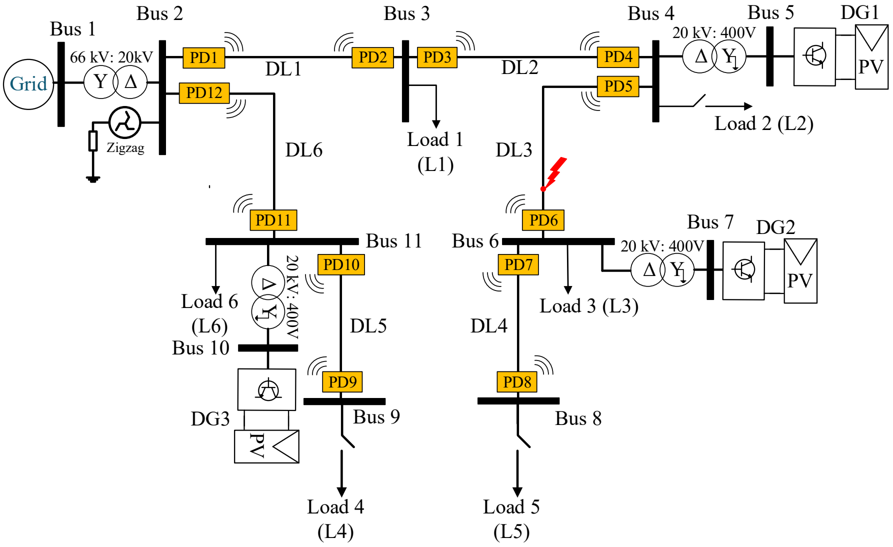
Bus 1
Bus 2
Bus 3
Bus 4
Bus 5
DG1
66 kV: 20kV
20 kV: 400V
Grid
Y
Δ
PD1
PD2
PD3
PD4
PD5
PD12
DL1
DL2
PV
Zigzag
Load 1
(L1)
Load 2 (L2)
DL6
DL3
PD11
PD6
Bus 11
Bus 6
Bus 7
DG2
20 kV: 400V
PD10
PD7
Load 6
(L6)
Bus 10
20 kV: 400V
DL5
DL4
Load 3 (L3)
PD9
PD8
DG3
Bus 9
Bus 8
Load 4
(L4)
Load 5
(L5)

Fig. 5.1 Single line diagram of the analysed radial DS with DG penetration

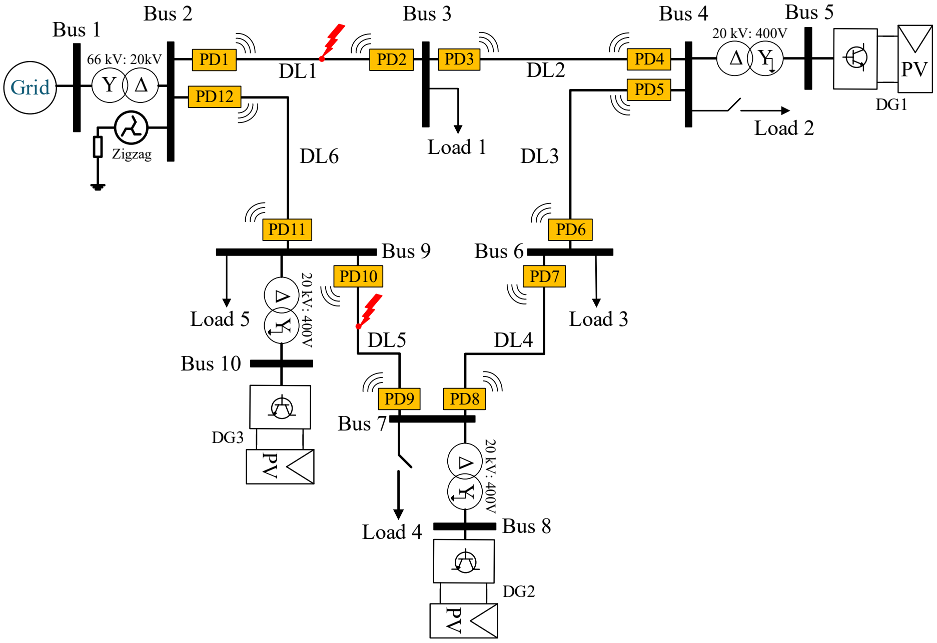
Bus 1
Bus 2
Bus 3
Bus 4
Bus 5
Grid
66 kV: 20kV
20 kV: 400V
Y
Δ
PD1
PD2
PD3
PD4
PD5
PD12
DL1
DL2
PV
DG1
Load 2
Zigzag
Load 1
DL6
DL3
PD11
PD6
Bus 9
Bus 6
PD10
PD7
Load 5
20 kV: 400V
Load 3
DL5
DL4
Bus 10
PD9
PD8
Bus 7
DG3
20 kV: 400V
Load 4
Bus 8
DG2

Fig. 5.2 Single line diagram of the analysed ring DS with DG penetration

5.2. Conventional protections (OCR/DR)

In order to emphasize the importance of the proposed protection strategy, the OCR and DR explained in [170] are used to emphasize the need for a new protection strategy in the case of ring or radial grids with high DG-based inverter penetration. The analysis of OCR, and DR protection algorithms' behaviour is shown for the radial grid represented in Fig. 5.1, because using this grid the main inconvenience can be highlighted. The currents at both ends of DL3 have been presented in Fig. 5.3 for the two protection strategies. Fig. 5.3(a) shows the case with 2 DG, Fig. 5.3(b) with 1 DG, and Fig. 5.3(c) without DG, respectively. These results correspond to a three-phase fault in DL3 with a value of the fault resistance of 0.1Ω. For the OCR and DR protection strategies, the relay settings used to obtain Fig. 5.3 are shown in Table 5.1 and Table 5.2.

Table 5.1 OCR settings with 2 DG

Parameter (OCR)	Value
Pick up current (pu)	1
Time dial (TD)	0.5
Current transformer (CT)	500 : 1

Table 5.2 DR settings with 2 DG

Parameter (DR)	Value
Differential current (pu)	1.08
Biased characteristic (K)	0.5
Current transformer (CT)	500 : 1

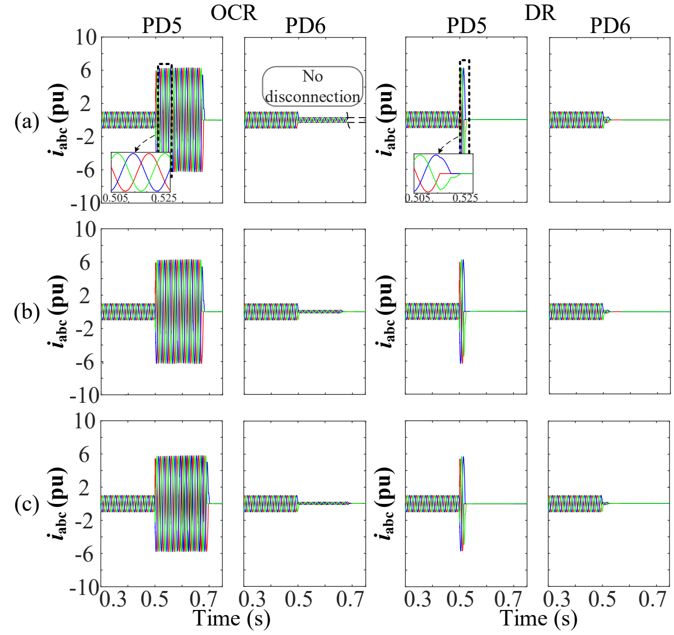

Fig. 5.3 Short-circuit current of OCR, and DR behaviour during a three-phase fault in DL3 with fault resistance $r = 0.1\ \Omega$ (a) with two DGs, (b) with one DG, (c) without DG

In order to highlight the limitations of classical protections, the following case has been analysed. In the case of two DGs connected at buses 4 and 6, and when a three-phase fault occurs at DL3, the faulted line will be fed from two points. The short-circuit current passing through PD5 is equal to the short-circuit current when one DG is connected at bus 4; however, the short-circuit current is different when DG2 is connected at bus 6, as PD6 will be supplied from DG2. This case is important to show the difference between OCR and the other protection strategies, because as seen in Fig. 5.3(a), PD5 will trip; however, PD6 will not trip as the settings of the relay needs to be updated.

When two DGs are connected at buses 4 and 6, the power flow and the current values are reduced in DL3 as DG1 and DG2 are close to the loads, so less power comes from bus 4 with DG penetration. In the case of single-phase to ground fault, as the ground connection is made through a zigzag transformer with grounding reactance, as shown in Fig. 5.1, the fault current during single-phase fault will be limited. Therefore, the relay will not trip in this case, as shown in Fig. 5.4, this case is important to highlight the limitation of DR in some scenarios. However, during a three-phase fault, the fault current will be high in both cases (with and without DGs), as there is no influence from the zigzag transformer, as shown in Fig. 5.3. The DR protection strategy is also affected by significant changes in DG penetration, which is averted using CE-ZO protection strategy.

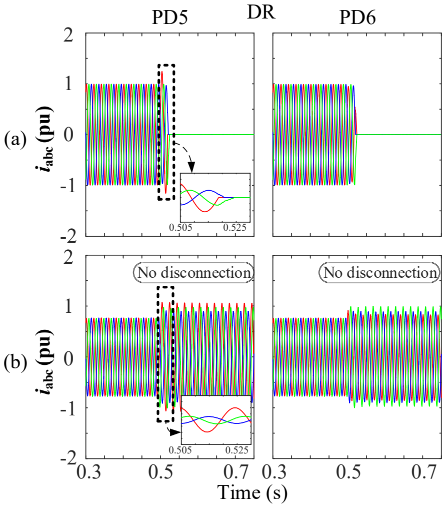

Fig. 5.4 Short-circuit current of DR behaviour during single-phase fault in DL3 with fault resistance *r* = 0.1 Ω (a) without DGs, (b) with two DG

As presented in previous paragraphs, the conventional relays may fail in some cases to guarantee complete protection in DS with high DG penetration. Therefore, the need for a genuine protection strategy adapted for radial and ring grids during different circumstances will be presented and discussed in the following sections.

5.3. Proposed fault protection algorithms

In this section, the proposed fault location algorithms will be explained. The proposed protection scheme is based on three-level of control. CE, ZO, and LO controllers. Fig. 5.5 Shows the content distribution of the proposed protection strategy in this section, referring to the subsection of each part.

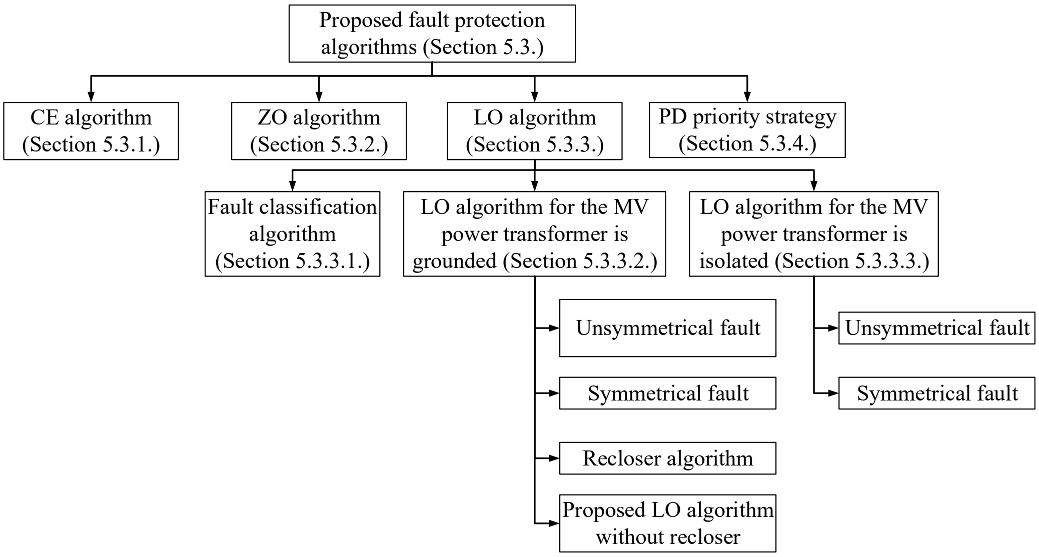
Proposed fault protection algorithms (Section 5.3.)
CE algorithm (Section 5.3.1.)
ZO algorithm (Section 5.3.2.)
LO algorithm (Section 5.3.3.)
PD priority strategy (Section 5.3.4.)
Fault classification algorithm (Section 5.3.3.1.)
LO algorithm for the MV power transformer is grounded (Section 5.3.3.2.)
LO algorithm for the MV power transformer is isolated (Section 5.3.3.3.)
Unsymmetrical fault
Symmetrical fault
Recloser algorithm
Proposed LO algorithm without recloser
Unsymmetrical fault
Symmetrical fault

Fig. 5.5 Distribution levels of the proposed protection algorithm for grounded/isolated power transformer

The proposed strategy will be based on the decision of two algorithms to provide more reliable and secure DS protection. The first algorithm (CE), is based on DPF data analysed from all PDs in the grid. These data will be transferred to the CE, where the controller will evaluate and analyze them and execute the relevant trip signal to isolate the faulty part of the grid, as shown on the left side of Fig. 5.6 and Fig. 5.7. The second algorithm is the ZO, located at each PD, which will rely on exchanging DPF data via the communication between both PDs in the same line to alter their status according to the faulty part of the grid, as shown on the right side of Fig. 5.6 and Fig. 5.7. The proposed CE and ZO algorithm decisions will be evaluated to have a consistent and effective process. During a fault, the CE controller will use network-wide comparative measurements to locate the fault and trip the corresponding PDs. ZO will be implemented to work in parallel with CE, then the decision of both controllers will be reviewed, in order to enhance the security and redundancy of the protection system. The ZO algorithm is based on the peer PDs in the same line and transmits their data to ZO located at each PD. Its advantages include encrypted communication, and the ability to adapt to temporary grid reconfigurations. If a communication problem is detected as a reason for errors or hacking, then, the decision priority shifts directly from one algorithm to the other. In addition, if the total communication channels have been lost due to accidents, storming, hacking, or noise interference, the LO will be able to localize the faulted part of the DS correctly.

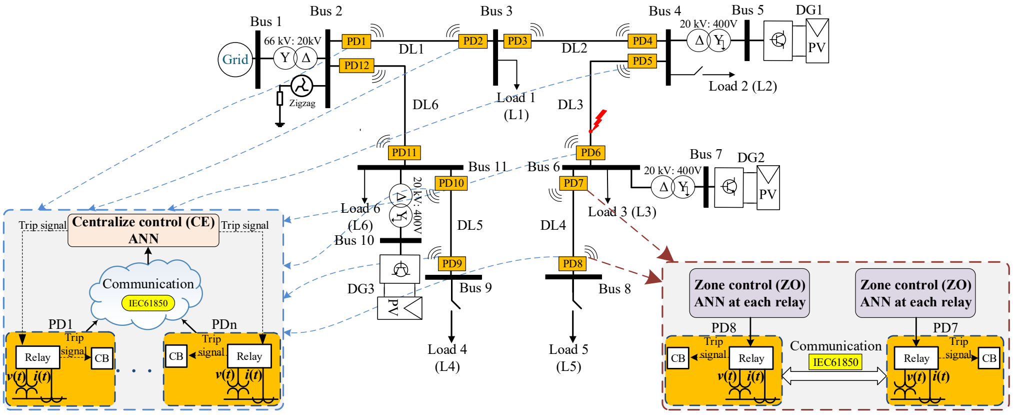
Bus 1
Bus 2
Bus 3
Bus 4
Bus 5
DG1
Grid
66 kV: 20kV
20 kV: 400V
PV
PD1
PD2
PD3
PD4
PD5
PD12
DL1
DL2
DL3
DL6
Zigzag
Load 1 (L1)
Load 2 (L2)
PD11
PD6
Bus 11
Bus 6
Bus 7
DG2
PD10
PD7
Load 6 (L6)
Load 3 (L3)
Bus 10
DL5
DL4
PD9
PD8
DG3
Bus 9
Bus 8
Load 4 (L4)
Load 5 (L5)
Trip signal
Centralize control (CE) ANN
Communication
IEC61850
PD1
PDn
Relay
CB
v(t) i(t)
Zone control (ZO) ANN at each relay
PD8
PD7

Fig. 5.6 Single line diagram of the analysed radial DS with DG penetration and CE/ZO algorithms

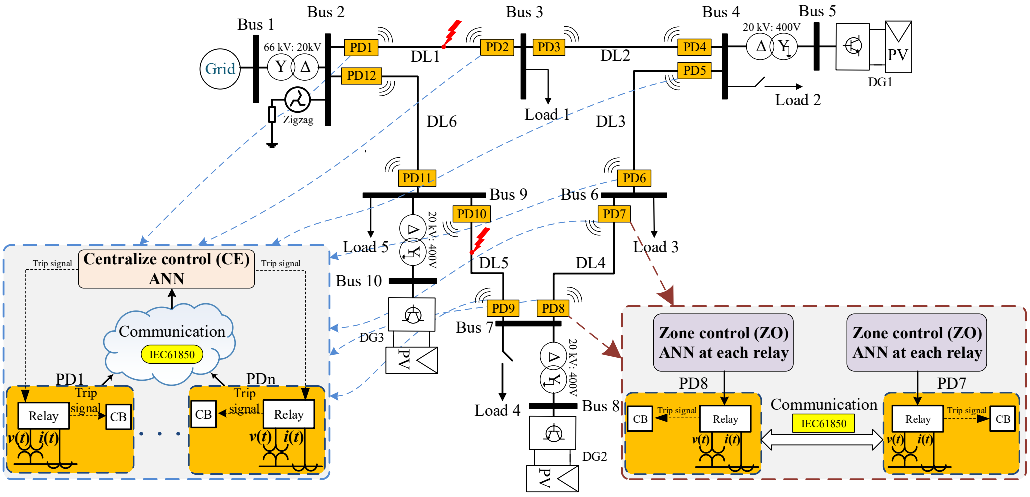
Bus 1
Bus 2
Bus 3
Bus 4
Bus 5
Grid
66 kV: 20kV
20 kV: 400V
PV
DG1
PD1
PD2
PD3
PD4
PD5
PD12
DL1
DL2
DL3
DL6
Zigzag
Load 1
Load 2
PD11
PD6
Bus 9
Bus 6
PD10
PD7
Load 5
Load 3
Bus 10
DL5
DL4
PD9
PD8
DG3
Bus 7
Bus 8
Load 4
DG2
Trip signal
Centralize control (CE) ANN
Communication
IEC61850
PD1
PDn
Relay
CB
v(t) i(t)
Zone control (ZO) ANN at each relay
PD8
PD7

Fig. 5.7 Single line diagram of the analysed ring system with DG penetration and CE/ZO algorithms

As mentioned in the introduction, due to the growth of DG penetration, traditional protection schemes have been evolved into new features due to the advent of standards such as IEC 61850 and the use of Ethernet-based communication capabilities, especially in smart grids, which will provide many possibilities to enhance the functioning of the electrical system in a wide scale. This communication module encrypts information for the electric field using various communication protocols; it also plays an essential role in communicating with the control center. By using a check signal to ensure communication availability, as specified in the communication standard (IEC 61850), it is feasible to determine the communication loss, besides by establishing a channel between PDs and control platforms, the standard offers the essential capabilities and services to act as a communication and automation tool for PDs. Manufacturing Message Specification (MMS), Generic Object Oriented Substation Event (GOOSE), and Sampled Values Protocol are all services provided by this standard (SVP). The GOOSE service is intended to replace current signal wiring in control systems while also adding additional functionality. Moreover, GOOSE can handle more information than just a cable, communicate rapidly across PDs, and provide quality service. The protection system allows PDs and the CE to interact in a variety of ways. TCP/IP-based Ethernet, Wi-Fi protocol, or Cellular networks communication are examples of these methods [85], [134]. Cellular networks are largely utilized for public wireless data services; however, they are not a reliable communication relay network since they are susceptible to discrepancy and hacking.

In Fig. 5.8, the proposed protection strategy's concept diagram is illustrated. Each PD receives a decision from the CE (blue arrow), and ZO (grey box) is performed internally at each PD at the same time, leveraging communication between peer PDs in the same line (red arrows). Finally, as discussed later in this chapter, both decisions will be compared and a priority check (grey box) will be used to select the optimum decision. The PD provides main protection for the corresponding DL along with backup protection for the PDs on adjacent lines, as will be explained later in this chapter (section 5.3.4.).

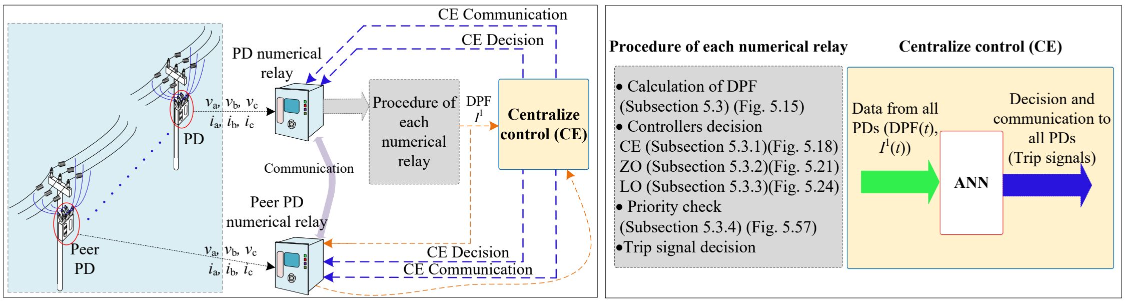
CE Communication
CE Decision
PD numerical relay
v_a, v_b, v_c
i_a, i_b, i_c
PD
Procedure of each numerical relay
DPF
I^1
Centralize control (CE)
Communication
Peer PD numerical relay
Peer PD
v_a, v_b, v_c
i_a, i_b, i_c
CE Decision
CE Communication
Procedure of each numerical relay
Centralize control (CE)
• Calculation of DPF (Subsection 5.3) (Fig. 5.15)
• Controllers decision
CE (Subsection 5.3.1)(Fig. 5.18)
ZO (Subsection 5.3.2)(Fig. 5.21)
LO (Subsection 5.3.3)(Fig. 5.24)
• Priority check (Subsection 5.3.4) (Fig. 5.57)
•Trip signal decision
Data from all PDs (DPF(t), I^1(t))
ANN
Decision and communication to all PDs (Trip signals)

(a) (b)

Fig. 5.8 Concept diagram of the proposed algorithm

In the following points, the ANN training, development, and DPF implementation, the calculation used in CE and ZO algorithms will be discussed.

➢ Artificial Neural Network (ANN)

The usage of CE and ZO algorithms is modeled and adapted by ANN to automatically coordinate the PD decision and locate the disturbance on the faulty line depending on various parameters. When a fault occurs, the control unit at each PD may use network-wide comparison measures to establish the fault location and trip the relevant PDs to isolate the fault.

The use of ANN provides the advantages of quick decision-making and massive data processing, making ANN preferred in DS with a high number of buses. The training procedure is dependent on the input data and expected outputs to produce the ANN function. It is easier and faster to employ ANN for this particular application than it is to use a scripted program that requires several adjustments for each change in the grid [91], [121], [124], which will complicate and decrease the precision of the algorithm decision, especially as the number of buses increases. Fig. 5.9 depicts the structure that describes the ANN fault location scheme. Each input to neuron (x) is given a weight (W) that corresponds to the input's contribution, then a bias (b) is added to the summation of all inputs (from 1 to 24); each input includes 64 samples per cycle.

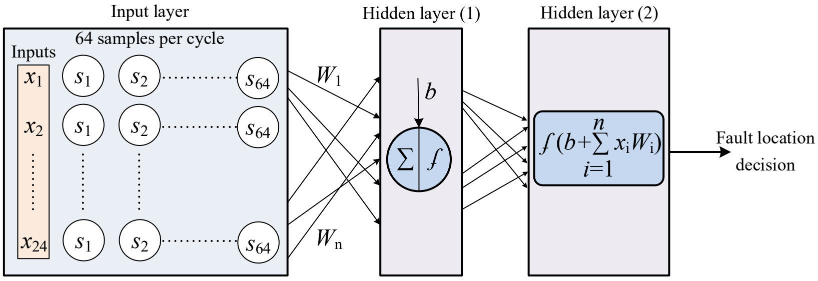
Input layer
64 samples per cycle
Inputs
x_1
x_2
x_{24}
s_1
s_2
s_{64}
W_1
W_n
Hidden layer (1)
b
$\sum$ f
Hidden layer (2)
$f(b+\sum_{i=1}^{n} x_i W_i)$
Fault location decision

Fig. 5.9 Structure of the ANN for fault location scheme

A significant number of cases are required to train the ANN, considering numerous variables such as variable DG penetration, location, various fault resistance, types, and locations. Fig. 5.10 represents the ANN train environment and the parameters that must be considered while training the ANN.

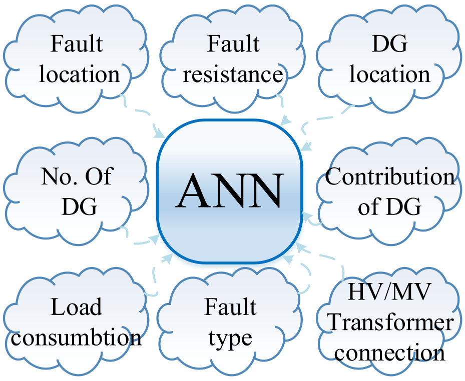

Fig. 5.10 ANN training environment

In order to simulate many cases and minimize the simulation time, PSCAD is used to implement the multiple run scenario instead of using MATLAB™ SIMULINK, which will take much more time, especially with a large number of cases that are needed to train the ANN. The same analysed radial and ring grids built in MATLAB™ are rebuilt in PSCAD to reproduce the same grid behaviour in both simulation platforms, as shown in Fig. 5.11, the transient and steady-state evolution in both simulation platforms are almost identical. Fig. 5.12 shows the flowchart of the ANN procedure starting from the system modeling, passing through the system simulation taking into consideration different grid scenarios (as load consumption change, various DG numbers connected to the grid, amount of DG power penetration, fault types, MV transformer connections, fault location, and fault resistance), and ending by ANN validation and testing.

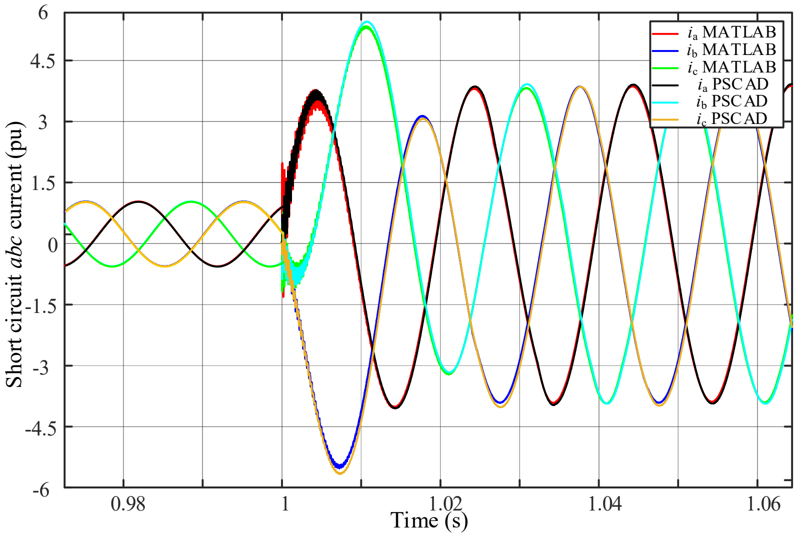

Fig. 5.11 short-circuit currents in PSCAD and MATLAB™ SIMULINK simulation platforms

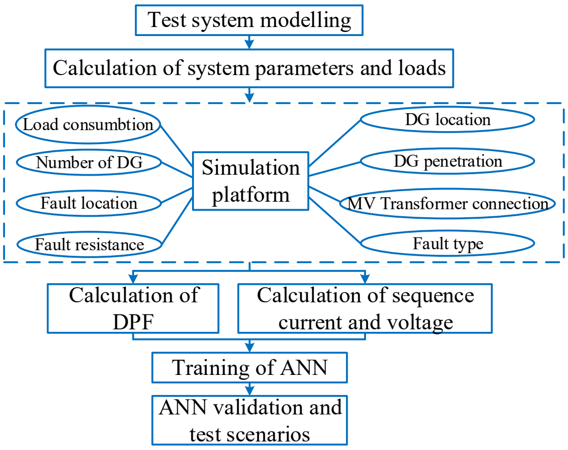
Test system modelling
Calculation of system parameters and loads
Load consumbtion
Number of DG
Fault location
Fault resistance
Simulation platform
DG location
DG penetration
MV Transformer connection
Fault type
Calculation of DPF
Calculation of sequence current and voltage
Training of ANN
ANN validation and test scenarios

Fig. 5.12 Flowchart of ANN training procedure

The control of DS protections will be studied using ANN, mainly because of their ability to recognize and classify patterns, making ANN ideal for this application. The goal is to locate the fault as quickly as possible and isolate the faulty part of the system. Some considerations must be taken to train ANN for specific grid behaviour. Grid behaviour must be investigated in multiple scenarios, as varying fault type, fault location, fault resistance, number of DG connected to the grid, location of DG, DG contribution, load consumption, and varied neutral connections for the MV side of the HV/MV transformer. The algorithm is evaluated on several neutral connections before being used to specific connections in this thesis (YNd11 grounded and YNd11 isolated) (Appendix A). The Neural Net Fitting tool (nftool) from the MATLAB^{TM} Toolbox is utilized to complete this task. After that, the most suitable training technique, "Levenberg Marquardt" was chosen. This approach necessitates a higher level of memory but requires less training time [171]. There is no exact method for determining the number of hidden layers and the number of neurons in each layer; nevertheless, because ANNs with more hidden layers are more difficult to train [172], therefore according to [173], the following equation is used to determine the number of hidden layers

$$\text{No. of hidden layers} = \sqrt{X+Y}+\sigma. \tag{33}$$

The ideal number of hidden layer neurons for the Minimum Mean Square Error (MSE) can be determined using trial and error, where X and Y are the numbers of inputs and outputs, respectively, and σ is a constant between (1~10). After the ANN has been trained, test scenarios must be performed to ensure the ANN's dependability and accuracy, and the test patterns must differ from the training patterns. The ANN is trained for about 5000 cases to manage parameter changes that impact the protection algorithm's decision. Fig. 5.13 shows in a 3-D preview, the Mean Square Error (MSE) for various neurons, and iteration. As seen, when the number of neurons is 20, the MSE equals 0.0014 n, and when the number of neurons increases the MSE also increases. Fig. 5.14 illustrates the decision of several ANN models with the estimated output. The results of the chosen ANN model (blue line) match with the estimated outputs (red lines), as seen in Fig. 5.14. The ANN will provide a faster decision instead of employing a script with loops to prolong the decision-making process.

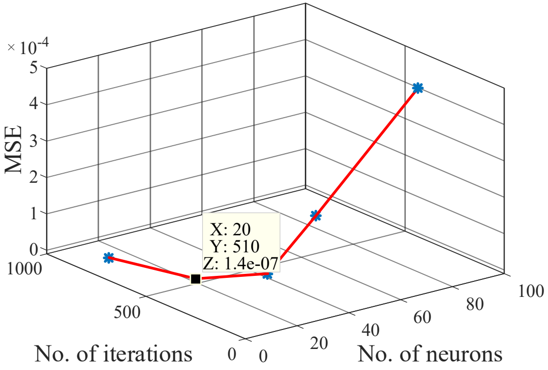

Fig. 5.13 ANN aspects for different trained ANN

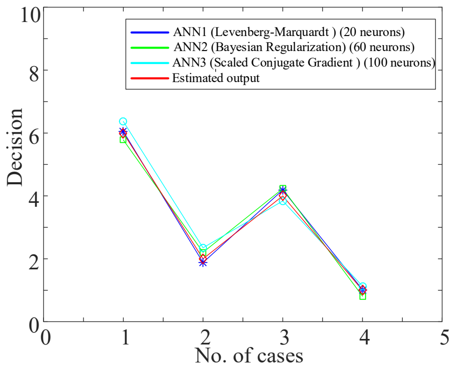

Fig. 5.14 Decision of different ANN models and the estimated output

For the output of ANN, a post-processing stage is needed to make a margin for each NN output. For example, for fault at Line 3, the output should be 3, so the margin of the ANN will be from (2.9 → 3.1).

- Calculation of direction of power flow

Due to the bi-directionality of fault currents in the presence of DG, detection of DPF has become an appealing alternative for ring grids. The behaviour of ring and radial grids with high DG penetration can be seen in Appendix B. An Intelligent Electronic Device (IED) with DSP TMS320F28335 is utilized to recognize DPF and develop the algorithm. Instrument transformers take voltage and current measurements (VT and CT) and convert them to lower-level signals that can be processed by PD.

The direction of the fault current injection can be estimated using the phase angle 'Ψ' between the fault current *i*(t) and the corresponding voltage *v*(t) to determine the direction of the fault. Lines are primarily inductive, therefore for forwarding line faults, *i*(t) lags *v*(t), and vice versa for reverse faults. Fig. 5.15(a) shows that the overlapping interval between voltage and current during normal conditions (-90° < Ψ < 90°) is longer than the non-overlapping interval, although during reversed power flow conditions (90°> Ψ > 270°) is the contrary, as shown in Fig. 5.15(b) [36]. This difference in the overlapping interval can be used to apply a relay's directional element under normal and reversed power flow conditions. The figure also shows the steps to model the directional element. Signals of current and voltage are transformed to a square wave of two levels; by multiplying the two output signals of (1) will be obtained during overlapping and (-1) during non-overlapping intervals (Fig. 5.15(c)). The outcome is then integrated with an upper limit of the integrator sets to '0' (Fig. 5.15(d)). During reversed power flow, the integral output drops under low level (L), the level is set to a value between (-0.01 ≤ L ≤ 0) to gain a faster response. The integral is always less than 0 under normal power flow conditions; as a result, the output of the directional element changes from '0' to '1', depending on achieving or not the lower limit (Fig. 5.15(e)) [37].

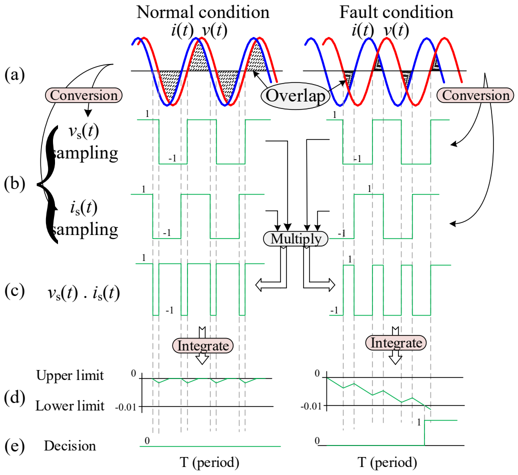

Fig. 5.15 Concept diagram for implementing directional element (a) *abc* current and voltage signals (b) square wave of current and voltage (c) current and voltage multiplication (d) integrator output (e) decision

During the normal condition, the power flow at both ends of the line will be the same. However, during a fault, the DPF will change at one end of the faulted line. Fig. 5.16 shows the Simulation diagram for DPF during fault.

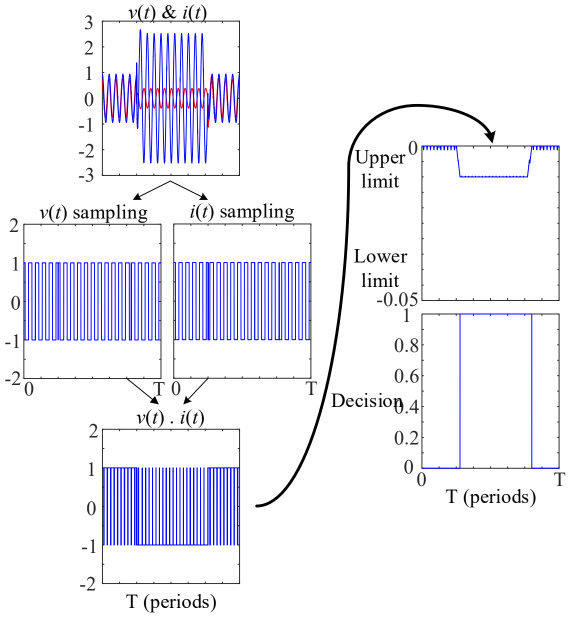

Fig. 5.16 Simulation diagram for DPF during fault

In the case of a healthy line, DPF at both PDs at both ends of the line will be the same. On the other hand, in case of a faulty line, the DPF will change at one end of the faulted line. By comparing the values of the DPF at both ends of the faulted line, the faulted line can be located, as shown in the figure below. Next, these data will be sent to the neural network to indicate the faulted line.

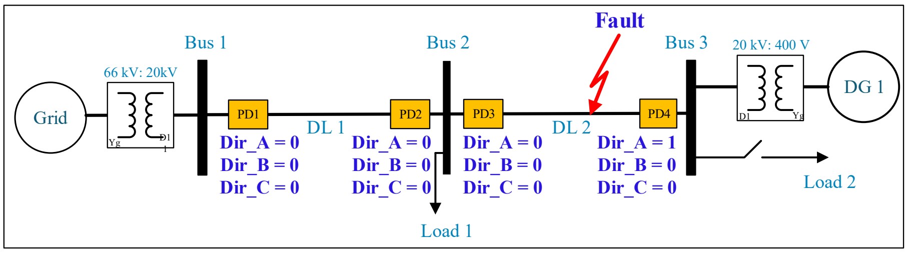

Fig. 5.17 Single phase to ground fault

5.3.1. Centralize control algorithm (CE)

In this section, the methodology to implement CE for radial and ring grids will be explained.

A control algorithm based on detecting the DPF of all the PDs in the ring and radial grids has been developed to locate and isolate the faulty section of the grid. In radial grids, (i^{+}) will be utilized instead of DPF since DPF will not change in some parts of the radial grid without DG penetration, causing the algorithm to fail. If the positive-sequence current (i^{+}) values are the same at both ends of the line, then there is no fault at this line, as shown in Fig. 5.18. These data were sent to the ANN instead of the DPF data. Then the same algorithm is used to locate and isolate the faulted part of the system. This can be done because the lines are short and the transversal capacitance is insufficient to provoke a big difference in current at both ends. Fig. 5.19 shows the concept diagram of CE controller.

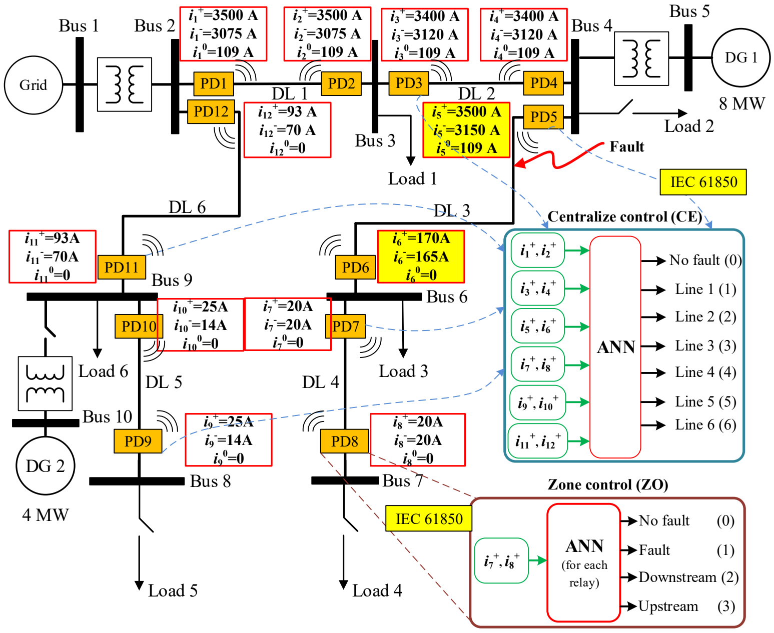
Bus 1
Bus 2
Grid
i_1^+=3500 A
i_1^-=3075 A
i_1^0=109 A
i_2^+=3500 A
i_2^-=3075 A
i_2^0=109 A
i_3^+=3400 A
i_3^-=3120 A
i_3^0=109 A
i_4^+=3400 A
i_4^-=3120 A
i_4^0=109 A
Bus 4
Bus 5
DG 1
8 MW
PD1
PD2
PD3
PD4
PD5
PD12
DL 1
DL 2
i_{12}^+=93 A
i_{12}^-=70 A
i_{12}^0=0
Bus 3
Load 1
i_5^+=3500 A
i_5^-=3150 A
i_5^0=109 A
Load 2
Fault
IEC 61850
DL 6
DL 3
Centralize control (CE)
i_{11}^+=93A
i_{11}^-=70A
i_{11}^0=0
PD11
Bus 9
PD6
i_6^+=170A
i_6^-=165A
i_6^0=0
Bus 6
i_{10}^+=25A
i_{10}^-=14A
i_{10}^0=0
i_7^+=20A
i_7^-=20A
i_7^0=0
PD10
PD7
Load 6
Load 3
DL 5
DL 4
Bus 10
PD9
i_9^+=25A
i_9^-=14A
i_9^0=0
PD8
i_8^+=20A
i_8^-=20A
i_8^0=0
DG 2
4 MW
Bus 8
Bus 7
Load 5
Load 4
i_1^+, i_2^+
i_3^+, i_4^+
i_5^+, i_6^+
i_7^+, i_8^+
i_9^+, i_{10}^+
i_{11}^+, i_{12}^+
ANN
No fault (0)
Line 1 (1)
Line 2 (2)
Line 3 (3)
Line 4 (4)
Line 5 (5)
Line 6 (6)
Zone control (ZO)
IEC 61850
i_7^+, i_8^+
ANN
(for each relay)
No fault (0)
Fault (1)
Downstream (2)
Upstream (3)

Fig. 5.18 Positive-sequence values for two-phase to ground fault at DL3, with fault resistance $r = 0.1\ \Omega$

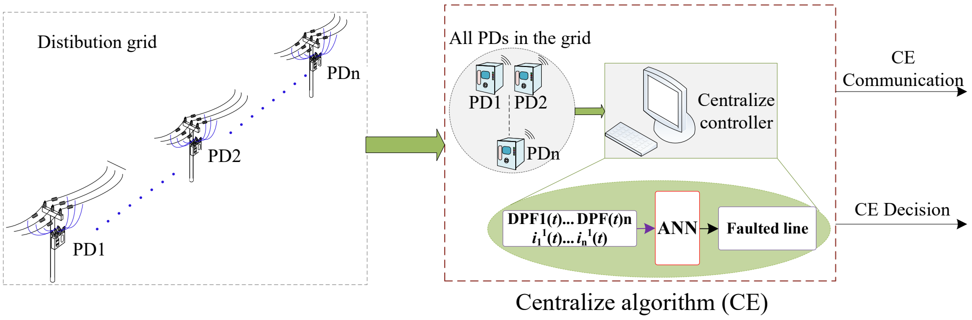
Distibution grid
PDn
PD2
PD1
All PDs in the grid
PD1
PD2
PDn
Centralize controller
DPF1(t)... DPF(t)n
$i_1^1(t)... i_n^1(t)$
ANN
Faulted line
CE
Communication
CE Decision
Centralize algorithm (CE)

Fig. 5.19 Concept diagram of CE algorithm

All connections between the PDs and the CE are considered to be available in this algorithm. The fundamental concept is to use DPF data for the ring grid and i^+ data for the radial grid as inputs to the CE to make the appropriate decision. Variations in short circuit current and DPF in each PD must be included in the ANN's training. The DPF and i^+ are calculated locally at each PD using voltage and current, and only the processed data is transmitted to the controller. Because there is no need to communicate voltages and currents to the CE, which would complicate the communication process, this step will make the learning process more accessible and decrease the error percentage. The next step is the training and testing of ANN. The method utilizes back-propagation that is a supervised learning technique employed by a multilayer perceptron. Finally, the ANN decision must have a minimal error value corresponding to the faulty line number and PD trip signal. The ANN parameters for CE are as follows: twenty four inputs relate to the DPF and i^+ of all PDs in the grid, six outputs equal to the faulty line, each output has seven statuses (0 → 6), as seen in Fig. 5.18, and two hidden layers. The ANN parameters are listed in Table 5.3.

Table 5.3 CE ANN fault location parameters

Number of ANN inputs	24
ANN training technique	Levenberg Marquardt
Number of hidden layers	2
Number of neurons in the hidden layer (1)	20
Number of neurons in the hidden layer (2)	1
Number of ANN Outputs	6 (0 to 6)

This idea is practical because no need to send voltage and current signals to the CE. Instead, these measurements signal are post-processed at each PD, then the processed information is sent to the controller, as seen in Fig. 5.20.

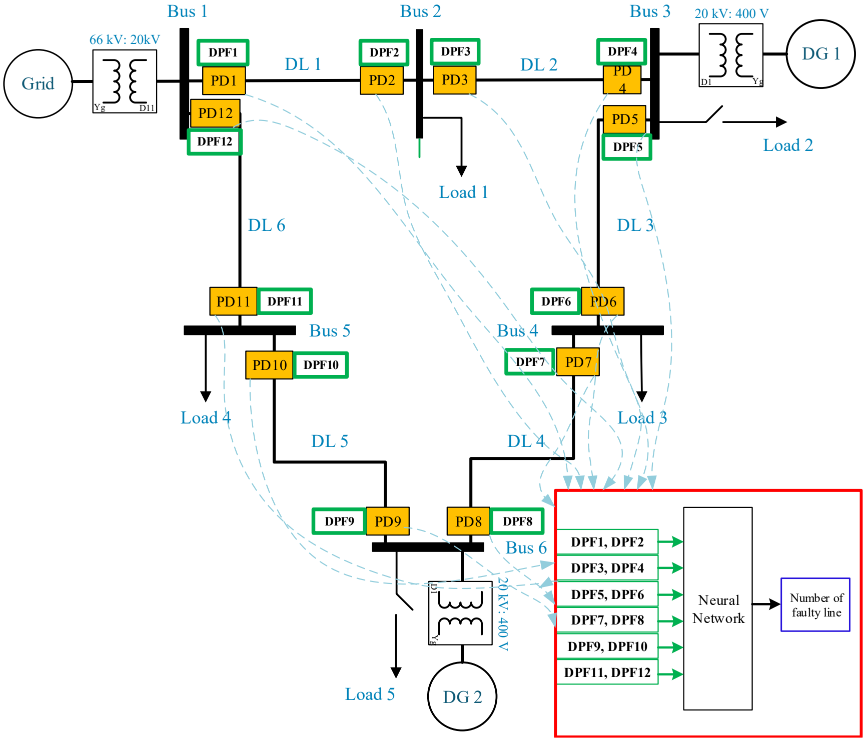
Bus 1
Bus 2
Bus 3
20 kV: 400 V
DG 1
66 kV: 20kV
Grid
Yg
D11
DPF1
PD1
DL 1
DPF2
PD2
DPF3
PD3
DL 2
DPF4
PD 4
D1
Yg
PD12
DPF12
PD5
DPF5
Load 2
Load 1
DL 6
DL 3
PD11
DPF11
DPF6
PD6
Bus 5
Bus 4
PD10
DPF10
DPF7
PD7
Load 4
Load 3
DL 5
DL 4
DPF9
PD9
PD8
DPF8
Bus 6
20 kV: 400 V
D1
Yg
Load 5
DG 2
DPF1, DPF2
DPF3, DPF4
DPF5, DPF6
DPF7, DPF8
DPF9, DPF10
DPF11, DPF12
Neural Network
Number of faulty line

Fig. 5.20 ANN connection in case of CE

The major benefits of this system are that it consolidates the security of the entire system into a single device, performing state estimation and security evaluations [86]. On the other side, Communications issues (due to failure or safety concerns) or CE unit failure, will result in a total loss of protection for the period it takes to restore services [84]. Furthermore, all input signals must be delivered to the same ANN, necessitating additional training time and a more complex training procedure. Furthermore, specific communication between all PDs and the controller must transfer all data to a CE [118], [135], [174]. In addition, communication delay must be taken into consideration; the total communication delay consists of four components: transmission delay, queuing delay, propagation delay, and processing delay. The total communication delay will be small enough to transfer the trip signals within a timescale lower than < 1ms [119]. An additional algorithm will coordinate with CE to resolve its disadvantages, and the decision will be based on both algorithms.

The total delay time of the clearing process consists of the delay time of the sensors, communication system, processing time, and circuit breaker delay, as shown in Fig. 5.21.

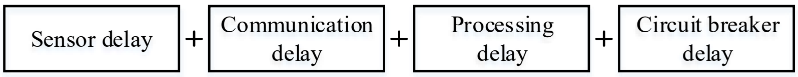
Sensor delay
+
Communication delay
+
Processing delay
+
Circuit breaker delay

Fig. 5.21 Delay components of the total fault clearing time

5.3.2. Zone control algorithm (ZO)

The CE will not pinpoint the exact location of the fault if certain information is missed due to poor communication. However, the faulty line in that zone may be identified by combining the data from the two PDs on the same line, as shown in Fig. 5.22. In order to improve the system’s redundancy, ZO is cooperating with CE. Every PD decides locally utilize the data acquired from the peer PD on the same line, as illustrated in Fig. 5.23, by employing the ZO, which can detect and update its decision based on the power flow at each end of the line. There is no necessity for communication between all of the PDs and a CE in this scenario. Typically, the communication system between two PDs on the same line is handled using a Power Line Carrier (PLC) with high-frequency signals or optical fiber cables, which improves the security of the connection [119], [175].

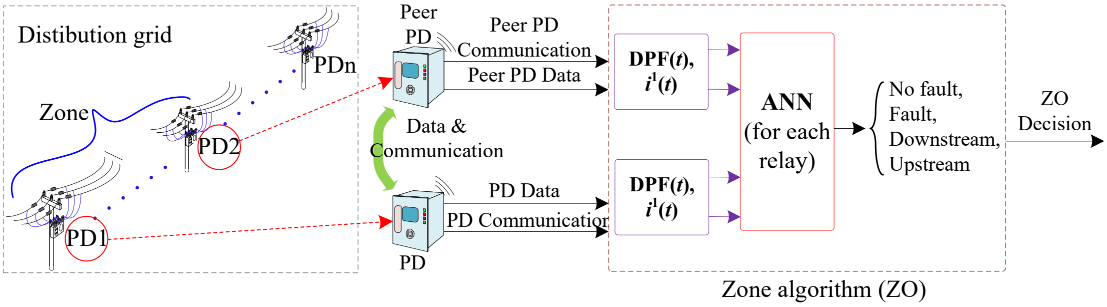

Fig. 5.22 Concept diagram of ZO algorithm

For example, if the fault is at DL5, as shown in Fig. 5.7, PD9 and PD10 will be able to locate the fault, while the rest of PDs will continue to operate normally since their controller identifies that the fault is on a different line. Each PD gets DPF data from its peers and compares it to its data to make an appropriate trip signal decision that isolates the faulty line. Furthermore, the ANN of each PD in the rest of the grid could determine the fault's direction, i.e., whether the fault is upstream or downstream of the PD. The ZO ANN consists of: two hidden layers, four inputs corresponding to the DPF and i^+ for PD of each line, and one output, which could be one of these options (no-fault, fault, fault downstream the line, and fault upstream the line), as seen in Fig. 5.18. The significant advantage of this technique is its flexibility to adapt to any alterations in the grid, even if they are just temporary, unlike the CE, which is fixed to the existing grid configuration. If another line is added to the grid, the CE must be retrained to adopt new inputs. However, for the ZO the same ANN used for each PD can be utilized for the newly added line. Another merit of this algorithm is that it makes a distinct decision for each line, takes less training time, and is simpler than CE.

Furthermore, there is no requirement for specific communication between the PDs and the controller, allowing for faster and more efficient PD response. As a result, the fault will be quickly located and eliminated by the closest PDs in a shorter time. Table 5.4 shows the parameters of the trained fault ZO ANN controller.

Table 5.4 ZO ANN fault location parameters

No. of ANN inputs	4
NN training technique	Levenberg Marquardt
No. of hidden layer	2
No. of neurons in the hidden layer (1)	12
No. of neurons in the hidden layer (2)	1
No. of ANN Outputs	4 (0 → 3)

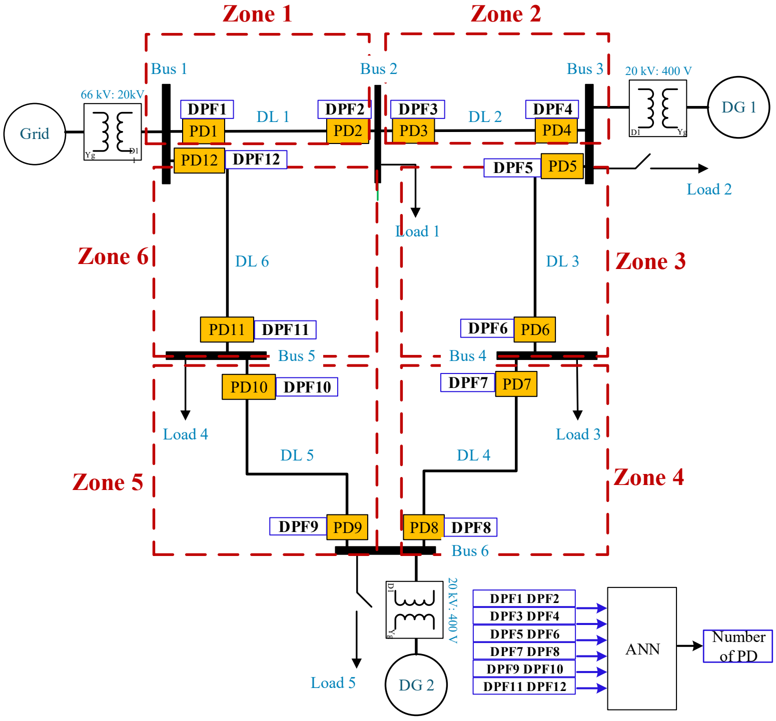
Zone 1
Zone 2
Bus 1
Bus 2
Bus 3
20 kV: 400 V
66 kV: 20kV
Grid
DG 1
DPF1
PD1
DL 1
DPF2
PD2
DPF3
PD3
DL 2
DPF4
PD4
PD12
DPF12
DPF5
PD5
Load 2
Load 1
Zone 6
DL 6
DL 3
Zone 3
PD11
DPF11
DPF6
PD6
Bus 5
Bus 4
PD10
DPF10
DPF7
PD7
Load 4
Load 3
DL 5
DL 4
Zone 5
Zone 4
DPF9
PD9
PD8
DPF8
Bus 6
20 kV: 400 V
DPF1 DPF2
DPF3 DPF4
DPF5 DPF6
DPF7 DPF8
DPF9 DPF10
DPF11 DPF12
ANN
Number of PD
Load 5
DG 2

Fig. 5.23 Zone identification for ZO algorithm, and ANN connection in case of CE

In order to verify the reliability and accuracy of the trained ANN, the CE-ZO algorithms have been tested using different cases (around 500 cases). Some of these cases are shown in Table 5.5.

Table 5.5 Some of the cases used to verify the protection algorithm

#	**Cases**
1	Analysed ring grid without DG
2	Analysed ring grid with one DG= 1 MW and high loads consumption
3	Analysed ring grid with one DG= 4 MW connected at bus 3 and low loads consumption
4	Analysed ring grid with one DG= 4 MW connected at bus 2 and low loads consumption
5	Analysed ring grid with one DG= 4 MW connected at bus 4 and low loads consumption
6	Analysed ring grid with one DG= 4 MW connected at bus 5 and low loads consumption
7	Analysed ring grid with one DG= 4 MW connected at bus 6 and low loads consumption
8	Analysed ring grid with two DG1= 8 MW, DG1= 8 MW, and high loads consumption
9	Analysed ring grid with two DG1= 8 MW, DG1= 6 MW, and low loads consumption
10	Analysed radial grid without DG
11	Analysed radial grid with one DG= 1 MW
12	Analysed radial grid with two DGs DG1= 8 MW, DG1= 8 MW

5.3.3. Local control algorithm (LO)

In this method, all communications between the PDs are not required, then in case of loss of communication, the protection system can work properly. In this case, each PD is able to detect the DPF, but it is not possible to identify the location of the fault. Each PD should be able to detect if the fault is located in the protected line or in another line, by using only the local information of the PD. The idea is based on using the sequence components of voltages and currents of each PD during fault conditions. In the bottom right corner of Fig. 5.24 and Fig. 5.25, the single line diagram of a radial and ring DS is shown, respectively, with DG penetration and LO algorithm.

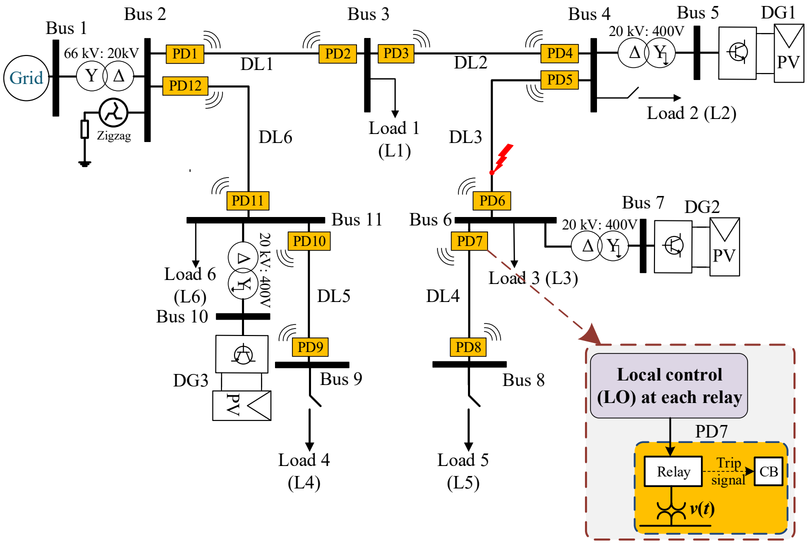
Bus 1
Bus 2
Bus 3
Bus 4
Bus 5
DG1
Grid
66 kV: 20kV
Y
Δ
Zigzag
PD1
PD12
DL1
PD2
PD3
DL2
PD4
PD5
20 kV: 400V
PV
Load 2 (L2)
Load 1
(L1)
DL6
DL3
PD11
Bus 11
PD10
Bus 6
PD6
PD7
Bus 7
DG2
20 kV: 400V
Load 3 (L3)
Load 6
(L6)
Bus 10
20 kV: 400V
DL5
DL4
PD9
PD8
DG3
Bus 9
Bus 8
Load 4
(L4)
Load 5
(L5)
Local control
(LO) at each relay
PD7
Relay
Trip signal
CB
v(t)

Fig. 5.24 Single line diagram of the analysed radial DS with DG penetration and LO

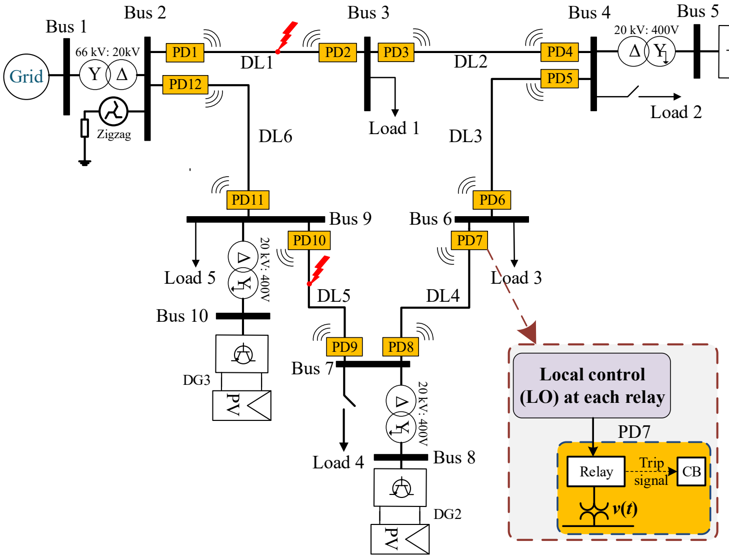
Bus 1
Bus 2
Bus 3
Bus 4
Bus 5
Grid
66 kV: 20kV
Y
Δ
Zigzag
PD1
PD12
DL1
PD2
PD3
DL2
PD4
PD5
20 kV: 400V
PV
DG1
Load 2
Load 1
DL6
DL3
PD11
Bus 9
Bus 6
PD6
PD10
PD7
Load 5
Load 3
20 kV: 400V
Bus 10
DL5
DL4
DG3
PD9
PD8
Bus 7
20 kV: 400V
Load 4
Bus 8
DG2
Local control
(LO) at each relay
PD7
Relay
Trip signal
CB
v(t)

Fig. 5.25 Single line diagram of the analysed ring DS with DG penetration and LO

Different fault location algorithm has been used for each type of fault. Because depending on the fault type (symmetrical/unsymmetrical), the sequence components will vary, which emphasizing the need for a fault classification technique to identify the type of fault before implementing the proposed LO algorithm. The fault classification method and the proposed LO protection algorithm for symmetrical and unsymmetrical faults are explained in the following subsections.

5.3.3.1. Fault classification algorithm

This section explains the methodology of fault type classification, aiming is to identify all types of faults. In order to achieve this objective, different methods had reviewed. The most well-known methods can be divided into two categories: (1) using AI techniques such as ANN [176], [177], FLC, or neuro-fuzzy [178]. (2) using DWT with AI techniques [125], [179]–[183]. In this work, ANN is chosen to be the tool to identify the fault type. The main merit of using ANN in this application is the fast and reliable decision, and the availability to use the same ANN in different grid voltage levels, then a preprocessing stage will be implemented before the ANN, to adapt the inputs signals.

In the preprocessing stage, the three *abc* instantaneous fundamental voltages ($v_a(t)$, $v_b(t)$, and $v_c(t)$) are divided by the base values of the system, in order always to obtain pu values that are easier to adapt to the ANN to different grid voltage levels. In order to identify the ground fault, the zero-sequence voltage is used (v^0), which is obtained from the *abc* voltages. These data are sent to an ANN to give the correct decision. Fig. 5.26 shows the conceptual diagram of the fault classification algorithm.

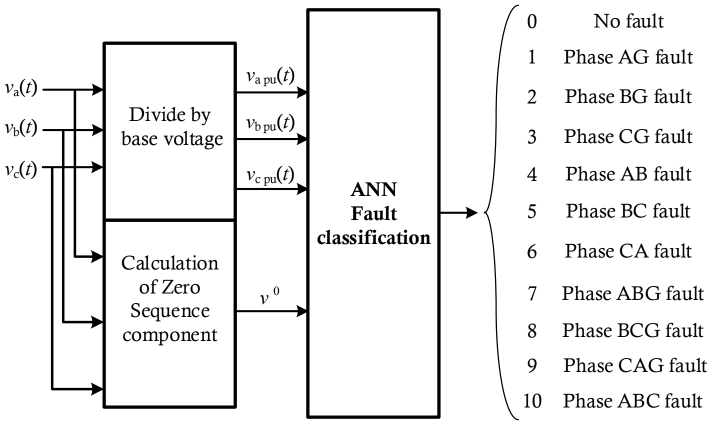
$v_a(t)$
$v_b(t)$
$v_c(t)$
Divide by base voltage
$v_{a\,pu}(t)$
$v_{b\,pu}(t)$
$v_{c\,pu}(t)$
Calculation of Zero Sequence component
v^0
ANN Fault classification
0 No fault
1 Phase AG fault
2 Phase BG fault
3 Phase CG fault
4 Phase AB fault
5 Phase BC fault
6 Phase CA fault
7 Phase ABG fault
8 Phase BCG fault
9 Phase CAG fault
10 Phase ABC fault

Fig. 5.26 preprocessing module block diagram and ANN to classify the fault

Table 5.6 shows the trained fault classification ANN parameters, where the inputs correspond to the *abc* voltages, and the zero-sequence voltage (used to discriminate the ground faults), ANN training technique is Levenberg Marquardt, Number of hidden layers are 2, and one output corresponds to the decision of fault type. Fig. 5.27 shows the flowchart of the fault classification algorithm. The ANN is trained for about 1000 cases to manage parameter changes that impact the decision of the algorithm. The number of cases for training the ANN, and the used training tool can be seen in Appendix B.

Table 5.6 ANN fault classification parameters

ANN fault classification	
No. of ANN inputs	4 ($v_a(t)$, $v_b(t)$, $v_c(t)$, v^0)
ANN training technique	Levenberg Marquardt
No. of hidden layer	2
No. of neurons in the hidden layer (1)	60
No. of neurons in hidden layer (2)	1
Number of NN Outputs	1 (0 → 10)

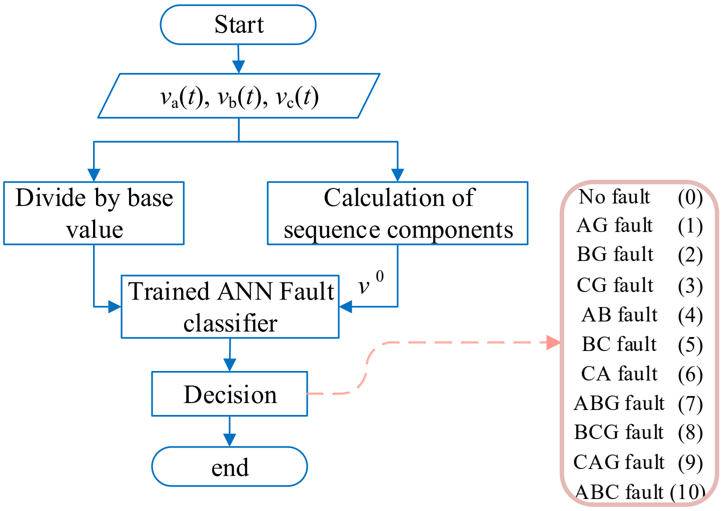
Start
$v_a(t)$, $v_b(t)$, $v_c(t)$
Divide by base value
Calculation of sequence components
v^0
Trained ANN Fault classifier
Decision
end
No fault (0)
AG fault (1)
BG fault (2)
CG fault (3)
AB fault (4)
BC fault (5)
CA fault (6)
ABG fault (7)
BCG fault (8)
CAG fault (9)
ABC fault (10)

Fig. 5.27 Flowchart of fault classification algorithm

The fault classification algorithm has been tested using different cases, in order to verify if it is possible to identify the fault in all possible situations; some cases are shown in Table 5.7. For the output of ANN, a post-processing stage is needed to make a margin for each ANN output. For example, for an AG fault, the output should be 1, so the margin of the ANN will be from (0.9 → 1), and other cases are shown in Table 5.8.

Table 5.7 Some of the cases used to test the classification algorithm

#	Cases
1	Analysed ring DS without DG
2	Analysed ring DS with one DG= 1 MW and high loads consumption
3	Analysed ring DS with one DG= 4 MW and low loads consumption
4	Analysed ring DS two DG1= 1 MW, DG1= 2 MW, and high loads consumption
5	Analysed ring DS two DG1= 4 MW, DG1= 2 MW, and low loads consumption
6	Analysed radial DS without DG
7	Analysed radial DS with one DG= 1 MW
8	Analysed radial DS with two DG= DG1= 1 MW, DG1= 2 MW

Table 5.8 Results of ANN decision in different fault scenarios

Fault Type	Fault location	Fault resistance	Number of DG	Contribution of DG	Load changes	ANN decision
AG	DL3	6 Ω	2	DG1 = 2 MW DG2 = 2 MW	L1 = 2 MVA, L3 = 4 MVA, L4 = 0.5 MVA,	1
AB	DL1	0.4 Ω	2	DG1 = 1 MW DG2 = 2 MW	L1 = 5 MVA, L3 = 1 MVA, L4 = 0.5 MVA,	4
CA	DL5	1.5 Ω	None	DG1 = Zero DG2 = Zero	L1 = 1 MVA, L2 = 0.25 MVA, L3 = 4 MVA, L4 = 2 MVA, L5 = 1 MVA	6
BCG	DL6	0.1 Ω	2	DG1 = 3 MW DG2 = 2 MW	L1 = 5 MVA, L3 = 10 MVA, L4 = 3 MVA,	8
ABC	DL3	5 Ω	2	DG1 = 1 MW DG2 = 1 MW	L1 = 2 MVA, L3 = 0.5 MVA, L4 = 2 MVA,	10

where: 1- Fault AG, 2- fault AG, 3- fault CG, 4- fault AB, 5- Fault BC, 6- fault CA, 7- fault ABG, 8- fault BCG, 9- fault CAG, 10- Fault ABC.

Table 5.9 Grounding connection of the HV/MV power transformer

Transformer connection (HV/MV)
YNd11
YNyn
YNyg grounded through a resistor
YNd11 grounded through zigzag
YNd11 grounded through zigzag and resistor

In the following subsections, the LO protection algorithm will be explained in detail for all the types of faults and for two scenarios. The first scenario is when the MV side of the HV/MV transformer is not isolated, and the second scenario is if it is isolated, because this connection will change the short circuit current magnitude in the studied grid.

The secondary of the HV power transformer (HV/MV) is connected for the Spanish electric utilities in one of the connections shown in Table 5.9.

As seen in Table 5.9, different connections can be obtained, because each company has its transformer connection [141], [143]. Moreover, each company have a different connection for each region, as it is shown in Table 2, page 7 of [141]. In this research, the most common connections have been chosen, YNyg grounded (not isolated in normal operation), and YNd11 grounded through zigzag (isolated in normal operation). In both cases, for the balanced condition or during single-phase to ground fault the zigzag has a large impedance to minimize the fault current; however, for unbalanced conditions (two-phase, two-phase to ground, and three-phase), the zigzag has a lower impedance.

5.3.3.2. LO algorithm in case symmetrical and unsymmetrical faults and the MV side of the (HV/MV) transformer is not isolated

The LO will be studied in this case for all types of faults. Depending on the fault type, the sequence components of the voltages and currents are studied to propose a local protection algorithm for each PD. In this subsection, each fault type with each proposed LO protection algorithm will be presented.

- Unsymmetrical fault

In the case of a single-phase fault with the un-isolated ground, one end of the faulted line can be located by using a zero-sequence current during the fault. The zero-sequence current at one end of the faulted line will be higher than any other zero-sequence value of other lines during the fault. Therefore, the highest value means faster disconnection. On the other hand, positive-sequence current cannot be used as the values before and during the fault do not change significantly, as shown in Fig. 5.28.

The next step is disconnecting the PD that presents a higher zero-sequence current and analyzing the grid after the disconnection. After the disconnection of one end of the faulted line, approximately the same value of the three-sequence currents at the other end of the faulted line will be obtained, as seen in Fig. 5.29(b). So, by using these data, the faulted line in a single-phase fault can be isolated.

It is important to mention that the previous strategy can work only in the case of not isolated ground, because in the case of isolated grounded, the i^0 is almost zero, so in this case, it cannot depend on the sequence current. Instead, the sequence voltages will be used, which will be explained later in this chapter.

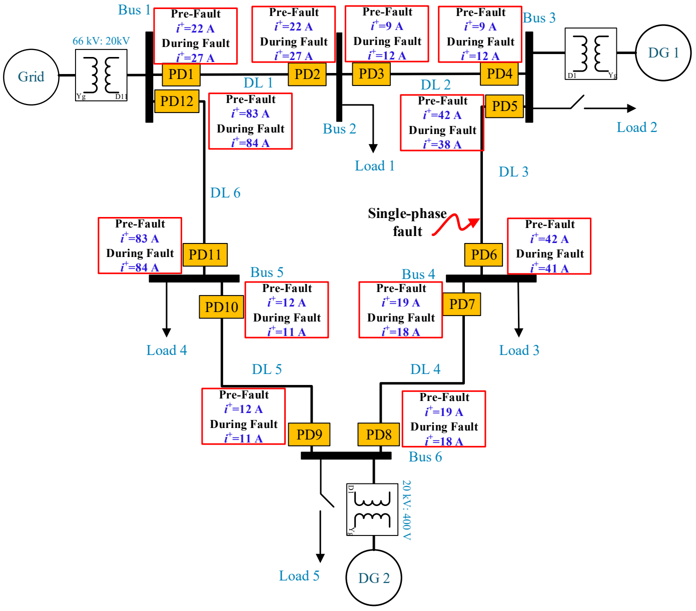
Bus 1
Pre-Fault
i^+=22 A
During Fault
i^+=27 A
Pre-Fault
i^+=22 A
During Fault
i^+=27 A
Pre-Fault
i^+=9 A
During Fault
i^+=12 A
Pre-Fault
i^+=9 A
During Fault
i^+=12 A
Bus 3
66 kV: 20kV
Grid
Yg
D11
PD1
DL 1
PD2
PD3
DL 2
PD4
D1
Yg
DG 1
PD12
Pre-Fault
i^+=83 A
During Fault
i^+=84 A
Bus 2
Pre-Fault
i^+=42 A
During Fault
i^+=38 A
PD5
Load 2
Load 1
DL 3
DL 6
Single-phase
fault
Pre-Fault
i^+=83 A
During Fault
i^+=84 A
PD11
PD6
Pre-Fault
i^+=42 A
During Fault
i^+=41 A
Bus 5
Bus 4
PD10
Pre-Fault
i^+=12 A
During Fault
i^+=11 A
Pre-Fault
i^+=19 A
During Fault
i^+=18 A
PD7
Load 4
Load 3
DL 5
DL 4
Pre-Fault
i^+=12 A
During Fault
i^+=11 A
PD9
PD8
Pre-Fault
i^+=19 A
During Fault
i^+=18 A
Bus 6
D1
Yg
20 kV: 400 V
Load 5
DG 2

Fig. 5.28 Positive-sequence current magnitude in case of healthy and faulty conditions in case of an isolated grounded transformer during a single-phase to ground fault at DL3

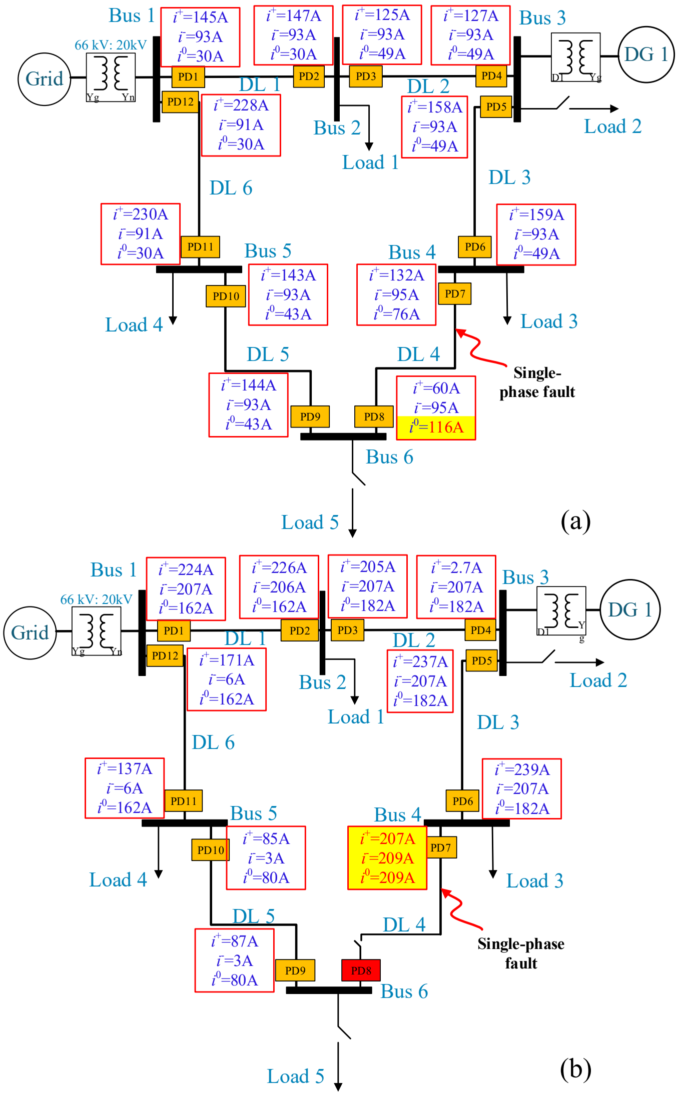
Bus 1
66 kV: 20kV
Grid
PD1
PD2
PD3
PD4
PD5
PD6
PD7
PD8
PD9
PD10
PD11
PD12
DL 1
DL 2
DL 3
DL 4
DL 5
DL 6
Bus 2
Bus 3
Bus 4
Bus 5
Bus 6
DG 1
Load 1
Load 2
Load 3
Load 4
Load 5
Single-phase fault
(a)
(b)

Fig. 5.29 Sequence current components during a single-phase to ground fault at DL4 (a) the first disconnection, (b) the second disconnection

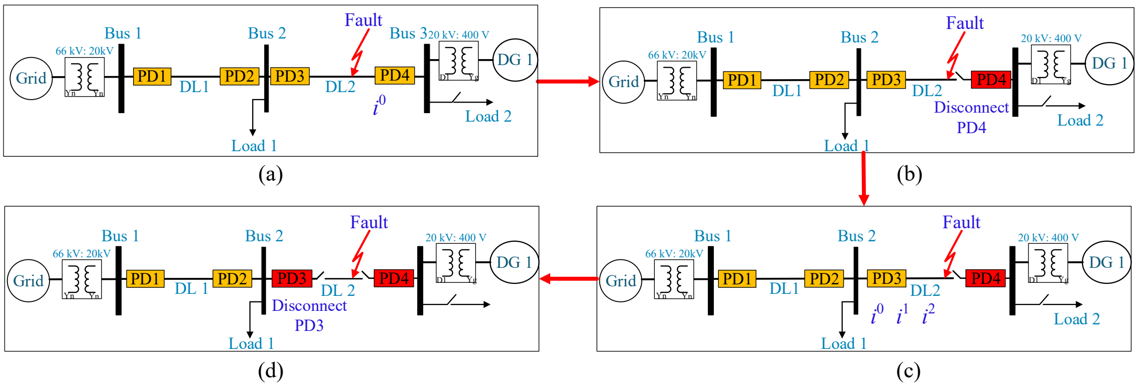
Grid
66 kV: 20kV
Bus 1
Bus 2
Bus 3
20 kV: 400 V
DG 1
PD1
PD2
PD3
PD4
DL1
DL2
Fault
Load 1
Load 2
Disconnect PD4
Disconnect PD3
(a)
(b)
(c)
(d)

Fig. 5.30 Fault isolation steps in case of a single-phase to ground fault

The changes in the *abc* voltages and currents in healthy conditions (without faults) and during a single-phase fault are approximately the same. Therefore, the grid can work safely with this fault. However, at the same time, it is possible to know that the grid has a single-phase fault using the fault classification algorithm. Even if it is not necessary to disconnect the faulted line, it is advisable because if there is a fault in another phase then high fault currents are expected. Fig. 5.30 shows the fault isolation steps in case of a single-phase to ground fault. When a single-phase to ground fault occurs at one end of DL2 the value of the zero-sequence current at that end will be the highest Fig. 5.30(a), so a disconnection of PD4 is executed Fig. 5.30(b). After the disconnection of PD4, the three sequence currents (positive, negative, and zero) at the other end of DL2 will be approximately the same Fig. 5.30(c), so a disconnection of PD3 is executed Fig. 5.30(d).

The flowchart of the LO in the case of a two-phase fault is shown in Fig. 5.31.

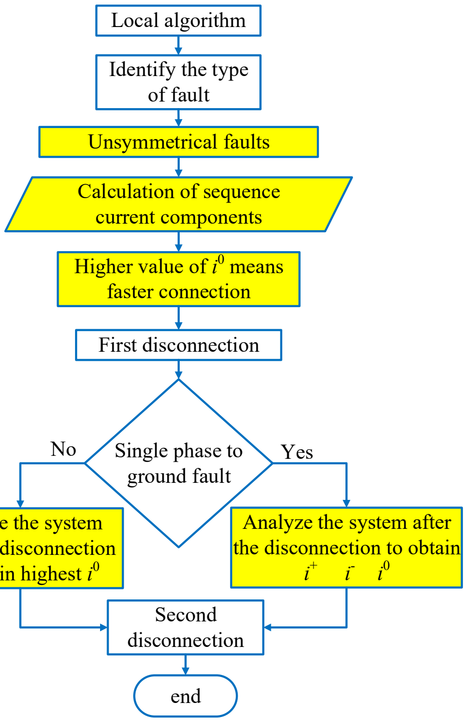
Local algorithm
Identify the type of fault
Unsymmetrical faults
Calculation of sequence current components
Higher value of i^0 means faster connection
First disconnection
Single phase to ground fault
No
Yes
Analyze the system after the disconnection to obtain highest i^0
Analyze the system after the disconnection to obtain i^+ i^- i^0
Second disconnection
end

Fig. 5.31 Flowchart of LO for unsymmetrical fault and recloser algorithm

In some cases, during a single-phase fault, the zero-sequence current will not be enough to distinguish the exact fault location after the first disconnection, especially if the fault is near DG. As seen in Fig. 5.32, with the presence of DG, the changes in zero-sequence current are too small (< 3 A) in PD4 and PD5, this is why the second disconnection does not only depend on the zero-sequence current. For example, if a single-phase fault occurred at DL3, which is near DG1, in this case, after the disconnection of PD6, the zero sequence currents will be the same at lines DL2 and DL3. In these cases, the second disconnection will depend on the three sequence current components as the three sequence components will approximately equal, as shown in Fig. 5.32. Fig. 5.33 shows the zero-sequence current profile in the case of single-phase to ground fault at DL1, DL3, and DL5. The figure shows that for the first disconnection the trip depends on the highest zero-sequence current Fig. 5.33(a), and for the second disconnection the trip depends on the approximately equal values of three sequence currents at the other end of the faulted line Fig. 5.33(b), and Fig. 5.33(c). The flowchart of the LO in case of single-phase fault is shown in Fig. 5.31.

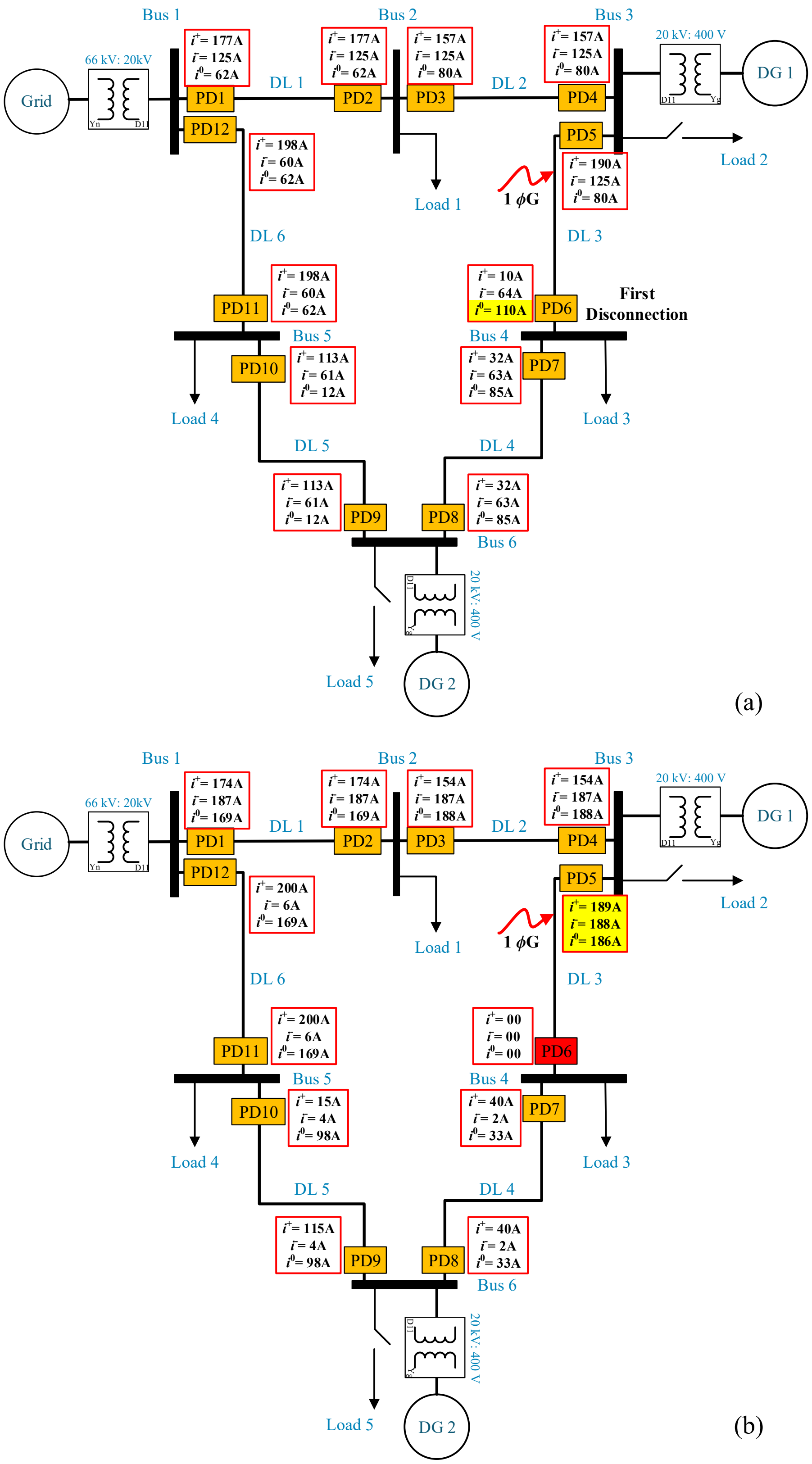
Bus 1
Bus 2
Bus 3
66 kV: 20kV
Grid
Yn
D11
20 kV: 400 V
D11
Yg
DG 1
i^+= 177A
i^-= 125A
i^0= 62A
PD1
DL 1
i^+= 177A
i^-= 125A
i^0= 62A
PD2
i^+= 157A
i^-= 125A
i^0= 80A
PD3
DL 2
i^+= 157A
i^-= 125A
i^0= 80A
PD4
PD12
i^+= 198A
i^-= 60A
i^0= 62A
Load 1
PD5
Load 2
1 ϕG
i^+= 190A
i^-= 125A
i^0= 80A
DL 6
DL 3
i^+= 198A
i^-= 60A
i^0= 62A
PD11
i^+= 10A
i^-= 64A
i^0= 110A
PD6
First
Disconnection
Bus 5
Bus 4
PD10
i^+= 113A
i^-= 61A
i^0= 12A
i^+= 32A
i^-= 63A
i^0= 85A
PD7
Load 4
Load 3
DL 5
DL 4
i^+= 113A
i^-= 61A
i^0= 12A
PD9
PD8
i^+= 32A
i^-= 63A
i^0= 85A
Bus 6
D11
Yg
20 kV: 400 V
Load 5
DG 2
(a)
Bus 1
Bus 2
Bus 3
66 kV: 20kV
Grid
Yn
D11
20 kV: 400 V
D11
Yg
DG 1
i^+= 174A
i^-= 187A
i^0= 169A
PD1
DL 1
i^+= 174A
i^-= 187A
i^0= 169A
PD2
i^+= 154A
i^-= 187A
i^0= 188A
PD3
DL 2
i^+= 154A
i^-= 187A
i^0= 188A
PD4
PD12
i^+= 200A
i^-= 6A
i^0= 169A
Load 1
PD5
Load 2
1 ϕG
i^+= 189A
i^-= 188A
i^0= 186A
DL 6
DL 3
i^+= 200A
i^-= 6A
i^0= 169A
PD11
i^+= 00
i^-= 00
i^0= 00
PD6
Bus 5
Bus 4
PD10
i^+= 15A
i^-= 4A
i^0= 98A
i^+= 40A
i^-= 2A
i^0= 33A
PD7
Load 4
Load 3
DL 5
DL 4
i^+= 115A
i^-= 4A
i^0= 98A
PD9
PD8
i^+= 40A
i^-= 2A
i^0= 33A
Bus 6
D11
Yg
20 kV: 400 V
Load 5
DG 2
(b)

Fig. 5.32 Sequence current single-phase fault at DL3 (a) before disconnection (b) after the first disconnection during

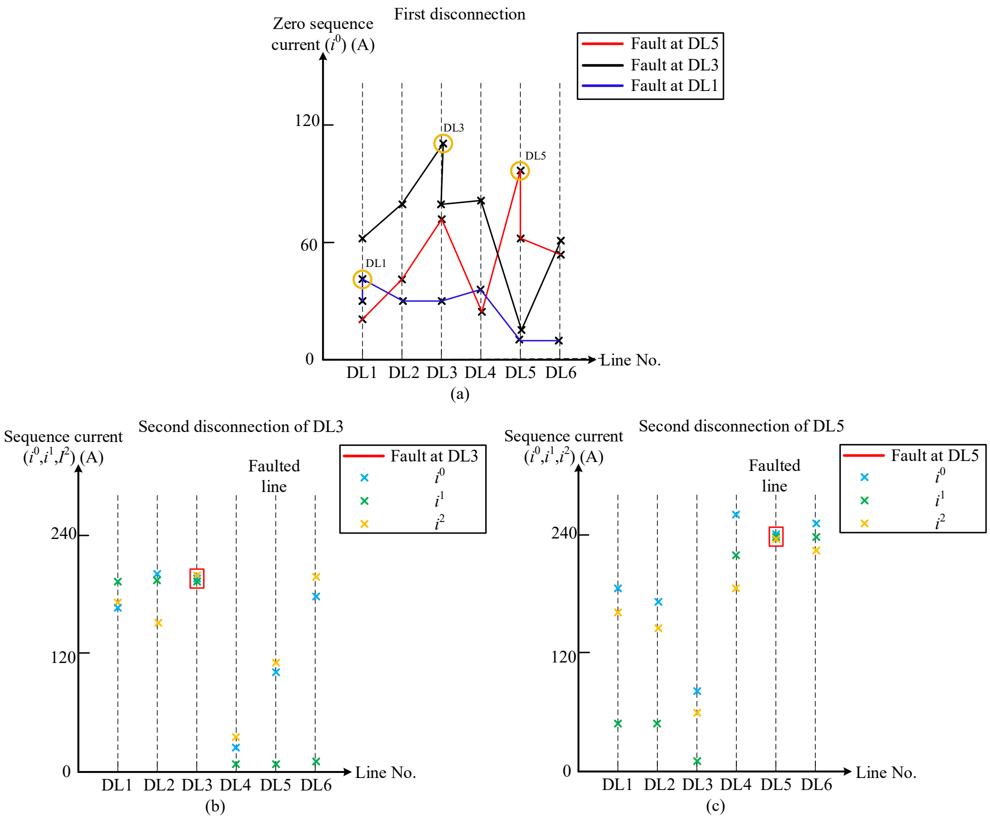

Fig. 5.33 Zero-sequence current profile with one DG connected at bus 3 (a) the first disconnection, (b) second disconnection when a single-phase fault at DL3, (c) second disconnection when a single-phase fault at DL5

In the case of two-phase or two-phase to ground faults, the same methodology used for single-phase faults can be applied for the first disconnection. Zero-sequence current during the fault at one end of the faulted line can be used to locate the fault, as shown in Fig. 5.34. After the first disconnection, the grid is analysed again. In this case, the highest value of zero sequence current at the other end of the faulted line will be obtained, and can be used to do the second disconnection.

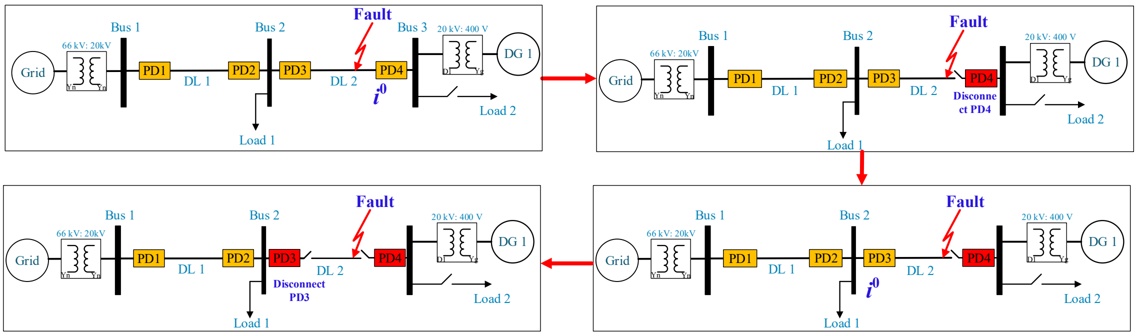

Fig. 5.34 Fault isolation steps in case of two-phase or two-phase to ground faults

Fig. 5.35 shows the zero-sequence current profile in the case of two-phase to ground fault at DL2 and two-phase fault at DL4. If the fault is at DL4, the highest i^0 is at this line (72 A). After the first disconnection, the highest i^0 is at the other end of DL4 (98 A), then both ends of the faulted line can be disconnected. Using the same concept, when the fault at DL2, the highest i^0 is at one end of DL2 (68 A), then after the first disconnection, i^0 at the other end of DL2 will be the highest (70 A), so the faulted line will be disconnected.

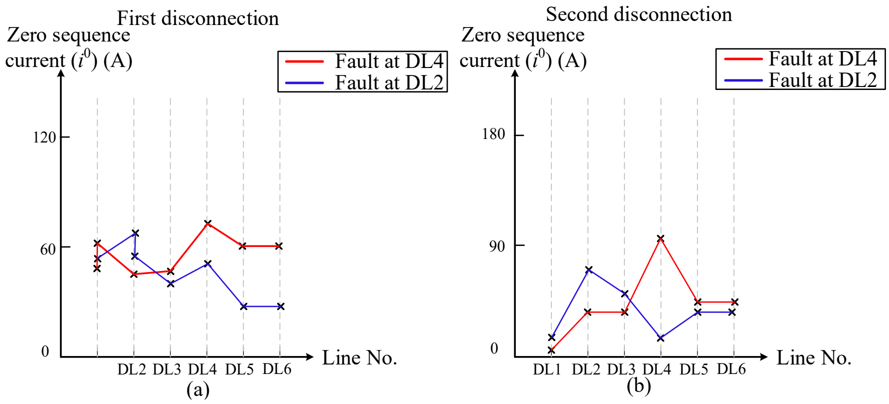

(a) (b)

Fig. 5.35 Zero-sequence current profile during two-phase fault at DL4 and two-phase to ground fault at DL2, with one DG connected at bus 3 (a) the first disconnection, (b) second disconnection

- Inverse Time current characteristic curve,

In order to design the inverse time-current characteristic curve, the IEEE extremely inverse standard curve is used, which is defined by the following equation:

$$t(I) = \left[\frac{k}{\left(I/I_s \right)^{\alpha} - 1} + c \right] * \mathrm{T_D}, \tag{34}$$

where t(I) is the trip time in seconds, I is the input current, I_s is the tripping set point (pickup) current, and $\mathrm{T_D}$ is the time dial. Table 5.10 shows the parameters for IEEE extremely inverse curve.

Table 5.10 Parameters for IEEE extremely inverse curve

Characteristic Curve	***k***	***c***	***α***
IEEE extremely inverse (EI)	5.64	0.02434	2

As mentioned before, the zero-sequence current is used to identify the location of the fault for unsymmetrical faults, which can be implemented using inverse time-current characteristic curve [184], [185]; therefore, the design of this curve will allow implementation of the LO efficiently. Fig. 5.36 shows the designed curve used in the case of unsymmetrical faults using the zero-sequence current.

The curve has been designed according to the values of the zero-sequence current in different grid configurations and scenarios. This curve can be adapted to other grid configurations and different grid voltage levels.

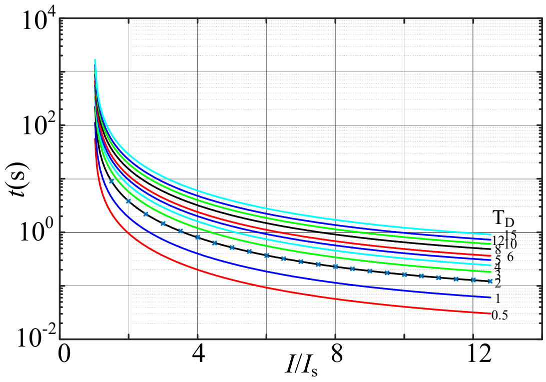

Fig. 5.36 Inverse time-current characteristic curve for unsymmetrical faults

- Symmetrical fault

In the case of a three-phase fault, the under-voltage relay will be used to disconnect one end of the faulted line. After the first disconnection, the same under-voltage criteria will be used again to disconnect the other end of the faulted line. As shown in Fig. 5.37, by using the under-voltage relay, two points with the same voltage are obtained, which means two PDs could disconnect simultaneously. So, to disconnect only the PD at the faulted line, an improvement with an additional algorithm will be used named recloser algorithm.

The design of the definite time curve will be explained at the end of the following subsection explaining the LO algorithm used for grounding the transformer with the zigzag transformer connected to the MV side.

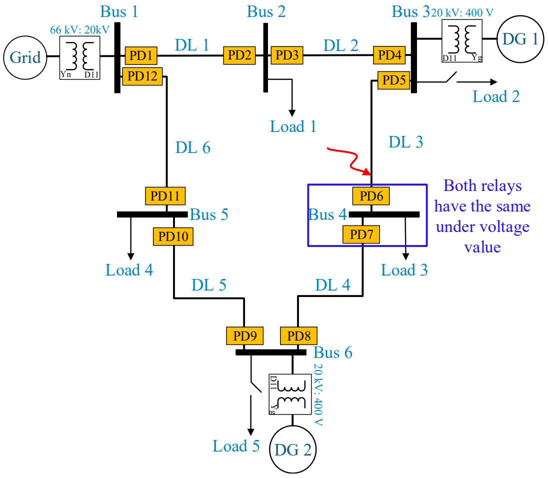
Bus 1
Bus 2
Bus 3
20 kV: 400 V
66 kV: 20kV
Grid
Yn D11
PD1
PD12
DL 1
PD2
PD3
DL 2
PD4
PD5
D11 Yg
DG 1
Load 2
Load 1
DL 6
DL 3
PD11
Bus 5
PD10
PD6
Bus 4
PD7
Both relays have the same under voltage value
Load 4
Load 3
DL 5
DL 4
PD9
PD8
Bus 6
20 kV: 400 V
Load 5
DG 2

Fig. 5.37 Three-phase fault at DL3

Fig. 5.38 shows the flowchart of the LO with the recloser algorithm.

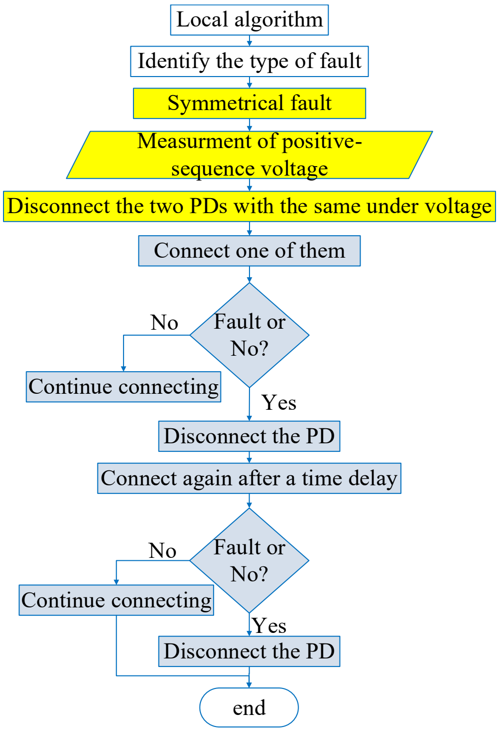
Local algorithm
Identify the type of fault
Symmetrical fault
Measurment of positive-sequence voltage
Disconnect the two PDs with the same under voltage
Connect one of them
Fault or No?
No
Continue connecting
Yes
Disconnect the PD
Connect again after a time delay
Fault or No?
No
Continue connecting
Yes
Disconnect the PD
end

Fig. 5.38 Flowchart of LO for symmetrical fault and recloser algorithm

The main idea of the algorithm is to use the recloser to open and close after a specific time interval (delay). The exact idea of the recloser algorithm will be discussed in the next subsection. Fig. 5.39 shows the voltage profile in the case of a three-phase fault. As shown, when a three-phase fault has occurred at DL3, the lowest v^{+} will be at DL3, and after the disconnection, the same behaviour is noticed to disconnect the other end of the faulted line. As seen in Fig. 5.39, similar behaviour is noticed when the fault is located at DL4.

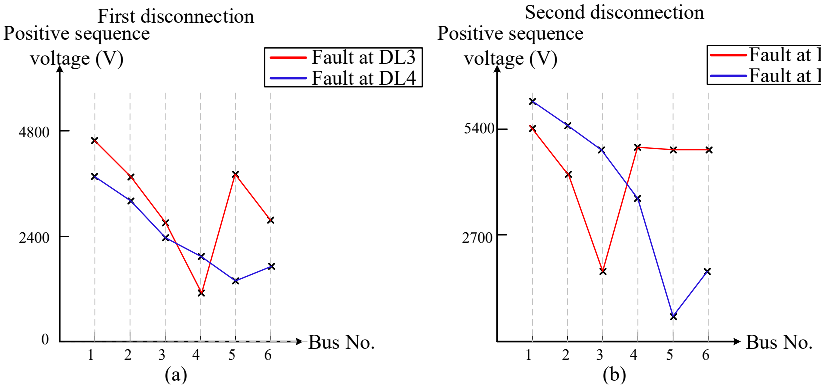

Fig. 5.39 Positive-sequence voltage profile during three-phase fault with one DG connected at bus 3 (a) the first disconnection, (b) second disconnection

- Recloser algorithm

As explained before, using an under-voltage relay two PDs connected to the same bus could be disconnected, because they have the same under-voltage. As shown in Fig. 5.40, two signals are used; the first is to turn on and off the PD and the second is to indicate if there is a fault or no-fault seen by the PD. As shown in Fig. 5.37, if there is a fault at line 3, PD6 and PD7 have the same under-voltage, so both of them could disconnect simultaneously. If PD6 is a little faster than PD7 then both disconnect, but, after a fixed delay, PD6 will be connected again. If there is a fault, then PD6 will disconnect permanently, and after a longer fixed delay, PD7 will connect, as presented in Fig. 5.40. On the other hand, if PD7 is faster than PD6, at the beginning both of them disconnect due to under-voltage. Then PD7 will connect first; in this case, there is no fault seen by PD7 because PD6 is still disconnected, so that PD7 will continue connected. After a delay, PD6 will connect and see the fault so that PD6 will disconnect again.

In case of fault at the middle of the line, as seen in Fig. 5.41, four PDs will have the same under-voltage (connected to the two buses at the end of the faulted line), and the recloser algorithm will be applied for each end of the line. For example, when a fault is in the middle of DL3, then PD4, PD5, PD6, and PD7 are disconnected as they have the same under voltage. Then, PD5 and PD6 will be connected simultaneously, and because they are exposed to the fault, both of them will be disconnected permanently, and then PD4 and PD7 will be connected. On the other hand, if PD4 and PD7 are faster than PD5 and PD6, then when PD4 and PD7 are connected, the fault is still cleared, so they will remain open permanently. Then, PD5 and PD6 will connect and recognize the fault and then disconnect permanently. As shown in Fig. 5.41, the recloser algorithm will also disconnect the PD at the faulted line only. The flowchart of the recloser algorithm is shown in Fig. 5.38 highlighted in blue color.

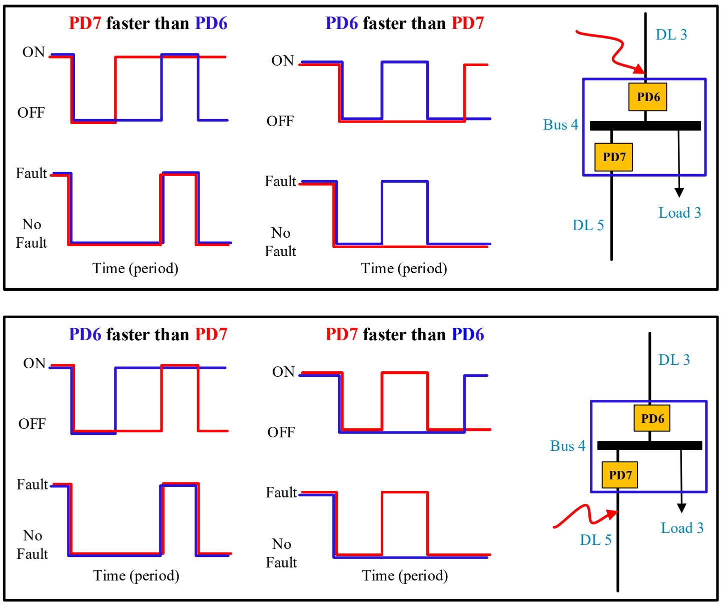
PD7 faster than PD6
PD6 faster than PD7
ON
OFF
Fault
No Fault
Time (period)
DL 3
PD6
Bus 4
PD7
Load 3
DL 5
PD6 faster than PD7
PD7 faster than PD6

Fig. 5.40 Recloser algorithm explanation when the fault in different lines

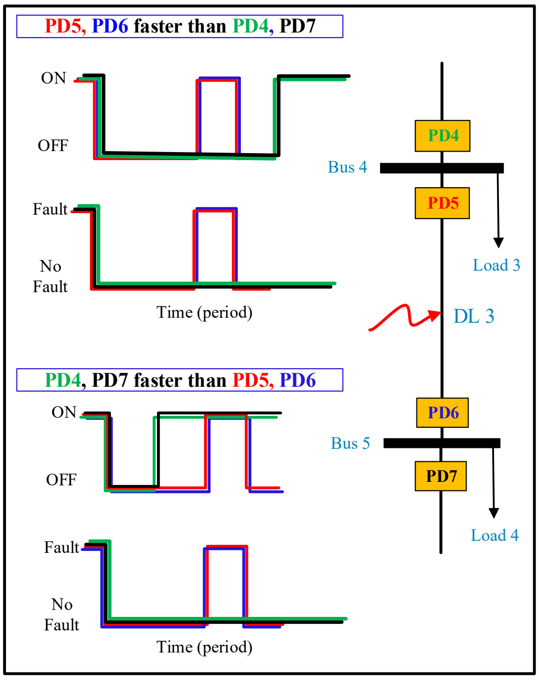
PD5, PD6 faster than PD4, PD7
ON
OFF
Fault
No Fault
Time (period)
PD4
Bus 4
PD5
Load 3
DL 3
PD4, PD7 faster than PD5, PD6
PD6
Bus 5
PD7
Load 4

Fig. 5.41 Recloser algorithm behaviour when a three-phase fault at the middle of the DL

- ➢ A line connected directly to the main grid

In the case of lines directly connected to the main grid, it is possible to use the inverse-time characteristic curve. Because Line 1 (DL1) and Line 4 (DL4) will have a considerable short-circuit current value compared to the other part of the system. Especially with the use of PV-based inverters.

- ➢ Flowchart of the proposed algorithm

Fig. 5.42 shows the flowchart of the complete protection strategy, but the details of LO are shown in Fig. 5.43.

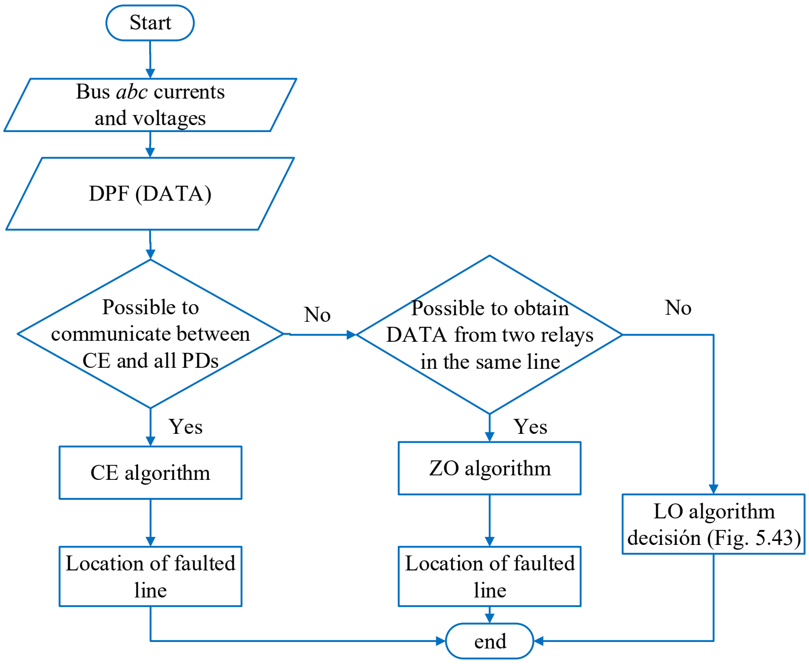
Start
Bus *abc* currents and voltages
DPF (DATA)
Possible to communicate between CE and all PDs
No
Possible to obtain DATA from two relays in the same line
No
Yes
CE algorithm
Yes
ZO algorithm
LO algorithm decisión (Fig. 5.43)
Location of faulted line
Location of faulted line
end

Fig. 5.42 Flowchart of the proposed CE, and ZO protection algorithms

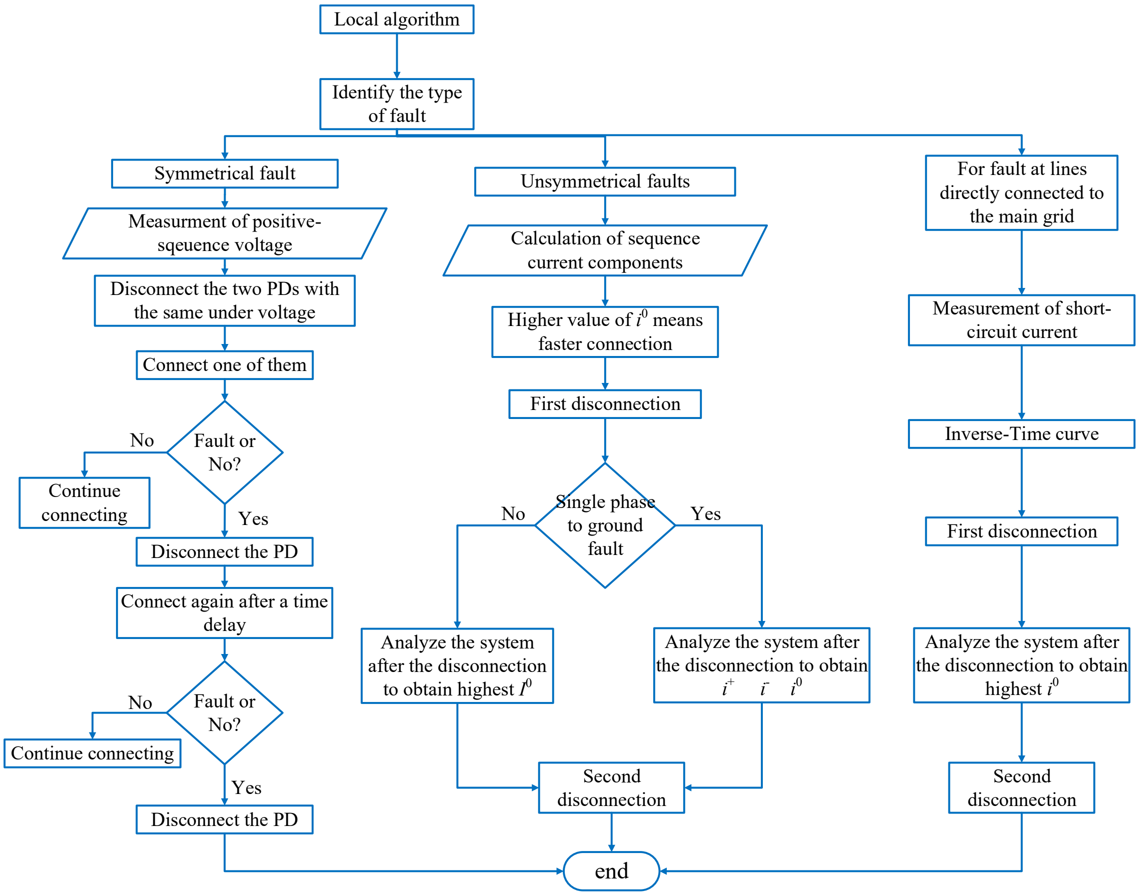
Local algorithm
Identify the type of fault
Symmetrical fault
Unsymmetrical faults
For fault at lines directly connected to the main grid
Measurment of positive-sqeuence voltage
Calculation of sequence current components
Disconnect the two PDs with the same under voltage
Higher value of i^0 means faster connection
Measurement of short-circuit current
Connect one of them
First disconnection
Inverse-Time curve
No
Fault or No?
Continue connecting
Yes
Single phase to ground fault
No
Yes
First disconnection
Disconnect the PD
Connect again after a time delay
Analyze the system after the disconnection to obtain highest I^0
Analyze the system after the disconnection to obtain i^+ i^- i^0
Analyze the system after the disconnection to obtain highest i^0
No
Fault or No?
Continue connecting
Yes
Disconnect the PD
Second disconnection
Second disconnection
end

Fig. 5.43 Flowchart of the LO proposed protection algorithm

- Proposed LO algorithm without recloser

The disadvantage of the recloser idea is that it needs more time and more steps to disconnect the fault. Therefore, another idea is proposed that is based on changing the location of the measurement signals. The idea is based on placing the measurement devices in front of the breaker (Fig. 5.44(b)) instead of behind it (Fig. 5.44(a)). Instead of using the recloser algorithm that will take time and more steps to clear the fault, the presence of a fault can be known directly using the measured voltages.

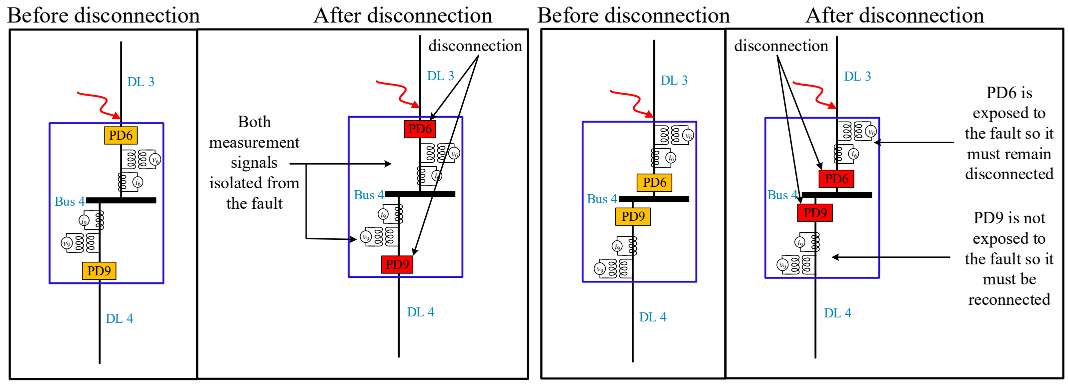
Before disconnection
After disconnection
Before disconnection
After disconnection
DL 3
PD6
Bus 4
PD9
DL 4
disconnection
Both measurement signals isolated from the fault
DL 3
PD6
Bus 4
PD9
DL 4
disconnection
PD6 is exposed to the fault so it must remain disconnected
PD9 is not exposed to the fault so it must be reconnected

(a) (b)

Fig. 5.44 measurement signals (a) behind the breaker, (b) in front of the breaker

As shown in Fig. 5.44, in the case of measurement devices placed between the bus and the breaker, after the disconnection of both beakers, both will see the same voltage and both of them will be disconnected from the fault. In this case, a recloser algorithm needs to be applied to disconnect the breaker in the faulted line.

However, in the case of placing the measurement signals in front of the breaker, after the disconnection of both breakers due to under-voltage, one of them will be disconnected from the fault and the other one will still be exposed to the fault. Therefore, there is no need for the recloser algorithm; instead, each breaker can take its own decision instantaneously with no delays. In this case, the time needed to disconnect the faulted part from the grid is reduced. Fig. 5.46 shows the flowchart of the proposed LO algorithm without recloser.

Table 5.11 and Fig. 5.45 show the clearing time needed to disconnect the faulted side of the line in case of a three-phase fault with LO. Considering that the delay time of the measuring instruments needs to be added to the total tripping time. That means for each open or close more delay time is obtained, which will indicate that with the recloser algorithm the clearing time of the fault will be more than the time needed to clear the fault without the recloser algorithm. It is important to note that using this idea will not affect the algorithms of the other fault types.

Table 5.11 Fault clearing time

	Clearing time
With recloser algorithm	0.47 Sec
Without recloser algorithm	0.39 Sec
Time difference	0.06 - 0.08 Sec

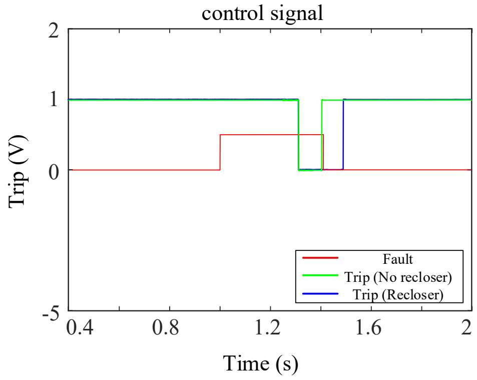

Fig. 5.45 Difference in trip signals with and without recloser algorithms

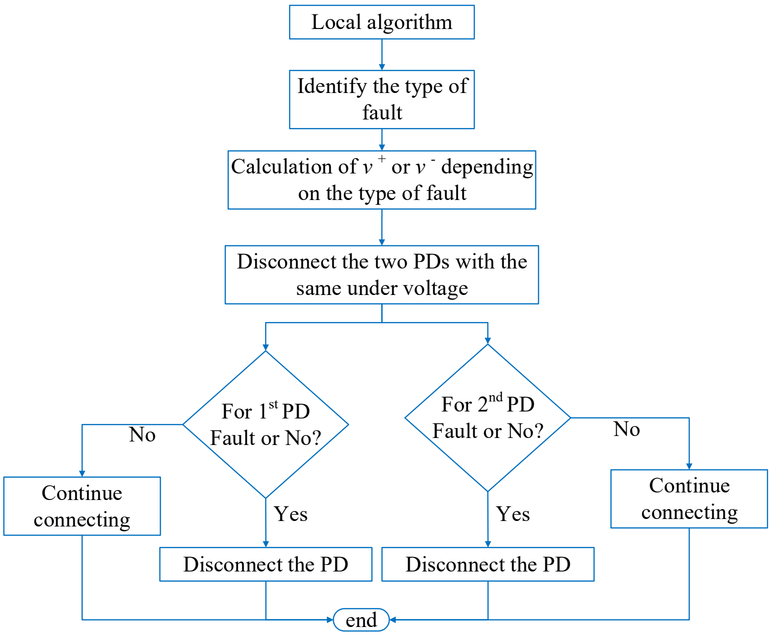
Local algorithm
Identify the type of fault
Calculation of v^+ or v^- depending on the type of fault
Disconnect the two PDs with the same under voltage
For 1st PD Fault or No?
For 2nd PD Fault or No?
No
No
Continue connecting
Continue connecting
Yes
Yes
Disconnect the PD
Disconnect the PD
end

Fig. 5.46 Flowchart of proposed LO algorithm without recloser

5.3.3.3. LO algorithm in case of symmetrical and unsymmetrical faults and the MV side of the (HV/MV) transformer grounded through a zigzag

The primary benefit of this algorithm is that it can operate independently of the HV/MV transformer's grounding connection since it is based on the value of the sequence *abc* voltages at each bus, and then use the recloser algorithm to disconnect the system's faulty part.

- Unsymmetrical faults

In the case of a single-phase fault, by using negative-sequence voltage during the fault, one end of the faulted line can be located. During the fault, the negative-sequence voltage of the two PDs at one end of the faulted line (bus 3) will be higher than any other negative-sequence voltage values of other lines, as shown in Fig. 5.47 and Fig. 5.48, then the recloser algorithm will be implemented to disconnect the PD at the faulted line. Therefore, the highest value means faster disconnection. Fig. 5.49 shows the steps to isolate the fault in case of a single-phase fault.

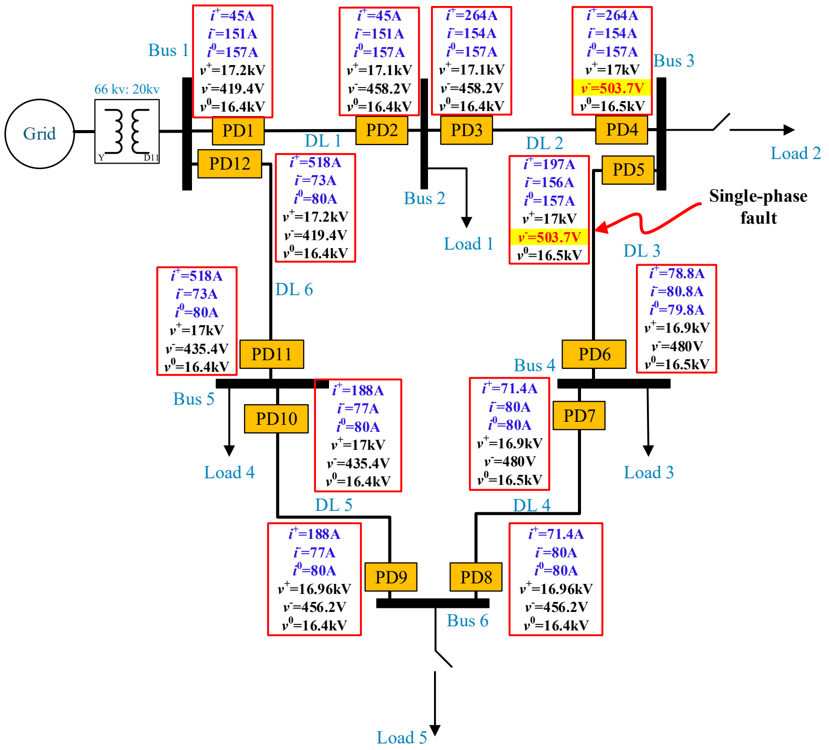
Grid
66 kv: 20kv
Y
D11
Bus 1
i^+=45A
i^-=151A
i^0=157A
v^+=17.2kV
v^-=419.4V
v^0=16.4kV
PD1
DL 1
i^+=45A
i^-=151A
i^0=157A
v^+=17.1kV
v^-=458.2V
v^0=16.4kV
PD2
i^+=264A
i^-=154A
i^0=157A
v^+=17.1kV
v^-=458.2V
v^0=16.4kV
PD3
DL 2
i^+=264A
i^-=154A
i^0=157A
v^+=17kV
v^-=503.7V
v^0=16.5kV
PD4
Bus 3
Load 2
PD12
i^+=518A
i^-=73A
i^0=80A
v^+=17.2kV
v^-=419.4V
v^0=16.4kV
Bus 2
Load 1
i^+=197A
i^-=156A
i^0=157A
v^+=17kV
v^-=503.7V
v^0=16.5kV
PD5
Single-phase fault
DL 3
DL 6
i^+=518A
i^-=73A
i^0=80A
v^+=17kV
v^-=435.4V
v^0=16.4kV
PD11
Bus 5
PD10
Load 4
i^+=188A
i^-=77A
i^0=80A
v^+=17kV
v^-=435.4V
v^0=16.4kV
i^+=78.8A
i^-=80.8A
i^0=79.8A
v^+=16.9kV
v^-=480V
v^0=16.5kV
PD6
Bus 4
i^+=71.4A
i^-=80A
i^0=80A
v^+=16.9kV
v^-=480V
v^0=16.5kV
PD7
Load 3
DL 5
DL 4
i^+=188A
i^-=77A
i^0=80A
v^+=16.96kV
v^-=456.2V
v^0=16.4kV
PD9
PD8
i^+=71.4A
i^-=80A
i^0=80A
v^+=16.96kV
v^-=456.2V
v^0=16.4kV
Bus 6
Load 5

Fig. 5.47 Single-phase to ground fault at DL3 with fault resistance r =0.1 Ω

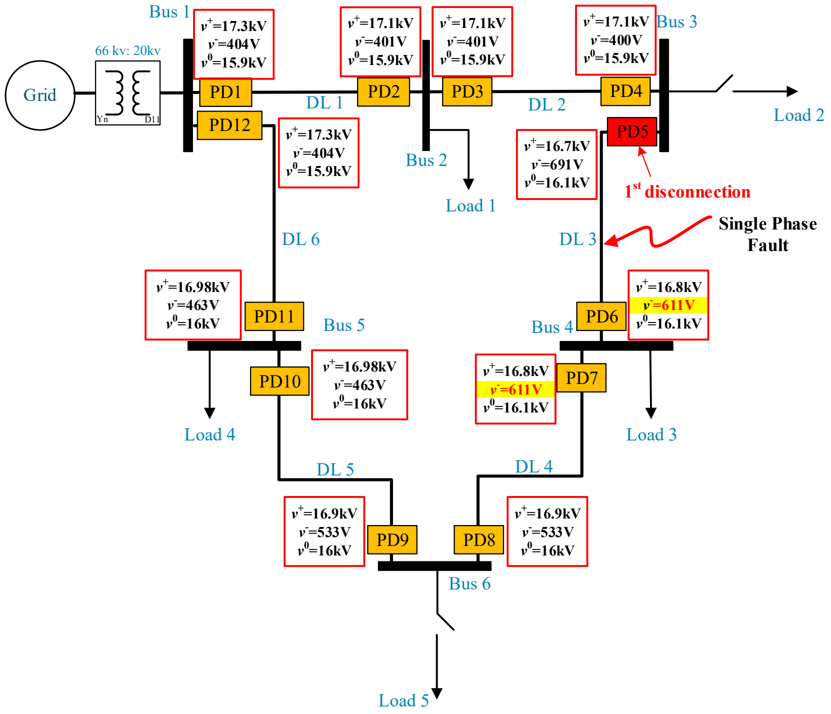
Grid
66 kv: 20kv
Yn
D11
Bus 1
v^+=17.3kV
v^-=404V
v^0=15.9kV
PD1
DL 1
v^+=17.1kV
v^-=401V
v^0=15.9kV
PD2
v^+=17.1kV
v^-=401V
v^0=15.9kV
PD3
DL 2
v^+=17.1kV
v^-=400V
v^0=15.9kV
PD4
Bus 3
Load 2
PD12
v^+=17.3kV
v^-=404V
v^0=15.9kV
Bus 2
Load 1
v^+=16.7kV
v^-=691V
v^0=16.1kV
PD5
1st disconnection
Single Phase Fault
DL 3
DL 6
v^+=16.98kV
v^-=463V
v^0=16kV
PD11
Bus 5
v^+=16.8kV
v^-=611V
v^0=16.1kV
PD6
Bus 4
PD10
v^+=16.98kV
v^-=463V
v^0=16kV
v^+=16.8kV
v^-=611V
v^0=16.1kV
PD7
Load 4
Load 3
DL 5
DL 4
v^+=16.9kV
v^-=533V
v^0=16kV
PD9
PD8
v^+=16.9kV
v^-=533V
v^0=16kV
Bus 6
Load 5

Fig. 5.48 Single-phase to ground fault at DL3 with fault resistance r =0.1 Ω, after 1st disconnection of PD5

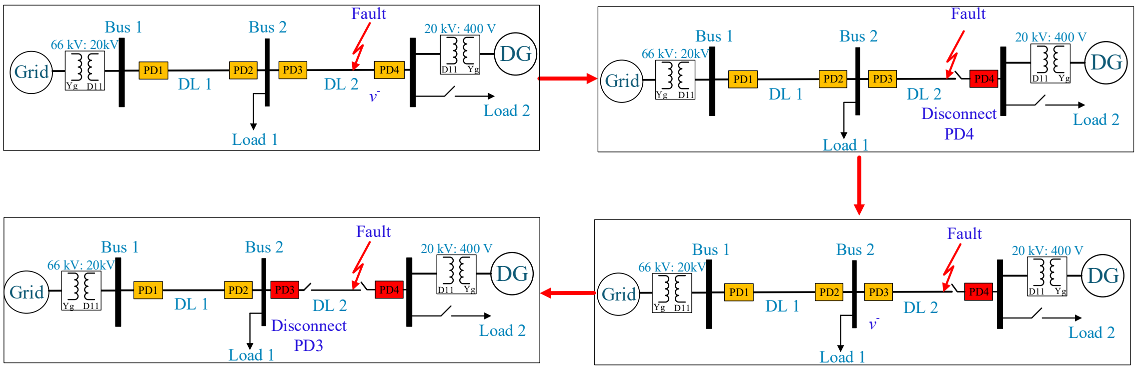
Grid
66 kV: 20kV
Yg D11
Bus 1
PD1
DL 1
Bus 2
PD2
PD3
Load 1
Fault
DL 2
v^-
PD4
20 kV: 400 V
D11 Yg
DG
Load 2
Disconnect PD4
Disconnect PD3

Fig. 5.49 Fault isolation steps in case of single-phase to ground fault

The flowchart of the LO algorithm when the HV/MV transformer side is connected as YNd11 grounded through a zigzag transformer is presented in Fig. 5.50.

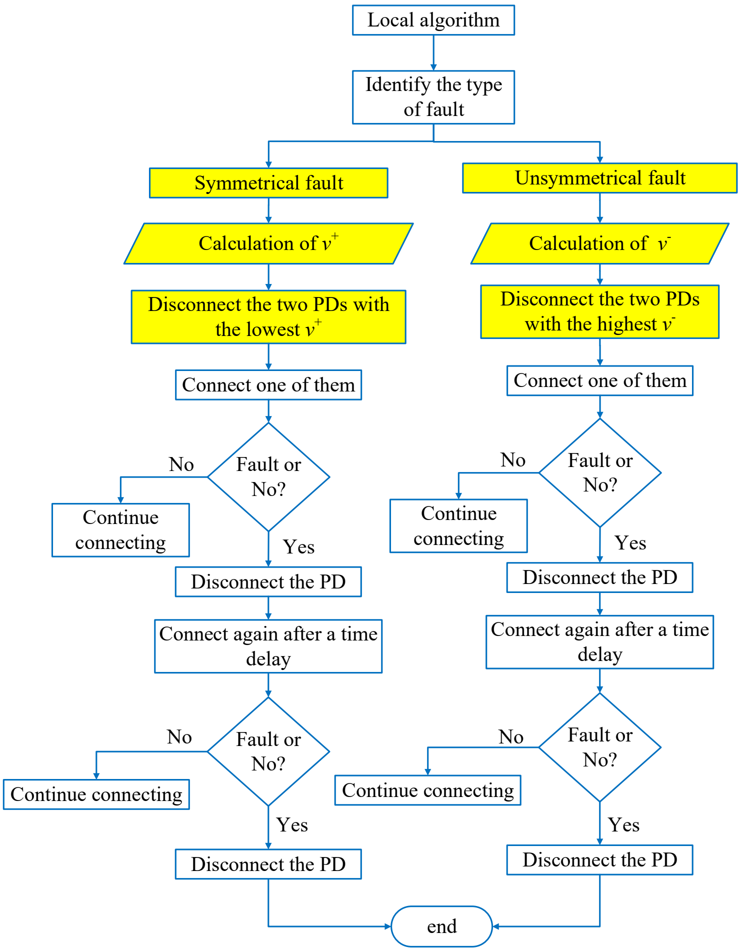
Local algorithm
Identify the type of fault
Symmetrical fault
Unsymmetrical fault
Calculation of v^+
Calculation of v^-
Disconnect the two PDs with the lowest v^+
Disconnect the two PDs with the highest v^-
Connect one of them
Connect one of them
Fault or No?
No
Yes
Continue connecting
Disconnect the PD
Connect again after a time delay
Fault or No?
No
Yes
Continue connecting
Disconnect the PD
end

Fig. 5.50 Flowchart of the proposed LO algorithm with YNd11 transformer connection grounded through a zigzag transformer

The next step is disconnecting the PD with the highest negative-sequence voltage and analyzing the grid after the disconnection. After the disconnection of one end of the faulted line, the highest value of the negative-sequence currents will be obtained at the other end of the faulted line, as shown in Fig. 5.47 and Fig. 5.48; which is used in case of single-phase fault to isolate the faulted line. Fig. 5.51 shows the zero-sequence current profile in the case of single-phase to ground fault. It can be illustrated that the v^- at the faulted line (DL5) has the highest value, so a first disconnection can be implemented, then using the same strategy the other end of the faulted line (DL5) is disconnected. Similar behaviour is obtained when the fault is at DL1, as seen in Fig. 5.51.

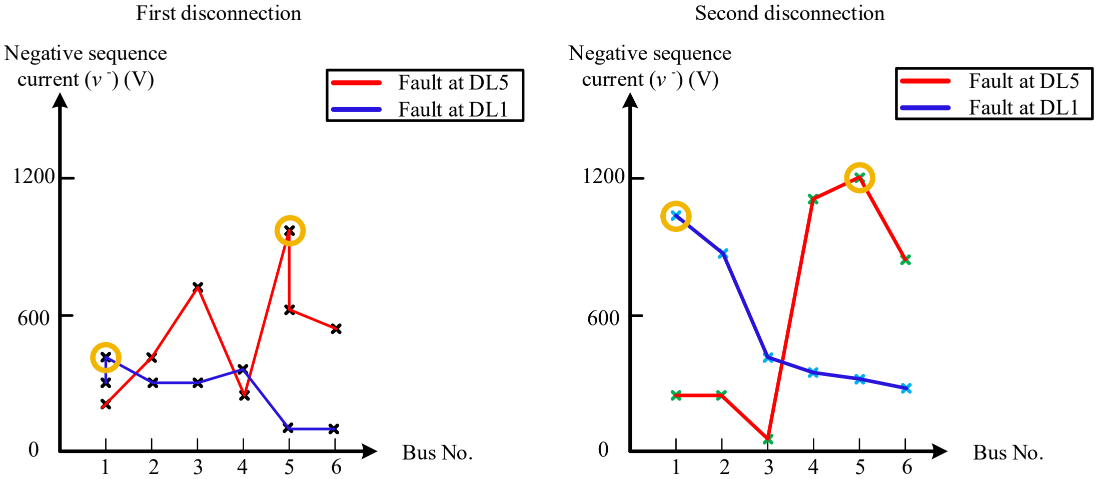

(a) (b)

Fig. 5.51 Negative-sequence voltage profile during single-phase fault with one DG connected at bus 3 (a) the first disconnection, (b) the second disconnection

In the case of two-phase or two-phase to ground faults, using the same idea applied in the case of single-phase fault through the negative-sequence voltage during the fault, one end of the faulted line can be located. Fig. 5.52 shows the negative-sequence voltage profile in the case of two-phase to ground and two-phase faults. The figure illustrates that the v^- at the faulted line (DL4 or DL2) has the highest value, so a first disconnection can be implemented, using the same strategy at the other end of the faulted line (DL4 or DL2) is disconnected.

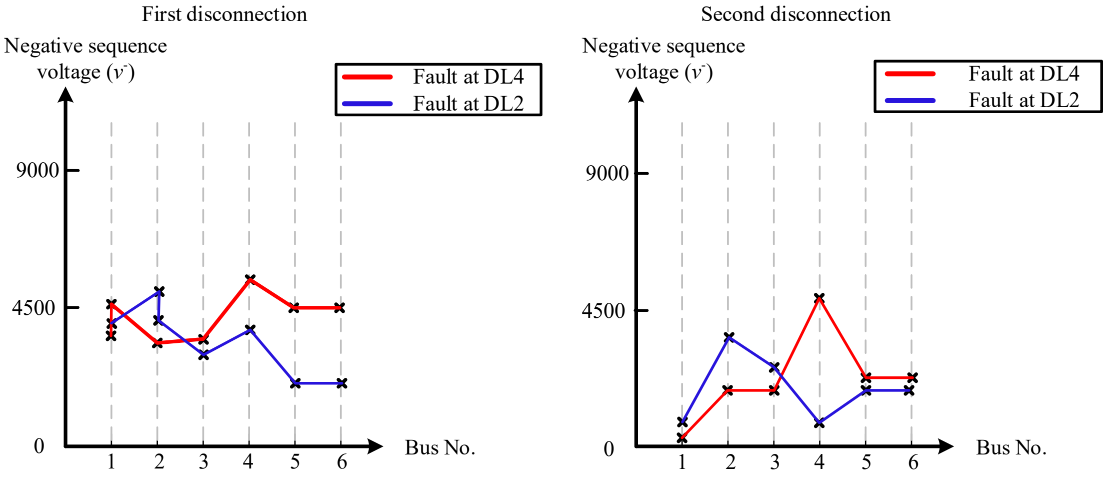

(a) (b)

Fig. 5.52 Negative-sequence voltage profile during two-phase fault with one DG connected at bus 3 (a) the first disconnection, (b) the second disconnection

- Symmetrical fault

In the case of a three-phase fault, positive-sequence voltage is used to distinguish the location of the fault and disconnect one end of the faulted line. The PD that detects a three-phase fault with the lowest positive-sequence voltage is the first to trip. After the first disconnection, the same criteria are used again to disconnect the other end of the faulted line, as shown in Fig. 5.53. Using this idea, two points with the same voltage will be obtained, which means two PDs will disconnect simultaneously, as shown in Fig. 5.55. Therefore, to disconnect only the PD at the faulted line, a recloser algorithm is needed.

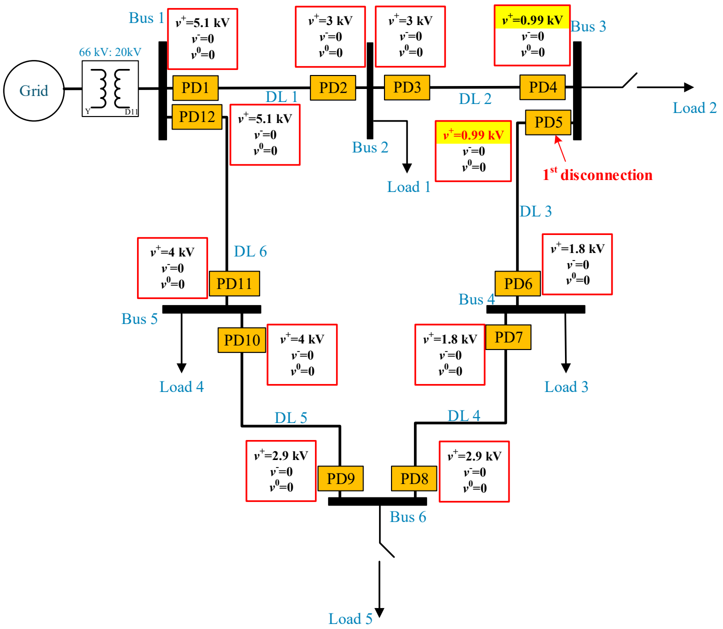
Grid
66 kV: 20kV
Bus 1
Bus 2
Bus 3
Bus 4
Bus 5
Bus 6
PD1
PD2
PD3
PD4
PD5
PD6
PD7
PD8
PD9
PD10
PD11
PD12
DL 1
DL 2
DL 3
DL 4
DL 5
DL 6
Load 1
Load 2
Load 3
Load 4
Load 5
1st disconnection
v+=5.1 kV v-=0 v0=0
v+=3 kV v-=0 v0=0
v+=3 kV v-=0 v0=0
v+=0.99 kV v-=0 v0=0
v+=5.1 kV v-=0 v0=0
v+=0.99 kV v-=0 v0=0
v+=1.8 kV v-=0 v0=0
v+=4 kV v-=0 v0=0
v+=4 kV v-=0 v0=0
v+=1.8 kV v-=0 v0=0
v+=2.9 kV v-=0 v0=0
v+=2.9 kV v-=0 v0=0

Fig. 5.53 Three-phase to ground fault at DL3, with fault resistance *r* = 0.1

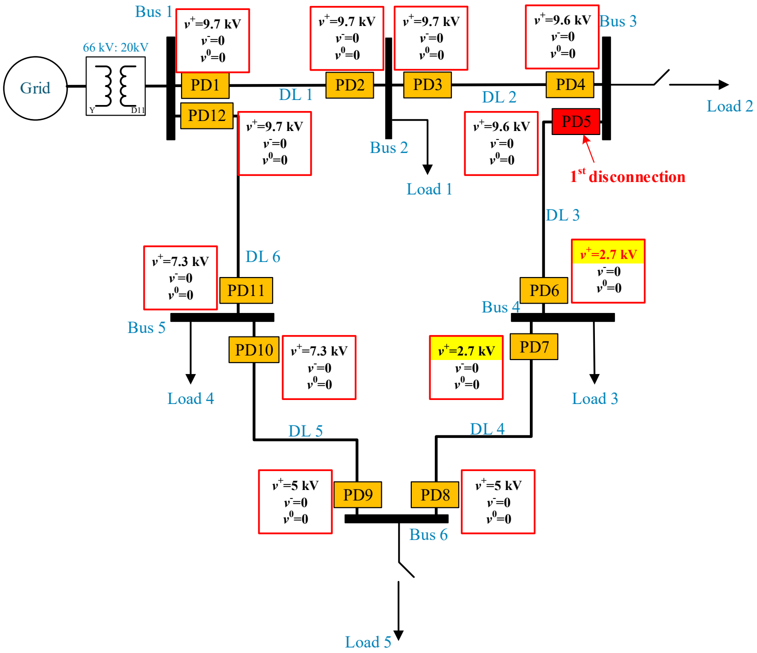
Grid
66 kV: 20kV
Bus 1
Bus 2
Bus 3
Bus 4
Bus 5
Bus 6
PD1
PD2
PD3
PD4
PD5
PD6
PD7
PD8
PD9
PD10
PD11
PD12
DL 1
DL 2
DL 3
DL 4
DL 5
DL 6
Load 1
Load 2
Load 3
Load 4
Load 5
1st disconnection
v+=9.7 kV v-=0 v0=0
v+=9.7 kV v-=0 v0=0
v+=9.7 kV v-=0 v0=0
v+=9.6 kV v-=0 v0=0
v+=9.7 kV v-=0 v0=0
v+=9.6 kV v-=0 v0=0
v+=2.7 kV v-=0 v0=0
v+=7.3 kV v-=0 v0=0
v+=7.3 kV v-=0 v0=0
v+=2.7 kV v-=0 v0=0
v+=5 kV v-=0 v0=0
v+=5 kV v-=0 v0=0

Fig. 5.54 Three-phase to ground fault at DL3 with fault resistance *r* =0.1 Ω, after 1st disconnection of PD5

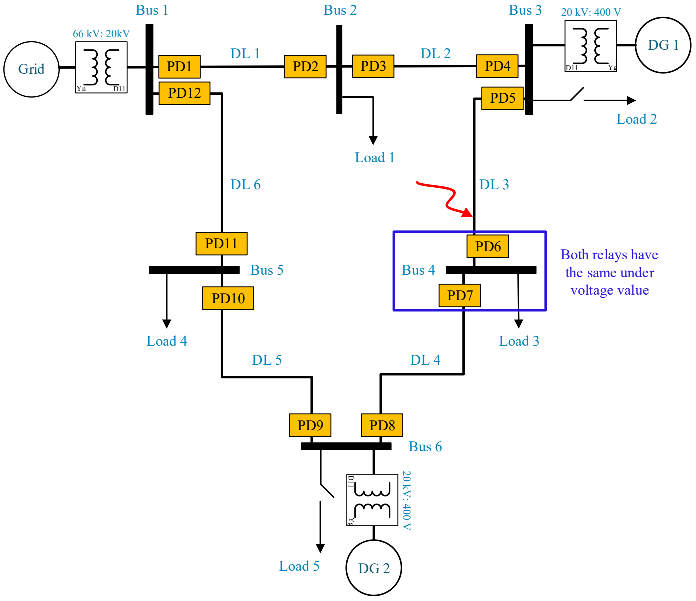
Bus 1
Bus 2
Bus 3
66 kV: 20kV
20 kV: 400 V
Grid
DG 1
PD1
PD2
PD3
PD4
PD5
PD12
DL 1
DL 2
Load 1
Load 2
DL 6
DL 3
PD11
PD6
Bus 5
Bus 4
PD10
PD7
Both relays have the same under voltage value
Load 4
Load 3
DL 5
DL 4
PD9
PD8
Bus 6
20 kV: 400 V
Load 5
DG 2

Fig. 5.55 Three-phase fault at DL3

The main idea of the algorithm is to use the recloser to open and close after some time. The exact idea of the recloser algorithm was explained in the previous subsection. Fig. 5.56 shows the voltage profile in the case of a three-phase fault.

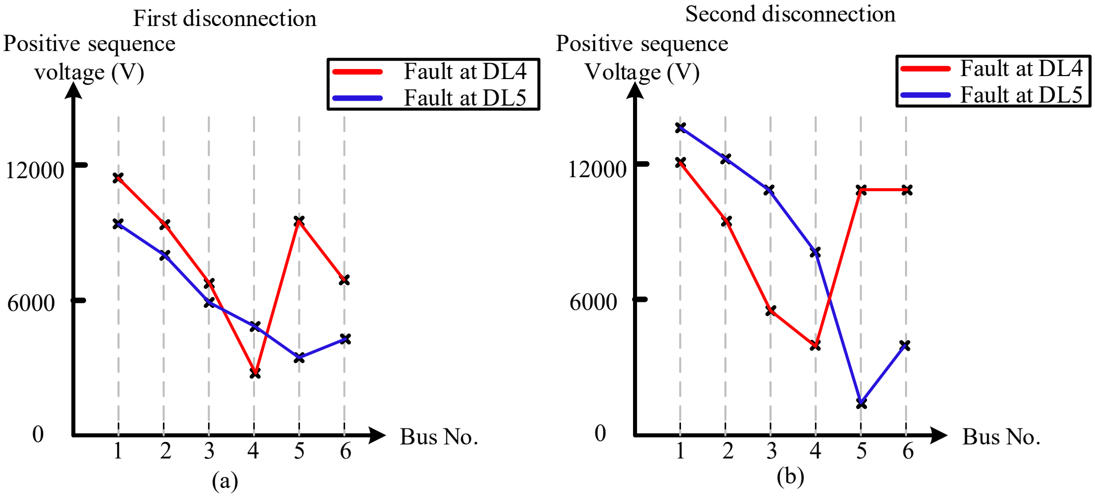

(a) (b)

Fig. 5.56 Voltage profile during three-phase fault with one DG connected at bus 3

- Definite time characteristic curve

The equation used for the definite time-voltage characteristic curve is based on IEEE definite Time standard [184], [185]. The disconnection of the first PD is based on the magnitude of the definite time curve of the positive-sequence or negative-sequence voltages, depending on the type of fault, as shown in Fig. 5.57. After that, the disconnection of the second PD is made depending on the fault type algorithm. The curve has been designed according to positive- and negative-sequence voltages for different grid configurations and scenarios. This curve can be adapted to other grid configurations and different grid voltage levels depending on the analysed grid.

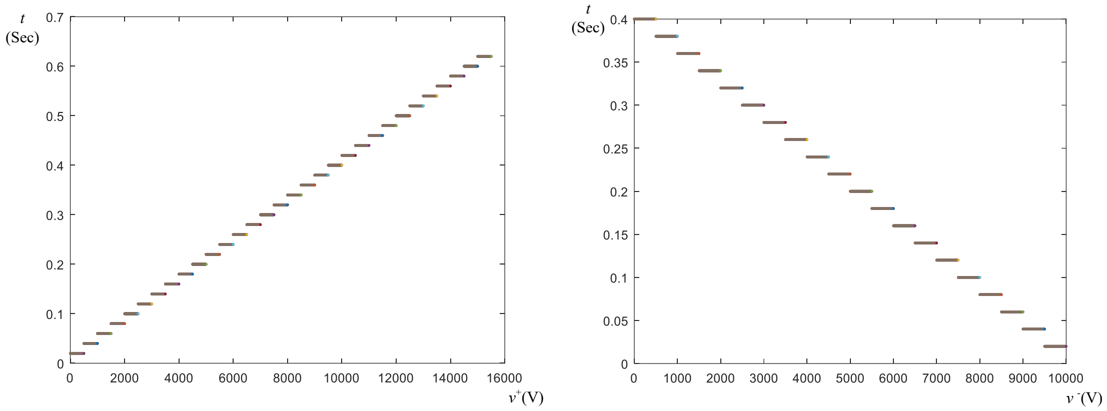

Fig. 5.57 Definite time curve (a) Positive-sequence voltage, (b) Negative-sequence voltage

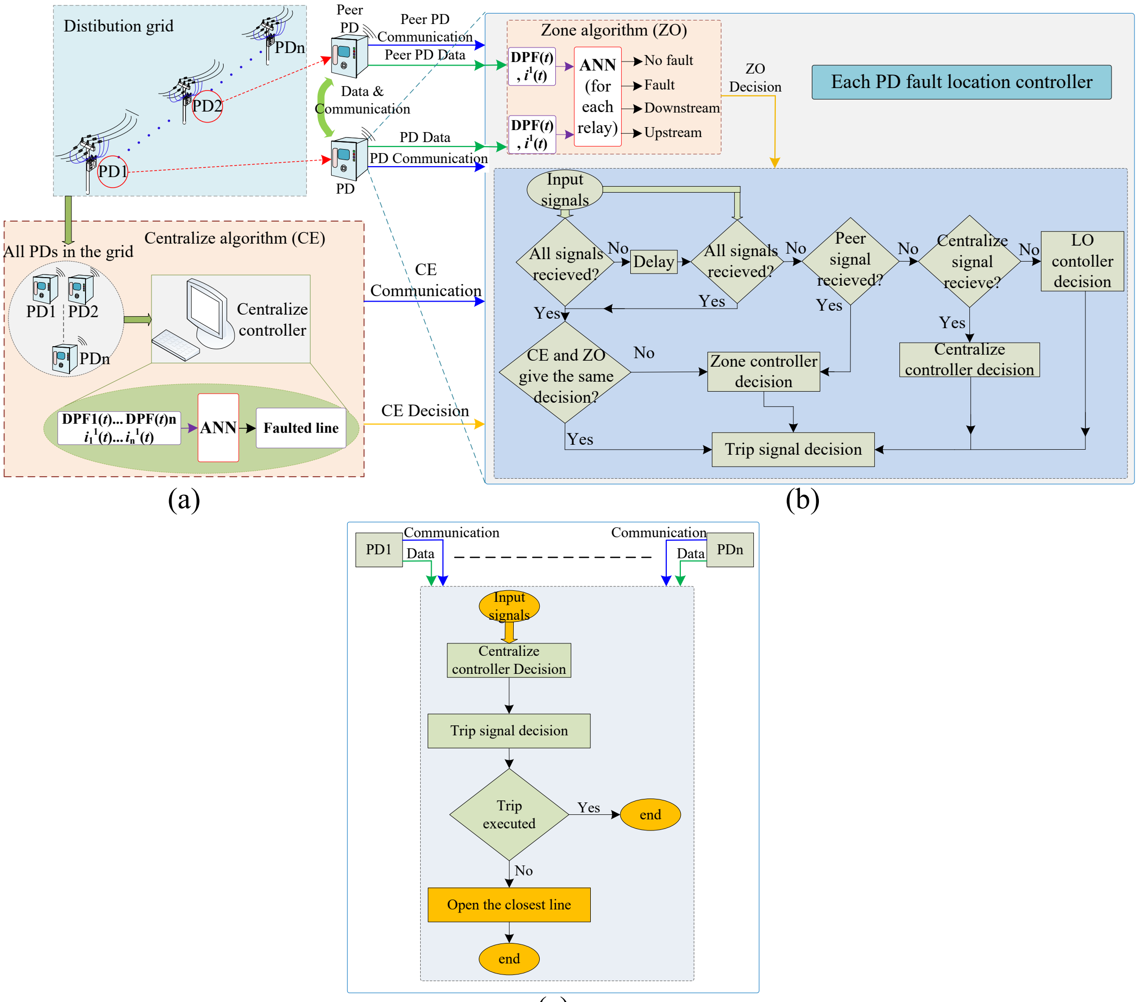
Distibution grid
PDn
PD2
PD1
Peer PD
Peer PD Communication
Peer PD Data
Data & Communication
PD Data
PD Communication
PD
Zone algorithm (ZO)
DPF(t), i¹(t)
ANN (for each relay)
No fault
Fault
Downstream
Upstream
ZO Decision
Each PD fault location controller
All PDs in the grid
Centralize algorithm (CE)
PD1
PD2
PDn
Centralize controller
DPF1(t)...DPF(t)n i₁¹(t)...iₙ¹(t)
ANN
Faulted line
CE Communication
CE Decision
Input signals
All signals recieved?
No
Delay
All signals recieved?
No
Peer signal recieved?
No
Centralize signal recieve?
No
LO contoller decision
Yes
Yes
Yes
Yes
CE and ZO give the same decision?
No
Zone controller decision
Centralize controller decision
Yes
Trip signal decision
(a)
(b)
PD1
Communication
Data
Communication
Data
PDn
Input signals
Centralize controller Decision
Trip signal decision
Trip executed
Yes
end
No
Open the closest line
end
(c)

Fig. 5.58 Concept diagram of (a) CE algorithm, (b) each PD fault location controller including ZO and LO algorithms, (c) post-processing algorithm

5.3.4. PD priority strategy

Depending on the outcomes of the two algorithms (CE-ZO), each PD must make a local decision. This step will increase the system's redundancy, enhancing security and reliability in the case of a failure. Furthermore, each algorithm must transmit a communication check signal (green arrows) to guarantee that the decision is available, as shown in Fig. 5.58(a).

Before performing the algorithm, the controller of each PD must verify that the signals are available. If one of the algorithms fails (for example, if one of the communication check signals is lost), a delay is created; the signals are rechecked to confirm that the system has a permanent fault rather than a temporary error. If the signals are received, the decisions of the CE and ZO controllers will be evaluated (orange arrows); if both agree, the decision will be made; if not, the ZO's decision will have priority because it has more encrypted communication (a secure channel of communication) signals. If the signals were not received, only the peer signal would be evaluated; if it were received, the ZO decision would be made. If not, the CE will be checked; if no signals are received, the decision will be made to use the LO algorithm and send a trip signal to the PD. Fig. 5.58(b) shows the flowchart of each PD fault location controller.

As the grounding connection of the (HV/MV) transformer changes the values of the short circuit current in the grid and modifies the setting of all the PDs in the grid, this method has the advantage of the algorithms operating correctly independent of the grounding connection. The new method would enhance the system's accuracy and efficiency, as well as accelerate the protection system's response to unanticipated grid disturbances.

If the CE controller transmits a trip signal to the PD but receives no response, the CE controller will initiate a post-processing step, as illustrated in Fig. 5.58(c), to disconnect the nearest line to the fault. For example, if a fault occurs at DL4 then PD7 and PD8 should be disconnected; however, if PD7 fails to disconnect, the CE controller will disconnect the closest line to the fault, by activating PD5 and PD6.

The pseudocode of each PD can be described as follows:

(1) Determine DPF, (2) transfer data and communication signals to the CE controller and the other PD on the same line, (3) apply the ZO controller, (4) acquire the CE decision, and (5) verify that all signals from the ZO and CE controllers have been received, (6) if not, make a delay and double-check the availability, (7) If all signals are received, check the ZO and CE controllers' decisions, (8) If the decisions are identical, send a trip signal to the breaker; (9) if otherwise, give the ZO decision higher precedence, (10) check the peer PD signals if none of the signals were received, (11) if the peer PD signals are received, apply the ZO algorithm and make a decision, (12) If not, double-check the CE's decision. (13) Send the trip signal to the breaker if it is received, (14) if neither CE nor ZO decisions are received, implement LO algorithm to send a disconnection signal, (15) if the trip signal did not activate, disconnect the nearest line to the fault.

In order to give the reader an easy way to follow and understand the behaviour of the protection algorithms (CE, ZO, and LO), as an example, the behaviour of the algorithms will be presented when a three-phase fault at DL3 has occurred for the grid shown in Fig. 5.59(a) with YNd11 transformer connection grounded through a zigzag transformer. DPF will be different in PD5 and PD6; however, DPF will be the same at both ends of DL for the rest of PDs. Therefore, CE can decide the appropriate trip signal using the received data (DPF, and i^{+}) of all the PDs in the grid. In this example, the CE makes the decision to trip PD5 and PD6, as shown in Fig. 5.59(c).

At the same time, the ZO at each PD will receive the data from the other PD at the same line, as shown in Fig. 5.59(b), so ZO at PD5 and PD6 will recognize the fault, and give a decision. However, the ZO of the other PD will be noticed that the fault is in another line. For example, the ZO decision of PD3 and PD4 has a value of two that indicates the fault is downstream DL2, and the ZO decision of PD7 and PD8 is equal to three, indicating the fault is upstream DL4. The decision of CE and ZO is compared, then according to the priority algorithm, the decision at each PD is executed, as shown in Fig. 5.59(d).

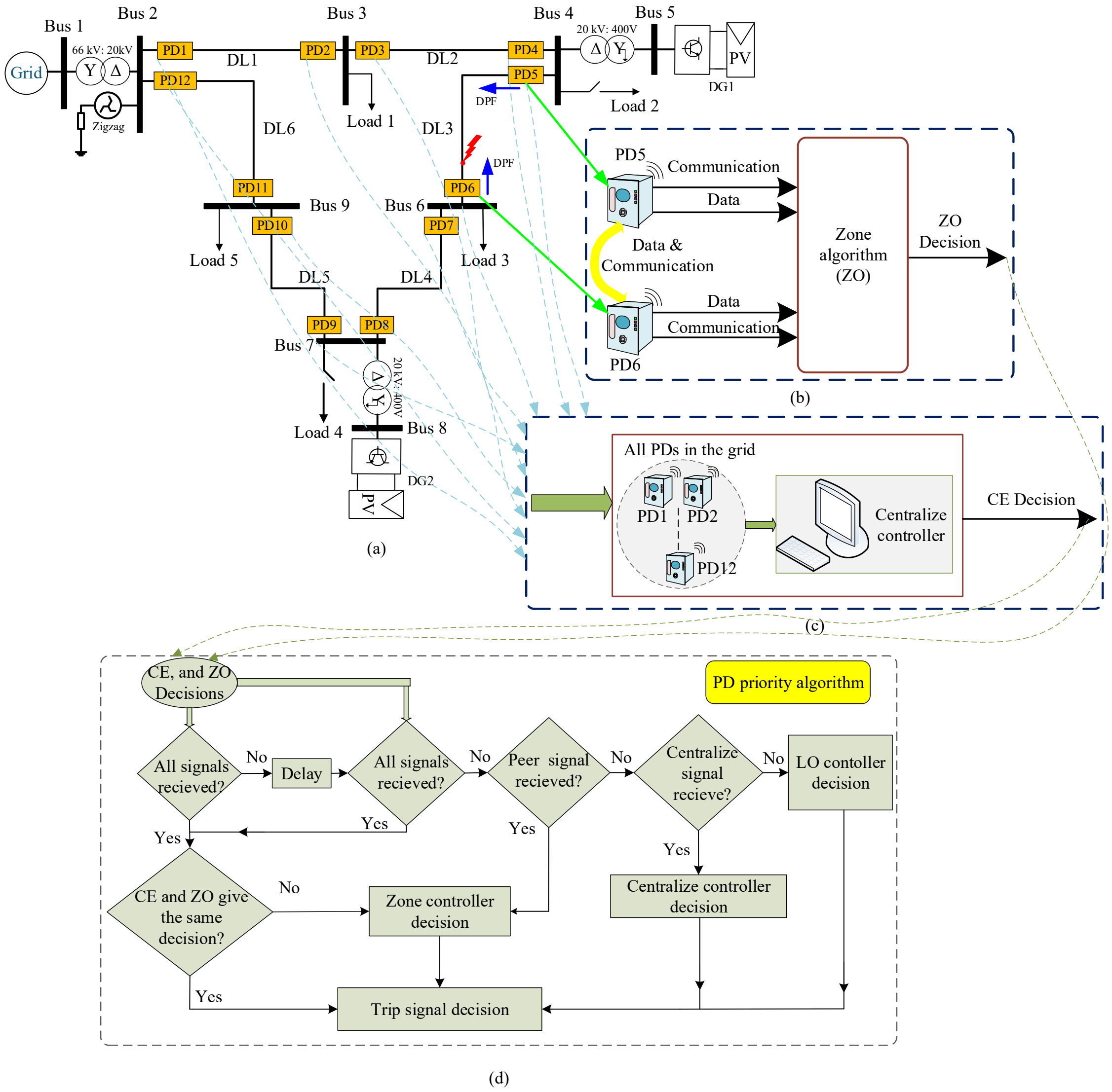
Bus 1
Bus 2
Bus 3
Bus 4
Bus 5
Grid
66 kV: 20kV
Y
Δ
Zigzag
PD1
PD2
PD3
PD4
PD5
PD6
PD7
PD8
PD9
PD10
PD11
PD12
DL1
DL2
DL3
DL4
DL5
DL6
20 kV: 400V
PV
DG1
Load 1
Load 2
Load 3
Load 4
Load 5
DPF
Bus 9
Bus 6
Bus 7
Bus 8
20 kV: 400V
DG2
PV
(a)
PD5
Communication
Data
Data &
Communication
Data
Communication
PD6
Zone
algorithm
(ZO)
ZO
Decision
(b)
All PDs in the grid
PD1
PD2
PD12
Centralize
controller
CE Decision
(c)
CE, and ZO
Decisions
PD priority algorithm
All signals
recieved?
No
Delay
All signals
recieved?
No
Peer signal
recieved?
No
Centralize
signal
recieve?
No
LO contoller
decision
Yes
Yes
Yes
Yes
CE and ZO give
the same
decision?
No
Zone controller
decision
Centralize controller
decision
Yes
Trip signal decision
(d)

Fig. 5.59 Concept diagram of (a) analysed ring grid with a three-phase fault at DL3, (b) ZO algorithm, (c) CE algorithm, and (d) PD priority algorithm

If CE-ZO fails to recognize the fault due to communication problems, the LO will be executed. In this example, as the fault is symmetrical and the grid is connected with YNd11 transformer connection grounded through a zigzag transformer, the v^+ will be used, so the minimum v^+ means faster disconnection In this case, v^+ at PD6 will be the minimum value (585 V), as shown in Fig. 5.60(a), and the trip time according to the Definite-Time curve is 0.4 s. So both of them are disconnected, then the recloser algorithm will be executed, as shown in Fig. 5.60(b). First, PD6 is reconnected, and as it can recognize the fault it will trip again, and after a delay, PD7 will be reconnected. The same idea is used after the first disconnection of PD6 at the other end of DL3 between PD4 and PD5, as its v^+ is the minimum value in this case (2260 V), and the trip time in this case according to the Definite-Time curve is 0.1 s, then PD5 will trip.

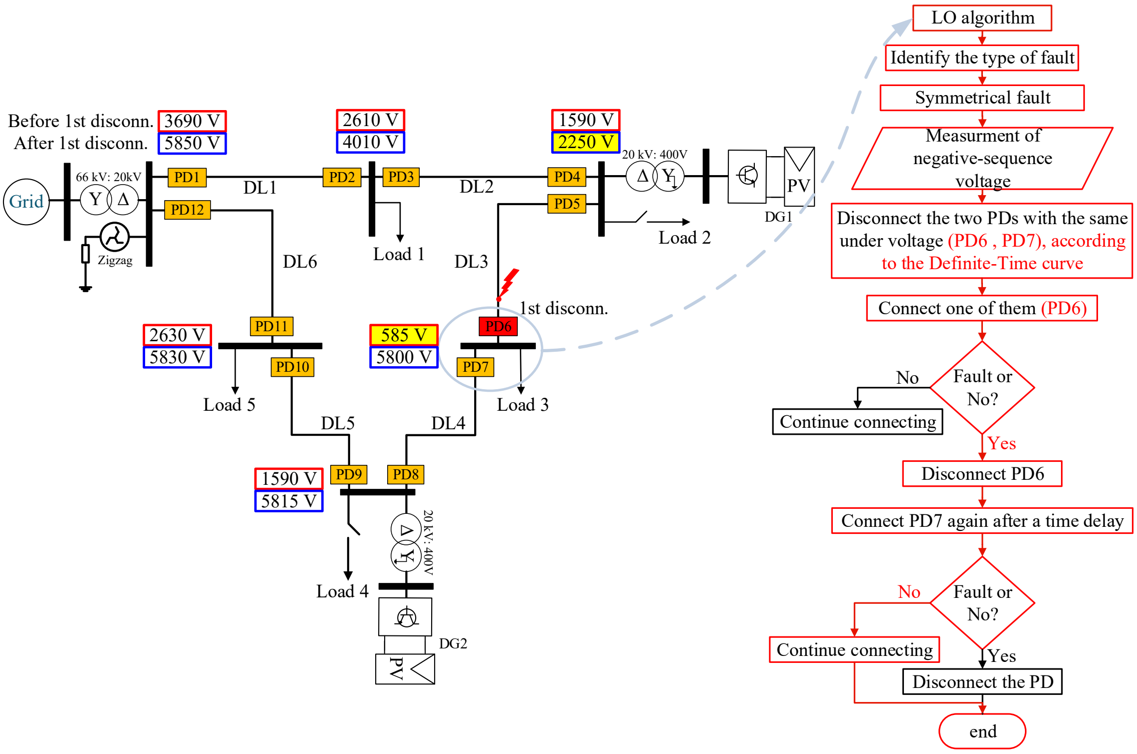
Before 1st disconn.
After 1st disconn.
3690 V
5850 V
2610 V
4010 V
1590 V
2250 V
Grid
66 kV: 20kV
Y
Δ
Zigzag
PD1
PD12
DL1
PD2
PD3
DL2
PD4
PD5
20 kV: 400V
PV
DG1
Load 1
Load 2
DL6
DL3
1st disconn.
2630 V
5830 V
PD11
PD10
585 V
5800 V
PD6
PD7
Load 5
Load 3
DL5
DL4
1590 V
5815 V
PD9
PD8
20 kV: 400V
Load 4
DG2
PV
LO algorithm
Identify the type of fault
Symmetrical fault
Measurment of negative-sequence voltage
Disconnect the two PDs with the same under voltage (PD6 , PD7), according to the Definite-Time curve
Connect one of them (PD6)
Fault or No?
No
Continue connecting
Yes
Disconnect PD6
Connect PD7 again after a time delay
Fault or No?
No
Continue connecting
Yes
Disconnect the PD
end

(a) (b)

Fig. 5.60 Analysed ring grid when a three-phase fault at DL3 and LO algorithm with YNd11 transformer connection grounded through a zigzag transformer

In order to analyze the proposed protection scheme, various cases have been studied, including different grid behaviour. In addition, a comparative study has been implemented to emphasize the functionality and reliability of the protection algorithm. Therefore, the next chapter presents some of the simulated tested cases to fulfill this aim.

6 Analysis and test results of the proposed protection algorithms

In this chapter, the analysis of the proposed protection algorithms (CE, ZO, and LO) in different scenarios are presented. Moreover, to show the dependability of the protection algorithms, a comparative study will be illustrated. The simulated results shown in this chapter are some examples of the whole of cases used to test the proposed algorithms with the grid in different operating conditions. the total number of simulated cases are approximately two hundred fifty cases. Some of these cases (forty-five cases) have been chosen to be represented in this chapter in order to show the functionality of the protection algorithms in different scenarios as changing the number of DG connected to the grid, DG penetration, fault location, fault type, fault resistance, strong and weak grids, and load consumption, changing grid configuration. The majority of the results are shown in Appendix B.

The response of the VSI control was implemented under grid faults combining the LVRT capabilities and the requirements of the Spanish grid code. VSI control is not discussed in this chapter, as it was explained in chapter 4 and Appendix E.

6.1. Analytical and test results for CE, ZO, and LO protection algorithms

In this section, the analysis of the protection algorithms test results obtained using MATLAB$^{\text{TM}}$ 2015b SIMULINK is presented. The studied ring grid is shown in Fig. 6.1, with DGs connected at buses 5, 8, and 10. This grid is chosen to be represented in this chapter as it guarantees different grid configurations. Other grid configurations can be seen in Appendix B. The proposed protection algorithms can be effectively treated with different grid structures and the number of buses, as will be discussed in this chapter.

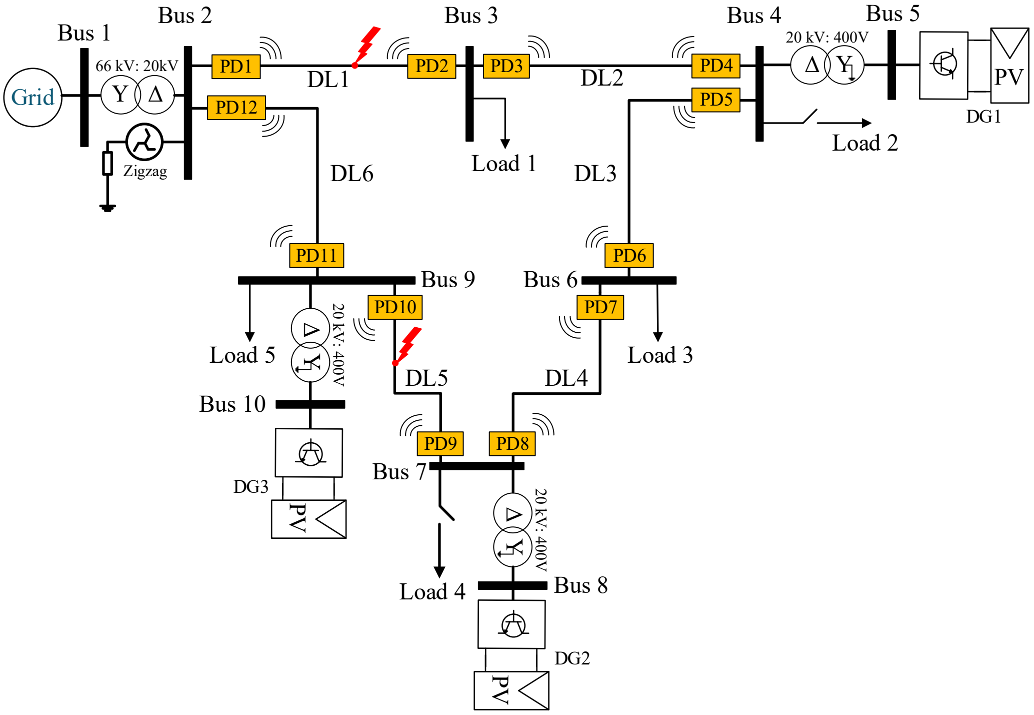

Fig. 6.1 Single line diagram of the analysed ring system with DG penetration

The PDs must be capable of holding a high current value for a specified time interval, depending on the protection algorithms, and the type of the relay [30]. For 95 % of the tested cases, PDs based on ANN provided low response times between 10 ms and 20 ms, and for the rest of the cases the response times are ≤ 25 ms, this time interval is based on the measurement devices and the speed of DPF.

The algorithms were tested by modifying the load consumption, DG penetration, fault location, fault type, fault resistance, and (HV/MV) transformer configuration on the studied grid in the ring and radial configurations (Appendix B). Some of the instances utilized to validate the protection algorithms are shown in Table 6.1. In every tested situation, the protection algorithms can identify the specific location of the fault.

Table 6.1 Some of the scenarios used to test the protection algorithms

Fault type	**Fault resistance (Ω)**	**Fault location**	**Load consumption (MVA)**					**DG penetration (MVA)**		
			***L*1**	***L*2**	***L*3**	***L*4**	***L*5**	**DG1**	**DG2**	**DG3**
Single-phase to ground	0.1	DL1	5	2	8	1	4	6	0	0
Two-phase to ground	2.5	DL2	5	2	8	4	4	5	5	0
Two-phase	1	DL4	1	2	8	1	0.5	5	3	0
Three-phase	4	DL6	5	4	8	1	4	6	5	6
Two-phase to ground	0.1	DL3	1	2	8	1	4	5	5	0
Three-phase	0.1	DL3	5	2	8	1	4	5	5	0

6.1.1. CE-ZO protection algorithms

The behaviour of CE-ZO algorithm is tested in different scenarios to demonstrate the functionality of the protection scheme. Fig. 6.2 shows the flowchart of the tested cases presented in this chapter.

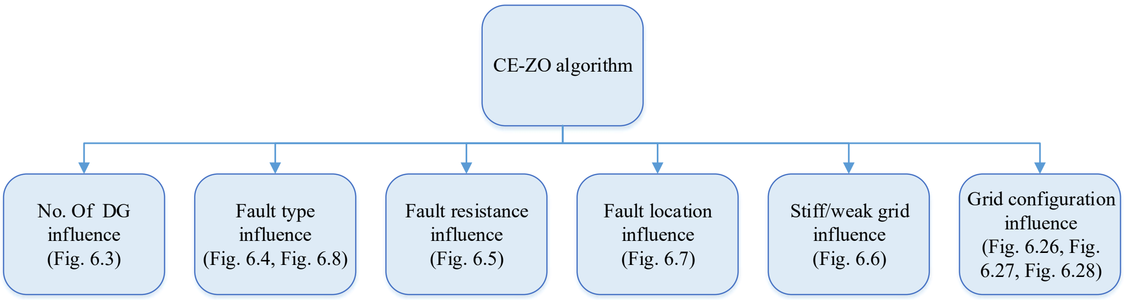
CE-ZO algorithm
No. Of DG influence (Fig. 6.3)
Fault type influence (Fig. 6.4, Fig. 6.8)
Fault resistance influence (Fig. 6.5)
Fault location influence (Fig. 6.7)
Stiff/weak grid influence (Fig. 6.6)
Grid configuration influence (Fig. 6.26, Fig. 6.27, Fig. 6.28)

Fig. 6.2 Flowchart of the studied cases

As an example of the acquired results, Fig. 6.3 depicts the behaviour of CE and ZO algorithms in two scenarios to demonstrate their performance. Fig. 6.3(a) illustrates CE and ZO decisions with two DGs during a three-phase fault in DL3, and Fig. 6.3(b) presents the results of both algorithms without DG. To demonstrate the values of the short-circuit current in different scenarios and the behaviour of the protection algorithms in these cases, the *abc* voltages, *abc* currents, DPF, CE decision, ZO decision, and trip signal have been displayed in Fig. 6.3.

As seen in Fig. 6.1, during a three-phase to ground fault in DL3, all phase voltages dropped, (*abc* voltages of PD5 and PD6 in Fig. 6.3(a)). Furthermore, due to the DG penetration into the fault, the values for three-phase currents rise to around 6.1 pu (PD5 currents in Fig. 6.3(a)). However, for the same type of fault without DG penetration (PD5 and PD6 in Fig. 6.3(b)), as the faulted current is supplied exclusively from the main grid, the short-circuit currents are less than 6.1 pu (approximately 4.8 pu). Also, the DPF varies in some PDs when a fault occurs. For example, in the case of a three-phase fault in DL3, the DPF for each phase will vary. The DPFs of the two PDs in DL3 are different during the fault; therefore, the DPF of PD6 changes from 1 to 0, but the DPF of PD5 does not chage (Fig. 6.3). Regarding the DPF of the other PDs, there is no difference in the DPF of the PDs located at the other lines. CE decision correlates to the faulty line number, with 0 indicating no-fault, and 1 to 6 indicating the faulted line number. When there is a fault in DL3, CE's decision is 3, which relates to the faulty line number. The ZO decision, on the other hand, corresponds to the PD in the faulty line. For example, when the fault occurs in DL3, only the ZO decision signals of PD5 and PD6 are triggered, and the other PDs will not trip, as there are no differences in the DPF. A trip signal is sent to PD5 and PD6, since both algorithms (CE and

ZO) can identify the fault (Fig. 6.3). According to [27], in order to not disconnect the line if the fault is temporary, a delay is performed before executing the trip signal to ensure that the fault is permanent, then the trip signal decision is performed after approximately 5 cycles.

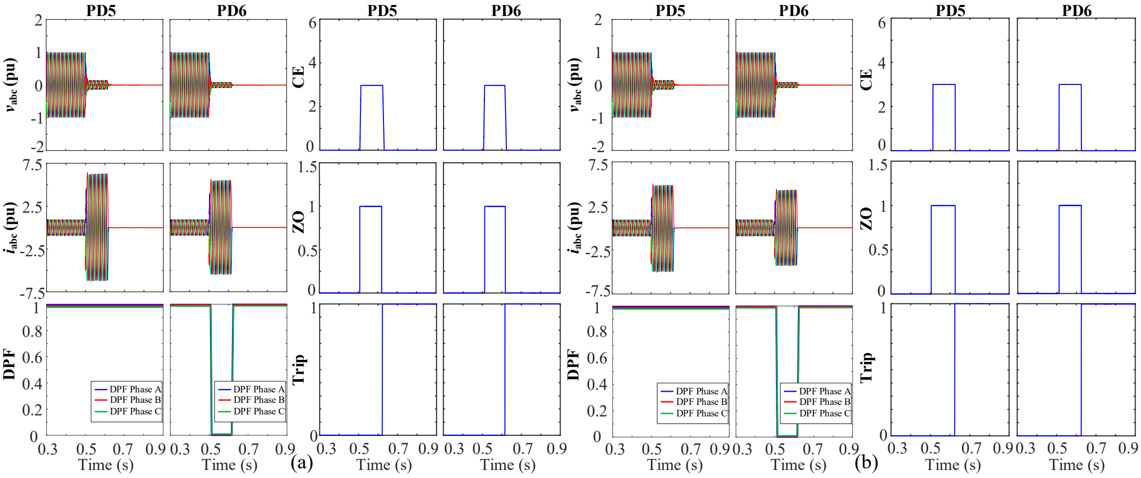

Fig. 6.3 CE and ZO behaviour during a three-phase fault in DL3 with fault resistance r = 0.1 Ω, (a) with two DGs, (b) without DG

Fig. 6.4 shows the DPF, CE, ZO decisions, and trip signals for the studied ring grid shown in Fig. 6.1, during symmetrical and unsymmetrical faults in DL3 and DL4, respectively. The figure represents the patterns of each signal for the 12 PDs in the grid in a 3-D preview. As seen in Fig. 6.4, the x-axis indicates the time in seconds, the y-axis represents the 12 PDs in the grid or represents the CE control device in the case of CE, and the z-axis represents the analysed signal (DPF, CE decision, ZO decision, and trip). For example, only PD5 and PD6 will have different DPFs during a symmetrical fault in DL3. In addition, if the fault is in DL4, only PD7 and PD8 will have a different DPF. The CE decision corresponds to the number of the faulty line; in the case of a fault at DL3 the value is 3, while the ZO decision signals of PD5 and PD6 are 1, as the remainder of the PDs will not trip. Besides, when a fault occurs in DL4, the CE decision is 4, and the ZO decision signals for PD7 and PD8 are 1. A post-processing step is performed to address the trip signal transmitted to the corresponding breaker in the faulty line based on the availability of both decision signals in each PD.

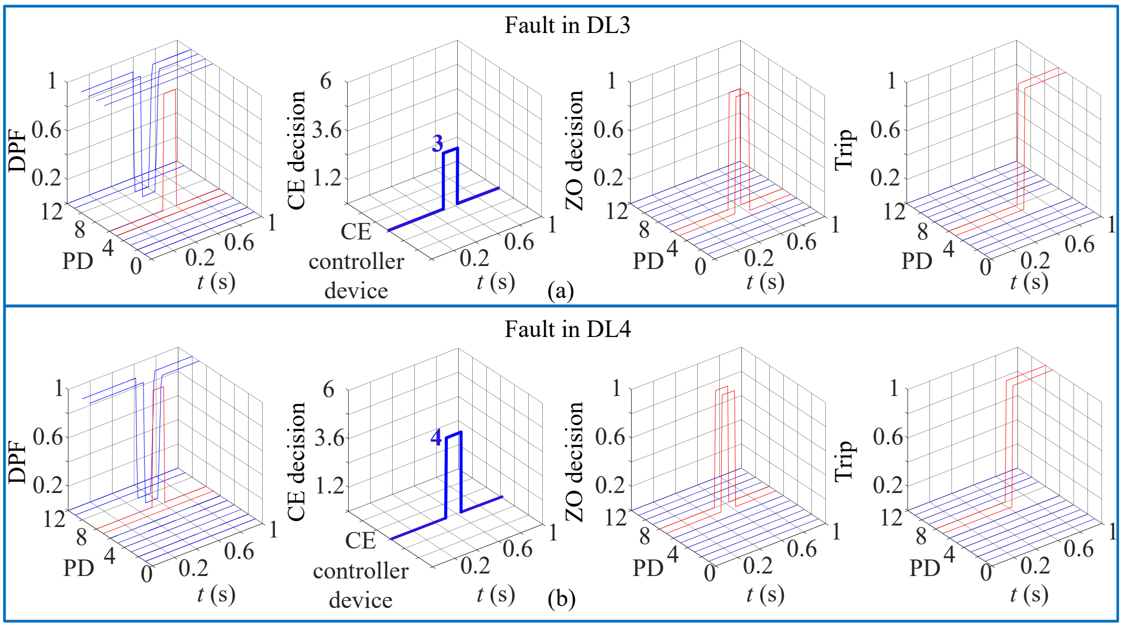

Fig. 6.4 Ring grid with two DGs during (a) three-phase fault in DL3, (b) single-phase fault in DL4

In the case of single-phase faults, the variations in short-circuit currents are not substantial due to the zigzag connection, as shown in Table 6.2, which limits the short-circuit currents. However, for two-phase to ground fault, due to the different paths of the fault current, the values are dramatically changed. As illustrated in Table 6.2, when a single-phase to ground fault is occurring at DL3, the values of the short-circuit current measured at PD5 and PD6 are not substantial; however, when a two-phase to ground fault is occurring at DL5 the short-circuit current values at PD9 and PD10 are different. Also, for the rest of the lines, the short-circuit currents are the same at both ends of each line (Table 6.2).

Table 6.2 Single-phase to ground, and two-phase to ground short-circuit currents, when loads consumption are: (L1 = 5, L2 =2, L3 = 1, L4 = 1, L5 = 4) MVA, and with fault resistance r = 0.1 Ω

Fault type	**Fault location**	**DG penetration (MVA)**			**DL1 (pu)**	**DL2 (pu)**	**DL3 (both ends) (pu)**	**DL4 (pu)**	**DL5 (both ends) (pu)**	**DL6 (pu)**
		DG 1	**DG 2**	**DG 3**						
Single-phase to ground	DL3	3	1.5	3	i^+=0.4, i^-=0.2, i^0=0.23	i^+=0.2, i^-=0.22, i^0=0.23	i^+_5=0.22, i^-_5=0.23, i^0_5=0.23. i^+_6=0.12, i^-_6=0.12, i^0_6=0.12	i^+=0.15, i^-=0.11, i^0=0.12	i^+=0.14, i^-=0.11, i^0=0.12	i^+=0.2, i^-=0.1, i^0=0.12
Two-phase to ground	DL5	3	1.5	3	i^+=1.97 ,i^-=1.8, i^0=0.06	i^+=1.8, i^-=1.8, i^0=0.06	i^+=1.96, i^-=1.91, i^0=0.06	i^+=1.93, i^-=1.9, i^0=0.06	i^+_9=2, i_9^-=1.97, i^0_9=0.06. i^+_{10}=3.9, i^-_{10}=3.82, i^0_{10}=0.12	i^+=3.9, i^-=3.7, i^0=0.12

The sub-index 5, 6, 9, and 10 correspond to the number of the PD.

As shown in Fig. 6.5(a) and Fig. 6.5(b), the protection scheme has been evaluated for various fault resistances changed from 6 Ω to 0.05 Ω, respectively, in order to test the protection scheme with very small and high fault resistance, the calculation of the fault resistance is shown in Appendix G. As shown, the decision is not affected in both cases. Also, the behaviour of the protection algorithms has been tested for stiff and weak grids. Fig. 6.6(a) shows the short-circuit current during two-phase to ground fault at DL3, as well as algorithms decision for the stiff grid. The stiff grid is supposed to be strong enough to impose the voltage and the frequency of the grid without any variation. However, in the case of a weak grid, a frequency or voltage variation from its steady-state value can occur during faults (voltage sags). The three-phase short-circuit power of the stiff grid S_{sc} equals 3600 MVA, and the weak grid equals 100 MVA. It is important to mention that the voltage and the frequency are imposed by the grid, not by the DG.

The same signals are shown in and Fig. 6.6(b) for the weak grid. From the evaluation of the short-circuit currents of both grids, it is evident that the stiff and weak grids have different short-circuit current values. For example, for the stiff grid and during a two-phase fault, the short-circuit current is near 5.6 pu, whereas the weak grid is about 1.2 pu. As shown in Fig. 6.6, the DPF criteria' reliability allows the algorithms to detect the faulty part of the grid in both cases.

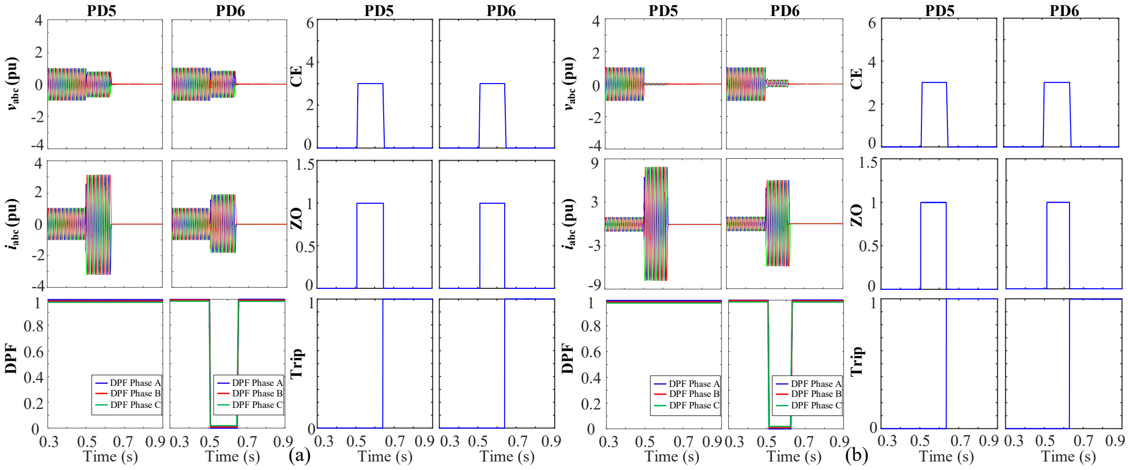

Fig. 6.5 CE and ZO behaviour during different fault resistance, with two DGs during a three-phase fault in DL3 (a) $r = 2\ \Omega$, (b) $r = 0.05\ \Omega$

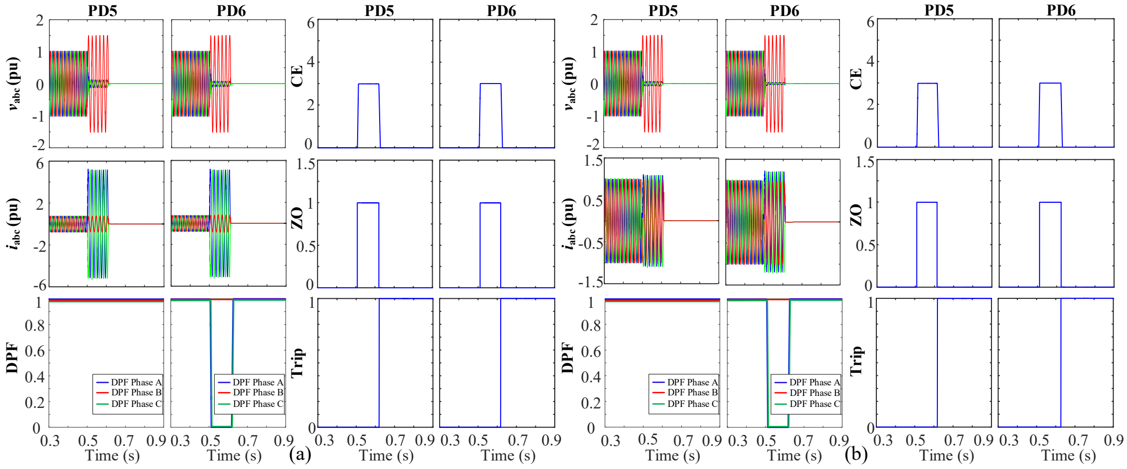

Fig. 6.6 CE and ZO behaviour during two-phase to ground fault in DL3, and $r = 0.1\ \Omega$, with two DGs, in case of (a) stiff grid, (b) weak grid

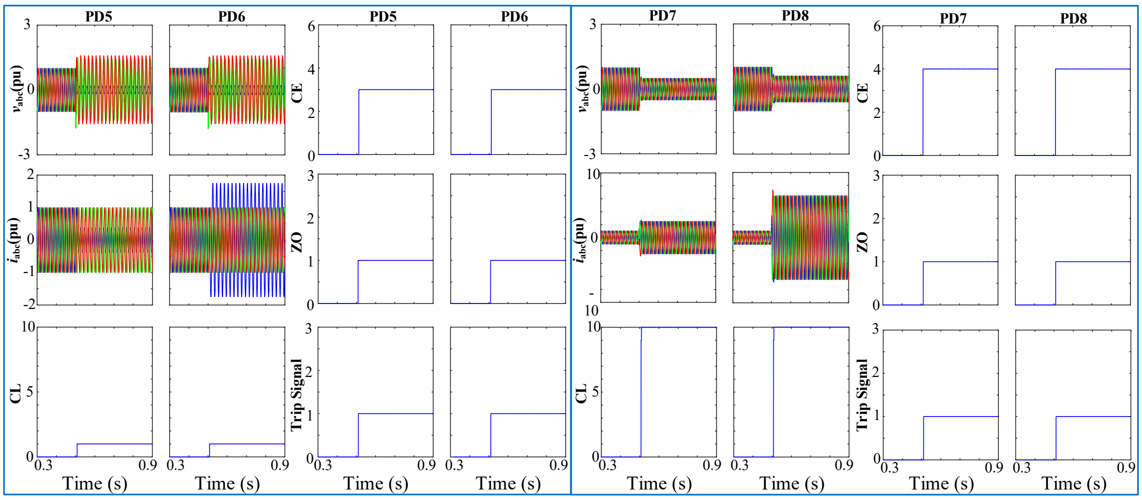

(a) (b)

Fig. 6.7 The analysed ring grid with 2 DG connected at buses 3 and 7 for CE-ZO algorithm, in case of (a) single-phase to ground fault at DL3, and (b) three-phase fault at DL4

Fig. 6.7 shows the CE-ZO algorithm with DG penetration when the fault at DL3, and DL4. The figure illustrates the behaviour of the fault location algorithms as seen in the first and second column of the third row; and the location algorithms as seen in the third and fourth column of the first row for CE, and the third and fourth column of the second row for ZO, for each figure. Also, the trip signal in both cases is shown in the last row of the figure. In the case of single-phase and three-phase faults, the fault classification algorithm (CL) gives 1 that is corresponds to a single-phase fault, and 10 that corresponds to a three-phase fault, respectively, as explained in chapter 5. In addition, when the fault is at DL3, the CE gives an output that corresponds to the location of the faulted line that equals 3; besides, when the fault is at DL4 the CE output will be 4. In the case of ZO, the output of each PD corresponds to the fault. Before the fault, the ZO output is 0, and during the fault, the ZO output is 1. Therefore, when there is a fault in DL3, PD5 and PD6 are tripped, and PD7 and PD8 are tripped if the fault occurs in DL4.

Fig. 6.9 shows the behaviour of the system during symmetrical faults at DL4. The figure shows the *abc* voltages, currents, DPF, fault Classification ANN (CL), and centralized ANN (CE) of all the relays in the grid. As shown in the figure, all the relays will be able to identify the type of fault correctly by using the fault classifier ANN, then the fault location algorithm can locate the fault, and if the fault is permanent to disconnect the faulted part of the network. As shown, for the breakers in the faulted line (DL4), the DPF is changed at one end of the faulted line from (1 → 0), which means the fault is at this line.

6.1.2. LO protection algorithm

The behaviour of the LO algorithm is tested in different scenarios to demonstrate the functionality of the protection scheme. Fig. 6.8 shows the flowchart of the tested cases presented in this chapter.

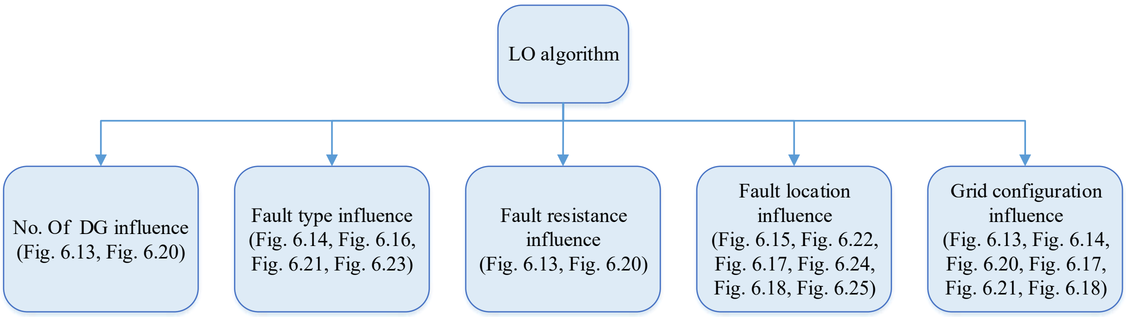
LO algorithm
No. Of DG influence (Fig. 6.13, Fig. 6.20)
Fault type influence (Fig. 6.14, Fig. 6.16, Fig. 6.21, Fig. 6.23)
Fault resistance influence (Fig. 6.13, Fig. 6.20)
Fault location influence (Fig. 6.15, Fig. 6.22, Fig. 6.17, Fig. 6.24, Fig. 6.18, Fig. 6.25)
Grid configuration influence (Fig. 6.13, Fig. 6.14, Fig. 6.20, Fig. 6.17, Fig. 6.21, Fig. 6.18)

Fig. 6.8 Flowchart of the studied cases

The idea is based on using only the data of each PD to identify the type and the location of the fault. Therefore, each relay should know that the fault is at its line or another line without knowing any information about the other relays. The data used for each relay is the sequence voltage or current of each relay, as shown in Fig. 6.10. For each type of fault, a different algorithm is implemented, as explained in chapter 5. The algorithm has been tested in different cases.

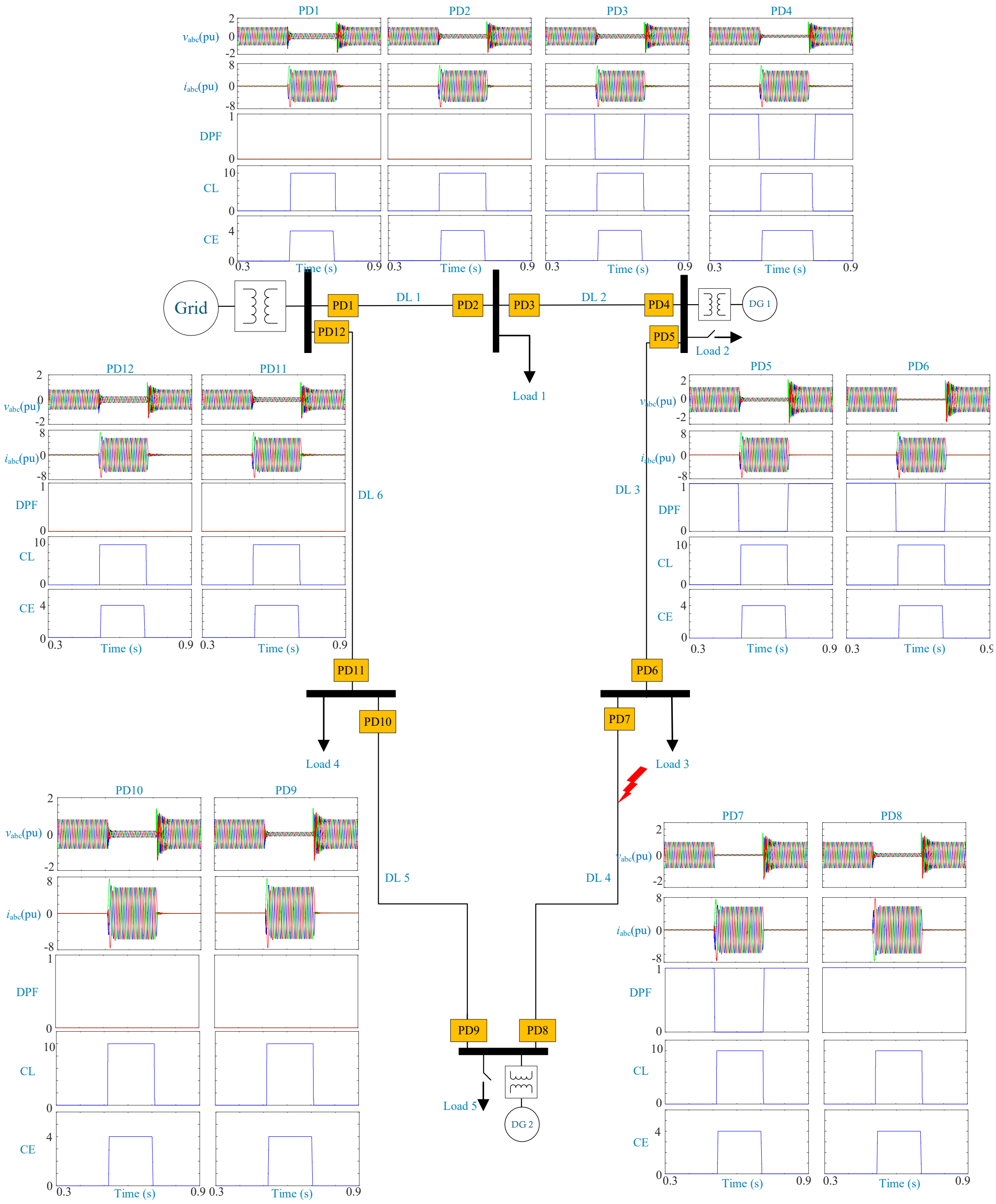

Fig. 6.9 System behaviour during symmetrical fault at DL4 with CE-ZO with $r = 0.1\ \Omega$

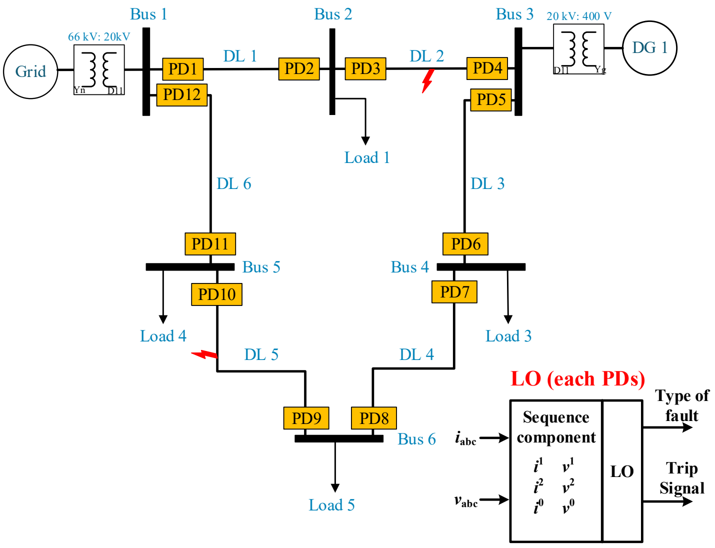
Bus 1
Bus 2
Bus 3
66 kV: 20kV
20 kV: 400 V
Grid
Yn
D11
DG 1
D11
Yg
PD1
DL 1
PD2
PD3
DL 2
PD4
PD12
PD5
Load 1
DL 6
DL 3
PD11
PD6
Bus 5
Bus 4
PD10
PD7
Load 4
Load 3
DL 5
DL 4
LO (each PDs)
PD9
PD8
Bus 6
Load 5
Sequence component
i_{abc}
v_{abc}
i^1 v^1
i^2 v^2
i^0 v^0
LO
Type of fault
Trip Signal

Fig. 6.10 LO scheme

The disconnection of the first and second PDs is based on the magnitude of the definite-time curve. Depending on the type of fault, the definite-time curve can correspond to positive sequence voltages (for symmetrical faults) or negative sequence voltages (for unsymmetrical faults), as explained in chapter 5, as shown in Fig. 6.11. As shown in Table 6.3, the disconnection is done in two steps, when a single-phase fault occurs at DL2, PD3 trip first, then PD4 will trip to disconnect DL2, where 0 and 1 correspond to close and open (trip) of the PD.

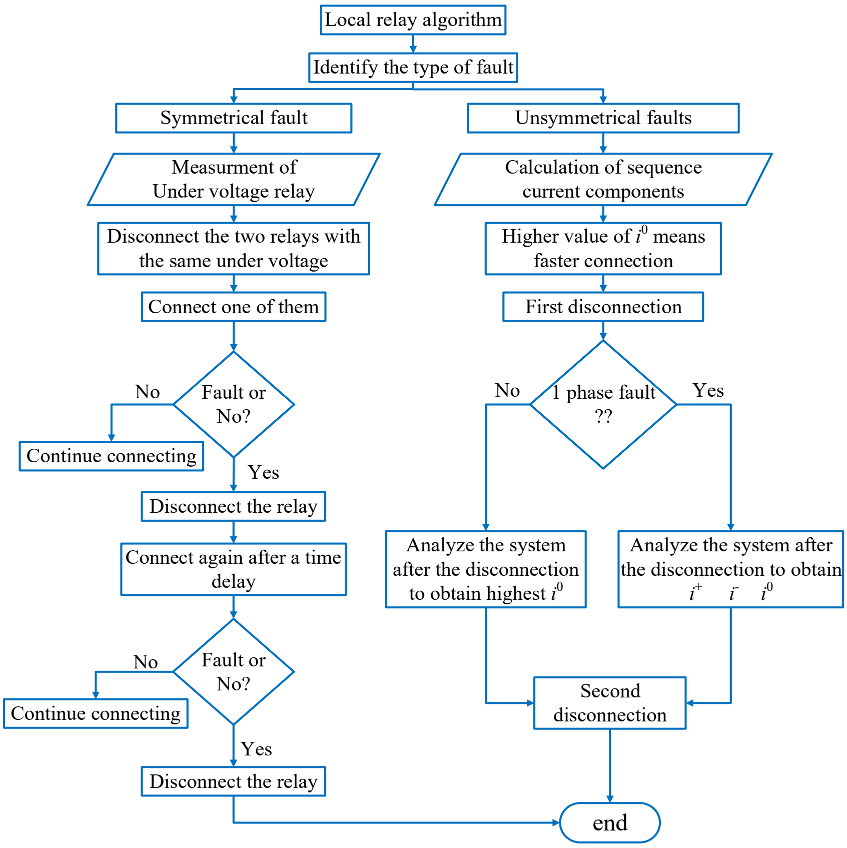
Local relay algorithm
Identify the type of fault
Symmetrical fault
Unsymmetrical faults
Measurment of Under voltage relay
Calculation of sequence current components
Disconnect the two relays with the same under voltage
Higher value of i^0 means faster connection
Connect one of them
First disconnection
No
Fault or No?
Continue connecting
Yes
No
1 phase fault ??
Yes
Disconnect the relay
Connect again after a time delay
Analyze the system after the disconnection to obtain highest i^0
Analyze the system after the disconnection to obtain i^+ i^- i^0
No
Fault or No?
Continue connecting
Second disconnection
Yes
Disconnect the relay
end

Fig. 6.11 Flowchart of the LO proposed protection algorithm

Table 6.3 Disconnections in case of single-phase fault at DL2

Fault		Direction Relays											
		PD1	PD2	PD3	PD4	PD5	PD6	PD7	PD8	PD9	PD10	PD11	PD12
DL2	1st Disconn.	0	0	1	0	0	0	0	0	0	0	0	0
	2nd Disconn.	0	0	1	1	0	0	0	0	0	0	0	0

Different types of fault at different locations are tested to verify the proposed LO protection algorithm. Fig. 6.13, Fig. 6.14, and Fig. 6.15 show the *abc* voltages, *abc* currents, and trip signals for the ring grid shown in Fig. 6.1, with symmetrical and unsymmetrical faults at different locations. In order to analyse the effect of DG penetration on the analysed ring grid, Fig. 6.13 is presented during unsymmetrical faults occurred at DL1 and DL5. Fig. 6.13(a) represents the ring grid in the case of two DGs and a single-phase to ground fault occurred at DL5 at (0.5 s). In this case, both PDs (PD8, PD9) will trip at the same time (0.86 s) (blue arrows in Fig. 6.13(a)), as both of them are exposed to the same negative-sequence voltage (1300 V) that corresponds to (0.36 s) as seen in Fig. 6.12. Then, the recloser algorithm will be applied, in this case, PD9 is closed before PD8, because PD9 is exposed to the fault, and when it closes again it will still have exposed to the fault, and as a consequence PD9 will trip, after that at (0.895 s) (green arrow in Fig. 6.13(a)) PD8 will be connected again and at that time the fault will be cleared so it will remain connected.

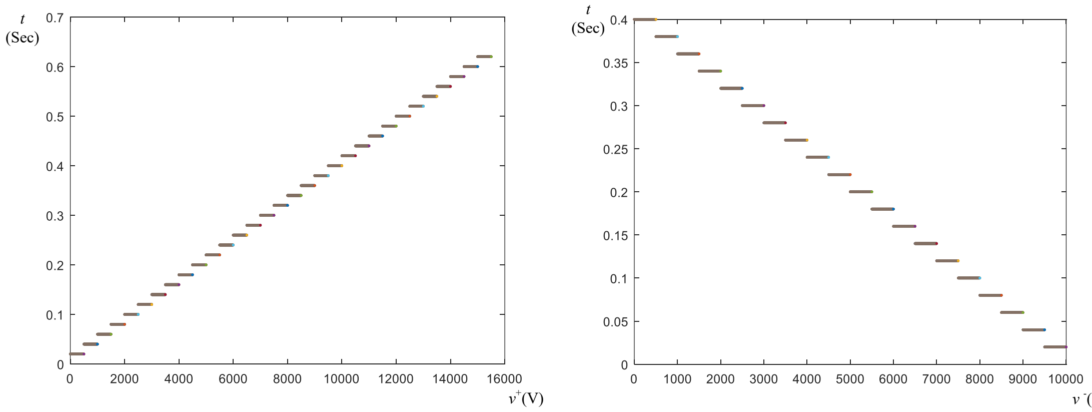

Fig. 6.12 Definite time curve (a) Positive-sequence voltage, (b) Negative-sequence voltage

The same idea is repeated between PD10 and PD11 as both are connected to the same bus, so both will measure the same negative-sequence voltage. Then, using the recloser algorithm, PD10 will be connected first, then trips as it is exposed to the fault, unlike PD11 that will be connected normally after a delay (0.015 s).

Fig. 6.14 is used to demonstrate the functionality of the LO algorithm with DG penetration during symmetrical and unsymmetrical faults. For example, in the case of a three-phase fault, the positive-sequence voltage will be used instead of the negative-sequence voltage, in this case, PD5 and PD4 will trip at (0.62 s) that is corresponds to (14860 V) then PD6 and PD7 will trip at (0.505 s) that is corresponds to (12220 V). After that, the recloser algorithm will be implemented to distinguish between PD5, PD4, and PD6, PD7, in order to disconnect the desired PDs at the faulted DL. Fig. 6.15 shows the behaviour of LO algorithm without DGs during unsymmetrical faults in various locations. The figure shows the operation of the LO algorithm, as the disconnection is faster in the case of a two-phase to ground fault because the short-circuit current is higher than a two-phase fault.

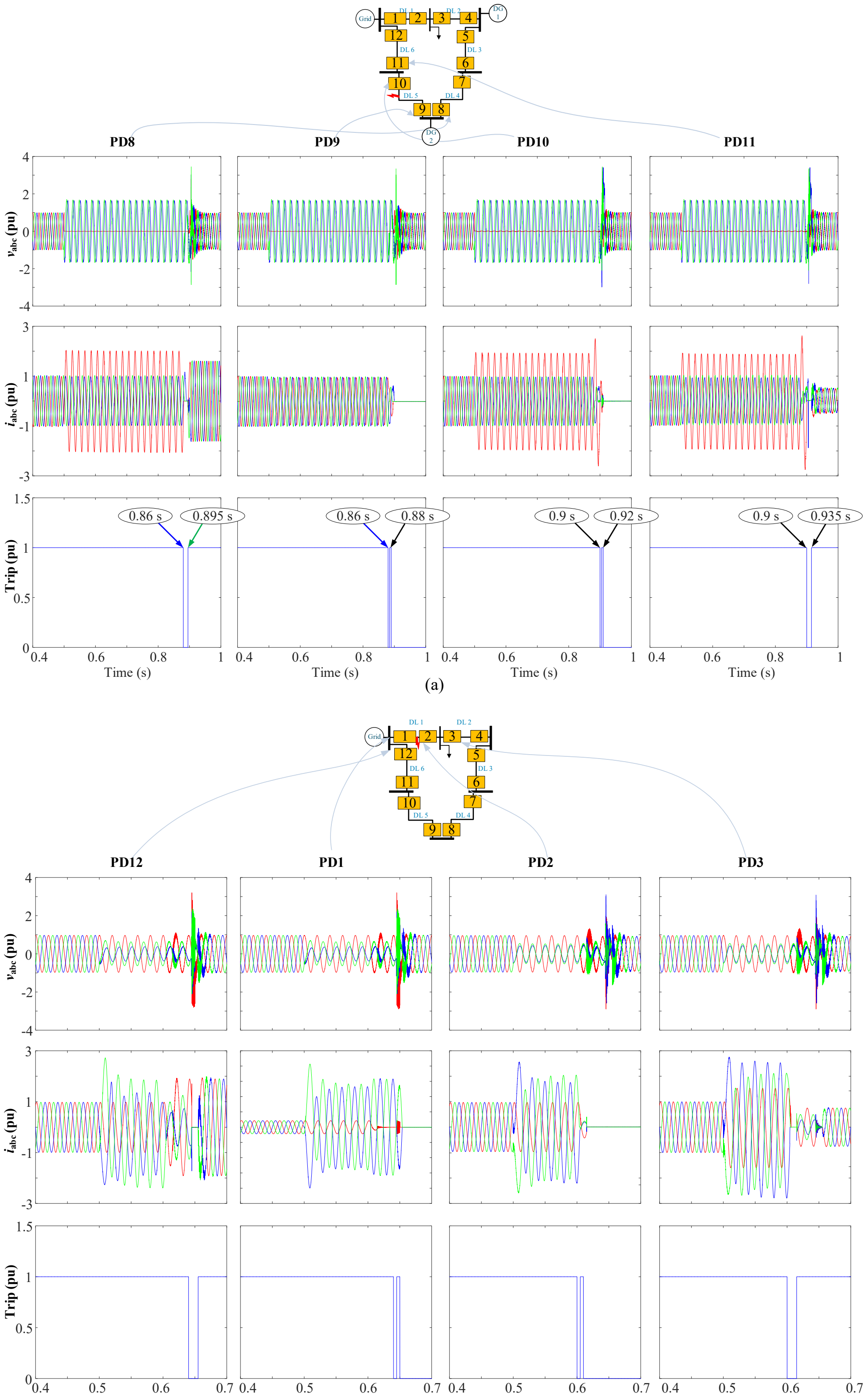

(a)

(b)

Fig. 6.13 *abc* voltages, *abc* currents, and trip signals for LO, with the analysed ring grid (a) with 2 DGs during 1 ph to ground (AG) at DL5, (b) without DG during 2 ph (BC) at DL1

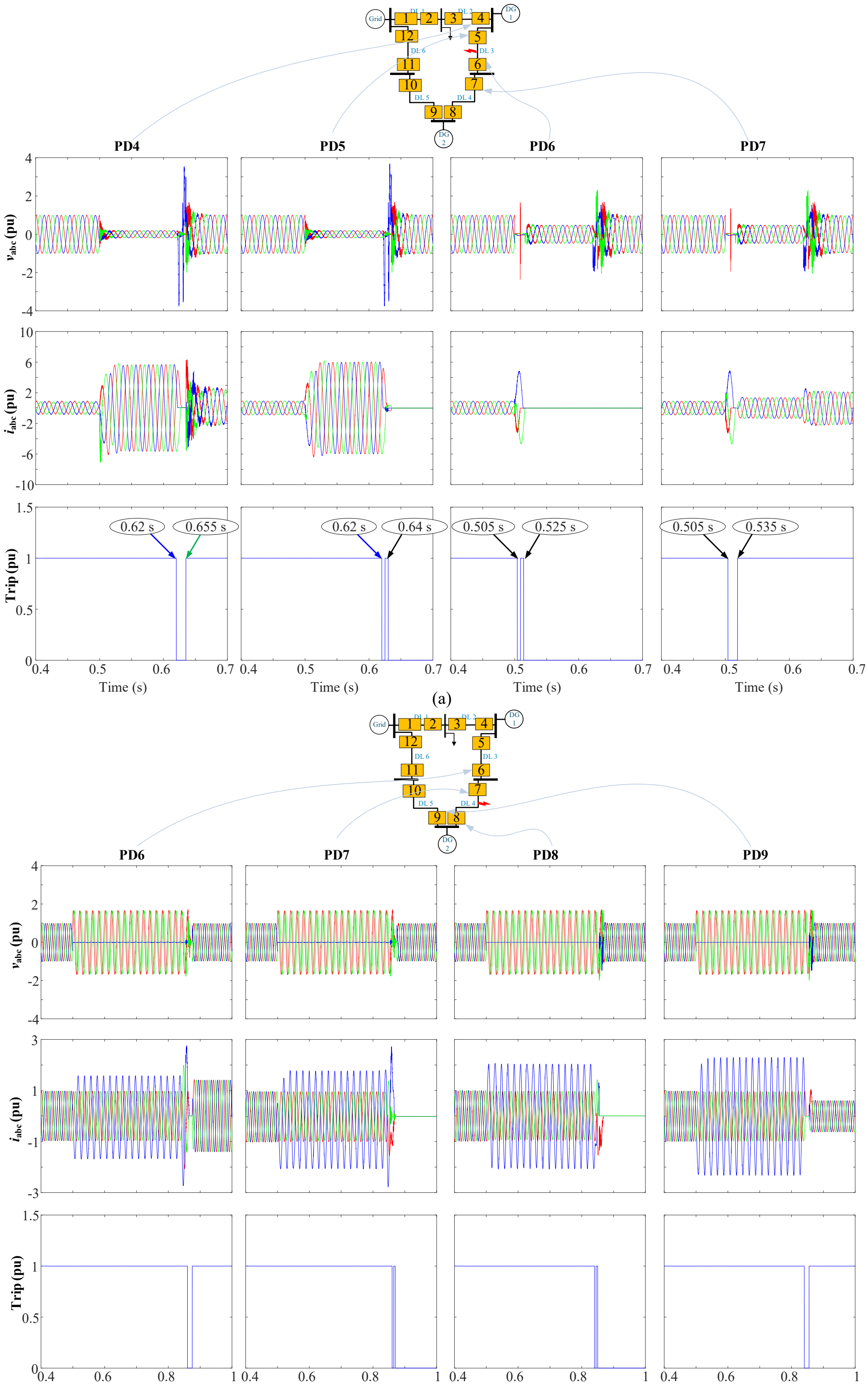

(a)

(b)

Fig. 6.14 *abc* voltages, *abc* currents, and trip signals for LO, with the analysed ring grid (a) with 2 DGs during three-phase fault at DL3, (b) with 2 DGs during single-phase to ground fault (BG) at DL4

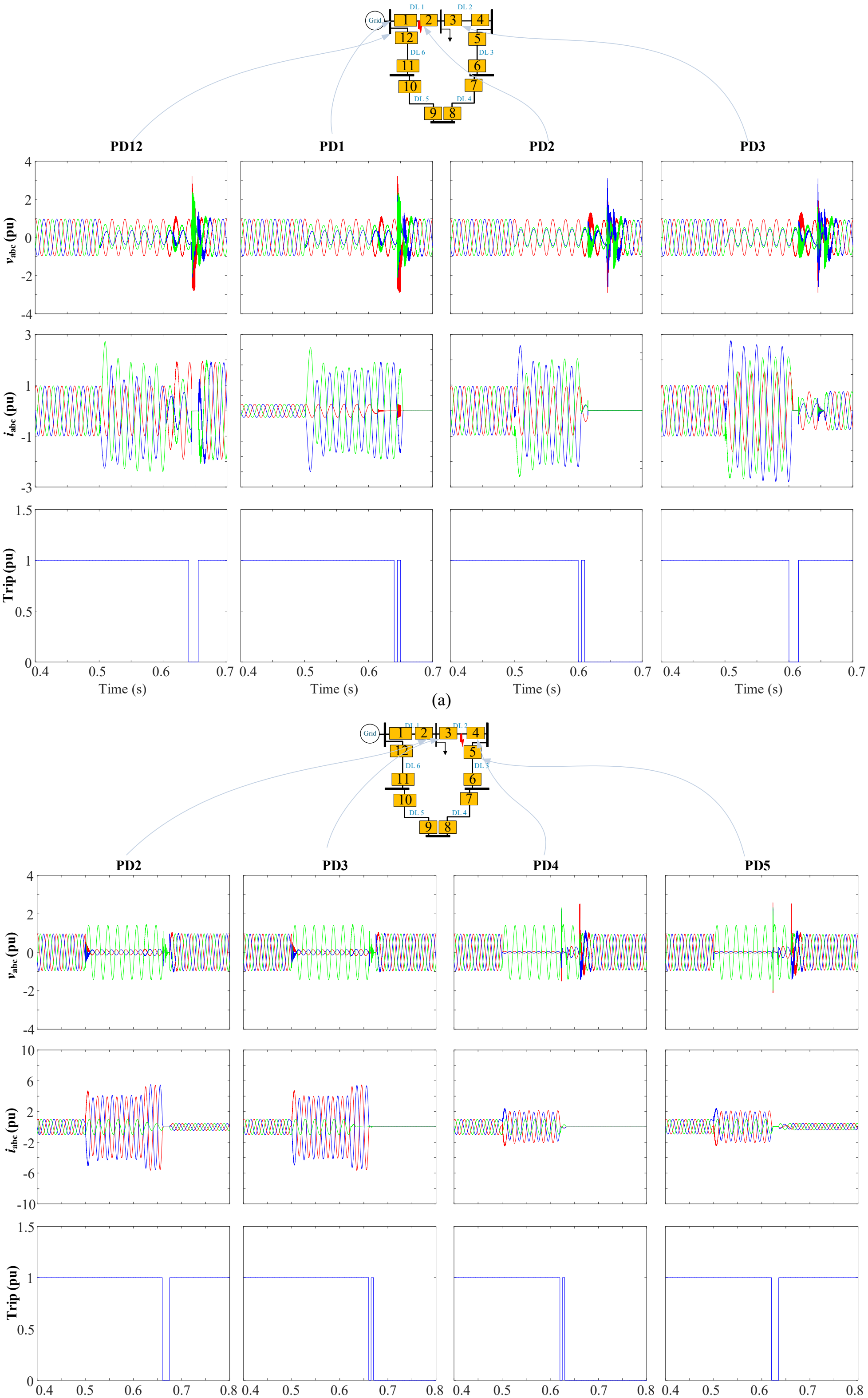

(a)

(b)

Fig. 6.15 *abc* voltages, *abc* currents, and trip signals for LO, with the analysed ring grid (a) without DG during 2 ph (BC) at DL1, (b) without DG during two-phase to ground fault (ABG) at DL2

A more precise interpretation of the LO with the recloser process (seen in Fig. 6.11), could be obtained from Fig. 6.16 and Fig. 6.17, when a symmetrical fault occurs at DL3 and an unsymmetrical faul is at DL4. These figures show the fault and trip signals in all the PDs connected to buses at the end of the faulted line.

As seen in Fig. 6.16(a), the protection algorithm depends on the definite-time curve corresponding to the positive-sequence voltage. The fault signal at PD4 and PD5 is the same because they are connected to the same bus (bus 3). The same happens for PD6 and PD7 connected to bus 4. Fig. 6.16(b) shows the trip signals of the same PDs. It is shown that the two PDs connected to the same bus trip at the same time, in this case, PD6 and PD7 have the first disconnection because they have the same minimum positive-sequence value, and PD4 and PD5 have the second disconnection because the positive-sequence value is higher than for the other two PDs (PD6 and PD7). After that, the recloser algorithm is applied by connecting PD6, which is exposed to the fault, so it trips again. After the disconnection of PD6, PD7 is connected, then PD7 is not exposed to the fault, and it does not trip. The previous conclusion can be obtained from Fig. 6.17, when an unsymmetrical fault occurs at DL4. The only difference is the protection algorithm in this case depends on the negative-sequence voltage.

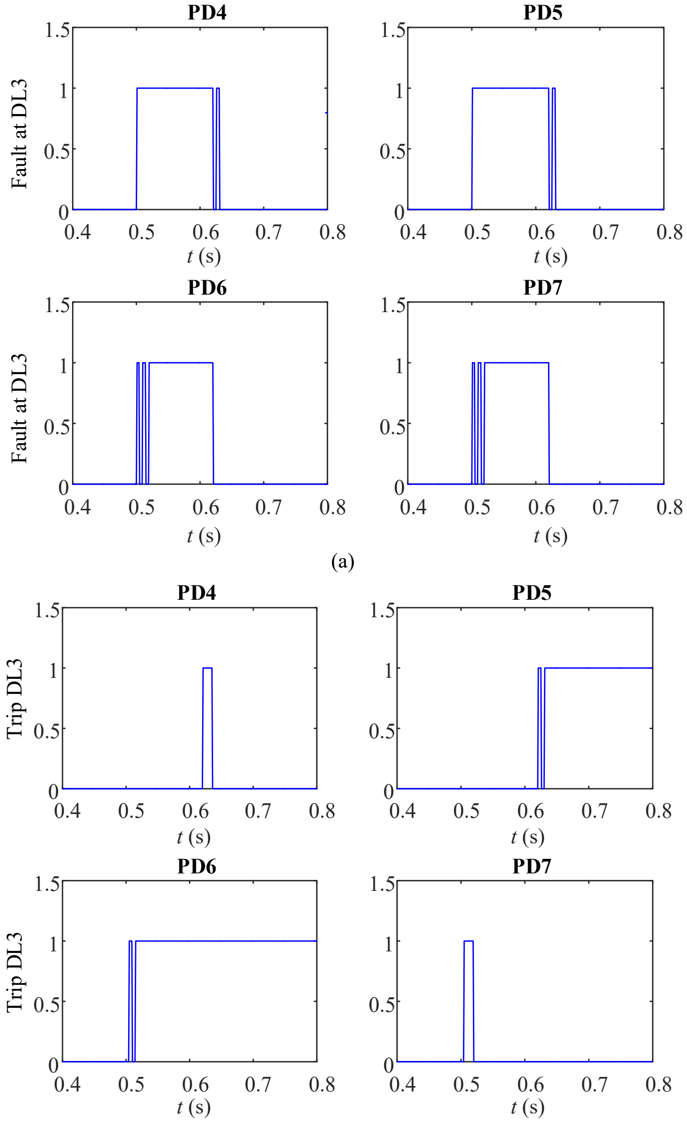

(a)

(b)

Fig. 6.16 Ring grid with 2 DGs during 3 ph (*abc*) at DL3, (a) fault, (b) trip.

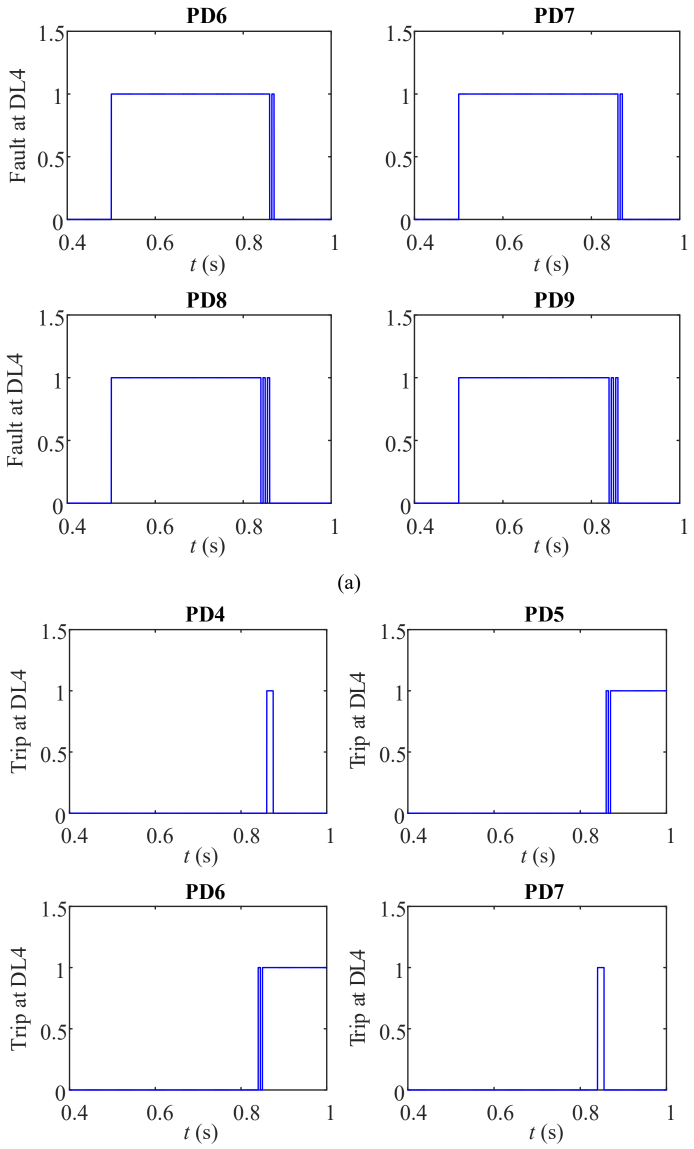

(a)

(b)

Fig. 6.17 Ring grid with 2 DGs during 1 ph (BG) at DL4, (a) fault, (b) trip.

The figures show in 3-D preview the patterns of fault and trip signals during symmeyrical fault in DL3 (Fig. 6.18(a)) and unsymmetrical fault in DL4 (Fig. 6.18(a)). The definition of the axises is considered as follow: *x* axis corresponds to the time evolution (*t*), *y* axis corresponds to the total number of PDs in the grid (PD), and *z* axis in the first colomn corresponds to the *fault signal*, and in the second colomn corresponds to the *trip signal*. For example, during symmetrical fault at DL3, the fault signals of PD4, PD5 go from 0 to 1 during the fault, as both of them have the same voltage. Then the recloser algorithm is applied, to diconnect PD5. The same idea is used for PD6 and PD7 to disconnect PD6. The trip signals of PD5 and PD6 equal 1; however, for the rest of the PDs in the grid the value equal 0 as the fault at DL3.

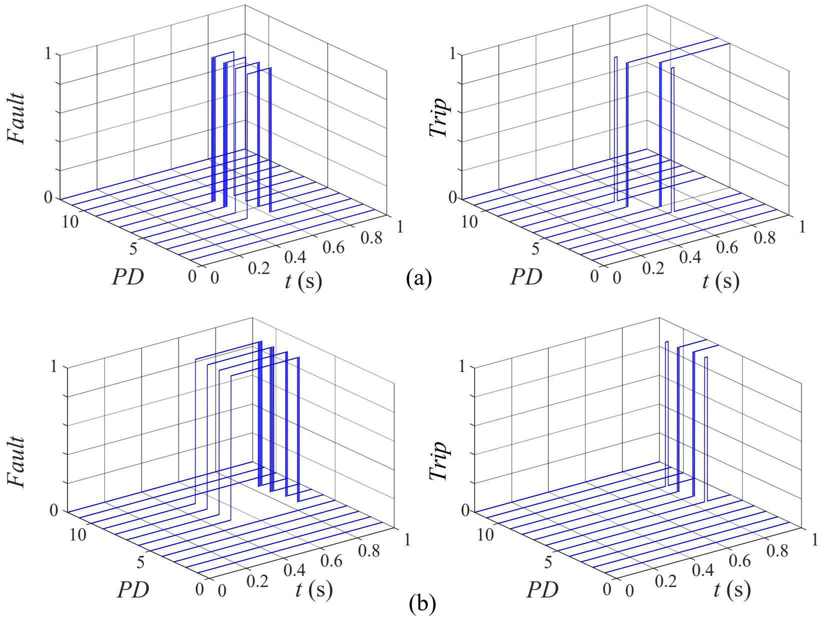

Fig. 6.18 ring grid with 2 DGs during (a) 3 ph (*abc*) at DL3, (b) 1 ph (BG) at DL4

Fig. 6.20, Fig. 6.21, and Fig. 6.22 show the *abc* voltages, *abc* currents, and trip signals for the radial grid shown in Fig. 6.19, with symmetrical and unsymmetrical faults at different locations. In order to analyse the effect of DG penetration on the analysed radial grid, Fig. 6.20 is presented during unsymmetrical faults occurred at DL1 and DL5. For example, during a single-phase to ground fault at DL5, both PDs (PD8, PD9) will trip simultaneously. Then, the recloser algorithm will be applied; in this case, PD9 is closed before PD8, because PD9 is exposed to the fault, then PD8 will be connected. The same idea is repeated between PD10 and PD11 to disconnect DL5. Fig. 6.21 illustrates the analysed radial grid with two DGs during symmetrical and unsymmetrical faults that occurred at DL3 and DL4, respectively. For example, in the case of a single-phase to ground fault, the negative-sequence voltage will be used, in this case, PD2 and PD3 will trip; then, the recloser algorithm is implemented to distinguish between PD2 and PD3, to disconnect the corresponding PDs at the faulted DL. The same methodology is used to disconnect the other end of the line between PD4 and PD5. Fig. 6.22 shows the behaviour of LO algorithm without DGs during unsymmetrical faults in different locations (DL1, and DL2). As seen, the LO is able to disconnect the appropriate PDs, which demonstrates the functionality of the LO.

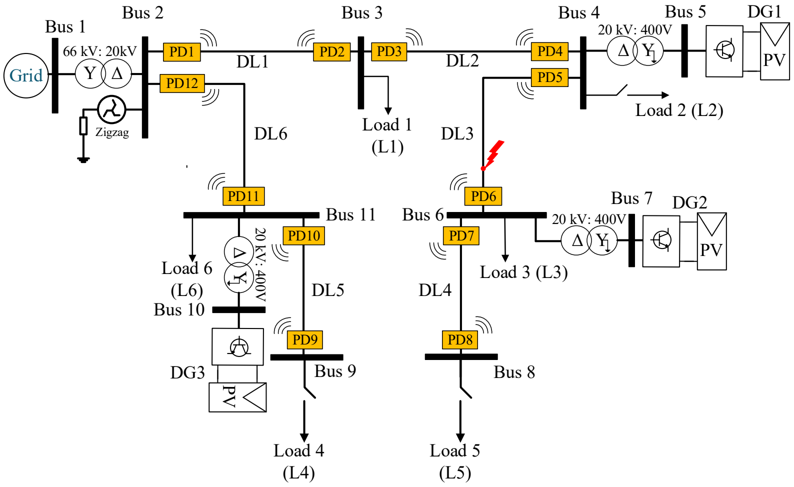
Grid
Bus 1
Bus 2
66 kV: 20kV
Y
Δ
Zigzag
PD1
PD12
DL1
Bus 3
PD2
PD3
Load 1 (L1)
DL2
DL6
Bus 4
PD4
PD5
20 kV: 400V
Bus 5
DG1
PV
Load 2 (L2)
DL3
PD6
Bus 6
PD7
Load 3 (L3)
Bus 7
DG2
20 kV: 400V
PV
DL4
PD8
Bus 8
Load 5 (L5)
PD11
Bus 11
PD10
20 kV: 400V
Load 6 (L6)
Bus 10
DG3
PV
DL5
PD9
Bus 9
Load 4 (L4)

Fig. 6.19 Single line diagram of a radial DS with DG penetration

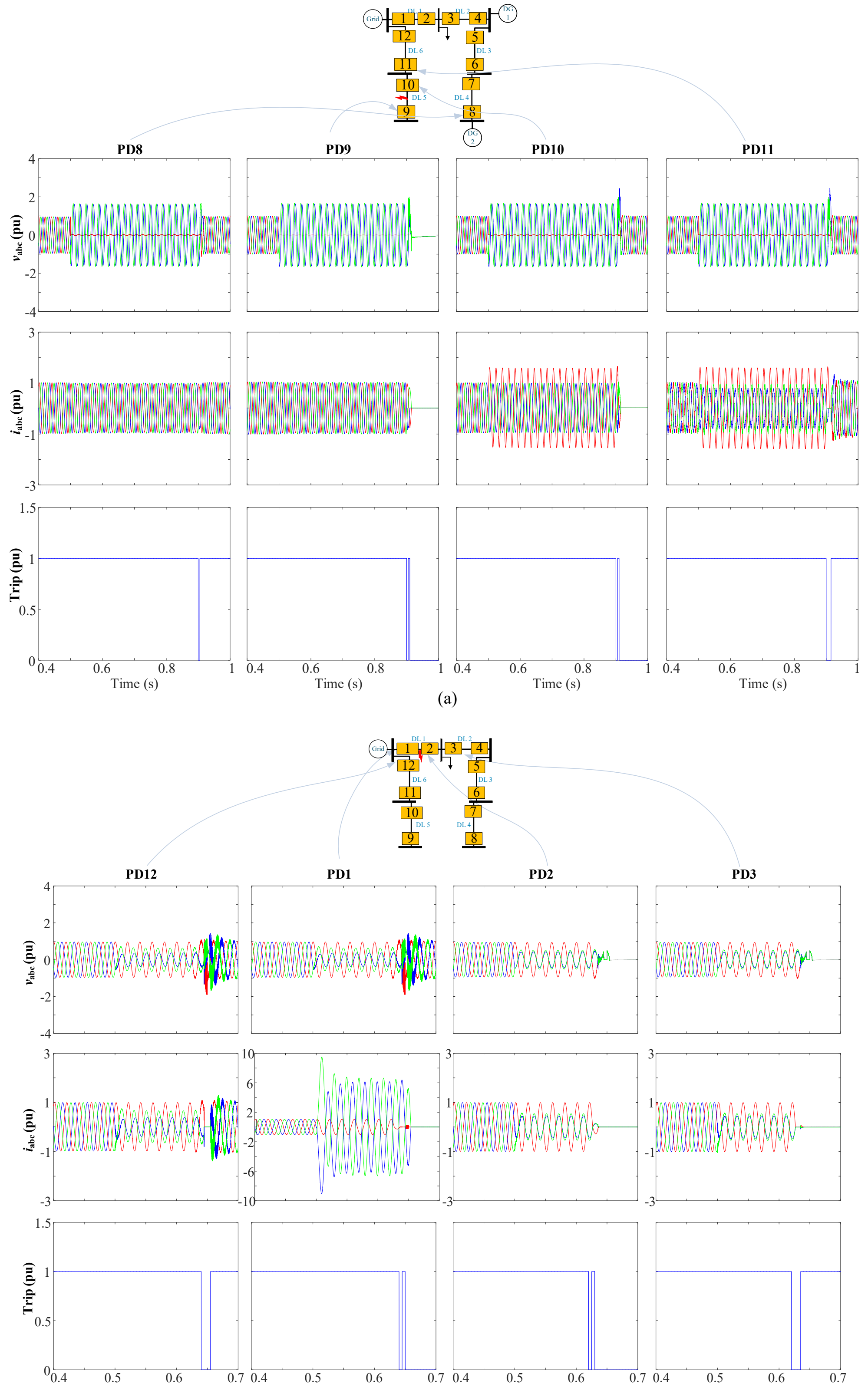

(a)

(b)

Fig. 6.20 *abc* voltages, *abc* currents, and trip signals for LO, with the analysed radial grid (a) with2 DGs during 1 ph to ground (AG) at DL5, (b) without DG during 2 ph (BC) at DL1

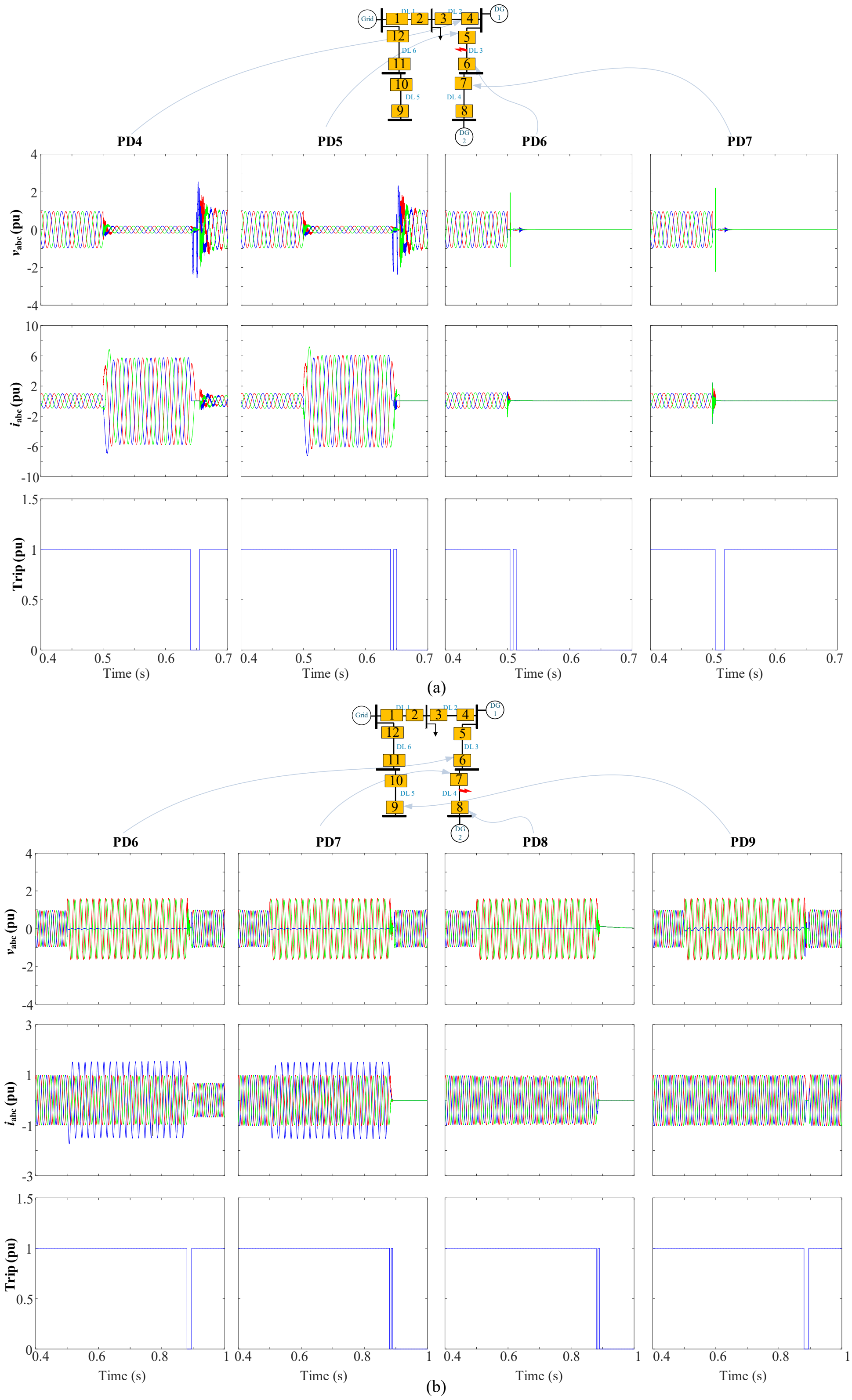

Fig. 6.21 *abc* voltages, *abc* currents, and trip signals for LO, with the analysed radial grid (a) with 2 DGs during three-phase fault at DL3, (b) with 2 DGs during single-phase to ground fault (BG) at DL4

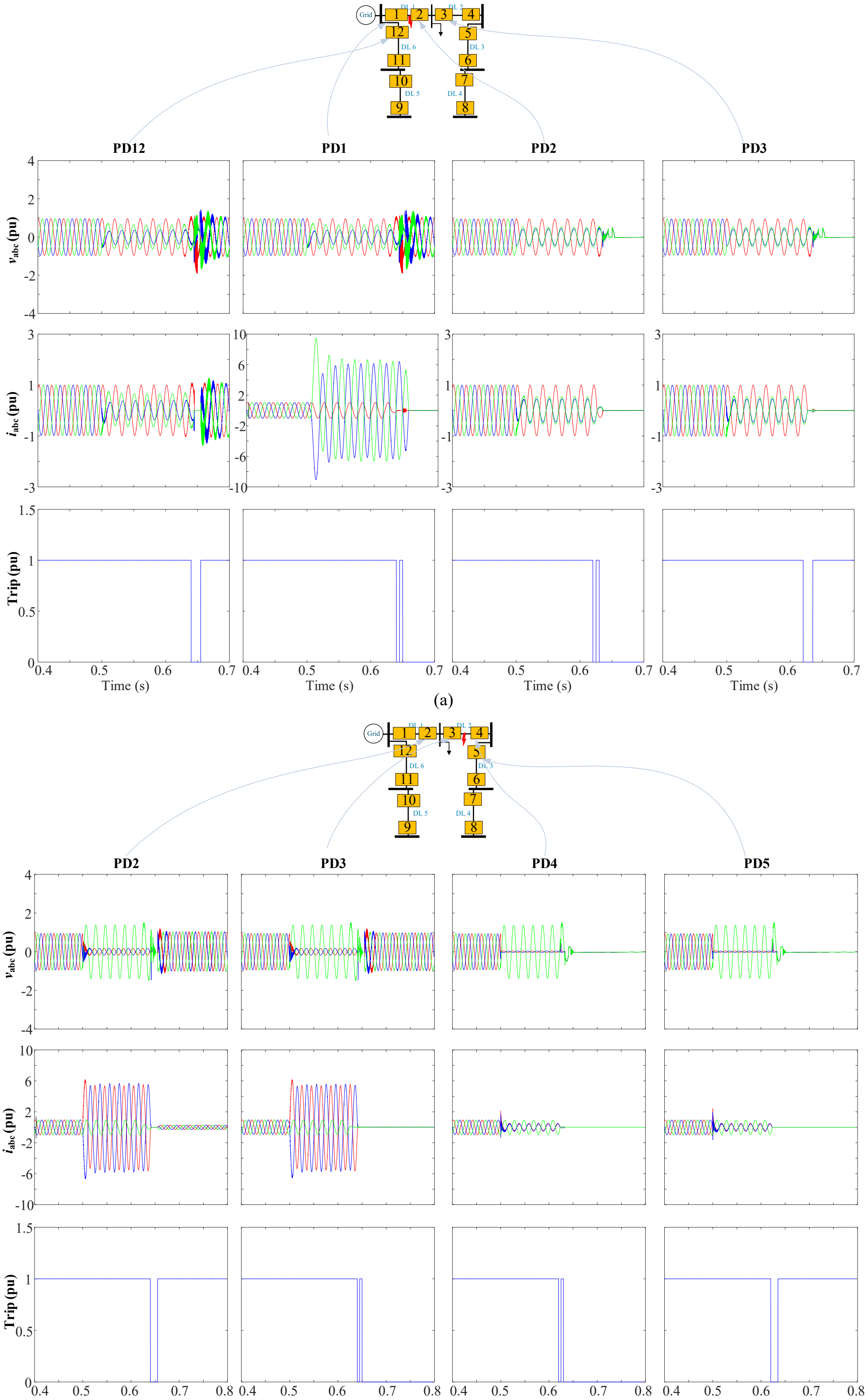

(a)

(b)

Fig. 6.22 *abc* voltages, *abc* currents, and trip signals for LO, with the analysed radial grid (a) without DG during 2 ph (BC) at DL1, (b) without DG during two-phase to ground fault (ABG) at DL2

Fig. 6.23 shows the fault and trip signals patterns during a symmetrical fault in DL4 (Fig. 6.23(a)) and an unsymmetrical fault in DL4 (Fig. 6.23(a)). The 3-D figures show the patterns of each signal for all the PDs to notice the behaviour of each of them during the fault. For example, during symmetrical fault at DL3, the trip signal is turned ON (1) only for breakers PD5 and PD6, because the rest of the breakers will not trip as the fault at DL3.

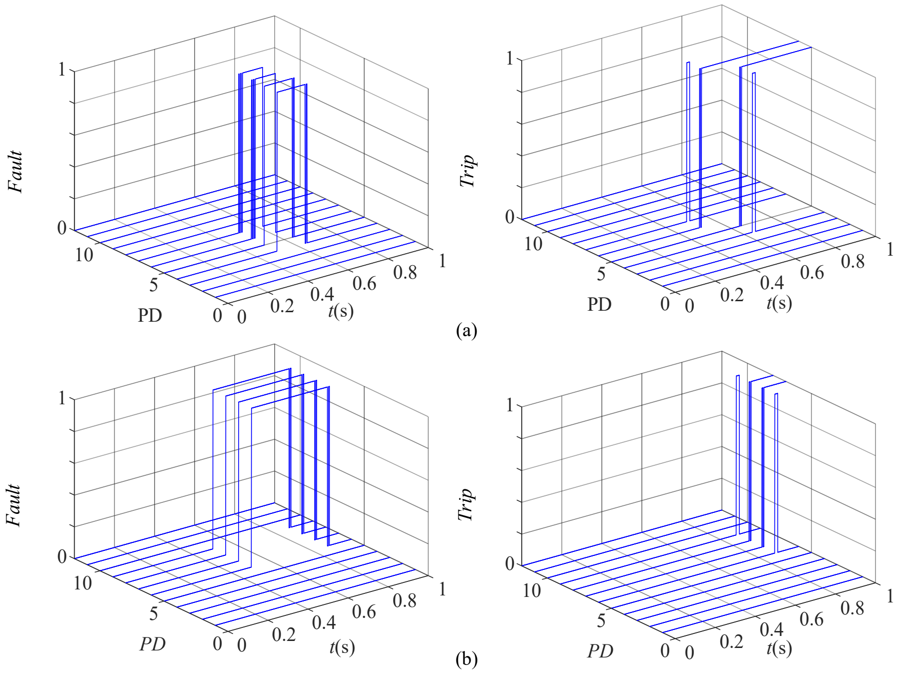

(a)

(b)

Fig. 6.23 Radial grid with 2 DGs during (a) 3 ph (*abc*) at DL3, (b) 1 ph (BG) at DL4

Fig. 6.24 and Fig. 6.25 show the fault and trip signals in all the PDs connected to buses at the end of the faulted line (DL3 in Fig. 6.24 and DL4 Fig. 6.25) for the radial grid shown in Fig. 6.19. For example, when a three-phase fault occurs at DL3 (Fig. 6.24(a)), the LO algorithm depends on the definite-time curve corresponds to the positive-sequence voltage at PD4 and PD5, so both of them will trip at the same time and the recloser algorithm is applied to disconnect the appropriate PD. The same methodology is used to disconnect the other end of the line between PD6 and PD7. Fig. 6.25 shows the trip signals of the four PDs connected to buses at the end of DL4, as seen, both PDs connected to the same bus trip at the same time, then the recloser algorithm is applied to disconnect the corresponding PD. In this case, the only difference is that the protection algorithm depends on the negative-sequence voltage, as the fault is unsymmetrical.

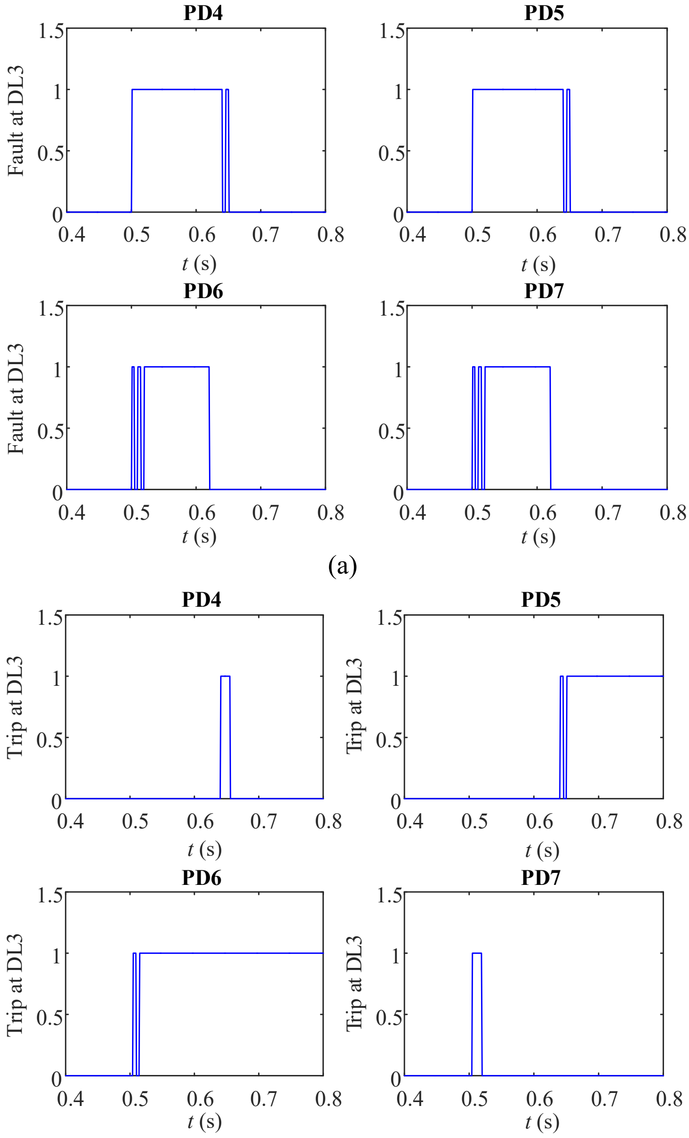

(a)

(b)

Fig. 6.24 Radial grid with 2 DGs during 3 ph (*abc*) at DL3, (a) fault, (b) trip.

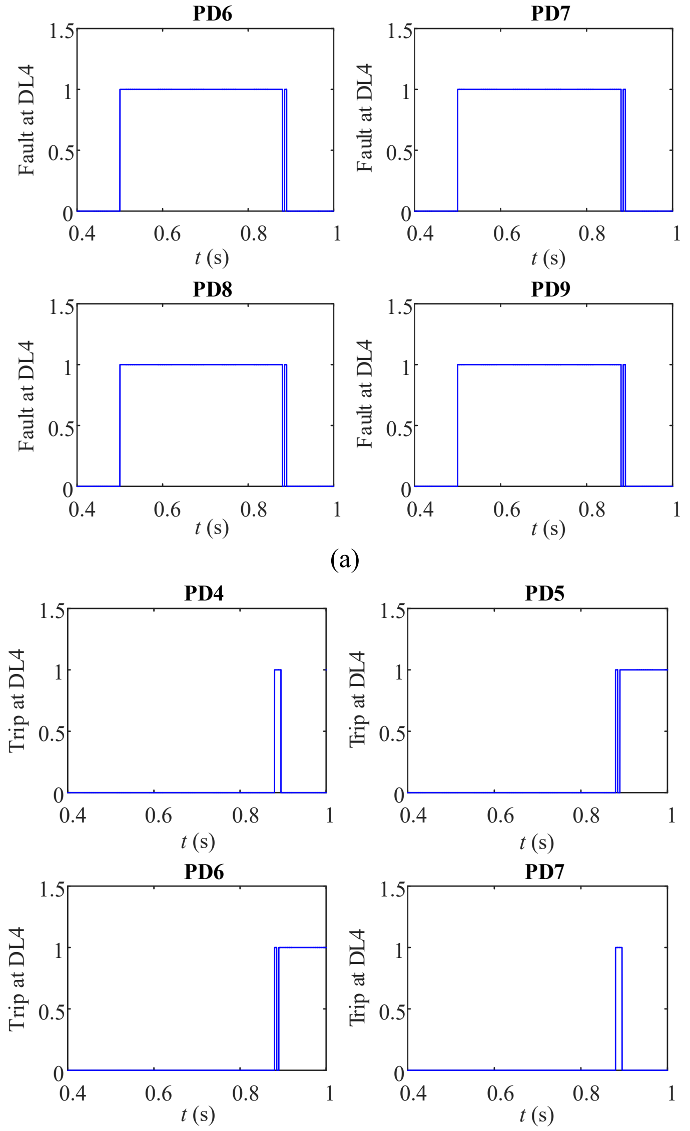

(a)

(b)

Fig. 6.25 Radial grid with 2 DGs during 1 ph (BG) at DL4, (a) fault, (b) trip.

6.2. Comparative study

A fair comparison between the proposed protection scheme and conventional protection techniques (OCR and DR) has been presented using MATLAB^{TM} SIMULINK to show the proposed protection scheme's preponderance and emphasize the importance of the proposed protection scheme.

The OCR and DR explained in [170] are used to compare classical protection schemes and the proposed protection scheme. The grid used to make the comparison is shown in Fig. 6.26. The flowchart of the tested cases presented in this section is shown in Fig. 6.27.

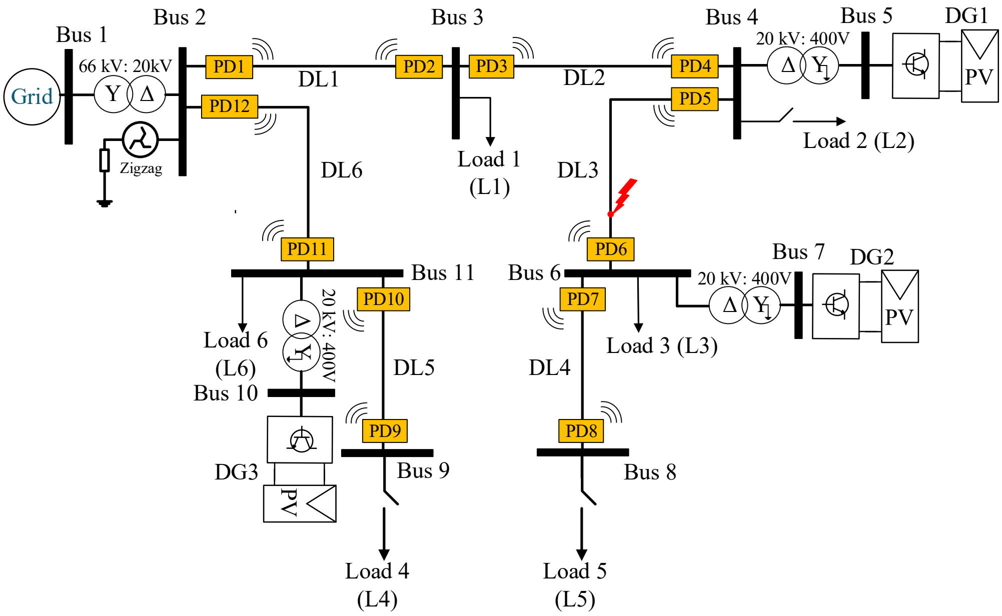
Bus 1
Bus 2
Bus 3
Bus 4
Bus 5
DG1
Grid
66 kV: 20kV
Y
Δ
Zigzag
PD1
PD2
PD3
PD4
PD5
PD12
DL1
DL2
20 kV: 400V
PV
Load 2 (L2)
Load 1
(L1)
DL6
DL3
PD11
PD6
Bus 11
Bus 6
Bus 7
DG2
20 kV: 400V
PV
PD10
PD7
Load 3 (L3)
Load 6
(L6)
20 kV: 400V
Bus 10
DL5
DL4
PD9
PD8
DG3
PV
Bus 9
Bus 8
Load 4
(L4)
Load 5
(L5)

Fig. 6.26 Single line diagram of a radial DS with DG penetration

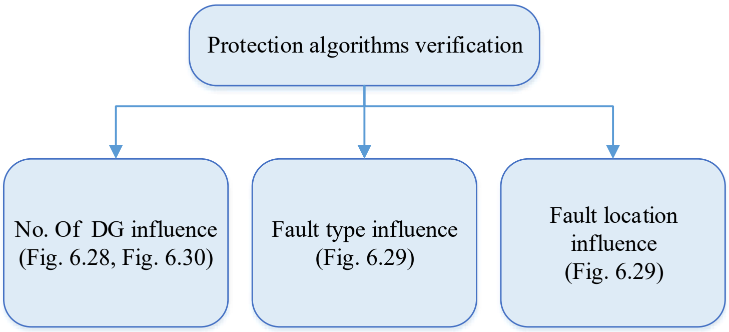
Protection algorithms verification
No. Of DG influence
(Fig. 6.28, Fig. 6.30)
Fault type influence
(Fig. 6.29)
Fault location
influence
(Fig. 6.29)

Fig. 6.27 Flowchart of the studied cases

The OCR, DR, and CE-ZO protection strategies have been tested for several DG penetrations, loads, fault resistance, fault type, and fault location. The analysis of OCR, DR, and CE-ZO protection algorithms' behaviour is shown for the grid represented in Fig. 6.19. The currents at both ends of DL3 have been presented in Fig. 6.28 for the three protection strategies. Fig. 6.28(a) shows the case with 2 DGs, Fig. 6.28(b) with 1 DG, and Fig. 6.28(c) without DG, respectively. These results correspond to a three-phase fault in DL3 with a value of the fault resistance of 0.1Ω. Fig. 6.28(a) shows the fault currents if two DGs are located at buses 4 and 6, respectively. It can be concluded that the DR and CE-ZO protection strategies can disconnect fast the faulted part of the system, and in the cases of OCR and DR, the relay settings have to be updated if there is any change in DG penetration or grid configuration. For the OCR and DR protection strategies, the relay settings used to obtain Fig. 6.28 are shown in Table 6.4 and Table 6.5. For the DR and CE-ZO protection strategies, the fault is cleared very fast (≈ half a period); however, as shown in Fig. 6.28(a), the disconnection is faster in the CE-ZO controller than DR because for DR the trip signal depends on the differential current value, while CE-ZO protection strategy depends on the criteria of power flow direction.

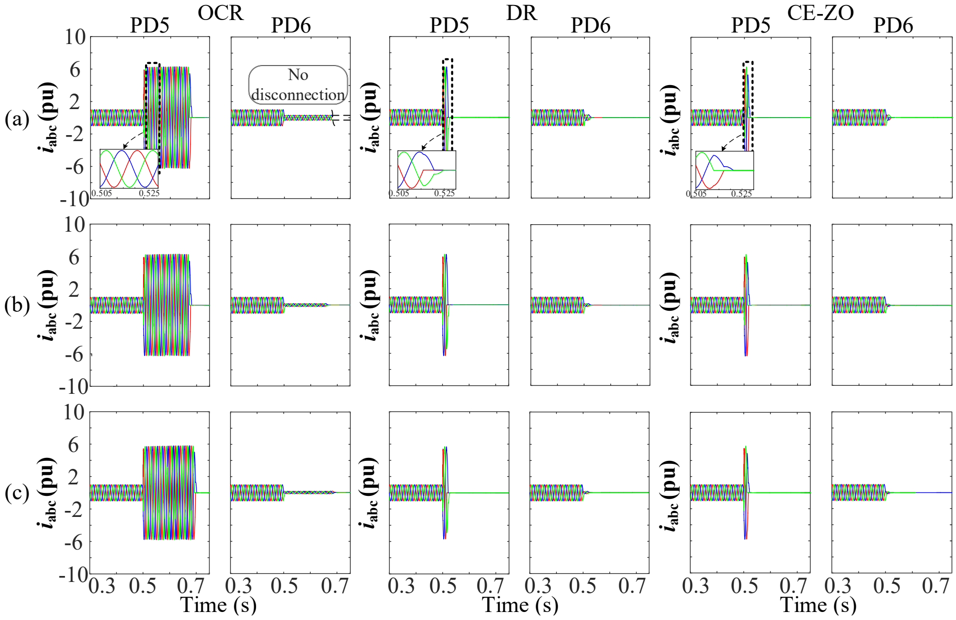

Fig. 6.28 Short-circuit current of OCR, DR, CE-ZO behaviour during a three-phase fault in DL3 with fault resistance $r = 0.1\ \Omega$ (a) with two DGs, (b) with one DG, (c) without DG

In the case of two DGs connected at buses 4 and 6, and when a three-phase fault occurs at DL3, the faulted line will be fed from two points. The current passing through PD5 is equal to the short-circuit current (current at the fault resistance) when one DG is connected at bus 4; however, this current through PD5 is different from the short-circuit current when DG2 is connected at bus 6 because PD6 will be supplied from DG2. This case is essential to show the difference between OCR and the other protection strategies because, as seen in Fig. 6.28(a), the relay trip depends on the settings. This figure shows that PD5 trips; however, PD6 does not trip as the settings of the relay need to be updated.

Table 6.4 OCR settings with 2 DG

Parameter (OCR)	Value
Pick up current (pu)	1
Time dial (TD)	0.5
Current transformer (CT)	500 : 1

Table 6.5 DR settings with 2 DG

Parameter (DR)	Value
Differential current (pu)	1.08
Biased characteristic (K)	0.5
Current transformer (CT)	500 : 1

In Fig. 6.29, the trip signals for three relays are presented in a 3-D preview for several DG penetrations, fault types, and fault resistance. It can be concluded that the OCR protection strategy is not a good option as the fault persists for many periods, and its trip is affected by the DG penetration.

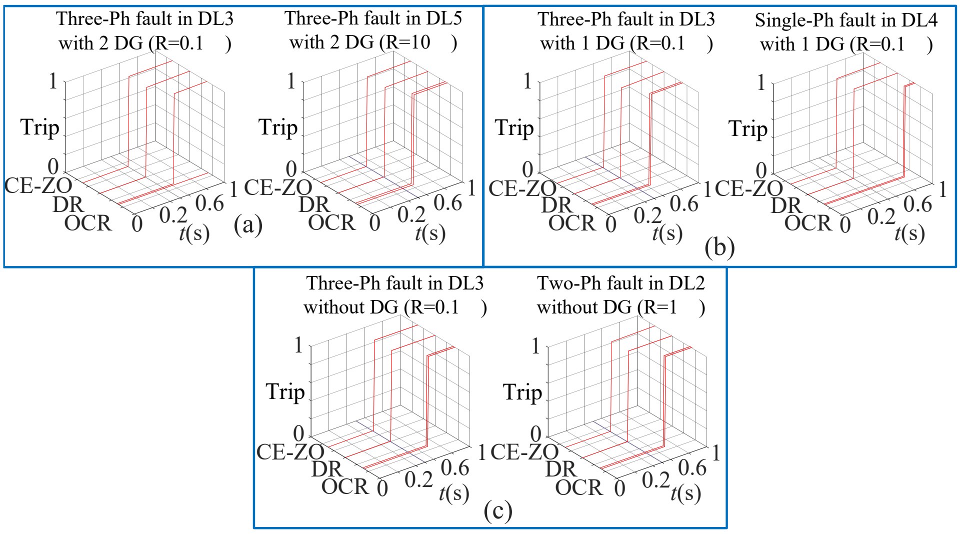

Fig. 6.29 Trip signal of OCR, DR, CE-ZO behaviour during symmetrical and unsymmetrical faults with different fault resistance (a) with two DGs, (b) with one DG, (c) without DG

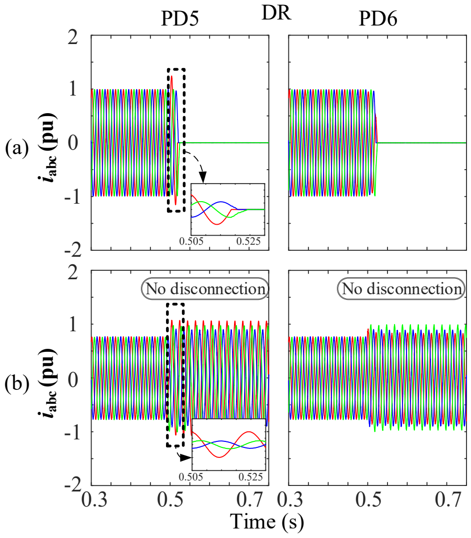

Fig. 6.30 Short-circuit current of DR behaviour during single-phase fault in DL3 with fault resistance $r = 0.1\ \Omega$ (a) without DGs, (b) with two DG

When two DGs are connected at buses 4 and 6, the power flow and the current values are reduced in DL3 as DG1 and DG2 are close to the loads, so less power comes from bus 4 with DG penetration. In the case of single-phase to ground fault, as the ground connection is made through a zigzag transformer with grounding reactance, as shown in Fig. 6.1, the fault current during single-phase fault is limited. Therefore, the relay does not trip, as shown in Fig. 6.30. However, during a three-phase fault, the fault current is high in both cases (with and without DGs), as there is no influence from the zigzag transformer, as shown in Fig. 6.28. The DR protection strategy is also affected by significant changes in DG penetration, which is averted using the CE-ZO protection strategy. CE-ZO protection strategy can disconnect the fault with several DG penetrations, as shown in Fig. 6.28 and Fig. 6.30. Moreover, the CE-ZO protection strategy can guarantee the fast disconnection of the fault even when the grid changes the operation conditions. The results are shown in Fig. 6.29 support these conclusions, where the OCR, DR, and CE-ZO protection strategies' trip signals during different fault types with different fault resistance in different locations are represented. It can be concluded that the CE-ZO protection strategy presents a better behaviour in different grid operation conditions (generation and consumption), fault conditions, and also with reconfigurations of the grid.

These results are some examples to emphasize the importance of the proposed CE-ZO protection strategy. This methodology can be adapted to other grid configurations. The scheme is tested with other grid configurations changing load consumption, DG penetration, different fault locations, fault types, and (HV/MV) transformer configuration [37].

Table 6.6 and Table 6.7 show the proposed protection strategy compared to other protection strategies. It can be concluded that the proposed algorithm is one of the few protection schemes used in case of high DG penetration, and at the same time can be applied in different grid configurations. Moreover, the protection algorithms have been tested experimentally using a scaled grid to emphasize their functionality, which is one of the key points of this research.

Table 6.6 Comparison between different protection strategies.

Inverter based	**Grid reconfiguration**	**Experimental verification**	**Trip signal**	**Strategy**	**References**
Yes	Yes	Yes	Very fast	Directional based ANN	Proposed method [37]
Yes	Yes	No	Fast	Linear programming	[110]
Yes	No	Yes	Very fast	Deep learning ANN (DNN)	[111]
Yes	No	No	Moderate	Directional relay	[112]
Yes	No	No	Fast	Discrete wavelet transform (DWT)	[114]
No	No	Yes	Not specified	Support Vector Machine (SVM) and ANN	[113]
No	No	No	Very fast	ANN	[115]
No	No	No	Moderate	communication-based	[116]
No	No	No	Moderate	OCR with DR	[109]

Table 6.7 Comparison of the proposed method with other methods for a similar problem.

References	**Protection Strategy**	**Experimental verification**	**Grid reconfiguration**	**Trip Time**	**Advantages**	**Disadvantages**
The proposed method [37]	CE-ZO (Directional relay-based ANN)	Yes	Yes	10 ms	Fast tripping, Variable DG penetration, Different fault locations, fault types, (HV/MV) transformer configuration, fault resistance-Stiff, and weak grids.	Communication problems
[110]	Centralize controller and Linear programming	No	Yes	421 ms	Variable DG penetration, No need for training, Obtain relay settings simultaneously	Communication problems, Knowledge of DG and PD status, More complex with large no. of buses
[103]	OCR	No	No	> 200 ms	High DG penetration, Different fault resistance	The offline calculation, Not adaptable for network modifications

Table 6.7 Cont'd

References	**Protection Strategy**	**Experimental verification**	**Grid reconfiguration**	**Trip Time**	**Advantages**	**Disadvantages**
[104]	MAS and OCR	No	No	300 ms	High DG penetration, No central controller	Communication problems
[102]	Dual setting OCR	No	Yes	> 100 ms	Variable DG penetration, High fault resistance	Offline calculation
[116]	Multi-terminal DR	Yes	No	90 ms	Fast tripping, Variable DG penetration, Different fault resistance	Communication problems
[111]	DNN	Yes	No	14 ms	Fast tripping, Variable DG penetration, Different fault resistance	Communication problems, The offline calculation, Not adaptable for network modifications

In the next chapter, the experimental validation of the protection algorithms, and a comparison between the conventional protection strategies (OCR/DR) and the proposed protection algorithms will be discussed.

7 Experimental implementation and results

First, the experimental implementation and results obtained to validate the control strategies of the three-phase grid-connected converter are presented, including the injected current control. Second, the experimental work for validating the proposed protection algorithms (CE, ZO, and LO) is illustrated. The validation of the algorithms is done in two steps: at the beginning, the idea is based on generating the voltage and currents signals of the faulted line in the dSPACE^{TM} and transmitting these data to the DSP, where the algorithms (CE, ZO, and LO) have been implemented. Then, a scaled entire grid has been constructed in the laboratory to validate the three control algorithms in different operation scenarios.

7.1. Experimental implementation of the three-phase grid-connected converter

In this section, the practical results of the inverter *abc* current control are presented.

7.1.1. Experimental implementation of the current control strategies

This section illustrates the experimental evaluation in a laboratory scaled model of the current control strategies and compares the considered control strategies. The experimental setup is shown in Fig. 7.1(a) is used to validate the analytical model and the simulation results in MATLAB^{TM} SIMULINK. The system components are shown in Appendix F.

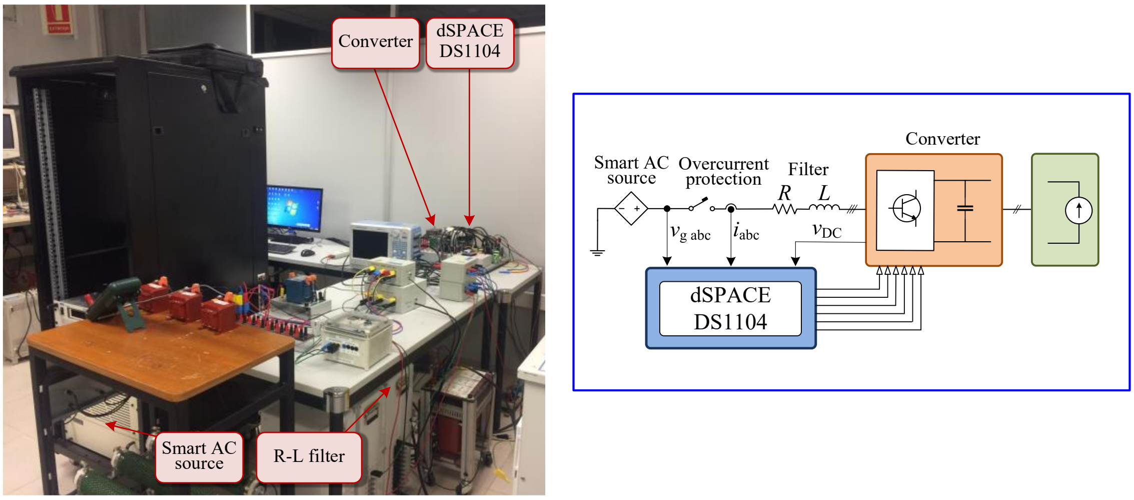

(a) (b)

Fig. 7.1 Experimental setup. (a) Real setup, (b) Electrical scheme.

Table 7.1 System parameters

Inverter	Rated power	10 kVA
	Rated voltage	400 V
Filter	Inductance (L)	10 mH
	Resistance (R)	0.2 Ω
DC bus	DC rated voltage	800 V

Table 7.1 shows the system parameters. The system consists of: a smart three-phase AC power source to emulate the grid and a converter connected to the grid through an RL filter. Fig. 7.1(b) depicts the electrical scheme of the experimental setup. Grid voltages ($v_{g\ abc}$), line currents (i_{abc}), and DC-link voltage (V_{DC}) need to be measured to implement the control algorithms using MATLAB^{TM} software and ControlDesk, which are sent to an oscilloscope and to the dSPACE^{TM} DS1104 that is connected to a PC.

- Without grid code validation

The following figures illustrate the *abc* injected current in steady-state and faulty conditions testing different types of sags. Fig. 7.2 shows the grid voltages and currents during the unfaulty steady-state condition (RMS phase voltage v_{abc} = 60 V, and *dq* reference currents i_d = 6 A, i_q = 0 A). These values have been chosen to start checking the experimental setup without harming any of the equipment. After that, the RMS phase voltage is calculated to match the pu value of the entire simulated grid. The figure shows that in a steady-state condition, the *abc* injected currents are perfectly balanced and symmetrical. In order to demonstrate the behaviour of BCC strategy during voltage sags, different sag types have been tested. The concentration on this strategy because it always injects balanced and symmetrical currents during the sags, also the other control strategies have been considered. The sag duration equals 0.2 s, this value has been chosen as the voltage sages can last from a few cycles to a few seconds, so using this value (0.2 s = 10 cycles) can guarantee the presence of the sag, and it is enough to analyze the behaviour of the injected current control strategies. The sag depth (*h*) equals 0.6, the control strategies have been tested with different sag depths, from *h* = 0.3 ~ 0.9.

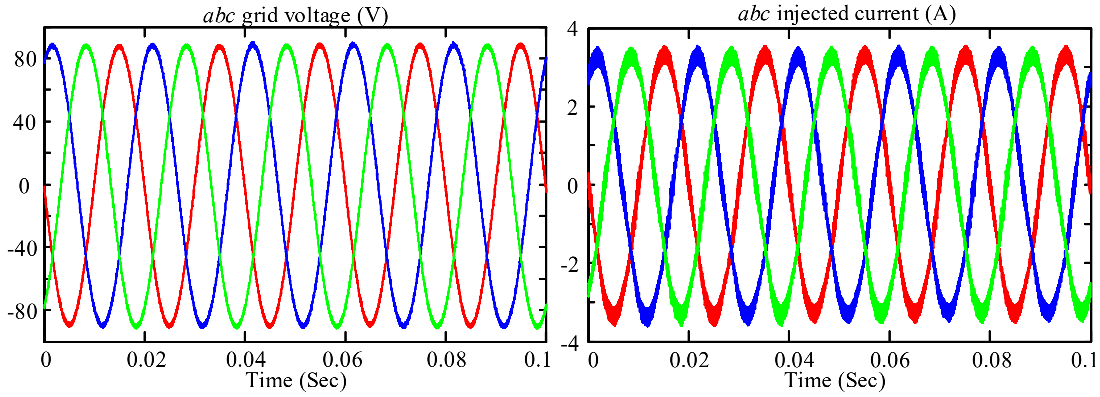

Fig. 7.2 Measured *abc* grid voltages and injected currents during the unfaulty steady-state condition

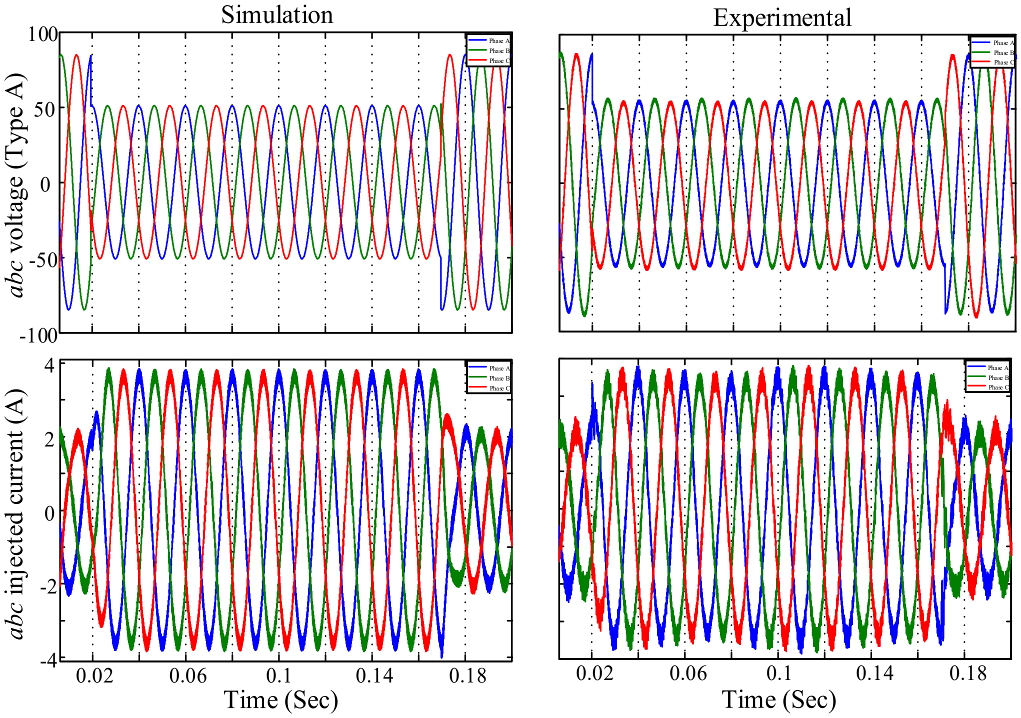

Fig. 7.3 Simulated and measured *abc* grid voltages and injected currents for a type A sag with BCC strategy

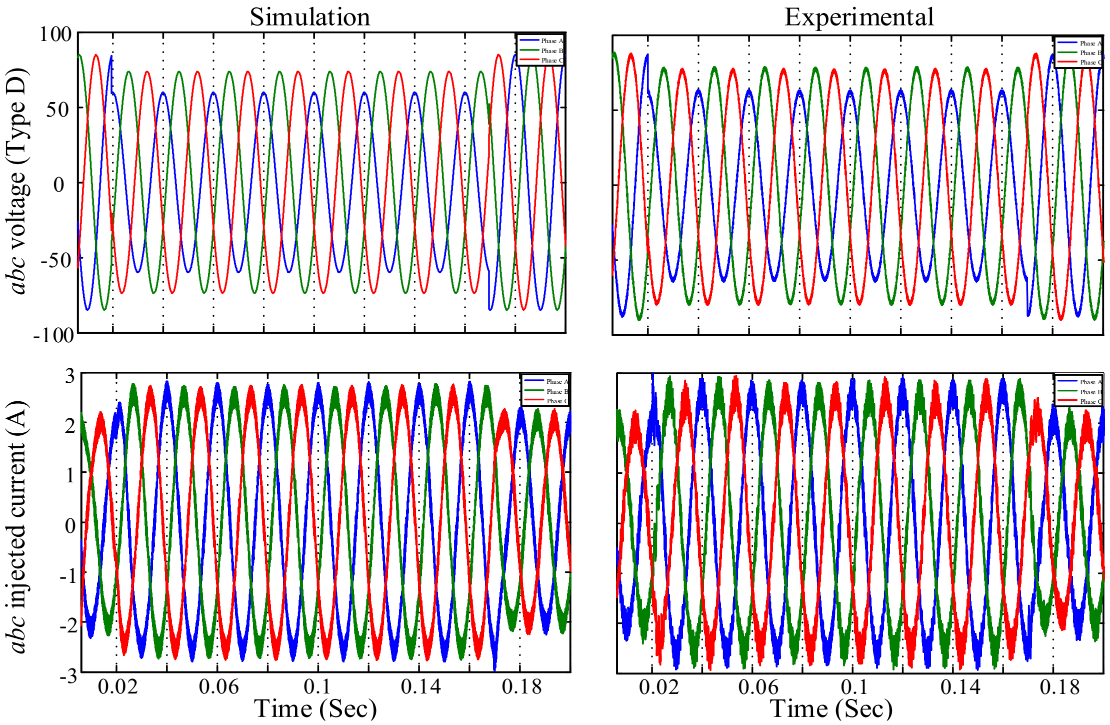

Fig. 7.4 Simulated and measured *abc* grid voltages and injected currents for a type D sag with BCC strategy

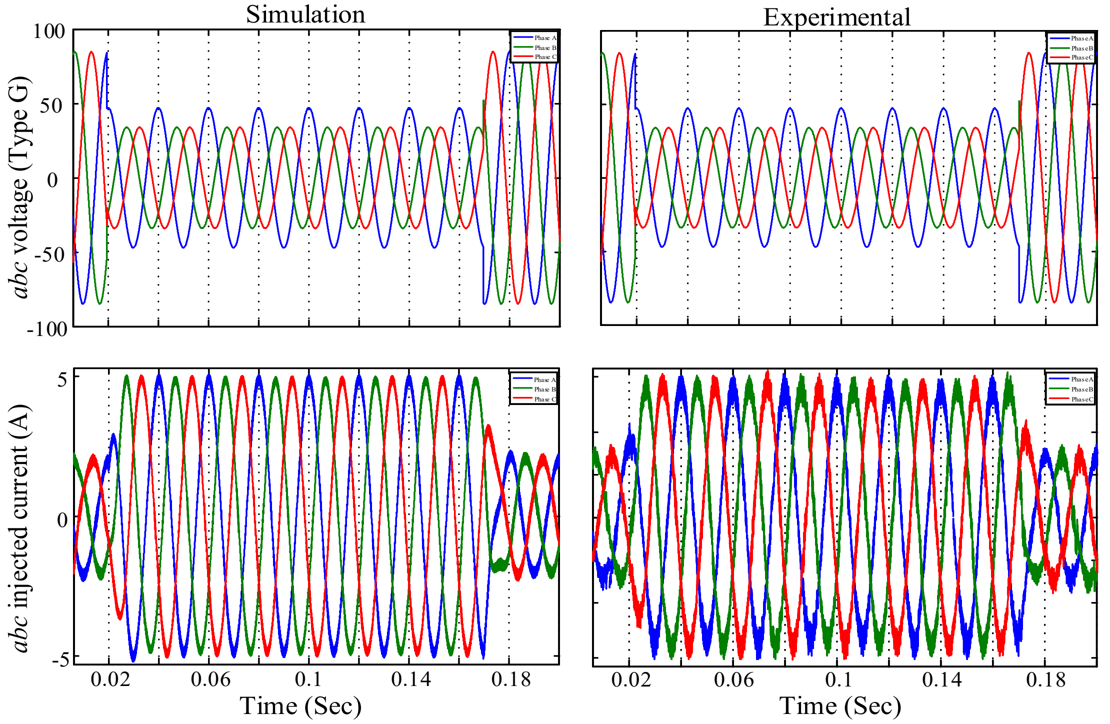

Fig. 7.5 Simulated and measured *abc* grid voltages and injected currents for a type G sag with BCC strategy

Fig. 7.3, Fig. 7.4, and Fig. 7.5 show the *abc* grid voltages and *abc* currents with different types of sags (A, D, and G), respectively. These sag types were chosen to test the control strategies for three-phase, two-phase, and single-phase faults. It is important to mention that previous results are obtained to demonstrate the functionality of the BCC strategy as it injects balanced current during voltage sags. However, the reference currents are imposed without verifying the grid code in this step, which will be presented later in this section. In addition, the experimental results and the simulation results have the same behaviour and values. The error percentage between the simulation and the experimental results during steady-state, fault, and recovery periods are 2 % for the instantaneous *abc* voltages, and 4 % for the instantaneous *abc* currents, which are less than 5 % in both cases; this is mainly due to the voltage and current sensors. The simulation results have some noise due to the actual model of the converter and its commutation frequency, and for experimental results, the same behaviour is obtained with more noise due to real system implementation.

- Under grid code validation

In the following results, the grid code validation (explained in chapter 4) is performed for various types of sags. When the system was in a steady-state, a voltage sag with a depth of $h = 0.5$ was applied. The control strategies have been tested for symmetrical and unsymmetrical sags, as illustrated in Fig. 7.6, to demonstrate their capability to fulfill the Spanish grid code requirements. The results demonstrate that both strategies inject the upper limit of the active current for symmetrical sags, because the negative-sequence voltage is zero; therefore, the injected current is balanced. However, for unsymmetrical sags, when the upper limit of the active current is injected, the injected currents do not exceed the grid code limitation for the BCC strategy. Moreover, because this strategy imposes zero value for the negative reference current, it injects symmetrical current. However, for the CPC strategy, if the upper limit of the active power is injected, the current surpasses these limitations; therefore, the active current must be reduced to avoid exceeding 1 pu (solid black line in Fig. 7.6 for type C sag with CPC). Furthermore, as the negative-sequence currents have a value other than zero, the injected current is unbalanced for CPC.

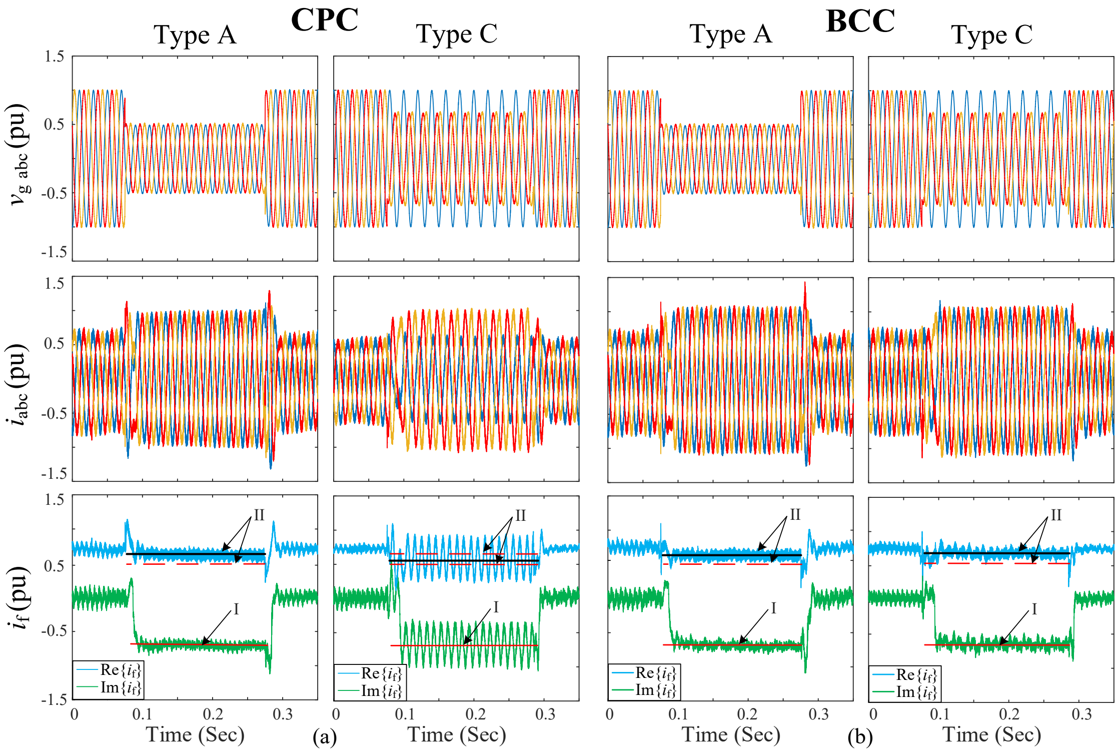

Fig. 7.6 Experimental results of grid voltage and injected current with the sag of h = 0.5 depth and 200 ms duration for (a) CPC strategy and (b) BCC strategy. I and II are the reactive and active current references, respectively, imposed by the Spanish grid code

During unsymmetrical sags (type C) with depth $h = 0.5$, the theoretical, simulated, and experimental grid voltage and injected current are shown in Fig. 7.7. Both control strategies are sorely tested in the same manner. When a voltage sag occurs, both strategies inject the rated current of the converter to ensure the grid code requirements are fulfilled. Because the voltage and current during the sag are balanced, the complex plane for both strategies will be a point in the case of symmetrical sags, as discussed in chapter 4. As illustrated in that figure, the CPC strategy injects unbalanced currents into the grid, causing the transformed variables (real and imaginary) of the injected current to oscillate, resulting in a circle in the complex plane. However, because the BCC method injects balanced currents during sags, its complex plane representation corresponds to a point. It should be noted that the representation in theoretical results is either a pure circle (for CPC strategy) or a point (for BCC strategy) and that the representation in simulation results includes some noise due to the actual converter model and its commutation frequency. Experimental results are similar, but with higher noise due to practical system implementation. Nevertheless, it can be concluded that theoretical, simulation and experimental results agree.

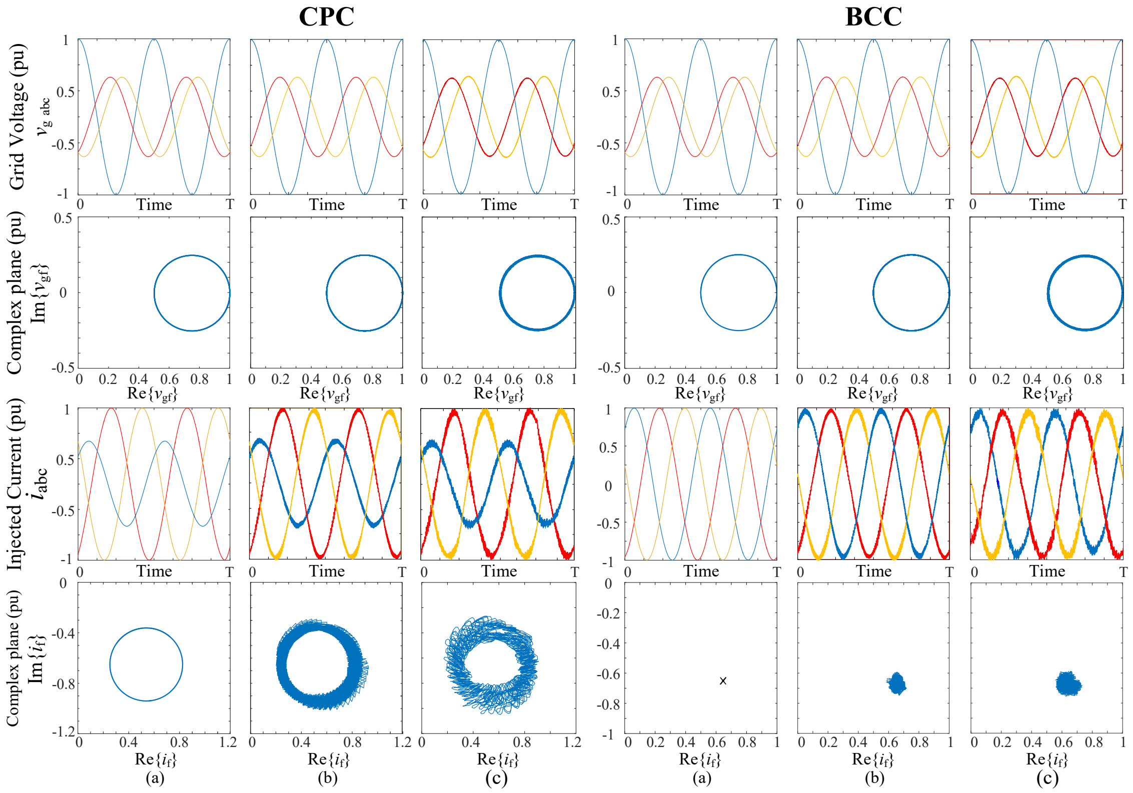

Fig. 7.7 (a) Theoretical, (b) simulation, and (c) experimental results of CPC and BCC control strategies during unsymmetrical sag (type C). T = period.

7.2. Experimental implementation of the proposed protection algorithms

In this section, the validation of the proposed protection algorithms will be presented. First, the SSR behaviour will be presented, then the algorithm verification using dSPACE^{TM}1104, and DSP TMS320F28335 will be demonstrated; finally, the experimental implementation of the proposed protection algorithm in a modeled scaled grid built in the laboratory is discussed.

- Solid State Relay (SSR)

Currently, mechanical circuit breakers (CBs), which take several 10 ms to clear the fault, are being used for this purpose. However, the slow switching time may be enough to distort power quality to unacceptable levels. Therefore, SSRs should be desired as a substitute for mechanical CBs, because they would be able to clear faults within 100 µs to 5 ms. Clearing time is adequate to retain a stable voltage in the power network. Additionally, due to the ultra-fast nature of solid-state machines, the fault current may be prevented from achieving its peak value, increasing system equipment lifetime. The main disadvantages of these devices, though, are their high initial costs. The SSR principle of operation is shown in Appendix C.

In this thesis, Crydom SSR is used as a breaker device for the protection system in the case of the radial grid. The use of SSR has the advantage of executing the trip signal and clearing the fault rapidly to guarantee the stability of the DS as fast as possible. It consists of an input DC circuit and an output AC circuit. The DC input is used to trigger the diac through a light-emitting diode to have a better isolation circuit between input and output voltages. The triac in the output is used for overvoltage protection. The SSR design is shown in Fig. 7.8.

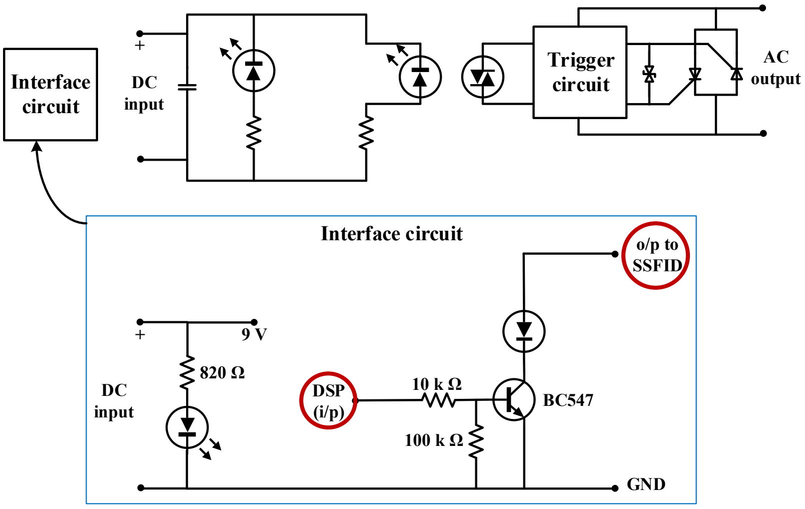

Fig. 7.8 Equivalent circuit of Crydom SSR with an interface circuit

The interface circuit shown in Fig. 7.8 is responsible for converting the output voltage of the DSP which is 3.3 V, to a voltage between (4 ~ 32) V to activate the SSR drive. In this case, the DSP voltage will be transformed to 12 V using the circuit shown in Fig. 7.8.

The operating voltage of the device has a range starting from 4 VDC until 32 VDC, which supports an operating voltage range from 48-660 V. This wide range gives flexibility for the control signal. Moreover, the turn on/off time is very fast, which is approximately half a cycle. The input and output specifications of the SSR are shown in Table 7.2.

Table 7.2 Specifications of SSR

Input specifications		**Output specifications**	
Control voltage range	4-32 VDC	Operating voltage	48-660 V
Minimum turn-on voltage	4 VDC	Transient overvoltage	1200 V
Minimum turn-off voltage	1 VDC	Maximum off-state leakage current at rated voltage	1 mA
Minimum input current	7 mADC	Maximum off-state dv/dt at maximum rated voltage	500 V/µs
Maximum input current	12 mADC	Maximum load current	25 mA
Maximum turn-on time	½ cycle		
Maximum turn-off time	½ cycle		

The location of the SSR is very important always to isolate the faulted part of the grid rapidly and effectively. Its position must coordinate with other PDs, and guarantee the disconnection of the faulty DL from both ends, as the line is fed from both ends when it is connected in a ring grid or a radial grid with DG penetration. The possible alternative locations of SSRs for the analysed grid are to place two PDs at each end of the DL, as shown in Fig. 7.9.

The performance of the Crydom SSR is tested in front of sudden changes in the input voltage (, as seen in Appendix C).

In the case of radial grids, the SSR is used as a PD. However, when it is connected in ring grids, as the impedance of the DLs is very small (less than 1.1 Ω), so the voltage difference across the SSR terminals is lower than the minimum value required by the SSR (more than 48 V as explained in the datasheet

[186]); otherwise, the SSR can not operate correctly (it is always disconnected), as it is demonstrated in Appendix C

As a solution for this problem, the SSR is replaced with a mechanical relay to overcome this problem, as explained in the following subsection. However, the main disadvantages of the mechanical relays are the slow response and noise production.

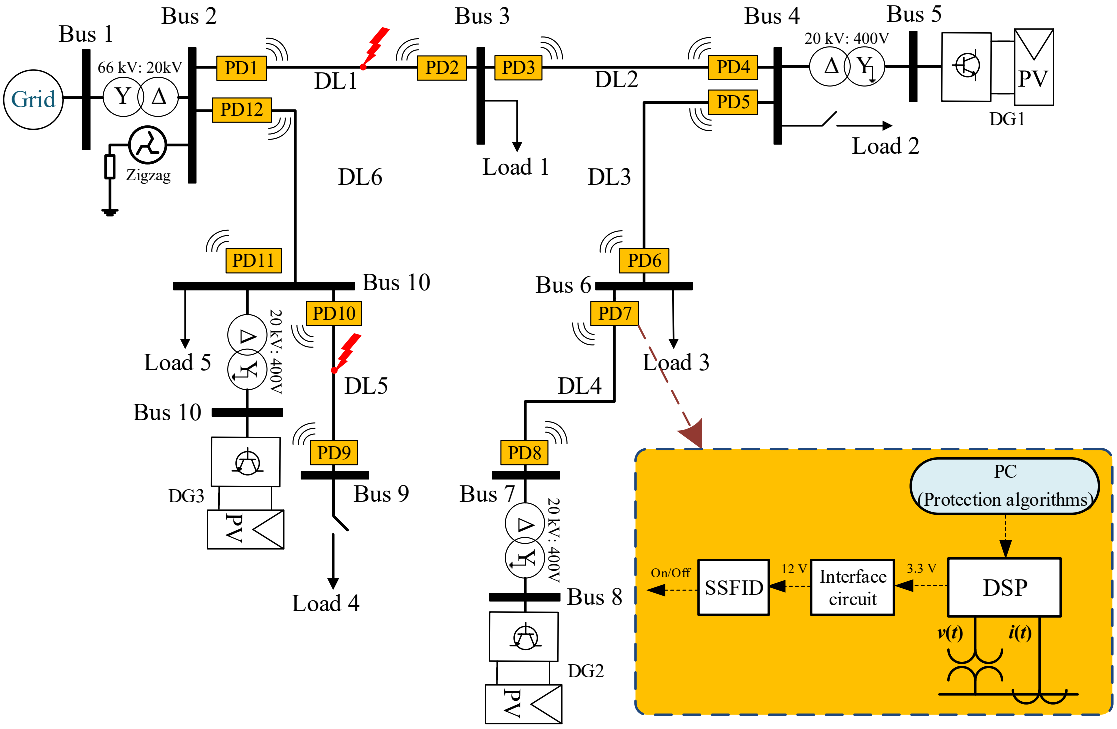
Bus 1
Bus 2
Bus 3
Bus 4
Bus 5
66 kV: 20kV
20 kV: 400V
Grid
Zigzag
PD1
PD2
PD3
PD4
PD5
PD6
PD7
PD8
PD9
PD10
PD11
PD12
DL1
DL2
DL3
DL4
DL5
DL6
Load 1
Load 2
Load 3
Load 4
Load 5
PV
DG1
DG2
DG3
Bus 6
Bus 7
Bus 8
Bus 9
Bus 10
20 kV: 400V
PC
(Protection algorithms)
DSP
Interface circuit
SSFID
On/Off
12 V
3.3 V
v(t)
i(t)

Fig. 7.9 Concept diagram of SSR

- Contactor and mechanical relay

As mentioned previously and in Appendix C, the SSR has the problem of the minimum required voltage for the current drive in the case of ring grid, but it works properly in the radial grid, this is the cause to change SSR to mechanical-breaker for the physical implementation of the ring grid only.

In order to control the contactors at both ends of the faulted line, an eight relay module is used to obtain the decision of the DSP, which is (0 – 3.3 V), and convert it to the appropriate value for the contactor control. The relay module shown at the left side of Fig. 7.10 is a low-level 5V relay interface board, and each channel needs a 15-20mA driver current. It can be used to control large current equipment. It is fitted with high-current relays that work under AC250V 10A or DC30V 10A. For protection criteria, this module is optically separated from the side of high voltage and also prevents ground loop when the interface to the controller (DSP). Each relay module has an NC (normally close), a NO (normally open), and a COM (Common) terminal.

The connection of the contactor with the relay is shown in Fig. 7.10. Each contactor at the end of each line is controlled from one relay that receives its control signal from the DSP controller. At steady-state, the DSP sends 0 V to the relay control part so the relay remains closed, and the contactor remains closed as well. However, during a fault, the DSP sends 3.3 V signal that opens the relays, and as a consequence, the contactor opens as well.

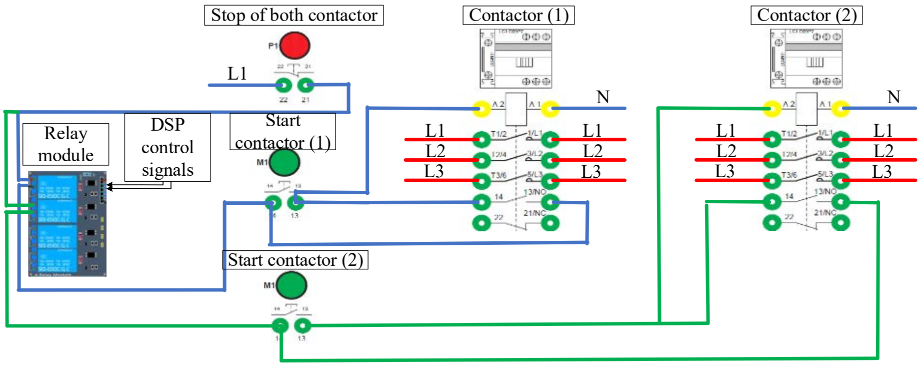
Stop of both contactor
Contactor (1)
Contactor (2)
L1
N
Relay module
DSP control signals
Start contactor (1)
Start contactor (2)
L1
L2
L3
L1
L2
L3
L1
L2
L3
L1
L2
L3
N

Fig. 7.10 Connection between the relay and mechanical contactor

In the following subsection, the validation of the proposed protection algorithms is discussed.

7.2.1. Protection algorithms practical verification using dSPACE^{TM} and DSP

In this subsection, the breaker actuation is tested to verify the behaviour of the algorithm, so in this case, the SSR can be used for ring and radial grids. After the physical grid, the SSR has the problem of the minimum required voltage for the current drive in the case of ring grid (Appendix C), but it works properly in the radial grid; this is the cause to change SSR to mechanical-breaker for ring grid.

In order to verify the proposed algorithms (CE-ZO) experimentally, the data of the simulated grid have been implemented in the laboratory using dSPACE^{TM}1104, then these data sent to the DSP for processing and decision-making step. In this section, this laboratory setup will be explained in detail. Several cases have been analysed for radial and ring grids with and without DG, and for different types of faults. Fig. 7.11 shows the control representation of the laboratory scheme, and Fig. 7.12 shows the conceptual diagram of the algorithm schemes tested in the laboratory.

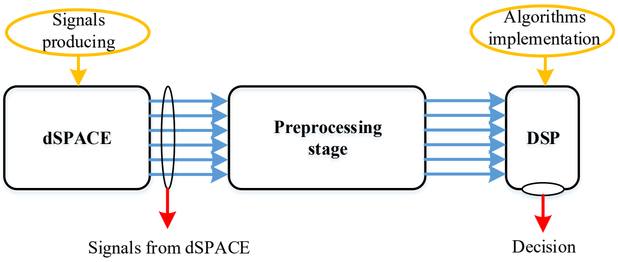
Signals producing
Algorithms implementation
dSPACE
Preprocessing stage
DSP
Signals from dSPACE
Decision

Fig. 7.11 Logic representation of laboratory scheme

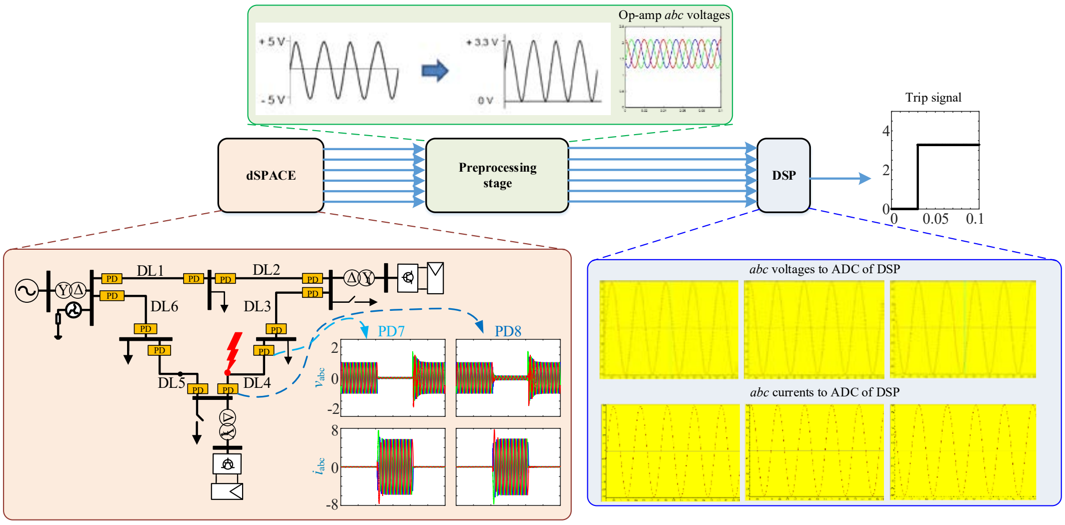
Op-amp abc voltages
+5V
-5V
+3.3V
0V
Trip signal
4
2
0
0
0.05
0.1
dSPACE
Preprocessing stage
DSP
DL1
DL2
DL6
DL3
DL5
DL4
PD
PD7
PD8
v_{abc}
2
0
-2
i_{abc}
8
0
-8
abc voltages to ADC of DSP
abc currents to ADC of DSP

Fig. 7.12 Conceptual diagram of the algorithm schemes tested in the laboratory

The total number of the implemented cases are shown in Appendix D. As an example of the analysed cases and to verify the proposed algorithm practically, the ring grid shown in Fig. 7.13(a) has been simulated using MATLAB^{TM} SIMULINK (Fig. 7.13(b)), and voltages and currents of the faulted line have been redeveloped practically using dSPACE^{TM}1104 (Fig. 7.13(c)). It should be noted that at this stage, the algorithms are tested using data collected from the dSPACETM1104, but because the physical grid had not yet been built at the time, the algorithm verification will take precedence. The explanation of the physical laboratory implementation and algorithm verification will be provided in the next subsection.

To execute the proposed algorithms and give the appropriate decision (trip signals), a numerical relay has been implemented using DSP TMS320F28335 and Crydom SSR. Fig. 7.13(a) shows the analysed ring grid, the parameters of the grid are shown in Table 7.4, and Table 7.5. The algorithm is tested during symmetrical and unsymmetrical faults at DL5. Fig. 7.13(c) shows the laboratory setup of the system, the trip signal from the DSP is sent to a three-phase SSRs at one end of the faulted line. Fig. 7.13(b) shows the conceptual diagram of the proposed algorithms to be implemented practically, respectively. Before sending the dSPACE^{TM} signals to the DSP, a pre-processing step has to be performed first to configure the analog output signals from the dSPACE^{TM} to the level of the DSP analog inputs by using an Operation Amplifier (Op-Amp) circuit, as shown in Fig. 7.13(b). The proposed algorithms use exclusively faulted line data. The faulted line data are sent from the dSPACE^{TM} to be processed by the DSP, and the data of the other healthy lines have been set internally inside the DSP. The trip signal is sent from the DSP digital outputs directly to the two SSRs located at the two ends of the faulted line. Using a graphical user interface (GUI), the signals (*abc* instantaneous voltages and currents of PD9 and PD10 generated from SIMULINK, shown in Fig. 7.14) produced from the dSPACE^{TM}, as seen in Fig. 7.13(c) are used to generate a fault indication signal to detect the start of the fault (grey color in Fig. 7.15). These signals are sent through the Digital to Analog Converter (DAC) of the dSPACE^{TM} to the Analog to Digital Converter (ADC) of the DSP to execute the algorithm and give the appropriate trip signal.

Fig. 7.15 shows the delay time between the fault occurrence and the output decision of the CE and ZO algorithms from the DSP in the case of three-phase fault and single-phase fault in DL5, as shown in Fig. 7.13(a). When the fault occurs, the level signal goes from 0 to 1 V (red color), which means the fault starts. Nevertheless, when the output of the DSP is 3.3 V, which means the trip signal has been activated (black color), this trip signal is obtained from the decision signals of the CE and ZO algorithms (Appendix D). For both algorithms, the system's response is similar, which strongly influences the accuracy and reliability of the proposed protection strategy.

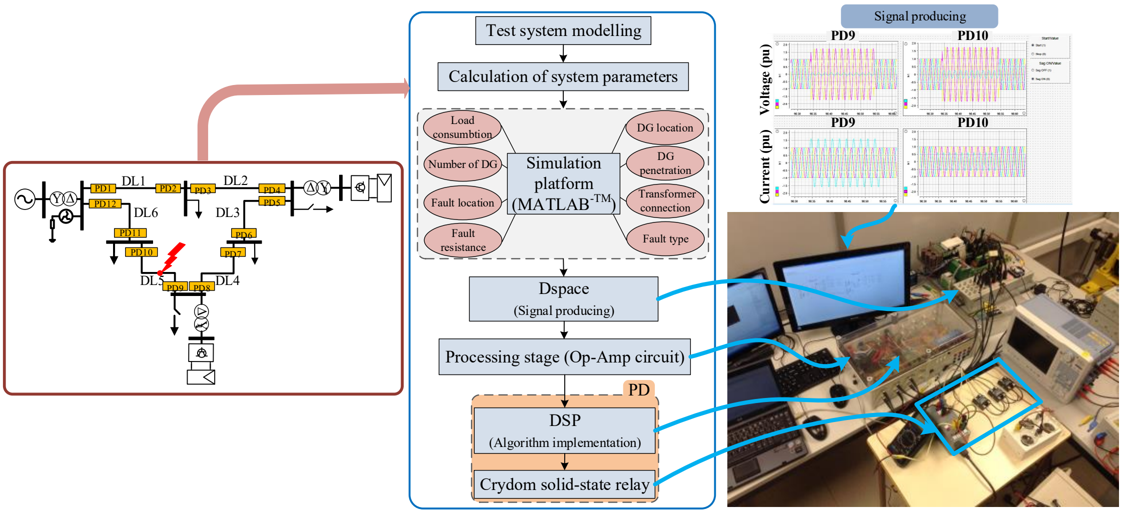
PD1
PD2
PD3
PD4
PD5
PD6
PD7
PD8
PD9
PD10
PD11
PD12
DL1
DL2
DL3
DL4
DL5
DL6
Test system modelling
Calculation of system parameters
Load consumbtion
Number of DG
Fault location
Fault resistance
Simulation platform (MATLAB-TM)
DG location
DG penetration
Transformer connection
Fault type
Dspace (Signal producing)
Processing stage (Op-Amp circuit)
PD
DSP (Algorithm implementation)
Crydom solid-state relay
Signal producing
PD9
PD10
Voltage (pu)
Current (pu)

(a) (b) (c)

Fig. 7.13 Procedure of the experimental verification (a) Analysed grid, (b) Concept diagram of the proposed algorithms practically, (c) Laboratory setup

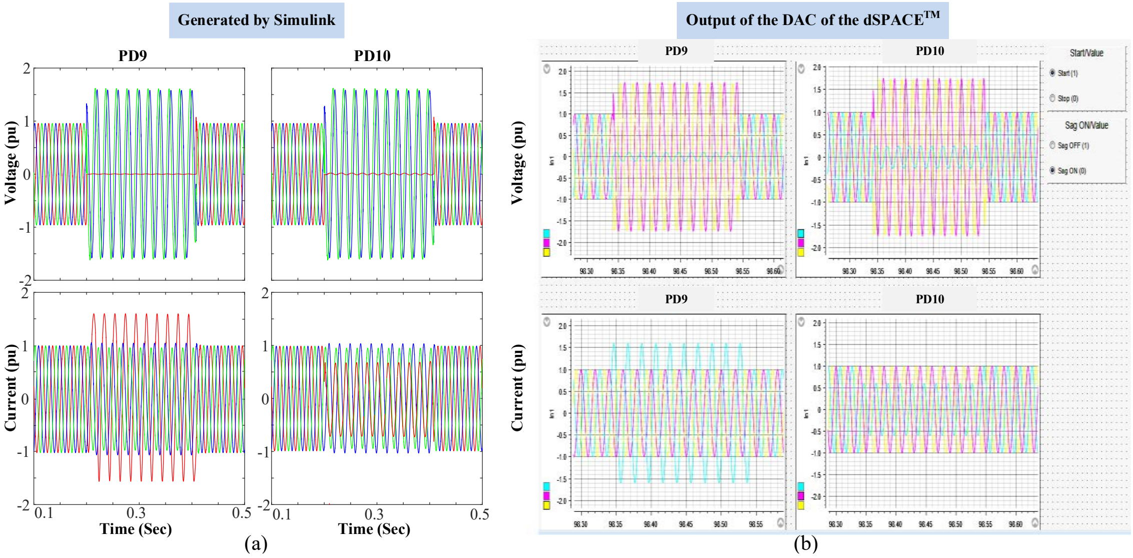

(a) (b)

Fig. 7.14 *abc* voltages and currents of PD9 and PD10 during a single-phase fault at DL5 (a) generated from SIMULINK, (b) Output of dSPACE™ DAC.

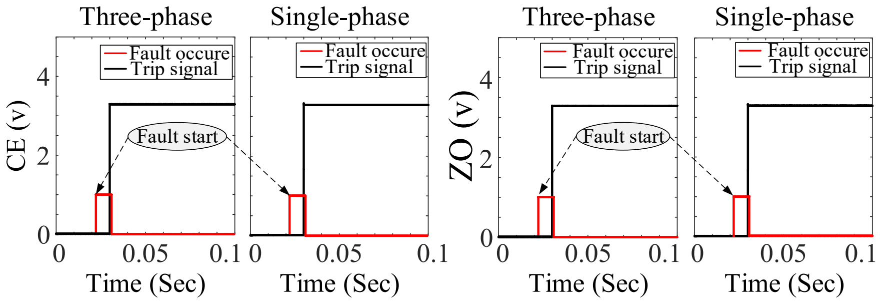

(a) (b)

Fig. 7.15 Digital output of the fault location algorithm decision and fault occurrence in case of three-phase fault, and single-phase fault for (a) CE and (b) ZO

In this section, CE-ZO algorithms are checked. In the following subsections, the three protection algorithms (CE-ZO, LO) have to be checked using the physical grid.

7.2.2. Experimental implementation and verification of the proposed protection algorithms using the physical scaled grid

In this section, the experimental verification of the proposed algorithms is presented using a physical scaled grid in a different grid configuration, along with comparing the conventional protection strategies (OCR, and DR) and the three proposed protection algorithms (CE, ZO, and LO). The system parameters can be seen in section 7.2.2.1.

In order to verify the proposed algorithm practically, an equivalent model has been built in the laboratory to give the same response and the same dynamic behaviour of the analysed ring and radial grid. Two network configurations have been studied, one ring and another radial grid, with and without DGs. In order to implement the proposed algorithm, a numerical relay based on DSP has been used to process the measurement data obtained from the sensors, then execute the algorithms, and finally give the appropriate decision (trip signals). The SSR is used as a PD in the analysed radial grids; however, the SSR is replaced by a mechanical relay in the analysed ring grids (section 7.2). Fig. 7.16 shows the ring grid implemented in the laboratory, and Table 7.3 shows the parameters of the devices used to implement the grid. The grid was built in the laboratory with aggregated lines to simplify the test but not affect the complete analysis due to the symmetry. Nevertheless, similar behaviour has been obtained. In addition, to emulate the impedance of the main grid, an inductor is added before bus 1 to emulate the grid, as shown in Fig. 7.16; the calculation of this inductance can be seen in Appendix G.

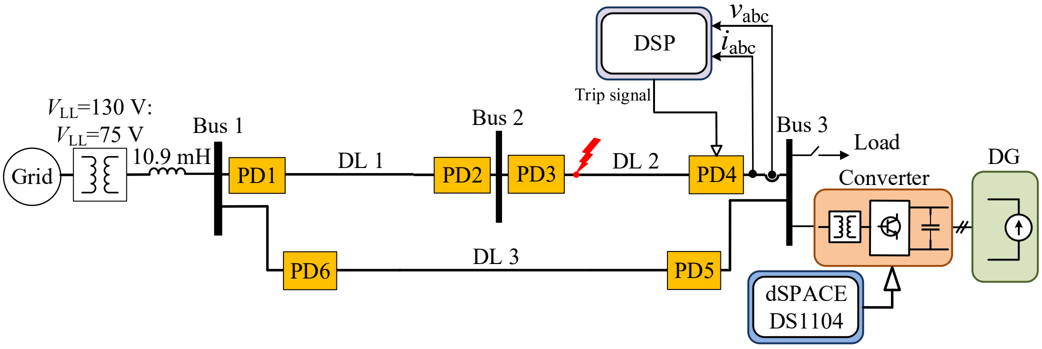

Fig. 7.16 Implemented ring grid in the laboratory

Table 7.3 List of grid components and their parameters:

Device	Parameters
Smart source	Rated power = 4.5 kVA
Three-phase power transformer	Rated power = 7.5 kVA, Rated L-L voltages: 380/220 V
Zigzag transformer inductance	L_{zigzag} = 6.9 mH
Inductor to emulate the grid	L_E = 10.94 mH ≈ 11 mH
Fault resistance per phase	R = 2.3 Ω

The calculation of the base values and the calculation of the laboratory grid parameters is explained in the next subsection. The complete explanation of the system parameters can be found in Appendix G.

7.2.2.1. Calculation of system parameters

It can be observed that the idea is to obtain the same voltages, currents, and impedances in pu in the implemented laboratory system with a perfect agreement with the real system. The base values of the real DS grid are: V_{Base} = 20kV, S_{Base} = 25 MVA, and I_{Base} = 721.69 A. The base values for both systems are shown in Table 7.5. These values are chosen to give the same pu voltage and current during steady-state in both grids; the idea is to fix the laboratory base values to work with reduced voltages and currents; nevertheless, the pu results are the same that the values obtained in the real grid. The calculation of these values is justified in Appendix G.

- Calculation of line parameters:

In order to calculate the base values of the grid implemented in the laboratory, the following equations are used, where V_{Base}, I_{Base}, S_{Base}, and Z_{Base} are the base voltage, current, apparent power, and grid impedance, respectively. The justification of these values is shown in Appendix G.

$$\begin{gathered} V_{\text{Base}} = 75\ \text{V}, \quad I_{\text{Base}_{\text{rms}}} = 2.4\ \text{A}, \\ S_{\text{Base}} = \sqrt{3} \cdot V_{\text{Base}} \cdot I_{\text{Base}_{\text{rms}}} = 540\ \text{W}, \quad Z_{\text{Base}} = \frac{V_{\text{Base}}}{I_{\text{Base}_{\text{rms}}}} = \frac{75}{2.4} = 31.25\ \Omega. \end{gathered} \tag{35}$$

The resistance of the analysed grid is 0.32 Ω, for 2 km, and since the base value of the grid is 16 Ω, as explained in chapter 3. Therefore, the pu value is

$$R_{\text{pu}} = \frac{0.32}{Z_{\text{Base}} = 16} = 0.02. \tag{36}$$

In order to calculate the corresponding resistance value for the grid implemented in the laboratory, (37) is used

$$R_{\text{Lab}} = R_{\text{pu}} \cdot Z_{\text{Base}} = 0.02 \cdot 31.25 = 0.625\ \Omega \ \text{ or } \ R_{\text{Lab}} = \frac{0.32 \cdot 31.25}{16} = 0.625\ \Omega. \tag{37}$$

The inductance of the analysed grid is 2*πf**L, L = 3.4696e-04 H. So, X_L = 0.218 Ω for 2 km. Since the base value of the real grid is 16 Ω. So, the pu value is

$$X_{\text{Lpu}} = \frac{0.218}{16} = 0.0136. \tag{38}$$

Therefore, the inductance of the implemented grid in the laboratory is calculated using (39).

$$X_{\text{LLab}} = X_{\text{Lpu}} \cdot Z_{\text{Base}} = 0.0136 \cdot 31.25 = 0.4304\ \Omega \text{ or } X_{\text{LLab}} = \frac{0.218 \cdot 31.25}{16} = 0.4304\ \Omega. \tag{39}$$

The capacitance of the analysed grid is $R_{\text{pu}} = \frac{1}{2\pi \text{f}C} = \frac{1}{2\pi(50)(0.309\text{e-}6)} = 1.0301\text{e+}04$. Since the base value of the real grid is 16 Ω. Therefore, the pu value is

$$X_{\text{Cpu}} = \frac{10301}{16} = 643.8307. \tag{40}$$

Therefore, the capacitance of the implemented grid in the laboratory is calculated using (42).

$$X_{\text{CLab}} = X_{\text{Cpu}} \cdot Z_{\text{Base}} = 643.83 \cdot 31.25 = 2.0120\text{e+}04\ \Omega \text{ or } X_{\text{CLab}} = \frac{10301 \cdot 31.25}{16} = 2.0120\text{e+}04\ \Omega \tag{41}$$

$$C = \frac{1}{2\pi \text{f} X_{\text{C}}} = 0.158\ \mu\text{F}. \tag{42}$$

- Calculation of zigzag impedance

The impedance of the zigzag grounding transformer for a fault current (I_f) = 500 A is calculated using

$$X_{\text{zigzag\_real}} = \frac{V_{\text{base}_{\text{ph}}}}{I_{\text{f}}/3} = \frac{20000/\sqrt{3}}{500/3} = 69.282\ \Omega, \tag{43}$$

and the pu value is calculated using

$$X_{\text{zigzag\_Lab}} = \frac{X_{\text{zigzag\_real}}}{Z_{\text{base\_real}}} * Z_{\text{base\_Lab}} = \frac{69.282}{16} * 31.25 = 135.32\ \Omega. \tag{44}$$

- Calculation of fault resistance:

The calculation of the fault resistance for the analysed grid and the grid implemented in the laboratory is obtained using

$$\begin{gathered} R_{\text{fault\_real}} = 1.193\ \Omega,\ R_{\text{fault\_pu}} = \frac{R_{\text{fault\_real}}}{Z_{\text{base\_real}}} = \frac{1.193}{16} = 0.0746 \\ R_{\text{fault\_Lab}} = R_{\text{fault\_pu}} * Z_{\text{base\_Lab}} = 0.0746 * 31.25 = 2.3312\ \Omega. \end{gathered} \tag{45}$$

Therefore, the pu values for the implemented grid in the laboratory can be summarized as follow

$$\begin{gathered} R_{\text{Line\_pu}} = 0.02,\ X_{\text{L}_{\text{Line\_pu}}} = j0.0138,\ C = \frac{1}{2\pi \text{f} X_{\text{C}}} = 0.158\ \mu\text{F},\ R_{\text{fault\_pu}} = 0.0746, \\ V_{\text{fault\_pu}} = 0.5911,\ I_{\text{fault\_pu}} = 6.183. \end{gathered} \tag{46}$$

Table 7.4 shows the laboratory grid parameters, and Table 7.5 compares these parameters with the analysed real grids.

Table 7.4 System parameters

CINERGIA^{TM} Inverter	Rated power	10 kVA
	Rated voltage	400 V
Filter	Inductance (L)	10 mH
	Resistance (R)	0.2 Ω
DC bus	DC rated voltage	800 V
Three-phase Pacific^{TM} Smart Power Source	345AMXT	4.5 kVA
SSR	Crydom H12WD4850	48-660 VAC
Distribution Lines (DL1, DL2, DL3)	Inductance (L_1, L_2, L_3)	1.37, 2.74, 4.11 mH
	Resistance (R_1, R_2, R_3)	625, 1250, 1875 mΩ
	Capacitance (C_1, C_2, C_3)	0.316, 0.632, 10, 30 µF
Loads	Inductance (L_1, L_2)	10, 30 mH
	Resistance (R_1, R_2)	14.5, 42 Ω

Table 7.5 Comparison between the real grid and the laboratory grid parameters

	Analysed grid	**Laboratory grid**
Base voltage	$V_{\text{Base}} = 20$ kV	$V_{\text{Base}} = 75$ V
Base apparent power	$S_{\text{Base}} = 25$ MVA	$S_{\text{Base}} = 540$ W
Base current	$I_{\text{Base}_{\text{rms}}} = 721.69$ A	$I_{\text{Base}_{\text{rms}}} = 2.4$ A
Base impedance	$Z_{\text{Base}} = 16\ \Omega$	$Z_{\text{Base}} = 31.25\ \Omega$
Line resistance	$R_{\text{Line\_pu}} = 0.02$ pu	$R_{\text{Line\_pu}} = 0.02$ pu
Line inductance	$X_{\text{L}_{\text{Line\_pu}}} = j0.0136$ pu	$X_{\text{L}_{\text{Line\_pu}}} = j0.0138$ pu
Fault resistance	$R_{\text{fault\_pu}} = 0.0746$ pu	$R_{\text{fault\_pu}} = 0.0746$ pu

Some conclusions can be deduced from Table 7.5: 1) the pu values are the same in both grids, so the same behaviour will be tested, 2) for CE and ZO techniques, no need to modify the algorithm because the idea in both techniques depends on the power flow direction, not the magnitude. However, for the LO, the algorithm needs to be adapted to the new grid scale.

In the next point, the results and discussion of the protection algorithms implemented practically in the laboratory is demonstrated.

7.2.2.2. Experimental results discussion of the proposed protection algorithms (CE, ZO, and LO)

Three grid configurations have been implemented and tested in the laboratory:

1- Simplified radial grid with one line, as shown in Fig. 7.17, to emulate a simplified grid.
2- A complete radial grid consists of three lines, as shown in Fig. 7.18, to emulate the real analysed grid. DL1 is equivalent to one DL, DL2 is equivalent to two DLs, and DL3 is equivalent to three DLs.
3- The ring grid consists of three lines, as shown in Fig. 7.19, to emulate the real analysed grid.

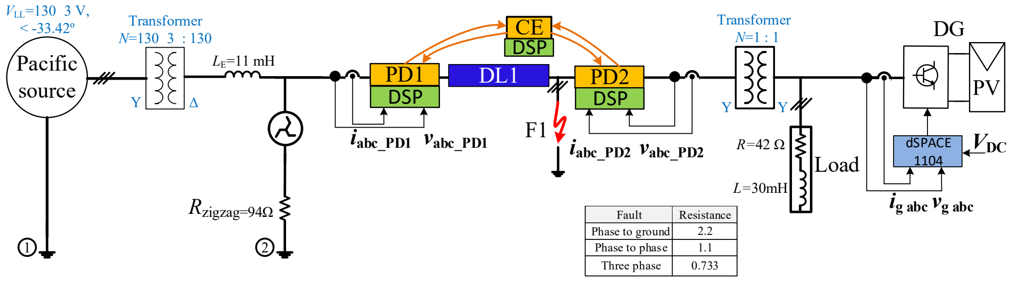
VLL=130 3 V,
< -33.42º
Pacific source
Transformer
N=130 3 : 130
Y
Δ
LE=11 mH
Rzigzag=94Ω
①
②
CE
DSP
PD1
DSP
DL1
PD2
DSP
F1
iabc_PD1 vabc_PD1
iabc_PD2 vabc_PD2
Transformer
N=1 : 1
Y
Y
R=42 Ω
L=30mH
Load
DG
PV
dSPACE 1104
VDC
ig abc vg abc
Fault | Resistance
Phase to ground | 2.2
Phase to phase | 1.1
Three phase | 0.733

Fig. 7.17 Simplified radial grid

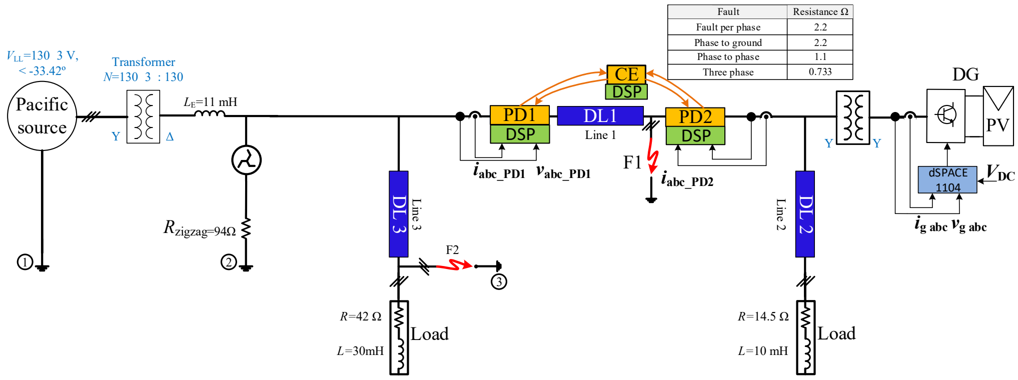
Fault | Resistance Ω
Fault per phase | 2.2
Phase to ground | 2.2
Phase to phase | 1.1
Three phase | 0.733
VLL=130 3 V,
< -33.42º
Pacific source
Transformer
N=130 3 : 130
Y
Δ
LE=11 mH
Rzigzag=94Ω
①
②
③
CE
DSP
PD1
DSP
DL1
Line 1
PD2
DSP
F1
F2
iabc_PD1 vabc_PD1
iabc_PD2
DL 3
Line 3
DL 2
Line 2
R=42 Ω
L=30mH
Load
R=14.5 Ω
L=10 mH
Load
DG
PV
dSPACE 1104
VDC
ig abc vg abc
Y
Y

Fig. 7.18 Complete Radial grid

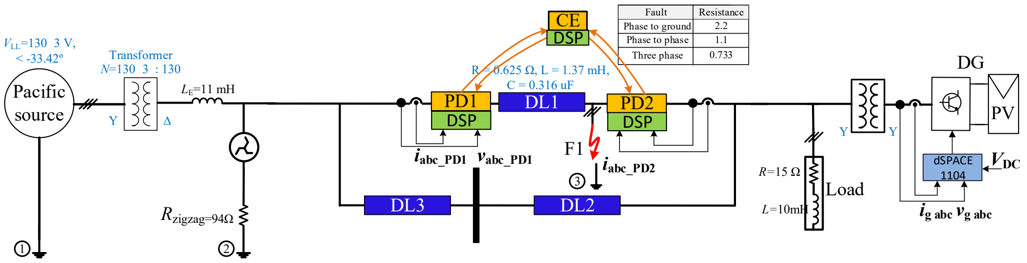
CE
DSP
Fault | Resistance
Phase to ground | 2.2
Phase to phase | 1.1
Three phase | 0.733
VLL=130 3 V,
< -33.42º
Pacific source
Transformer
N=130 3 : 130
Y
Δ
LE=11 mH
Rzigzag=94Ω
①
②
③
R = 0.625 Ω, L = 1.37 mH,
C = 0.316 uF
PD1
DSP
DL1
PD2
DSP
F1
iabc_PD1 vabc_PD1
iabc_PD2
DL3
DL2
R=15 Ω
L=10mH
Load
DG
PV
dSPACE 1104
VDC
ig abc vg abc
Y
Y

Fig. 7.19 Ring grid

Points 1, 2, and 3 in the previous figures are connected to the same point, which is the ground of the pacific smart source; also, the load is connected in an isolated star connection.

The following results are some examples of the total 70 cases to emphasize the importance of the CE, ZO, and LO protection algorithms; the rest of the results can be seen in Appendix D. The flowchart of the selected cases is shown in Fig. 7.20. For each algorithm, various grid scenarios have been studied, as the influence of grid configurations, fault type, fault location, DG penetration, classical and AI protection algorithms, and current control strategies.

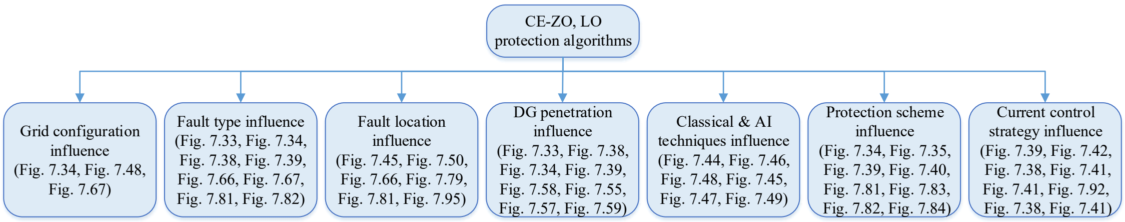
CE-ZO, LO protection algorithms
Grid configuration influence (Fig. 7.34, Fig. 7.48, Fig. 7.67)
Fault type influence (Fig. 7.33, Fig. 7.34, Fig. 7.38, Fig. 7.39, Fig. 7.66, Fig. 7.67, Fig. 7.81, Fig. 7.82)
Fault location influence (Fig. 7.45, Fig. 7.50, Fig. 7.66, Fig. 7.79, Fig. 7.81, Fig. 7.95)
DG penetration influence (Fig. 7.33, Fig. 7.38, Fig. 7.34, Fig. 7.39, Fig. 7.58, Fig. 7.55, Fig. 7.57, Fig. 7.59)
Classical & AI techniques influence (Fig. 7.44, Fig. 7.46, Fig. 7.48, Fig. 7.45, Fig. 7.47, Fig. 7.49)
Protection scheme influence (Fig. 7.34, Fig. 7.35, Fig. 7.39, Fig. 7.40, Fig. 7.81, Fig. 7.83, Fig. 7.82, Fig. 7.84)
Current control strategy influence (Fig. 7.39, Fig. 7.42, Fig. 7.38, Fig. 7.41, Fig. 7.41, Fig. 7.92, Fig. 7.38, Fig. 7.41)

Fig. 7.20 Flowchart of the studied cases

The methodology can be adapted to other grid configurations. The scheme is tested with other grid configurations changing load consumption, DG penetration, different fault locations, fault types, and (HV/MV) transformer configuration [37]. The analysed grid is an example to test the functionality of the protection algorithms. The proposed algorithms could be applied to other grids, but in this case, CE and LO algorithms have to be modified according to the explanations in chapter 5. ZO algorithm can be applied to other grids without any change. If the topology of the grid changes, the CE needs to be adapted to the new number of PDs; LO has to consider the new grid scale; however, ZO does not require any adaptation, as shown in Fig. 7.21, and Fig. 7.22.

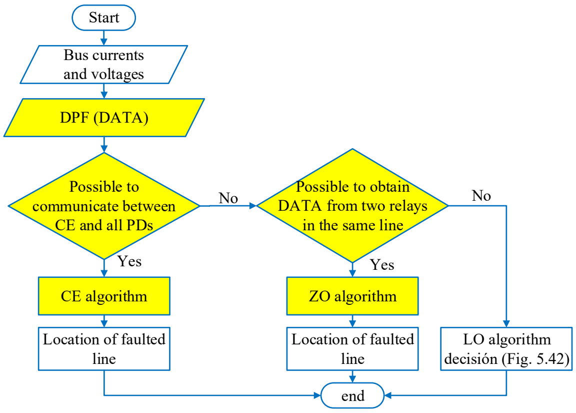
Start
Bus currents and voltages
DPF (DATA)
Possible to communicate between CE and all PDs
No
Possible to obtain DATA from two relays in the same line
No
Yes
Yes
CE algorithm
ZO algorithm
Location of faulted line
Location of faulted line
LO algorithm decisión (Fig. 5.42)
end

Fig. 7.21 Flowchart of the proposed CE-ZO protection algorithms

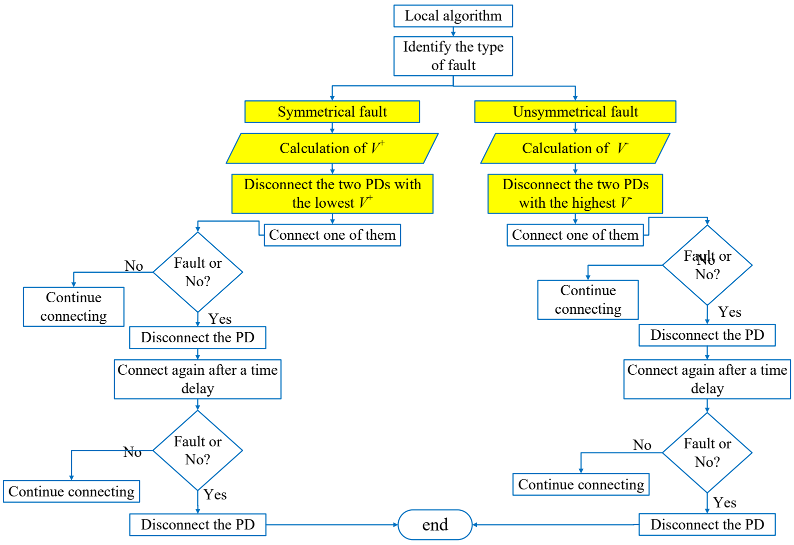
Local algorithm
Identify the type of fault
Symmetrical fault
Unsymmetrical fault
Calculation of V^+
Calculation of V^-
Disconnect the two PDs with the lowest V^+
Disconnect the two PDs with the highest V^-
Connect one of them
Connect one of them
No
Fault or No?
Fault or No?
No
Continue connecting
Continue connecting
Yes
Yes
Disconnect the PD
Disconnect the PD
Connect again after a time delay
Connect again after a time delay
Fault or No?
No
Fault or No?
No
Continue connecting
Continue connecting
Yes
Yes
Disconnect the PD
end
Disconnect the PD

Fig. 7.22 Flowchart of the LO proposed protection algorithm

The protection strategy is tested practically for which the grid shown in Fig. 7.9 has been adapted, and an equivalent system has been built experimentally in the laboratory as shown in Fig. 7.23(c), and Fig. 7.24. The base values for the DS shown in Fig. 7.9 are: v_B = 20 kV, i_B = 721.7 A, Z_B = 16 Ω, and for the grid shown in Fig. 7.19 are: v_B = 75*√3 V, i_B = 2.4 A, Z_B = 31.25 Ω. Fig. 7.23(a) shows the conceptual diagram of the algorithms to be implemented practically. Three DSPs TMS320F28335 have been used to implement the CE and ZO protection algorithms, as seen in Fig. 7.23(c). As explained in the previous section, the ZO control is implemented in both PDs in the same DL (two DSPs), and the CE control obtains signals from all the devices (one DSPs). Besides, the inverter control was implemented using ControlDesk and dSPACE^{TM} DS1104. All the protection algorithms and inverter control have been programmed using MATLAB^{TM} software because the software selected to ease the implementation of the control system, considering the laboratory components. As seen in Fig. 7.23(b), the CE controller obtains the faulted line data from the DSPs located at the ends of this line. However, the data corresponding to the rest of the PDs are imposed in the DSP of the CE controller due to the lack of the DSPs in all the lines.

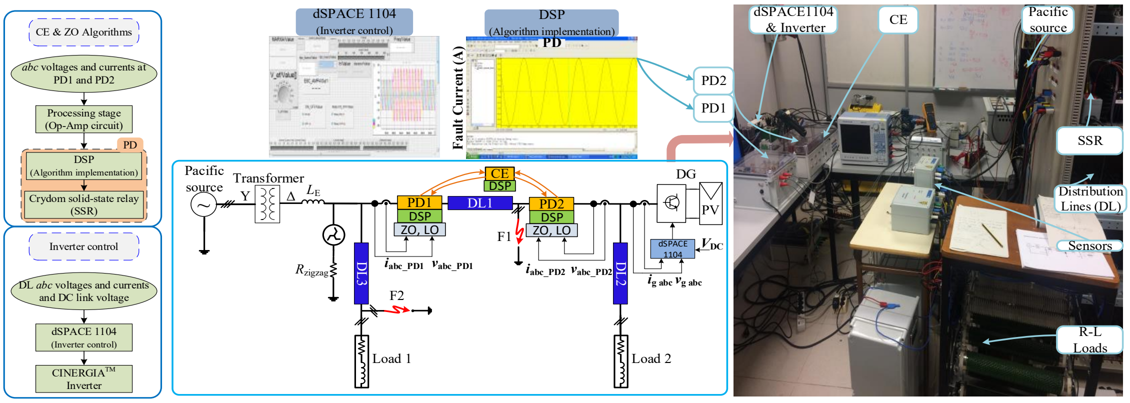
CE & ZO Algorithms
abc voltages and currents at PD1 and PD2
Processing stage (Op-Amp circuit)
PD
DSP (Algorithm implementation)
Crydom solid-state relay (SSR)
Inverter control
DL abc voltages and currents and DC link voltage
dSPACE 1104 (Inverter control)
CINERGIA™ Inverter
dSPACE 1104 (Inverter control)
DSP (Algorithm implementation)
PD
Fault Current (A)
PD2
PD1
Pacific source
Transformer
Y
Δ
L_E
CE
DSP
PD1
DSP
ZO, LO
DL1
PD2
DSP
ZO, LO
F1
DG
PV
dSPACE 1104
V_{DC}
R_{zigzag}
DL3
i_{abc_PD1}
v_{abc_PD1}
i_{abc_PD2}
v_{abc_PD2}
DL2
$i_{g\ abc}$
$v_{g\ abc}$
F2
Load 1
Load 2
dSPACE1104 & Inverter
CE
Pacific source
SSR
Distribution Lines (DL)
Sensors
R-L Loads

Fig. 7.23 Procedure of the experimental verification (a) Concept diagram of the proposed algorithms (b) Analysed grid, (c) Laboratory setup

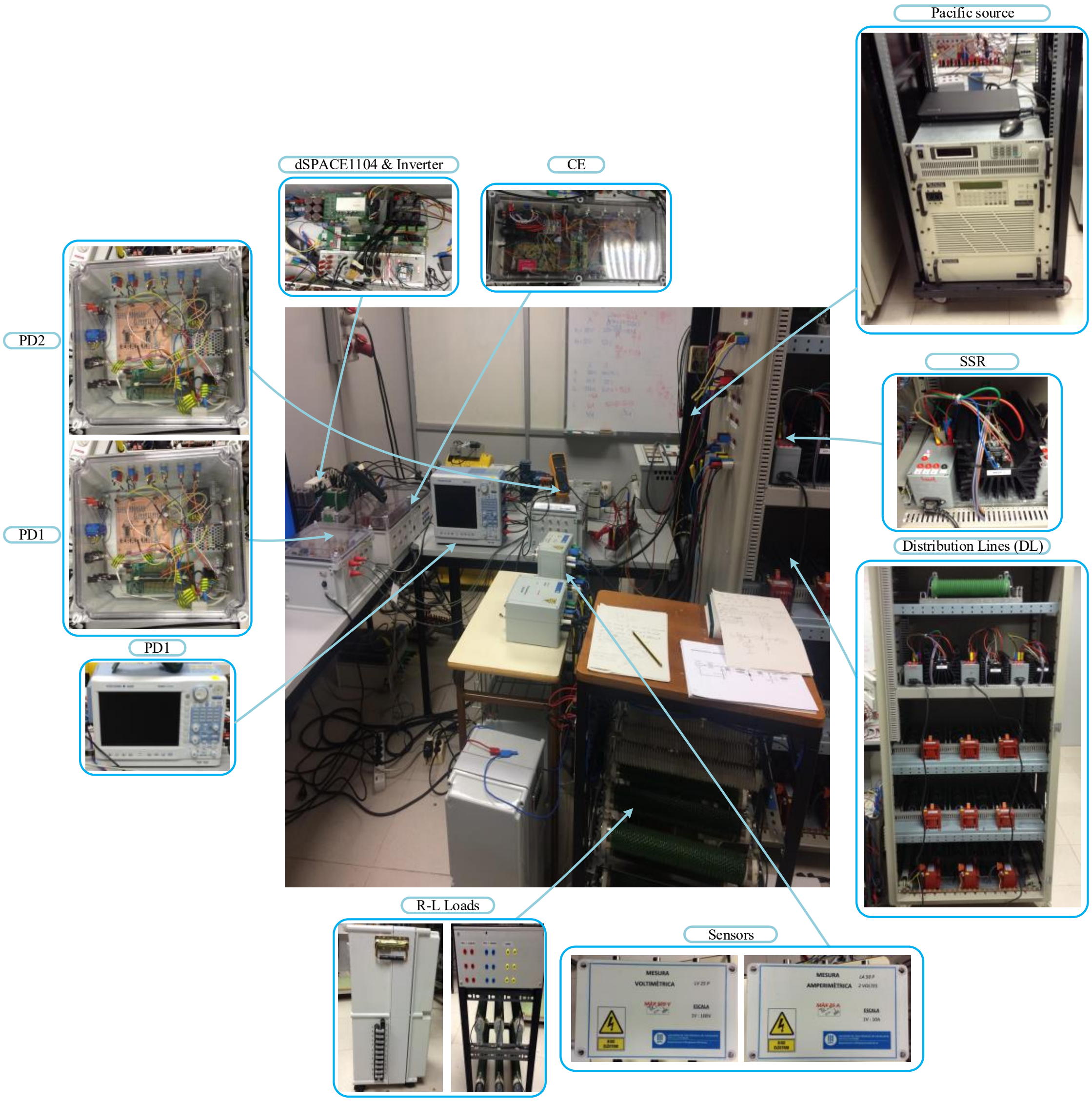
Pacific source
dSPACE1104 & Inverter
CE
PD2
PD1
PD1
SSR
Distribution Lines (DL)
R-L Loads
Sensors

Fig. 7.24 Complete laboratory setup

In the case of radial grids, the proposed algorithms have been tested practically with different scenarios as shown in Table 7.6. Also, in the case of ring grids, the proposed algorithms have been tested practically with different scenarios, as shown in Table 7.7.

Table 7.6 Some of the experimentally tested cases for radial grids

Experiment	Fault location	DG penetration	Protection Algorithm	Fault type
(1)	DL1	No	OCR	1 phG
			DR	3 ph
			CE & ZO	
			LO	
(2)	DL1	Yes	OCR	1 phG
			DR	3 ph
			CE & ZO	
			LO	
(3)	DL3	No	OCR	1 phG
			DR	3 ph
			CE & ZO	
			LO	
(4)	DL3	Yes	OCR	1 phG
			DR	3 ph
			CE & ZO	
			LO	

Table 7.7 Some of the experimentally tested cases for ring grid

Experiment	Fault location	DG penetration	Protection algorithm	Fault type
(1)	DL1	No	CE & ZO	1 phG
				3 ph
				2 phG
			LO	1 phG
				3 ph
				2 phG
(2)	DL1	Yes	CE & ZO	1 phG
				3 ph
				2 phG
			LO	1 phG
				3 ph
				2 phG
(3)	DL3	No	CE & ZO	1 phG
				3 ph
			LO	1 phG
				3 ph
(4)	DL3	Yes	CE & ZO	1 phG
				3 ph
			LO	1 phG
				3 ph
(5)	DL2	No	CE & ZO	1 phG
				3 ph
			LO	1 phG
				3 ph
(6)	DL2	Yes	CE & ZO	1 phG
				3 ph
			LO	1 phG
				3 ph

Table 7.7 Cont'd

Experiment	Fault location	DG penetration	Protection algorithm	Fault type
(7)	DL1	No	LO (No Recloser)	1 phG
				3 ph
			LO (Recloser)	1 phG
				3 ph
(8)	DL1	Yes	LO (No Recloser)	1 phG
				3 ph
			LO (Recloser)	1 phG
				3 ph

Where 1phG refers to single-phase to ground faults, 2phG refers to two-phase to ground faults, and 3ph refers to three-phase faults.

In the following subsections, some of the cases implemented in the laboratory shown in Table 7.6, and Table 7.7 is presented to show the functionality of the proposed protection schemes practically in different scenarios. In addition, the practical and simulation experiments are compared to validate the results. The rest of the results are presented in Appendix E.

It is essential to mention that the sensor and communications delay (0.5 ms) in the experimental results are included in the simulation to show that the results agree, as shown in Fig. 7.25, which strongly influences the accuracy reliability of the proposed protection algorithms.

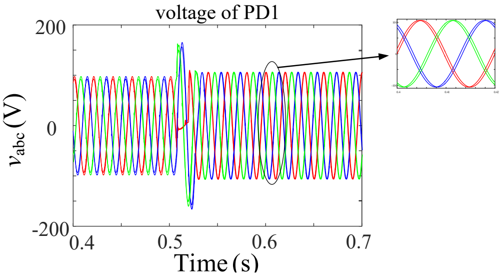

Fig. 7.25 delay between experimental and simulated *abc* voltage at PD1

7.2.2.3. Simplified radial grid without DG

Fig. 7.26 shows the grid implemented in the laboratory to emulate the simplified radial grid without DG. The protection algorithms have been tested for both symmetrical (three-phase) and unsymmetrical (single-phase to ground) faults. The algorithms are tested for the rest of the fault types by simulation, as seen in Appendix B. As seen in Fig. 7.28 and Fig. 7.29 the behaviour of CE-ZO algorithm has been tested for both types of faults. The figures show the *abc* voltages and *abc* currents for both PDs (PD1, and PD2) at each end of DL1. Also, the third row shows the trip signal versus the fault. As shown, the trip signal is executed in approximately 12 ms, and as the grid consists of one line, the trip of one or two PDs will result in a complete disconnection of the line. CE and ZO are checked together as the trip signal depends on the priority check explained in chapter 5, and can be seen in Fig. 7.27. In addition, the simulation and experimental results (in Fig. 7.28 and Fig. 7.29) have been compared to highlight and confirm the correctness of the practical results.

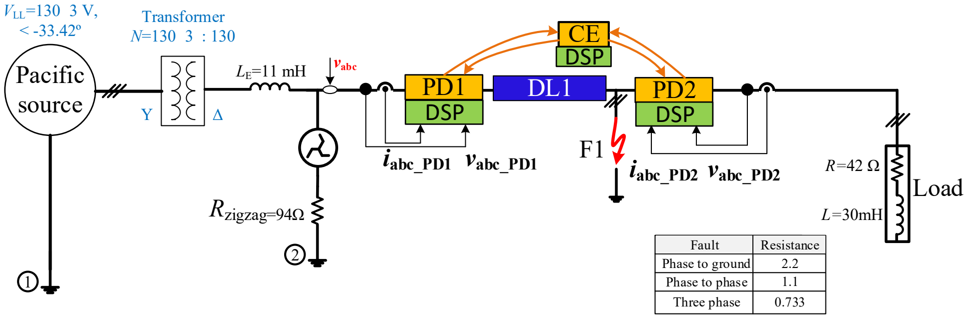

Fault	Resistance
Phase to ground	2.2
Phase to phase	1.1
Three phase	0.733

Fig. 7.26 Scheme of the simplified radial grid without DG

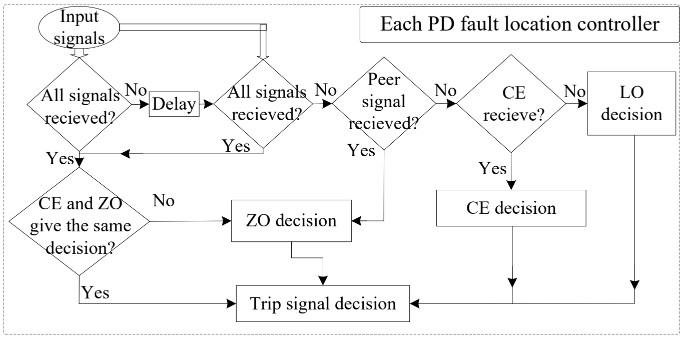
Input signals
Each PD fault location controller
All signals recieved?
No
Delay
All signals recieved?
No
Peer signal recieved?
No
CE recieve?
No
LO decision
Yes
Yes
Yes
Yes
CE and ZO give the same decision?
No
ZO decision
CE decision
Yes
Trip signal decision

Fig. 7.27 Flowchart of the priority algorithm

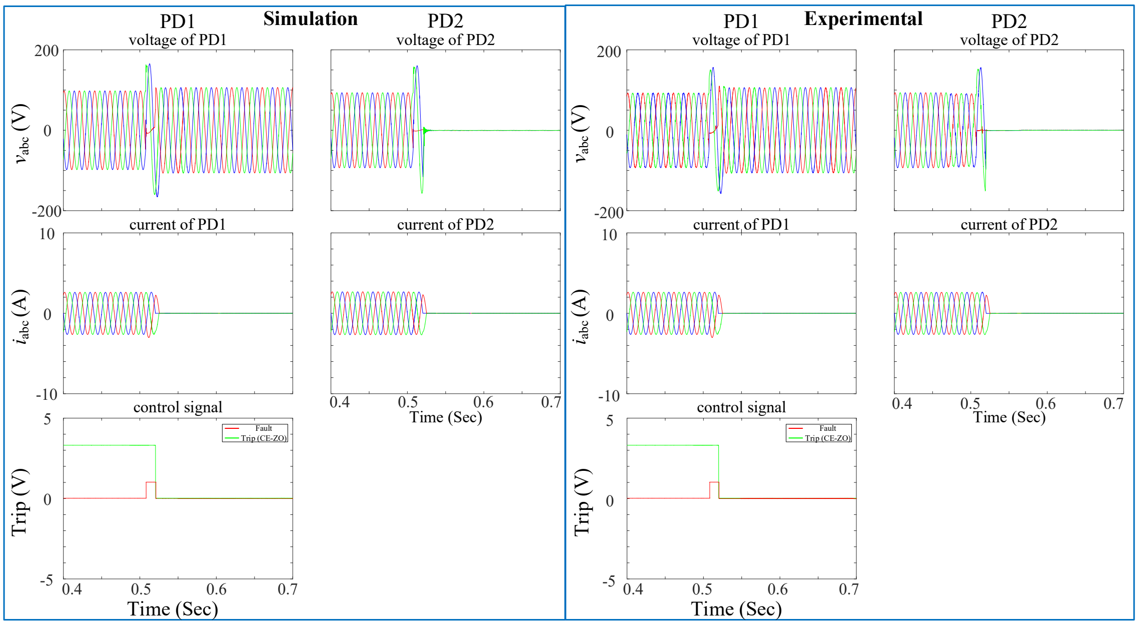

Fig. 7.28 Behaviour of CE-ZO control for single-phase to ground fault

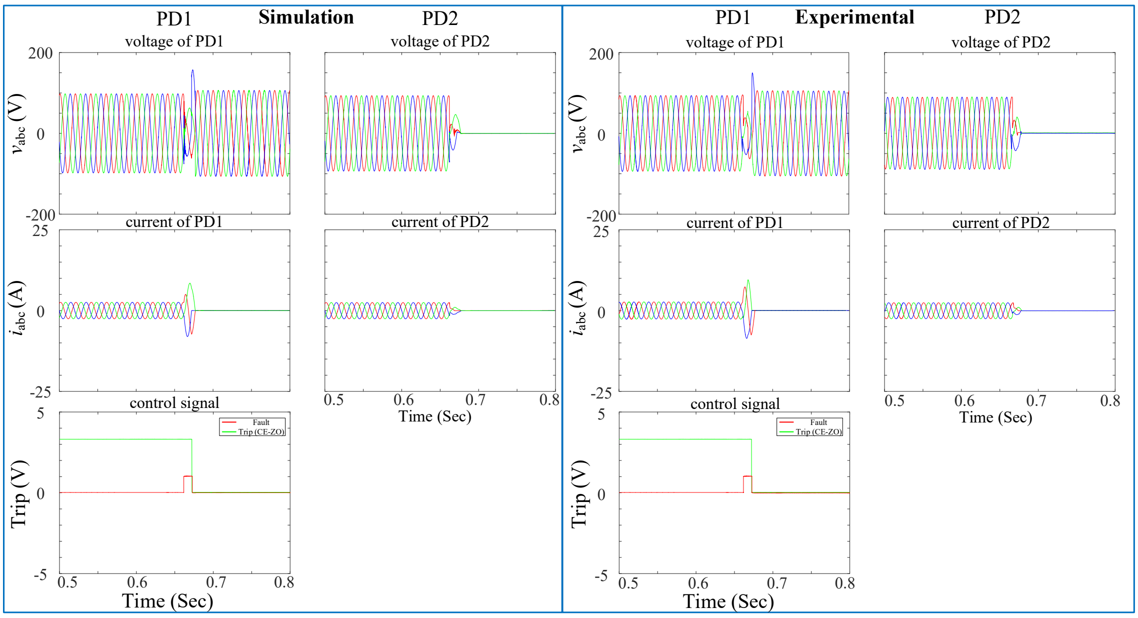

Fig. 7.29 Behaviour of CE-ZO control for three-phase fault

In addition, Fig. 7.30 shows the *abc* voltages, currents and trip signals at PD1 and PD2 located at each end of DL1. The behaviour of the LO algorithm for a three-phase fault has been analysed (more results can be seen in Appendix B). As the fault is near PD2, PD2 will disconnect first at $t \approx 0.17$ s, and then PD1 will disconnect later at $t \approx 0.21$ s. Because the value of the positive-sequence voltage at PD2 is less than the value at PD1, therefore, using the definite-time curve explained in chapter 5, the trip time can be determined for both PDs. It must be mentioned that the values of the positive- and negative sequence voltages obtained from the definite-time curve must be scaled to the values of the implemented grid in the laboratory, to have suitable values.

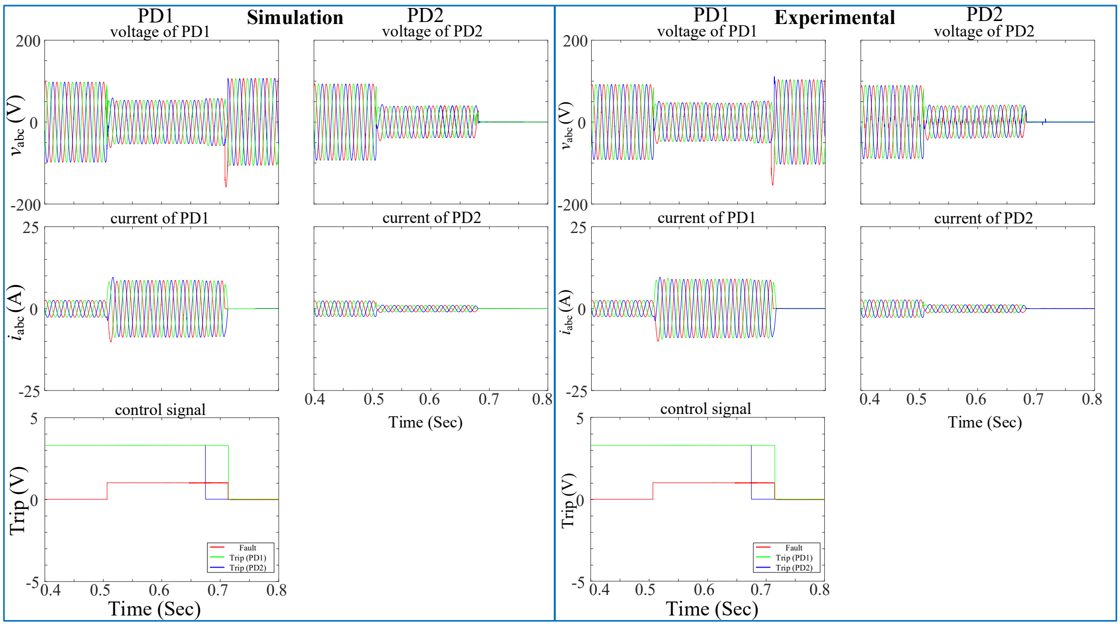

Fig. 7.30 Behaviour of LO control for three-phase fault

Fig. 7.31 shows the scaled definite-time curves for the positive-sequence voltage divided by 100 and the negative-sequence voltage divided by 300. These values are chosen to scale the definite-time curves to a lower value match with the values obtained in the laboratory. Fig. 7.32 shows the difference in the trip time between CE-ZO algorithms (green line) and LO algorithm (black and blue lines for PD1 and PD2, respectively) when a three-phase fault occurs at DL1 as shown in Fig. 7.26. As seen, the trip time is faster in the case of CE-ZO as they do not depend on the definite-time curve, but depend on the DPF.

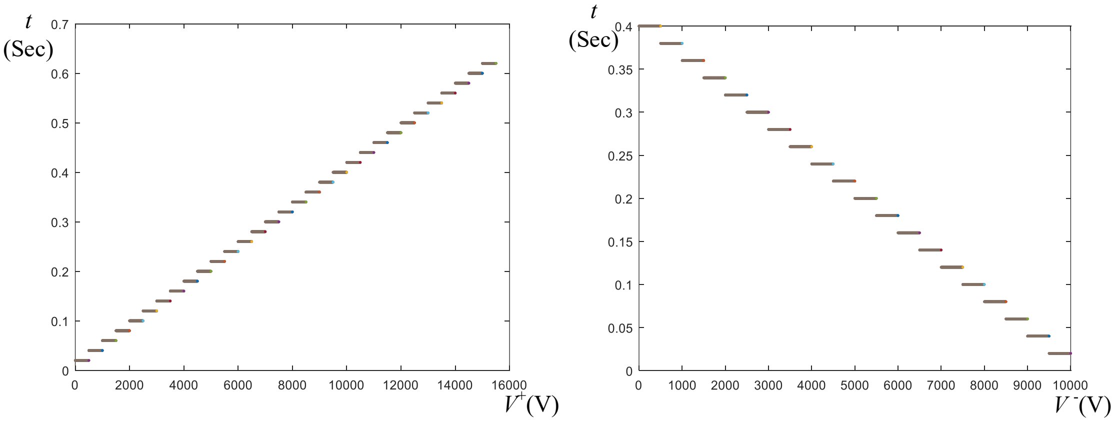

Fig. 7.31 Definite time curve (a) Positive sequence voltage, (b) Negative sequence voltage

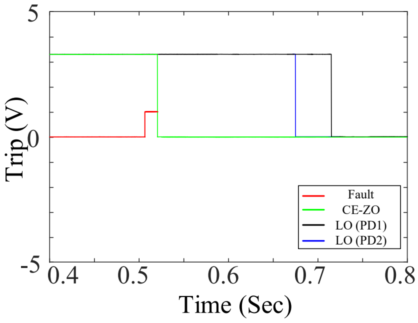

Fig. 7.32 Trip time difference between CE-ZO and LO

7.2.2.4. Simplified radial grid with DG

Fig. 7.33 shows the grid implemented in the laboratory to emulate a Simplified radial grid with DG. In this case, the load value has been modified, as shown in the figure, to have more power and consumption. The protection algorithms have been tested for symmetrical (three-phase) and unsymmetrical (single-phase to ground) faults. Fig. 7.34 and Fig. 7.35 show the behaviour of the CE-ZO algorithms for both types of faults. These figures show the *abc* voltages and *abc* currents for both PDs at each end of DL1. Moreover, the injected current from the DG's inverter has been presented using the BCC control technique, because this technique injects symmetrical and balanced abc currents and verifies the grid code during grid faults, as explained in chapter 4. Also, the third row shows the trip signal vs. the fault. In this case, the CE-ZO controller can locate the fault and send trip signals to both PDs at the same time to disconnect the faulted line. The slight unbalance in the *abc* voltages of Fig. 7.34 is due to the calibration of the voltage sensors.

In case of a fault, the DG is disconnected when the faulted line is disconnected because the inverter control is based on the voltage and frequency of the grid (not islanded), nevertheless, in the case of ring grids, the DG will always be connected to the grid, and the inverter control will not face problems in this case. This point could be improved by modifying the inverter control to be adapted to islanded grids, considered in future work.

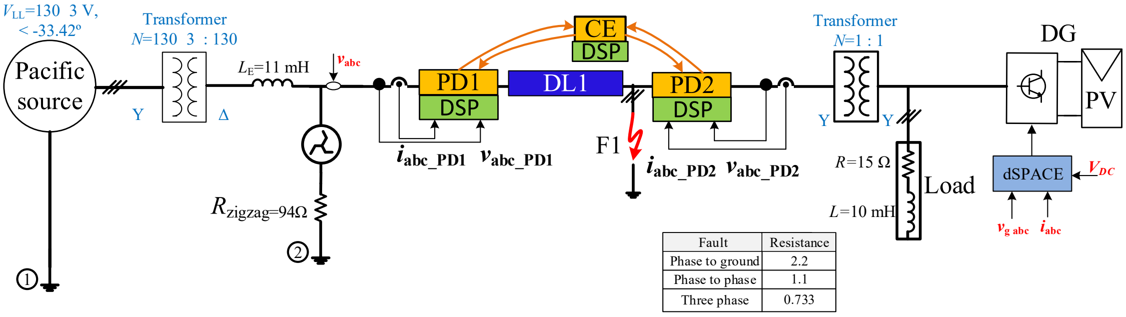
V_{LL}=130 3 V,
< -33.42°
Pacific source
Transformer
N=130 3 : 130
Y
Δ
L_E=11 mH
v_{abc}
R_{zigzag}=94Ω
①
②
CE
DSP
PD1
DSP
DL1
PD2
DSP
F1
i_{abc_PD1}
v_{abc_PD1}
i_{abc_PD2}
v_{abc_PD2}
Transformer
N=1 : 1
Y
Y
R=15 Ω
L=10 mH
Load
DG
PV
dSPACE
V_{DC}
$v_{g\ abc}$
i_{abc}

Fault	Resistance
Phase to ground	2.2
Phase to phase	1.1
Three phase	0.733

Fig. 7.33 Scheme of the Simplified radial grid with DG

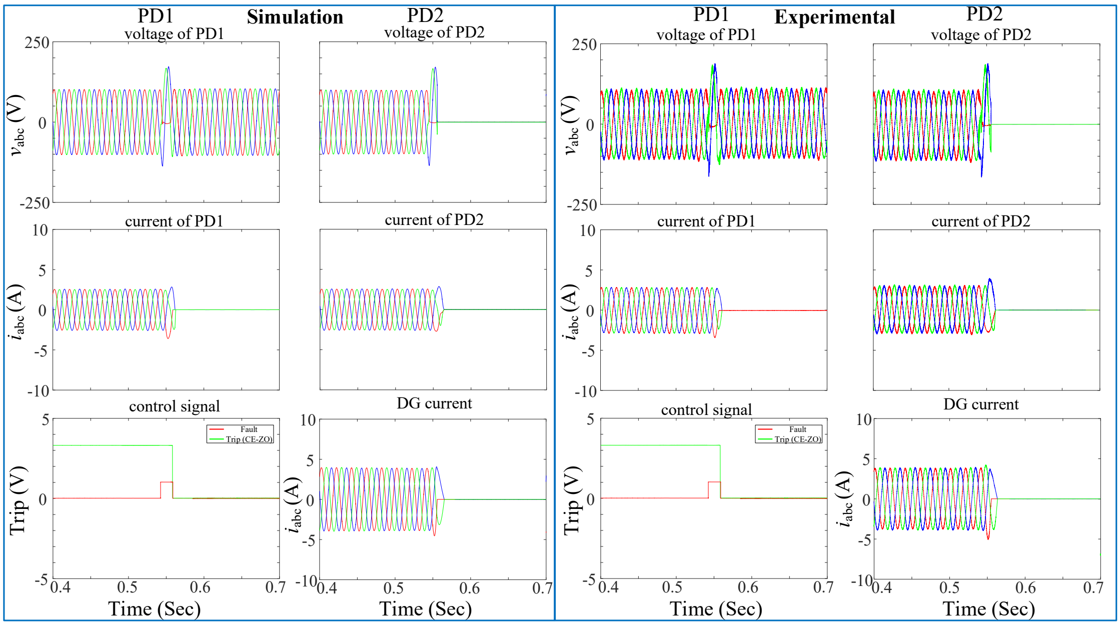

Fig. 7.34 Behaviour of CE-ZO control for single-phase to ground fault with BCC

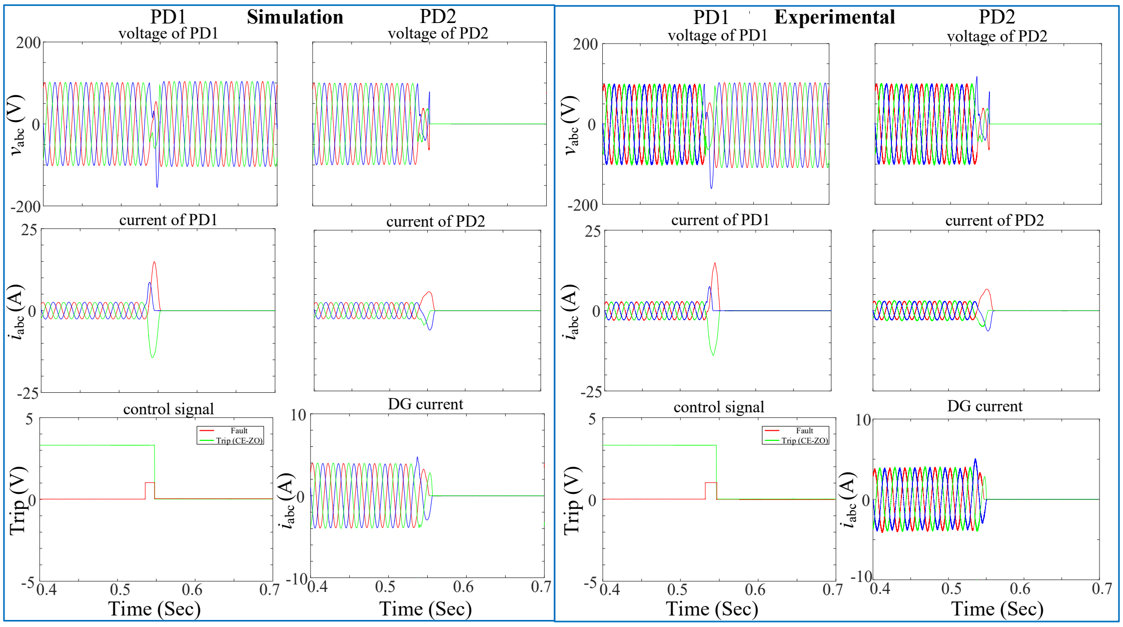

Fig. 7.35 Behaviour of CE-ZO control for three-phase fault with BCC

Fig. 7.36 shows the *abc* voltages, currents and trip signals at PD1 and PD2 located at each end of DL1. The behaviour of the LO algorithm for a three-phase fault is presented. PD2 will be disconnected first as the fault is at the end of the line (see Fig. 7.33). In this case, the fault is supplied from two locations (the main grid, and the DG). Threfore, the DPF will change in PD2, and the CE-ZO gives the decision to trip.

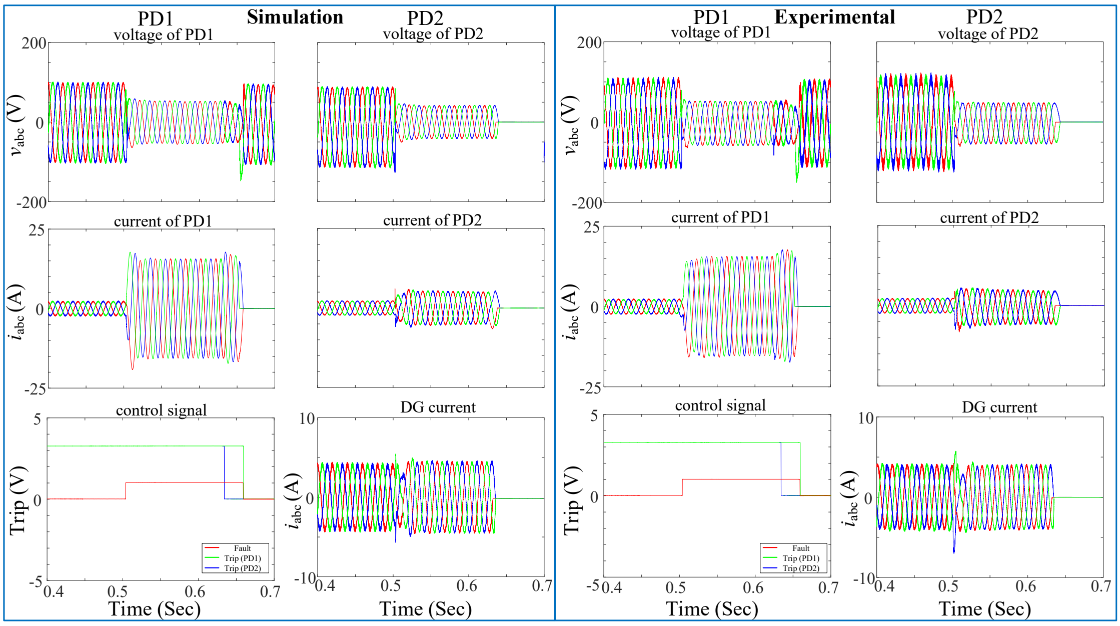

Fig. 7.36 Behaviour of LO control for three-phase fault with BCC

In Fig. 7.37 and Fig. 7.38 the inverter control is implemented using CPC and CRC control techniques, respectively, as explained in chapter 4 (more results can be seen in Appendix B). As seen in the figure, the *abc* injected currents are sinusoidal but not symmetrical because the CPC strategy injects constant active power and oscillates the reactive power. However, for CRC, the reactive power is constant and the active power oscillates, as explained in chapter 4. Trip signals have been implemented after approximately 100 ms, to assure the fault is permanent, not a transient fault, as explained in chapters 5 and chapter 6.

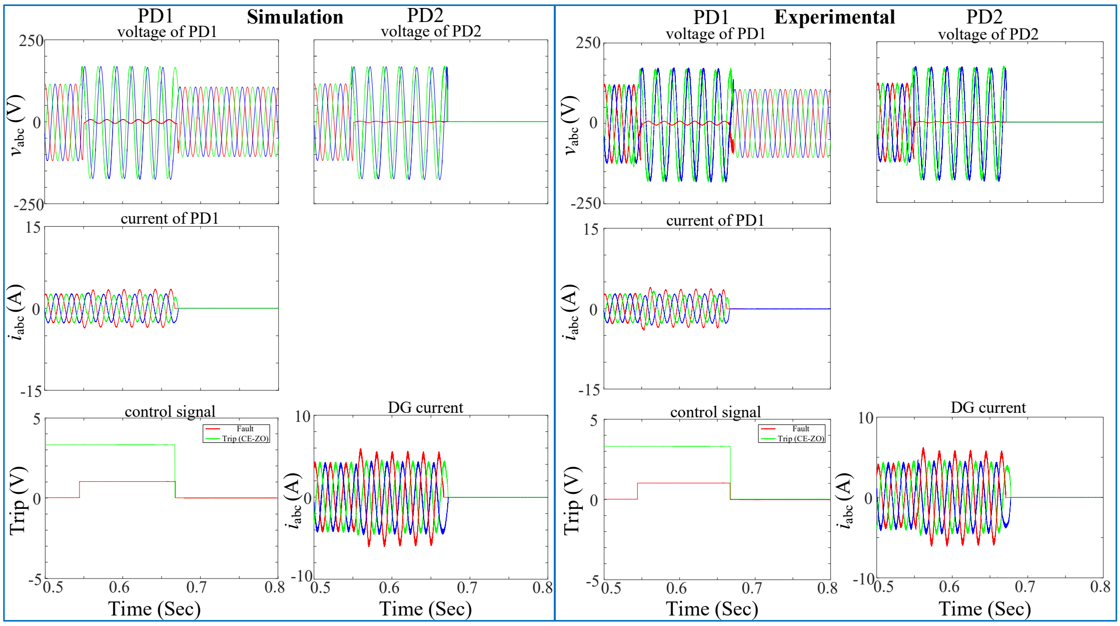

Fig. 7.37 Behaviour of CE-ZO control for single-phase to ground fault with CPC

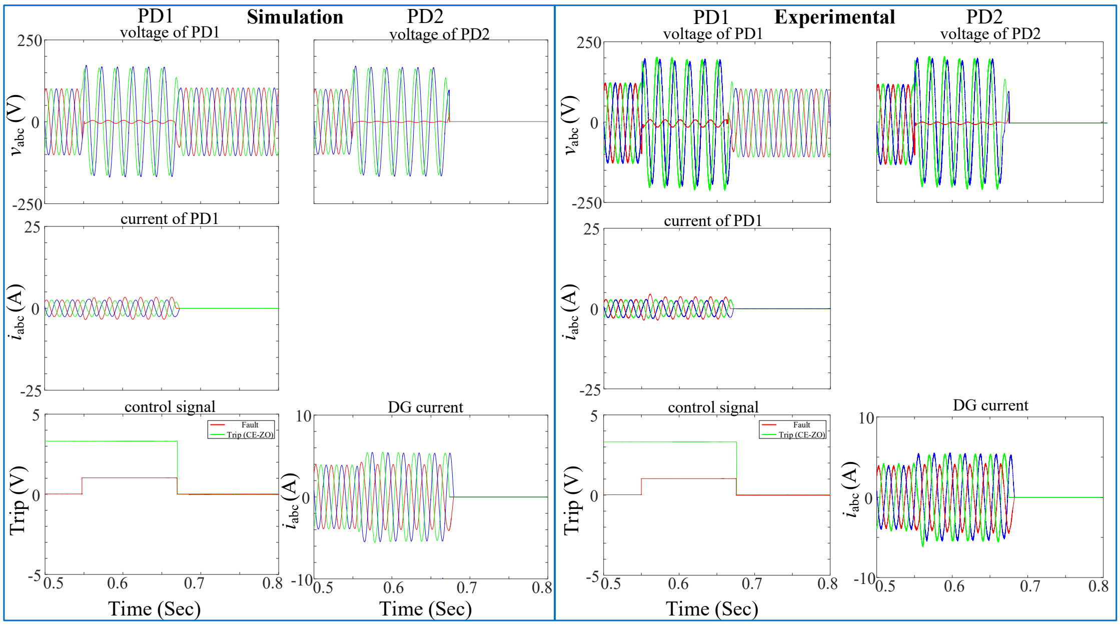

Fig. 7.38 Behaviour of CE-ZO control for three-phase fault with CRC

7.2.2.5. Complete radial grid without DG

Fig. 7.39 shows the grid implemented in the laboratory to emulate the complete radial grid without DG. The protection algorithms have been tested for symmetrical (three-phase) and unsymmetrical (single-phase to ground) faults. The behaviour of OCR, DR, and CE-ZO algorithms have been tested for both types of faults when the fault is at F1 or F2 (fault location can be seen in Fig. 7.39), and the results are shown from Fig. 7.40 to Fig. 7.48. The figures show the *abc* voltages, *abc* currents and trip signals for both PDs at each end of the faulted line (DL1). Moreover. Also, the third row shows the trip signal versus the fault (more experimental results can be seen in Appendix B). The relay settings for the OCR and DR protection strategies have been updated for each operating condition.

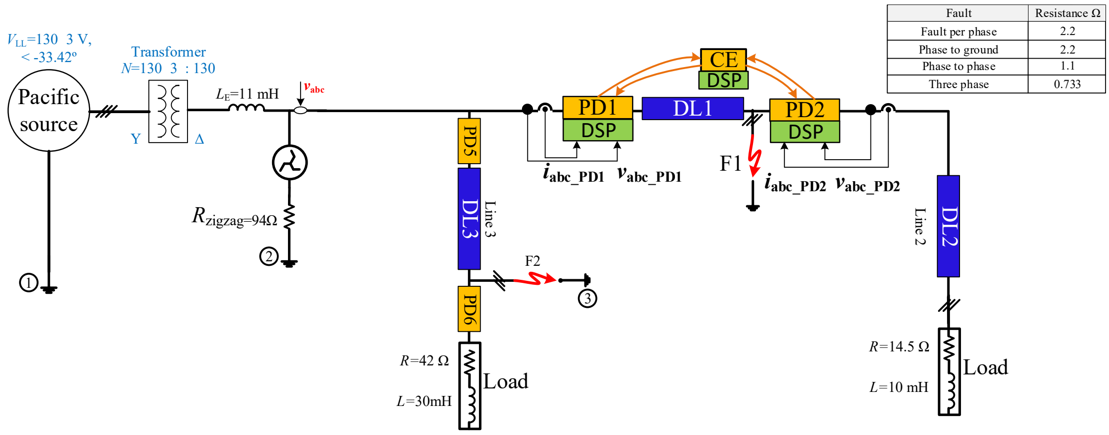
V_{LL}=130 3 V,
< -33.42°
Transformer
N=130 3 : 130
Pacific
source
Y
Δ
L_E=11 mH
v_{abc}
R_{zigzag}=94Ω
①
②
③
CE
DSP
PD1
DSP
DL1
PD2
DSP
i_{abc_PD1} v_{abc_PD1}
F1
i_{abc_PD2} v_{abc_PD2}
PD5
DL3
Line 3
F2
PD6
R=42 Ω
L=30mH
Load
DL2
Line 2
R=14.5 Ω
L=10 mH
Load

Fault	Resistance Ω
Fault per phase	2.2
Phase to ground	2.2
Phase to phase	1.1
Three phase	0.733

Fig. 7.39 Scheme of the complete radial grid without DG

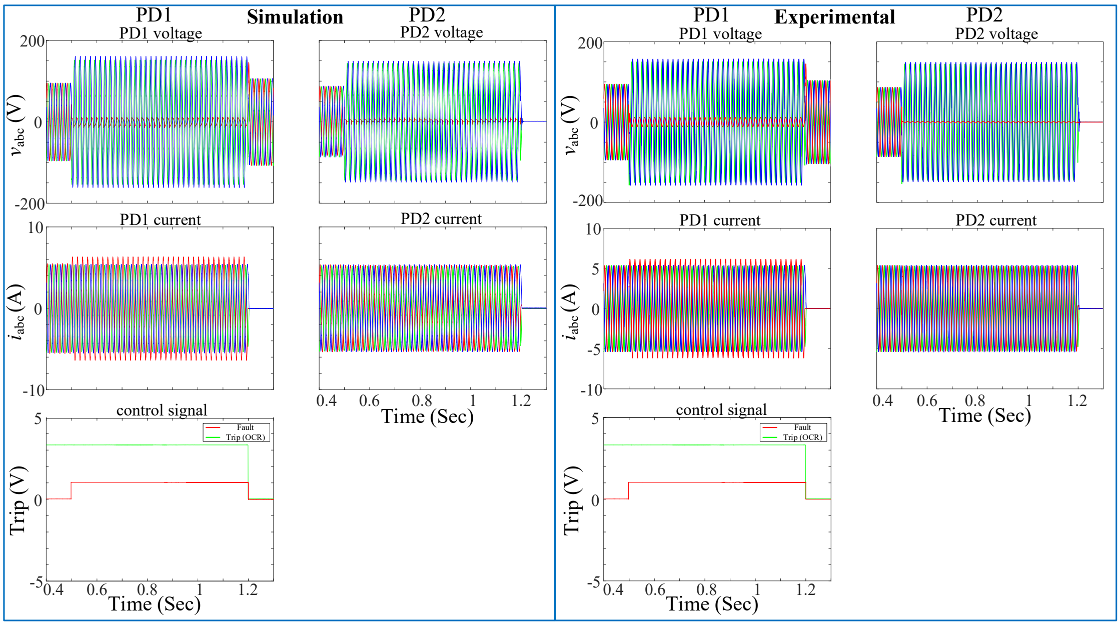

Fig. 7.40 Behaviour of OCR for single-phase to ground fault when the fault at F1

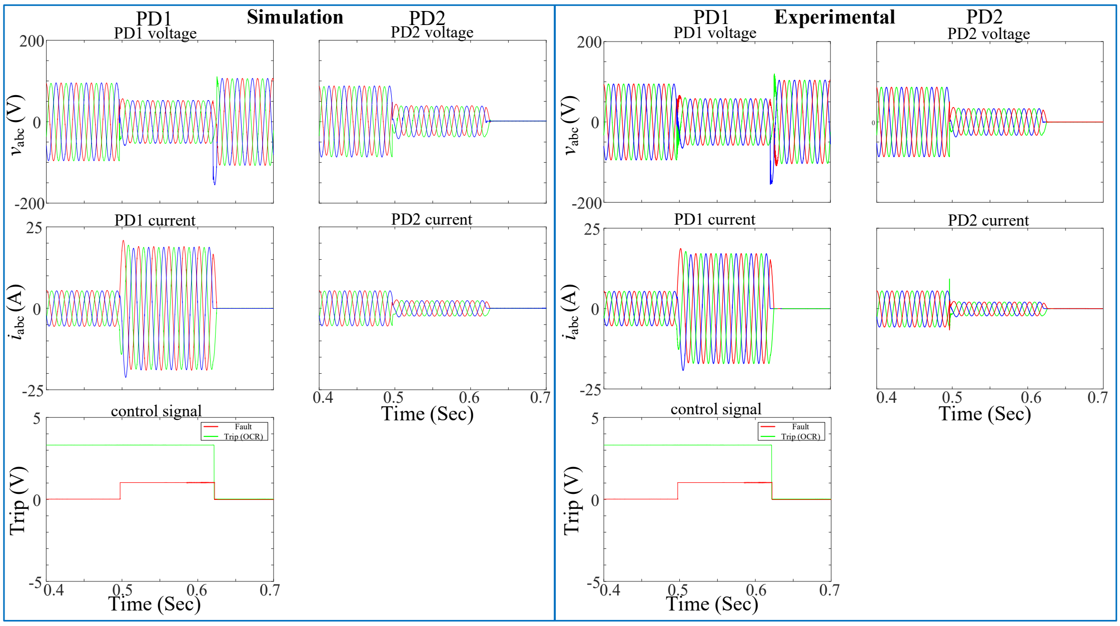

Fig. 7.41 Behaviour of OCR for the three-phase fault when the fault at F1

As seen in Fig. 7.40, during a single-phase to ground fault at F1, the OCR will disconnect the fault after ≈ 0.75 s. Also, during a three-phase fault at F1, the OCR will trip faster in this case as the short-circuit current is larger (Fig. 7.41). Therefore, the OCR will trip after ≈ 0.12 s.

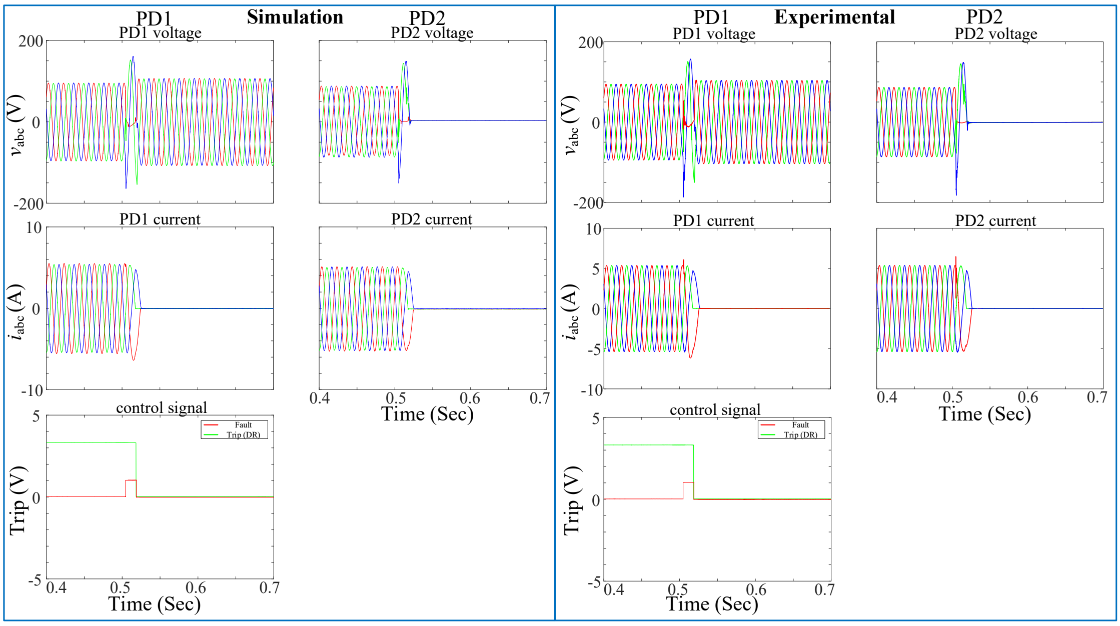

Fig. 7.42 Behaviour of DR for single-phase to ground fault when the fault at F1

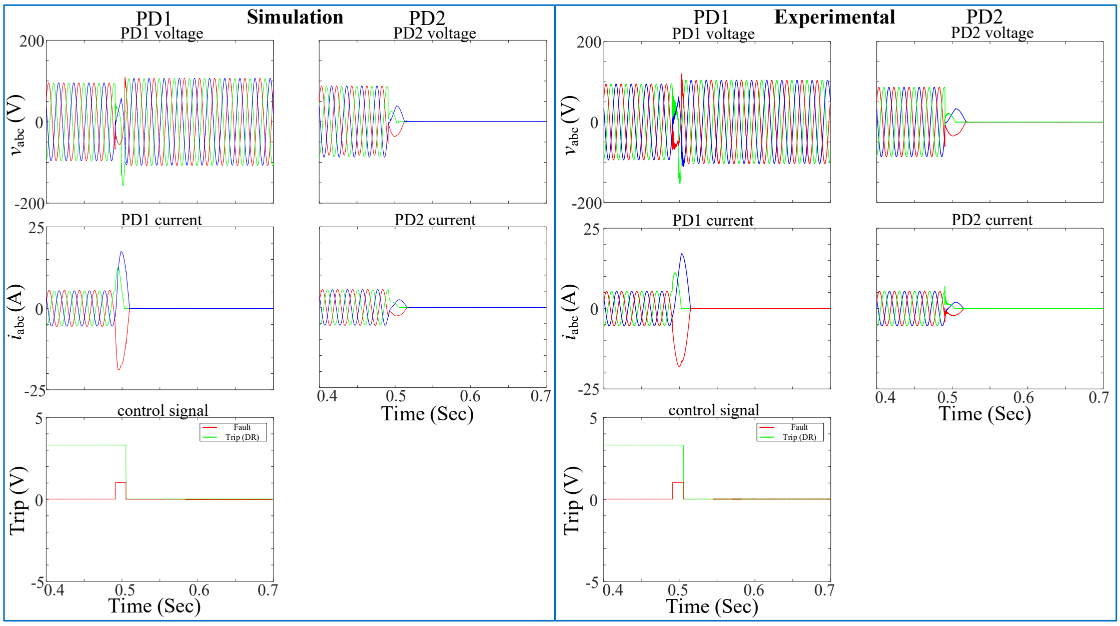

Fig. 7.43 Behaviour of DR for the three-phase fault when the fault at F1

In the case of DR, as seen in Fig. 7.42 and Fig. 7.43, the disconnection of both PDs located at the ends of the faulted line will be faster than OCR (≈ 0.015 s). Moreover, the type of fault does not affect the tripping time of the relay.

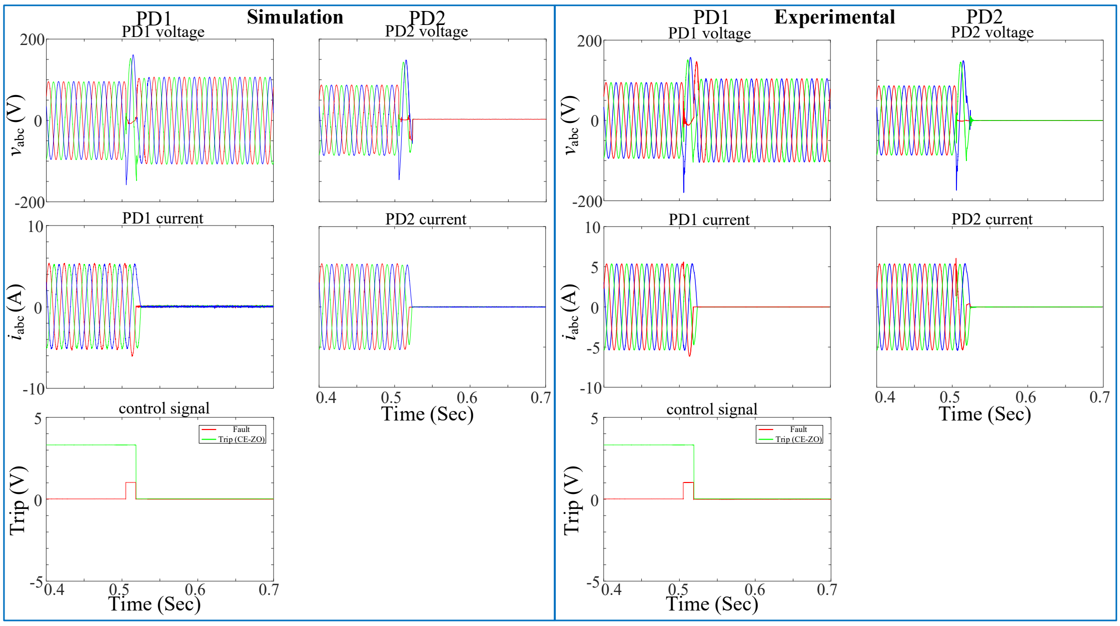

Fig. 7.44 Behaviour of CE-ZO for single-phase to ground fault when the fault at F1

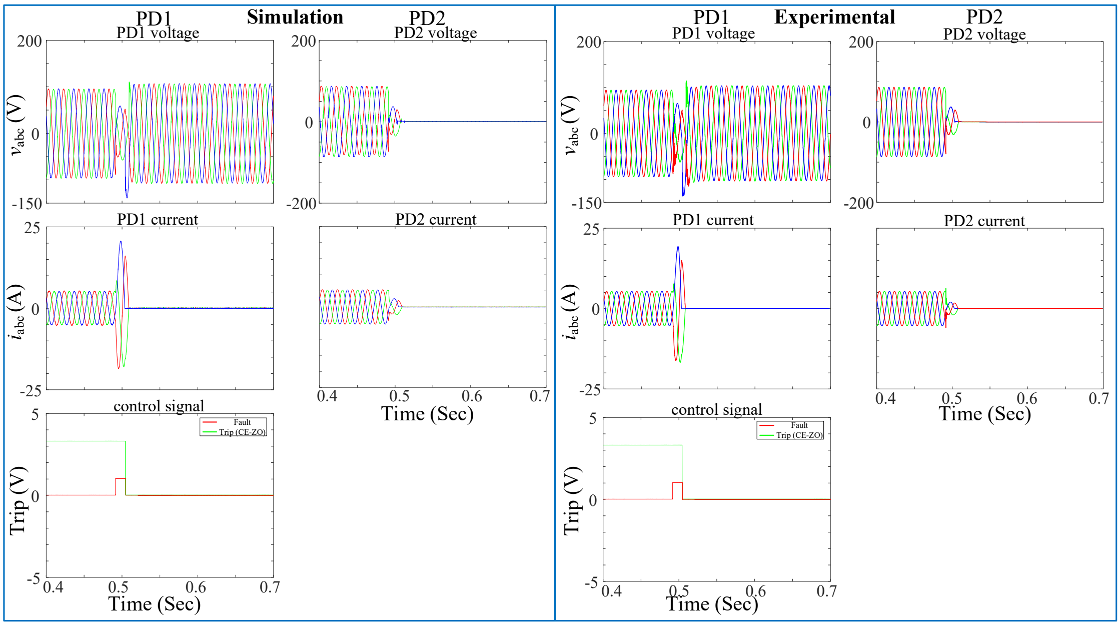

Fig. 7.45 Behaviour of CE-ZO for the three-phase fault when the fault at F1

Fig. 7.44 and Fig. 7.45 show the *abc* voltages, *abc* currents and trip signals during a single-phase to ground fault and three-phase fault at F1. The disconnection of the two PDs located at the end of the faulted line (DL1) will be decided depending on the comparison between the positive-sequence currents at PD1 and PD2. If both disagree, then the decision is to trip the PDs and disconnect the faulted part of the grid. in addition, the trip signal does not depend on the type of fault, as in both fault types the disconnection is executed at the same time (≈ 0.012 s).

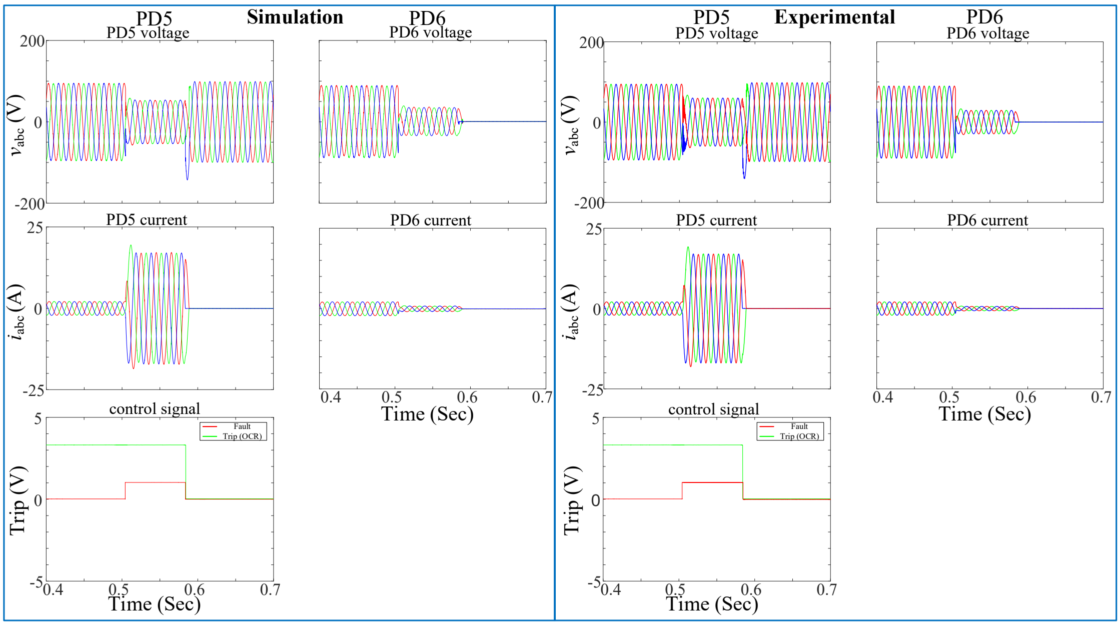

Fig. 7.46 Behaviour of OCR for the three-phase fault when the fault at F2

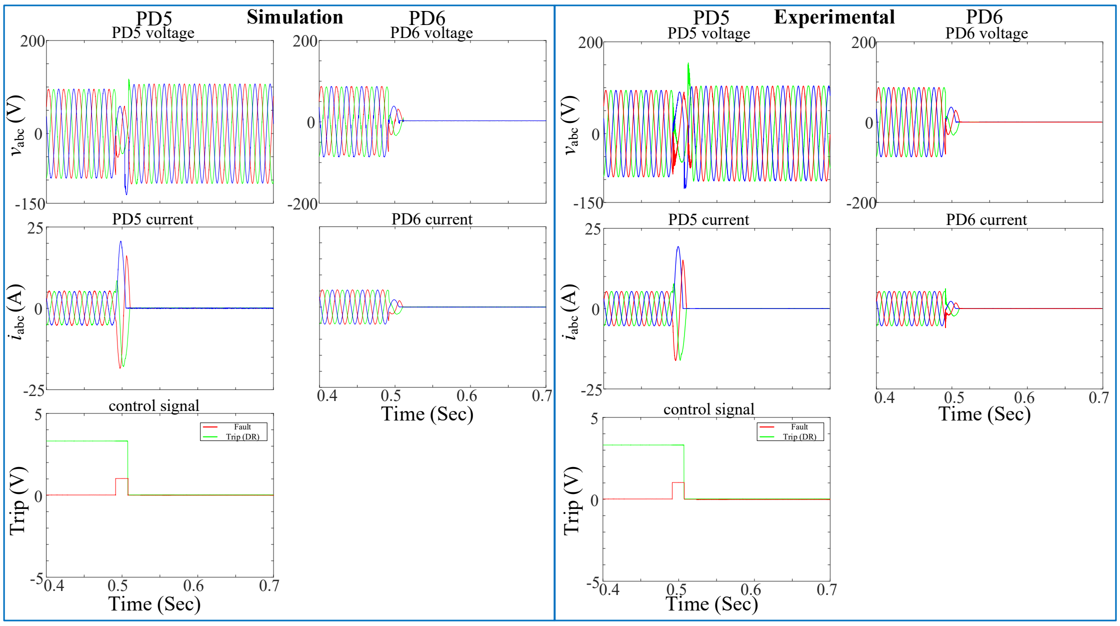

Fig. 7.47 Behaviour of DR for the three-phase fault when the fault at F2

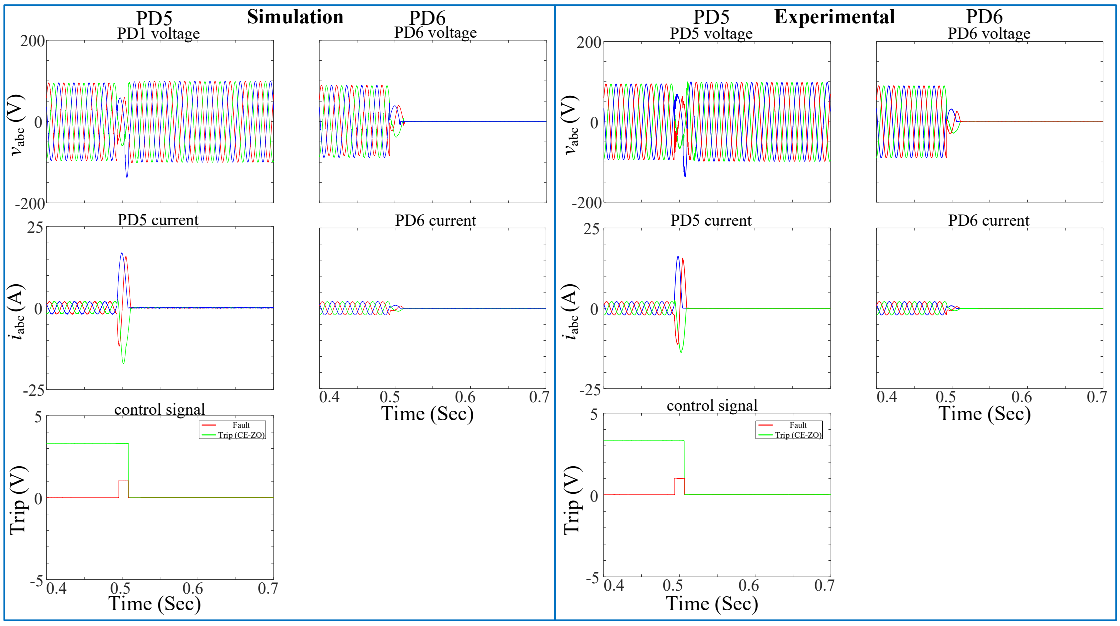

Fig. 7.48 Behaviour of CE-ZO for the three-phase fault when the fault at F2

Fig. 7.40, Fig. 7.42, and Fig. 7.44 show the behaviour of OCR, DR, and CE-ZO, respectively, for single-phase fault at F1. As seen, the OCR needs more periods to disconnect the fault as it depends on the inverse time characteristic curve. However, for the DR and CE-ZO algorithms, the response is much faster. The same conclusion can be obtained from Fig. 7.41, Fig. 7.43, and Fig. 7.45 but for a three-phase fault at F1. In addition, Fig. 7.46, Fig. 7.47, and Fig. 7.48 show the behaviour of the algorithms when the fault is at F2. In the case of CE-ZO and DR, the trip time is much faster than OCR, because the CE-ZO depend on the DPF at both PDs located at the end of the faulted line, and DR depends on the differential current at both ends of the faulted line.

As can be seen, the simulation and experimental results match, and the CE-ZO protection strategy provides the best behaviour, because they can respond rapidly to the fault and operate with different fault locations and types regardless of the grid topology, as stated in chapter 5 (5.3.1, and 5.3.2). Furthermore, there is no need to update the relay settings.

7.2.2.6. Complete radial grid with DG

Fig. 7.49 shows the grid implemented in the laboratory to emulate the complete radial grid with DG. The protection algorithms have been tested for symmetrical (three-phase) and unsymmetrical (single-phase to ground) faults. The behaviour of the OCR, DR, and CE-ZO algorithm has been tested for both types of faults. Fault location was at F1 or F2, and the results are shown from Fig. 7.50 – Fig. 7.58.

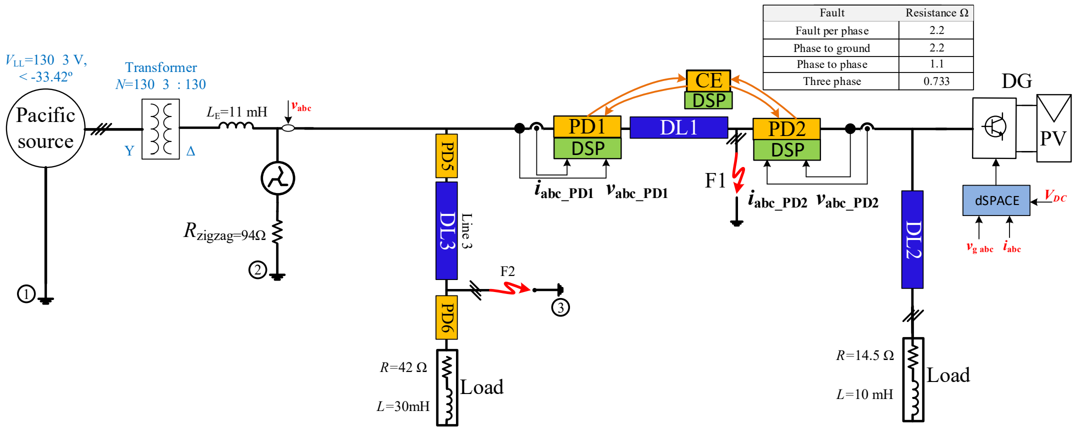
Fault
Resistance Ω
Fault per phase 2.2
Phase to ground 2.2
Phase to phase 1.1
Three phase 0.733
V_{LL}=130 3 V,
< -33.42°
Transformer
N=130 3 : 130
Pacific source
Y
Δ
L_E=11 mH
v_{abc}
R_{zigzag}=94Ω
①
②
③
PD5
DL3
Line 3
F2
PD6
R=42 Ω
L=30mH
Load
PD1
DSP
DL1
CE
DSP
PD2
DSP
F1
i_{abc_PD1} v_{abc_PD1}
i_{abc_PD2} v_{abc_PD2}
DL2
R=14.5 Ω
L=10 mH
Load
DG
PV
dSPACE
V_{DC}
$v_{g\ abc}$ i_{abc}

Fig. 7.49 Scheme of the complete radial grid with DG

The figures show the *abc* voltages and *abc* currents for both PDs at each end of DL1 or DL3. Moreover, the injected current from the DG's inverter has been presented using the BCC control technique explained in chapter 4, as this technique injects balanced and symmetrical currents during the fault, and verifies the grid code. Also, the third row shows the trip signal vs. the fault (more results can be seen in Appendix B).

In case of a fault in F1, the DG is disconnected when the faulted line is disconnected, because the inverter control is based on the voltage and frequency of the grid (not islanded), However, when the fault at F2, the DG will not be disconnected, and the inverter control can operate normally in this case, as the voltage and frequency continue to be imposed by the main grid.

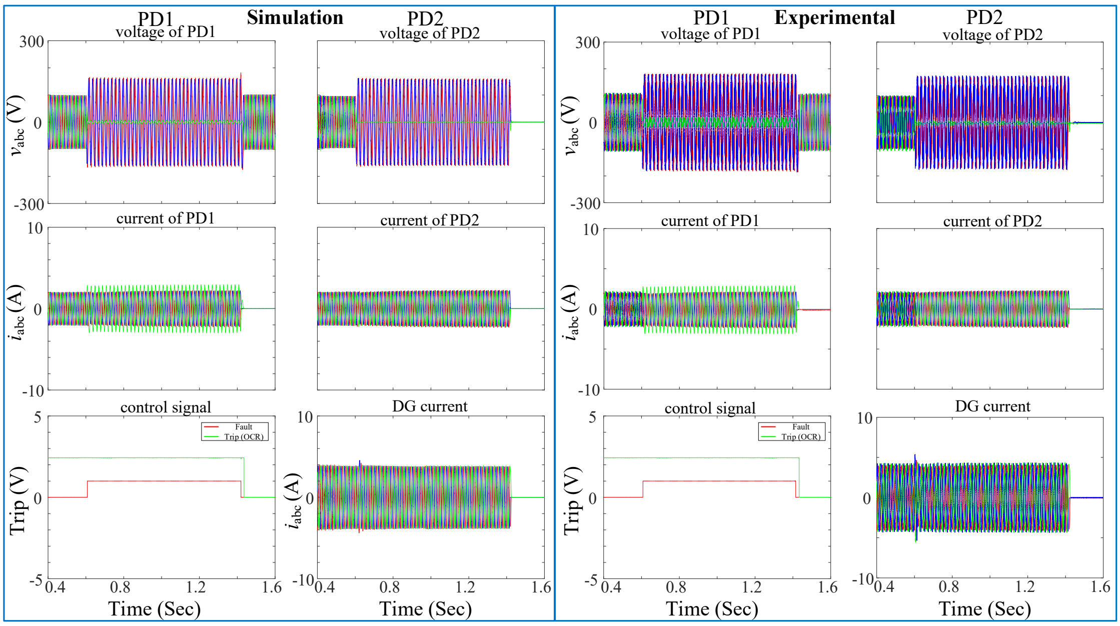

Fig. 7.50 Behaviour of OCR for single-phase to ground fault when the fault at F1

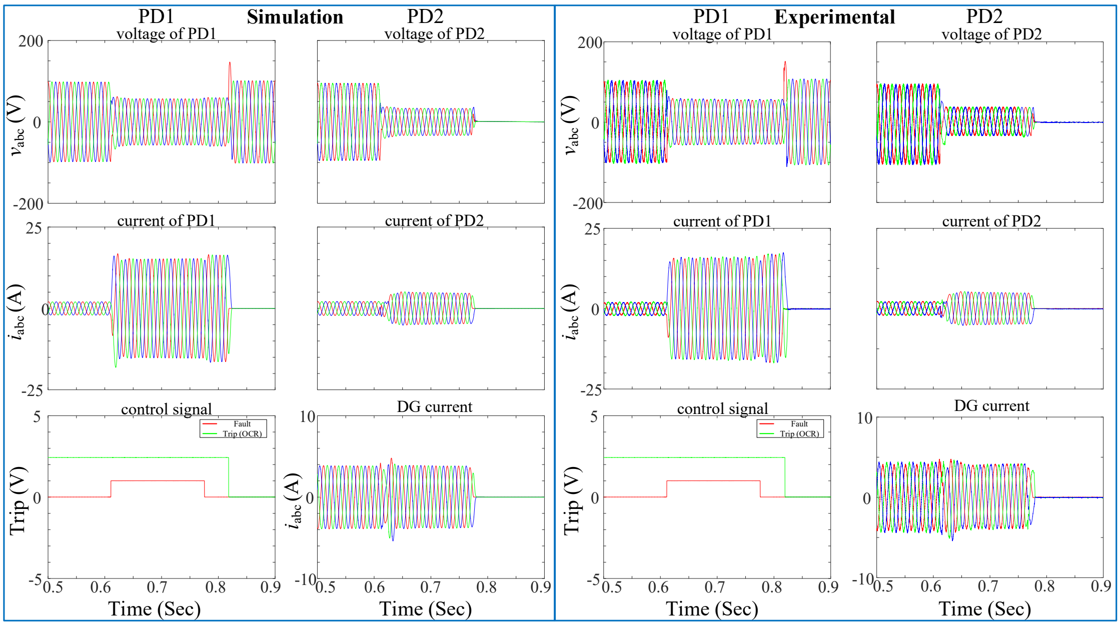

Fig. 7.51 Behaviour of OCR for the three-phase fault when the fault at F1

As seen in Fig. 7.50, during a single-phase fault at F1, in the case of OCR, the first disconnection is PD2 (≈ 0.8 s), because the fault is close to the end of DL1, then PD1 is disconnected (≈ 0.9 s). The difference between the case with DG penetration (Fig. 7.50) and without (Fig. 7.40) is that with DG the grid contribution to the fault is reduced as the DG also contributes the short-circuit current. Fig. 7.51 shows the disconnection of PD1 and PD2 during a three-phase fault at F1. As seen in the figure, PD2 is disconnected at (≈ 0.17 s), and PD1 is disconnected later at (≈ 0.23 s) because when the fault is at DL1, the fault is supplied from two points with DG penetration.

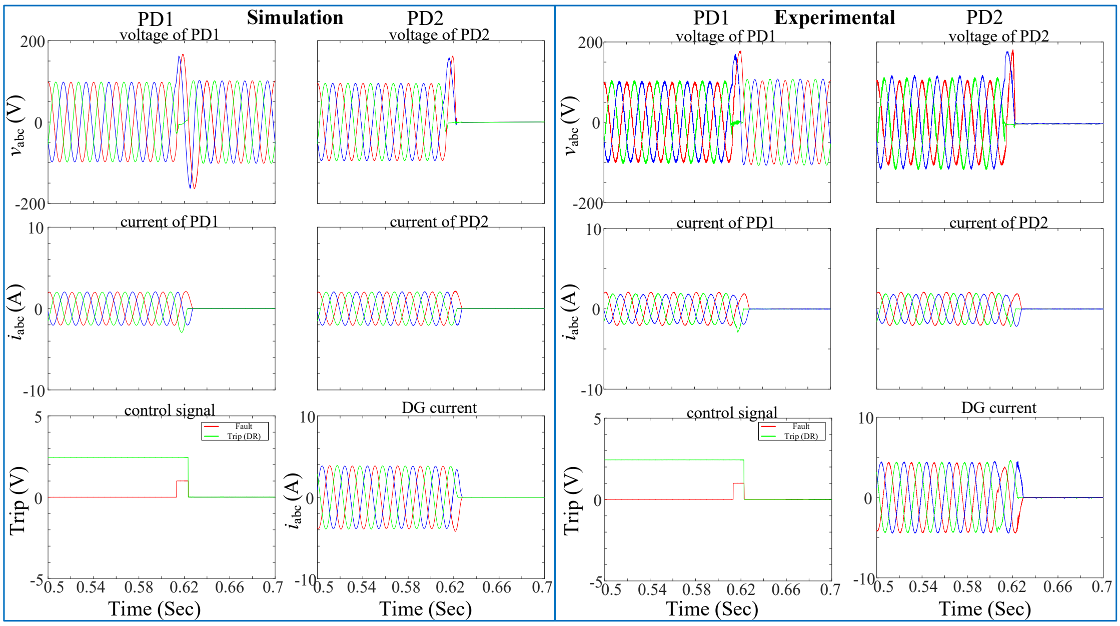

Fig. 7.52 Behaviour of DR for single-phase to ground fault when the fault at F1

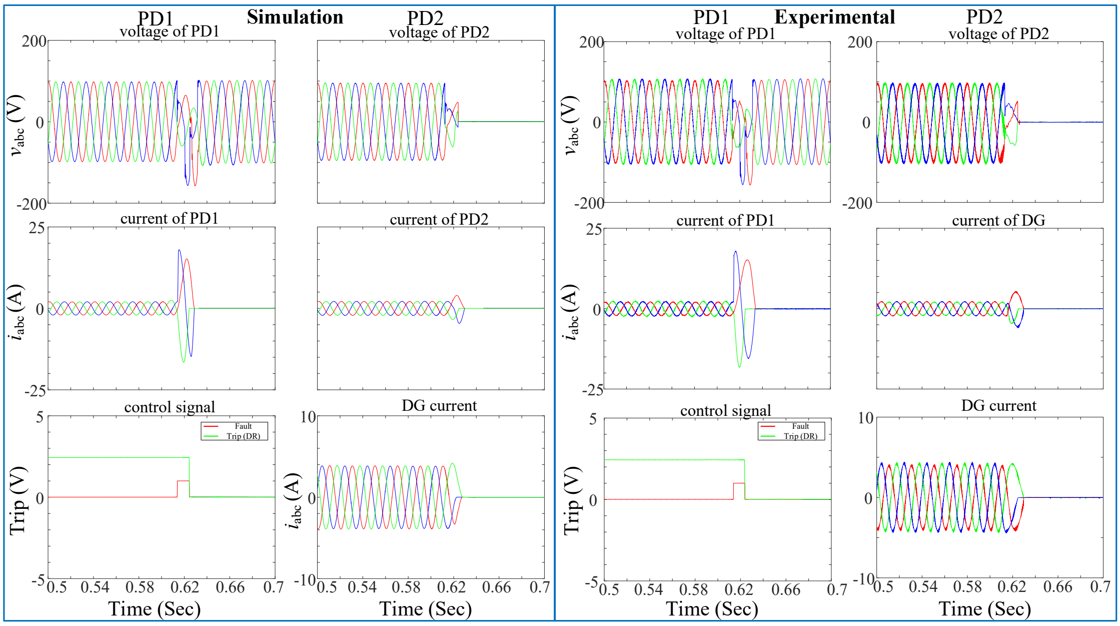

Fig. 7.53 Behaviour of DR for the three-phase fault when the fault at F1

Fig. 7.52 and Fig. 7.53 show the behaviour of the DR during single-phase to ground and three-phase faults. As seen, the disconnection of the two PDs located at the ends of the faulted line (DL1) is tripped at the same time (≈ 0.015 s). In addition, the disconnection of the PDs is executed at the same time for both PDs.

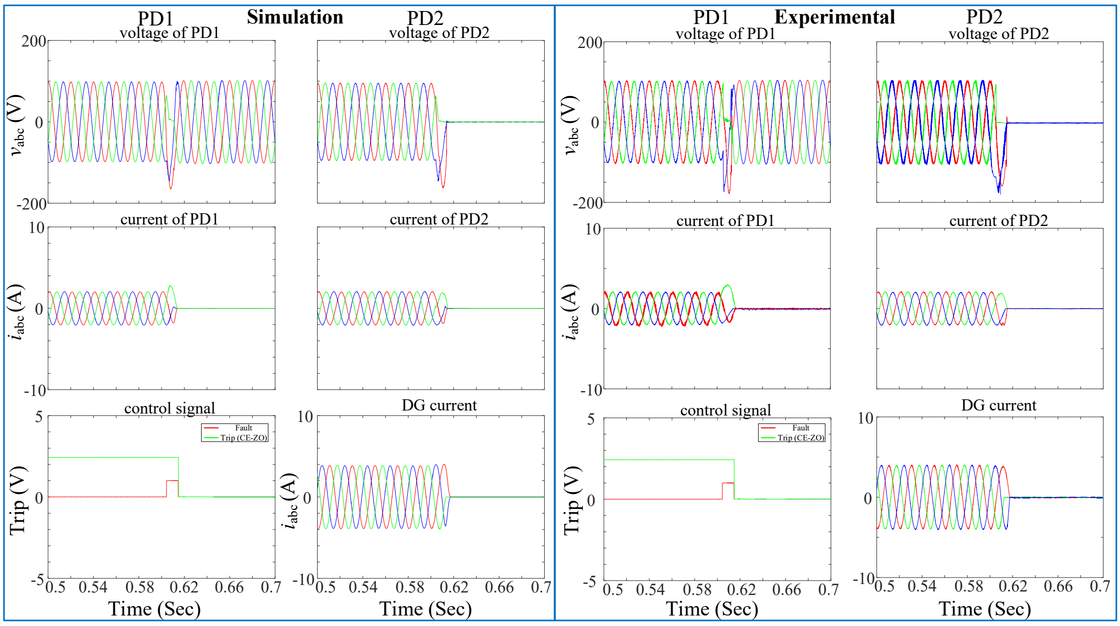

Fig. 7.54 Behaviour of CE-ZO for single-phase to ground fault when the fault at F1

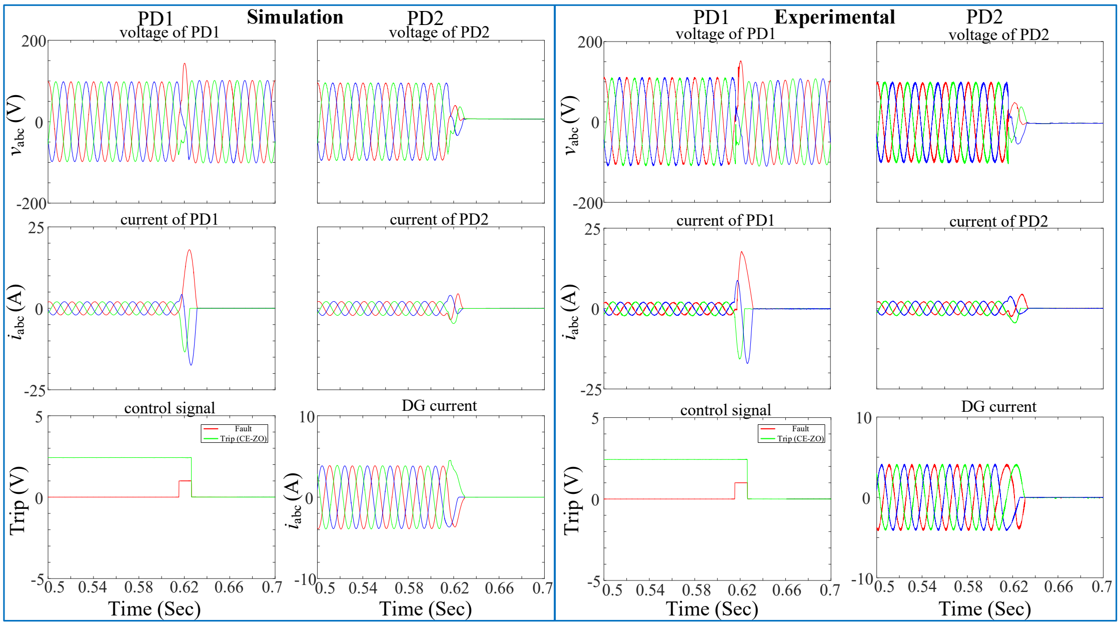

Fig. 7.55 Behaviour of CE-ZO for the three-phase fault when the fault at F1

Fig. 7.54 and Fig. 7.55 show the behaviour of CE-ZO during single-phase to ground and three-phase faults at F1. The trip signal for both types of faults is executed at the same time, because the algorithm does not depend on the type of fault. In addition, it can be summarized that the trip time (≈ 0.012 s) with DG penetration (Fig. 7.45) is equal to the trip time without DG (Fig. 7.55). Because the algorithm does not depend on the value of short-circuit currents but the DPF.

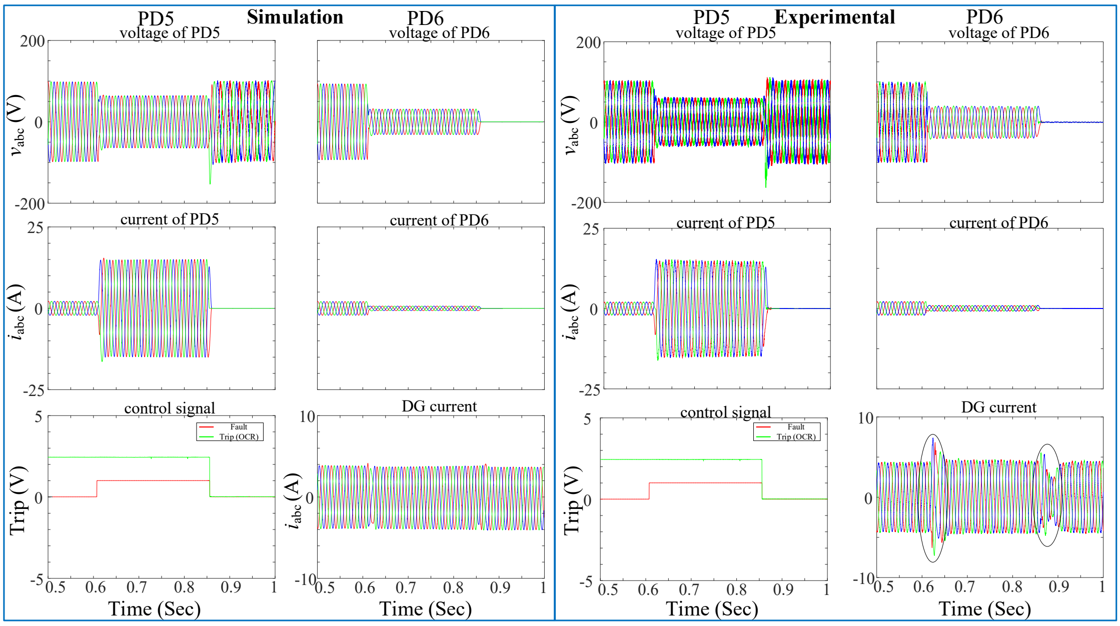

Fig. 7.56 Behaviour of OCR for the three-phase fault when the fault at F2

Fig. 7.56, Fig. 7.57, and Fig. 7.58 show the behaviour of OCR, DR, and CE-ZO during a three-phase fault at F2, respectively. For OCR, when PD6 is disconnected, the current at DL3 will be equal to zero, as this line is supplied from one end (Fig. 7.39). The disconnection of DL3 will not affect the supply of DG connected between DL1 and DL2. For the DR and CE-ZO the trip signal is sent to PD5 and PD6 made at the same time to disconnect the faulted line.

As explained in Appendix E, the current of the DG shown in the fourth column and third row of Fig. 7.56 can be improved, especially during transient by modifying the current limiting technique.

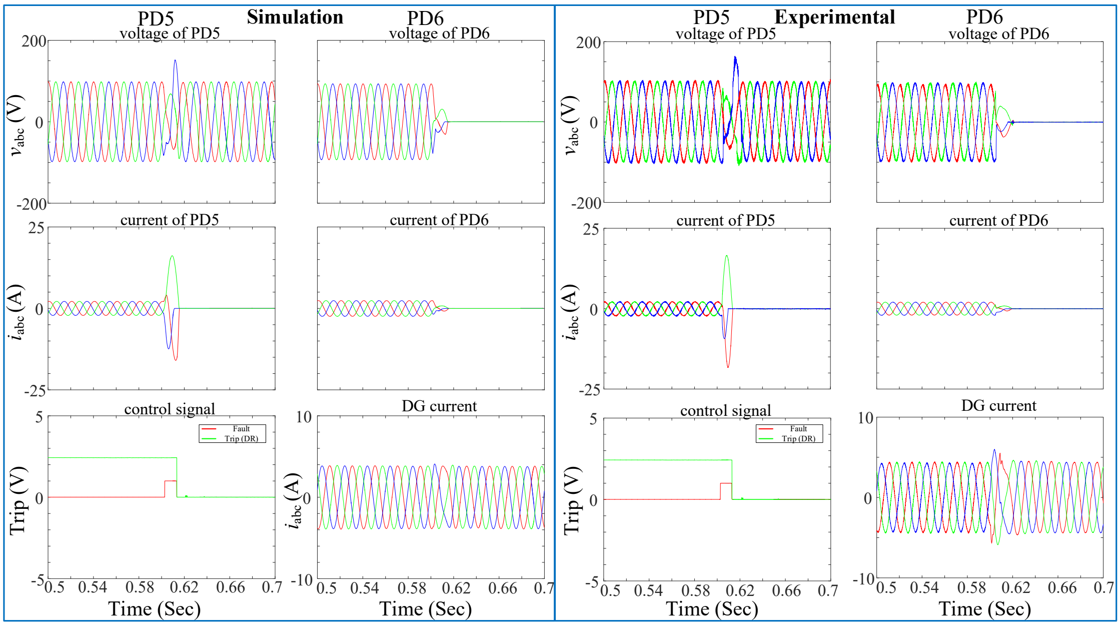

Fig. 7.57 Behaviour of DR for the three-phase fault when the fault at F2

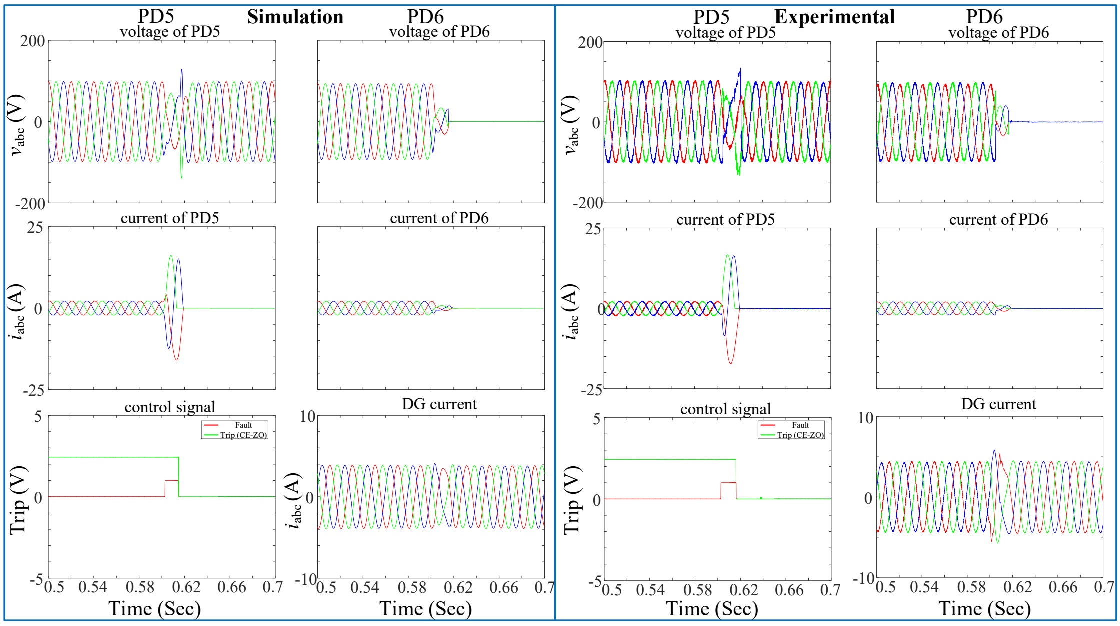

Fig. 7.58 Behaviour of CE-ZO for the three-phase fault when the fault at F2

Several tests have been done in the laboratory; for example, Fig. 7.59 presents the trip signals of OCR, DR, and CE-ZO protection strategies for symmetrical and unsymmetrical faults when the fault is located at F1 and F2. Also, Fig. 7.60 shows the trip signals of OCR, DR, LO, and CE-ZO protection strategies for symmetrical faults when the fault is located at F1 and F2. The relay settings for the OCR and DR protection strategies have been updated for each operation condition in the presence of DG. In this case, it is observed that DR and CE almost give the same results, but OCR is worse due to the trip curve. The trip times obtained for the reduced scale grid implemented in the laboratory are close to the obtained by simulation of the real studied grid. CE-ZO algorithm has been tested for different grid reconfiguration experimentally and using simulation. One experimental case is shown in Fig. 7.61 to present the evolution of the *abc* voltages and currents for symmetrical and unsymmetrical faults with CE-ZO algorithms. As seen, the simulation and experimental results agree, and as is explained in chapter 5, the CE-ZO protection strategy gives the best behaviour. Moreover, no relay settings updating is required. The trip times obtained for the reduced scale grid implemented in the laboratory are close to those obtained by simulation of the real studied grid, as seen in Fig. 7.61.

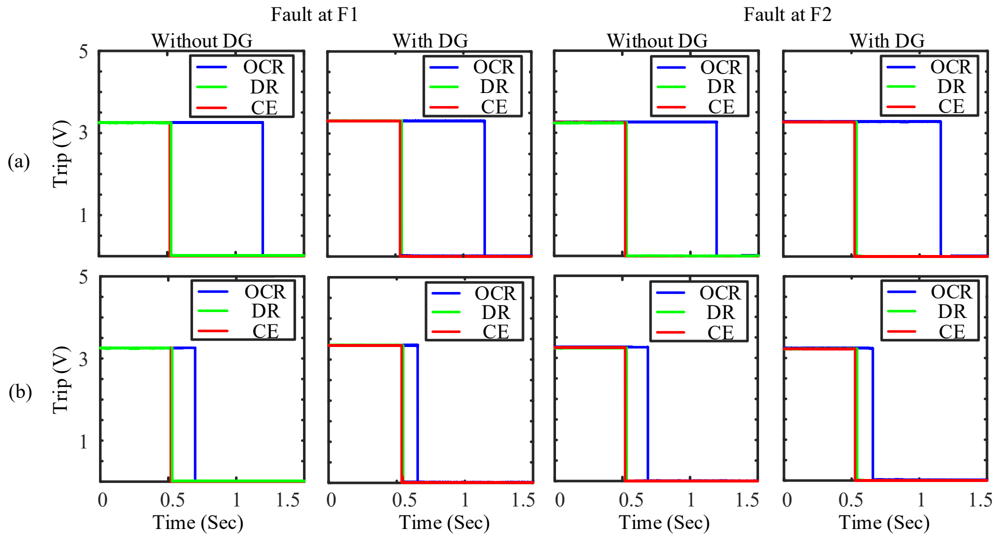

Fig. 7.59 Digital output of OCR, DR, and CE-ZO with DG during (a) Single-phase fault, (b) Three-phase fault

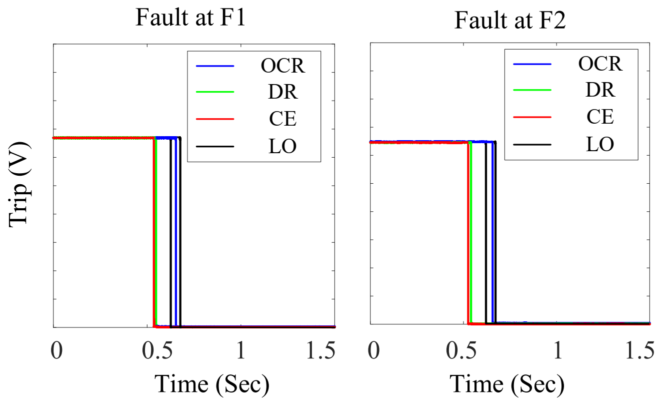

Fig. 7.60 Digital output of OCR, DR, LO, and CE-ZO with DG during Three-phase fault

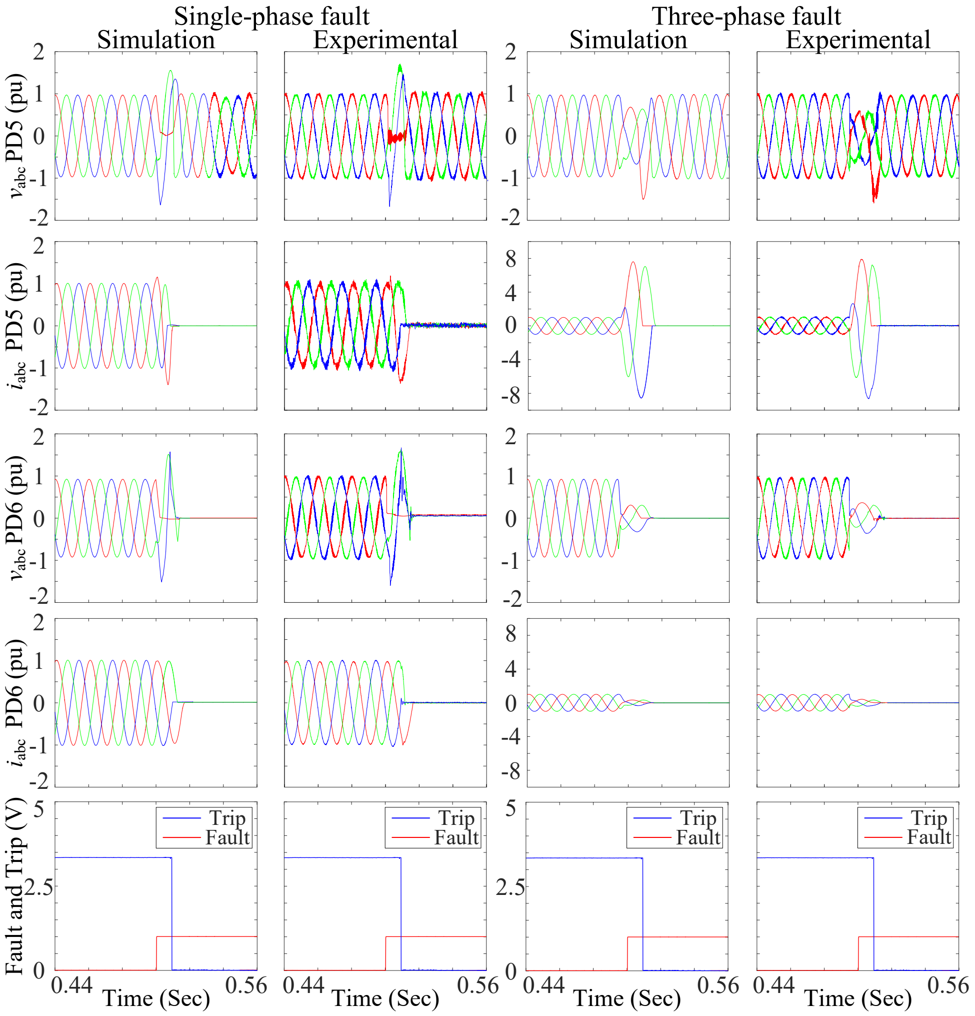

Fig. 7.61 Simulation and Experimental *abc* voltages and currents of PD5, PD6, and Trip signals of the CE-ZO algorithm decision in case of three-phase fault, and single-phase.

7.2.2.7. Complete ring grid without DG

Fig. 7.62 shows the grid implemented in the laboratory to emulate the complete ring grid without DG. The protection algorithms have been tested for both symmetrical (three-phase) and unsymmetrical (single-phase to ground) faults; the algorithms are tested for the rest of the fault types by simulation, as seen in Appendix B. Faults at DL1or DL2 (the complete grid is shown in Fig. 7.62) are considered. The behaviour of the CE-ZO algorithm has been tested for both types of faults. The results are shown in Fig. 7.63 and Fig. 7.64. CE obtains the data of one line and the data of the other PDs are imposed in the DSP of the CE controller due to the lack of the DSPs in all the lines. The figures show the *abc* voltages and *abc* currents for both PDs at each end of the faulted line; the trip signal is executed after a delay of approximately 100 ms to assure the fault is a permanent fault, as explained in chapter 6. Moreover. Also, the third row shows the trip signal vs. the fault (more experimental results can be seen in Appendix B). In the case of ring grids, the PDs have been changed from SSR to mechanical relays. As mentioned earlier (beginning of section 7.2) in this chapter, the problem could be that when the two lines are connected in parallel with DL1, the voltage difference across the SSR terminals will be small, as the values of the resistance and the impedance of the DLs are very small (less than 1.1 Ω). The SSR needs a minimum voltage difference across its ends to operate correctly; otherwise, if the voltage difference is less than a certain value (48 V) then the SSR is always disconnected, as explained in Appendix C.

It must be highlighted that the mechanical breaker has a different behaviour than the presented in the ideal breaker used for the simulation, but the SSR has a close behaviour to the ideal breaker. The explanation of the mechanical relay behaviour can be seen in Appendix C [187]–[193]. In Fig. 7.63 the experimental *abc* currents of PD1 at the second row and the third column have a big overcurrent that is different from the simulated result. This is mainly because for ring grids, the SSRs are replaced with mechanical contactors, which opens at any instance causing a spark, and as a result the current increases to almost more than the double. During the tripping of the mechanical-breaker, there is an overshot in the *abc* current for PD1 as seen in Fig. 7.63 (black ellipses), this overshoot is produced from the arcing process during the disconnection of the breaker. Therefore, the disconnection of the breaker will last for 2 or more cycles before it disconnects, which is a disadvantage, if it is compared to the SSR that disconnects fast and at zero current. As seen, there is a drop of voltage in the three phases, which means the single-phase fault during the sag is transformed to a three-phase fault, which produces an increase in the *abc* currents (Appendix C). The air is ionized in the first two cycles, and metal vapors and other impurities create several low impedance pathways to the ground, resulting in the formation of further arcs and the fault soon becomes a three-phase to ground fault with several arcs [194]–[196]. On the contrary, the SSRs only disconnect when the current goes to zero (zero current turn-offs). The aim is to verify that the algorithms work properly, but the improvement in the simulation with mechanical-breaker is future work. In addition, the improvement of the electronic breaker to work in these kinds of grids is future work.

The same is true for the three-phase fault shown in Fig. 7.64, but the results of the *abc* current at PD1 seem to be better as during the three-phase fault, as the short-circuit current is high to be near the overcurrent during the spark when the breaker trips.

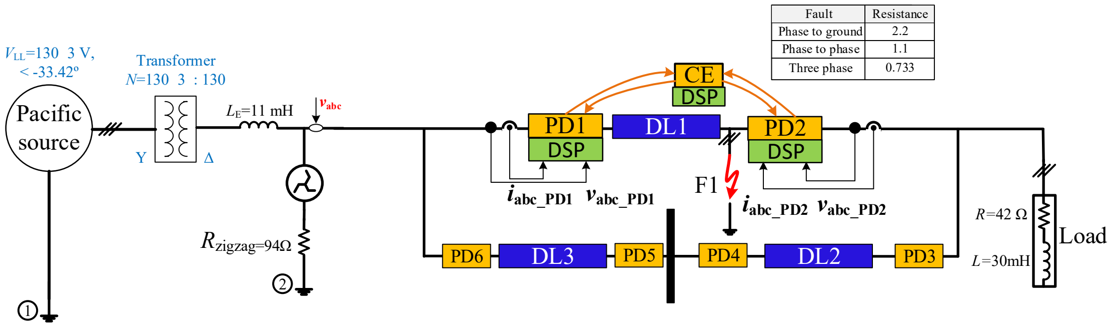

Fault	Resistance
Phase to ground	2.2
Phase to phase	1.1
Three phase	0.733

Fig. 7.62 Scheme of ring grid without DG

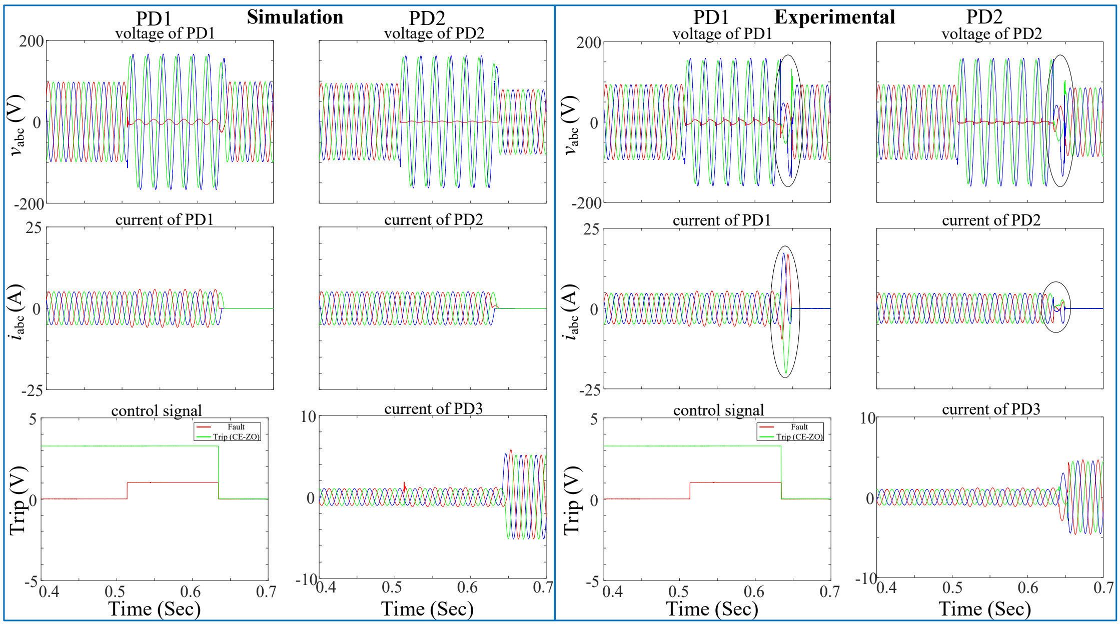

Fig. 7.63 Behaviour of CE-ZO for single-phase to ground fault when the fault at DL1

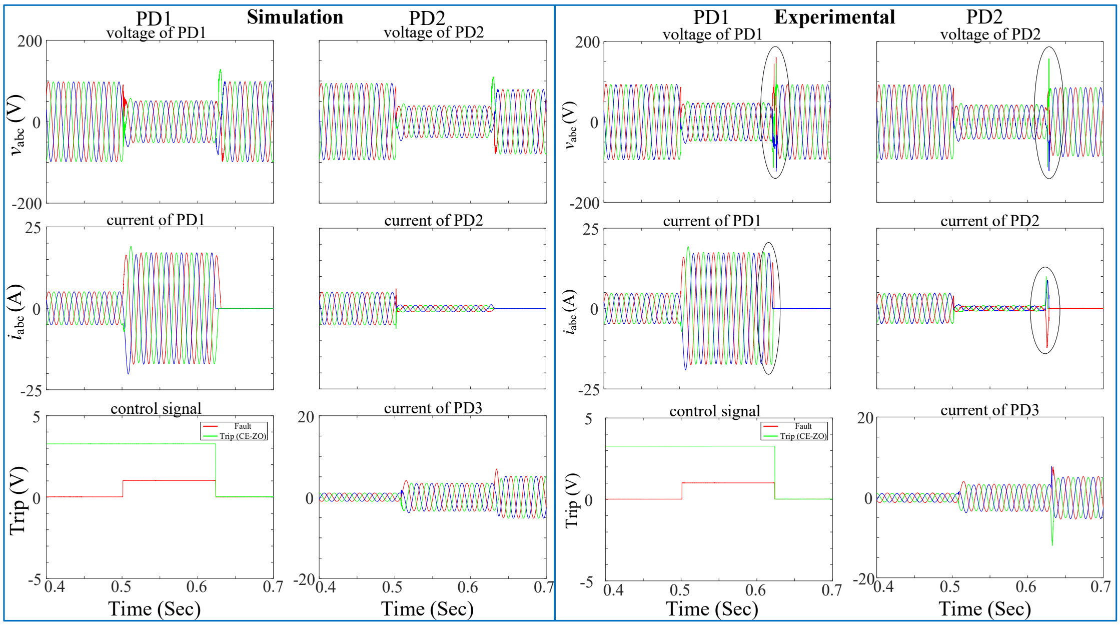

Fig. 7.64 Behaviour of CE-ZO for the three-phase fault when the fault at DL1

Fig. 7.65 and Fig. 7.66 show the *abc* voltages, *abc* currents and trip signals during a single-phase to groundand three-phase faults at DL1. The behaviour of the LO algorithm for PD2 and PD3 without the recloser algorithm is analysed. As seen in the third row of the figure, the PD exposed to the fault will always be disconnected (green line), and the other PDs that are far from the fault is closed again (blue line). The difference when the sag recovers are due to the trip of the mechanical contactor.

In the case of the LO algorithm, when a single-phase fault occurs at DL1 and the fault is near PD2, so PD2 will disconnect first at $t \approx 0.34$ s, and then PD1 will disconnect later at $t \approx 0.36$ s. Because the value of the negative-sequence voltage at PD2 is higher than the value at PD1, therefore, using the definite-time curve explained in chapter 5, the trip time can be determined for both PDs. Also, in the case of a three-phase fault, the trip time will depend on the value of the positive-sequence voltage at PD2 and PD1, so PD2 will disconnect first ($t \approx 0.16$ s), as it measures the lowest value, then PD2 will be disconnected ($t \approx 0.2$ s).

In the case of the LO algorithm, the protection algorithm has been tested in two scenarios: first with recloser (breakers placed behind the measurement devices), and second without recloser (breakers placed in front of the measurement devices), as explained in chapter 5.

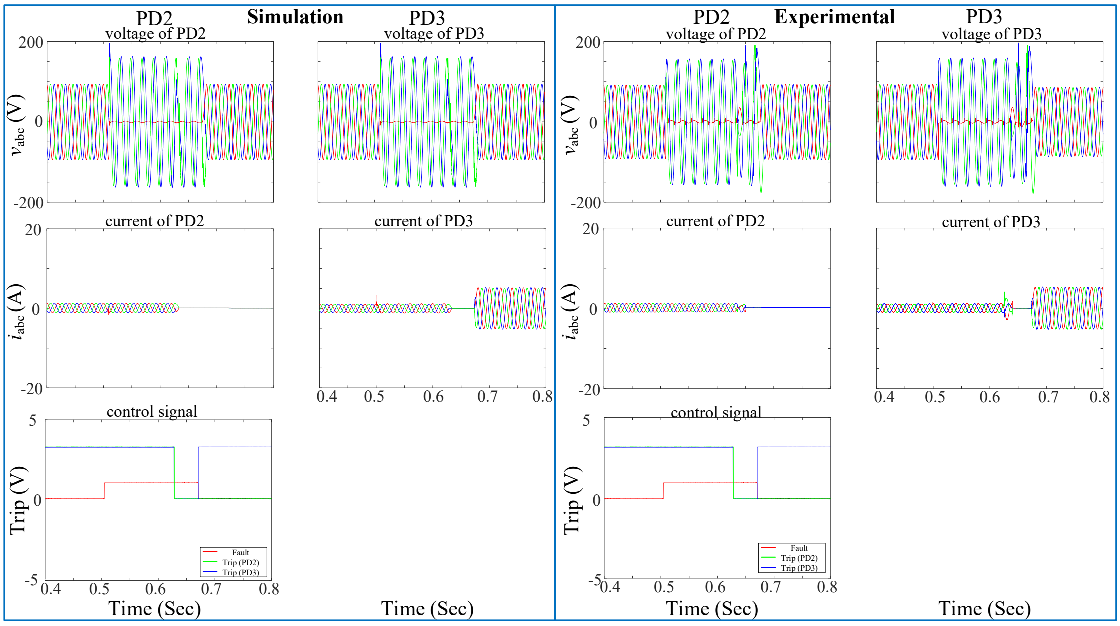

Fig. 7.65 Behaviour of LO without recloser for single-phase to ground fault when the fault at DL1

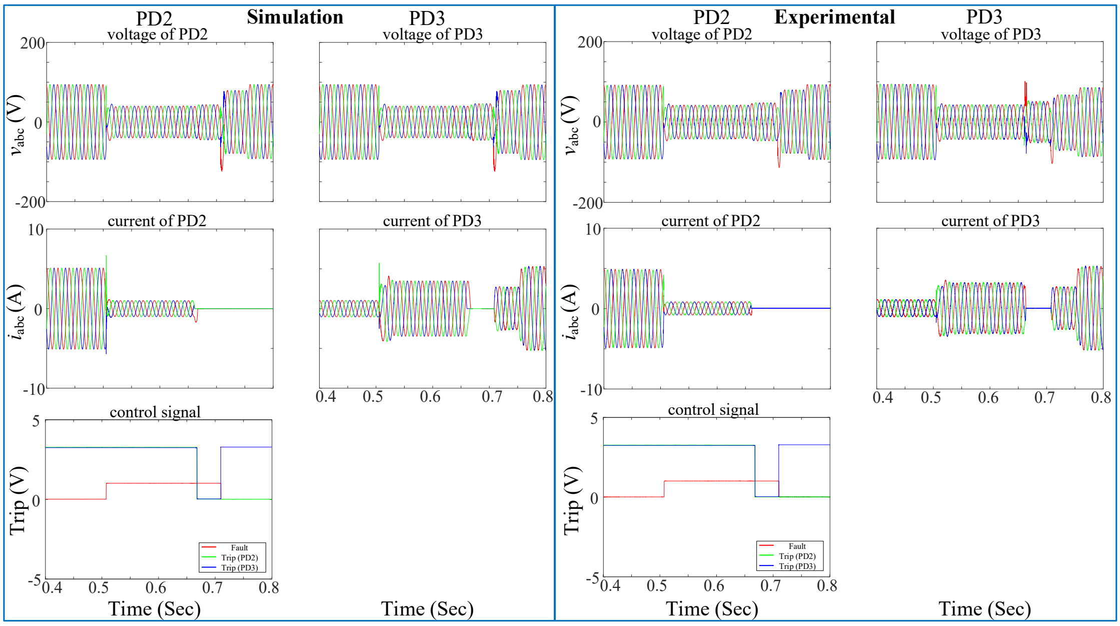

Fig. 7.66 Behaviour of LO without recloser for the three-phase fault when the fault at DL1

Fig. 7.67 and Fig. 7.68 show the behaviour of the LO algorithm with the recloser algorithm. The recloser algorithm is applied in this case, as explained in chapter 5 and Fig. 7.22. As shown in the third row of the figure, both PDs are disconnected simultaneously (blue and green lines), then one PD is connected, and if the PD is still exposed to the fault, a permanent disconnection is executed (green line). After that, the other PD is connected (blue line).

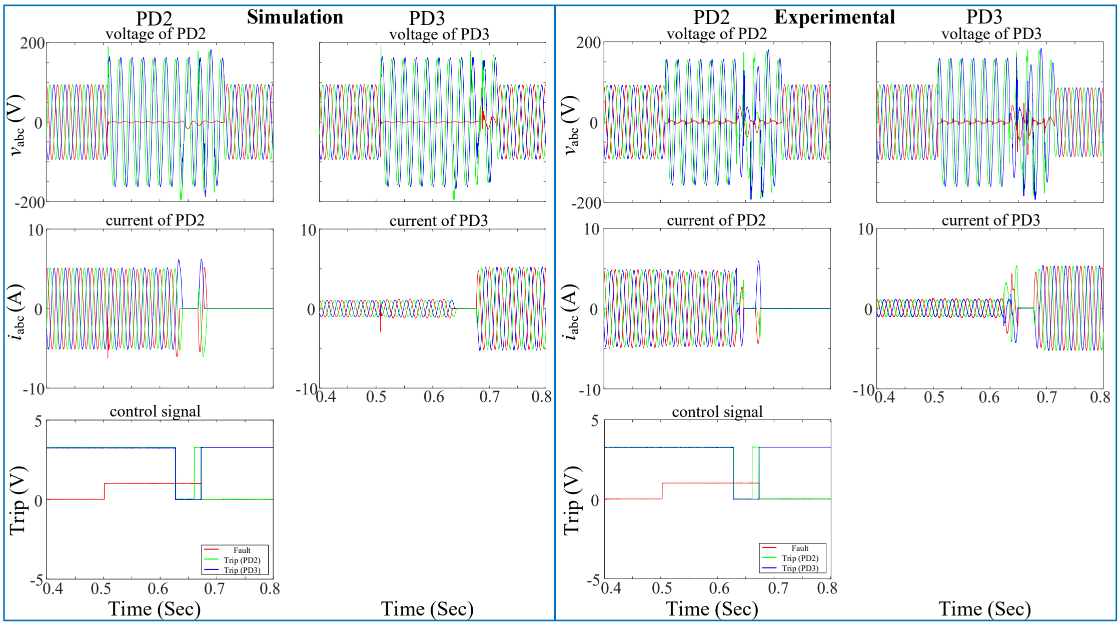

Fig. 7.67 Behaviour of LO with recloser for single-phase to ground fault when the fault at DL1

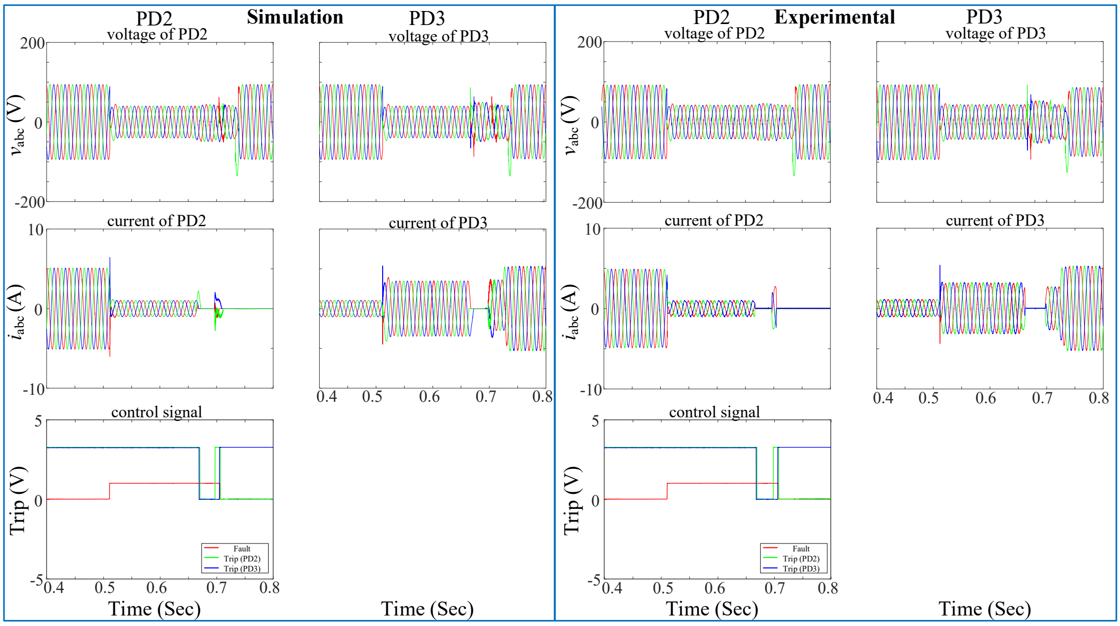

Fig. 7.68 Behaviour of LO with recloser for the three-phase fault when the fault at DL1

Previous figures show the behaviour of both PDs connected to the same bus (PD2 and PD3). To show the complete procedure of the LO algorithm, four PDs need to be demonstrated and analysed. For example, if the fault at DL1, the behaviour of PD1, PD2, PD3, and PD6 need to be studied. In this case, PD1 and PD6 are connected to the same bus, while PD2 and PD3 are connected to the same bus at the other end of the faulted line. Due to the limitation of the breakers in the laboratory, this case will be divided into two steps. First, the study of PD2 and PD3 will be tested, and then the study of PD1 and PD6 located at the other end of the faulted line will be tested.

Fig. 7.69 and Fig. 7.70 show the recloser algorithm between PD2 and PD3, then the disconnection of PD1 is implemented later. Also, Fig. 7.71 and Fig. 7.72 show the recloser algorithm between PD1 and PD6, when PD2 is already disconnected first.

For example, when a single-phase fault occurs at DL1 close to the end of the line (Fig. 7.62), the positive-sequence voltage (is the minimum for symmetrical faults) or negative-sequence voltage (is the maximum for unsymmetrical faults) at PD2 and PD3 are equal as they are connected to the same bus. Therefore, PD2 and PD3 are tripped first. Then, the recloser algorithm is applied to trip the PD at the faulted line (DL1). At this stage, PD3 is connected and because it is isolated from the fault, it remains connected. Then, PD2 is connected and as it is exposed to the fault as a consequence it is trip again (Fig. 7.69).

The other end of the faulted line is tripped in the next stage because it has the same highest positive-sequence voltage or the lowest negative-sequence voltage depending on the type of fault. PD1 and PD6 are tripped simultaneously, as they are connected to the same bus. Then, PD6 is connected and as it is isolated from the fault it will remain connected. Then, PD1 is connected and because it is exposed to the fault it will trip again (Fig. 7.71). At this stage, both ends of the line are disconnected and the faulted line is isolated from the grid. Fig. 7.70 and Fig. 7.72 represent the *abc* voltages, *abc* currents, and trip signals for the corresponding PDs in the case of a three-phase fault.

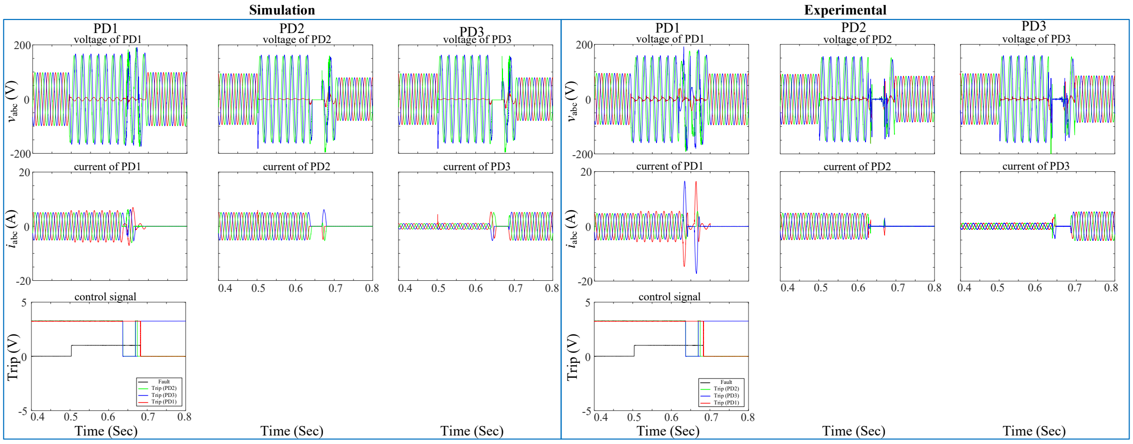

Fig. 7.69 Behaviour of PD1, PD2, and PD3 for single-phase to ground fault when the fault at DL1

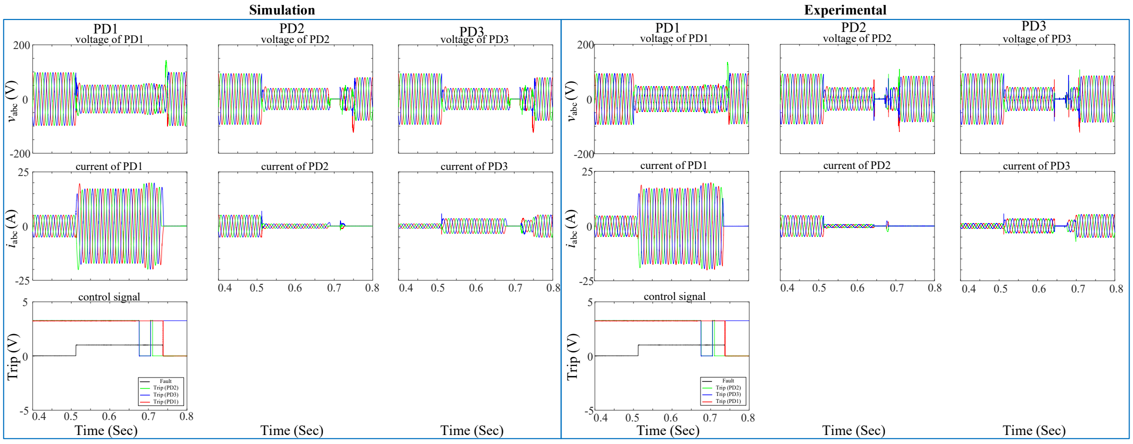

Fig. 7.70 Behaviour of PD1, PD2, and PD3 for the three-phase fault when the fault at DL1

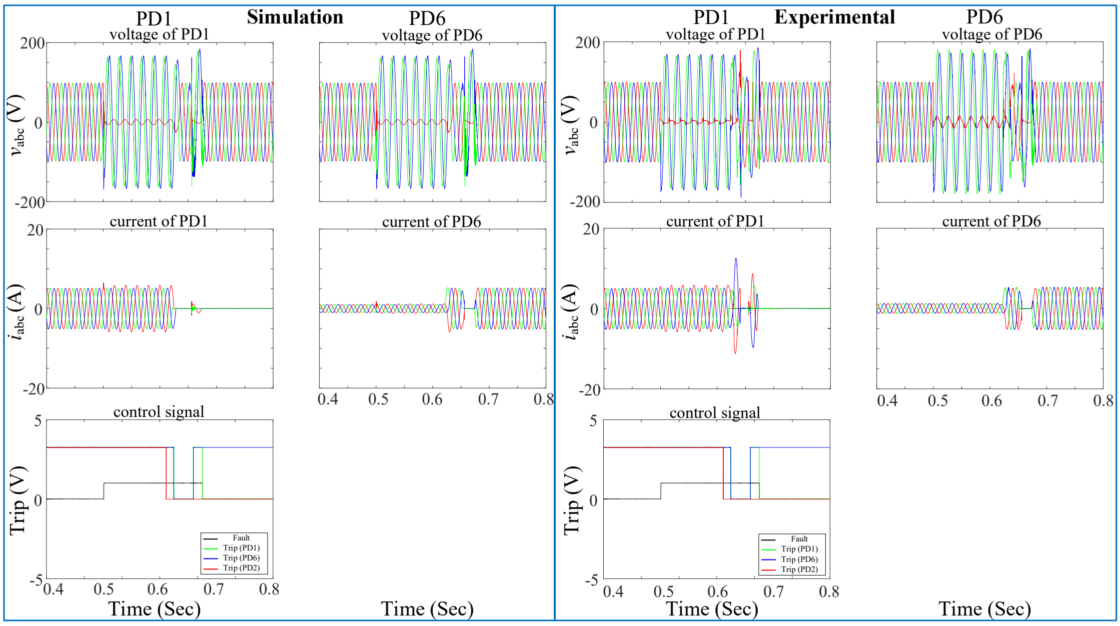

Fig. 7.71 Behaviour of PD1, PD2, and PD6 for single-phase to ground fault when the fault at DL1

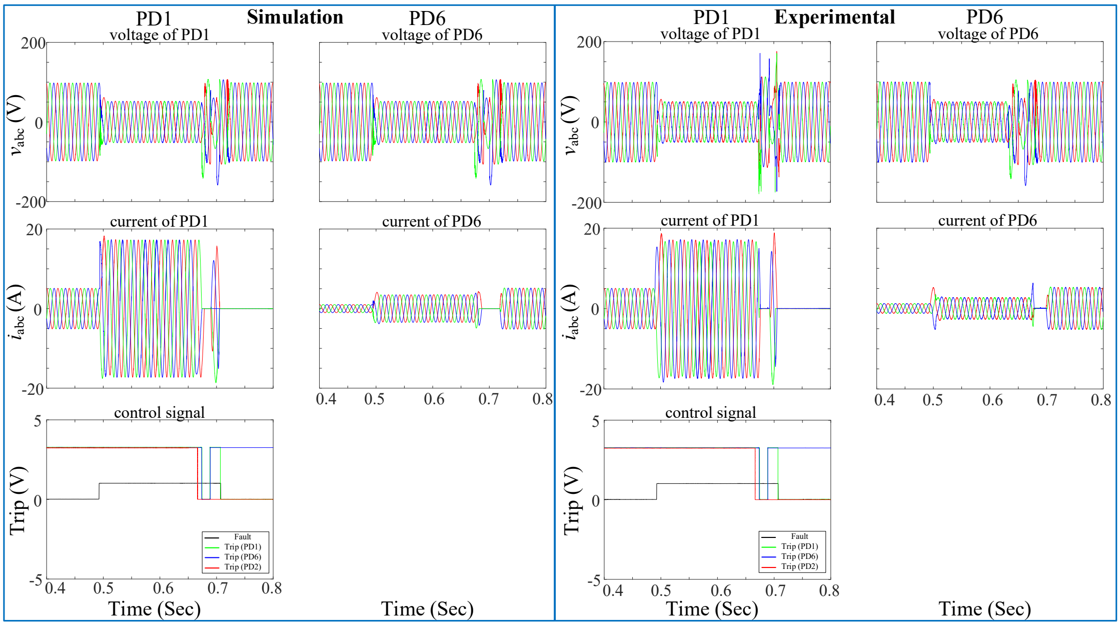

Fig. 7.72 Behaviour of PD1, PD2, and PD6 for the three-phase fault when the fault at DL1

- Breakers in DL1 and fault in DL3

In order to test the behaviour of the protection algorithms in different scenarios, the fault is moved from DL1 to DL3 as shown in Fig. 7.73. In this case, the PDs are located at DL1 to see the behaviour of the protection algorithm if a three-phase fault occurs in another line, the fault duration, in this case, is (200 ms). As seen in Fig. 7.74, for CE-ZO, the PDs did not trip because the fault is in another line.

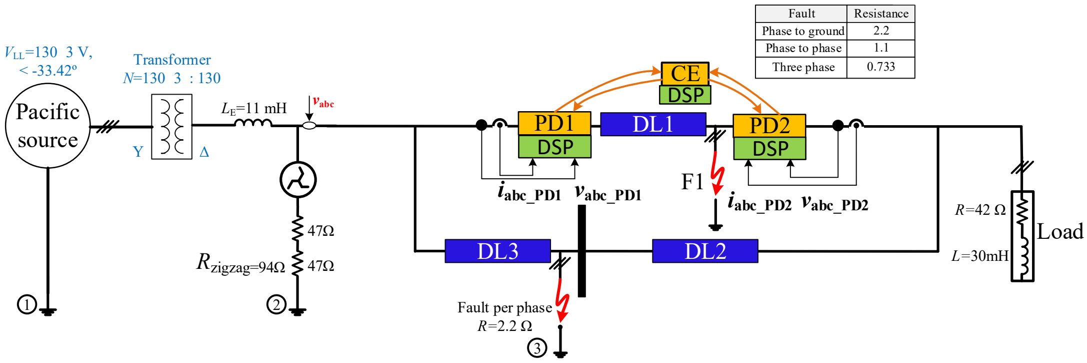

Fault | Resistance
Phase to ground 2.2
Phase to phase 1.1
Three phase 0.733
V_{LL}=130 3 V, < -33.42°
Transformer N=130 3 : 130
Pacific source
Y Δ
L_E=11 mH
v_{abc}
CE DSP
PD1 DSP
DL1
PD2 DSP
F1
i_{abc_PD1} v_{abc_PD1}
i_{abc_PD2} v_{abc_PD2}
47Ω
47Ω
R_{zigzag}=94Ω
R=42 Ω
L=30mH
Load
DL3
DL2
Fault per phase R=2.2 Ω
①
②
③

Fig. 7.73 Scheme of ring grid when the fault at DL3

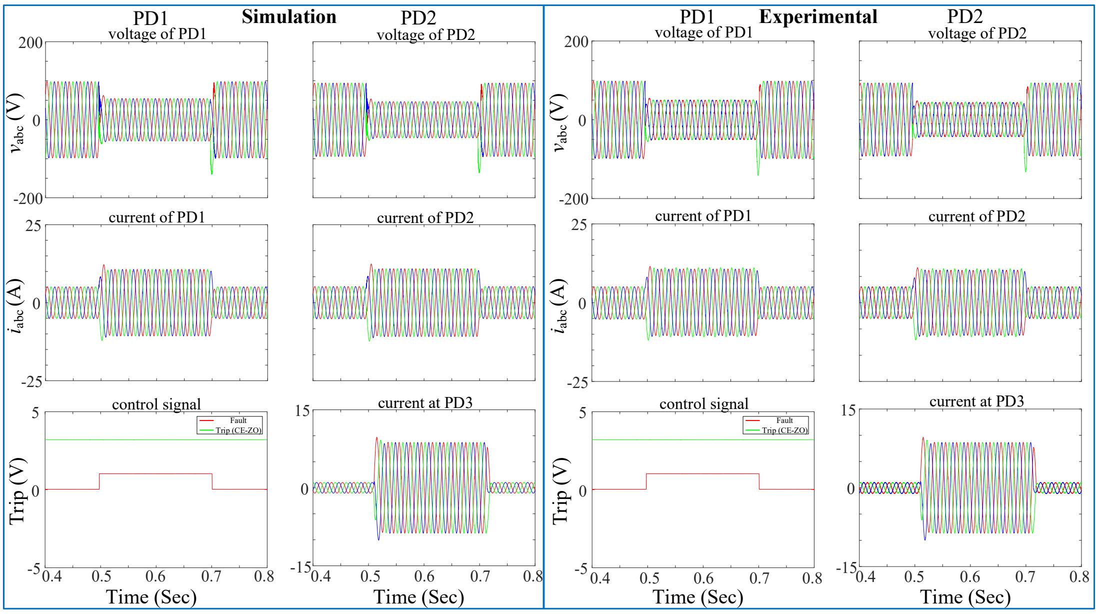

Fig. 7.74 Behaviour of CE-ZO for the three-phase fault when the fault at DL3

- ➢ Breakers in DL2 and fault in DL2

In order to test the protection algorithms in different locations, another test has been made when the PDs are placed in DL2 and the fault is in DL2, as shown in Fig. 7.75. In this case, the PDs must trip as the fault is in the same line, as shown in Fig. 7.76. The figure shows that during a single-phase to ground fault at DL2, the CE-ZO algorithm can detect and isolate the fault. The same behaviour is recognized at the recuperation of the fault due to the breaker opening.

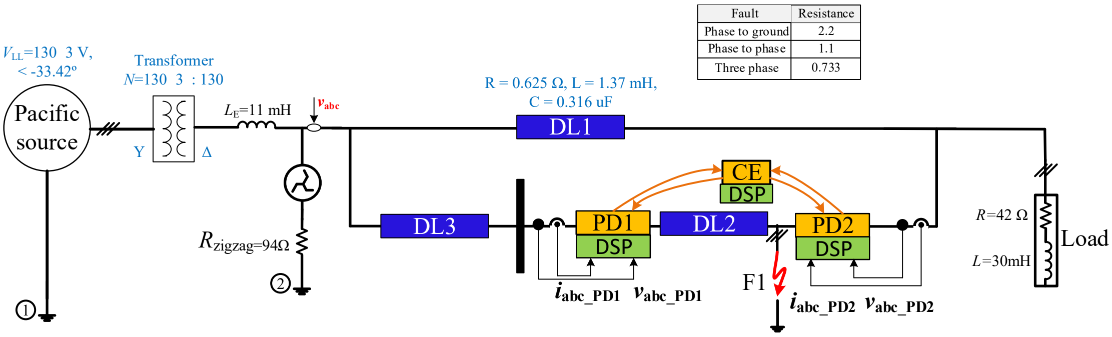

Fault | Resistance
Phase to ground 2.2
Phase to phase 1.1
Three phase 0.733
V_{LL}=130 3 V, < -33.42°
Transformer N=130 3 : 130
Pacific source
Y Δ
L_E=11 mH
v_{abc}
R = 0.625 Ω, L = 1.37 mH, C = 0.316 uF
DL1
CE DSP
DL3
PD1 DSP
DL2
PD2 DSP
R_{zigzag}=94Ω
F1
i_{abc_PD1} v_{abc_PD1}
i_{abc_PD2} v_{abc_PD2}
R=42 Ω
L=30mH
Load
①
②

Fig. 7.75 Scheme of ring grid when the fault at DL2

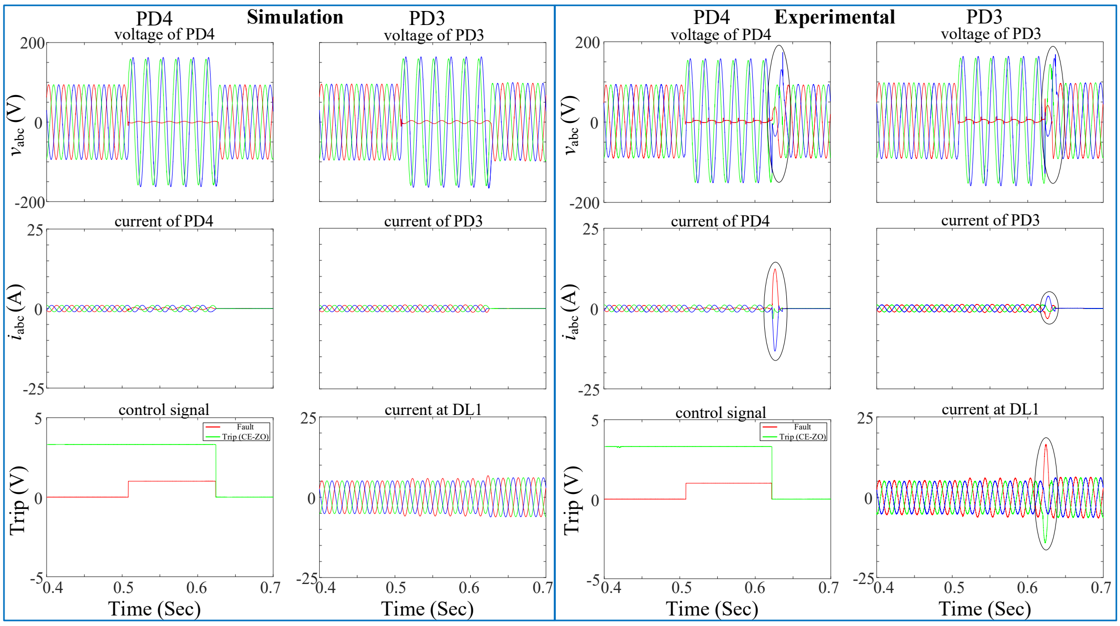

Fig. 7.76 Behaviour of CE-ZO for single-phase to ground fault when the fault at DL2

7.2.2.8. Complete ring grid with DG

Fig. 7.77 shows the grid implemented in the laboratory to emulate the complete ring grid with DG. The protection algorithms have been tested for both symmetrical (three-phase) and unsymmetrical (single-phase to ground) faults. As seen in Fig. 7.78 and Fig. 7.79, the CE-ZO algorithm behaviour has been tested for both types of faults. The faults are located at DL1 or DL2, as seen in Fig. 7.77. The figures show the *abc* voltages and *abc* currents for both PDs at each end of the faulted line. Moreover. Also, the third row shows the trip signal vs. the fault (more results can be seen in Appendix B). CE obtains the data of one line and the data of the other PDs imposed in the DSP of the CE controller.

In Fig. 7.78 the experimental *abc* currents of PD1 at the second row and the third column have a big overcurrent that is different from the simulated result. This is mainly because for ring grids, the SSRs are replaced with mechanical contactors, as explained in 7.2.2.7. However, the behaviour of the proposed protection algorithms does not affect by this change, as the algorithms are independent of the type of contactor.

In Fig. 7.78, and Fig. 7.79 the simulation and the experimental results agree. The noise on the injected voltage, and current is due to the accurate model of the converter and its commutation frequency. Also, as shown in Fig. 7.77, the inverter of the DG is connected directly to the DLs, another idea is to connected through a Y-Y transformer to isolate the two circuits that will be considered in the future work.

During steady-state, fault, and recovery periods, the error percentage between simulation and experimental measurements is 5% for instantaneous *abc* voltages and 2% for instantaneous *abc* currents.

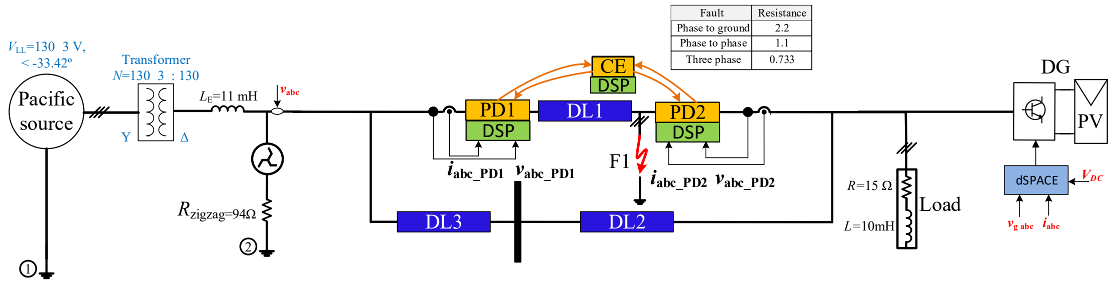

Fault	Resistance
Phase to ground	2.2
Phase to phase	1.1
Three phase	0.733

Fig. 7.77 Scheme of ring grid with DG

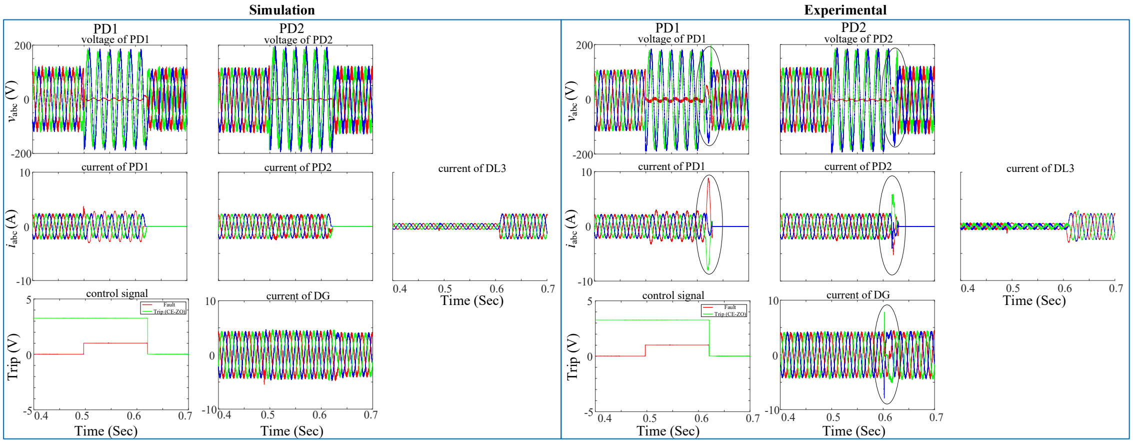

Fig. 7.78 Behaviour of CE-ZO for single-phase to ground fault when the fault at DL1

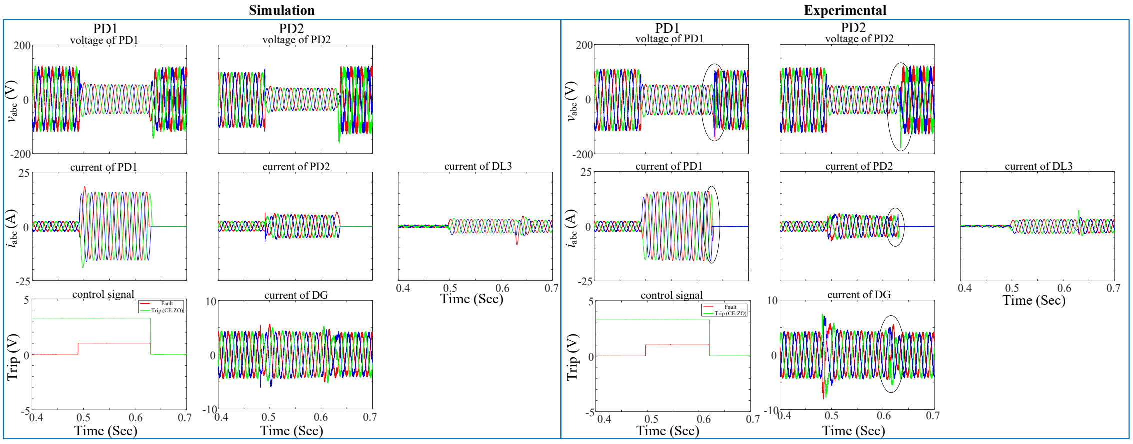

Fig. 7.79 Behaviour of CE-ZO for the three-phase fault when the fault at DL1

In the case of the LO algorithm, the protection algorithm has been tested in both scenarios, with and without recloser. Fig. 7.80 and Fig. 7.81 show the behaviour of the LO algorithm for PD2 and PD3 without the recloser algorithm. When a DG is connected to the ring grid, the values of the positive- and negative-sequence voltages are changed.

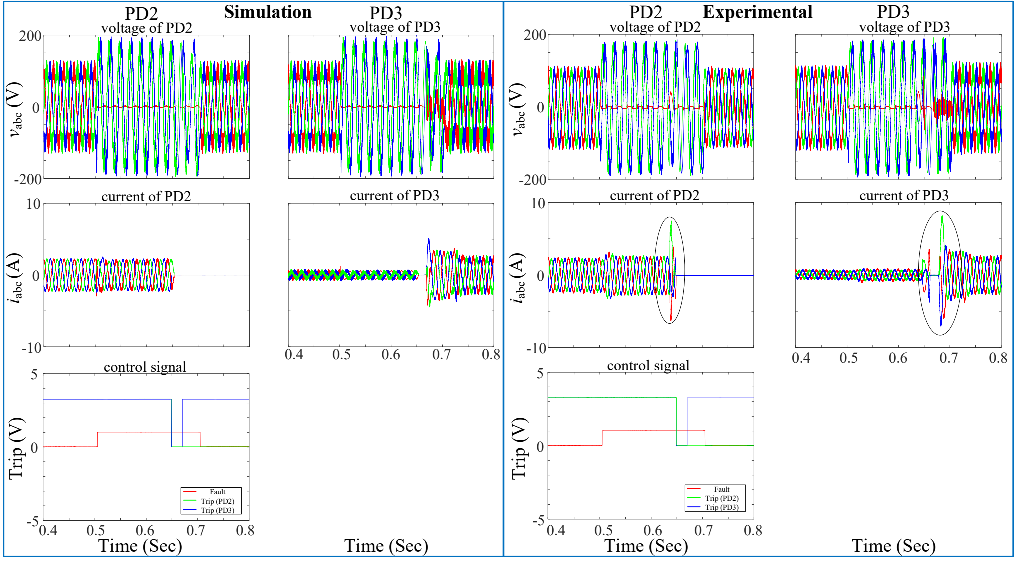

Fig. 7.80 Behaviour of LO without recloser for single-phase to ground fault when the fault at DL1

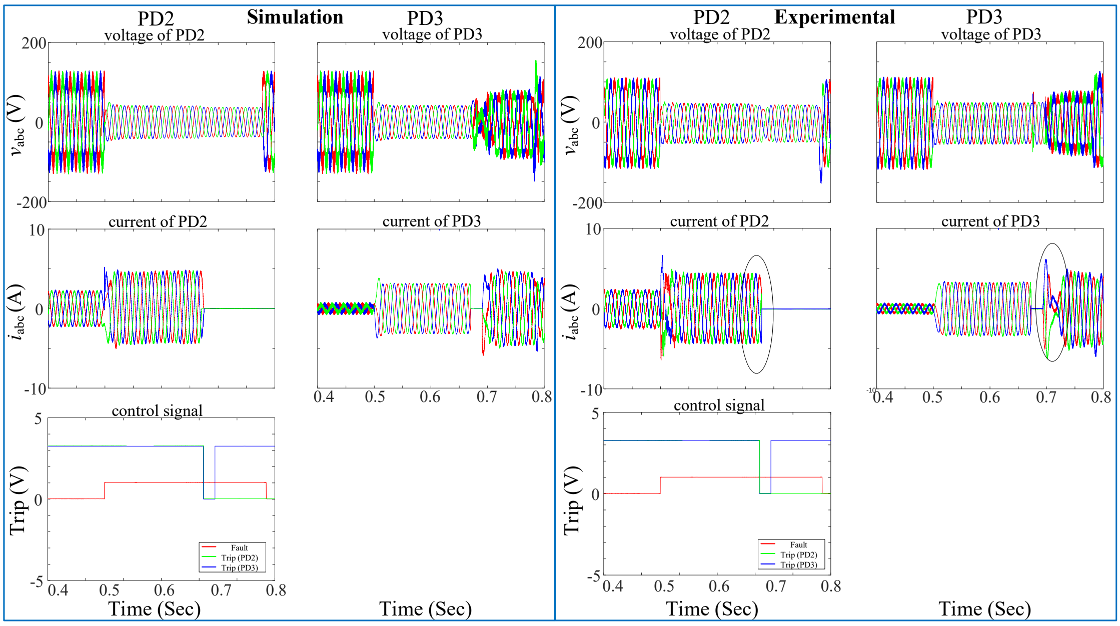

Fig. 7.81 Behaviour of LO without recloser for the three-phase fault when the fault at DL1

Fig. 7.82 and Fig. 7.83 show the behaviour of the LO algorithm with the recloser algorithm. In this case, the recloser algorithm is applied, as explained in chapter 5.

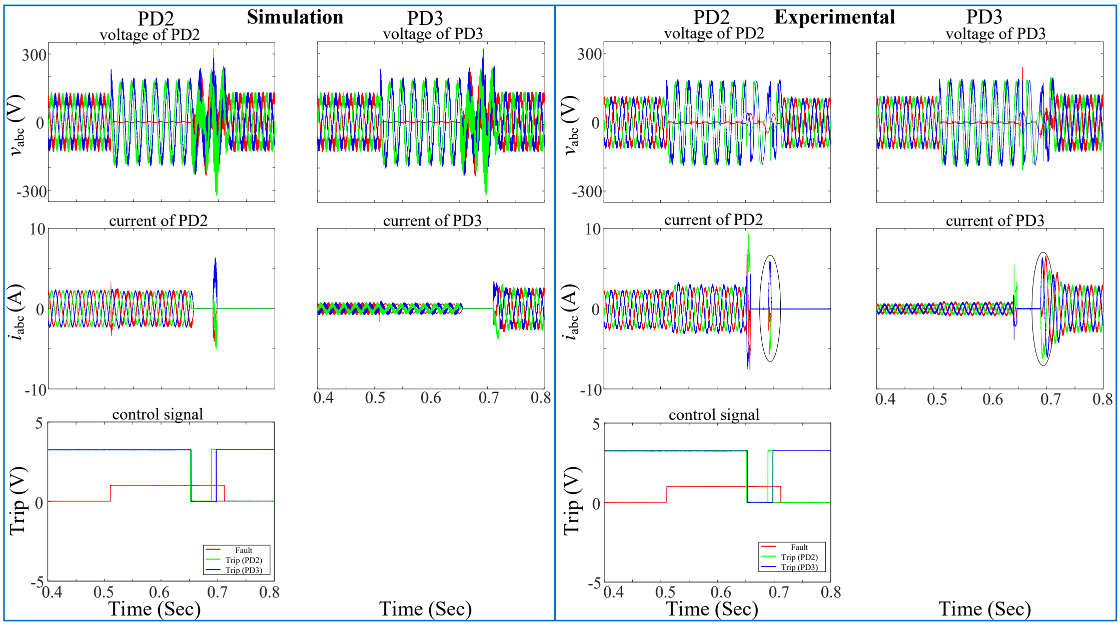

Fig. 7.82 Behaviour of LO with recloser for single-phase to ground fault when the fault at DL1

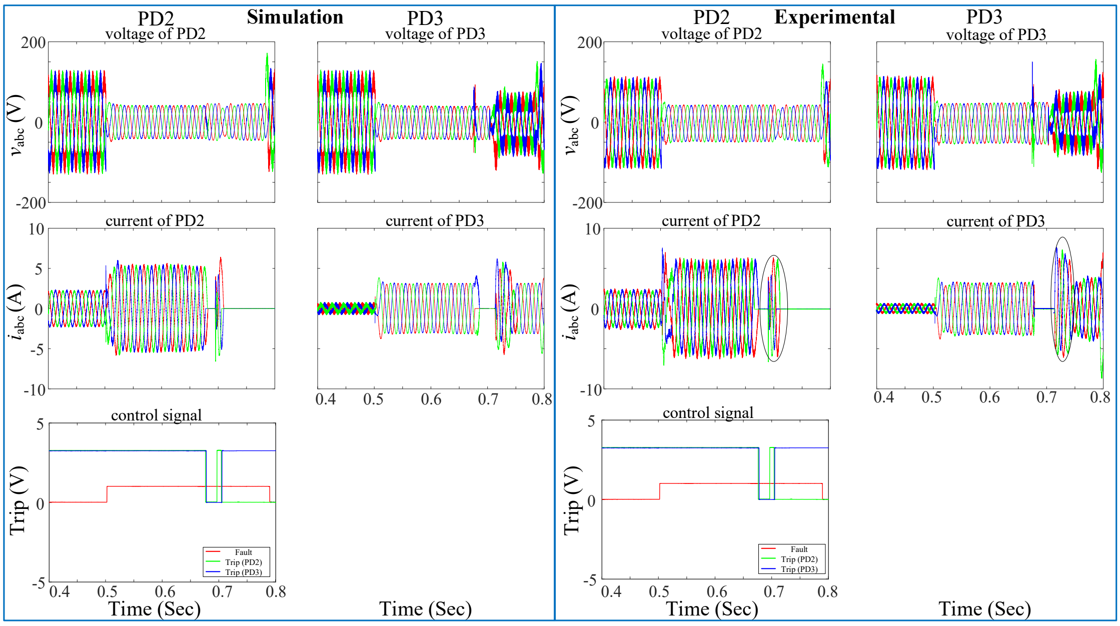

Fig. 7.83 Behaviour of LO with recloser for the three-phase fault when the fault at DL1

First, the study of PD2 and PD3 will be tested, and then the study of PD1 and PD6 located at the other end of the faulted line will be tested. Fig. 7.85 and Fig. 7.86 show the recloser algorithm between PD2 and PD3, then the disconnection of PD1 is implemented later. Also, Fig. 7.87 and Fig. 7.88 show the recloser algorithm between PD1 and PD2, when PD2 is disconnected first.

When PD2 and PD3 are disconnected, then the recloser algorithm is executed. During this time the DG inverter is disconnected from the grid. As the inverter control depends on the voltage and frequency of the grid, then as seen, a loss in the synchronization is happened for a short interval (Fig. 7.85 and Fig. 7.86). This point can be enhanced by implementing droop control to impose the voltage and frequency, which is one of the future points of this research. The same behaviour is obtained when PD1 and PD6 (Fig. 7.87 and Fig. 7.88).

Fig. 7.84 shows the steps of disconnection if a fault occurs at DL1, at the beginning PD2 and PD3 disconnect at the same time (Fig. 7.84(a)) as they are connected to the same bus and have the same voltage, then the recloser algorithm is applied, so PD3 is reconnected (Fig. 7.84(b)). After that, PD1 and PD6 trip at the same time (Fig. 7.84(c)), then the recloser algorithm is applied to reconnect PD6 (Fig. 7.84(d)).

Due to the direct connection between the inverter and the grid, without using an isolated transformer, distorted signals of the *abc* voltage are obtained in some figures, as seen in Fig. 7.79 - Fig. 7.83. However, the protection algorithms can work properly without problems. This point can be considered in future work to enhance the results.

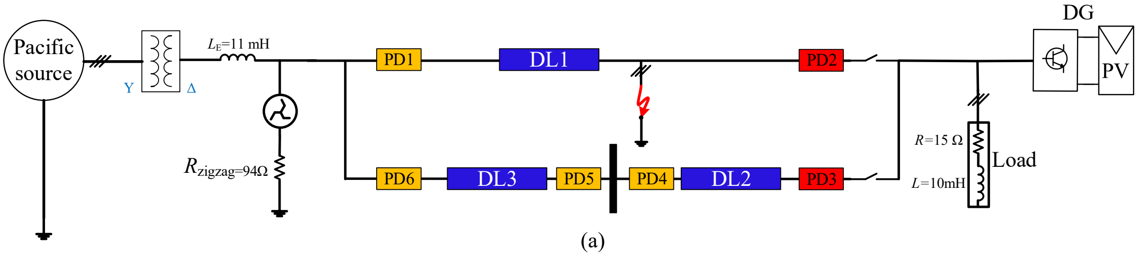

(a)

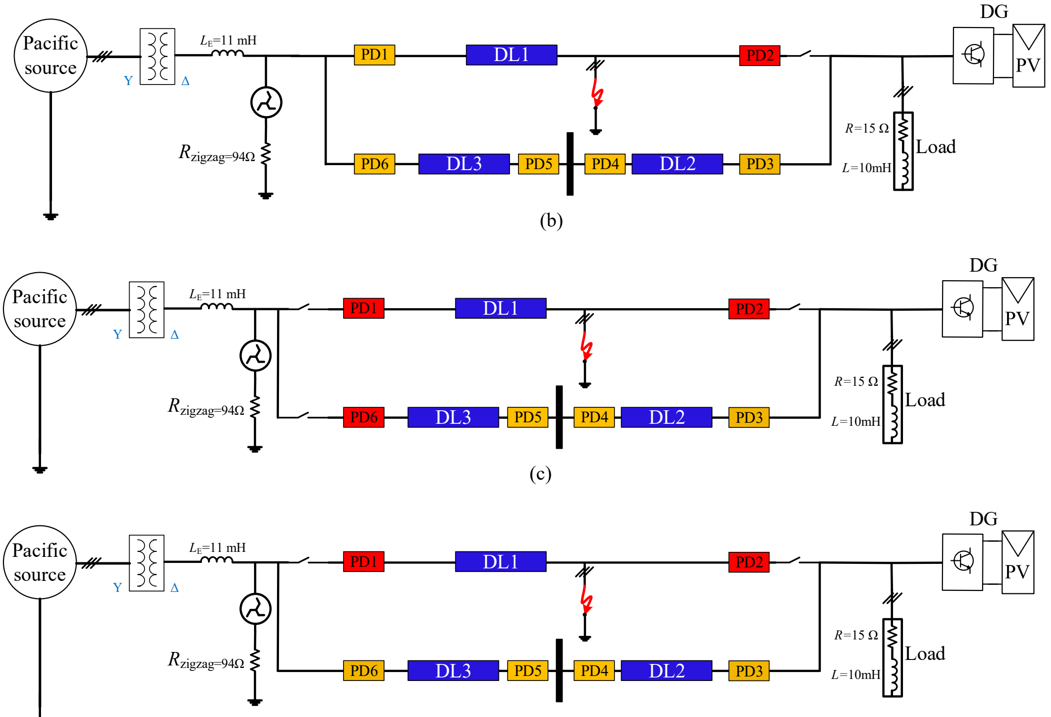
Pacific source
Y
Δ
L_E=11 mH
R_{zigzag}=94Ω
PD1
DL1
PD2
PD6
DL3
PD5
PD4
DL2
PD3
DG
PV
R=15 Ω
L=10mH
Load

(b)

(c)

(d)

Fig. 7.84 Scheme of ring grid with DG

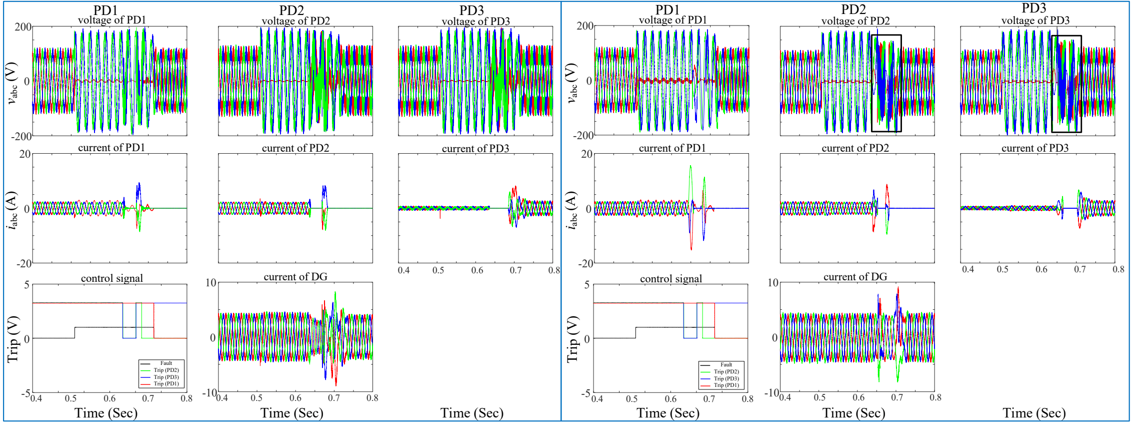

Fig. 7.85 Behaviour of PD1, PD2, and PD3 for single-phase to ground fault when the fault at DL1

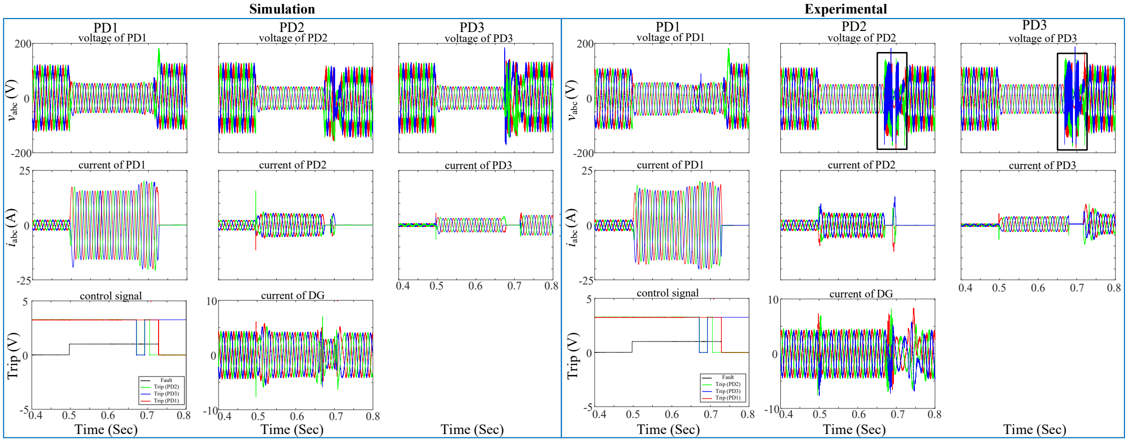

Fig. 7.86 Behaviour of PD1, PD2, and PD3 for the three-phase fault when the fault at DL1

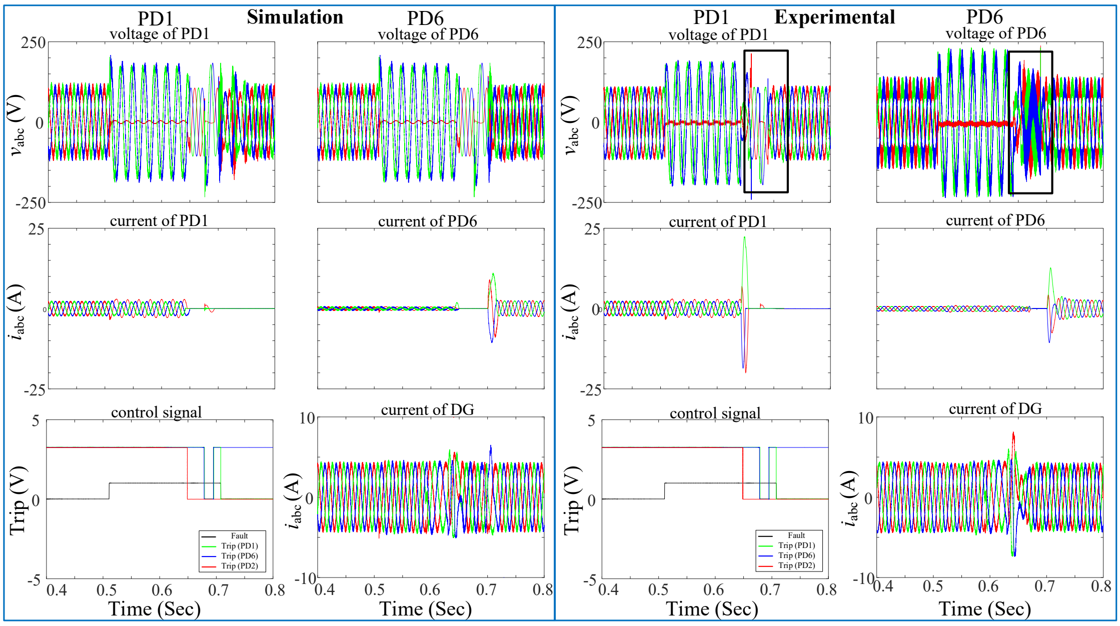

Fig. 7.87 Behaviour of PD1, PD2, and PD6 for single-phase to ground fault when the fault at DL1

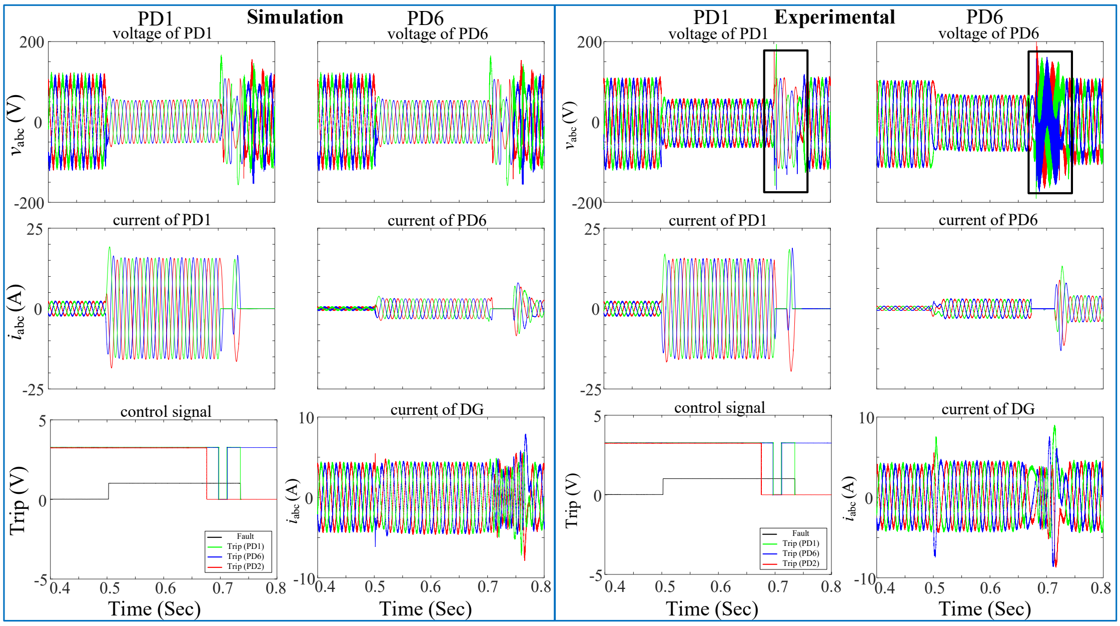

Fig. 7.88 Behaviour of PD1, PD2, and PD6 for the three-phase fault when the fault at DL1

In Fig. 7.89 and Fig. 7.90 the inverter control is implemented using CPC and CRC control techniques respectively (more results can be seen in Appendix B). As seen, the injected *abc* currents are sinusoidal but not symmetrical, because in both techniques the *dq* negative-sequence currents are not null. CPC injects constant active power, and CRC injects constant reactive power.

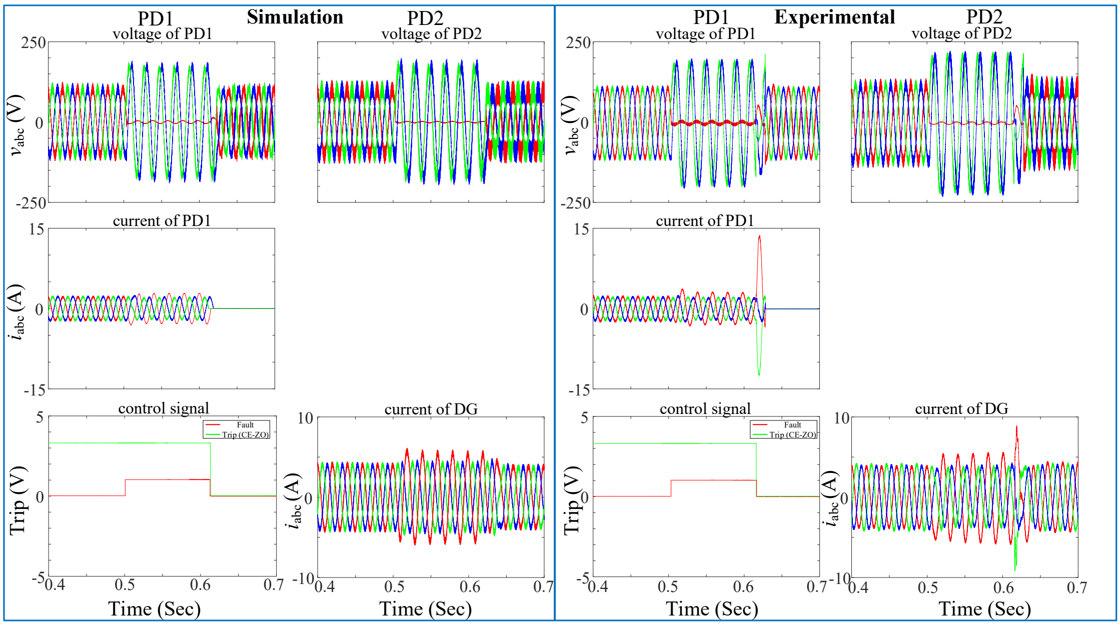

Fig. 7.89 Behaviour of CE-ZO control for single-phase to ground fault with CPC

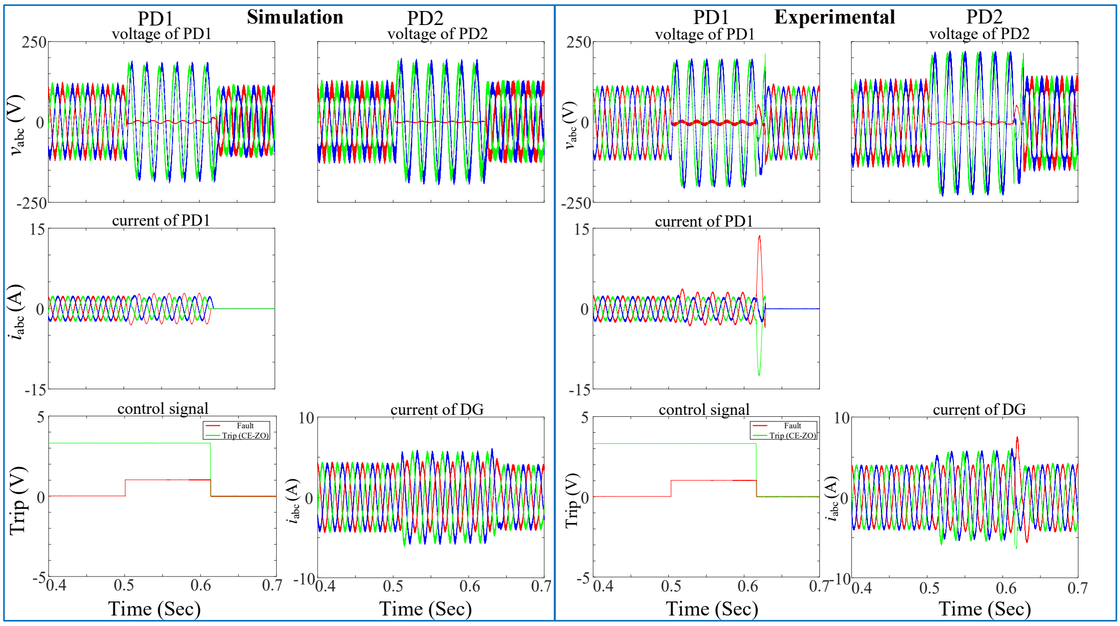

Fig. 7.90 Behaviour of CE-ZO control for single-phase to ground fault with CRC

- Breakers in DL1 and fault in DL3

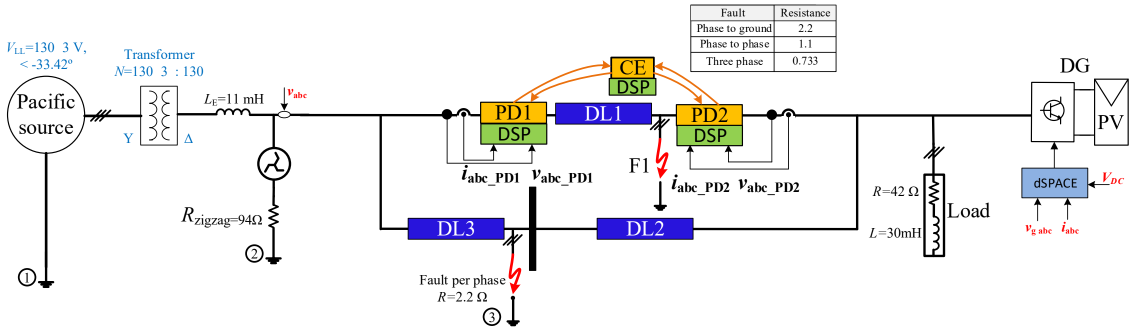
Fault | Resistance
Phase to ground | 2.2
Phase to phase | 1.1
Three phase | 0.733
V_{LL}=130 3 V, < -33.42°
Transformer N=130 3 : 130
Pacific source
Y Δ
L_E=11 mH
v_{abc}
R_{zigzag}=94Ω
①
②
③
CE
DSP
PD1
DSP
DL1
PD2
DSP
F1
i_{abc_PD1} v_{abc_PD1}
i_{abc_PD2} v_{abc_PD2}
DL3
DL2
Fault per phase R=2.2 Ω
R=42 Ω
L=30mH
Load
DG
PV
dSPACE
V_{DC}
$v_{g\ abc}$ i_{abc}

Fig. 7.91 Scheme of ring grid with DG when the fault at DL3

In order to test the behaviour of the protection algorithms, different scenarios have been considered. In this case, the fault location is moved from DL1 to DL3, as shown in Fig. 7.91. In this case, for CE, the PDs in DL1 did not trip because the fault is in another line, as seen in Fig. 7.92.

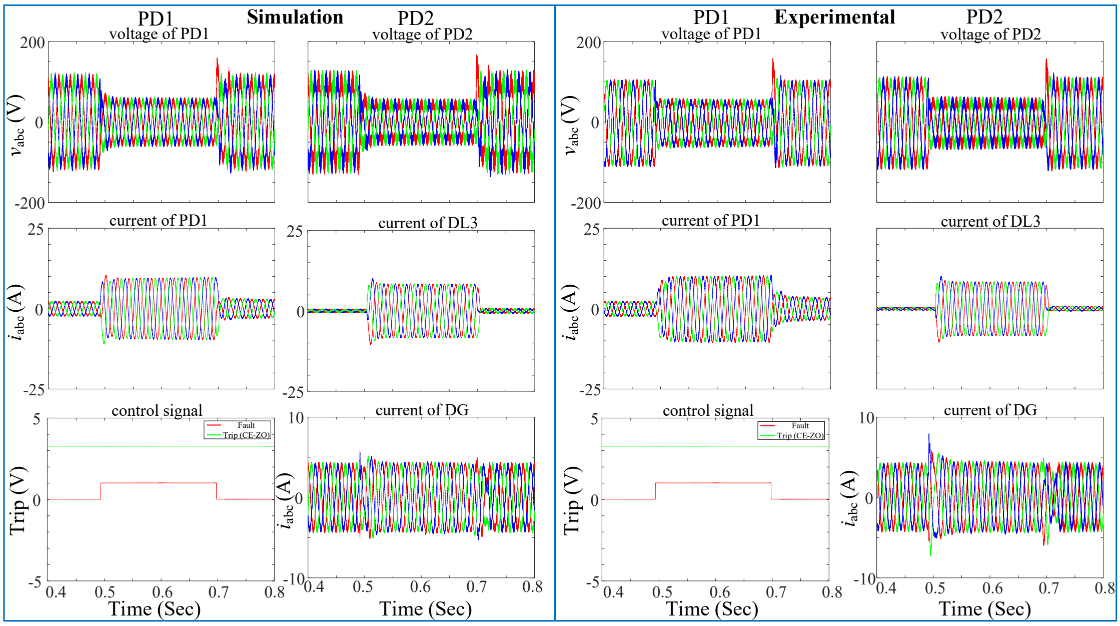

Fig. 7.92 Behaviour of CE-ZO for the three-phase fault when the fault at DL3

- ➢ Breakers in DL2 and fault in DL2

Another test has been made when the PDs are placed in DL2, and the fault is located at DL2 (Fig. 7.93). In this case, the PDs must trip as the fault is in the same line, as shown in Fig. 7.94.

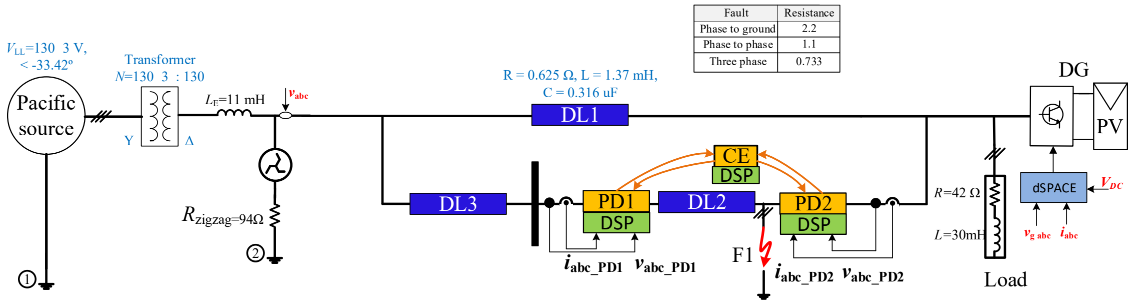
Fault | Resistance
Phase to ground | 2.2
Phase to phase | 1.1
Three phase | 0.733
V_{LL}=130 3 V, < -33.42°
Transformer N=130 3 : 130
Pacific source
Y Δ
L_E=11 mH
v_{abc}
R_{zigzag}=94Ω
①
②
R = 0.625 Ω, L = 1.37 mH, C = 0.316 uF
DL1
DL3
CE
DSP
PD1
DSP
DL2
PD2
DSP
F1
i_{abc_PD1} v_{abc_PD1}
i_{abc_PD2} v_{abc_PD2}
R=42 Ω
L=30mH
Load
DG
PV
dSPACE
V_{DC}
$v_{g\ abc}$ i_{abc}

Fig. 7.93 Scheme of ring grid when the fault at DL2

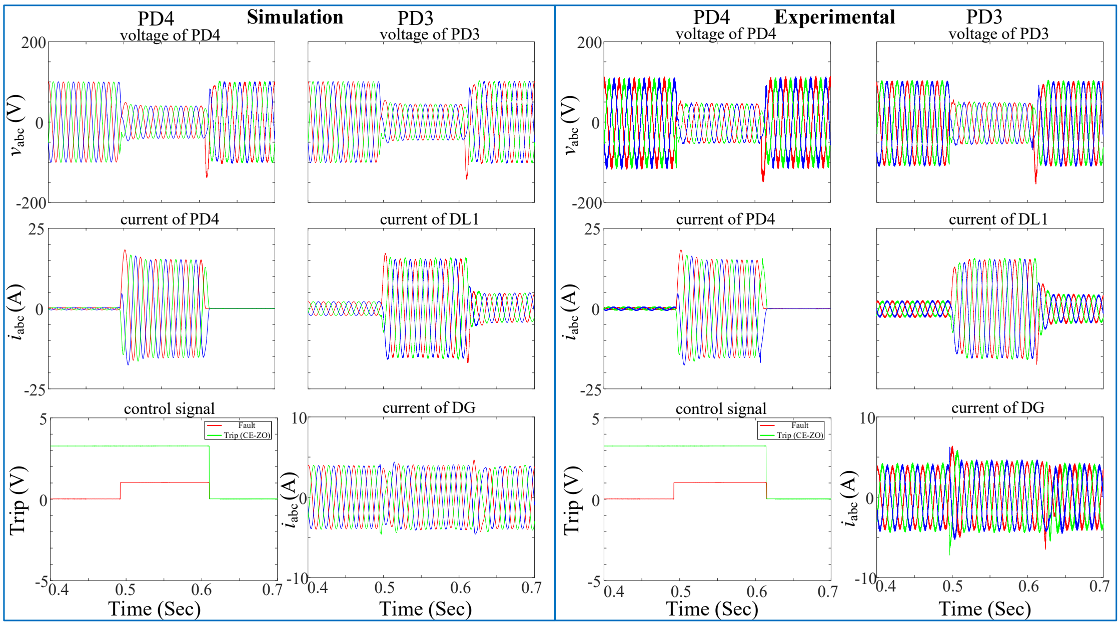

Fig. 7.94 Behaviour of CE-ZO for single-phase to ground fault when the fault at DL2

Previous results show the full functionality of the proposed protection algorithms (CE, ZO, and LO) in all the studied cases. In addition, the comparative study between the simulation results and the practical implementation gives strong reliability and accuracy of the proposed algorithms in different grid scenarios for radial and ring structures with and without DG penetration.

8 Conclusions, and recommendations for future work

8.1. Conclusions

In the present doctoral thesis, a study has been carried out of the effect of the Distributed Generator (DG) on the protection of Medium Voltage (MV) distribution system (DS), and protection algorithms have been proposed with the control of the DG converter during grid faults verifying grid code requirements. Once the thesis is finished, the conclusions that have been reached can be defined as follow:

- About the injected current control strategies under grid code

Controlling the positive and negative reference currents is required to control the active and reactive power during grid disturbances. Therefore, according to the Spanish grid code, this study has proposed different control strategies for a grid-connected inverter under voltage sags; two scenarios have been considered: the first imposes only positive sequence current, and the second imposes both positive and negative sequence current. In addition, a proposed limiting strategy is demonstrated.

In addition, the importance of complying with grid code requirements for DGs operating in a faulty grid with both balanced and unbalanced conditions, as well as ensuring the power converter voltage and current limits are not exceeded have been demonstrated. It is essential to highlight that grid codes consider balanced grid faults, yet most grid faults are unbalanced. An analytical study has been presented by using the *Park* and *Ku* transformation in order to represent the sag influence on the converter voltage and injected current in an easy way, as well as on the injected active and reactive powers. Comprehensive simulations have been carried out for all sag types throughout a wide range of durations and depths. Converter limits are considered to analyze the situations in which the PV system can be controlled.

The control strategies have been validated analytically, using simulation and laboratory experiments, considering symmetrical and unsymmetrical sags with different durations and depths. The effect of these sag parameters has also been illustrated in the complex plane.

The results show that for symmetrical sags, non of the proposed strategies violate the grid code. However, for unsymmetrical sags, the proposed Balanced Current Control (BCC) with grid code requirements is the optimum control method since it assures Fault Ride Through (FRT) for all sag types throughout the broadest range of durations and depths while also meeting grid code requirements. However, it has the drawback of power oscillation. On the other hand, the Constant Active Power Control (CPC) strategy allows constant active power injection, and the Constant Reactive Power Control (CRC) strategy allows constant reactive power injection; however, both strategies do not meet grid code requirements under unsymmetrical sags because transformed current oscillations are always outside the grid code limits. Also, the Constant Active Reactive Control (CPRC) strategy injects constant active and reactive powers, but the injected *abc* currents are distorted.

Consequently, the author suggested that future grid code versions include recommendations for dealing with unsymmetrical sags. Grid codes might, for example, define whether unbalanced injected currents or oscillations in the instantaneous active or reactive powers are permitted.

- About classical protection

MV DSs can have several configurations due to load consumption, reconfigurations due to faults or maintenance, and DG penetration dynamic changes. So, DS with DGs based on voltage source inverters requires advanced protection strategies to avoid undesired tripping. Therefore, the parameters of OverCurrent Relay (OCR) protection strategies are complicated to be fitted and cannot be adapted to these changes in some cases. On the other hand, Differential Relay (DR) protection strategies are faster and can adapt to the penetration of DG due to their ability to identify power flow changes. However, when the DG penetration change significantly, the DR protections could face problems.

Therefore, the OCR and DR drawbacks are highlighted, and a new protection strategy is developed using AI and validated experimentally to protect smart grids effectively. A comparison between conventional (OCR, DR) and Artificial Intelligent Centralize-Zone (CE-ZO) protection strategies illustrates the effectiveness of the selected protection strategy.

- About the proposed protection algorithms

This study has proposed different algorithms for fault location in the MV DS ring grid with high DG penetration to avoid undesirable tripping when inverter-based DGs are connected to a grid. The inverter control integrates the capabilities of the Low Voltage Ride Through (LVRT) and the requirements of the Spanish grid code.

The proposed protection scheme consists of three levels of protection algorithms, named Centralize (CE), Zone (ZO), and Local (LO) algorithms. The three algorithms provided can pinpoint the location of a fault and isolate the faulty part of the system with high precision. In order to have a more secure and redundant protection system, the study presents a novel usage of a communication-based directional relay system using an Artificial Neural Network (ANN).

In the CE, all Protective Device (PDs) data (Direction of Power Flow (DPF) and the positive-sequence current) in the grid are gathered and transmitted to a centralized controller. The ANN's training must incorporate variations in short circuit current and DPF in each PD. The main advantages are that it combines the security of the entire system into a single device. However, if some data is lost because of poor communication, the CE will not locate the exact location of the fault. As a result, ZO is proposed, based on zone control utilizing peer-to-peer communication, by integrating the data from the two PDs on the same line. Compared to the CE, which is fixed to the existing grid configuration, this approach can adapt to any modifications in the grid, even if they are just temporary. A third protection algorithm (LO) is also developed to locate the exact fault location based solely on local measurements gathered at each PD. According to the type (symmetrical or unsymmetrical), different algorithms will be applied depending on the calculation of the sequence components. The LO has been proposed independently of the communication between the PD; then in case of communication loss, the protection system can work effectively. The main advantage of this algorithm is the independence in the decision of each PD, which eliminates communication problems. The proposed (CE-ZO) algorithm compares the decisions of the two algorithms (CE and ZO) to generate a more dependable and redundant system. Furthermore, each algorithm serves as a backup for the others. Each PD can give decisions locally according to the signals received at each of them.

In order to analyze the proposed protection scheme, various cases have been studied, including different grid behaviour. In addition, a comparative study has been implemented to emphasize the functionality and reliability of the protection algorithm. The algorithms were tested for symmetrical and unsymmetrical faults, various fault resistance, different fault locations, and stiff and weak grids. For ring and radial grids, the results demonstrated that the faulted line can be located and isolated fast and efficiently. The proposed protection strategies can provide a more secure and dependable system against system faults, discrepancy, and hacking.

The protection strategies can adapt to different grid reconfiguration. Also, the trip decision is faster than conventional relays. Furthermore, a comparison of simulation results and the experimental implementation shows strong reliability and accuracy of the proposed algorithms in different grid scenarios for radial and ring structures with and without DG penetration.

8.2. Recommendations for future work

The following research points could be a future expansion to the work done in this thesis;

- The proposed protection strategies and current control strategies have been studied for DG connected to a stiff grid; however, for a very weak grid or a Micro Grid (MG), another study needs to be done in order to validate the proposed control for these types of grids.

  This can be done by changing the control strategies of the injected current that is based on controlling the active and reactive powers to another strategy that depends on imposing the voltage and frequency and does not depend on the voltage and the frequency of the grid. A hierarchical droop-based control could be studied and implemented to ensure inverter control during islanding and enhance the DGs' reliability during disturbances, load shadings, or faults.

- Provide a MATLAB^{TM} code to simulate the analysed grid and provide a Graphical User Interface (GUI) to implement the protection algorithm. In order to reduce the simulation time significantly, especially for large grids, that is able to decide the number of lines in the grid, the fault type and resistance, the penetration, and the location of each DG in the grid. Also, calculate the short-circuit current of the fault, and finally decide the fault's location and the trip signals need to be sent to the protective devices in the faulted line.
- If the fault is in the transmission grid, the behaviour of the protection system in MV DS could be studied, and a new protection strategy could be proposed by analyzing the effect of the faults on the *abc* voltages and currents and proposing a protection methodology.
- Study and experimentally verify how to integrate Solid State Relays (SSRs) in a ring grid using Insulated-Gate Bipolar Transistors (IGBTs) drivers or circuit triggers, as this option will give an advantage for the protection of ring grids, as the IGBTs, unlike thyristors, do not require a minimum voltage difference to operate. In addition, the IGBT has a low power requirement to run the gate drive. Also, to improve its reliability it could be paired with a snubber circuit, metal oxide varistor, and freewheeling diode.

  In addition, Simulate the mechanical-breaker including arc modeling, and improve its behaviour compared to other models.
- MPPT methods can be incorporated in the protection system analysis in future work by considering different generation scenarios during grid faults with partial weather conditions (Appendix H). In addition, the effect of the change in the power of photovoltaic generation during grid faults on the protection of the MV DS could be analysed, and a modification could be presented.

List of references

[1] J. Watson, M. Schmela,: "Global Market Outlook for Solar Power". Solar Power Europe, Brussels, Belgium (2018).

[2] A. S. Sánchez, “Automatic Fault Location in Electrical Distribution Networks with Distributed Generation.” Doctoral Thesis, Universitat Politècnica de Catalunya, 2018.

[3] T. T. Maor, “Impacts of Power System-Tied Distributed Generation on the Performance of Protection Systems,”, Master thesis, University of Texas at Tyler, 2017.

[4] “The spanish electricity system 2017,” Red Eléctrica de España, 2018.

[5] P. Janssen, “Monitoring, protection and fault location in power distribution using system-wide-measurements,” Doctoral Thesis, Ecole Polytechnique de Bruxelles, 2014.

[6] M. Esmaeili, M. Sedighizadeh, and M. Esmaili, “Multi-objective optimal reconfiguration and DG (Distributed Generation) power allocation in distribution networks using Big Bang-Big Crunch algorithm considering load uncertainty,” *Energy*, vol. 103, pp. 86–99, 2016.

[7] K. Kirubarani and A. Peer Fathima, “Impact of distribution generation on losses of distribution system,” *Lect. Notes Electr. Eng.*, vol. 394, pp. 395–403, 2017.

[8] A. A. Chen, A. J. Stephens, R. Koon Koon, M. Ashtine, and K. Mohammed-Koon Koon, “Pathways to climate change mitigation and stable energy by 100% renewable for a small island: Jamaica as an example,” *Renew. Sustain. Energy Rev.*, vol. 121, p. 109671, 2020.

[9] D. Mills, “Advances in solar thermal electricity technology,” *Sol. Energy*, vol. 76, no. 1–3, pp. 19–31, 2004.

[10] J. I. Marvik, "Fault Localization in Medium Voltage Distribution Networks with Distributed Generation", Doctoral Thesis, Norwegian University of Science and Technology, 2011.

[11] S. Marzal, R. Salas, R. González-Medina, G. Garcerá, and E. Figueres, “Current challenges and future trends in the field of communication architectures for microgrids,” *Renew. Sustain. Energy Rev.*, vol. 82, pp. 3610–3622, 2018.

[12] A. Villalón, M. Rivera, Y. Salgueiro, J. Muñoz, T. Dragičević, and F. Blaabjerg, “Predictive control for microgrid applications: A review study,” *Energies*, vol. 13, no. 10, pp. 1–32, 2020.

[13] E. McGlynn *et al.*, “The Future of Neuroscience: Flexible and Wireless Implantable Neural Electronics,” *Adv. Sci.*, vol. 8, no. 10, pp. 1–33, 2021.

[14] M. M. Saha, J. Izykowski, E. Rosolowski, *Fault Location on Power Networks*, 1st ed. Springer, London, 2010.

[15] L. Alzubaidi et al., Review of deep learning: concepts, CNN architectures, challenges, applications, future directions, vol. 8, no. 1. *Springer International Publishing*, 2021.

[16] K. Ncibi, T. Sadraoui, M. Faycel, and A. Djenina, “A Multilayer Perceptron Artificial Neural Networks Based a Preprocessing and Hybrid Optimization Task for Data Mining and Classification,” *Int. J. Econom. Financ. Manag.,* vol. 5, no. 1, pp. 12–21, 2017.

[17] B. K. Panigrahi, A. Abraham, S. Das, *Computational Intelligence in Power Engineering*., 1st ed. Springer, Berlin, 2010.

[18] R. Mechouma, B. Azoui, and M. Chaabane, “Three-phase grid connected inverter for photovoltaic systems, a review,” *2012 1st Int. Conf. Renew. Energies Veh. Technol. REVET 2012*, pp. 37–42, 2012.

[19] M. A. Leon and S. Kumar, “Mathematical modeling and thermal performance analysis of unglazed transpired solar collectors,” *Sol. Energy*, vol. 81, no. 1, pp. 62–75, 2007.

[20] A. Jäger-Waldau, *PV Status Report 2019*, publications Office of the European Union, 2019.

[21] NREL/BK -550-47514, “Utility-scale PV Variability Workshop,” 2009.

[22] G. Karagiannis, S. Chondrogiannis, E. Krausmann, I. Turksezer, *Power grid recovery after natural hazard impact*, publications Office of the European Union, 2017.

[23] A. Chandra, G. K. Singh, and V. Pant, “Protection of AC microgrid integrated with renewable energy sources – A research review and future trends,” *Electr. Power Syst. Res.*, vol. 193, p. 107036, 2021.

[24] Y. Li, “A fault location al tion algorithm for unbal thm for unbalanced Distribution sy distribution system wi stem without f thout fault type inform ype information,” Doctoral thesis, *UKnowledge*, University of Kentucky, 2018.

[25] S. S. Gururajapathy, H. Mokhlis, and H. A. Illias, “Fault location and detection techniques in power

distribution systems with distributed generation : A review," *Renew. Sustain. Energy Rev.*, vol. 74, pp. 949–958, 2017.

[26] S. Vasilic, "Fuzzy neural network pattern recognition algorithm for classification of the events in power system networks," Doctoral thesis, Texas A&M University, 2004.

[27] J. L. Blackburn, T. J. Domin, *Protective Relaying Principles and Applications*, 2nd ed. Marcel Dekker, New York, 1998.

[28] S. Beheshtaein, R. Cuzner, M. Savaghebi, and J. M. Guerrero, "Review on microgrids protection," *IET Gener. Transm. Distrib.*, vol. 13, no. 6, pp. 743–759, 2019.

[29] S. Hodder, B. Kasztenny, and N. Fischer, "Backup considerations for line current differential protection," *2012 65th Annu. Conf. Prot. Relay Eng.*, pp. 96–107, 2012.

[30] B. Bhalja, et al., *Protection and Switchgear*. 1st ed. University Press, Oxford, 2011.

[31] Y. L. Goh, A. K. Ramasamy, F. H. Nagi, A. Azwin, and Z. Abidin, "Evaluation of DSP based Numerical Relay for Overcurrent Protection," I*nternational journal of systems applications, engineering & development*, Vol. 5, no.3, 2011.

[32] E. Coster, *Distribution grid operation including distributed generation - Impact on grid protection and the consequenses of fault ride-through behaviour*, Doctoral thesis, Technische Universiteit Eindhoven, 2010.

[33] M. Singh, "Protection coordination in distribution systems with and without distributed energy resources- a review," *Prot. Control Mod. Power Syst.*, vol. 2, no. 1, pp. 1–17, 2017.

[34] F. Blaabjerg, Y. Yang, D. Yang, and X. Wang, "Distributed Power-Generation Systems and Protection," *Proc. IEEE*, vol. 105, no. 7, pp. 1311–1331, 2017.

[35] Z. Liang, X. Lin, Y. Kang, B. Gao, and H. Lei, "Short Circuit Current Characteristics Analysis and Improved Current Limiting Strategy for Three-phase Three-leg Inverter under Asymmetric Short Circuit Fault," *IEEE Trans. Power Electron.*, vol. 33, no. 8, pp. 7214–7228, 2018.

[36] C. Yeh *et al.*, "Design of Special Protection System for an Offshore Island With High-PV Penetration," *IEEE Trans. Ind. Appl.*, vol. 53, no. 2, pp. 947–953, 2017.

[37] M. Bakkar, S. Bogarra, F. Córcoles, and J. Iglesias, "Overcurrent protection based on ANNs for smart distribution networks with grid-connected VSIs," *IET Gener. Transm. Distrib.*, no. October, pp. 1–16, 2020.

[38] R. Teodorescu, M., Liserre, P., Rodriguez,: 'Grid converters for photovoltaic and wind power systems' 1st Edn., John Willey & Sons, Chichester, 2011.

[39] SRZ001: Particular technical specifications of HV / MV substations. Endesa, Spain (2018).

[40] A. Yazdaninejadi, A. Hamidi, S. Golshannavaz, F. Aminifar, and S. Teimourzadeh, "Impact of inverter-based DERs integration on protection, control, operation, and planning of electrical distribution grids," *Electr. J.*, vol. 32, no. 6, pp. 43–56, 2019.

[41] I. Kim and M. Begovic, "On impact of randomly distributed PV systems on distribution networks," *Proc. Annu. Hawaii Int. Conf. Syst. Sci.*, pp. 2418–2425, 2016.

[42] R. A. Walling, R. Saint, R. C. Dugan, J. Burke and L. A. Kojovic, "Summary of Distributed Resources Impact on Power Delivery Systems," in *IEEE Transactions on Power Delivery*, vol. 23, no. 3, pp. 1636-1644, July 2008.

[43] Yuping Lu, Jiao Du, Xia Lin and Jinjie Ma, "An asymmetrical fault line selection based on I2 scalar product research in distribution system with DGs," 2008 IEEE Power and Energy Society General Meeting - Conversion and Delivery of Electrical Energy in the 21st Century, 2008, pp. 1-6.

[44] J. Driesen and R. Belmans, "Distributed Generation : Challenges and Possible Solutions," *2006 IEEE Power Eng. Soc. Gen. Meet.*, p. 8 pp., 2006.

[45] T. Ackermann and V. Knyazkin, "Interaction between distributed generation and the distribution network: Operation aspects," *Proc. IEEE Power Eng. Soc. Transm. Distrib. Conf.*, vol. 2, pp. 1357–1362, 2002.

[46] H. Musa, "A Review of Distributed Generation Resource Types and Their Mathematical Models for Power Flow Analysis," *Int. J. Sci. Technol. Soc.*, vol. 3, no. 4, p. 204, 2015.

[47] A. Girgis and S. Brahma, "Effect of distributed generation on protective device coordination in distribution system," *LESCOPE 2001 - 2001 Large Eng. Syst. Conf. Power Eng. Powering Beyond 2001, Conf. Proc.*, pp. 115–119, 2001.

[48] B. Han, H. Li, G. Wang, D. Zeng, and Y. Liang, "A Virtual Multi-Terminal Current Differential Protection Scheme for Distribution Networks with Inverter-Interfaced Distributed Generators,"

IEEE Trans. Smart Grid, vol. 9, no. 5, pp. 5418–5431, 2018.

[49] F. Coffele, C. Booth, A. Dyśko, and G. Burt, “Quantitative analysis of network protection blinding for systems incorporating distributed generation,” *IET Gener. Transm. Distrib.*, vol. 6, no. 12, pp. 1218–1224, 2012.

[50] N. A. Rufa’I, L. Zhang, and B. Chong, “Constrained optimised flexible power control for grid-connected converters under unbalanced faults,” *J. Eng.*, no. March, pp. 321–333, 2021.

[51] V. Valouch, M. Bejvl, P. Šimek, and J. Škramlík, “Power Control of Grid-Connected Converters Under Unbalanced Voltage Conditions,” *IEEE Trans. Ind. Electron.*, vol. 62, no. 7, pp. 4241–4248, 2015.

[52] L. Monjo, J. J. Mesas, L. Sainz, J. Saura, and J. Pedra, “Impact of Voltage Sags on DC Bus Voltage in Unipolar LVDC Systems,”, pp. 1–4, 2015.

[53] P. Zhang, G. Zhang, and H. Wang, “Control Strategy of Low Voltage Ride-Through for Grid-Connected Photovoltaic Inverter,” *2015 IEEE 6th Int. Symp. Power Electron. Distrib. Gener. Syst.*, pp. 1–6, 2015.

[54] M. Mirhosseini, J. Pou, B. Karanayil, and V. G. Agelidis, “Positive- and Negative-Sequence Control of Grid- Connected Photovoltaic Systems under Unbalanced Voltage Conditions,” *2013 Australas. Univ. Power Eng. Conf.*, pp. 1–6, 2013.

[55] F. Wang, S. Member, J. L. Duarte, and M. A. M. Hendrix, “Pliant Active and Reactive Power Control for Grid-Interactive Converters Under Unbalanced Voltage Dips,” *IEEE Trans. Power Electron.*, vol. 26, no. 5, pp. 1511–1521, 2011.

[56] K. Li, J. Liu, Z. Wang, and B. Wei, “Strategies and Operating Point Optimization of STATCOM Control for Voltage Unbalance Mitigation in Three-Phase Three-Wire Systems,” vol. 22, no. 1, pp. 413–422, 2007.

[57] P. Rodriguez, G. Medeiros, M. C. Cavalcanti, and R. Teodorescu, “Safe Current Injection Strategies for a STATCOM under Asymmetrical Grid Faults,” *2010 IEEE Energy Convers. Congr. Expo.*, pp. 3929–3935, 2010.

[58] I. Candela, “Control of D-STATCOM During Unbalanced Grid Faults Based on DC Voltage Oscillations and Peak,” *IEEE Trans. Ind. Appl.*, vol. 54, no. 2, pp. 1680–1690, 2018.

[59] M. Garc, N. El Halabi, and H. Ajami, “Integrated Control Technique for Compliance of Solar Photovoltaic Installation Grid Codes,” vol. 27, no. 3, pp. 792–798, 2012.

[60] M. Bakkar, S. Bogarra, A. Rolán, F. Córcoles, and J. Saura, “Voltage sag influence on controlled threephase grid-connected inverters according to the Spanish grid code,” *IET Gener. Transm. Distrib.*, vol. 14, no. 10, pp. 1882–1892, 2020.

[61] G. B. Huka, W. Li, P. Chao, and S. Peng, “A comprehensive LVRT strategy of two-stage photovoltaic systems under balanced and unbalanced faults,” *Int. J. Electr. Power Energy Syst.*, vol. 103, pp. 288–301, 2018.

[62] M. Castilla, J. Miret, J. L. Sosa, J. Matas, and L. G. De Vicuña, “Grid-fault control scheme for three-phase photovoltaic inverters with adjustable power quality characteristics,” *IEEE Trans. Power Electron.*, vol. 25, no. 12, pp. 2930–2940, 2010.

[63] N. H. Viet and A. Yokoyama, “Impact of fault ride-through characteristics of high-penetration photovoltaic generation on transient stability,” *2010 Int. Conf. Power Syst. Technol. Technol. Innov. Mak. Power Grid Smarter, POWERCON2010*, pp. 1–7, 2010.

[64] J. M. G. and A. M.-S. I. Sadeghkhani, M. E. Hamedani Golshan, “A Current Limiting Strategy to Improve Fault Ride-Through of Inverter Interfaced Autonomous Microgrids,” *IEEE Trans. Smart Grid*, vol. 8, no. 5, pp. 2138–2148, 2017.

[65] N. Bottrell and T. C. Green, “Comparison of current-limiting strategies during fault ride-through of inverters to prevent latch-up and wind-up,” *IEEE Trans. Power Electron.*, vol. 29, no. 7, pp. 3786–3797, 2014.

[66] F. Wang, J. L. Duarte, and M. A. M. Hendrix, “Design and analysis of active power control strategies for distributed generation inverters under unbalanced grid faults,” *IET Gener. Transm. Distrib.*, vol. 4, no. 8, pp. 905–916, 2010.

[67] S. Abbasi, A. A. Ghadimi, A. H. Abolmasoumi, M. R. Miveh, and F. Jurado, “Enhanced control scheme for a three-phase grid-connected pv inverter under unbalanced fault conditions,” *Electron.*, vol. 9, no. 8, pp. 1–24, 2020.

[68] A. Camacho, M. Castilla, J. Miret, A. Borrell, and L. G. De Vicuña, “Active and Reactive Power

Strategies With Peak Current Limitation for Distributed Generation Inverters During Unbalanced Grid Faults," vol. 62, no. 3, pp. 1515–1525, 2015.

[69] L. Huang, H. Xin, Z. Wang, L. Zhang, K. Wu, and J. Hu, "Transient Stability Analysis and Control Design of Droop-Controlled Voltage Source Converters Considering Current Limitation," *IEEE Trans. Smart Grid*, vol. 10, no. 1, pp. 578–591, 2019, doi: 10.1109/TSG.2017.2749259.

[70] F. Nejabatkhah, Y. Li, and B. Wu, "Control strategies of three-phase distributed generation inverters for grid unbalanced voltage compensation," *2015 IEEE Energy Convers. Congr. Expo. ECCE 2015*, vol. 31, no. 7, pp. 6467–6474, 2015, doi: 10.1109/ECCE.2015.7310566.

[71] B. Mahamedi, M. Eskandari, J. E. Fletcher, and J. Zhu, "Sequence-Based Control Strategy with Current Limiting for the Fault Ride-Through of Inverter-Interfaced Distributed Generators," *IEEE Trans. Sustain. Energy*, vol. 11, no. 1, pp. 165–174, 2018, doi: 10.1109/TSTE.2018.2887149.

[72] H. Chen *et al.*, "A Low-Voltage Ride-Through Technique for Grid-Connected Converters With Reduced Power Transistors Stress," *IEEE Trans. Power Electron.*, vol. 31, no. 12, pp. 8562–8571, 2016, doi: 10.1109/TPEL.2016.2522511.

[73] H. D. Tafti, A. I. Maswood, G. Konstantinou, J. Pou, and P. Acuna, "Active / reactive power control of photovoltaic grid-tied inverters with peak current limitation and zero active power oscillation during unbalanced voltage sags," *IET power electronics*, vol. 11 no. 6, 2018, doi: 10.1049/iet-pel.2017.0210.

[74] M. A. Garnica López, J. L. García de Vicuña, J. Miret, M. Castilla and R. Guzmán, "Control Strategy for Grid-Connected Three-Phase Inverters During Voltage Sags to Meet Grid Codes and to Maximize Power Delivery Capability," in IEEE Transactions on Power Electronics, vol. 33, no. 11, pp. 9360-9374, Nov. 2018, doi: 10.1109/TPEL.2018.2792478.

[75] E. Afshari et al., "Control Strategy for Three-Phase Grid-Connected PV Inverters Enabling Current Limitation Under Unbalanced Faults," in IEEE Transactions on Industrial Electronics, vol. 64, no. 11, pp. 8908-8918, Nov. 2017, doi: 10.1109/TIE.2017.2733481.

[76] A. Camacho, M. Castilla, J. Miret, L. G. de Vicuña and R. Guzman, "Positive and Negative Sequence Control Strategies to Maximize the Voltage Support in Resistive–Inductive Grids During Grid Faults," in IEEE Transactions on Power Electronics, vol. 33, no. 6, pp. 5362-5373, June 2018, doi: 10.1109/TPEL.2017.2732452.

[77] A. B. Rey-Boué and J. S. and T. I. S. , N. F. Guerrero-Rodríguez, "Modeling and Design of the Vector Control for a Three-Phase Single-Stage Grid-Connected PV System with LVRT Capability according to the Spanish Grid Code," *Energies*, 2019.

[78] J. C. Hernández, J. De La Cruz, and B. Ogayar, "Electrical protection for the grid-interconnection of photovoltaic- distributed generation," *Electr. Power Syst. Res.*, vol. 89, pp. 85–99, 2012, doi: 10.1016/j.epsr.2012.03.002.

[79] M. Mirhosseini, J. Pou, and V. G. Agelidis, "Single- and Two-Stage Inverter-Based Grid-Connected Photovoltaic Power Plants With Ride-Through Capability Under Grid Faults," *IEEE Trans. Sustain. Energy*, vol. 6, no. 3, pp. 1150–1159, 2015, doi: 10.1109/TSTE.2014.2347044.

[80] A. Raza, A. Benrabah, T. Alquthami, and M. Akmal, "A review of fault diagnosing methods in power transmission systems," *Appl. Sci.*, vol. 10, no. 4, 2020, doi: 10.3390/app10041312.

[81] M. A. Aftab, S. M. S. Hussain, I. Ali, and T. S. Ustun, "Dynamic protection of power systems with high penetration of renewables: A review of the traveling wave based fault location techniques," *Int. J. Electr. Power Energy Syst.*, vol. 114, p. 105410, 2020, doi: 10.1016/j.ijepes.2019.105410.

[82] F. Aminifar, M. Abedini, T. Amraee, et al. "A review of power system protection and asset management with machine learning techniques". *Energy Syst* (2021). https://doi.org/10.1007/s12667-021-00448-6.

[83] S. K. Salman and Z. G. Wan, "Comparison between conventional and fuzzy logic controller-based AVC relay for voltage control application of distribution networks," 2007 International Power Engineering Conference (IPEC 2007), 2007, pp. 526-531.

[84] P. Tendayi and R. Bansal, "Renewable distributed generation : The hidden challenges – A review from the protection perspective," *Renew. Sustain. Energy Rev.*, vol. 58, pp. 1457–1465, 2016, doi: 10.1016/j.rser.2015.12.276.

[85] M. Norshahrani, H. Mokhlis, A. H. A. Bakar, J. J. Jamian, and S. Sukumar, "Progress on protection strategies to mitigate the impact of renewable distributed generation on distribution systems," *Energies*, vol. 10, no. 11, 2017, doi: 10.3390/en10111864.

[86] H. L. R. Van Der Walt, R. C. Bansal, and R. Naidoo, “PV based distributed generation power system protection: A review,” *Reinf. Plast.*, vol. 24, pp. 33–40, 2018, doi: 10.1016/j.ref.2017.12.002.

[87] N. Hussain, M. Nasir, J.C. Vasquez, J.M. Guerrero, "Recent Developments and Challenges on AC Microgrids Fault Detection and Protection Systems–A Review". *Energies 2020*, 13, 2149. https://doi.org/10.3390/en13092149.

[88] Y. Firouz, S. Farhadkhani, J. Lobry, F. Vallée, A. Khakpour, and O. Durieux, “Numerical comparison of the effects of different types of distributed generation units on overcurrent protection systems in MV distribution grids,” *Renew. Energy*, vol. 69, pp. 271–283, 2014, doi: 10.1016/j.renene.2014.03.035.

[89] H. C. Kiliçkiran, İ. Şengör, H. Akdemir, B. Kekezoğlu, O. Erdinç, and N. G. Paterakis, “Power system protection with digital overcurrent relays: A review of non-standard characteristics,” *Electr. Power Syst. Res.*, vol. 164, pp. 89–102, 2018, doi: 10.1016/j.epsr.2018.07.008.

[90] S. Jamali and H. Borhani-Bahabadi, “Non-communication protection method for meshed and radial distribution networks with synchronous-based DG,” *Int. J. Electr. Power Energy Syst.*, vol. 93, pp. 468–478, 2017, doi: 10.1016/j.ijepes.2017.06.019.

[91] A. A. Kida, A. E. Labrador Rivas, and L. A. Gallego, “An improved simulated annealing–linear programming hybrid algorithm applied to the optimal coordination of directional overcurrent relays,” *Electr. Power Syst. Res.*, vol. 181, p. 106197, 2020, doi: 10.1016/j.epsr.2020.106197.

[92] A. Shabani and K. Mazlumi, “Evaluation of a Communication-Assisted Overcurrent Protection Scheme for Photovoltaic-Based DC Microgrid,” *IEEE Trans. Smart Grid*, vol. 11, no. 1, pp. 429–439, 2020, doi: 10.1109/TSG.2019.2923769.

[93] H. Hooshyar, M. E. Baran, and L. Vanfretti, “Coordination assessment of overcurrent relays in distribution feeders with high penetration of PV systems,” *2013 IEEE Grenoble Conf. PowerTech, POWERTECH 2013*, 2013, doi: 10.1109/PTC.2013.6652117.

[94] W. El-khattam and T. S. Sidhu, “Resolving the impact of distributed renewable generation on directional overcurrent relay coordination: a case study,” *IET Renew. Power Gener.*, vol. 3, no. 4, p. 415, 2009, doi: 10.1049/iet-rpg.2008.0015.

[95] S. D. Saldarriaga-Zuluaga, J. M. López-Lezama, and N. Muñoz-Galeano, “Adaptive protection coordination scheme in microgrids using directional over-current relays with non-standard characteristics,” *Heliyon*, vol. 7, no. 4, p. 06665, 2021, doi: 10.1016/j.heliyon.2021.e06665.

[96] S. Mirsaeidi, D. Mat Said, M. Wazir Mustafa, M. Hafiz Habibuddin, and K. Ghaffari, “An analytical literature review of the available techniques for the protection of micro-grids,” *Int. J. Electr. Power Energy Syst.*, vol. 58, pp. 300–306, 2014, doi: 10.1016/j.ijepes.2014.01.032.

[97] B. K. Chaitanya, A. Yadav, and M. Pazoki, “An improved differential protection scheme for micro-grid using time-frequency transform,” *Int. J. Electr. Power Energy Syst.*, vol. 111, no. September 2018, pp. 132–143, 2019, doi: 10.1016/j.ijepes.2019.04.015.

[98] S. Xu, Y. Lu, and C. Cai, “Study of novel sine fitting differential protection algorithm in distribution system with high penetration of DGs,” *IEEE Power Energy Soc. Gen. Meet.*, pp. 1–6, 2012, doi: 10.1109/PESGM.2012.6344633.

[99] T. S. Aghdam, H. Kazemi Karegar, and H. H. Zeineldin, “Variable tripping time differential protection for microgrids considering DG stability,” *IEEE Trans. Smart Grid*, vol. 10, no. 3, pp. 2407–2415, 2019, doi: 10.1109/TSG.2018.2797367.

[100] T. S. Ustun and R. H. Khan, “Multiterminal Hybrid Protection of Microgrids over Wireless Communications Network,” *IEEE Trans. Smart Grid*, vol. 6, no. 5, pp. 2493–2500, 2015, doi: 10.1109/TSG.2015.2406886.

[101] V. Nougain, S. Mishra, and A. K. Pradhan, “MVDC Microgrid Protection Using a Centralized Communication With a Localized Backup Scheme of Adaptive Parameters,” *IEEE Trans. Power Deliv.*, vol. 34, no. 3, pp. 869–878, 2019, doi: 10.1109/TPWRD.2019.2899768.

[102] H. M. Sharaf, H. H. Zeineldin, and E. El-Saadany, “Protection coordination for microgrids with grid-connected and islanded capabilities using communication assisted dual setting directional overcurrent relays,” *IEEE Trans. Smart Grid*, vol. 9, no. 1, pp. 143–151, 2018, doi: 10.1109/TSG.2016.2546961.

[103] M. N. Alam, R. Gokaraju, and S. Chakrabarti, “Protection coordination for networked microgrids using single and dual setting overcurrent relays,” *IET Gener. Transm. Distrib.*, vol. 14, no. 14, pp.

2818–2828, 2020, doi: 10.1049/iet-gtd.2019.0557.

[104] M. Y. Shih, A. Conde, Z. Leonowicz, and L. Martirano, "An Adaptive Overcurrent Coordination Scheme to Improve Relay Sensitivity and Overcome Drawbacks due to Distributed Generation in Smart Grids," *IEEE Trans. Ind. Appl.*, vol. 53, no. 6, pp. 5217–5228, 2017, doi: 10.1109/TIA.2017.2717880.

[105] M. Y. Shih *et al.*, "A two stage fault current limiter and directional overcurrent relay optimization for adaptive protection resetting using differential evolution multi-objective algorithm in presence of distributed generation," *Electr. Power Syst. Res.*, vol. 190, p. 106844, 2021, doi: 10.1016/j.epsr.2020.106844.

[106] W. Li, Y. Tan, Y. Li, Y. Cao, C. Chen, and M. Zhang, "A New Differential Backup Protection Strategy for Smart Distribution Networks: A Fast and Reliable Approach," *IEEE Access*, vol. 7, pp. 38135–38145, 2019, doi: 10.1109/ACCESS.2019.2905604.

[107] S. Amir, H. Askarian, S. Hossein, H. Sadeghi, F. Razavi, and A. Nasiri, "An overview of microgrid protection methods and the factors involved," *Renew. Sustain. Energy Rev.*, vol. 64, pp. 174–186, 2016, doi: 10.1016/j.rser.2016.05.089.

[108] S. Kar, S. R. Samantaray, and M. D. Zadeh, "Data-Mining Model Based Intelligent Differential Microgrid Protection Scheme," *IEEE Syst. J.*, vol. 11, no. 2, pp. 1161–1169, 2017, doi: 10.1109/JSYST.2014.2380432.

[109] M. Y. Shih, A. Conde Enríquez, T. Y. Hsiao, and L. M. Torres Treviño, "Enhanced differential evolution algorithm for coordination of directional overcurrent relays," *Electr. Power Syst. Res.*, vol. 143, pp. 365–375, 2017, doi: 10.1016/j.epsr.2016.09.011.

[110] P. Mishra, A. Kumar Pradhan, and P. Bajpai, "Adaptive Relay Setting for Protection of Distribution System with Solar PV," *2018 20th Natl. Power Syst. Conf.*, vol. 2, no. 1, pp. 1–5, 2019, doi: 10.1109/npsc.2018.8771786.

[111] M. Manohar, E. Koley, and S. Ghosh, "Enhancing the reliability of protection scheme for PV integrated microgrid by discriminating between array faults and symmetrical line faults using sparse auto encoder," *IET Renew. Power Gener.*, vol. 13, no. 2, pp. 308–317, 2019, doi: 10.1049/iet-rpg.2018.5627.

[112] C. Yuan, S. Member, M. A. Haj-ahmed, S. Member, M. S. Illindala, and S. Member, "Protection Strategies for Medium-Voltage Direct-Current Microgrid at a Remote Area Mine Site," *IEEE Trans. Ind. Appl.*, vol. 51, no. 4, pp. 2846–2853, 2015, doi: 10.1109/TIA.2015.2391441.

[113] A. C. Adewole, "Investigation of Methodologies for Fault Detection and Diagnosis in Electric Power System Protection," Master thesis, Cape Peninsula University of Technology, 2012.

[114] G. S. Yogee *et al.*, "An algorithm for recognition of fault conditions in the utility grid with renewable energy penetration," *Energies*, vol. 13, no. 9, pp. 1–22, 2020, doi: 10.3390/en13092383.

[115] R. F. Pujiantara, M. Pujiantara, A. Priyadi and D. A. Asfani, "Protection coordination using zone selective interlocking method and neural network in IEEE 9 bus plan," 2018 International Conference on Information and Communications Technology (ICOIACT), 2018, pp. 196-201, doi: 10.1109/ICOIACT.2018.8350817.

[116] J. He, L. Liu, Y. Xu, F. Ding, and D. Zhang, "A two-step protection algorithm for smart distribution systems with DGs," *Int. Trans. Electr. Energy Syst.*, vol. 28, no. 3, pp. 1–15, 2018, doi: 10.1002/etep.2506.

[117] M. E. Baran, H. Hooshyar, Z. Shen, and A. Huang, "Accommodating high PV penetration on distribution feeders," *IEEE Trans. Smart Grid*, vol. 3, no. 2, pp. 1039–1046, 2012, doi: 10.1109/TSG.2012.2190759.

[118] H. Bisheh and B. Fani, "Local penetration-free control approach against numerous changes in PV generation level in MAS-based protection schemes," *IET renewable power generation*, vol. 13, pp. 1197–1204, 2019, doi: 10.1049/iet-rpg.2018.6083.

[119] A. Shabani and K. Mazlumi, "Evaluation of a Communication-Assisted Overcurrent Protection Scheme for Photovoltaic-Based DC Microgrid," in *IEEE Transactions on Smart Grid*, vol. 11, no. 1, pp. 429-439, Jan. 2020, doi: 10.1109/TSG.2019.2923769.

[120] K. Solak, W. Rebizant, and A. Klimek, "Fuzzy adaptive transmission-line differential relay immune to CT saturation," *IEEE Trans. Power Deliv.*, vol. 27, no. 2, pp. 766–772, 2012, doi: 10.1109/TPWRD.2011.2179815.

[121] A. Samadi and R. Mohammadi Chabanloo, “Adaptive coordination of overcurrent relays in active distribution networks based on independent change of relays’ setting groups,” *Int. J. Electr. Power Energy Syst.*, vol. 120, p. 106026, 2020, doi: 10.1016/j.ijepes.2020.106026.

[122] S. A. M. Javadian, M. R. Haghifam, and N. Rezaei, “A fault location and protection scheme for distribution systems in presence of DG using MLP neural networks,” *2009 IEEE Power Energy Soc. Gen. Meet. PES ’09*, pp. 1–8, 2009, doi: 10.1109/PES.2009.5275863.

[123] M. Mishra, R. R. Panigrahi, and P. K. Rout, “A combined mathematical morphology and extreme learning machine techniques based approach to micro-grid protection,” *Ain Shams Eng. J.*, vol. 10, no. 2, pp. 307–318, 2019, doi: 10.1016/j.asej.2019.03.011.

[124] M. Ghotbi-Maleki, R. M. Chabanloo, H. H. Zeineldin and S. M. Hosseini Miangafsheh, "Design of Setting Group-Based Overcurrent Protection Scheme for Active Distribution Networks Using MILP," in *IEEE Transactions on Smart Grid*, vol. 12, no. 2, pp. 1185-1193, March 2021, doi: 10.1109/TSG.2020.3027371.

[125] J. J. Q. Yu, Y. Hou, A. Y. S. Lam and V. O. K. Li, "Intelligent Fault Detection Scheme for Microgrids With Wavelet-Based Deep Neural Networks," in *IEEE Transactions on Smart Grid*, vol. 10, no. 2, pp. 1694-1703, March 2019, doi: 10.1109/TSG.2017.2776310.

[126] V. A. Papaspiliotopoulos, T. A. Kurashvili and G. N. Korres, "Optimal coordination of directional overcurrent relays in distribution systems with distributed generation based on a hybrid PSO-LP algorithm," MedPower 2014, 2014, pp. 1-6, doi: 10.1049/cp.2014.1697.

[127] S. Barakat, M. B. Eteiba, and W. I. Wahba, “Fault location in underground cables using ANFIS nets and discrete wavelet transform,” *J. Electr. Syst. Inf. Technol.*, vol. 1, no. 3, pp. 198–211, 2014, doi: 10.1016/j.jesit.2014.12.003.

[128] H. Zayandehroodi, A. Mohamed, H. Shareef, and M. Mohammadjafari, “Determining exact fault location in a distribution network in presence of DGs using RBF neural networks,” *2011 IEEE Int. Conf. Inf. Reuse Integr.*, pp. 434–438, 2011, doi: 10.1109/IRI.2011.6009587.

[129] H. Zayandehroodi, A. Mohamed, M. Farhoodnea, and M. Mohammadjafari, “An optimal radial basis function neural network for fault location in a distribution network with high penetration of DG units,” *Meas. J. Int. Meas. Confed.*, vol. 46, no. 9, pp. 3319–3327, 2013, doi: 10.1016/j.measurement.2013.05.002.

[130] S. Sadat and H. Kamangar, “Optimal Combined Overcurrent and Distance Relays Coordination Using a New Genetic Algorithm Method,” *International Journal of Innovations in Energy Systems and Power,* vol. 5, no. 1, pp. 17–21, 2010.

[131] M. T. Scholar, “Optimal Coordination of Over Current and Distance Relays,”, *International Journal of Engineering Research & Technology*, vol. 3, no. 10, pp. 748–753, 2014.

[132] S. K. Salman and Z. G. Wan, “Fuzzy logic-based AVC relay for voltage control of distribution network with and without distributed/embedded generation,” *2007 IEEE Lausanne POWERTECH, Proc.*, pp. 2128–2132, 2007, doi: 10.1109/PCT.2007.4538647.

[133] I. Xyngi and M. Popov, “An Intelligent Algorithm for the Protection of Smart Power Systems,” *IEEE Trans. Smart Grid*, vol. 4, no. 3, pp. 1541–1548, 2013, doi: 10.1109/TSG.2013.2244621.

[134] Q. Yang, J. A. Barria, T. C. Green, and S. Member, “Communication Infrastructures for Distributed Control of Power Distribution Networks,” *IEEE Trans. Ind. Informatics*, vol. 7, no. 2, pp. 316–327, 2011, doi: 10.1109/TII.2011.2123903.

[135] T. S. Ustun, C. Ozansoy, and A. Zayegh, “Modeling of a Centralized Microgrid Protection System and Distributed Energy Resources According to IEC 61850-7-420,” *IEEE Trans. Power Syst.*, vol. 27, no. 3, pp. 1560–1567, 2012, doi: 10.1109/TPWRS.2012.2185072.

[136] H. Karimi, G. Shahgholian, B. Fani, I. Sadeghkhani, and M. Moazzami, “A protection strategy for inverter-interfaced islanded microgrids with looped configuration,” *Electr. Eng.*, vol. 101, no. 3, pp. 1059–1073, 2019, doi: 10.1007/s00202-019-00841-6.

[137] M. P. Nthontho, S. P. Chowdhury, S. Winberg and S. Chowdhury, "Communication networks for domestic photovoltaic based microgrid protection," 11th IET International Conference on Developments in Power Systems Protection (DPSP 2012), 2012, pp. 1-6, doi: 10.1049/cp.2012.0007.

[138] L. I. Bin, W. U. Honglin, and G. A. O. Xiaoqi, “Investigation of Protection Schemes for High Penetration Rooftop Pho - tovoltaic System,” *2011 Int. Conf. Adv. Power Syst. Autom. Prot.*, vol. 2, pp. 1299–1303, 2011, doi: 10.1109/APAP.2011.6180579.

[139] S. E. Razavi *et al.*, “Impact of distributed generation on protection and voltage regulation of distribution systems: A review,” *Renew. Sustain. Energy Rev.*, vol. 105, pp. 157–167, 2019, doi: 10.1016/j.rser.2019.01.050.

[140] P.O.12.2: Technical requirements of wind power and photovoltaic facilities (draft), Red Electra, Madrid, Spain (2008)

[141] SRZ001: Particular technical specifications of HV / MV substations. Endesa, Spain (2018).

[142] MT. 2.00.03, “Particular regulations for customer facilities in HV,” Iberdrola, Spain, 2014.

[143] NTP-GEN, “Technical and safety conditions of the FECSA ENDESA distribution facilities,” pp. 14510–14512, 2007.

[144] L. R. Rodríguez, J. A. Torres Santana, J. M. García Muñoz, J. Sánchez Paz “Problems in the protection against single phase faults in medium voltage networks with neutral on grounded through reactance.”, 2012, http://hdl.handle.net/11531/5009.

[145] IT.0116.ES.RE.PTP, “Underground power cables type project up to 20kV.”, UNION FENOSA, 2011.

[146] Y. C. Kuo, T. J. Liang, and J. F. Chen, “Novel maximum-power-point-tracking controller for photovoltaic energy conversion system,” *IEEE Trans. Ind. Electron.*, vol. 48, no. 3, pp. 594–601, 2001, doi: 10.1109/41.925586.

[147] F. Blaabjerg, Z. Chen, and S. B. Kjaer, “Power electronics as efficient interface in dispersed power generation systems,” *IEEE Trans. Power Electron.*, vol. 19, no. 5, pp. 1184–1194, 2004, doi: 10.1109/TPEL.2004.833453.

[148] M. F. Schonardie, R. F. Coelho, R. Schweitzer, and D. C. Martins, “Control of the active and reactive power using dq0 transformation in a three-phase grid-connected PV system,” *IEEE Int. Symp. Ind. Electron.*, pp. 264–269, 2012, doi: 10.1109/ISIE.2012.6237095.

[149] M. Bakkar, M. Abd El-Geliel and M. A. Zied, "Control of photovoltaic grid connected using different control strategies," 22nd Mediterranean Conference on Control and Automation, 2014, pp. 710-715, doi: 10.1109/MED.2014.6961457.

[150] M. Bakkar, M. Abdel-Geliel, and M. Abozied, “Photovoltaic maximum power point grid connected based on power conditioning technique employing fuzzy controller,” in *Renewable Energy and Power Quality Journal*, 2015, vol. 1, no. 13, pp. 339–344, doi: 10.24084/repqj13.320.

[151] Z. Yu, X. Hu, Z. Yao, L. Chen, M. Zhang and S. Jiang, "Analysis and design of a transformerless boost inverter for stand-alone photovoltaic generation systems," in CPSS Transactions on Power Electronics and Applications, vol. 4, no. 4, pp. 310-319, Dec. 2019, doi: 10.24295/CPSSTPEA.2019.00029.

[152] M. Baran and I. El-Markabi, "Adaptive over current protection for distribution feeders with distributed generators," *IEEE PES Power Systems Conference and Exposition*, 2004, pp. 715-719 vol.2, doi: 10.1109/PSCE.2004.1397672.

[153] Bollen, M.: ‘Understanding power quality problems voltage sags and interruptions’, 1st Edn., Wiley-IEEE Press., New York, 2000.

[154] S. Babaei, S. Member, and B. Fardanesh, “High-Power VSC-Based Simultaneous Positive- and Negative-Sequence Voltage Regulator,” *IEEE Trans. Power Deliv.*, vol. 29, no. 5, pp. 2124–2135, 2014, doi: 10.1109/TPWRD.2014.2325773.

[155] J. L. Sosa, M. Castilla, and J. Miret, “Control Strategy to Maximize the Power Capability of PV Three-Phase Inverters During Voltage Sags,” *IEEE Trans. Power Electron.*, vol. 31, no. 4, pp. 3314–3323, 2016, doi: 10.1109/TPEL.2015.2451674.

[156] J. Roldán-pérez, A. García-cerrada, J. L. Zamora-macho, and M. Ochoa-giménez, “Helping all generations of photo-voltaic inverters ride-through voltage sags,” *IET Power Electronics*, vol. 7, no. 10, pp. 2555–2563, 2014, doi: 10.1049/iet-pel.2013.0552.

[157] P.O.12.2: Technical requirements of wind power and photovoltaic facilities (draft), Red Electra, Madrid, Spain (2008).

[158] DL M 34272, “Ministry of industry, tourism and trade,” Madrid, 2006.

[159] I. Y.-H. G. Math H. J. Bollen, *Signal Processing of Power Quality Disturbances.*, 1st ed., Wiley-IEEE Press, 2006.

[160] L. Guasch, F. Corcoles and J. Pedra, "Effects of unsymmetrical voltage sag types E, F and G on induction motors," *Ninth International Conference on Harmonics and Quality of Power. Proceedings* (Cat. No.00EX441), 2000, pp. 796-803 vol.3, doi: 10.1109/ICHQP.2000.896831.

[161] M. Bakkar, et al.: "Voltage sag influence on controlled three-phase gridconnected inverters according to the Spanish grid code". *IET Gener. Transm. Distrib.* vol. 14, no.10, pp.1882–1892 2020.

[162] A. Rolán, P. Giménez, S. J. Yagüe, S. Bogarra, J. Saura, and M. Bakkar, “Voltage recovery influence on three-phase grid-connected inverters under voltage sags,” *IET Gener. Transm. Distrib.*, vol. 13, no. 3, 2019, doi: 10.1049/iet-gtd.2018.5607.

[163] M. Akagi, H.;Watanabe, E-H.; Aredes, *Instantaneous power theory and applications to power conditioning*, 2nd ed. IEEE Press., Hoboken, 2007.

[164] SRZ001: Particular technical specifications of HV / MV substations. Endesa, Spain (2018).

[165] DOUE-L-2016-80721, “Reglamento (UE) 2016/631 de la Comisión de 14 de abril de 2016 que establece un código de red sobre requisitos de conexión de generadores a la red,” *Department Of Unión Europea.*, no. 112, 2016.

[166] A. Rolán, S. Bogarra and M. Bakkar, "Integration of Distributed Energy Resources to Unbalanced Grids under Voltage Sags with Grid Code Compliance," in IEEE Transactions on Smart Grid, doi: 10.1109/TSG.2021.3107984..

[167] M. Bakkar, S., Bogarra, F., Córcoles, et al.: ‘Power control strategies during voltage sags according to spanish grid code’. Int. Conf. on Renewable Energies and Power Quality, Spain, 2018, pp. 493–498.

[168] A. Q. Al-Shetwi, M. A. Hannan, K. P. Jern, A. A. Alkahtani, and A. E. P. G. Abas, “Power quality assessment of grid-connected PV system in compliance with the recent integration requirements,” *Electron.*, vol. 9, no. 2, pp. 1–22, 2020, doi: 10.3390/electronics9020366.

[169] M. Garnica, L. G. De Vicuña, J. Miret, A. Camacho, and R. Guzmán, “Voltage support experimental analysis of a low-voltage ride-through strategy applied to grid-connected distributed inverters,” *Energies*, vol. 11, no. 8, pp. 1–20, 2018, doi: 10.3390/en11081949.

[170] M. Kezunovic, J. Ren, S. Lotfifard, *Design, Modeling and Evaluation of Protective Relays for Power Systems*, 1st ed., Springer, London, 2016.

[171] M. Kayri, “Predictive abilities of Bayesian regularization and levenberg-marquardt algorithms in artificial neural networks: A comparative empirical study on social data,” *Math. Comput. Appl.*, vol. 21, no. 2, 2016, doi: 10.3390/mca21020020.

[172] J. Heaton,: *Introduction to Neural Networks with Java*, 2nd ed. Heaton Research Inc., Washington 2008.

[173] K. Z. Mao and G. Bin Huang, “Neuron selection for RBF neural network classifier based on data structure preserving criterion,” *IEEE Trans. Neural Networks*, vol. 16, no. 6, pp. 1531–1540, 2005, doi: 10.1109/TNN.2005.853575.

[174] A. Silos, A. Señís, R.M. De Pozuelo, A. Zaballos, "Using IEC 61850 GOOSE Service for Adaptive ANSI 67/67N Protection in Ring Main Systems with Distributed Energy Resources." *Energies*, vol. 10, no. 11, pp.1685, 2017. https://doi.org/10.3390/en10111685.

[175] J. Momoh, *Smart Grid: Fundamentals of Design and Analysis*, 1st ed. New Jersey: JOHN WILEY & SONS, 2012.

[176] Q. Yang, J. Li, S. Le Blond, and C. Wang, “Artificial Neural Network Based Fault Detection and Fault Location in the DC Microgrid,” *Energy Procedia*, vol. 103, pp. 129–134, 2016, doi: 10.1016/j.egypro.2016.11.261.

[177] M. F. Guo, N. C. Yang, and W. F. Chen, “Deep-Learning-Based Fault Classification Using Hilbert-Huang Transform and Convolutional Neural Network in Power Distribution Systems,” *IEEE Sens. J.*, vol. 19, no. 16, pp. 6905–6913, 2019, doi: 10.1109/JSEN.2019.2913006.

[178] H. R. S. Bernardes and C. R. Minussi, “Fault Classification in Power Distribution Systems using Multiresolution Analysis and a Fuzzy - ARTMAP Neural Network,” vol. 19, no. 11, pp. 1824–1831, 2021.

[179] S. Barakat, M. B. Eteiba, and W. I. Wahba, “Fault location in underground cables using ANFIS nets and discrete wavelet transform,” *J. Electr. Syst. Inf. Technol.*, vol. 1, no. 3, pp. 198–211, 2014, doi: 10.1016/j.jesit.2014.12.003.

[180] A. C. Adewole, R. Tzoneva, and S. Behardien, “Distribution network fault section identification and fault location using wavelet entropy and neural networks,” *Appl. Soft Comput. J.*, vol. 46, pp. 296–306, 2016, doi: 10.1016/j.asoc.2016.05.013.

[181] J. Liang, T. Jing, H. Niu, and J. Wang, “Two-Terminal Fault Location Method of Distribution

Network Based on Adaptive Convolution Neural Network," *IEEE Access*, vol. 8, pp. 54035–54043, 2020, doi: 10.1109/ACCESS.2020.2980573.

[182] M. Dehghani, M. H. Khooban, and T. Niknam, "Fast fault detection and classification based on a combination of wavelet singular entropy theory and fuzzy logic in distribution lines in the presence of distributed generations," *Int. J. Electr. Power Energy Syst.*, vol. 78, pp. 455–462, 2016, doi: 10.1016/j.ijepes.2015.11.048.

[183] I. M. Karmacharya and R. Gokaraju, "Fault Location in Ungrounded Photovoltaic System Using Wavelets and ANN," *IEEE Trans. Power Deliv.*, vol. 33, no. 2, pp. 549–559, 2018, doi: 10.1109/TPWRD.2017.2721903.

[184] G. Benmouyal *et al.*, "IEEE standard inverse-time characteristic equations for overcurrent relays," *IEEE Trans. Power Deliv.*, vol. 14, no. 3, pp. 868–871, 1999, doi: 10.1109/61.772326.

[185] VIP400-VIP410, "Electrical Network Protection Reference Manual", Schneider-electric, 2013.

[186] H12WD, "Solid State Relay," *Crydom*, 2013, [Online]. Available: www.crydom.com.

[187] P. Schavemaker and L. Van der Sluis, "The arc model blockset," *P Second IASTED International Conference POWER AND ENERGY SYSTEMS (EuroPES)*, pp. 644–648, 2002.

[188] I. Pramudya, M. W. Hadi, J. Y. Koo, B. W. Lee, U. A. Khan, and Suwarno, "Modelling of high voltage AC circuit breaker based on circuit breaker's technical data: Using Schwarz black box arc model," *Int. Conf. High Volt. Eng. Power Syst. ICHVEPS 2017 - Proceeding*, pp. 83–86, 2017, doi: 10.1109/ICHVEPS.2017.8225917.

[189] M. Kezunovic, J. Ren, S. Lotfifard, *Design, Modeling and Evaluation of Protective Relays for Power Systems*, 1st ed., Springer, London, 2016.

[190] T. Ohtaka, V. Kertesz, and R. P. P. Smeets, "Novel Black-Box Arc Model Validated by High-Voltage Circuit Breaker Testing," *IEEE Trans. Power Deliv.*, vol. 33, no. 4, pp. 1835–1844, 2018, doi: 10.1109/TPWRD.2017.2764108.

[191] S. W. Lim, U. A. Khan, J. G. Lee, B. W. Lee, K. S. Kim, and C. W. Gu, "Simulation analysis of DC arc in circuit breaker applying with conventional black box arc model," *2015 3rd Int. Conf. Electr. Power Equip. - Switch. Technol. ICEPE-ST 2015*, pp. 332–336, 2015, doi: 10.1109/ICEPE-ST.2015.7368330.

[192] J. Magnusson, "On the design of hybrid DC-breakers consisting of a mechanical switch and semiconductor devices.", doctoral thesis, KTH Royal Institute of Technology, Stockholm, 2015.

[193] Y. Pei, "Computer Simulation of Fundamental Processes in High Voltage Circuit Breakers Based on an Automated Modelling Platform," doctoral thesis, University of Liverpool, Liverpool, 2014.

[194] K. Malmedal and P. K. Sen, "Arcing fault current and the criteria for setting ground fault relays in solidly-grounded low voltage systems," *2000 IEEE Industrial and Commercial Power Systems Technical Conference. Conference Record (Cat. No.00CH37053)*, 2000, pp. 185-191, doi: 10.1109/ICPS.2000.854370.

[195] J. A. Kay, J. Arvola and L. Kumpulainen, "Protecting at the speed of light: Combining arc flash sensing and arc-resistant technologies," *Conference Record of 2010 Annual Pulp & Paper Industry Technical Conference*, 2010, pp. 1-7, doi: 10.1109/PAPCON.2010.5556507.

[196] D. G. Loucks, "Calculating Incident Energy Released With Varying Ground Fault Magnitudes on Solidly Grounded Systems," in *IEEE Transactions on Industry Applications*, vol. 46, no. 2, pp. 761-769, March-april 2010, doi: 10.1109/TIA.2009.2039843.

[197] M. H. Weik, *Data switching exchanget.*, 1st ed., Springer, Boston, MA, 2017.

[198] C. L. Fortescue, "Method of Symmetrical Co-Ordinates Applied to the Solution of Polyphase Networks," in *Transactions of the American Institute of Electrical Engineers*, vol. XXXVII, no. 2, pp. 1027-1140, July 1918, doi: 10.1109/T-AIEE.1918.4765570.

[199] Y. H. Ku, "Transient Analysis of A-C. Machinery," in *Transactions of the American Institute of Electrical Engineers*, vol. 48, no. 3, pp. 707-714, July 1929, doi: 10.1109/T-AIEE.1929.5055273.

[200] BOE-A-2004-5562, 12 of March Royal Decree 436/2004, "Establishing the methodology for updating and systematizing the legal and economic regime of the activity of electric power production under a special regime.," pp. 13217–13238, 2004.

[201] S. K. Chung, "A phase tracking system for three phase utility interface inverters," *IEEE Trans. Power Electron.*, vol. 15, no. 3, pp. 431–438, 2000, doi: 10.1109/63.844502.

[202] A. Junyent-Ferre, "Control of power electronic converters for the operation of wind generation systems under grid disturbances,", *International Journal of Industrial Electronics and Drives*,

vol. 2, no. 1, pp. 43-61, 2015. DOI:10.1504/IJIED.2015.068769 2011.

[203] T. V. Tran, T. W. Chun, H. H. Lee, H. G. Kim, and E. C. Nho, “PLL-based seamless transfer control between grid-connected and islanding modes in grid-connected inverters,” *IEEE Trans. Power Electron.*, vol. 29, no. 10, pp. 5218–5228, 2014, doi: 10.1109/TPEL.2013.2290059.

[204] D. Zhu, S. Zhou, X. Zou, and Y. Kang, “Improved Design of PLL Controller for LCL-Type Grid-Connected Converter in Weak Grid,” *IEEE Trans. Power Electron.*, vol. 35, no. 5, pp. 4715–4727, 2020, doi: 10.1109/TPEL.2019.2943634.

[205] A. Ali *et al.*, “Review of online and soft computing maximum power point tracking techniques under non-uniform solar irradiation conditions,” *Energies*, vol. 13, no. 12, 2020.

[206] D. Verma, S. Nema, A. M. Shandilya, and S. K. Dash, “Comprehensive analysis of maximum power point tracking techniques in solar photovoltaic systems under uniform insolation and partial shaded condition,” *J. Renew. Sustain. Energy*, vol. 7, no. 4, 2015.

[207] A. Mohapatra, B. Nayak, P. Das, and K. B. Mohanty, “A review on MPPT techniques of PV system under partial shading condition,” *Renew. Sustain. Energy Rev.*, vol. 80, pp. 854–867, 2017.

[208] G. F. T. Kebir, C. Larbes, A. Ilinca, T. Obeidi, and S. T. Kebir, “Study of the intelligent behaviour of a maximum photovoltaic energy tracking fuzzy controller,” *Energies*, vol. 11, no. 12, 2018.

[209] Y. Wang *et al.*, “An advanced maximum power point tracking method for photovoltaic systems by using variable universe fuzzy logic control considering temperature variability,” *Electron.*, vol. 7, no. 12, 2018.

[210] L. Bouselham, M. Hajji, B. Hajji, and H. Bouali, “A New MPPT-based ANN for Photovoltaic System under Partial Shading Conditions,” *Energy Procedia*, vol. 111, pp. 924–933, 2017.

[211] R. S. Pal and V. Mukherjee, “Metaheuristic based comparative MPPT methods for photovoltaic technology under partial shading condition,” *Energy*, vol. 212, p. 118592, 2020.

[212] Z. Zhao *et al.*, “A dynamic particles MPPT method for photovoltaic systems under partial shading conditions,” *Energy Convers. Manag.*, vol. 220, p. 113070, 2020.

[213] M. Mansoor, A. F. Mirza, and Q. Ling, “Harris hawk optimization-based MPPT control for PV systems under partial shading conditions,” *J. Clean. Prod.*, vol. 274, p. 122857, 2020.

[214] M. Seyedmahmoudian *et al.*, “Maximum power point tracking for photovoltaic systems under partial shading conditions using bat algorithm,” *Sustain.*, vol. 10, no. 5, pp. 1–16, 2018.

[215] J. Gosumbonggot and G. Fujita, “Partial shading detection and global maximum power point tracking algorithm for photovoltaic with the variation of irradiation and temperature,” *Energies*, vol. 12, no. 2, 2019.

[216] Y. Zou, F. Yan, X. Wang, and J. Zhang, “An efficient fuzzy logic control algorithm for photovoltaic maximum power point tracking under partial shading condition,” *J. Franklin Inst.*, vol. 357, no. 6, pp. 3135–3149, 2020.

[217] P. Verma, R. Garg, and P. Mahajan, “Asymmetrical interval type-2 fuzzy logic control based MPPT tuning for PV system under partial shading condition,” *ISA Trans.*, vol. 100, pp. 251–263, 2020.

[218] H. Hassan, M. A. Geliel, and M. Abu-Zeid, “A proposed fuzzy controller for MPPT of a photovoltaic system,” *2014 IEEE Conf. Energy Conversion, CENCON 2014*, pp. 164–169, 2014.

[219] W. Li, G. Zhang, T. Pan, Z. Zhang, Y. Geng, and J. Wang, “A Lipschitz Optimization-Based MPPT Algorithm for Photovoltaic System under Partial Shading Condition,” *IEEE Access*, vol. 7, pp. 126323–126333, 2019, doi: 10.1109/ACCESS.2019.2939095.

[220] M. A. Abdel-Geliel, “Fault Diagnosis and Performance Recovery Based on the Dynamic Safety Margin,” Doctoral thesis, Inauguraldissertation zur Erlangung des akademischen Grades eines Doktors der Naturwissenschaften der Universität Mannheim, 2006.

[221] M. Abdel-Geliel, E. Badredden, and A. Gambier, “Application of Dynamic Safety Margin in robust fault detection and fault tolerant control,” *Proc. IEEE Int. Conf. Control Appl.* , pp. 337–342, 2006, doi: 10.1109/CCA.2006.285915.

[222] M. Bakkar, A. Aboelhassan, M. Abdelgeliel, and M. Galea, “PV systems control using fuzzy logic controller employing dynamic safety margin under normal and partial shading conditions,” *Energies*, vol. 14, no. 4, 2021, doi: 10.3390/en14040841.

[223] N. Patcharaprakiti, S. Premrudeepreechacharn, and Y. Sriuthaisiriwong, “Maximum power point

tracking using adaptive fuzzy logic control for grid-connected photovoltaic system," *Renew. Energy*, vol. 30, no. 11, pp. 1771–1788, 2005, doi: 10.1016/j.renene.2004.11.018.
[224] C. Pesce, J. Riedemann, R. Pena, W. Jara, C. Maury, and R. Villalobos, "A modified step-up DC-DC flyback converter with active snubber for improved efficiency," *Energies*, vol. 12, no. 11, 2019, doi: 10.3390/en12112066.
[225] NE-80EJEA, "Off grid 80 watt module from the world's trusted source for solar", Sharp, 2008.
[226] ETD 44, "Flyback transformers 120 to 160 W," Myrra, 2008.
[227] LV 25-P, "Voltage transducer LV 25-P," *LEM*, 2014, [Online]. Available: www.lem.com.
[228] LA 100-NP, "Current Transducer LA 100-NP", *LEM*, 2014, [Online]. Available: www.lem.com..